Transactions of the ASME, Journal of Applied Mechanics (ISSN 0021-8936) is published bimonthly (Jan., Mar., May, July, Sept., Nov.) The American Society of Mechanical Engineers, Three Park Avenue, New York, NY 10016. Periodicals postage paid at New York, NY and additional mailing office. POSTMASTER: Send address changes to Transactions of the ASME, Journal of Applied Mechanics, c/o THE AMERICAN SOCIETY OF MECHANICAL ENGINEERS, 22 Law Drive, Box 2300, Fairfield, NJ 07007-2300. **CHANGES OF ADDRESS** must be received at Society headquarters seven weeks before they are to be effective. Please send old label and new address. **STATEMENT from By-Laws.** The Society shall not be responsible for statements or opinions advanced in papers or . . . printed in its publications (B7.1, Para. 3).

Journal of Applied Mechanics

Published Bimonthly by The American Society of Mechanical Engineers

VOLUME 70 • NUMBER 2 • MARCH 2003

TECHNICAL PAPERS

(**Contents continued on inside back cover**)

This journal is printed on acid-free paper, which exceeds the ANSI Z39.48-1992 specification for permanence of paper and library materials. ♾™
♻ 85% recycled content, including 10% post-consumer fibers.

Journal of Applied Mechanics **Volume 70, Number 2** **MARCH 2003**

BRIEF NOTES

ANNOUNCEMENTS AND SPECIAL NOTES

The ASME Journal of Applied Mechanics is abstracted and indexed in the following:

Alloys Index, Aluminum Industry Abstracts, Applied Science & Technology Index, AMR Abstracts Database, Ceramic Abstracts, Chemical Abstracts, Civil Engineering Abstracts, Compendex (The electronic equivalent of Engineering Index), Computer & Information Systems Abstracts, Corrosion Abstracts, Current Contents, EEA (Earthquake Engineering Abstracts Database), Electronics & Communications Abstracts Journal, Engineered Materials Abstracts, Engineering Index, Environmental Engineering Abstracts, Environmental Science and Pollution Management, Fluidex, Fuel & Energy Abstracts, GeoRef, Geotechnical Abstracts, INSPEC, International Aerospace Abstracts, Journal of Ferrocement, Materials Science Citation Index, Mechanical Engineering Abstracts, METADEX (The electronic equivalent of Metals Abstracts and Alloys Index), Metals Abstracts, Nonferrous Metals Alert, Polymers Ceramics Composites Alert, Referativnyi Zhurnal, Science Citation Index, SciSearch (Electronic equivalent of Science Citation Index), Shock and Vibration Digest, Solid State and Superconductivity Abstracts, Steels Alert, Zentralblatt MATH

Elastic Fields of Quantum Dots in Multilayered Semiconductors: A Novel Green's Function Approach

B. Yang[1]
Structures Technology, Inc.,
543 Keisler Drive, Suite 204,
Cary, NC 27511
e-mail: boyang@boulder.nist.gov
Mem. ASME

E. Pan
Department of Civil Engineering,
University of Akron,
Akron, OH 44325
Mem. ASME

We present an efficient and accurate continuum-mechanics approach to predict the elastic fields in multilayered semiconductors due to buried quantum dots (QDs). Our approach is based on a novel Green's function solution in anisotropic and linearly elastic multilayers, derived within the framework of generalized Stroh formalism and Fourier transforms, in conjunction with the Betti's reciprocal theorem. By using this approach, the induced elastic fields due to QDs with general misfit strains are expressed as a volume integral over the QDs domains. For QDs with uniform misfit strains, the volume integral involved is reduced to a surface integral over the QDs boundaries. Further, for QDs that can be modeled as point sources, the induced elastic fields are then derived as a sum of the point-force Green's functions. In the last case, the solution of the QD-induced elastic field is analytical, involving no numerical integration, except for the evaluation of the Green's functions. As numerical examples, we have studied a multilayered semiconductor system of QDs made of alternating GaAs-spacer and InAs-wetting layers on a GaAs substrate, plus a freshly deposited InAs-wetting layer on the top. The effects of vertical and horizontal arrays of QDs and of thickness of the top wetting layer on the QD-induced elastic fields are examined and some new features are observed that may be of interest to the designers of semiconductor QD superlattices. [DOI: 10.1115/1.1544540]

1 Introduction

Owing to their great advantages over those processed by lithography and etching, self-assembled quantum semiconductor heterostructures have attracted tremendous attention in recent years. The processing of the heterostructures is based on the spontaneous growth of small islands from a wetting layer due to its mismatch strain to the substrate, i.e., a Stranski-Krastanow growth mechanism. The islands include quasi-zero-dimensional dots (or quantum dots (QDs)) and quasi-one-dimensional wires, on the scale of 1–100 nanometers. Experimental studies have shown that such QD nanostructures possess certain special electronic and optical features, rendering fascinating and novel devices, such as the low-threshold laser, resonant tunneling device, and huge-capacity memory media, possible, [1,2]. These features are in part related to the strain fields induced by the QDs and thus it is important to understand the latter before the design of devices, [1–3]. In their device applications, it is often desirable to fabricate the QDs in successive stacks with both vertical and lateral orderings, [4–8]. The final product is then a multilayered structure with buried arrays of QDs and with each layer being anisotropic. Therefore, an efficient and accurate numerical tool for predicting the mechanical fields, based on the theory of generally anisotropic elasticity for layered media, would be much appreciated.

To quantitatively explain and numerically model the QD nanostructures, various numerical methods have been proposed, including the continuum finite element (FE) and finite difference (FD) methods, [9–14], and the discrete atomic-level simulations, [15–17]. However, the domain-based FE and FD methods and the atomic models are computationally expensive, making them difficult to perform parametric studies in order to interpret the experimental phenomena or to reach an economic design strategy. This difficulty is manifested especially in the case of multilayered heterostructures. Recently, various analytical and semi-analytical methods, in particular, those related to the Green's function solutions, have been proposed and applied to the QD modeling, [18,19]. Because of their robust features in terms of accuracy and efficiency, these analytical methods, particularly the Green's function method, have been found to be very useful in the study of QD structures, [18–24]. For QDs in a three-dimensional isotropic infinite space, Pearson and Faux [23] derived the exact-closed-form solution for the QD-induced strain when the QDs are in the form of pyramids. When the infinite domain is anisotropic, Faux and Pearson [19] and Andreev et al. [22] derived the induced strain using, respectively, the Fourier transform method and the series expansion method. More recently, Pan and Yang [24] examined the elastic field due to a buried QD in an anisotropic half-space substrate using the point-force Green's function, which is derived within the framework of generalized Stroh formalism and Fourier transforms, in conjunction with the Betti's reciprocal theorem. Their result has shown clearly the effects of material anisotropy and free surface on the elastic fields.

In this paper, we propose a novel Green's function approach for the elastic analyses of buried QDs in multilayered semiconductors, advanced from the authors' previous works, [24,25]. The QDs and surrounding matrix are assumed to have the same material property, within the classical inclusion approach of eigenstrain, [26]. In this approach, the elastic fields induced by QDs with general misfit strains (i.e., eigenstrains) are expressed as a volume integral over the QDs domains. For QDs with a uniform misfit strain, the volume integral can be reduced to a surface integral over the QDs boundaries. Further, for QDs that can be modeled as point sources, the induced elastic fields can then be derived as a sum of the point-force Green's functions. In the last case, the QD solution is analytical, except for the numerical evaluation of the point-force Green's functions. The proposed approach then is applied to examine a multilayered system of QDs with alternating GaAs-spacer and InAs-wetting layers on a GaAs sub-

[1]To whom correspondence should be addressed. Present address: Materials Reliability Division, National Institute of Standards and Technology, Boulder, CO 80305.

Contributed by the Applied Mechanics Division of THE AMERICAN SOCIETY OF MECHANICAL ENGINEERS for publication in the ASME JOURNAL OF APPLIED MECHANICS. Manuscript received by the Applied Mechanics Division, Dec. 16, 2001; final revision, June 8, 2002. Associate Editor: H. Gao. Discussion on the paper should be addressed to the Editor, Prof. Robert M. McMeeking, Chair, Department of Mechanics and Environmental Engineering, University of California–Santa Barbara, Santa Barbara, CA 93106-5070, and will be accepted until four months after final publication in the paper itself in the ASME JOURNAL OF APPLIED MECHANICS.

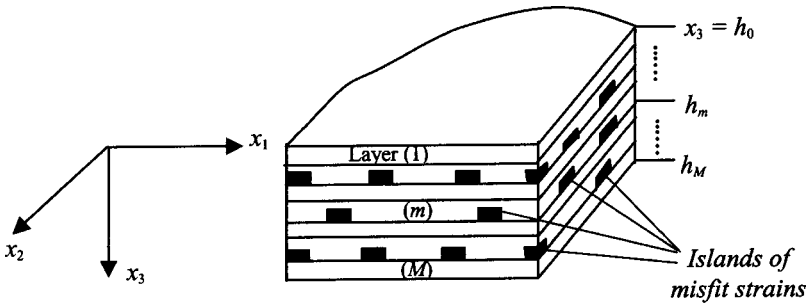

Fig. 1 A multilayered heterostructure with embedded islands of misfit strains

strate, plus a ''freshly'' deposited wetting layer on the top. The theory is described in Section 2. The numerical results are presented and discussed in Section 3. Conclusions are drawn in Section 4.

2 Theory

2.1 Integral Equation Formulation of Quantum Dots. Inclusion problem of misfit strains, [26], in a heterogeneous, anisotropic, linearly elastic matrix can be described in terms of an integral-equation formulation with the integral kernel being the point-force Green's function in the same media. This integral-equation formulation is a consequence of the Betti's reciprocal theorem. Let us assume that there are two states associated with the matrix domain D: one for the misfit-strain problem due to a given misfit strain $\varepsilon^0_{ij}(\mathbf{x})$, and the other for the Green's function problem due to a point force at $\mathbf{y}$. In these two problems, the boundary conditions along ∂D (boundary of D) are identical. Applying the Betti's reciprocal theorem, we find that the displacement $u_p(\mathbf{y})$ due to the misfit strain $\varepsilon^0_{ij}(\mathbf{x})$ can be expressed in terms of the following integral-equation formulation, as, [26],

$$u_p(\mathbf{y}) = \int_D u^*_{pi}(\mathbf{x};\mathbf{y})[-C_{ijlm}(\mathbf{x})\varepsilon^0_{lm}(\mathbf{x})]_{,j} dV(\mathbf{x}), \tag{1}$$

where $u^*_{pi}(\mathbf{x};\mathbf{y})$ is the Green's ith displacement component at $\mathbf{x}$ due to a point force in the pth direction applied at $\mathbf{y}$, C_{ijlm} is the elastic stiffness, heterogeneous in general, and a repeated index implies the conventional summation over its range. Note that $_{,j}$ indicates the partial derivative with respect to field coordinate x_j while $_{,y_p}$ is used for the partial derivative with respect to source coordinate y_p. Making use of the Gauss theorem, Eq. (1) can be rewritten as

$$u_p(\mathbf{y}) = \int_D u^*_{pi,j}(\mathbf{x};\mathbf{y}) C_{ijlm}(\mathbf{x})\varepsilon^0_{lm}(\mathbf{x}) dV(\mathbf{x}) - \int_{\partial D} u^*_{pi}(\mathbf{x};\mathbf{y}) C_{ijlm}(\mathbf{x})\varepsilon^0_{lm}(\mathbf{x}) n_j(\mathbf{x}) d\Gamma(\mathbf{x}), \tag{2}$$

where n_j is the outward normal at a boundary point.

We now consider a special heterogeneous matrix structure and a special misfit strain distribution, as shown in Fig. 1. The special heterogeneous matrix structure consists of multiple planar layers of different media. They are homogeneous, anisotropic, and linearly elastic. The special misfit-strain field is nonzero only in a number of interior islands $\Omega^{(n)}(n=1,\ldots,N)$. To apply the above theory, we assume that the islands have the same elastic property as their surrounding layer media. This special system represents a multilayered semiconductor with coherently strained QDs, [1]. We remark that there should exist nonzero eigenstrain field in some of the layers (i.e., wetting layers from which the QDs grow), similar to that in the QDs. In this case, the elastic field to be derived under the above assumption of nonzero eigenstrain only in the QDs is in fact the part of a total field induced by the QDs. The total field can be obtained by applying the rule of superposition of the induced field to the homogeneous field that is caused by the nonzero matrix eigenstrain alone (i.e., in the absence of the QDs) under the same boundary and interfacial conditions. For the present multilayered structure, the homogeneous elastic field can be solved by applying the classical laminate theory, [27].

Under these assumptions, Eq. (2) can be simplified. First, by using the fact that the misfit strain along the domain boundary ∂D is zero, the term of boundary integral in Eq. (2) is eliminated, which yields

$$u_p(\mathbf{y}) = \int_D u^*_{pi,j}(\mathbf{x};\mathbf{y}) C_{ijlm}(\mathbf{x})\varepsilon^0_{lm}(\mathbf{x}) dV(\mathbf{x}). \tag{3}$$

Then, reducing the integral domain from D to $\Omega^{(n)}(n=1,\ldots,N)$, Eq. (3) is rewritten as

$$u_p(\mathbf{y}) = \sum_{n=1}^{N} \int_{\Omega^{(n)}} u^*_{pi,j}(\mathbf{x};\mathbf{y}) C_{ijlm}(\mathbf{x})\varepsilon^0_{lm}(\mathbf{x}) dV(\mathbf{x}). \tag{4}$$

Further, the domain integrals in Eq. (4) can be reduced to the surface of $\Omega^{(n)}$ for those QDs in which the misfit strain distribution is uniform. Assuming that all of the islands have a uniform misfit strain field, we arrive at

$$u_p(\mathbf{y}) = \sum_{n=1}^{N} C^{(n)}_{ijlm}\varepsilon^{0(n)}_{lm} \int_{\partial\Omega^{(n)}} u^*_{pi}(\mathbf{x};\mathbf{y}) n_j(\mathbf{x}) dS(\mathbf{x}), \tag{5}$$

where $C^{(n)}_{ijlm}$ and $\varepsilon^{0(n)}_{lm}$ are, respectively, the (uniform) elastic stiffness and misfit strain in the nth island. Note that a uniform distribution of misfit strain in a QD may occur when the QD and matrix (generally mismatched in thermal expansion coefficients) are subjected to a uniform temperature change and if their mismatch of elastic constants can be neglected.

In order to find the induced elastic strain field, the displacement in Eq. (5) is differentiated with respect to the observation point $\mathbf{y}$ (i.e., the source point where the point force is located in the corresponding Green's function problem), which yields

$$\varepsilon^*_{pq}(\mathbf{y}) = \sum_{n=1}^{N} \frac{1}{2} C^{(n)}_{ijlm}\varepsilon^{0(n)}_{lm} \int_{\partial\Omega^{(n)}} [u^*_{pi,y_q}(\mathbf{x};\mathbf{y}) + u^*_{qi,y_p}(\mathbf{x};\mathbf{y})] n_j(\mathbf{x}) dS(\mathbf{x}). \tag{6}$$

Subsequently, the stress field is obtained as

$$\sigma_{pq}(\mathbf{y}) = C_{pqst}(\mathbf{y})[\varepsilon_{st}(\mathbf{y}) - \varepsilon^0_{st}(\mathbf{y})]. \tag{7}$$

Note that $\varepsilon^0_{st}(\mathbf{y})$ in Eq. (7) is nonzero only if $\mathbf{y}$ is within a QD.

Finally, the above expressions can be further reduced if the observation point $\mathbf{y}$ is remote to some or all of the QDs compared to their individual sizes. These remote QDs can be modeled as

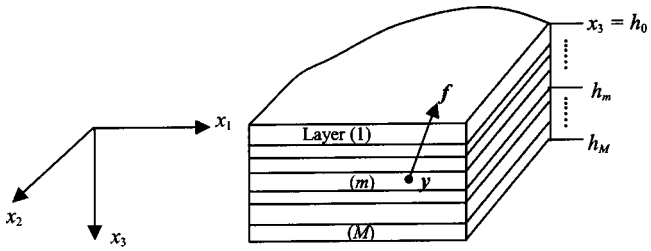

Fig. 2 Point-force Green's function problem of a multilayered heterostructure (Fig. 1)

point sources of misfit strain. Without the loss of generality, assuming the remoteness of **y** to all QDs, the misfit strain field is then expressed as

$$\varepsilon^0_{lm}(\mathbf{x}) = \sum_{n=1}^{N} \varepsilon^{0(n)}_{lm} V^{(n)} \delta(\mathbf{x} - \mathbf{x}^{(n)}), \tag{8}$$

where $V^{(n)}$ and $\mathbf{x}^{(n)}$ are, respectively, the volume and location of the nth QD, and $\delta(\mathbf{x})$ is the Dirac delta function. By substituting Eq. (8) in Eq. (3), the induced displacement and strain at **y** due to the point sources of misfit strain are analytically found to be

$$u_p(\mathbf{y}) = \sum_{n=1}^{N} u^*_{pi,j}(\mathbf{x}^{(n)};\mathbf{y}) C^{(n)}_{ijlm} \varepsilon^{0(n)}_{lm} V^{(n)}$$

$$= \sum_{n=1}^{N} \sigma^*_{plm}(\mathbf{x}^{(n)};\mathbf{y}) \varepsilon^{0(n)}_{lm} V^{(n)}, \tag{9}$$

$$\varepsilon_{pq}(\mathbf{y}) = \sum_{n=1}^{N} \frac{1}{2} [\sigma^*_{plm,y_q}(\mathbf{x}^{(n)};\mathbf{y}) + \sigma^*_{qlm,y_p}(\mathbf{x}^{(n)};\mathbf{y})] \varepsilon^{0(n)}_{lm} V^{(n)}. \tag{10}$$

In the derivation of the right-hand side of Eq. (9), the Hooke's law, $\sigma_{lm} = C_{ijlm} u_{i,j}$, was effected. It is observed in Eq. (9) that the displacement field in the pth direction at **y** due to point sources of misfit strain with components (lm) at $\mathbf{x}^{(n)}$ $(n = 1, \ldots, N)$ is equivalent to the stress field with components (lm) at $\mathbf{x}^{(n)}$ due to a point force in the pth direction at **y**, [28].

We remark that Eqs. (4), (5), and (9) (and their corresponding expressions for strain and stress) can be used whenever and wherever applicable to most efficiently compute the elastic fields due to a QD. The idea of applying the point-source approach to describe the elastic field remote to a QD, the inclusion approach to describe the field in an intermediate distance to a QD, and the imhomogeneity approach to describe the field close to or inside a QD, has been elaborated recently by Romanov et al. [29]. The different approaches require different computational tools to efficiently and accurately solve the problem. The present work proposes to apply a special Green's function for anisotropic multilayers to solve the problem of QDs approached as inclusions. It enables a simulation of a relatively large system of QDs in multilayered semiconductors. This special Green's function is described next.

2.2 Green's Function for Anisotropic Multilayers. Three-dimensional point-force Green's function in anisotropic multilayers, as shown in Fig. 2, can be solved within the framework of generalized Stroh formalism and Fourier transforms, [25,30]. The elegancy of the formulation has been demonstrated by applying the derived Green's functions to the boundary element analyses of stress around a hole in a composite laminate, [31], and the corresponding delamination crack problem, [32]. In the following, we summarize the Green's functions for anisotropic elastostatic multilayers. For details of the theory, one may refer to the authors' previous work, [25], and articles cited therein.

The equilibrium of a multilayered system subjected to a point force requires that

$$C_{pjlm}(\mathbf{x}) u_{l,mj}(\mathbf{x}) = -f_p \delta(\mathbf{x} - \mathbf{y}), \tag{11}$$

where f_p is the pth component of a point force applied at **y**. To solve this problem, the following two-dimensional Fourier transform (k_1, k_2) is first applied to the in-plane variables (x_1, x_2) of $u_i(x_1, x_2, x_3)$,

$$\tilde{u}_i(k_1, k_2, x_3) = \int \int u_i(x_1, x_2, x_3) e^{i x_\alpha k_\alpha} dx_1 dx_2, \tag{12}$$

where e stands for the *exponential* function, and i in the exponent denotes the unit of imaginary number, $\sqrt{-1}$, and the Greek index takes a value in the range from 1 to 2. The integral limits are $(-\infty, \infty)$ along both the coordinates x_1 and x_2. Thus, in the Fourier transformed domain, the governing Eq. (11) becomes

$$C_{p3i3}\tilde{u}_{i,33} - i(C_{p\alpha i3} + C_{p3i\alpha}) k_\alpha \tilde{u}_{i,3} - C_{p\alpha i\beta} k_\alpha k_\beta \tilde{u}_i = -f_p e^{i y_\alpha k_\alpha} \delta(x_3 - y_3), \tag{13}$$

which is valid for each individual homogeneous layer in the system.

Solving this ordinary differential equation in terms of x_3 with **f** being a unit force in the pth direction yields the general expression for the transformed-domain Green's displacement in the ith direction, $\tilde{u}^*_{ip}$, as

$$\tilde{\mathbf{u}}^*_m(x_3) = e^{i k_\alpha y_\alpha} [\tilde{\mathbf{u}}^{*(s)}_m(x_3) + i\eta^{-1} (\overline{\mathbf{A}}_m \langle e^{-i\overline{\mathbf{p}}_m \eta (x_3 - h_{m-1})} \rangle \mathbf{V}_m + \mathbf{A}_m \langle e^{-i\mathbf{p}_m \eta (x_3 - h_m)} \rangle \mathbf{W}_m)], \tag{14}$$

where the subscript m indicates the association of a quantity to the mth layer where the field point **x** resides; $\tilde{\mathbf{u}}^*_m$ is a function of k_1, k_2 and **y** as well as x_3; $\tilde{\mathbf{u}}^{*(s)}_m$, a special solution, is a given function of k_1, k_2 and **y** as well as x_3; and $\mathbf{V}_m$ and $\mathbf{W}_m$ are a pair of unknown tensors, being functions of k_1, k_2 and y_3, to be determined by imposing boundary and interfacial conditions. The dummy arguments in these functions, which are not relevant directly to the enforcement of boundary and interfacial conditions, are omitted for simplicity. In addition, the overbar denotes the complex conjugate, (η, θ) are the polar coordinates related to (k_1, k_2) by $k_1 = \eta \cos\theta$ and $k_2 = \eta \sin\theta$, and

$$\langle e^{-i\mathbf{p}\eta x_3} \rangle \equiv \mathrm{diag}[e^{-ip_1 \eta x_3}, e^{-ip_2 \eta x_3}, e^{-ip_3 \eta x_3}]. \tag{15}$$

In addition, **p** and $\mathbf{A} = (\mathbf{a}_1, \mathbf{a}_2, \mathbf{a}_3)$ are, respectively, the eigenvalues and eigenmatrix, related to each other by the following characteristic eigenrelation, [33–35], in an oblique plane spanned by $(n_1 = \cos\theta, n_2 = \sin\theta, 0)^T$ and $(0,0,1)^T$, as

$$[\mathbf{Q} + p_i(\mathbf{R} + \mathbf{R}^T) + p_i^2 \mathbf{T}] \mathbf{a}_i = 0, \tag{16}$$

with $Q_{ij} \equiv C_{i\alpha j\beta} n_\alpha n_\beta$, $R_{ij} \equiv C_{i\alpha j3} n_\alpha$, and $T_{ij} \equiv C_{i3j3}$.

Let us define **s** as a vector consisting of the in-plane stress components in the horizontal plane, and **t** as a vector consisting of the corresponding out-of-plane stress components. The combination of these two vectors represents the full stress tensor because of its symmetry. The corresponding Green's functions are given by $\mathbf{s}^* \equiv (\sigma^*_{11p}, \sigma^*_{12p}, \sigma^*_{22p})$ and $\mathbf{t}^* \equiv (\sigma^*_{13p}, \sigma^*_{23p}, \sigma^*_{33p})$, with subscript p indicating the unit point-force direction. By applying the Hooke's law, $\mathbf{t}^*$ and $\mathbf{s}^*$ can be derived from Eq. (14), in the transformed domain, as

$$\tilde{\mathbf{t}}^*_m(x_3) = e^{i k_\alpha y_\alpha} [\tilde{\mathbf{t}}^{*(s)}_m(x_3) + (\overline{\mathbf{B}}_m \langle e^{-i\overline{\mathbf{p}}_m \eta (x_3 - h_{m-1})} \rangle \mathbf{V}_m + \mathbf{B}_m \langle e^{-i\mathbf{p}_m \eta (x_3 - h_m)} \rangle \mathbf{W}_m)], \tag{17}$$

$$\tilde{\mathbf{s}}^*_m(x_3) = e^{i k_\alpha y_\alpha} [\tilde{\mathbf{s}}^{*(s)}_m(x_3) + (\overline{\mathbf{C}}_m \langle e^{-i\overline{\mathbf{p}}_m \eta (x_3 - h_{m-1})} \rangle \mathbf{V}_m + \mathbf{C}_m \langle e^{-i\mathbf{p}_m \eta (x_3 - h_m)} \rangle \mathbf{W}_m)], \tag{18}$$

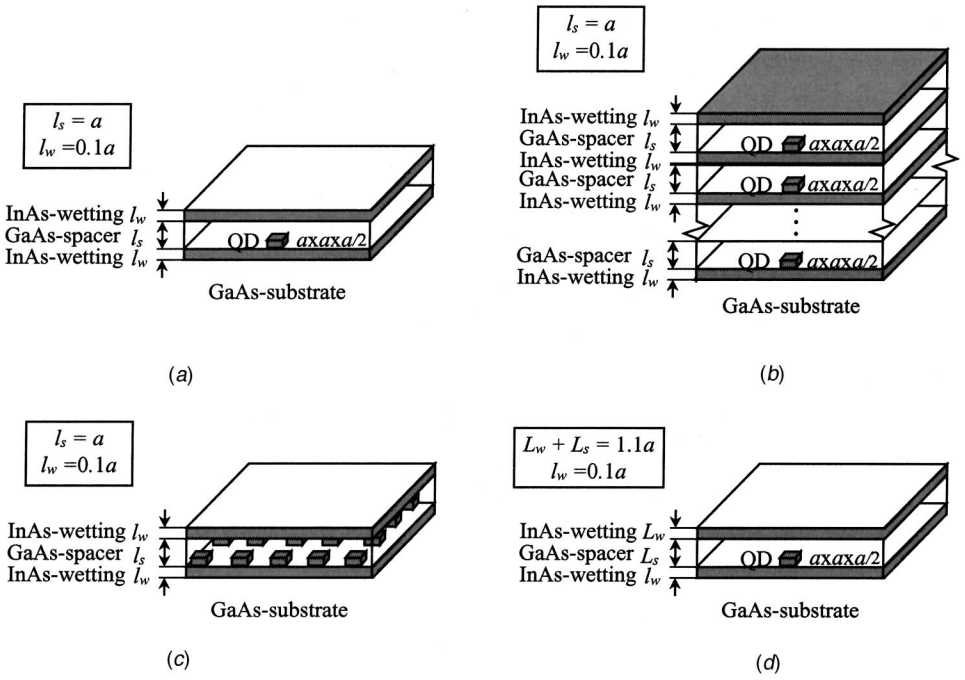

Fig. 3 Four examples of a heterostructure with alternating layers of GaAs-spacer and InAs-wetting on a GaAs substrate, plus a fresh wetting layer on the top: (*a*) a single QD; (*b*) a vertical array of QDs; (*c*) a horizontal rectangular array of QDs; (*d*) a single QD with varying ratio of thickness between top wetting and spacer layers

where $\tilde{\mathbf{t}}^{*(s)}_m$ and $\tilde{\mathbf{s}}^{*(s)}_m$ are derived from $\tilde{\mathbf{u}}^{*(s)}_m$ and matrix **B** and **C** are related to **A** and **p**, [35]. The matrix **C** here is different from the fourth-rank tensor of elastic stiffness C_{ijkl}.

The derivatives of $\tilde{\mathbf{u}}^*$, $\tilde{\mathbf{t}}^*$, and $\tilde{\mathbf{s}}^*$ with respect to source coordinates **y** can be obtained from the above expressions, as

$$\tilde{\mathbf{u}}^*_{m,y_\alpha}(x_3) = ik_\alpha \tilde{\mathbf{u}}^*_m(x_3), \quad \tilde{\mathbf{t}}^*_{m,y_\alpha}(x_3) = ik_\alpha \tilde{\mathbf{t}}^*_m(x_3),$$
$$\tilde{\mathbf{s}}^*_{m,y_\alpha}(x_3) = ik_\alpha \tilde{\mathbf{s}}^*_m(x_3), \tag{19}$$

$$\tilde{\mathbf{u}}^*_{m,y_3}(x_3) = e^{ik_\alpha y_\alpha}[\tilde{\mathbf{u}}^{*(s)}_{m,y_3}(x_3) + i\eta^{-1}(\overline{\mathbf{A}}_m\langle e^{-i\overline{\mathbf{p}}_m\eta(x_3-h_{m-1})}\rangle \mathbf{V}'_m + \mathbf{A}_m\langle e^{-i\mathbf{p}_m\eta(x_3-h_m)}\rangle \mathbf{W}'_m)], \tag{20}$$

$$\tilde{\mathbf{t}}^*_{m,y_3}(x_3) = e^{ik_\alpha y_\alpha}[\tilde{\mathbf{t}}^{*(s)}_{m,y_3}(x_3) + (\overline{\mathbf{B}}_m\langle e^{-i\overline{\mathbf{p}}_m\eta(x_3-h_{m-1})}\rangle \mathbf{V}'_m + \mathbf{B}_m\langle e^{-i\mathbf{p}_m\eta(x_3-h_m)}\rangle \mathbf{W}'_m)], \tag{21}$$

$$\tilde{\mathbf{s}}^*_{m,y_3}(x_3) = e^{ik_\alpha y_\alpha}[\tilde{\mathbf{s}}^{*(s)}_{m,y_3}(x_3) + (\overline{\mathbf{C}}_m\langle e^{-i\overline{\mathbf{p}}_m\eta(x_3-h_{m-1})}\rangle \mathbf{V}'_m + \mathbf{C}_m\langle e^{-i\mathbf{p}_m\eta(x_3-h_m)}\rangle \mathbf{W}'_m)], \tag{22}$$

where $\mathbf{V}'_m$ and $\mathbf{W}'_m$ are a new pair of unknown tensors, as a function of k_1, k_2 and y_3.

The above unknown tensors $\mathbf{V}_m$, $\mathbf{W}_m$, $\mathbf{V}'_m$, and $\mathbf{W}'_m$ can be solved by imposing appropriate boundary and interfacial conditions provided that the special solutions are given. Yang and Pan [25] took the first few terms of the expansion solution of trimaterials, [36], to be the special solutions and solved the problem with traction-free top-boundary and symmetric bottom-boundary conditions and with the perfectly bonded interfacial conditions. The special solutions may also be taken as the infinite-space Green's function, [37], or the bimaterials solution, [30]. The difference would be in the resulting efficiency in evaluating the physical-domain Green's functions, [25]. By applying the boundary and interfacial conditions to the multilayers, a linear system of equations with the same number of unknowns can be formed and solved for each set of (k_1, k_2) in the transformed plane. Then, the physical-domain Green's functions are obtained by using the Fourier inverse transform, for example, the displacement field, as

$$u_i(x_1,x_2,x_3) = \frac{1}{(2\pi)^2}\int\int \tilde{u}_i(k_1,k_2,x_3)e^{-ix_\alpha k_\alpha}dk_1dk_2, \tag{23}$$

where the integral limits in both k_1 and k_2 are $(-\infty,\infty)$.

Above, we have only described the key steps in the derivation of the three-dimensional Green's functions for anisotropic elastostatic multilayers within the framework of generalized Stroh formalism and Fourier transforms. For details of the theory and relevant computational issues, one may refer to [25,30,35,36], and articles cited therein.

3 Results and Discussions

In this section, we apply the integral-equation formulation, described in the previous section, to investigate the elastic fields due to embedded QDs in a multilayered semiconductor system. Effects of vertical and lateral orderings of QDs and of thickness of wetting layer on the elastic fields will be addressed. The multilayered semiconductor consists of up to four sets of alternating GaAs-spacer and InAs-wetting layers on a GaAs substrate, plus a ''freshly'' deposited InAs-wetting layer on the top. Four different examples as shown in Figs. 3(*a–d*) are studied. The top surface is assumed to be traction-free while the interfaces are in the perfect-bonding condition. The far-field stress and displacement are zero. The thickness of the wetting and spacer layers is denoted by l_w and l_s, respectively. It is taken that $l_w = 0.1a$ and $l_s = a$ with the exception in the last example (Fig. 3(*d*)). The QDs are assumed to be cuboidal with dimensions $a \times a \times a/2$. They are seated on the top of a wetting layer and embedded in the above adjacent GaAs-spacer, as shown in Fig. 3(*a–d*). It is mentioned that the sides of the QDs are taken to be along the global coordinates (x_1, x_2, x_3). For simplicity, we also assume that the QDs have the same elastic property as its surrounding GaAs-spacer, and the misfit strain in the QDs is hydrostatic, i.e., $\varepsilon^0_{ij} = \varepsilon^0 \delta_{ij}$. The elastic constants for

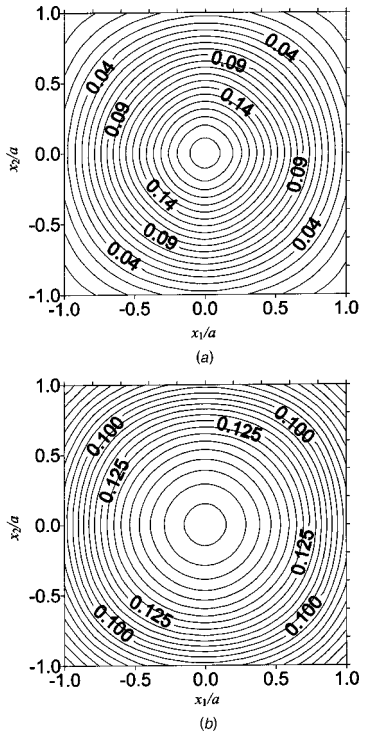

Fig. 4 Elastic fields on top surface induced by a single QD (Fig. 3*a*): (*a*) normalized hydrostatic strain $\varepsilon_{kk}/\varepsilon^0$; (*b*) normalized vertical displacement component $-u_3/(\varepsilon^0 a)$

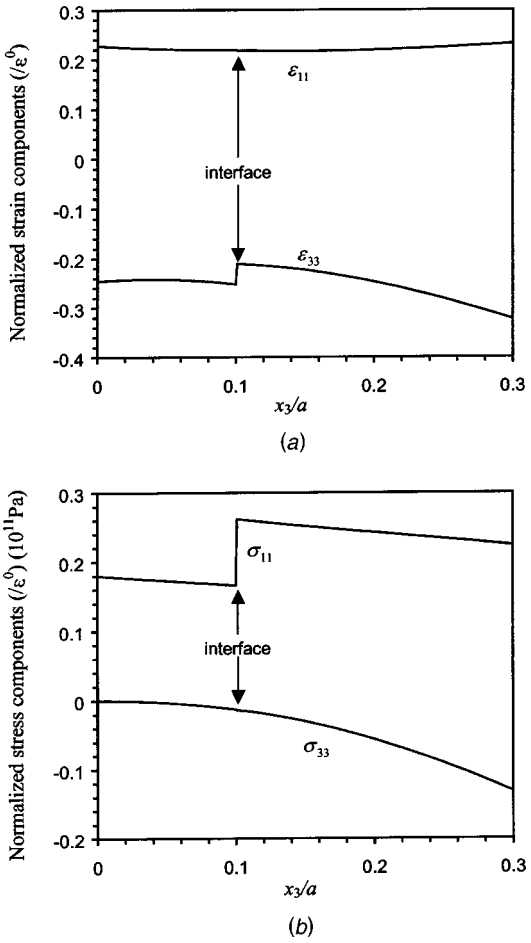

Fig. 5 Vertical variation of normalized nonzero strain and stress components over a single QD (Fig. 3*a*): (*a*) $\varepsilon_{11}(\varepsilon_{22}=\varepsilon_{11})$ and $\varepsilon_{33}/\varepsilon^0$; (*b*) $\sigma_{11}(\sigma_{22}=\sigma_{11})$ and $\sigma_{33}/\varepsilon^0$ in 10^{11} Pa

GaAs are $C_{11}=118$, $C_{12}=54$, $C_{44}=59$ and for InAs $C_{11}=83$, $C_{12}=45$, $C_{44}=40$ (GPa), with their crystallographic directions [100], [010], and [001] coinciding with the global coordinates x_1, x_2, and x_3, respectively. We remark that there should exist nonzero eigenstrain in the wetting layers, similar to that in the QDs. Because of the linearity of the problem, the QD-induced elastic field discussed below and the homogenous field due to the nonzero eigenstrain in the wetting layers can be superposed. In the present multilayer structure, the homogenous field can be obtained by applying the classical laminate theory, [27].

3.1 Example 1: A Single Quantum Dot. A buried single QD in the layered semiconductor system of top-InAs-wetting/GaAs-spacer/InAs-wetting/GaAs-substrate, as shown in Fig. 3(*a*), is first studied. The cuboidal QD is seated on the top of the internal wetting layer and embedded in the spacer, with its center located at $(0,0,0.85a)$. The top InAs layer represents a "freshly" deposited wetting layer where a next generation of QDs is expected to grow. Figures 4(*a*) and 4(*b*) show, respectively, the contour plots of the normalized hydrostatic strain $\varepsilon_{kk}/\varepsilon^0$ and normalized vertical displacement $-u_3/(\varepsilon^0 a)$ on the top surface (i.e., the free surface of the freshly deposited InAs-wetting layer) above the QD. Figure 5 shows the vertical variation of the normalized nonzero strain and stress components over the center of the QD. It is noted that, in this example, only the diagonal components, ε_{11}, $\varepsilon_{22}(=\varepsilon_{11})$, ε_{33}, σ_{11}, $\sigma_{22}(=\sigma_{11})$, and σ_{33}, are nonzero.

It is observed from Fig. 4 that due to the coincidence of the crystallographic orientations of the wetting and spacer crystals with the side orientations of the cuboidal QD, the normalized hydrostatic strain and vertical displacement are symmetric relative to the in-plane axes. They reach their maximum values at the origin, (0,0,0), right above the QD center on the free surface. We remark, however, that should the GaAs (111) be used in place of GaAs (001) for the spacer, the contour plots will be distorted with completely different features. The characteristics may be correlated to the electronic and optical behaviors of the semiconductor system, and to the growth direction and vertical correlation of new QDs, [38,39].

Due to the mismatch between the wetting and spacer layer crystals, the out-of-plane strain component, ε_{33}, and the in-plane stress components, σ_{11} and σ_{22}, are discontinuous across the interface, as shown in Fig. 5. However, the other in-plane strain and out-of-plane stress components, as well as all the displacement components, are continuous, as enforced in the Green's function solution, and in turn reflected in the inclusion solution of eigenstrains, [26]. It is also interesting to note from Fig. 5 that in the wetting layer, the magnitude of the in-plane strain and stress components increases when the observation point approaches the traction-free top surface, a phenomenon that may be explained by the free-surface bending effect.

3.2 Example 2: A Vertical Array of Quantum Dots. Effect of a vertical array of QDs on the elastic fields is examined in this example. Figure 3(*b*) schematically shows the geometry of the problem. Simulations were performed with repeated sets of alternating spacer and wetting layers with a QD embedded in each set. The variation of the normalized hydrostatic strain and vertical displacement along a line $(x_1,0,0)$ on the top surface is shown in Figs. 6(*a*) and 6(*b*). In these two figures, the results for *n* QD correspond to a semiconductor model made of *n* set of GaAs/InAs (plus a fresh InAs on the top and a GaAs substrate on the bottom). For instance, the results for one QD correspond to a semiconductor model with only one set of GaAs/InAs (plus a fresh InAs on the top and a GaAs substrate on the bottom, exactly the same as in

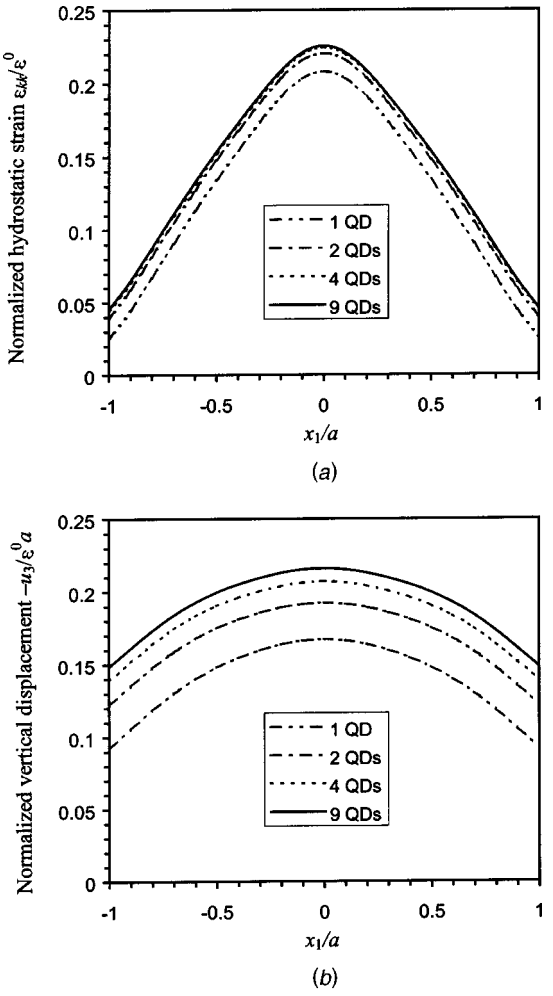

Fig. 6 Induced elastic fields along a line $(x_1,0,0)$ on top surface due to a vertical array of up to nine QDs (Fig. 3*b*): (*a*) normalized hydrostatic strain $\varepsilon_{kk}/\varepsilon^0$; (*b*) normalized vertical displacement component $-u_3/(\varepsilon^0 a)$

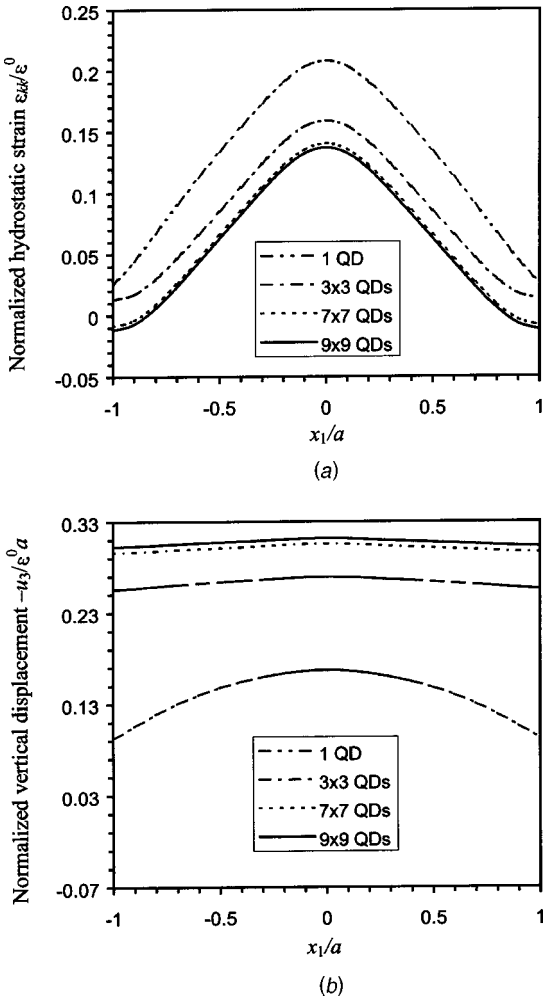

Fig. 7 Induced elastic fields along a line $(x_1,0,0)$ on top surface due to a horizontal rectangular array of up to 9×9 QDs (Fig. 3*c*): (*a*) normalized hydrostatic strain $\varepsilon_{kk}/\varepsilon^0$; (*b*) normalized vertical displacement component $-u_3/(\varepsilon^0 a)$

the previous case), and results for four QDs correspond to a semiconductor model consisting of four sets of GaAs/InAs, i.e., top-InAs/GaAs/InAs/GaAs/InAs/GaAs/InAs/GaAs-substrate, with a QD in each GaAs-spacer layer.

It can be observed from Fig. 6(*a*) that the magnitude of the hydrostatic strain on the surface increases with increasing number of QDs and converges quickly to the maximum values. This suggests that a vertical array of QDs should sum up their effects of elastic relaxation on the freshly deposited wetting layer (top wetting layer) where a new generation of QDs is expected to grow. The displacement field, on the contrary, has not shown its tendency of convergence with the number of QDs of the vertical array so far.

3.3 Example 3: A Horizontal Array of Quantum Dots. Now, effect of a horizontal array of QDs on the elastic fields is studied. Simulations were performed with a horizontal rectangular array of QDs located in the spacer. The semiconductor system consists of only one set of alternating spacer and wetting layers, as shown in Fig. 3(*c*). The spacing between the adjacent QDs (from center to center) in both in-plane directions is $2a$, with size of array varying from 3×3 to 9×9. Variations of the normalized hydrostatic strain and vertical displacement on the surface above the central QD are plotted in Fig. 7.

These results show that, with increasing number of QDs laterally around the central one, the magnitude of the surface elastic-strain field decreases and converges to its minimum value. Therefore, the surrounding QDs in the lateral directions play a role in relaxing the induced elastic field due to the central QD, an effect opposite to that of a vertical array of QDs as observed earlier. Consequently, the existence of laterally neighboring QDs would suppress the effect of the central QD on the growth of a new QD above it. The vertical displacement component converges with increasing number of QDs, again in contrast to that in the case of a vertical array of QDs.

3.4 Example 4: A Single QD With Varied Thickness of Top Wetting Layer. At last, effect of top wetting layer thickness on the QD-induced elastic field is studied. The geometry is similar to that studied in the first example (Fig. 3(*a*)), but with varied thickness of the top-wetting layer and spacer layer. The total thickness of these two layers is fixed at $1.1a$, as shown in Fig. 3(*d*). Similar to that in the first example, a single QD is located at the bottom of the spacer layer. To distinguish this example from the previous ones, the varied thicknesses of the top wetting and spacer layers are now indicated by L_w and L_s, respectively. On the top surface at three locations (0,0,0), $(0.5a,0,0)$, and $(a,0,0)$, the normalized hydrostatic strain, $\varepsilon_{kk}/\varepsilon^0$, and vertical displacement component, $-u_3/(\varepsilon^0 a)$, are evaluated with various combinations of thickness

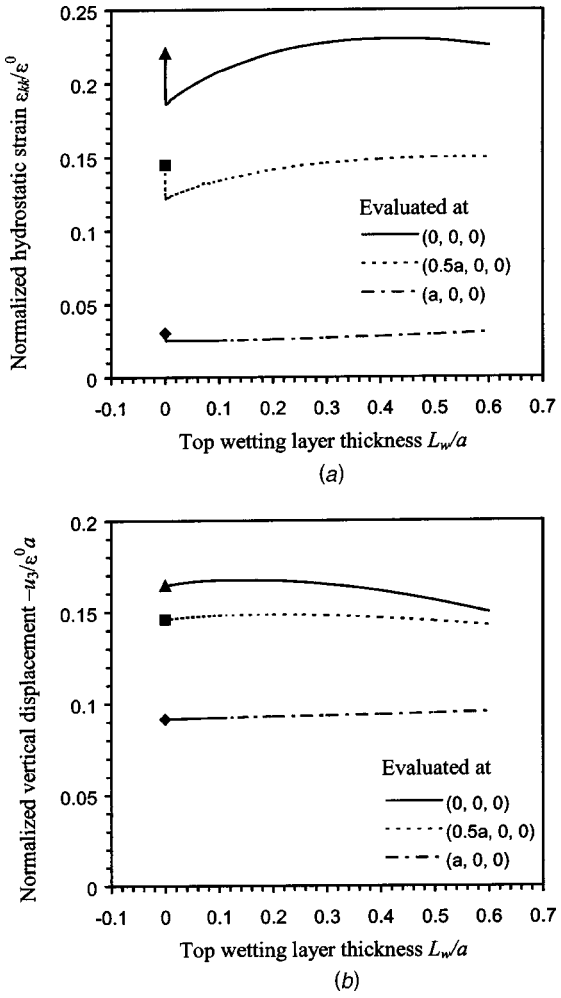

Fig. 8 Variation of elastic fields at three locations on top surface with top wetting layer thickness L_w (Fig. 3*d*): (*a*) normalized hydrostatic strain $\varepsilon_{kk}/\varepsilon^0$; (*b*) normalized vertical displacement component $-u_3/(\varepsilon^0 a)$. The results for the extreme case $L_w=0$ are indicated by symbols.

of these two layers. In addition, the extreme case without the top wetting layer (i.e., $L_w=0$) is solved. The results are shown in Fig. 8.

It can be seen that the variations of these quantities are continuous with thickness ratio between the top wetting and spacer layers. However, when $L_w=0$, the strain, as well as stress which is not shown, exhibits a jump. Meanwhile, the vertical displacement converges at $L_w=0$. The jumps in the strain and stress fields at $L_w=0$ are due to the material mismatch between the wetting and spacer layers. It is also observed that the variations of these QD-induced elastic fields may not be monotonic with the varying thickness ratio. This may be due not only to the materials mismatch between the wetting and spacer layers but also to the free-surface bending effect. Therefore, these elastic fields in the freshly deposited wetting layer cannot be modeled accurately by assigning identical elastic property to the wetting and spacer layers, no matter how thin the wetting layer is, in the multilayered semiconductor system of InAs and GaAs.

4 Conclusions

In this paper, we have proposed a novel Green's function approach to the elastic field in multilayered semiconductors with embedded coherently strained QDs. The problem of QDs with misfit strains is modeled as an anisotropic elastostatic inclusion problem of eigenstrains, [26]. The unique feature of the approach is that the point-force Green's function used for the multilayer system satisfies the boundary and interfacial-continuity conditions. By applying the Betti's reciprocal theorem, the elastic field induced by QDs with general misfit strains is expressed in terms of a domain integral with the point-force Green's function as integral kernel. The domain integral is reduced to a surface integral along the boundary of a QD that has a uniform misfit-strain distribution. Further, for QDs that can be modeled as point sources, the induced elastic field is then derived as a sum of the point-force Green's functions. These novel features make the present continuum-mechanics approach both accurate and efficient for carrying out a parametric study of QDs-induced elastic field in multilayered semiconductors.

By applying the Green's function approach, we have analyzed the elastic field due to embedded QDs in a system of alternating GaAs-spacer and InAs-wetting layers on a GaAs substrate, plus a freshly deposited InAs-wetting layer on the top. The QDs embedded in the spacer layers are assumed to have the same elastic constants as the spacer medium. The effects of vertical and horizontal arrays of QDs and of thickness of the top wetting layer on the elastic fields are examined and discussed in detail. The following features have been observed:

- First, the QD-induced out-of-plane strain and in-plane stress components exhibit discontinuities across the interface between the wetting and spacer layers due to the materials mismatch between these layers.
- Second, the magnitude of the induced in-plane strain and stress components increases when the observation point moves away from the QD source towards the top free surface. This may be explained by the free-surface bending effect.
- Third, a vertical array of QDs sums up their effects of elastic relaxation on the freshly deposited wetting layer, where a new generation of QDs is expected to grow. However, a horizontal array of QDs plays a role in deducting the elastic relaxation effect of the central QD on the top wetting layer, in contrast to that of a vertical array of QDs.
- Finally, when the thickness of the top wetting layer varies, the induced elastic field on the top surface changes continuously. However, when the top wetting layer totally disappears, some of the elastic strain and stress components exhibit a jump, due to the difference of elastic property between the wetting and spacer layers.

Acknowledgment

The authors would like to thank Dr. Vinod Tewary of the NIST at Boulder, Colorado for discussion and encouragement.

References

[1] Bimberg, D., Grundmann, M., and Ledentsov, N. N., 1998, *Quantum Dot Heterostructures*, John Wiley and Sons, New York.
[2] Brunner, K., 2002, "Si/Ge Nanostructures," Rep. Prog. Phys., **65**, pp. 27–72.
[3] Freund, L. B., and Johnson, H. T., 2001, "Influence of Strain on Functional Characteristics of Nanoelectronic Devices," J. Mech. Phys. Solids, **49**, pp. 1925–1935.
[4] Xie, Q., Madhukar, A., Chen, P., and Kobayashi, N. P., 1995, "Vertically Self-Organized InAs Quantum Box Islands on GaAs(100)," Phys. Rev. Lett., **75**, pp. 2542–2545.
[5] Tersoff, J., Teichert, C., and Lagally, M. G., 1996, "Self-Organization in Growth of Quantum Dot Supperlattices," Phys. Rev. Lett., **76**, pp. 1675–1678.
[6] Ishikawa, H., Shoji, H., Nakata, Y., Mukai, K., Sugawara, M., Egawa, M., Otsuka, N., Sujiyama, Y., Futatsugi, T., and Yokoyama, N., 1998, "Self-Organized Quantum Dots and Lasers," J. Vac. Sci. Technol. A, **16**, pp. 794–800.
[7] Springholz, G., Pinczolits, M., Holy, V., Zerlauth, S., Vavra, I., and Bauer, G., 2001, "Vertical and Lateral Ordering in Self-Organized Quantum Dot Supperlattices," Physica E (Amsterdam), **9**, pp. 149–163.
[8] Le Ru, E. C., Bennett, A. J., Roberts, C., and Murray, R., 2002, "Strain and Electronic Interactions in InAs/GaAs Quantum Dot Multilayers for 1300 nm Emission," J. Appl. Phys., **91**, pp. 1365–1370.
[9] Grundmann, M., Stier, O., and Bimberg, D., 1995, "InAs/GaAs Pyramidal

Quantum Dots: Strain Distribution, Optical Phonons, and Electronic Structure,'' Phys. Rev. B, **52**, pp. 11,969–11,981.
[10] Benabbas, T., Francois, P., Androussi, Y., and Lefebvre, A., 1996, ''Stress Relaxation in Highly Strained InAs/GaAs Structures as Studied by Finite Element Analysis and Transmission Electron Microscopy,'' J. Appl. Phys., **80**, pp. 2763–2767.
[11] Johnson, H. T., Freund, L. B., Akyuz, C. D., and Zaslavsky, A., 1998, ''Finite Element Analysis of Strain Effects on Electronic and Transport Properties in Quantum Dots and Wires,'' J. Appl. Phys., **84**, pp. 3714–3725.
[12] Kret, S., Benabbas, T., Delamarre, C., Androussi, Y., Dubon, A., Laval, J. Y., and Lefebvre, A., 1999, ''High Resolution Electron Microscope Analysis of Lattice Distortions and in Segregation in Highly Strained In0.35Ga0.65As Coherent Islands Grown on GaAs(001),'' J. Appl. Phys., **86**, pp. 1988–1993.
[13] Jogai, B., 2001, ''Three-Dimensional Strain Field Calculations in Multiple InN/AIN Wuutzite Quantum Dots,'' J. Appl. Phys., **90**, pp. 699–704.
[14] Johnson, H. T., and Freund, L. B., 2001, ''The Influence of Strain on Confined Electronic States in Semiconductor Quantum Structures,'' Int. J. Solids Struct., **38**, pp. 1045–1062.
[15] Daruka, I., Barabasi, A. L., Zhou, S. J., Germann, T. C., Lomdahl, P. S., and Bishop, A. R., 1999, ''Molecular-Dynamics Investigation of the Surface Stress Distribution in a Ge/Si Quantum Dot Superlattice,'' Phys. Rev. B, **60**, pp. R2150–R2153.
[16] Kikuchi, Y., Sugii, H., and Shintani, K., 2001, ''Strain Profiles in Pyramidal Quantum Dots by Means of Atomistic Simulation,'' J. Appl. Phys., **89**, pp. 1191–1196.
[17] Makeev, M. A., and Maduhukar, A., 2001, ''Simulations of Atomic Level Stresses in Systems of Buried Ge/Si Islands,'' Phys. Rev. Lett., **86**, pp. 5542–5545.
[18] Ru, C. Q., 1999, ''Analytic Solution for Eshelby's Problem of an Inclusion of Arbitrary Shape in a Plane or Half Plane,'' ASME J. Appl. Mech., **66**, pp. 315–322.
[19] Faux, D. A., and Pearson, G. S., 2000, ''Green's Tensors for Anisotropic Elasticity: Application to Quantum Dots,'' Phys. Rev. B, **62**, pp. R4798–R4801.
[20] Davies, J. H., 1998, ''Elastic and Piezoelcetric Fields around a Buried Quantum Dot: A Simple Picture,'' J. Appl. Phys., **84**, pp. 1358–1365.
[21] Davies, J. H., 1999, ''Quantum Dots Induced by Strain from Buried and Surface Stressors,'' Appl. Phys. Lett., **75**, pp. 4142–4144.
[22] Andreev, A. D., Downes, J. R., Faux, D. A., and O'Reilly, E. P., 1999, ''Strain Distributions in Quantum Dots of Arbitrary Shape,'' J. Appl. Phys., **86**, pp. 297–305.
[23] Pearson, G. S., and Faux, D. A., 2000, ''Analytical Solutions for Strain in Pyramidal Quantum Dots,'' J. Appl. Phys., **88**, pp. 730–736.
[24] Pan, E., and Yang, B., 2001, ''Elastostatic Fields in an Anisotropic Substrate due to a Buried Quantum Dot,'' J. Appl. Phys., **90**, pp. 6190–6196.
[25] Yang, B., and Pan, E., 2001, ''Efficient Evaluation of Three-Dimensional Green's Functions for Anisotropic Elastostatic Multilayered Composites,'' Eng. Anal. Boundary Elem., **26**, pp. 355–366.
[26] Mura, T., 1987, *Micromechanics of Defects in Solids*, Martinus Nijhoff, Boston.
[27] Tsai, S. W., and Hahn, H. T., 1980, *Introduction to Composite Materials*, Technomic Publishing, Westport, CT.
[28] Pan, E., 1991, ''Dislocation in an Infinite Poroelastic Medium,'' Acta Mech., **87**, pp. 105–115.
[29] Romanov, A. E., Beltz, G. E., Fischer, W. T., Petroff, P. M., and Speck, J. S., 2001, ''Elastic Fields of Quantum Dots in Subsurface Layers,'' J. Appl. Phys., **89**, pp. 4523–4531.
[30] Pan, E., and Yuan, F. G., 2000, ''Three-Dimensional Green's Functions in Anisotropic Bimaterials,'' Int. J. Solids Struct., **37**, pp. 5329–5351.
[31] Pan, E., Yang, B., Cai, X., and Yuan, F. G., 2001, ''Stress Analyses Around Holes in Composite Laminates Using Boundary Element Method,'' Eng. Anal. Boundary Elem., **25**, pp. 31–40.
[32] Yang, B., 2002, ''Examination of Free-Edge Crack Nucleation Around an Open Hole in Composite Laminates,'' Int. J. Fract., **115**, pp. 173–191.
[33] Stroh, A. N., 1958, ''Dislocations and Cracks in Anisotropic Elasticity,'' Philos. Mag., **3**, pp. 625–646.
[34] Stroh, A. N., 1962, ''Steady State Problems in Anisotropic Elasticity,'' J. Math. Phys., **41**, pp. 77–103.
[35] Ting, T. C. T., 1996, *Anisotropic Elasticity*, Oxford University Press, Oxford, UK.
[36] Yang, B., and Pan, E., 2001, ''Three-Dimensional Green's Functions in Anisotropic Trimaterials,'' Int. J. Solids Struct., **39**, pp. 2235–2255.
[37] Tonon, F., Pan, E., and Amadei, B., 2001, ''Green's Functions and Boundary Element Formulation for 3D Anisotropic Media,'' Comput. Struct., **79**, pp. 469–482.
[38] Holy, V., Springholz, G., Pinezolits, M., and Bauer, G., 1999, ''Strain Induced Vertical and Lateral Correlations in Quantum Dot Superlattices,'' Phys. Rev. Lett., **83**, pp. 356–359.
[39] Harrison, P., 2000, *Quantum Wells, Wires and Dots: Theoretical and Computational Physics*, John Wiley and Sons, New York.

Indentation Problems of Two-Dimensional Anisotropic Thermoelasticity With Perturbed Boundaries

C.-K. Chao
Professor

B. Gao

Department of Mechanical Engineering,
National Taiwan University of Science and Technology,
43, Keelung Road, Section 4,
Taipei, Taiwan

Complex variable representations in the Stroh formalism are used to analyze the problem of rigid stamp indentation on an irregularly shaped surface of an anisotropic thermoelastic body. The shape of boundary surface considered in this work includes a cosine wave-shaped surface and a triangular hole that are assumed to be slightly different from a straight line and an ellipse, respectively, for which the exact solutions exist. Based on a perturbation technique, an approximate solution for the punch problem of rigid stamp indentation on a wave-shaped surface or a triangular hole that is viewed as being perturbed from a straight line or an elliptical hole is provided. First-order perturbation solutions for both temperature and stress functions are given explicitly. Numerical results of contact stress under the punch face are discussed in detail and shown in graphic form. [DOI: 10.1115/1.1554414]

1 Introduction

In the theory of two-dimensional linear elasticity one of the most powerful techniques for the solution of boundary value problems with awkwardly shaped regions is to transform the region into one of simpler shape. For example, the boundary value problem associated with an elliptic hole or a polygonal hole for isotropic materials can be solved by the transformation of the simpler geometry such as a circle hole whose solution is easy to achieve. The success of the above method lies in the property that the transformation must be conformal and one-to-one. However, there are many cases that a one-to-one mapping function cannot be found such as the problem with a wave-shaped boundary or a triangular hole boundary for anisotropic materials. In order to illustrate the above argument, let the hole boundary be Γ and its image by $z_\alpha = x + p_\alpha y$ be Γ_α with p_α ($\alpha = 1,2,3$) being the eigenvalues for anisotropic materials. Obviously, $f_\alpha(z_\alpha)$ is analytic outside Γ_α in the z_α-plane. It is expected that the transformed functions $f_\alpha(m_\alpha(\zeta))$ can be determined by transforming the original boundary conditions on an elliptic hole Γ onto the unit circle in the ζ-plane. However, one could not expect that the transformed functions $f_\alpha(m_\alpha(\zeta))$ can be found by transforming the boundary conditions on a nonelliptic hole Γ onto the unit circle since three unknown functions $f_\alpha(m_\alpha(\zeta))$ appearing in the transformed boundary conditions on the unit circle in the ζ-plane will take different values at three different points. The relations between these three points are too much complex in general for a nonelliptic hole Γ and it is impossible to choose the mappings $m_\alpha(\zeta)$ so that the three image points on the unit circle in the ζ-plane be always coincident.

When the boundary geometries are simple like the straight boundary, the main task is the development of a systematic approach for solving the mixed boundary value problem. For example, the punch problem for an anisotropic elasticity with straight edges was solved by Fan and Keer [1] in detail by employing the formalism of Eshelby et al. [2] and the method of analytical continuation (Muskhelishvili [3]). As to the problems with elliptic boundaries, the introduction of conformal mapping functions was used by Fan and Hwu [4]. As discussed in the above paragraph, the method based on the conformal mapping functions is not valid for solving the problem with awkwardly shaped regions. An alternative approach for solving such problems is based on the perturbation method by introducing a small parameter which denotes the deviation of the opening from that of a straight line or an ellipse (Hwu and Fan [5]). The solution for the anisotropic media with a straight edge or an elliptical opening will be used as a reference. Then, by the perturbation technique an approximate solution for the anisotropic media with openings slightly different from a straight edge or an elliptical opening can be found.

The research noted above has considered only the isothermal case. When heat flows between two conducting solids, there will be some resistance to heat flow across the interface and the contact stress will be influenced by the temperature distribution in the bodies. In certain conditions, separation will occur at the corners of the punch resulting in incomplete indentation that makes the problem more difficult to solve. The literature on this subject includes works by Barber [6,7], Clements and Toy [8], and Panek and Dundurs [9]. More specifically, for the problem with a frictionless rigid flat-ended punch, Comninou et al. [10] indicated that, depending on the magnitude and the direction of the total heat flux, either perfect thermal contact throughout the punch face or an imperfect contact region at the center with adjacent perfect contact regions occurs. In this paper, based on a perturbation technique, we like to solve the more complicated problem with perturbed boundaries. Two kinds of perturbed boundaries will be considered here. One is a boundary perturbed from a straight line such as a cosine wave-shaped surface indented by a rigid flat-ended punch, the other is a boundary perturbed from an ellipse such as a triangular hole boundary indented by a rigid stamp. In order to make an analytical solution tractable in the current work, the stamp is considered to completely adhere to the surface of an elastic body over the contact region such that the displacement along the contact region can be assumed to be a constant value. Moreover, the magnitude of the total heat flux is properly chosen such that the condition of perfect thermal contact is always satisfied during the indentation. A general solution up to the first-order

Contributed by the Applied Mechanics Division of THE AMERICAN SOCIETY OF MECHANICAL ENGINEERS for publication in the ASME JOURNAL OF APPLIED MECHANICS. Manuscript received by the ASME Applied Mechanics Division, Dec. 9, 2001; final revision, Sept. 4, 2002. Associate Editor: J. R. Barber. Discussion on the paper should be addressed to the Editor, Prof. Robert M. McMeeking, Department of Mechanical and Environmental Engineering University of California–Santa Barbara, Santa Barbara, CA 93106-5070, and will be accepted until four months after final publication of the paper itself in the ASME JOURNAL OF APPLIED MECHANICS.

perturbation will be obtained by using Stroh's formalism (Stroh [11]), analytical continuation, conformal mapping function, and perturbation technique. As to higher-order perturbation solutions, general procedure is depicted in this paper. Two numerical examples of punch problems associated with a cosine wave shaped surface and a triangular hole boundary are studied in detail and shown in graphic form.

2 Basic Equations for Two-Dimensional Anisotropic Thermoelasticity

The basic equations for linear anisotropic thermoelasticity are the equations for the stress-strain, the equilibrium, the heat conduction, and the balance of energy, which can be expressed as

$$\begin{gathered}\sigma_{ij}=C_{ijks}u_{k,s}-\beta_{ij}T\\ \sigma_{ij,j}=0\\ h_i=-k_{ij}T_{,j}\\ h_{i,i}=0\end{gathered}\tag{2.1}$$

where u_i, σ_{ij}, h_i, T stand for the displacement, stress, heat flux, and temperature, respectively, and β_{ij}, k_{ij}, C_{ijks} are, respectively, the thermal moduli, the heat conduction, and the elastic constants.

For two-dimensional problems which depend on x_1 and x_2 only, the general solution to (2.1) may be written by means of four holomorphic functions which satisfy all the basic equations given in (2.1) as (Ting [12])

$$\begin{gathered}T=2\ \mathrm{Re}[g'(z_t)]\\ Q=\int h_1dx_2-h_2dx_1=2\ \mathrm{Re}[ikg'(z_t)]\\ \mathbf{u}=2\ \mathrm{Re}[\mathbf{A}\mathbf{f}(z)+\mathbf{c}g(z_t)]\\ \phi=2\ \mathrm{Re}[\mathbf{B}\mathbf{f}(z)+\mathbf{d}g(z_t)]\end{gathered}\tag{2.2}$$

with $\mathbf{A}=[\mathbf{a}_1\ \mathbf{a}_2\ \mathbf{a}_3]$, $\mathbf{B}=[\mathbf{b}_1\ \mathbf{b}_2\ \mathbf{b}_3]$, $\mathbf{f}(z)=[f_1(z_1)\ f_2(z_2)\ f_3(z_3)]^T$, $k=\sqrt{k_{11}k_{22}-k_{12}^2}$, $z_t=x_1+\tau x_2$, $z_\alpha=x_1+p_\alpha x_2$, $\alpha=1,2,3$, in which g and $\mathbf{f}$ are functions of the complex variables z_t and z_α, respectively. In the above equation, $\mathbf{u}=(u_1,u_2,u_3)$ is the displacement vector, $\phi=(\phi_1,\phi_2,\phi_3)$ stands for the stress function vector, which is related to the stresses σ_{ij} by $\sigma_{i1}=-\phi_{i,2}$, $\sigma_{i2}=\phi_{i,1}$, and the additional multipliers in (2.2) are defined by

$$\begin{gathered}\mathbf{c}=[\mathbf{Q}+\tau(\mathbf{R}+\mathbf{R}^T)+\tau^2\mathbf{T}]^{-1}\{\boldsymbol{\beta}_1+\tau\boldsymbol{\beta}_2\},\\ \mathbf{d}=(\mathbf{R}^T+\tau\mathbf{T})\mathbf{c}-\boldsymbol{\beta}_2\end{gathered}\tag{2.3}$$

where

$$\begin{gathered}Q_{ik}=C_{i1k1},\quad R_{ik}=C_{i1k2},\quad T_{ik}=C_{i2k2},\\ \boldsymbol{\beta}_1=[\beta_{11}\beta_{12}\beta_{13}]^T,\quad \boldsymbol{\beta}_2=[\beta_{21}\beta_{22}\beta_{23}]^T.\end{gathered}\tag{2.4}$$

For the latter derivation by means of the analytical continuation, the argument of each component function of $\mathbf{f}(z)$ is written as $z=x_1+px_2$ without referring to its associated eigenvalues p_α. Once the solutions of the holomorphic functions are obtained, a replacement of z_1, z_2, and z_3 (or z_t) should be made for $\mathbf{f}(z)$ (or $g(z)$) to calculate the field quantities from (2.2).

3 Straight Boundary Perturbation

Let an anisotropic elastic body occupy the lower half-plane whose boundary is a wave-shaped surface perturbed from the straight line $x_2=0$ which can be expressed in terms of a small parameter ε as

$$x_2=\varepsilon\varphi(x_1)\tag{3.1}$$

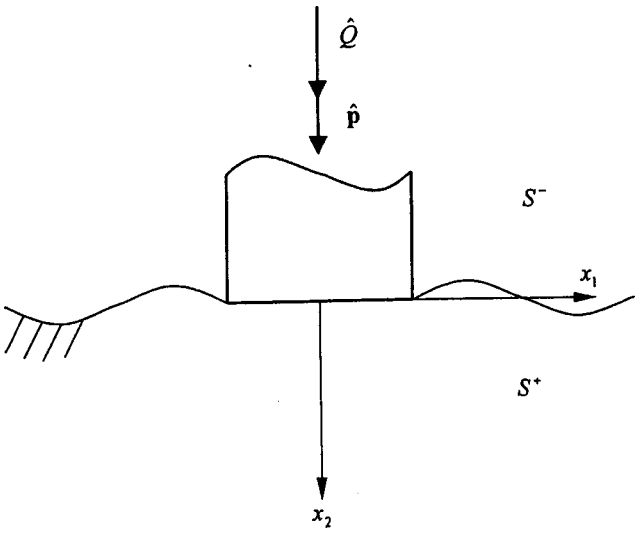

Fig. 1 A rigid stamp indentation on a wave-shaped surface of an elastic half-plane

where $\varphi(x_1)$ is a wave-shaped function. Consider a rigid punch of width $2a$ which is pressed into a wave-shaped surface by a compressive force $\hat{\mathbf{p}}$ and the total heat flux $\hat{Q}$ from the punch to the half plane as shown in Fig. 1. In this section we consider a material occupying the lower half-plane $x_2>0$ and denote this region by S^+, using the notation S^- for the half-plane $x_2<0$.

3.1 Temperature Field. In order to solve such a mixed boundary value problem, we let the temperature function $g'(z)$ be expanded in the following perturbation form:

$$g'(z)=g_0'(z)+\varepsilon g_1'(z)+\varepsilon^2g_2'(z)+\ \ldots\ .\tag{3.2}$$

For the convenience of formulating boundary conditions along the perturbed boundary, a new variable $\hat{z}$ in place of z is introduced as

$$z=\hat{z}+\tau\varepsilon\varphi(x_1),\quad \hat{z}=x_1+\tau[x_2-\varepsilon\varphi(x_1)].\tag{3.3}$$

With the aid of (3.3), each term $g_i'(z)$ in (3.2) can be expanded into

$$\begin{gathered}g_i'(z)=g_i'(\hat{z})+\tau\varepsilon\varphi(x_1)g_i''(\hat{z})+\frac{1}{2}[\tau\varepsilon\varphi(x_1)]^2g_i'''(\hat{z})+\ \ldots,\\ i=0,1,2\ \ldots\ .\end{gathered}\tag{3.4}$$

Substituting (3.4) into (3.2), we can obtain

$$\begin{aligned}g'(z)=&g_0'(\hat{z})+\varepsilon[g_1'(\hat{z})+\tau\varphi(x_1)g_0''(\hat{z})]\\ &+\varepsilon^2\left[g_2'(\hat{z})+\tau\varphi(x_1)g_1''(\hat{z})+\frac{1}{2}\tau^2\varphi^2(x_1)g_0'''(\hat{z})\right]+\ \ldots\ .\end{aligned}\tag{3.5}$$

If there is perfect thermal contact throughout the region L pressed by the punch and the remaining part of the half-plane surface is assumed to be thermally insulated, the boundary conditions along the perturbed boundary $x_2\to\varepsilon\varphi(x_1^+)$ give

$$\begin{gathered}\frac{dT}{dx_1}=\frac{d}{dx_1}2\ \mathrm{Re}[g'(x_1^+)]=0,\quad x_1\in L\\ h_2=-\frac{d}{dx_1}2\ \mathrm{Re}[ikg'(x_1^+)]=0,\quad x_1\notin L.\end{gathered}\tag{3.6}$$

Note that $(3.6)_1$ implies that the interface offers no resistance to heat flow in the regions with solid to solid contact while $(3.6)_2$ presumes that no heat is exchanged between the bodies in the regions out of contact.

Substituting (3.5) into (3.6), we have

$$\begin{aligned}\frac{dT}{dx_1}&=\frac{d}{dx_1}2\,\mathrm{Re}\{g_0'(x_1^+)+\varepsilon[g_1'(x_1^+)+\tau\varphi(x_1^+)g_0''(x_1^+)]+\ \dots\}\\&=0,\quad x_1\in L\qquad\text{and}\\h_2&=-\frac{d}{dx_1}2\,\mathrm{Re}\{ik(g_0'(x_1^+)+\varepsilon[g_1'(x_1^+)+\tau\varphi(x_1^+)g_0''(x_1^+)]\\&\quad+\ \dots)\}=0,\quad x_1\notin L\end{aligned}\tag{3.7}$$

Comparing the coefficients of ε^λ $(\lambda=0,1,2\ \dots)$ on both equations of (3.7), we obtain

$$\begin{cases}\dfrac{d}{dx_1}2\,\mathrm{Re}[g_0'(x_1^+)]=0, & x_1\in L\\[2mm]\dfrac{d}{dx_1}2\,\mathrm{Re}[ikg_0'(x_1^+)]=0, & x_1\notin L\end{cases}$$

$$\begin{cases}\dfrac{d}{dx_1}2\,\mathrm{Re}[g_1'(x_1^+)+\tau\varphi(x_1^+)g_0''(x_1^+)]=0, & x_1\in L\\[2mm]\dfrac{d}{dx_1}2\,\mathrm{Re}[ik(g_1'(x_1^+)+\tau\varphi(x_1^+)g_0''(x_1^+))]=0, & x_1\notin L\end{cases}\tag{3.8}$$

$$\vdots$$

The first set of equations in (3.8) for the zero-order perturbation is identical to that for the mixed boundary value problems with straight boundary whose solution has been found in (Chao et al. [13]) as

$$g_0''(\hat z)=\frac{-\hat Q}{2\pi k\sqrt{(\hat z-a)(\hat z+a)}},\quad \hat z\in S^+.\tag{3.9}$$

Using $g_0''(\hat z)$ as a reference solution, the second set of Eqs. (3.8) for the first-order perturbation can be treated in a similar way and the final result is

$$g_1''(\hat z)=-\frac{d}{dz}[\tau\varphi(\hat z)g_0''(\hat z].\tag{3.10}$$

In a similar way, the higher-order perturbation solutions can be solved step by step.

3.2 Stress Field. Let the derivative of the complex function $\mathbf{f}(z)$ be expanded in the following perturbation form:

$$\mathbf{f}'(z)=\mathbf{f}_0'(z)+\varepsilon\mathbf{f}_1'(z)+\varepsilon^2\mathbf{f}_2'(z)+\ \dots\ .\tag{3.11}$$

If we introduce a new variable $\hat z$ in place of z by

$$z=\hat z+p\varepsilon\varphi(x_1),\quad \hat z=x_1+p[x_2-\varepsilon\varphi(x_1)],\tag{3.12}$$

each term $\mathbf{f}_i'(z)$ in (3.11) can be expanded into

$$\begin{aligned}\mathbf{f}_i'(z)&=\mathbf{f}_i'(\hat z)+p\varepsilon\varphi(x_1)\mathbf{f}_i''(\hat z)+\frac{1}{2}[p\varepsilon\varphi(x_1)]^2\mathbf{f}_i'''(\hat z)+\ \dots,\\&\quad i=0,1,2,\dots\ .\end{aligned}\tag{3.13}$$

Substituting (3.13) into (3.11), we obtain

$$\begin{aligned}\mathbf{f}'(z)&=\mathbf{f}_0'(\hat z)+\varepsilon[\mathbf{f}_1'(\hat z)+p\varphi(x_1)\mathbf{f}_0''(\hat z)]\\&\quad+\varepsilon^2\left[\mathbf{f}_2'(\hat z)+p\varphi(x_1)\mathbf{f}_1''(\hat z)+\frac{1}{2}p^2\varphi(x_1)^2\mathbf{f}_0'''(\hat z)\right]+\ \dots\ .\end{aligned}\tag{3.14}$$

Since a rigid punch of width $2a$ is pressed into a wave-shaped half-plane surface by a compressive force, the boundary conditions for this problem are

$$\begin{aligned}\frac{d\mathbf{u}}{dx_1}&=\hat{\mathbf{u}}'(x_1),\quad x_1\in L\\\frac{d\phi}{dx_1}&=0,\quad x_1\notin L\end{aligned}\tag{3.15}$$

where $\hat{\mathbf{u}}'(x_1)$ can be expressed in terms of ε as

$$\hat{\mathbf{u}}'(x_1)=\hat{\mathbf{u}}_0'(x_1)+\varepsilon\hat{\mathbf{u}}_1'(x_1)+\varepsilon^2\hat{\mathbf{u}}_2'(x_1)+\ \dots\ .$$

Along the perturbed boundary $x_2\to\varepsilon\varphi(x_1^+)$ the boundary conditions (3.15) become

$$\begin{aligned}\frac{d\mathbf{u}}{dx_1}&=2\,\mathrm{Re}\{\mathbf{A}(\mathbf{f}_0'(x_1^+)+\varepsilon[\mathbf{f}_1'(x_1^+)+p\varphi(x_1^+)\mathbf{f}_0''(x_1^+)]+\ \dots)\\&\quad+\mathbf{c}(g_0'(x_1^+)+\varepsilon[g_1'(x_1^+)+\tau\varphi(x_1^+)g_0''(x_1^+)]+\ \dots)\}\\&=\hat{\mathbf{u}}'(x_1),\quad x_1\in L\qquad\text{and}\\\frac{d\phi}{dx_1}&=2\,\mathrm{Re}\{\mathbf{B}(\mathbf{f}_0'(x_1^+)+\varepsilon[\mathbf{f}_1'(x_1^+)+p\varphi(x_1^+)\mathbf{f}_0''(x_1^+)]+\ \dots)\\&\quad+\mathbf{d}(g_0'(x_1^+)+\varepsilon[g_1'(x_1^+)+\tau\varphi(x_1^+)g_0''(x_1^+)]+\ \dots)\}\\&=0,\quad x_1\notin L.\end{aligned}\tag{3.16}$$

By comparing the coefficients of ε^λ $(\lambda=0,1,2,\dots)$ on both sides of (3.16), we obtain

$$\begin{cases}2\,\mathrm{Re}[\mathbf{A}\mathbf{f}_0'(x_1^+)+\mathbf{c}g_0'(x_1^+)]=\hat{\mathbf{u}}_0'(x_1), & x_1\in L\\2\,\mathrm{Re}[\mathbf{B}\mathbf{f}_0'(x_1^+)+\mathbf{d}g_0'(x_1^+)]=0, & x_1\notin L\end{cases}$$

$$\begin{cases}2\,\mathrm{Re}[\mathbf{A}(\mathbf{f}_1'(x_1^+)+p\varphi(x_1^+)\mathbf{f}_0''(x_1^+))+\mathbf{c}(g_1'(x_1^+)+\tau\varphi(x_1^+)g_0''(x_1^+))]=\hat{\mathbf{u}}_1'(x_1), & x_1\in L\\2\,\mathrm{Re}[\mathbf{B}(\mathbf{f}_1'(x_1^+)+p\varphi(x_1^+)\mathbf{f}_0''(x_1^+))+\mathbf{d}(g_1'(x_1^+)+\tau\varphi(x_1^+)g_0''(x_1^+))]=0, & x_1\notin L\end{cases}\tag{3.17}$$

$$\vdots$$

The first set of equations in (3.17) for the zero-order perturbation is the same as the one corresponding to the mixed boundary value problems with straight boundary whose solution has been found in (Chao et al. [13]) as

$$\mathbf{f}_0'(\hat{z})=\mathbf{B}^{-1}\left\{\frac{1}{2\pi i}\mathbf{X}(\hat{z})\int_L\frac{1}{t-\hat{z}}[\mathbf{X}^+(t)]^{-1}\mathbf{M}\{i\hat{\mathbf{u}}_0'(t)+2\ \mathrm{Im}[\mathbf{c}-\mathbf{A}\mathbf{B}^{-1}\mathbf{d}]g_0'(t)\}dt+\mathbf{X}(\hat{z})\mathbf{p}_0(\hat{z})-\mathbf{d}g_0'(\hat{z})\right\} \tag{3.18}$$

where $\mathbf{M}=-i\mathbf{B}\mathbf{A}^{-1}$ is the impedance matrix and $\mathbf{X}(\hat{z})$ is the Plemelj function for the problem with the straight line boundary given by

$$\mathbf{X}(\hat{z})=\mathbf{\Lambda}\mathbf{\Gamma}(\hat{z}) \tag{3.19}$$

with

$$\mathbf{\Lambda}=[\lambda_1,\lambda_2,\lambda_3],\quad \mathbf{\Gamma}(\hat{z})=\langle\langle(\hat{z}-a)^{-1-\delta_\alpha}(\hat{z}+a)^{\delta_\alpha}\rangle\rangle. \tag{3.20}$$

The angular bracket $\langle\langle\ \rangle\rangle$ stands for the diagonal matrix in which each component is varied according to the Greek index α, δ_α and λ_α, $\alpha=1,2,3$ are the eigenvalues and eigenvectors of (Ting [12])

$$(\overline{\mathbf{M}}^{-1}+e^{2\pi i\delta}\mathbf{M}^{-1})\lambda=0. \tag{3.21}$$

The polynomial function $\mathbf{p}_0(\hat{z})$ in (3.18) has the form

$$\mathbf{p}_0(\hat{z})=\frac{1}{2\pi i}\mathbf{\Lambda}^{-1}\hat{\mathbf{p}}_0. \tag{3.22}$$

The zero-order solution $\mathbf{f}_0'(\hat{z})$ given in (3.18) can be used as a reference to solve the other unknown functions $\mathbf{f}_i'(\hat{z})$ in (3.17). In order to employ the method of analytical continuation, the second set of equations in (3.17) is now rewritten as

$$\begin{cases}\mathbf{A}[\mathbf{f}_1'(x_1^+)+{}^*\mathbf{f}_1'(x_1^+)]+\mathbf{c}[g_1'(x_1^+)+{}^*g_1'(x_1^+)]+\overline{\mathbf{A}}[\overline{\mathbf{f}_1'(x_1^+)}+\overline{{}^*\mathbf{f}_1'(x_1^+)}]+\overline{\mathbf{c}}[\overline{g_1'(x_1^+)}+\overline{{}^*g_1'(x_1^+)}]=\hat{\mathbf{u}}_1'(x_1), & x_1\in L\\ \mathbf{B}[\mathbf{f}_1'(x_1^+)+{}^*\mathbf{f}_1'(x_1^+)]+\mathbf{d}[g_1'(x_1^+)+{}^*g_1'(x_1^+)]+\overline{\mathbf{B}}[\overline{\mathbf{f}_1'(x_1^+)}+\overline{{}^*\mathbf{f}_1'(x_1^+)}]+\overline{\mathbf{d}}[\overline{g_1'(x_1^+)}+\overline{{}^*g_1'(x_1^+)}]=0, & x_1\notin L\end{cases} \tag{3.23}$$

where ${}^*\mathbf{f}_1'(\hat{z})\equiv p\varphi(\hat{z})\mathbf{f}_0''(\hat{z})$ and ${}^*g_1'(\hat{z})\equiv\tau\varphi(\hat{z})g_0''(\hat{z})$.

By using the analytic continuation method, a new holomorphic function is introduced as

$$\mathbf{\Theta}_1'(\hat{z})=\begin{cases}\mathbf{B}[\mathbf{f}_1'(\hat{z})+{}^*\mathbf{f}_1'(\hat{z})]+\mathbf{d}[g_1'(\hat{z})+{}^*g_1'(\hat{z})], & \hat{z}\in S^+\\ -\overline{\mathbf{B}}[\overline{\mathbf{f}_1'(\hat{z})}+\overline{{}^*\mathbf{f}_1'(\hat{z})}]-\overline{\mathbf{d}}[\overline{g_1'(\hat{z})}+\overline{{}^*g_1'(\hat{z})}], & \hat{z}\in S^-\end{cases}. \tag{3.24}$$

With the aid of (3.24), (3.23) becomes

$$\begin{cases}\mathbf{\Theta}_1'(x_1^+)+\mathbf{M}\overline{\mathbf{M}}^{-1}\mathbf{\Theta}_1'(x_1^-)=i\mathbf{M}\{\hat{\mathbf{u}}_1'(x_1)-2\ \mathrm{Re}[(\mathbf{c}-\mathbf{A}\mathbf{B}^{-1}\mathbf{d})(g_1'(x_1^+)+{}^*g_1'(x_1^+))]\}, & x_1\in L\\ \mathbf{\Theta}_1'(x_1^+)-\mathbf{\Theta}_1'(x_1^-)=0, & x_1\notin L\end{cases}. \tag{3.25}$$

Equation (3.25) is in the form of Hilbert problem whose solution is obtained as

$$\mathbf{\Theta}_1'(\hat{z})=\frac{1}{2\pi}\mathbf{X}(\hat{z})\int_L\frac{1}{t-\hat{z}}[\mathbf{X}(t)]^{-1}\mathbf{M}\{\hat{\mathbf{u}}_1'(t)-2\ \mathrm{Re}[(\mathbf{c}-\mathbf{A}\mathbf{B}^{-1}\mathbf{d})(g_1'(t^+)+{}^*g_1'(t^+))]\}dt+\mathbf{X}(\hat{z})\mathbf{p}_1(\hat{z}),\quad \hat{z}\in S^+ \tag{3.26}$$

where the polynomial vector $\mathbf{p}_1(\hat{z})$ can be determined by the loading condition. The first-order perturbation solution $\mathbf{f}_1'(\hat{z})$ can be immediately obtained by substituting (3.26) into (3.24). In a similar way, the higher-order perturbation solutions can also be solved step by step.

4 Elliptical Boundary Perturbation

Next we consider an anisotropic body containing an opening whose boundary is slightly different from an ellipse which can be expressed in terms of a small parameter ε as

$$\begin{aligned}x_1&=a\left[\cos\vartheta+\varepsilon\sum_{n=1}^{N}(a_n\cos n\vartheta+b_n\sin n\vartheta)\right]\\ x_2&=a\left[c\sin\vartheta+\varepsilon\sum_{n=1}^{N}(-a_n\sin n\vartheta+b_n\cos n\vartheta)\right].\end{aligned} \tag{4.1}$$

When $\varepsilon=0$ an ellipse with semi-axes a and ac can be described. In other cases with $\varepsilon=0$, $c=1$, and $\varepsilon=0$, $c\to0$, the contour stands for, respectively, a circle and a crack. If $N=2$, $a_1=b_1=b_2=0$, $a_2=1$, $\varepsilon=0.25$, a triangle with rounded corners can be plotted. The other cases can be obtained by setting the different values of the coefficients on (4.1).

An infinite plane with an opening (4.1) can be transformed to the ς-plane with a unit circle $|\varsigma|=1$. The transform function is written as

$$z_\alpha=z_\alpha^e+\varepsilon\varphi_\alpha(\varsigma),\quad \alpha=1,2,3,t \tag{4.2}$$

where $z_\alpha=x_1+p_\alpha x_2$ and

$$z_\alpha^e=\omega_\alpha(\varsigma)=\frac{1}{2}a\left\{(1-ip_\alpha c)\varsigma+(1+ip_\alpha c)\frac{1}{\varsigma}\right\}$$

$$\varphi_\alpha(\varsigma)=\frac{1}{2}a\sum_{n=1}^{N}\left\{(a_n-ib_n)(1+ip_\alpha)\varsigma^n+(a_n+ib_n)(1-ip_\alpha)\frac{1}{\varsigma^n}\right\}.$$

Note that the superscript "e" denotes that the transformation is related to the corresponding elliptical opening. With this transformation function (4.2), all the solutions given in (2.2) are expressed in terms of the new variable ς instead of z (or z_t). On transforming to the region $|\varsigma|\geqslant1$ of the ς-plane, the perfect contact and perfect insulation conditions can then be expressed as

$$T_{,n}(\sigma)=0,\quad \mathbf{u}_{,n}=\hat{\mathbf{u}}'(\sigma),\quad \sigma\in L \tag{4.3}$$

$$h_m=\mathbf{t}_m=0,\quad \sigma\notin L \tag{4.4}$$

where $\sigma=e^{i\vartheta}$ denotes the point on the unit circle of the ς-plane; L is an arc defined as $L=(e^{-i\varphi},e^{i\varphi})$, $\hat{\mathbf{u}}'(\sigma)$ is the given function of the displacement gradient along the tangent direction $\mathbf{n}$; h_m and $\mathbf{t}_m$

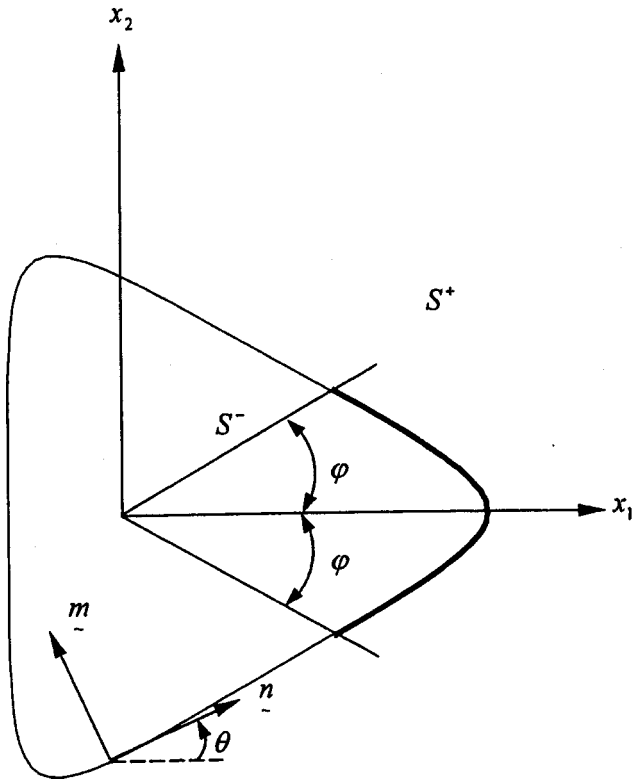

Fig. 2 A rigid stamp indentation on a triangular hole boundary embedded in an elastic infinite body

are the heat flux and the traction function, respectively, along the normal direction $\mathbf{m}$; $\mathbf{n}^T=(\cos\theta,\sin\theta,0)$, $\mathbf{m}^T=(-\sin\theta,\cos\theta,0)$; and θ is the angle measured counterclockwise between the tangent vector $\mathbf{n}$ and the positive x_1-axis (Fig. 2). In this section we consider a material occupying the region $|\varsigma|>1$ as denoted by S^+ and the region $|\varsigma|<1$ by S^-.

4.1 Temperature Field. Like the problem of straight boundary perturbation, the complex function $g'(z)$ can be expressed as

$$g'(z)=g_0'(z)+\varepsilon g_1'(z)+\varepsilon^2 g_2'(z)+\ldots. \tag{4.5}$$

With the definition (4.2), each term $g_i'(z)$ in (4.5) can be rewritten as

$$g_i'(z)=g_i'(z^e+\varepsilon\varphi(\varsigma))=g_i'(z^e)+\varepsilon\varphi(\varsigma)g_i''(z^e)+\frac{1}{2}[\varepsilon\varphi(\varsigma)]^2 g_i'''(z^e)+\ldots. \tag{4.6}$$

Substituting (4.6) into (4.5), we have

$$g'(z)=g_0'(z^e)+\varepsilon[g_1'(z^e)+\varphi(\varsigma)g_0''(z^e)]+\varepsilon^2\left[g_2'(z^e)+\varphi(\varsigma)g_1''(z^e)+\frac{1}{2}\varphi^2(\varsigma)g_0'''(z^e)\right]+\ldots. \tag{4.7}$$

Since $z_t^e=\omega_t(\varsigma)$, we can express $g_i'(z^e)$ in terms of $g_i'(\varsigma)$ as

$$g'(\varsigma)=g_0'(\varsigma)+\varepsilon[g_1'(\varsigma)+\varphi(\varsigma)g_0''(\varsigma)]+\varepsilon^2\left[g_2'(\varsigma)+\varphi(\varsigma)g_1''(\varsigma)+\frac{1}{2}\varphi^2(\varsigma)g_0'''(\varsigma)\right]+\ldots. \tag{4.8}$$

Let an anisotropic body contain an opening as indicated in (4.1) be indented by a rigid stamp under the resultant heat flow $\hat{Q}$ and resultant force $\hat{\mathbf{p}}$ over a segment, which is mapped onto an arc $L=(e^{-i\varphi},e^{i\varphi})$ in the ς-domain. Along the perturbed boundary $z_t=\omega_t(\sigma)+\varepsilon\varphi_t(\sigma)$ with $\sigma=e^{i\vartheta}$ the boundary conditions (4.3) and (4.4) can be rewritten as

$$\frac{dT}{dn}=\frac{d}{dn}2\,\mathrm{Re}[g'(\sigma^+)]=0,\quad \sigma\in L$$

and

$$h_m=\frac{d}{dn}2\,\mathrm{Re}[ikg'(\sigma^+)]=0,\quad \sigma\notin L. \tag{4.9}$$

Substituting (4.8) into (4.9) and comparing the coefficients of ε^λ ($\lambda=0,1,2\ldots$) on both sides, we have

$$\begin{cases}\dfrac{d}{dn}2\,\mathrm{Re}[g_0'(\sigma^+)]=0, & \sigma\in L\\[2mm] \dfrac{d}{dn}2\,\mathrm{Re}[ikg_0'(\sigma^+)]=0, & \sigma\notin L\end{cases}$$

$$\begin{cases}\dfrac{d}{dn}2\,\mathrm{Re}[g_1'(\sigma^+)+\varphi(\sigma^+)g_0''(\sigma^+)]=0, & \sigma\in L\\[2mm] \dfrac{d}{dn}2\,\mathrm{Re}[ik\{g_1'(\sigma^+)+\varphi(\sigma^+)g_0''(\sigma^+)\}]=0, & \sigma\notin L\end{cases} \tag{4.10}$$

$$\vdots$$

In view of $(4.10)_1$, the expression for the zero-order perturbation is identical to the mixed boundary value problems with elliptical boundary whose solution has been found in (Chao and Gao [14]) as

$$g_0''(\varsigma)=\varsigma^{-1}X_0(\varsigma)p_0(\varsigma),\quad \varsigma\in S^+ \tag{4.11}$$

where $X_0(\varsigma)$ is the Plemelj function for the arc given by

$$X_0(\varsigma)=(\varsigma-e^{-i\varphi})^{-1/2}(\varsigma-e^{i\varphi})^{-1/2} \tag{4.12}$$

and $p_0(\varsigma)$ is a polynomial function, which can be determined by the thermal loading condition, expressed as

$$p_0(\varsigma)=\frac{-\hat{Q}}{4\pi\rho}(1+\varsigma) \tag{4.13}$$

with

$$\rho=a\sqrt{\sin^2\vartheta+c^2\cos^2\vartheta}. \tag{4.14}$$

Once $g_0''(\varsigma)$ is obtained, it can be used as a reference to solve the other unknown functions $g_i'(\varsigma)$. The second set of (4.10) can be rewritten as

$$\begin{cases} -\dfrac{i\sigma}{\rho}[g_1''(\sigma^+)+\varphi'(\sigma^+)g_0''(\sigma^+)+\varphi(\sigma^+)g_0'''(\sigma^+)] \\ \quad +\dfrac{i}{\rho\sigma}[\overline{g_1''(\sigma^+)}+\overline{\varphi'(\sigma^+)g_0''(\sigma^+)}+\overline{\varphi(\sigma^+)g_0'''(\sigma^+)}]=0, \quad \sigma\in L \\ \dfrac{k\sigma}{\rho}[g_1''(\sigma^+)+\varphi'(\sigma^+)g_0''(\sigma^+)+\varphi(\sigma^+)g_0'''(\sigma^+)] \\ \quad +\dfrac{k}{\rho\sigma}[\overline{g_1''(\sigma^+)}+\overline{\varphi'(\sigma^+)g_0''(\sigma^+)}+\overline{\varphi(\sigma^+)g_0'''(\sigma^+)}]=0, \quad \sigma\notin L. \end{cases} \tag{4.15}$$

In view of (4.15), the terms $\varphi'(z)g_0''(z)$ and $\varphi(z)g_0'''(z)$ are not holomorphic in S^+ or S^-. In order to employ the analytical continuation theorem, we need the following relationship by differentiating $(4.10)_1$ with respect to σ as

$$2g_0''(\sigma^+)+\sigma g_0'''(\sigma^+)=-\frac{1}{\sigma^3}\overline{g_0'''\left(\frac{1}{\bar{\sigma}}\right)}, \quad \sigma\in L$$

and

$$g_0'''(\sigma^+)=\frac{2}{\sigma^3}\overline{g_0''\left(\frac{1}{\bar{\sigma}}\right)}+\frac{1}{\sigma^4}\overline{g_0'''\left(\frac{1}{\bar{\sigma}}\right)}, \quad \sigma\notin L \tag{4.16}$$

and introducing

$$\theta_1'(\varsigma)=\begin{cases} \varsigma g_1''(\varsigma)+\dfrac{a}{2}\displaystyle\sum_{n=1}^{N}\left\{(a_n+ib_n)(1-ip)\frac{1}{\varsigma^n}\right\}\{-ng_0''(\varsigma)+\varsigma g_0'''(\varsigma)\} \\ \quad +\dfrac{a}{2}\displaystyle\sum_{n=1}^{N}\left\{(a_n+ib_n)(1-i\bar{p})\frac{1}{\varsigma^n}\right\}\varsigma^2\{-ng_0''(\varsigma)+2g_0''(\varsigma)+\varsigma g_0'''(\varsigma)\}, & \varsigma\in S^+ \\ -\dfrac{1}{\varsigma}\overline{g_1''\left(\frac{1}{\bar{\varsigma}}\right)}+\dfrac{a}{2}\displaystyle\sum_{n=1}^{N}\{(a_n-ib_n)(1+ip)\varsigma^n\}\left\{\frac{n}{\varsigma^2}\overline{g_0''\left(\frac{1}{\bar{\varsigma}}\right)}-\frac{2}{\varsigma^2}\overline{g_0''\left(\frac{1}{\bar{\varsigma}}\right)}-\frac{1}{\varsigma^3}\overline{g_0'''\left(\frac{1}{\bar{\varsigma}}\right)}\right\} \\ \quad -\dfrac{a}{2}\displaystyle\sum_{n=1}^{N}\{(a_n-ib_n)(1+i\bar{p})\varsigma^n\}\left\{-n\overline{g_0''\left(\frac{1}{\bar{\varsigma}}\right)}+\frac{1}{\varsigma}\overline{g_0'''\left(\frac{1}{\bar{\varsigma}}\right)}\right\}, & \varsigma\in S^-. \end{cases} \tag{4.17}$$

With the aid of (4.16) and (4.17), Eq. (4.15) can be rearranged to the following Hilbert problem

$$\begin{cases} \theta_1'(\sigma^+)+\theta_1'(\sigma^-)=0, & \sigma\in L \\ \theta_1'(\sigma^+)-\theta_1'(\sigma^-)=0, & \sigma\notin L. \end{cases} \tag{4.18}$$

The first-order perturbation solution to (4.18) is found as

$$\theta_1'(\varsigma)=X_0(\varsigma)p_1(\varsigma), \quad \varsigma\in S^+ \tag{4.19}$$

where the polynomial function $p_1(\varsigma)$, similar to the previous approach, can be determined by the thermal loading condition. Thus, $g_1''(\varsigma)$ can be directly obtained by substituting (4.19) into (4.17). Similarly, the higher-order perturbation solutions $g_i'(\varsigma)$ can also be determined step by step.

4.2 Stress Field. Similar to the problem of straight boundary perturbation, the complex function $\mathbf{f}(z)$ can be expanded into

$$\mathbf{f}(z)=\mathbf{f}_0(z)+\varepsilon\mathbf{f}_1(z)+\varepsilon^2\mathbf{f}_2(z)+\ldots. \tag{4.20}$$

Each term $\mathbf{f}_i(z)$ in (4.20) can be written as

$$\mathbf{f}_i(z)=\mathbf{f}_i(z^e+\varepsilon\varphi(\zeta))=\mathbf{f}_i(z^e)+\varepsilon\varphi(\zeta)\mathbf{f}_i'(z^e)+\frac{1}{2}[\varepsilon\varphi(\zeta)]^2\mathbf{f}_i''(z^e)+\ldots. \tag{4.21}$$

Substituting (4.21) into (4.20), we have

$$\mathbf{f}(z)=\mathbf{f}_0(z^e)+\varepsilon[\mathbf{f}_1(z^e)+\varphi(\varsigma)\mathbf{f}_0'(z^e)]+\varepsilon^2\left[\mathbf{f}_2(z^e)+\varphi(\varsigma)\mathbf{f}_1'(z^e)+\frac{1}{2}\varphi^2(\varsigma)\mathbf{f}_0''(z^e)\right]+\ldots. \tag{4.22}$$

Since $z_\alpha^e=\omega_\alpha(\varsigma)$, we can express $\mathbf{f}_i(z^e)$ in terms of $\mathbf{f}_i(\varsigma)$ as

$$\mathbf{f}(\varsigma)=\mathbf{f}_0(\varsigma)+\varepsilon[\mathbf{f}_1(\varsigma)+\varphi(\varsigma)\mathbf{f}_0'(\varsigma)]+\varepsilon^2\left[\mathbf{f}_2(\varsigma)+\varphi(\varsigma)\mathbf{f}_1'(\varsigma)+\frac{1}{2}\varphi^2(\varsigma)\mathbf{f}_0''(\varsigma)\right]+\ldots. \tag{4.23}$$

Along the boundary $\sigma=e^{i\vartheta}$ the boundary conditions (4.3) and (4.4) are written as

$$\begin{aligned} \frac{d\mathbf{u}}{dn}&=\frac{d}{dn}2\,\mathrm{Re}[\mathbf{A}\mathbf{f}(\sigma^+)+\mathbf{c}g(\sigma^+)]=\hat{\mathbf{u}}_{,n}, \quad \sigma\in L \\ \mathbf{t}_m&=\frac{d\phi}{dn}=\frac{d}{dn}2\,\mathrm{Re}[\mathbf{B}\mathbf{f}(\sigma^+)+\mathbf{d}g(\sigma^+)]=0, \quad \sigma\notin L \end{aligned} \tag{4.24}$$

where

$$\hat{\mathbf{u}}_{,n}(\sigma)=\hat{\mathbf{u}}_{0,n}(\sigma)+\varepsilon\hat{\mathbf{u}}_{1,n}(\sigma)+\varepsilon^2\hat{\mathbf{u}}_{2,n}(\sigma)+\ldots.$$

Substituting (4.23) and (4.8) into (4.24) for $\varsigma\to\sigma^+$ and comparing the coefficients of ε^λ $(\lambda=0,1,2\ldots)$ on both sides of (4.24), we have

$$\begin{cases} \dfrac{d}{dn}2\,\mathrm{Re}[\mathbf{A}\mathbf{f}_0(\sigma^+)+\mathbf{c}g_0(\sigma^+)]=\hat{\mathbf{u}}_{0,n}(\sigma), & \sigma\in L \\ \dfrac{d}{dn}2\,\mathrm{Re}[\mathbf{B}\mathbf{f}_0(\sigma^+)+\mathbf{d}g_0(\sigma^+)]=0, & \sigma\notin L \end{cases}$$

$$\begin{cases} \dfrac{d}{dn}2\,\mathrm{Re}[\mathbf{A}(\mathbf{f}_1(\sigma^+)+\varphi(\sigma^+)\mathbf{f}_0'(\sigma^+))+\mathbf{c}(g_1(\sigma^+)+\varphi(\sigma^+)g_0'(\sigma^+))]=\hat{\mathbf{u}}_{1,n}, & \sigma\in L \\ \dfrac{d}{dn}2\,\mathrm{Re}[\mathbf{B}(\mathbf{f}_1(\sigma^+)+\varphi(\sigma^+)\mathbf{f}_0'(\sigma^+))+\mathbf{d}(g_1(\sigma^+)+\varphi(\sigma^+)g_0'(\sigma^+))]=0, & \sigma\notin L \end{cases} \tag{4.25}$$

$$\vdots$$

Like the problem of straight perturbed boundary, the first set of (4.25) is the equation for the zero-order perturbation which is identical to that for the punch problem with elliptical boundary, whose solution has been found in (Chao and Gao [14]) as

$$\mathbf{f}_0'(\varsigma)=\mathbf{B}^{-1}(\varsigma^{-1}\boldsymbol{\Theta}_0'(\varsigma)-\mathbf{d}g_0'(\varsigma)) \tag{4.26}$$

with

$$\boldsymbol{\Theta}_0'(\varsigma)=\frac{1}{2\pi i}\mathbf{X}(\varsigma)\int_L\frac{1}{t-\varsigma}[\mathbf{X}^+(t)]^{-1}\mathbf{M}\{-\rho\hat{\mathbf{u}}_{0,n}+2\,\mathrm{Im}[(\mathbf{c}-\mathbf{A}\mathbf{B}^{-1}\mathbf{d})tg_0'^+(t)]\}dt+\mathbf{X}(\varsigma)\mathbf{p}_0(\varsigma),\quad \varsigma\in S^+ \tag{4.27}$$

where $\mathbf{X}(\varsigma)$ is the Plemelj function for the arc and $\mathbf{p}_0(\varsigma)$ is a polynomial function which can be determined by the loading conditions. Once $\mathbf{f}_0(\varsigma)$ is obtained, it can be used as a reference to find the other unknown functions $\mathbf{f}_i(\varsigma)$.

The second set of (4.25) can be expressed as

$$\begin{aligned}&\sigma^2\{\mathbf{A}[\mathbf{f}_1'(\sigma^+)+\varphi(\sigma^+)\mathbf{f}_0''(\sigma^+)+\varphi'(\sigma^+)\mathbf{f}_0'(\sigma^+)]\\&\quad+\mathbf{c}[g_1'(\sigma^+)+\varphi(\sigma^+)g_0''(\sigma^+)+\varphi'(\sigma^+)g_0''(\sigma^+)]\}\\&\quad-\{\overline{\mathbf{A}}[\overline{\mathbf{f}_1'(\sigma^+)}+\overline{\varphi(\sigma^+)}\,\overline{\mathbf{f}_0''(\sigma^+)}+\overline{\varphi'(\sigma^+)}\,\overline{\mathbf{f}_0'(\sigma^+)}]\\&\quad+\overline{\mathbf{c}}[\overline{g_1'(\sigma^+)}+\overline{\varphi(\sigma^+)}\,\overline{g_0''(\sigma^+)}+\overline{\varphi'(\sigma^+)}\,\overline{g_0''(\sigma^+)}]\}\\&\quad=i\rho\sigma\hat{\mathbf{u}}_{1,n},\quad \sigma\in L\end{aligned} \tag{4.28}$$

and

$$\begin{aligned}&-\sigma^2\{\mathbf{B}[\mathbf{f}_1'(\sigma^+)+\varphi(\sigma^+)\mathbf{f}_0''(\sigma^+)+\varphi'(\sigma^+)\mathbf{f}_0'(\sigma^+)]\\&\quad+\mathbf{d}[g_1'(\sigma^+)+\varphi(\sigma^+)g_0''(\sigma^+)+\varphi'(\sigma^+)g_0''(\sigma^+)]\}\\&\quad+\{\overline{\mathbf{B}}[\overline{\mathbf{f}_1'(\sigma^+)}+\overline{\varphi(\sigma^+)}\,\overline{\mathbf{f}_0''(\sigma^+)}+\overline{\varphi'(\sigma^+)}\,\overline{\mathbf{f}_0'(\sigma^+)}]\\&\quad+\overline{\mathbf{d}}[\overline{g_1'(\sigma^+)}+\overline{\varphi(\sigma^+)}\,\overline{g_0''(\sigma^+)}+\overline{\varphi'(\sigma^+)}\,\overline{g_0''(\sigma^+)}]\}\\&\quad=0,\quad \sigma\notin L.\end{aligned}$$

Unlike the problem of straight boundary perturbation, due to the form of $\varphi_\alpha(\varsigma)$ in (4.2) $\varphi(z)\mathbf{f}_0''(z)$ and $\varphi'(z)\mathbf{f}_0'(z)$ in (4.28) will not be holomorphic in S^+ or S^-. To overcome this difficulty, one needs the additional relationships (see Appendix) such that (4.28) can be rewritten as the following Hilbert problem of vector form

$$\begin{cases} \boldsymbol{\Theta}_1'(\sigma^+)-\boldsymbol{\Theta}_1'(\sigma^-)=0, & \sigma\notin L \\ \boldsymbol{\Theta}_1'(\sigma^+)+\mathbf{M}\overline{\mathbf{M}}^{-1}\boldsymbol{\Theta}_1'(\sigma^-)=-i\mathbf{M}\tilde{\mathbf{u}}_1(\sigma), & \sigma\in L \end{cases} \tag{4.29}$$

where

$$\mathbf{M}=-i\mathbf{B}\mathbf{A}^{-1},$$

$$\tilde{\mathbf{u}}_1(\sigma)=-i\rho\hat{\mathbf{u}}_{1,n}+\frac{a}{2}\sum_{n=1}^{N}\{(a_n-ib_n)(1+ip)\sigma^n\}i\rho\left[\frac{n-1}{\sigma}\hat{\mathbf{u}}_{0,n}+\hat{\mathbf{u}}_{0,n}'\right]-\frac{a}{2}\sum_{n=1}^{N}\left\{(a_n+ib_n)(1-i\overline{p})\frac{1}{\sigma^n}\right\}i\rho[(1-n)\sigma\hat{\mathbf{u}}_{0,n}+\sigma^2\hat{\mathbf{u}}_{0,n}']+2i\,\mathrm{Im}\left\{(\mathbf{c}-\mathbf{A}\mathbf{B}^{-1}\mathbf{d})\left[\sigma g_1'(\sigma^+)+\frac{a}{2}\sum_{n=1}^{N}(a_n+ib_n)(1-ip)\frac{1}{\sigma^n}[\sigma g_0''(\sigma^+)-ng_0'(\sigma^+)]+\frac{a}{2}\sum_{n=1}^{N}(a_n+ib_n)(1-i\overline{p})\frac{1}{\sigma^n}((2-n)\sigma^2g_0'(\sigma^+)+\sigma^3g_0''(\sigma^+))\right]\right\}.$$

The solution to (4.29) is found as

$$\boldsymbol{\Theta}_1'(\varsigma)=\frac{-1}{2\pi}\mathbf{X}(\varsigma)\int_L\frac{1}{t-\varsigma}[\mathbf{X}^+(t)]^{-1}\mathbf{M}\tilde{\mathbf{u}}_1(t)dt+\mathbf{X}(\varsigma)\mathbf{p}_1(\varsigma),\quad \varsigma\in S^+ \tag{4.30}$$

where the polynomial vector can be determined by the loading conditions. Thus $\boldsymbol{\Theta}_1'(\varsigma)$ is completely solved and the first-order perturbation solution $\mathbf{f}_1'(\varsigma)$ can be obtained by substituting (4.30) into $(A3)_1$. The higher-order perturbation solutions $\mathbf{f}_i'(\varsigma)$ can be also solved in a similar way.

5 Examples

In order to demonstrate the use of the present approach and to understand clearly the physical behavior of the indentation problems, numerical examples associated with a cosine wave-shaped boundary and a triangular hole boundary will be discussed in this section.

5.1 A Rigid Flat Punch on a Cosine Wave-Shaped Boundary. We first consider a rigid punch indenting into the cosine wave-shaped surface of an anisotropic elastic half-plane by a total resultant force $\hat{\mathbf{p}}=(0,p,0)$ and a resultant heat flow $\hat{Q}$ (see Fig. 1). The wave-shaped surface is slightly perturbed from a straight line by a small amount ε in amplitude represented as

$$x_2=\varepsilon\varphi(x_1),\quad \varphi(x_1)=\cos x_1. \tag{5.1}$$

The material properties considered in the present study are chosen as

$$E_{11}=144.8\ \text{Gpa},\quad E_{22}=E_{33}=9.7\ \text{Gpa},$$

$$G_{12}=G_{23}=G_{13}=4.1\ \text{Gpa},$$

$$\nu_{12}=\nu_{23}=\nu_{13}=0.3,\quad \alpha_{11}=-0.3\times10^{-6}\ \text{K}^{-1},$$

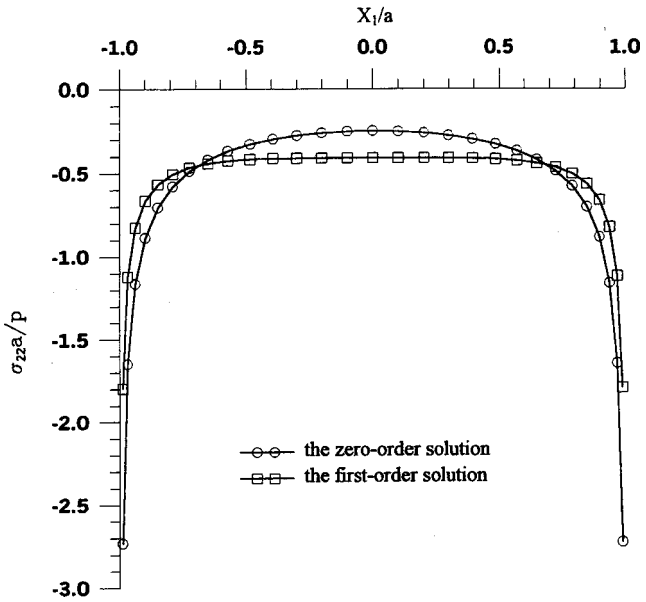

Fig. 3 The normal contact stress along a cosine wave-shaped surface indented by a rigid stamp with $\lambda^*=-0.5$

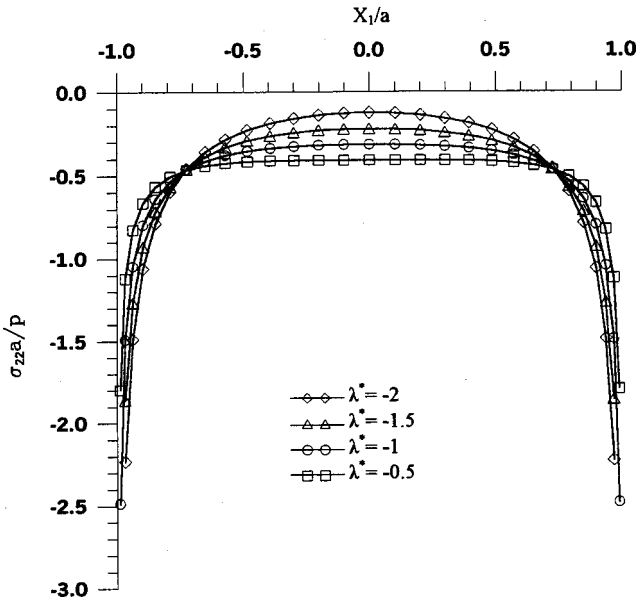

Fig. 4 The normal contact stress along a cosine wave-shaped surface indented by a rigid stamp for different values of λ^*

$$\alpha_{22}=\alpha_{33}=28.1\times10^{-6}\ \ \mathrm{K}^{-1}, \tag{5.2}$$

$$k_{11}=4.62\ \ \mathrm{Wm}^{-1}\,\mathrm{K}^{-1},\quad k_{22}=k_{33}=0.72\ \ \mathrm{Wm}^{-1}\,\mathrm{K}^{-1}.$$

During the indentation, we assume that the punch is completely adhered to the half-plane over the contact region $|x_1|\leq a$ in such a way that no slip occurs. Based on this assumption, the displacement of the surface of the half-plane is given as

$$\hat{\mathbf{u}}(\tilde{z})=(c+\varepsilon\cos x_1))\mathbf{i}_2 \tag{5.3}$$

where $\mathbf{i}_2=(010)^T$ and c is the relative depth of indentation.

For the purpose of clearly expressing the effect of material properties, geometric configuration and applied loading on the contact stress, the nondimensional parameter λ^* defined as

$$\lambda^*=\frac{\alpha_{11}\hat{Q}E_{11}a}{k_{11}p} \tag{5.4}$$

is used which must be properly chosen such that the condition of a negative (compressive) contact stress is satisfied. In the present case with $\varepsilon=0.1$, perfect contact is found to maintain throughout the punch face as λ^* ranges from -4.965 to 0.020 up to the first-order perturbation solution. When λ^* is beyond this region, either separation to occur near the ends of the punch or imperfect contact to occur at the central region will be predicted (Comninou et al. [10]). Both the zero-order and first-order perturbation solutions for the contact stress $\sigma_{22}a/p$ with $\lambda^*=-0.5$ are displayed in Fig. 3 which shows that the stress singularity is found near the ends of a rigid stamp. We also observed that the contact stress for the first-order perturbation solution with cosine wave-shaped surface is larger (or less) than that for the zero-order perturbation solution with flat surface near the central part (or the edge) of a rigid punch. The contact stress under the punch face for different values of λ^* is shown in Fig. 4. The result indicates that the contact stress near the center of the punch face decreases with increasing the value of $-\lambda^*$. Based on this finding, we anticipate that a central region of imperfect contact will be developed for $\lambda^*<-4.965$. On the other hand, if $p/\hat{Q}$ is sufficiently large (or λ^* approaches zero), perfect contact will be maintained throughout the punch face for either direction of heat flow.

5.2 A Rigid Stamp on a Triangular Hole Boundary With Rounded Corners. As a second example we consider that an equilateral triangular hole, which is embedded in an infinite body having the material properties listed in (5.2), represented by $N=2$, $a_1=b_1=b_2=0$, $a_2=1$, $\varepsilon=0.25$ and $a=c=1$ in (4.1) is subjected to a resultant force $\hat{\mathbf{p}}=(p,0,0)$ and a resultant heat flow $\hat{Q}$ approached from the negative x_1-axis along the segment $\phi=30°$ (see Fig. 2). Since the stamp completely adheres to the hole boundary, the displacement along the contact region will be a constant value, i.e., $\hat{\mathbf{u}}(\tilde{z})=\text{const}$. Note that this assumption is different from that given in (5.3). In that case the punch profile differs from the wavy surface on initial contact, while in this example, the surfaces of the stamp and the hole boundary are assumed to be perfectly matched on initial contact as well as during the subsequent indentation. The nondimensional parameter λ^* for the problem with triangular hole boundary is defined as

$$\lambda^*=\frac{\alpha_{11}E_{11}\hat{Q}a(c\sin\varphi-\varepsilon\sin 2\varphi)}{k_{11}p}. \tag{5.5}$$

In the present case, perfect contact is found to maintain throughout the punch face as λ^* ranges from -0.712 to 0.013 up to the first-order perturbation solution. The first-order perturbation solution for the contact stress $\sigma_{mm}/(p/2a(c\sin\varphi-\varepsilon\sin 2\varphi))$ with $\lambda^*=-0.3$ is shown in Fig. 5 that also reveals the stress singularity behavior at the ends of the rigid stamp. The contact stress for different values of λ^* is displayed in Fig. 6 which indicates that imperfect contact will be developed at $\varphi=\pm15°$ if the value of $-\lambda^*$ increases and exceeds 0.712. On the other hand, perfect contact will be maintained throughout the punch face if $p/\hat{Q}$ is sufficiently large for either direction of heat flow.

6 Conclusion

The mixed boundary value problems of two-dimensional anisotropic thermoelasticity with perturbed boundaries are solved in this paper. The boundary surface considered in this work is the one perturbed by a straight line or an ellipse. Based on the Stroh's formulation, analytical continuation theorem, conformal mapping function, and perturbation technique, a general solution up to the

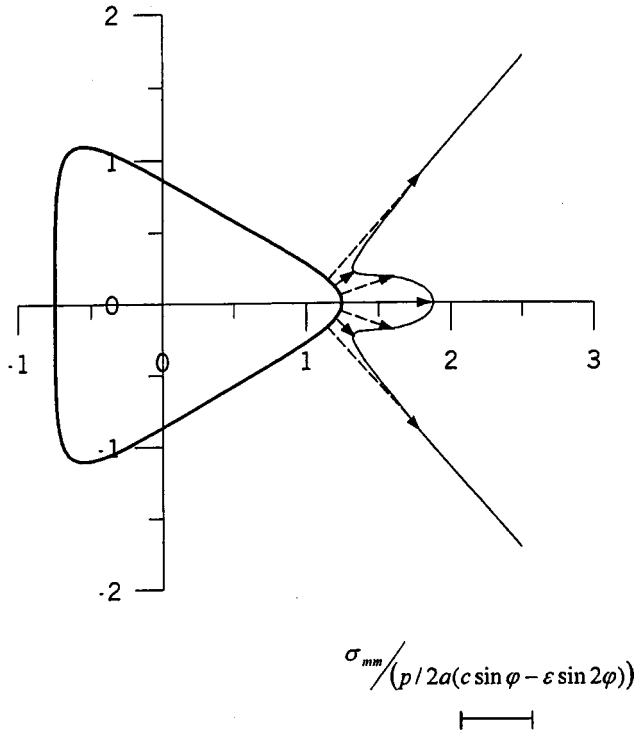

Fig. 5 The normal contact stress along an equilateral triangular hole boundary indented by a rigid stamp with $\lambda^*=-0.3$

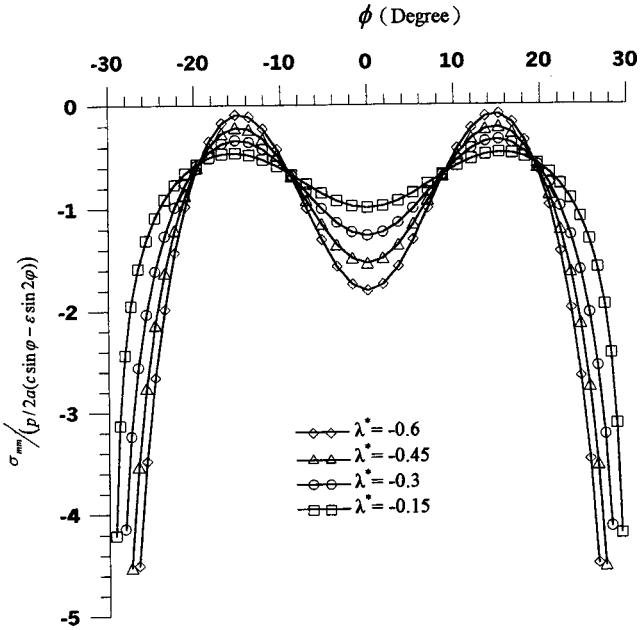

Fig. 6 The normal contact stress along an equilateral triangular hole boundary indented by a rigid stamp for different values of λ^*

first-order perturbation has been solved explicitly. Two numerical examples of rigid stamp indentation on a perturbed boundary of an anisotropic elastic body are solved completely and shown in graphic form. As discussed in the preceding chapter, in order to make an analytical solution accessible in this work, we assume that the stamp is considered to completely adhere to the surface of an elastic body over the contact region during the indentation. In reality, when a rigid indenter is pressed into a half-plane (or a triangular hole boundary), the contact area on the half-plane will not be stationary, but will move over the half-plane with time. For this case the heat conduction problem will be transient and needs to be posed in a moving frame of reference. The correct formulation of such physical problems requires an incremental treatment that is beyond the scope of the present study.

Acknowledgments

The authors would like to thank the support by National Science Council, Republic of China, through Grant No. NSC 90-2212-E-011-062.

Appendix

In order to obtain the Hilbert problem given in (4.29), we first substitute (4.2) into $(4.28)_2$ as

$$-\sigma[\mathbf{Bf}_1'(\sigma^+)+\mathbf{d}g_1'(\sigma^+)]+\frac{1}{\sigma}[\overline{\mathbf{Bf}_1'(\sigma^+)}+\overline{\mathbf{d}g_1'(\sigma^+)}]-\frac{a}{2}\sum_{n=1}^{N}\left\{(a_n-ib_n)(1+ip)\sigma^{n+1}+(a_n+ib_n)(1-ip)\frac{1}{\sigma^{n-1}}\right\}[\mathbf{Bf}_0''(\sigma^+)$$
$$+\mathbf{d}g_0''(\sigma^+)]+\frac{a}{2}\sum_{n=1}^{N}\left\{(a_n+ib_n)(1-i\overline{p})\overline{\sigma}^{n+1}+(a_n-ib_n)(1+i\overline{p})\frac{1}{\overline{\sigma}^{n-1}}\right\}[\overline{\mathbf{Bf}_0''(\sigma^+)}+\overline{\mathbf{d}g_0''(\sigma^+)}]$$
$$-\frac{a}{2}\sum_{n=1}^{N}\left\{(a_n-ib_n)(1+ip)n\sigma^n+(a_n+ib_n)(1-ip)\frac{-n}{\sigma^n}\right\}[\mathbf{Bf}_0'(\sigma^+)+\mathbf{d}g_0'(\sigma^+)]+\frac{a}{2}\sum_{n=1}^{N}\left\{(a_n+ib_n)(1-i\overline{p})n\overline{\sigma}^n\right.$$
$$\left.+(a_n-ib_n)(1+i\overline{p})\frac{-n}{\overline{\sigma}^n}\right\}[\overline{\mathbf{Bf}_0'(\sigma^+)}+\overline{\mathbf{d}g_0'(\sigma^+)}]=0,\quad \sigma\notin L. \tag{A1}$$

Differentiating $(4.25)_1$ with respect to σ yields

$$[\mathbf{Af}_0''(\sigma^+)+\mathbf{c}g_0''(\sigma^+)]=\frac{-2}{\sigma^3}\left[\overline{\mathbf{A}}\overline{\mathbf{f}_0'\left(\frac{1}{\overline{\sigma}}\right)}+\overline{\mathbf{c}}\overline{g_0'\left(\frac{1}{\overline{\sigma}}\right)}\right]-\frac{1}{\sigma^4}\left[\overline{\mathbf{A}}\overline{\mathbf{f}_0''\left(\frac{1}{\overline{\sigma}}\right)}+\overline{\mathbf{c}}\overline{g_0''\left(\frac{1}{\overline{\sigma}}\right)}\right]+i\rho\left[\frac{-1}{\sigma^2}\hat{\mathbf{u}}_{0,n}+\frac{1}{\sigma}\hat{\mathbf{u}}_{0,n}'\right],\quad \sigma\in L$$

$$\left[\overline{\mathbf{A}}\overline{\mathbf{f}_0''\left(\frac{1}{\overline{\sigma}}\right)}+\overline{\mathbf{c}}\overline{g_0''\left(\frac{1}{\overline{\sigma}}\right)}\right]=-\sigma^4[\mathbf{Af}_0''(\sigma^+)+\mathbf{c}g_0''(\sigma^+)]-2\sigma^3[\mathbf{Af}_0'(\sigma^+)+\mathbf{c}g_0'(\sigma^+)]+i\rho[\sigma^2\hat{\mathbf{u}}_{0,n}+\sigma^3\hat{\mathbf{u}}_{0,n}'],\quad \sigma\in L$$

and

$$
\begin{aligned}
&[\mathbf{B}\mathbf{f}_0''(\sigma^+)+\mathbf{d}g_0''(\sigma^+)]=\frac{-2}{\sigma^3}\left[\overline{\mathbf{B}}\overline{\mathbf{f}_0'\left(\frac{1}{\bar{\sigma}}\right)}+\overline{\mathbf{d}}\overline{g_0'\left(\frac{1}{\bar{\sigma}}\right)}\right]-\frac{1}{\sigma^4}\left[\overline{\mathbf{B}}\overline{\mathbf{f}_0''\left(\frac{1}{\bar{\sigma}}\right)}+\overline{\mathbf{d}}\overline{g_0''\left(\frac{1}{\bar{\sigma}}\right)}\right],\quad \sigma\notin L\\
&\left[\overline{\mathbf{B}}\overline{\mathbf{f}_0''\left(\frac{1}{\bar{\sigma}}\right)}+\overline{\mathbf{d}}\overline{g_0''\left(\frac{1}{\bar{\sigma}}\right)}\right]=-\sigma^4[\mathbf{B}\mathbf{f}_0''(\sigma^+)+\mathbf{d}g_0''(\sigma^+)]-2\sigma^3[\mathbf{B}\mathbf{f}_0'(\sigma^+)+\mathbf{d}g_0'(\sigma^+)],\quad \sigma\notin L
\end{aligned}
\tag{A2}
$$

Based on the relationship expressed in the last two equations of (*A*2), (*A*1) allows us to introduce a new holomorphic function expressed as

$$
\boldsymbol{\Theta}_1'(\varsigma)=\begin{cases}
\varsigma[\mathbf{B}\mathbf{f}_1'(\varsigma)+\mathbf{d}g_1'(\varsigma)]+\dfrac{a}{2}\displaystyle\sum_{n=1}^{N}\left\{(a_n+ib_n)(1-ip)\frac{1}{\varsigma^{n-1}}\right\}[\mathbf{B}\mathbf{f}_0''(\varsigma)+\mathbf{d}g_0''(\varsigma)]\\
\quad-\dfrac{a}{2}\displaystyle\sum_{n=1}^{N}\left\{(a_n+ib_n)(1-i\bar{p})\frac{1}{\varsigma^{n+1}}\right\}\{-\varsigma^4[\mathbf{B}\mathbf{f}_0''(\varsigma)+\mathbf{d}g_0''(\varsigma)]-2\varsigma^3[\mathbf{B}\mathbf{f}_0'(\varsigma)+\mathbf{d}g_0'(\varsigma)]\}\\
\quad+\dfrac{a}{2}\displaystyle\sum_{n=1}^{N}\left\{(a_n+ib_n)(1-ip)\frac{-n}{\varsigma^{n}}\right\}[\mathbf{B}\mathbf{f}_0'(\varsigma)+\mathbf{d}g_0'(\varsigma)]-\frac{a}{2}\sum_{n=1}^{N}\left\{(a_n+ib_n)(1-i\bar{p})\frac{n}{\varsigma^{n}}\right\}\varsigma^2[\mathbf{B}\mathbf{f}_0'(\varsigma)+\mathbf{d}g_0'(\varsigma)],\\
\quad\varsigma\in S^+\\
\dfrac{1}{\varsigma}\left[\overline{\mathbf{B}}\overline{\mathbf{f}_1'\left(\frac{1}{\varsigma}\right)}+\overline{\mathbf{d}}\overline{g_1'\left(\frac{1}{\varsigma}\right)}\right]+\dfrac{a}{2}\displaystyle\sum_{n=1}^{N}\{(a_n-ib_n)(1+i\bar{p})\varsigma^{n-1}\}\left[\overline{\mathbf{B}}\overline{\mathbf{f}_0''\left(\frac{1}{\varsigma}\right)}+\overline{\mathbf{d}}\overline{g_0''\left(\frac{1}{\varsigma}\right)}\right]\\
\quad-\dfrac{a}{2}\displaystyle\sum_{n=1}^{N}\{(a_n-ib_n)(1+ip)\varsigma^{n+1}\}\left\{-\frac{2}{\varsigma^3}\left[\overline{\mathbf{B}}\overline{\mathbf{f}_0'\left(\frac{1}{\varsigma}\right)}+\overline{\mathbf{d}}\overline{g_0'\left(\frac{1}{\varsigma}\right)}\right]-\frac{1}{\varsigma^4}\left[\overline{\mathbf{B}}\overline{\mathbf{f}_0''\left(\frac{1}{\varsigma}\right)}+\overline{\mathbf{d}}\overline{g_0''\left(\frac{1}{\varsigma}\right)}\right]\right\}\\
\quad+\dfrac{a}{2}\displaystyle\sum_{n=1}^{N}\{(a_n-ib_n)(1+i\bar{p})(-n)\varsigma^{n}\}\left[\overline{\mathbf{B}}\overline{\mathbf{f}_0'\left(\frac{1}{\varsigma}\right)}+\overline{\mathbf{d}}\overline{g_0'\left(\frac{1}{\varsigma}\right)}\right]-\frac{a}{2}\sum_{n=1}^{N}\{(a_n-ib_n)(1+ip)n\varsigma^{n}\}\frac{1}{\varsigma^2}\left[\overline{\mathbf{B}}\overline{\mathbf{f}_0'\left(\frac{1}{\varsigma}\right)}+\overline{\mathbf{d}}\overline{g_0'\left(\frac{1}{\varsigma}\right)}\right],\\
\quad\varsigma\in S^-
\end{cases}
\tag{A3}
$$

On the other hand, substitution of (4.2) into $(4.28)_1$ and using the first two equations of (*A*2) gives

$$
\begin{aligned}
&-\mathbf{A}\left\{\sigma\mathbf{f}_1'(\sigma^+)+\frac{a}{2}\sum_{n=1}^{N}\left[(a_n+ib_n)(1-ip)\frac{1}{\sigma^n}\right][\sigma\mathbf{f}_0''(\sigma^+)-n\mathbf{f}_0'(\sigma^+)]+\frac{a}{2}\sum_{n=1}^{N}\left[(a_n+ib_n)(1-i\bar{p})\frac{1}{\sigma^n}\right][(2-n)\sigma^2\mathbf{f}_0'(\sigma^+)+\sigma^3\mathbf{f}_0''(\sigma^+)]\right\}\\
&\quad-\mathbf{c}\left\{\sigma g_1'(\sigma^+)+\frac{a}{2}\sum_{n=1}^{N}\left[(a_n+ib_n)(1-ip)\frac{1}{\sigma^n}\right][\sigma g_0''(\sigma^+)-ng_0'(\sigma^+)]+\frac{a}{2}\sum_{n=1}^{N}\left[(a_n+ib_n)(1-i\bar{p})\frac{1}{\sigma^n}\right][(2-n)\sigma^2 g_0'(\sigma^+)\right.\\
&\quad\left.+\sigma^3 g_0'''(\sigma^+)]\right\}+\overline{\mathbf{A}}\left\{\frac{1}{\sigma}\overline{\mathbf{f}_1'\left(\frac{1}{\bar{\sigma}}\right)}+\frac{a}{2}\sum_{n=1}^{N}[(a_n-ib_n)(1+ip)\sigma^n]\left[\frac{2-n}{\sigma^2}\overline{\mathbf{f}_0'\left(\frac{1}{\bar{\sigma}}\right)}+\frac{1}{\sigma^3}\overline{\mathbf{f}_0''\left(\frac{1}{\bar{\sigma}}\right)}\right]+\frac{a}{2}\sum_{n=1}^{N}[(a_n-ib_n)(1+i\bar{p})\sigma^n]\right.\\
&\quad\left.\times\left[\frac{1}{\sigma}\overline{\mathbf{f}_0''\left(\frac{1}{\bar{\sigma}}\right)}-n\overline{\mathbf{f}_0'\left(\frac{1}{\bar{\sigma}}\right)}\right]\right\}+\overline{\mathbf{c}}\left\{\frac{1}{\sigma}\overline{g_1'\left(\frac{1}{\bar{\sigma}}\right)}+\frac{a}{2}\sum_{n=1}^{N}[(a_n-ib_n)(1+ip)\sigma^n]\left[\frac{2-n}{\sigma^2}\overline{g_0'\left(\frac{1}{\bar{\sigma}}\right)}+\frac{1}{\sigma^3}\overline{g_0''\left(\frac{1}{\bar{\sigma}}\right)}\right]\right.\\
&\quad\left.+\frac{a}{2}\sum_{n=1}^{N}[(a_n-ib_n)(1+i\bar{p})\sigma^n]\left[\frac{1}{\sigma}\overline{g_0''\left(\frac{1}{\bar{\sigma}}\right)}-n\overline{g_0'\left(\frac{1}{\bar{\sigma}}\right)}\right]\right\}-\frac{a}{2}\sum_{n=1}^{N}[(a_n-ib_n)(1+ip)\sigma^n]i\rho\left[\frac{n-1}{\sigma}\hat{\mathbf{u}}_{0,n}+\hat{\mathbf{u}}_{0,n}'\right]\\
&\quad+\frac{a}{2}\sum_{n=1}^{N}\left[(a_n+ib_n)(1-i\bar{p})\frac{1}{\sigma^n}\right]i\rho[(1-n)\sigma\hat{\mathbf{u}}_{0,n}+\sigma^2\hat{\mathbf{u}}_{0,n}']=-i\rho\hat{\mathbf{u}}_{1,n},\quad \sigma\in L.
\end{aligned}
\tag{A4}
$$

Furthermore, Eq. (*A*3) can be rearranged as

$$
\begin{aligned}
&\sigma\mathbf{f}_1'(\sigma^+)+\frac{a}{2}\sum_{n=1}^{N}\left[(a_n+ib_n)(1-ip)\frac{1}{\sigma^n}\right][\sigma\mathbf{f}_0''(\sigma^+)-n\mathbf{f}_0'(\sigma^+)]+\frac{a}{2}\sum_{n=1}^{N}\left[(a_n+ib_n)(1-i\bar{p})\frac{1}{\sigma^n}\right][(2-n)\sigma^2\mathbf{f}_0'(\sigma^+)+\sigma^3\mathbf{f}_0''(\sigma^+)]\\
&\quad=\mathbf{B}^{-1}\left\{\boldsymbol{\Theta}_1'(\sigma^+)-\mathbf{d}\left(\sigma g_1'(\sigma^+)+\frac{a}{2}\sum_{n=1}^{N}\left[(a_n+ib_n)(1-ip)\frac{1}{\sigma^n}\right][\sigma g_0''(\sigma^+)-ng_0'(\sigma^+)]\right.\right.\\
&\quad\left.\left.+\frac{a}{2}\sum_{n=1}^{N}\left[(a_n+ib_n)(1-i\bar{p})\frac{1}{\sigma^n}\right][(2-n)\sigma^2 g_0'(\sigma^+)+\sigma^3 g_0''(\sigma^+)]\right)\right\}
\end{aligned}
$$

and

$$\frac{1}{\sigma}\overline{\mathbf{f}_1'\left(\frac{1}{\bar{\sigma}}\right)}+\frac{a}{2}\sum_{n=1}^{N}\left[(a_n-ib_n)(1+i\bar{p})\sigma^n\right]\left[\frac{1}{\sigma}\overline{\mathbf{f}_0''\left(\frac{1}{\bar{\sigma}}\right)}-n\overline{\mathbf{f}_0'\left(\frac{1}{\bar{\sigma}}\right)}\right]+\frac{a}{2}\sum_{n=1}^{N}\left[(a_n-ib_n)(1+ip)\sigma^n\right]\left[\frac{2-n}{\sigma^2}\overline{\mathbf{f}_0'\left(\frac{1}{\bar{\sigma}}\right)}+\frac{1}{\sigma^3}\overline{\mathbf{f}_0''\left(\frac{1}{\bar{\sigma}}\right)}\right]$$

$$=\bar{\mathbf{B}}^{-1}\left\{\boldsymbol{\Theta}_1'(\sigma^-)-\bar{\mathbf{d}}\left(\frac{1}{\sigma}\overline{g_1'\left(\frac{1}{\bar{\sigma}}\right)}+\frac{a}{2}\sum_{n=1}^{N}\left[(a_n-ib_n)(1+i\bar{p})\sigma^n\right]\left[\frac{1}{\sigma}\overline{g_0''\left(\frac{1}{\bar{\sigma}}\right)}-n\overline{g_0'\left(\frac{1}{\bar{\sigma}}\right)}\right]\right.\right.$$

$$\left.\left.+\frac{a}{2}\sum_{n=1}^{N}\left[(a_n-ib_n)(1+ip)\sigma^n\right]\left[\frac{2-n}{\sigma^2}\overline{g_0'\left(\frac{1}{\bar{\sigma}}\right)}+\frac{1}{\sigma^3}\overline{g_0''\left(\frac{1}{\bar{\sigma}}\right)}\right]\right)\right\}. \tag{A5}$$

With the aid of (*A*5), (*A*1) and (*A*4) can be rewritten as the following Hilbert problem of vector form given in (4.29).

References

[1] Fan, H., and Keer, L. M., 1994, ''Two-Dimensional Contact on an Anisotropic Elastic Half-Space,'' ASME J. Appl. Mech., **61**, pp. 250–255.

[2] Eshelby, J. D., Read, W. T., and Shockley, W., 1953, ''Anisotropic Elasticity With Applications to Dislocation Theory,'' Acta Metall., **1**, pp. 251–259.

[3] Muskhelishvili, N. I., 1953, *Some Basic Problems of Mathematical Theory of Elasticity*, P. Noordhoff, Groningen.

[4] Fan, C. W., and Hwu, C., 1998, ''Rigid Stamp Indentation on a Curvilinear Hole Boundary of an Anisotropic Elastic Body,'' ASME J. Appl. Mech., **65**, pp. 389–397.

[5] Hwu, C., and Fan, C. W., 1998, ''Mixed Boundary-Value Problems of Two-Dimensional Anisotropic Elasticity With Perturbed Boundaries,'' Proc. R. Soc. London, Ser. A, **454**, pp. 1269–1282.

[6] Barber, J. R., 1973, ''Indentation of the Semi-Infinite Elastic Solid by a Hot Sphere,'' Int. J. Mech. Sci., **15**, pp. 813–819.

[7] Barber, J. R., 1978, ''Contact Problems Involving a Cooled Punch,'' J. Elast., **8**, pp. 404–423.

[8] Clements, D. L., and Toy, G. D., 1976, ''Two Contact Problems in an Anisotropic Thermoelasticity,'' J. Elast., **6**, pp. 137–147.

[9] Panek, C., and Dundurs, J., 1979, ''Thermoelastic Contact Between Bodies With Wavy Surfaces,'' ASME J. Appl. Mech., **46**, pp. 854–860.

[10] Comninou, M., Barber, J. R., and Dundurs, J., 1981, ''Heat Conduction Through a Flat Punch,'' ASME J. Appl. Mech., **48**, pp. 871–875.

[11] Stroh, A. N., 1958, ''Dislocations and Cracks in Anisotropic Elasticity,'' Philos. Mag., **7**, pp. 625–646.

[12] Ting, T. C. T., 1996, *Anisotropic Elasticity—Theory and Applications*, Oxford Science Publications, New York.

[13] Chao, C. K., Wu, S. P., and Kao, B., 1999, ''Thermoelastic Contact Between a Flat Punch and an Anisotropic Half-Space,'' ASME J. Appl. Mech., **66**, pp. 548–552.

[14] Chao, C. K., and Gao, B., 2001, ''Mixed Boundary-Valued Problems of Two-Dimensional Thermoelasticity With Elliptic Boundaries,'' Int. J. Solids Struct., **38**, pp. 5975–5994.

Three-Dimensional Green's Functions in Anisotropic Elastic Bimaterials With Imperfect Interfaces

E. Pan[1]
Structures Technology, Inc.,
543 Keisler Drive, Suite 204,
Cary, NC 27511
Mem. ASME

In this paper, three-dimensional Green's functions in anisotropic elastic bimaterials with imperfect interface conditions are derived based on the extended Stroh formalism and the Mindlin's superposition method. Four different interface models are considered: perfect-bond, smooth-bond, dislocation-like, and force-like. While the first one is for a perfect interface, other three models are for imperfect ones. By introducing certain modified eigenmatrices, it is shown that the bimaterial Green's functions for the three imperfect interface conditions have mathematically similar concise expressions as those for the perfect-bond interface. That is, the physical-domain bimaterial Green's functions can be obtained as a sum of a homogeneous full-space Green's function in an explicit form and a complementary part in terms of simple line-integrals over $[0,\pi]$ suitable for standard numerical integration. Furthermore, the corresponding two-dimensional bimaterial Green's functions have been also derived analytically for the three imperfect interface conditions. Based on the bimaterial Green's functions, the effects of different interface conditions on the displacement and stress fields are discussed. It is shown that only the complementary part of the solution contributes to the difference of the displacement and stress fields due to different interface conditions. Numerical examples are given for the Green's functions in the bimaterials made of two anisotropic half-spaces. It is observed that different interface conditions can produce substantially different results for some Green's stress components in the vicinity of the interface, which should be of great interest to the design of interface. Finally, we remark that these bimaterial Green's functions can be implemented into the boundary integral formulation for the analysis of layered structures where imperfect bond may exist. [DOI: 10.1115/1.1546243]

Introduction

Interface modeling has been the subject of numerous studies in material science and composite structure. The importance of researches in this topic cannot be overemphasized as it is directly related to the prediction of the overall material properties, delamination, transmission of force, etc. (see, e.g., [1–13]). The most ideal interface model, as is well known, is the so-called perfect-bond interface where the displacements and tractions are continuous across the interface. However, interfaces are seldom perfect, and therefore various imperfect models have been introduced, such as the three-phase and linear spring-like models (see, i.e., [14–16]). Although these models are more capable of representing the imperfect interface, the associated Green's functions are very difficult to derive ([14–17]). Perhaps the most frequently studied imperfect interface model is the smooth-bond interface where the normal components of the displacement and traction are continuous across the interface while the shear traction components are zero on the interface from both sides of the bimaterials (see, e.g., [1,2,18]). This model is much simpler than the three-phase and linear spring-like models, and has been used to describe the connection between two materials at elevated temperature ([17]), and to model the bone implants in biomechanics ([19]). Recently, Shuvalov and Gorkunova [18] studied the corresponding wave propagation in anisotropic bimaterials with smooth-bond interface where they found certain special features associated with the smooth-bond interface. Besides various homogeneous interface models mentioned above, Ru [20,21] has recently proposed an inhomogeneously imperfect interface model where the interface parameters are functions of the position variable along the interface, instead of constants along the whole interface for the homogeneous case.

While various interface-related studies have been carried out for two-dimensional deformation problems, relatively very few literatures are available for the corresponding three-dimensional deformations, especially with a planar interface. An apparent reason is that most three-dimensional problems are complicated and need to be solved numerically. Since singular stress field is usually associated with problems involving interface, a more suitable numerical tool would be the boundary integral equation method (i.e., [22]). However, successful application of the boundary integral equation method depends upon the variability of the related Green's functions. Unfortunately, as far as the three-dimensional bimaterial Green's functions with imperfect interface are concerned, only those with the smooth-bond interface for isotropic [1,23,24]) and transversely isotropic ([25]) materials were obtained previously. More recently, Yu [14] introduced a dislocation-like model where the interface condition is similar to the linear spring-like model but with the displacement on one side of the interface being assumed to be linearly proportional to that on the other side of the interface. This dislocation-like model enjoys at least two advantages: (1) The interface shear stress predicted by this model agreed qualitatively with experimental measurements ([15]), a suitable description on the effect of an imperfect interface

[1]Currently at the Department of Civil Engineering, University of Akron, Akron, OH 44325-3905. e-mail: pan2@uakron.edu

Contributed by the Applied Mechanics Division of THE AMERICAN SOCIETY OF MECHANICAL ENGINEERS for publication in the ASME JOURNAL OF APPLIED MECHANICS. Manuscript received by the ASME Applied Mechanics Division, May 8, 2001; final revision, Mar. 5, 2002. Associate Editor: D. A. Kouris. Discussion on the paper should be addressed to the Editor, Prof. Robert M. McMeeking, Department of Mechanical and Environmental Engineering University of California–Santa Barbara, Santa Barbara, CA 93106-5070, and will be accepted until four months after final publication of the paper itself in the ASME JOURNAL OF APPLIED MECHANICS.

on the load transfer and (2) For this model, the exact closed-form bimaterial Green's functions can be derived ([14,15]).

Besides their application as kernel functions in the boundary integral equation method, the three-dimensional Green's functions, in particular, the three-dimensional bimaterial Green's functions with various interface conditions, are of special values in the numerical studies of strained semiconductor quantum devices where the strain-induced quantum dot growth in semiconductor nanostructures is crucial to the electronic performance ([26–28]). While under two-dimensional deformation, the strain-induced elastic fields can be easily analyzed using the analytical solution ([29]), for those in the three-dimensional bimaterial space, the Green's functions, as embedded in the Eshelby tensor ([30,31]), are required in the corresponding studies. Unfortunately, for problems with material anisotropy, as for the strained semiconductor quantum devices, the involved three-dimensional Green's functions are very difficult to derive.

In recent years, the Stroh formalism, originally developed by Stroh ([32,33]) for the two-dimensional deformation problems, has been extended to certain three-dimensional Green's function solutions ([34–37]). This opens a new door to further exploring the Stroh formalism. The most promising feature, perhaps, is the application of the extended three-dimensional Stroh formalism combined with the Mindlin's superposition method ([38]), as in Pan and Yuan [37]. In doing so, the three-dimensional bimaterial Green's functions can be expressed as a sum of the Kelvin solution (the full-space Green's function) and a Mindlin's complimentary part ([37]). While the former has an explicit expression ([39–42]), the latter is expressed in terms of a simple and regular line integral over $[0,\pi]$. This is perhaps the most simple and concise approach available since a direct application of the Fourier transform would end up with a Green's function expression in terms of three-dimensional Fourier integrals for the homogeneous full-space and four-dimensional Fourier integrals for the bimaterial full-space ([43]).

In this paper, we further extend the three-dimensional Stroh formalism and Mindlin's superposition method to the study of the three-dimensional Green's functions in anisotropic elastic bimaterials with imperfect interface. Four different interface models, namely perfect-bond, smooth-bond, dislocation-like, and force-like, are considered. While the first model is for a perfect interface for which the corresponding bimaterial Green's functions were derived by Pan and Yuan [37], other three models are for imperfect interfaces for which the corresponding bimaterial Green's functions are derived in this paper. Furthermore, the dislocation-like model has been generalized by introducing an interface spring-like matrix, instead of only two parameters, and the force-like model is a complete new one resembling the recently proposed traction-jump model ([16,44,45]) with its potential application yet to be found. We will show that even for the three imperfect interface models, the bimaterial Green's functions can still enjoy the same simple and concise structure as that for the perfect interface model. This is actually achieved by carefully introducing certain modified eigenmatrices corresponding to the imperfect interface conditions. We also remark that while the generalized Mindlin's problem in an anisotropic elastic half-space with general boundary conditions has been recently solved by the author ([46]), the corresponding two-dimensional bimaterial Green's functions with the three imperfect interface models are derived analytically in the Appendix of this paper.

A typical numerical example on the Green's stress distribution is given for a bimaterial full-space made of two orthotropic half-spaces with the four different interface models. It is demonstrated clearly that by varying the interface parameters in the dislocation-like and force-like models, various load transfer states can be simulated. It is observed that, for most Green's stresses, the four different interface models affect only their local distribution behaviors in the vicinity of the interface, and that among the three imperfect interface models, the smooth-bond model shows the greatest variation as compared to the perfect-bond results. These features should be of great interest to the composite structure analysis, in particular, to the interface design. Since the bimaterial Green's functions for the four interface conditions can be obtained very efficiently and accurately, they can also be implemented into a boundary integral formulation to investigate the deformation, stress, and fracture problems in anisotropic and layered structures with imperfect interfaces.

Problem Description

Consider an anisotropic elastic bimaterial full-space where $x_3>0$ and $x_3<0$ are occupied, respectively, by materials 1 and 2 with interface at $x_3=0$ plane. Without loss of generality, we assume that a point force $\mathbf{f}=(f_1,f_2,f_3)$ is applied in material 1 at source point $\mathbf{d}\equiv(d_1,d_2,d_3\equiv d>0)$, with the field point being denoted by $\mathbf{x}\equiv(x_1,x_2,x_3\equiv z)$[2]. Following Pan and Yuan [36], the problem domain is now artificially divided into three regions: $z>d$ (in material 1), $0\leqslant z<d$ (in material 1), and $z<0$ (in material 2).

Since each region is now free of the body force, the equation of equilibrium in terms of the elastic displacements u_k can thus be written as

$$C_{ijkl}u_{k,lj}=0 \tag{1}$$

where C_{ijkl} is the elastic stiffness tensor of the corresponding region. As a convention, summation is taken for the repeated index from 1 to 3, and an index following the subscript comma denotes the partial differentiation with respect to the field coordinate.

Equation (1) needs to be solved for each region with suitable continuity conditions along the interface and at the source level. In this paper, four different interface models are considered, with one being perfect and three being imperfect.

Model 1. The displacement and traction vectors are continuous across the interface, i.e.,

$$u_j^{(1)}|_{z=0^+}=u_j^{(2)}|_{z=0^-},\quad t_j^{(1)}|_{z=0^+}=t_j^{(2)}|_{z=0^-};\quad j=1,2,3 \tag{2a}$$

where the superscripts (1) and (2) are used exclusively to denote the quantities in materials 1 and 2, respectively. It is seen that, for this model, the two half-spaces are perfectly bonded together, and such an interface is also called perfect-bond (or ideal, welded) interface (see, e.g., [1,17,24]). We further mention that the anisotropic bimaterial Green's functions with this interface condition have been derived recently by Pan and Yuan [37] and are included here for the purpose of comparison to the bimaterial Green's functions with imperfect interface conditions.

Model 2. The displacement and traction vectors are required to satisfy the following conditions across the interface:

$$\begin{gathered} u_3^{(1)}|_{z=0^+}=u_3^{(2)}|_{z=0^-},\quad t_3^{(1)}|_{z=0^+}=t_3^{(2)}|_{z=0^-} \\ t_\alpha^{(1)}|_{z=0^+}=t_\alpha^{(2)}|_{z=0^-}=0,\quad \alpha=1,2. \end{gathered} \tag{2b}$$

This is perhaps one of the most frequently studied imperfect interface models and is called smooth-bond (or frictionless, slipping, or sliding) interface ([1,17,24,25]).

Model 3. Across the interface, the traction vector is continuous and the displacement vector is discontinuous:

$$u_i^{(1)}|_{z=0^+}=k_{ij}^u u_j^{(2)}|_{z=0^-},\quad t_i^{(1)}|_{z=0^+}=t_i^{(2)}|_{z=0^-};\quad i=1,2,3 \tag{2c}$$

where the constant matrix $\mathbf{k}^u=[k_{ij}^u]$ describes the bonding condition along the interface. Yu ([14]) recently proposed this imperfect interface model for the isotropic bimaterial full-space with the

[2]Thereafter, the scalar variables z and d will be used exclusively for the third field coordinate x_3 and third source coordinate d_3, respectively.

constant matrix $\mathbf{k}^u$ being diagonal. This new model is called dislocation-like because of its similarity to the Somigliana's dislocation ([31]). Yu [14] proved that for this new interface model, the three-dimensional isotropic bimaterial Green's function possesses the same simple structure as that for the perfect-bond model, and that the load transfer at the interface predicted with this model is quantitatively comparable to the experimental measurement. Furthermore, two special cases can be reduced from this model: (a) If k_{ij}^u is an identity matrix, implying vanishing of the displacement jumps at the interface, the dislocation-like model is then reduced to Model 1, i.e., the perfect-bond interface and (b) if k_{ij}^u is a zero matrix, then the bimaterial problem is reduced to two separate half-space problems. With a point force being applied in material 1, the half-space problem for material 1 can be first solved subject to a rigid surface boundary condition (i.e., the surface displacements are zero). Then, the solution in the half-space of material 2 can be solved using the traction surface condition of Eq. (2*c*). Therefore, with the element values of the matrix k_{ij}^u varying from 0 (for rigid-bond) to 1 (for perfect-bond), the dislocation-like model can actually simulate various intermediate interface conditions between these two extreme cases. Another interesting feature associated with this model is that when the matrix k_{ij}^u is diagonal, the first two elements on the diagonal are related to the interface conditions in the tangential directions and the third one to the condition in the normal direction of the interface. In the following analysis, we assume that the matrix k_{ij}^u is diagonal with values in the interval (0,1) and that its inverse exists.

Model 4. In contrast with Model 3, here across the interface, the displacement vector is continuous while the traction vector is discontinuous:

$$u_i^{(1)}|_{z=0^+}=u_i^{(2)}|_{z=0^-},\quad t_i^{(1)}|_{z=0^+}=k_{ij}^t t_j^{(2)}|_{z=0^-};\quad i=1,2,3. \tag{2d}$$

Similarly, the constant matrix $\mathbf{k}^t=[k_{ij}^t]$ describes the bonding condition along the interface. This new model, being named as force-like model, describes a traction jump at the interface. We remark that this force-like model resembles the traction-jump model proposed recently by Benveniste [16], Benveniste and Chen [44], and Hashin [45] and that it includes two previous models as its special cases: (a) If k_{ij}^t is an identity matrix, implying vanishing of the traction jumps at the interface, the force-like model is then reduced to Model 1, i.e., the perfect-bond interface; and (b) if k_{ij}^t is a zero matrix, then the bimaterial problem is reduced to two separate half-space problems. With a point force being applied in material 1, the half-space problem for material 1 can be first solved subject to a traction-free surface boundary condition. Then, the solution in the half-space of material 2 can be derived using the displacement surface condition of Eq. (2*d*). Consequently, with the element values of the matrix k_{ij}^t varying from 0 (traction-free) to 1 (perfect-bond), the force-like model can actually be used to simulate the load transfer along various intermediate interfaces between these two extreme cases. Furthermore, similar to Model 3, if the matrix k_{ij}^t is diagonal, then the first two elements on the diagonal are related to the interface conditions in the tangential directions and the third one to the condition in the normal direction of the interface. Again, we assume that the inverse of the matrix k_{ij}^t exists.

Besides the interface conditions at $z=0$, one will also need the condition at the source level in order to solve the bimaterial Green's functions. It is found that, at the source level $z=d$ where the point force is applied, the displacement and traction vectors are required to satisfy the following conditions:

$$\begin{aligned}\mathbf{u}^{(1)}|_{z=d^-}&=\mathbf{u}^{(1)}|_{z=d^+}\\ \mathbf{t}^{(1)}|_{z=d^-}-\mathbf{t}^{(1)}|_{z=d^+}&=\delta(x_1-d_1)\,\delta(x_2-d_2)\mathbf{f}\end{aligned} \tag{3}$$

where the displacement and traction vectors $\mathbf{u}$ and $\mathbf{t}$ are defined as

$$\begin{aligned}\mathbf{u}&=(u_1,u_2,u_3)\\ \mathbf{t}&\equiv(\sigma_{13},\sigma_{23},\sigma_{33})\equiv(t_1,t_2,t_3).\end{aligned} \tag{4}$$

Finally, the Green's function solutions are required to vanish as $|\mathbf{x}|$ approaches infinity.

Bimaterial Green's Functions in the Transformed Domain

To solve the problem described in the previous section, the two-dimensional Fourier transform, i.e., for the displacement,

$$\tilde{u}_k(y_1,y_2,z;\mathbf{d})=\int\int u_k(x_1,x_2,z;\mathbf{d})e^{iy_\alpha x_\alpha}dx_1dx_2 \tag{5}$$

is applied to Eq. (1) for the three regions. In Eq. (5), α takes the summation from 1 to 2. We point out that, when carrying out the double Fourier inverse transforms later on, a polar coordinate system that relates the Fourier variables (y_1,y_2) as

$$y_1=\eta\cos\theta;\quad y_2=\eta\sin\theta \tag{6}$$

will be used, [37].

Applying the two-dimensional Fourier transform to the continuity conditions (2*a*–*d*) at the interface $z=0$ and the condition (3) at the source level $z=d$, the general solution in the transformed domain that satisfies the source level condition can be expressed in terms of the Stroh eigenvalues and the corresponding eigenmatrices as ([34,37]):

For $z>d$ (in material 1):

$$\begin{aligned}\tilde{\mathbf{u}}^{(1)}(y_1,y_2,z;\mathbf{d})&=-i\eta^{-1}\overline{\mathbf{A}}^{(1)}\langle e^{-i\overline{p}_*^{(1)}\eta(z-d)}\rangle\overline{\mathbf{q}}^{\infty}-i\eta^{-1}\overline{\mathbf{A}}^{(1)}\\ &\quad\times\langle e^{-i\overline{p}_*^{(1)}\eta z}\rangle\overline{\mathbf{q}}^{(1)}\\ \tilde{\mathbf{t}}^{(1)}(y_1,y_2,z;\mathbf{d})&=-\overline{\mathbf{B}}^{(1)}\langle e^{-i\overline{p}_*^{(1)}\eta(z-d)}\rangle\overline{\mathbf{q}}^{\infty}-\overline{\mathbf{B}}^{(1)}\langle e^{-i\overline{p}_*^{(1)}\eta z}\rangle\overline{\mathbf{q}}^{(1)}\\ \tilde{\mathbf{s}}^{(1)}(y_1,y_2,z;\mathbf{d})&=-\overline{\mathbf{C}}^{(1)}\langle e^{-i\overline{p}_*^{(1)}\eta(z-d)}\rangle\overline{\mathbf{q}}^{\infty}-\overline{\mathbf{C}}^{(1)}\langle e^{-i\overline{p}_*^{(1)}\eta z}\rangle\overline{\mathbf{q}}^{(1)}.\end{aligned} \tag{7}$$

For $0\leq z<d$ (in material 1):

$$\begin{aligned}\tilde{\mathbf{u}}^{(1)}(y_1,y_2,z;\mathbf{d})&=i\eta^{-1}\mathbf{A}^{(1)}\langle e^{-ip_*^{(1)}\eta(z-d)}\rangle\mathbf{q}^{\infty}-i\eta^{-1}\overline{\mathbf{A}}^{(1)}\\ &\quad\times\langle e^{-i\overline{p}_*^{(1)}\eta z}\rangle\overline{\mathbf{q}}^{(1)}\\ \tilde{\mathbf{t}}^{(1)}(y_1,y_2,z;\mathbf{d})&=\mathbf{B}^{(1)}\langle e^{-ip_*^{(1)}\eta(z-d)}\rangle\mathbf{q}^{\infty}-\overline{\mathbf{B}}^{(1)}\langle e^{-i\overline{p}_*^{(1)}\eta z}\rangle\overline{\mathbf{q}}^{(1)}\\ \tilde{\mathbf{s}}^{(1)}(y_1,y_2,z;\mathbf{d})&=\mathbf{C}^{(1)}\langle e^{-ip_*^{(1)}\eta(z-d)}\rangle\mathbf{q}^{\infty}-\overline{\mathbf{C}}^{(1)}\langle e^{-i\overline{p}_*^{(1)}\eta z}\rangle\overline{\mathbf{q}}^{(1)}.\end{aligned} \tag{8}$$

For $z<0$ (in material 2):

$$\begin{aligned}\tilde{\mathbf{u}}^{(2)}(y_1,y_2,z;\mathbf{d})&=i\eta^{-1}\mathbf{A}^{(2)}\langle e^{-ip_*^{(2)}\eta z}\rangle\mathbf{q}^{(2)}\\ \tilde{\mathbf{t}}^{(2)}(y_1,y_2,z;\mathbf{d})&=\mathbf{B}^{(2)}\langle e^{-ip_*^{(2)}\eta z}\rangle\mathbf{q}^{(2)}\\ \tilde{\mathbf{s}}^{(2)}(y_1,y_2,z;\mathbf{d})&=\mathbf{C}^{(2)}\langle e^{-ip_*^{(2)}\eta z}\rangle\mathbf{q}^{(2)}\end{aligned} \tag{9}$$

where

$$\langle e^{-ip_*\eta z}\rangle=\mathrm{diag}[e^{-ip_1\eta z},e^{-ip_2\eta z},e^{-ip_3\eta z}] \tag{10}$$

and

$$\mathbf{q}^{\infty}=(\mathbf{A}^{(1)})^T\mathbf{f}e^{iy_\alpha d_\alpha},\quad \overline{\mathbf{q}}^{\infty}=(\overline{\mathbf{A}}^{(1)})^T\mathbf{f}e^{iy_\alpha d_\alpha}. \tag{11}$$

In Eqs. (7)–(9), p_j $(j=1,2,3)$, and $\mathbf{A}$, $\mathbf{B}$, and $\mathbf{C}$ are the Stroh eigenvalues and the corresponding eigenmatrices, and their expressions, being functions of the elastic stiffness tensor and the Fourier angular variable θ, can be found in Pan and Yuan [37]. Also in Eqs. (7)–(9), η is the Fourier radial variable defined by Eq. (6), and $\tilde{\mathbf{s}}$ the Fourier transform of the in-plane stress vector $\mathbf{s}$ defined by

$$\mathbf{s}\equiv(\sigma_{11},\sigma_{12},\sigma_{22}). \tag{12}$$

One important feature associated with the extended three-dimensional Stroh formalism is that the Stroh eigenvalues p_j and the corresponding eigenmatrices **A**, **B**, and **C** in Eqs. (7)–(9) are all independent of the Fourier radial variable η! This is actually the key in success of carrying out exactly the infinite integral with respect to the Fourier radial variable η, reducing the bimaterial Green's function to an expression in terms of a simple line integral of θ over a finite interval $[0,\pi]$ ([37]). Furthermore, as will be shown next, similar concise expression can also be obtained even for the three imperfect interface models, upon introducing certain modified eigenmatrics associated with the imperfect interface conditions.

To determine the complex vectors $\overline{\mathbf{q}}^{(1)}$ and $\mathbf{q}^{(2)}$ in Eqs. (7)–(9), one of the interface models should be applied, and they are discussed below one by one.

Model 1. For the perfect bond, we found ([37])

$$\mathbf{A}^{(1)}\langle e^{ip_*^{(1)}\eta d}\rangle\mathbf{q}^{\infty}-\overline{\mathbf{A}}^{(1)}\overline{\mathbf{q}}^{(1)}=\mathbf{A}^{(2)}\mathbf{q}^{(2)} \tag{13a}$$

$$\mathbf{B}^{(1)}\langle e^{ip_*^{(1)}\eta d}\rangle\mathbf{q}^{\infty}-\overline{\mathbf{B}}^{(1)}\overline{\mathbf{q}}^{(1)}=\mathbf{B}^{(2)}\mathbf{q}^{(2)}. \tag{13b}$$

Model 2. For the smooth bond, the interface conditions for the complex vectors $\overline{\mathbf{q}}^{(1)}$ and $\mathbf{q}^{(2)}$ are

$$\begin{pmatrix} B_{11}^{(1)} & B_{12}^{(1)} & B_{13}^{(1)} \\ B_{21}^{(1)} & B_{22}^{(1)} & B_{23}^{(1)} \\ B_{31}^{(1)} & B_{32}^{(1)} & B_{33}^{(1)} \end{pmatrix}\langle e^{ip_*^{(1)}\eta d}\rangle\mathbf{q}^{\infty}-\begin{pmatrix} \overline{B}_{11}^{(1)} & \overline{B}_{12}^{(1)} & \overline{B}_{13}^{(1)} \\ \overline{B}_{21}^{(1)} & \overline{B}_{22}^{(1)} & \overline{B}_{23}^{(1)} \\ \overline{B}_{31}^{(1)} & \overline{B}_{32}^{(1)} & \overline{B}_{33}^{(1)} \end{pmatrix}\overline{\mathbf{q}}^{(1)}$$
$$=\begin{pmatrix} -B_{11}^{(2)} & -B_{12}^{(2)} & -B_{13}^{(2)} \\ -B_{21}^{(2)} & -B_{22}^{(2)} & -B_{23}^{(2)} \\ B_{31}^{(2)} & B_{32}^{(2)} & B_{33}^{(2)} \end{pmatrix}\mathbf{q}^{(2)} \tag{14a}$$

$$(A_{31}^{(1)}\ A_{32}^{(1)}\ A_{33}^{(1)})\langle e^{ip_*^{(1)}\eta d}\rangle\mathbf{q}^{\infty}-(\overline{A}_{31}^{(1)}\ \overline{A}_{32}^{(1)}\ \overline{A}_{33}^{(1)})\overline{\mathbf{q}}^{(1)}$$
$$=(A_{31}^{(2)}\ A_{32}^{(2)}\ A_{33}^{(2)})\mathbf{q}^{(2)} \tag{14b}$$

$$(B_{31}^{(1)}\ B_{32}^{(1)}\ B_{33}^{(1)})\langle e^{ip_*^{(1)}\eta d}\rangle\mathbf{q}^{\infty}-(\overline{B}_{31}^{(1)}\ \overline{B}_{32}^{(1)}\ \overline{B}_{33}^{(1)})\overline{\mathbf{q}}^{(1)}$$
$$=(B_{31}^{(2)}\ B_{32}^{(2)}\ B_{33}^{(2)})\mathbf{q}^{(2)} \tag{14c}$$

$$\begin{pmatrix} B_{11}^{(1)} & B_{12}^{(1)} & B_{13}^{(1)} \\ B_{21}^{(1)} & B_{22}^{(1)} & B_{23}^{(1)} \end{pmatrix}\langle e^{ip_*^{(1)}\eta d}\rangle\mathbf{q}^{\infty}-\begin{pmatrix} \overline{B}_{11}^{(1)} & \overline{B}_{12}^{(1)} & \overline{B}_{13}^{(1)} \\ \overline{B}_{21}^{(1)} & \overline{B}_{22}^{(1)} & \overline{B}_{23}^{(1)} \end{pmatrix}\overline{\mathbf{q}}^{(1)}=0 \tag{14d}$$

$$\begin{pmatrix} B_{11}^{(2)} & B_{12}^{(2)} & B_{13}^{(2)} \\ B_{21}^{(2)} & B_{22}^{(2)} & B_{23}^{(2)} \end{pmatrix}\overline{\mathbf{q}}^{(2)}=0. \tag{14e}$$

It is observed that solving directly these equations for the complex vectors $\overline{\mathbf{q}}^{(1)}$ and $\mathbf{q}^{(2)}$ is very complicated. However, by performing certain simple additions and subtractions, these equations can be grouped equivalently into two matrix equations:

$$\begin{pmatrix} B_{11}^{(1)} & B_{12}^{(1)} & B_{13}^{(1)} \\ B_{21}^{(1)} & B_{22}^{(1)} & B_{23}^{(1)} \\ A_{31}^{(1)} & A_{32}^{(1)} & A_{33}^{(1)} \end{pmatrix}\langle e^{ip_*^{(1)}\eta d}\rangle\mathbf{q}^{\infty}-\begin{pmatrix} \overline{B}_{11}^{(1)} & \overline{B}_{12}^{(1)} & \overline{B}_{13}^{(1)} \\ \overline{B}_{21}^{(1)} & \overline{B}_{22}^{(1)} & \overline{B}_{23}^{(1)} \\ \overline{A}_{31}^{(1)} & \overline{A}_{32}^{(1)} & \overline{A}_{33}^{(1)} \end{pmatrix}\overline{\mathbf{q}}^{(1)}$$
$$=\begin{pmatrix} B_{11}^{(2)} & B_{12}^{(2)} & B_{13}^{(2)} \\ B_{21}^{(2)} & B_{22}^{(2)} & B_{23}^{(2)} \\ A_{31}^{(2)} & A_{32}^{(2)} & A_{33}^{(2)} \end{pmatrix}\mathbf{q}^{(2)} \tag{15a}$$

$$\begin{pmatrix} B_{11}^{(1)} & B_{12}^{(1)} & B_{13}^{(1)} \\ B_{21}^{(1)} & B_{22}^{(1)} & B_{23}^{(1)} \\ B_{31}^{(1)} & B_{32}^{(1)} & B_{33}^{(1)} \end{pmatrix}\langle e^{ip_*^{(1)}\eta d}\rangle\mathbf{q}^{\infty}-\begin{pmatrix} \overline{B}_{11}^{(1)} & \overline{B}_{12}^{(1)} & \overline{B}_{13}^{(1)} \\ \overline{B}_{21}^{(1)} & \overline{B}_{22}^{(1)} & \overline{B}_{23}^{(1)} \\ \overline{B}_{31}^{(1)} & \overline{B}_{32}^{(1)} & \overline{B}_{33}^{(1)} \end{pmatrix}\overline{\mathbf{q}}^{(1)}$$
$$=\begin{pmatrix} -B_{11}^{(2)} & -B_{12}^{(2)} & -B_{13}^{(2)} \\ -B_{21}^{(2)} & -B_{22}^{(2)} & -B_{23}^{(2)} \\ B_{31}^{(2)} & B_{32}^{(2)} & B_{33}^{(2)} \end{pmatrix}\mathbf{q}^{(2)}. \tag{15b}$$

It is very interesting that these two equations have a similar structure as that for the bimaterial Model 1 with perfectly bonded interface conditions (13*a*) and (13*b*). Therefore, the solution for the complex vectors $\overline{\mathbf{q}}^{(1)}$ and $\mathbf{q}^{(2)}$ can be found following the same procedure as for the perfect-bond interface. We further remark that this analogue method also works for other well-posed homogeneous interface conditions, as long as the displacement and traction vectors do not coupled in the same interface equation. If the displacement and traction components are mixed together in any interface condition, e.g., the spring-like model with interface displacement jump proportional to the interface traction, the infinite integral over η cannot be carried out exactly even for the two-dimensional isotropic bimaterial plane case ([17]).

Model 3. For the dislocation-like model, we have

$$\mathbf{A}^{(1)}\langle e^{ip_*^{(1)}\eta d}\rangle\mathbf{q}^{\infty}-\overline{\mathbf{A}}^{(1)}\overline{\mathbf{q}}^{(1)}=\mathbf{K}^{u}\mathbf{A}^{(2)}\mathbf{q}^{(2)} \tag{16a}$$

$$\mathbf{B}^{(1)}\langle e^{ip_*^{(1)}\eta d}\rangle\mathbf{q}^{\infty}-\overline{\mathbf{B}}^{(1)}\overline{\mathbf{q}}^{(1)}=\mathbf{B}^{(2)}\mathbf{q}^{(2)}. \tag{16b}$$

Model 4. For the force-like model, we have

$$\mathbf{A}^{(1)}\langle e^{ip_*^{(1)}\eta d}\rangle\mathbf{q}^{\infty}-\overline{\mathbf{A}}^{(1)}\overline{\mathbf{q}}^{(1)}=\mathbf{A}^{(2)}\mathbf{q}^{(2)} \tag{17a}$$

$$\mathbf{B}^{(1)}\langle e^{ip_*^{(1)}\eta d}\rangle\mathbf{q}^{\infty}-\overline{\mathbf{B}}^{(1)}\overline{\mathbf{q}}^{(1)}=\mathbf{K}^{t}\mathbf{B}^{(2)}\mathbf{q}^{(2)}. \tag{17b}$$

Since all the equations for $\overline{\mathbf{q}}^{(1)}$ and $\mathbf{q}^{(2)}$ have similar structures, the solutions for them can therefore be expressed uniformly as

$$\begin{aligned}\overline{\mathbf{q}}^{(1)}&=\mathbf{G}_1\langle e^{ip_*^{(1)}\eta d}\rangle\mathbf{q}^{\infty}\\ \mathbf{q}^{(2)}&=\mathbf{G}_2\langle e^{ip_*^{(1)}\eta d}\rangle\mathbf{q}^{\infty}.\end{aligned} \tag{18}$$

In this equation, the matrices $\mathbf{G}_1$ and $\mathbf{G}_2$ for the four different models are found to be

$$\begin{aligned}\mathbf{G}_1&=-(\overline{\hat{\mathbf{A}}^{(1)}})^{-1}(\overline{\hat{\mathbf{M}}^{(1)}}+\hat{\mathbf{M}}^{(2)})^{-1}(\hat{\mathbf{M}}^{(1)}-\hat{\mathbf{M}}^{(2)})\hat{\mathbf{A}}^{(1)}\\ \mathbf{G}_2&=(\hat{\mathbf{A}}^{(2)})^{-1}(\overline{\hat{\mathbf{M}}^{(1)}}+\hat{\mathbf{M}}^{(2)})^{-1}(\hat{\mathbf{M}}^{(1)}+\overline{\hat{\mathbf{M}}^{(1)}})\hat{\mathbf{A}}^{(1)}\end{aligned} \tag{19}$$

where $\hat{\mathbf{M}}^{(\alpha)}$ are the modified impedance tensors defined by

$$\hat{\mathbf{M}}^{(\alpha)}=-i\hat{\mathbf{B}}^{(\alpha)}(\hat{\mathbf{A}}^{(\alpha)})^{-1}\quad(\alpha=1,2) \tag{20}$$

with the modified eigenmatrices $\hat{\mathbf{A}}^{(\alpha)}$ and $\hat{\mathbf{B}}^{(\alpha)}$ being given below for the four different interface models.

Model 1. For the perfect bond ([37]),

$$\hat{\mathbf{A}}^{(\alpha)}=\mathbf{A}^{(\alpha)},\quad \hat{\mathbf{B}}^{(\alpha)}=\mathbf{B}^{(\alpha)};\quad(\alpha=1,2). \tag{21}$$

Model 2. For the smooth bond,

$$\hat{\mathbf{A}}^{(\alpha)}=\begin{pmatrix} B_{11}^{(\alpha)} & B_{12}^{(\alpha)} & B_{13}^{(\alpha)} \\ B_{21}^{(\alpha)} & B_{22}^{(\alpha)} & B_{23}^{(\alpha)} \\ A_{31}^{(\alpha)} & A_{32}^{(\alpha)} & A_{33}^{(\alpha)} \end{pmatrix};\quad(\alpha=1,2) \tag{22a}$$

$$\hat{\mathbf{B}}^{(1)}=\mathbf{B}^{(1)};\quad \hat{\mathbf{B}}^{(2)}=\begin{pmatrix} -B_{11}^{(2)} & -B_{12}^{(2)} & -B_{13}^{(2)} \\ -B_{21}^{(2)} & -B_{22}^{(2)} & -B_{23}^{(2)} \\ B_{31}^{(2)} & B_{32}^{(2)} & B_{33}^{(2)} \end{pmatrix}. \tag{22b}$$

Model 3. For the dislocation-like model,

$$\hat{\mathbf{A}}^{(1)}=\mathbf{A}^{(1)};\quad \hat{\mathbf{A}}^{(2)}=\mathbf{K}^{u}\mathbf{A}^{(2)}$$
$$\hat{\mathbf{B}}^{(\alpha)}=\mathbf{B}^{(\alpha)};\quad (\alpha=1,2). \tag{23}$$

Model 4. For the force-like model,

$$\hat{\mathbf{A}}^{(\alpha)}=\mathbf{A}^{(\alpha)};\quad (\alpha=1,2)$$
$$\hat{\mathbf{B}}^{(1)}=\mathbf{B}^{(1)};\quad \hat{\mathbf{B}}^{(2)}=\mathbf{K}^{t}\mathbf{B}^{(2)}. \tag{24}$$

Equations (7)–(9) are the bimaterial Green's displacements and stresses in the Fourier transformed domain. For the four different interface models, the complex vectors $\overline{\mathbf{q}}^{(1)}$ and $\mathbf{q}^{(2)}$ in Eqs. (7)–(9) have been derived in a unified form. With the exception of the perfect-bond interface, the bimaterial Green's functions for the three imperfect interface models are new. Similar to the perfect-bond bimaterial Green's functions ([37]), there are several important features pertained to these Green's functions. While a detailed discussion can be found in Pan and Yuan [37], we restate only one of the features closely related to the present work and add three new observations associated with the imperfect interface conditions:

1. As has been observed by Pan and Yuan [37], for the solutions in material 1 ($z>0$), the first term in Eqs. (7) and (8) is the Fourier-domain Green's function for the anisotropic full-space. The inverse of this Green's function, i.e., the physical-domain solution, has been developed by Tewary [39], Ting and Lee [40], Sales and Gray [41], and Tonon et al. [42] in an explicit form. Therefore, the Fourier inverse transform needs to be carried out only for the second term of the solutions, which is similar to the complementary part of the Mindlin solution, [38].
2. The modified eigenmatrices are introduced only for the purpose of determining the complex vectors $\overline{\mathbf{q}}^{(1)}$ and $\mathbf{q}^{(2)}$. The matrices **A**, **B**, and **C** in Eqs. (7)–(9) and later in the final expressions for the physical-domain Green's functions (Eqs. (25), (27), (28)) are the original ones and should not be altered.
3. The methodology is not restricted to the four interface models presented in this paper. The complex vectors $\overline{\mathbf{q}}^{(1)}$ and $\overline{\mathbf{q}}^{(2)}$ in Eqs. (7)–(9) for other imperfect interface models can be derived similarly by introducing the corresponding modified eigenmatrices. The only requirement is that the displacement and traction components are uncoupled in the interface conditions.
4. Under the assumption of two-dimensional deformation, the corresponding anisotropic bimaterial Green's functions in the physical domain with the three imperfect interface models can be derived analytically. This is given in the Appendix of this paper.

Bimaterial Green's Functions in the Physical Domain

Having obtained the bimaterial Green's function in the transformed domain, we now apply the inverse Fourier transform to Eqs. (7)–(9). To handle the double infinite integrals, the polar coordinate transform (6) is applied. In doing so, the infinite integral with respect to the radial variable η can be carried out exactly. Thus, the final bimaterial Green's function in the physical domain is expressed in terms of a regular line-integral over $[0,2\pi]$ in the source-free half-space, and as a sum of the homogeneous full-space Green's function and a regular line-integral over $[0,2\pi]$ in the point-force loaded half-space. Furthermore, the line integral over $[0,2\pi]$ can be reduced to $[0,\pi]$ using certain properties of the Stroh eigenvalues and the corresponding modified eigenvectors ([46,47]). The procedure is very similar to the perfect-bond interface ([37]) and one needs only to replace the matrices $\mathbf{G}_1$ and $\mathbf{G}_2$ with those corresponding to the given interface conditions. Listed below are the final physical-domain bimaterial Green's functions for the four different interface models.

Assuming that $z\neq 0$ or $d\neq 0$, the 3×3 Green's displacement tensor in material 1, with the first index for the displacement component and the second for the point-force direction, is found to be

$$\mathbf{U}^{(1)}(\mathbf{x};\mathbf{d})=\mathbf{U}^{\infty}(\mathbf{x};\mathbf{d})+\frac{1}{2\pi^2}\left[\int_0^{\pi}\overline{\mathbf{A}}^{(1)}\mathbf{G}_u^{(1)}(\mathbf{A}^{(1)})^T d\theta\right] \tag{25}$$

$$(\mathbf{G}_u^{(1)})_{ij}=\frac{(\mathbf{G}_1)_{ij}}{-\overline{p}_i^{(1)}z+p_j^{(1)}d-[(x_1-d_1)\cos\theta+(x_2-d_2)\sin\theta]}. \tag{26}$$

In Eq. (25), $\mathbf{U}^{\infty}(\mathbf{x};\mathbf{d})$ denotes the homogeneous full-space Green's displacement tensor with elastic properties of material 1 for which an explicit expression is available ([39–42]). In Eq. (26), the indices i and j take the range from 1 to 3.

Similarly, the bimaterial Green's stresses (traction and in-plane stress) in material 1 and the Green's displacements and stresses in material 2 can be derived as

$$\mathbf{T}^{(1)}(\mathbf{x};\mathbf{d})=\mathbf{T}^{\infty}(\mathbf{x};\mathbf{d})+\frac{1}{2\pi^2}\left[\int_0^{\pi}\overline{\mathbf{B}}^{(1)}\mathbf{G}_t^{(1)}(\mathbf{A}^{(1)})^T d\theta\right]$$
$$\mathbf{S}^{(1)}(\mathbf{x};\mathbf{d})=\mathbf{S}^{\infty}(\mathbf{x};\mathbf{d})+\frac{1}{2\pi^2}\left[\int_0^{\pi}\overline{\mathbf{C}}^{(1)}\mathbf{G}_t^{(1)}(\mathbf{A}^{(1)})^T d\theta\right] \tag{27}$$

$$\mathbf{U}^{(2)}(\mathbf{x};\mathbf{d})=-\frac{1}{2\pi^2}\left[\int_0^{\pi}\mathbf{A}^{(2)}\mathbf{G}_u^{(2)}(\mathbf{A}^{(1)})^T d\theta\right]$$
$$\mathbf{T}^{(2)}(\mathbf{x};\mathbf{d})=-\frac{1}{2\pi^2}\left[\int_0^{\pi}\mathbf{B}^{(2)}\mathbf{G}_t^{(2)}(\mathbf{A}^{(1)})^T d\theta\right] \tag{28}$$
$$\mathbf{S}^{(2)}(\mathbf{x};\mathbf{d})=-\frac{1}{2\pi^2}\left[\int_0^{\pi}\mathbf{C}^{(2)}\mathbf{G}_t^{(2)}(\mathbf{A}^{(1)})^T d\theta\right].$$

In Eq. (27), $\mathbf{T}^{\infty}(\mathbf{x};\mathbf{d})$ and $\mathbf{S}^{\infty}(\mathbf{x};\mathbf{d})$ denote the explicit Green's stresses in the homogeneous full-space with the elastic properties of material 1 ([42]) and

$$(\mathbf{G}_t^{(1)})_{ij}=\frac{(\mathbf{G}_1)_{ij}}{\{-\overline{p}_i^{(1)}z+p_j^{(1)}d-[(x_1-d_1)\cos\theta+(x_2-d_2)\sin\theta]\}^2} \tag{29}$$

$$(\mathbf{G}_u^{(2)})_{ij}=\frac{(\mathbf{G}_2)_{ij}}{-p_i^{(2)}z+p_j^{(1)}d-[(x_1-d_1)\cos\theta+(x_2-d_2)\sin\theta)]} \tag{30}$$

$$(\mathbf{G}_t^{(2)})_{ij}=\frac{(\mathbf{G}_2)_{ij}}{\{-p_i^{(2)}z+p_j^{(1)}d-[(x_1-d_1)\cos\theta+(x_2-d_2)\sin\theta]\}^2}. \tag{31}$$

Therefore, in material 1, the bimaterial Green's function is expressed as a sum of the explicit full-space Green's function and a complementary part in terms of a line integral over $[0,\pi]$; In material 2, the bimaterial Green's function is expressed in terms of a line integral over $[0,\pi]$ only. Although the bimaterial Green's function problem is complicated in nature, the final solution is very concise, indicating that the modified three-dimensional Stroh formalism is truly mathematically elegant and numerically powerful ([34,35]), especially when used jointly with the Mindlin's superposition method. Indeed, a direct application of the Fourier transform would require a three-dimensional integral for the full-space Green's function and four-dimensional integral for the half-space Green's function ([43]). Furthermore, with regard to these physical-domain bimaterial Green's functions (Eqs. (25), (27), and (28)), the following important observations can be made, with some of them being similar to those made in Pan and Yuan [37]:

1. For the complementary part of the solution in material 1 and the solution in material 2, the dependence of the solutions on the

field point $\mathbf{x}$ and source point $\mathbf{d}$ appears only through matrices $\mathbf{G}_u^{(1)}$, $\mathbf{G}_t^{(1)}$, $\mathbf{G}_u^{(2)}$, and $\mathbf{G}_t^{(2)}$ defined in Eqs. (26) and (29)–(31). Therefore, the derivatives of the bimaterial Green's functions with respect to either the field or source point can be exactly carried out under the integral sign. These derivatives are required in the boundary integral formulation for the internal stress and fracture analyses in bimaterial solids ([48]).

2. The integrals in Eqs. (25), (27), and (28) are regular if $z \neq 0$ or $d \neq 0$, and thus can be easily carried out by any standard numerical integral method such as the Gauss quadrature. Actually, Pan and Yang [49] have recently applied an adaptive integration version in order to calculate the perfect-bond bimaterial Green's function.

3. If $z \neq 0$ and $d = 0$, the bimaterial Green's function is still mathematically regular although some of its components may not have a direct and apparent physical meaning ([1]). However, the author ([46]) has recently given an indirect physical explanation using an equivalent relation between the Green's function due to a point force and that due to a point dislocation (or infinitesimal dislocation loop).

4. When the field and source points are both on the interface (i.e., $z = d = 0$), the bimaterial Green's function is then reduced to the interfacial Green's function. For this special case, the line integral involved in the Green's function expression becomes singular and the resulting finite-part integral needs to be handled with special approaches. A detailed study for the perfect-bond interface can be found in Pan and Yang ([49]) and a similar approach can be followed for the imperfect interface models.

Effects of Interface Conditions

The effect of different interface conditions on the displacement and stress fields was studied by Dundurs and Hetenyi [1], Mura [31], and Yu [14] for the isotropic bimaterial full-space. However, a systematic discussion on this issue has not been carried out yet, not to mention the complexity due to the general anisotropy. Based on the extended three-dimensional Stroh formalism and Mindlin's superposition method, we have found that the effect of different interface conditions on the displacement and stress fields can be studied with a unified formalism.

When studying the difference of the elastic fields due to different imperfect interface conditions relative to those with the perfect-bond interface (i.e., Model 1), it is noted that the full-space Green's function has no influence at all to this difference. It is the complementary part of the bimaterial solution that contributes to it! We also notice that it is the matrix $\mathbf{G}_1$ or $\mathbf{G}_2$ that totally controls such a difference. This is actually no surprising since when deriving the bimaterial solution, it is the complementary part that takes care of the different interface conditions, and it is the matrix $\mathbf{G}_1$ or $\mathbf{G}_2$ that directly accomplishes the task! Therefore, the difference of the displacement and stress fields due to imperfect and perfect interface conditions is directly proportional to the difference of the integral involving the matrix $\mathbf{G}_1$ or $\mathbf{G}_2$.

In the study presented below, we restrict ourselves to the case where the source point d is within the material 1 ($d > 0$) but the field point x can be anywhere in the bimaterials. Again, the difference is relative to the bimaterial Green's function solution corresponding to the perfect-bond interface (i.e., Model 1). We also mention that results for the derivatives of the displacements and stresses will not be given but can be obtained trivially.

For the field point in material 1 (i.e., $z > 0$), we found

$$\mathbf{U}^{(1)}(\mathbf{x};\mathbf{d})|_m - \mathbf{U}^{(1)}(\mathbf{x};\mathbf{d})|_1 = \frac{1}{2\pi^2}\left[\int_0^{\pi} \overline{\mathbf{A}}^{(1)} \Delta\mathbf{G}_u^{(1)} (\mathbf{A}^{(1)})^T d\theta\right] \tag{32}$$

$$\mathbf{T}^{(1)}(\mathbf{x};\mathbf{d})|_m - \mathbf{T}^{(1)}(\mathbf{x};\mathbf{d})|_1 = \frac{1}{2\pi^2}\left[\int_0^{\pi} \overline{\mathbf{B}}^{(1)} \Delta\mathbf{G}_t^{(1)} (\mathbf{A}^{(1)})^T d\theta\right] \tag{33}$$

$$\mathbf{S}^{(1)}(\mathbf{x};\mathbf{d})|_m - \mathbf{S}^{(1)}(\mathbf{x};\mathbf{d})|_1 = \frac{1}{2\pi^2}\left[\int_0^{\pi} \overline{\mathbf{C}}^{(1)} \Delta\mathbf{G}_t^{(1)} (\mathbf{A}^{(1)})^T d\theta\right]$$

where

$$(\Delta\mathbf{G}_u^{(1)})_{ij} = \frac{(\mathbf{G}_1|_m - \mathbf{G}_1|_1)_{ij}}{-\overline{p}_i^{(1)} z + p_j^{(1)} d - [(x_1 - d_1)\cos\theta + (x_2 - d_2)\sin\theta]} \tag{34}$$

$$(\Delta\mathbf{G}_t^{(1)})_{ij} = \frac{(\mathbf{G}_1|_m - \mathbf{G}_1|_1)_{ij}}{\{-\overline{p}_i^{(1)} z + p_j^{(1)} d - [(x_1 - d_1)\cos\theta + (x_2 - d_2)\sin\theta]\}^2}. \tag{35}$$

In Eqs. (32)–(35), the displacement and stress fields with a vertical line followed by subscript 1 are the bimaterial Green's functions corresponding to the perfect-bond interface (i.e., Model 1), and those by subscript m (=2, 3, and 4) correspond to the three imperfect interface models.

Similarly, for the field point in material 2 (i.e., $z < 0$), we obtained

$$\mathbf{U}^{(2)}(\mathbf{x};\mathbf{d})|_m - \mathbf{U}^{(2)}(\mathbf{x};\mathbf{d})|_1 = -\frac{1}{2\pi^2}\left[\int_0^{\pi} \mathbf{A}^{(2)} \Delta\mathbf{G}_u^{(2)} (\mathbf{A}^{(1)})^T d\theta\right]$$

$$\mathbf{T}^{(2)}(\mathbf{x};\mathbf{d})|_m - \mathbf{T}^{(2)}(\mathbf{x};\mathbf{d})|_1 = -\frac{1}{2\pi^2}\left[\int_0^{\pi} \mathbf{B}^{(2)} \Delta\mathbf{G}_t^{(2)} (\mathbf{A}^{(1)})^T d\theta\right] \tag{36}$$

$$\mathbf{S}^{(2)}(\mathbf{x};\mathbf{d})|_m - \mathbf{S}^{(2)}(\mathbf{x};\mathbf{d})|_1 = -\frac{1}{2\pi^2}\left[\int_0^{\pi} \mathbf{C}^{(2)} \Delta\mathbf{G}_t^{(2)} (\mathbf{A}^{(1)})^T d\theta\right]$$

where

$$(\Delta\mathbf{G}_u^{(2)})_{ij} = \frac{(\mathbf{G}_2|_m - \mathbf{G}_2|_1)_{ij}}{-p_i^{(2)} z + p_j^{(1)} d - [(x_1 - d_1)\cos\theta + (x_2 - d_2)\sin\theta)]} \tag{37}$$

$$(\Delta\mathbf{G}_t^{(2)})_{ij} = \frac{(\mathbf{G}_2|_m - \mathbf{G}_2|_1)_{ij}}{\{-p_i^{(2)} z + p_j^{(1)} d - [(x_1 - d_1)\cos\theta + (x_2 - d_2)\sin\theta]\}^2}. \tag{38}$$

Numerical Examples

Having derived the bimaterial Green's functions for the four different interface models, and discussed the effect of different imperfect interface conditions on the displacement and stress fields, we now present numerical examples for these bimaterial Green's functions. We first mention that the present bimaterial Green's functions have been checked with previously available solutions ([1,37]) for some special cases in isotropic and anisotropic bimaterials.

In the present examples, materials 1 and 2 are both orthotropic. Material 1 is the NASA fabric, a composite material made by stacking layers of a carbon warp-knit fabric that was stitched with Kevlar-29 thread prior to introducing 3501-6 epoxy resin ([37]). Material 2 is a graphite/epoxy composite with strong material anisotropy ([37]). In using these two materials, their principal material axes (E_1 and E_2), originally coincide with the x-y–axes, have been rotated 45 deg counterclockwise with respect to the x-axis. Thus the stiffness tensor C_{ijkl} of both materials in the structural coordinates (x,y,z) is monoclinic with symmetry plane at $z = 0$. This bimaterial full-space actually corresponds to the case III in Pan and Yuan ([37]), and the elastic stiffness in the reduced and dimensionless form for materials 1 and 2 are given, respectively, in Tables 1 and 2.

Some dimensionless Green's stress components in such a bimaterial full-space are presented in Figs. 1 to 5. In these figures, the point force of a unit magnitude is applied at $(0,0,d=1)$. The stresses are plotted at field points $(x,y,z) = (1,1,z)$ with z varying from -3 to 3.

Table 1 Elastic stiffness C_{ij} in material 1

.83514624D1	.33934624D1	.57053231D0	.0	.0	.17804512D1
	.83514624D1	.57053231D0	.0	.0	.17804512D1
		.15949776D1	.0	.0	.65283587D-2
			.605	.035	.0
				.605	.0
					.34414318D1

First, the effect of the interface matrices k_{ij}^u and k_{ij}^t (in Models 3 and 4) upon the bimaterial Green's stresses is studied. For simplicity, these interface matrices are assumed to have the same diagonal structure, i.e.,

$$\mathbf{K}^u = \mathbf{K}^t = \text{diag}[k,k,1] \tag{39}$$

where k varies from 0 and 1. Therefore, for Model 3, the normal displacement component is assumed to be continuous while the tangential components are not. Similarly, for Model 4, the normal traction component is assumed to be continuous but the shear components are not.

Shown in Figs. 1(a) and 1(b) are the variations of the dimensionless Green's stress component σ_{xx} due to a point force applied in the z-direction for Models 3 and 4, respectively. For both models, the interface parameter k in Eq. (39) takes the values of 1, 0.5, 0.1, 0.01, and 0.0001. While $k=1$ corresponds to the perfect-bond interface (i.e., Model 1), other k values are for the imperfect bond with $k=0.0001$ simulating the tangential zero-displacement and shear traction-free interfaces, respectively, for the dislocation-like and force-like models (the result for $k=0.0001$ is nearly identical to that for $k=0.000001$). It is observed from Figs. 1(a) and 1(b) that this Green's stress component is discontinuous across the interface for both models. Furthermore, it is found that for the dislocation-like model (Fig. 1(a)), the amount of discontinuity is the largest for the perfect-bond interface and decreases in general with decreasing k, reaching a final value when the tangential displacements are zero (i.e., $k=0$). For the force-like model (Fig. 1(b)), however, the amount of discontinuity is the smallest for the perfect-bond interface and increases with decreasing k, reaching a final value when the shear tractions are zero (i.e., $k=0$). Therefore, by varying the k value in the dislocation-like and force-like models, various load transfer situations across the interface can be simulated.

We now compare the stress distributions for the four models. In Figs. 2 to 5, cases 1, 2, 3, and 4 correspond to the perfect-bond, smooth-bond, dislocation-like, and force-like models, respectively. For models 3 and 4, the interface matrices k_{ij}^u and k_{ij}^t are given by Eq. (39) with k being fixed at 0.5.

The variations of the Green's stresses σ_{xx} and σ_{xy} due to a point force in the x and z-directions are shown in Figs. 2 and 3, with all of them being discontinuous across the interface. It is observed that the magnitudes of the Green's stress components due to the point force in x-direction are much larger than those due to the point force in z-direction (about four-five times). It is also clear that, locally, i.e., in the vicinity of the interface, different interface models can have a great influence on the stress distribution. Among the four models, the smooth interface model, i.e., model 2, shows the largest influence on the stress field near

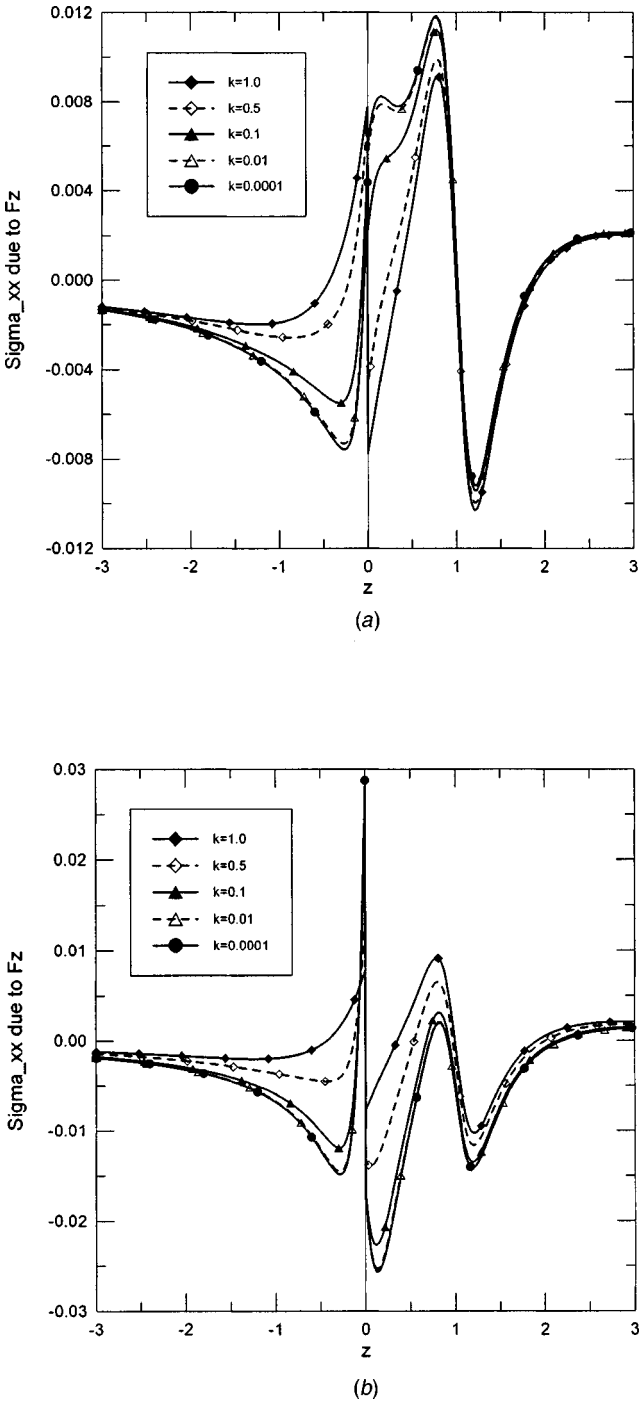

Fig. 1 Variation of the bimaterial Green's stress σ_{xx} with field point (1,1,$z\in[-3,3]$) due to a point force at d=(0,0,1) in the z-direction for different interface parameter k of dislocation-like model (*a*) and force-like model (*b*)

Table 2 Elastic stiffness C_{ij} in material 2

.71726275D1	.54524875D1	.62233525D0	.0	.0	.51191753D1
	.71726275D1	.62233525D0	.0	.0	.51191753D1
		.16217043D1	.0	.0	.11350357D0
			.64977	−.03046	.0
				.64977	.0
					.54251991D1

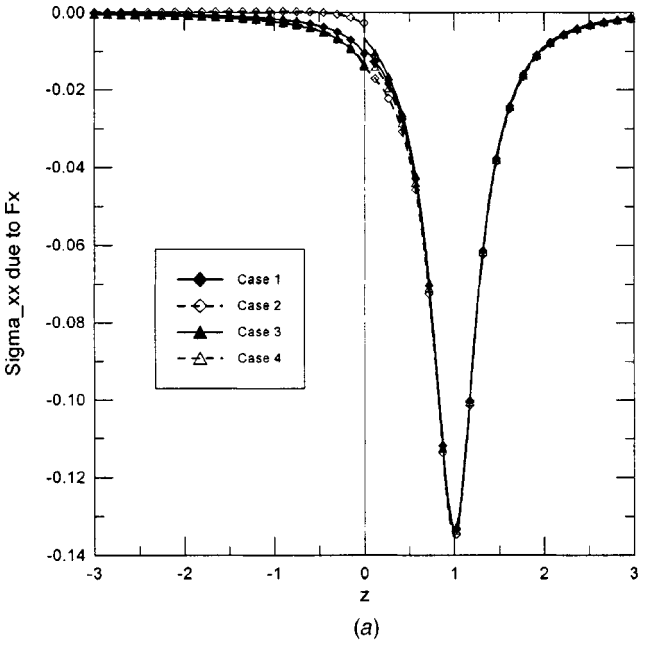

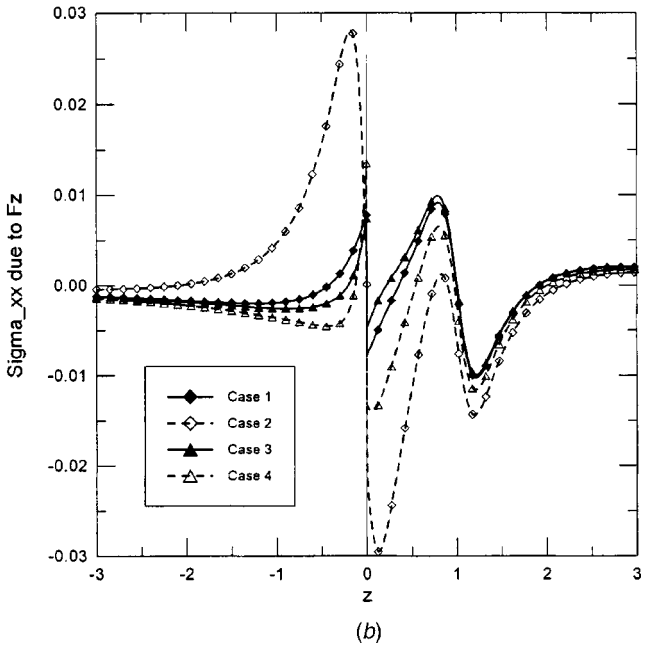

Fig. 2 Variation of the bimaterial Green's stress σ_{xx} with field point (1,1,$z\in[-3,3]$) due to a point force at d=(0,0,1) in the *x*-direction (*a*) and *z*-direction (*b*). Cases 1, 2, 3, and 4 correspond to models 1, 2, 3, and 4, respectively.

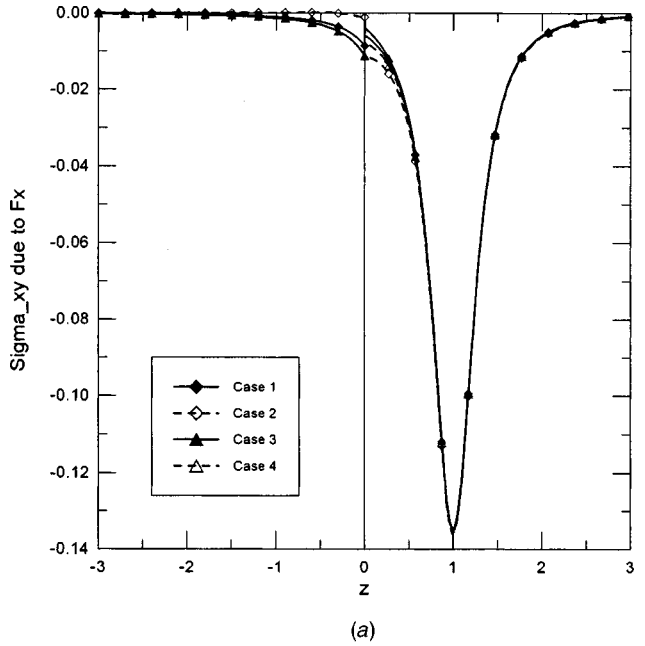

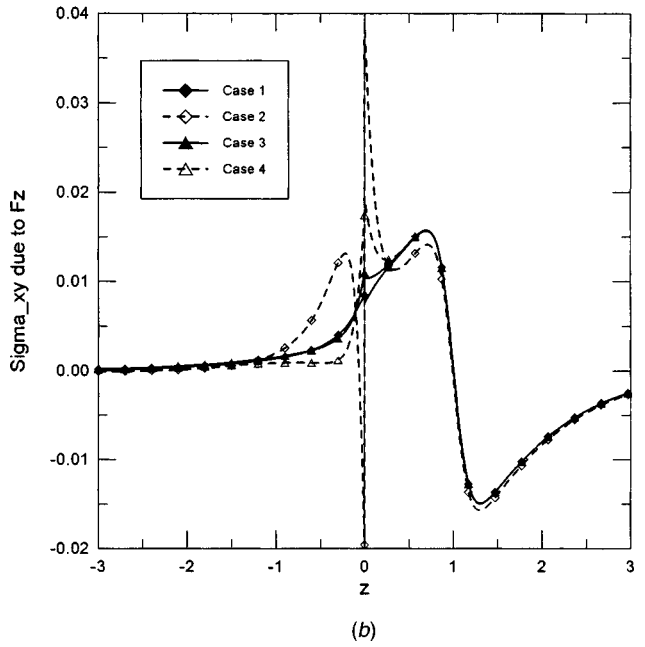

Fig. 3 Variation of the bimaterial Green's stress σ_{xy} with field point (1,1,$z\in[-3,3]$) due to a point force at d=(0,0,1) in the *x*-direction (*a*) and *z*-direction (*b*). Cases 1, 2, 3, and 4 correspond to models 1, 2, 3, and 4, respectively.

the interface. Furthermore, such an influence can be extended to a relatively far distance away from the interface, as compared to the perfect-bond model (Figs. 2(*b*) and 3(*b*)).

Shown in Figs. 4(*a*) and 4(*b*) are the variation of the shear stress σ_{xz} due to the point force in *x* and *z*-directions, respectively. For this shear stress component, its magnitudes due to the point force in *x* and *z*-directions are roughly the same. Similar to the behavior of the stresses σ_{xx} and σ_{xy}, the most affected region by the different interface models is found in the vicinity of the interface. Again, the smooth-bond model causes the greatest variation relative to the perfect-bond model. We also mention that across the interface, while σ_{xz} is continuous for models 1–3, it is discontinuous for model 4 as assumed in the model.

Finally, shown in Figs. 5(*a*) and 5(*b*) are the variations of the vertical stress σ_{zz} due to the point force in *x* and *z*-directions, respectively. For this case, the magnitude of the stress due to the point force in *z*-direction is about three times larger than that due to the point force in *x*-direction. An interesting feature is that while different interface models have nearly no effect on this stress component, the smooth-bond model, however, has a strong

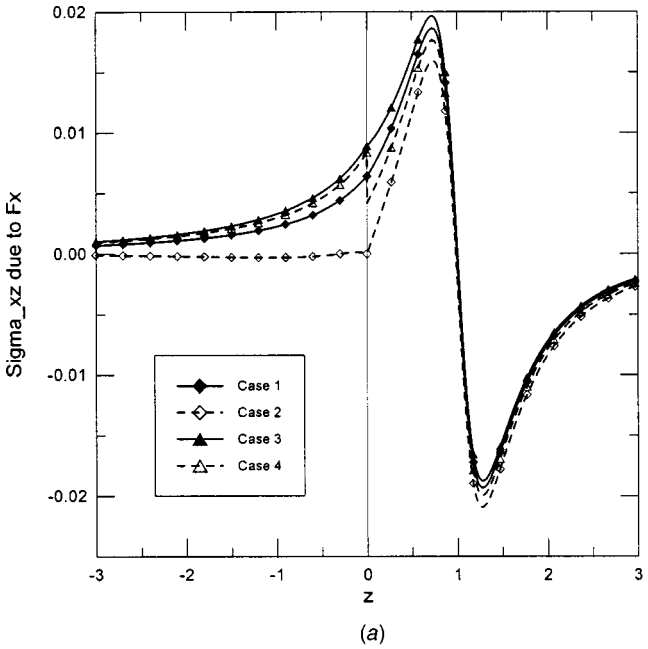

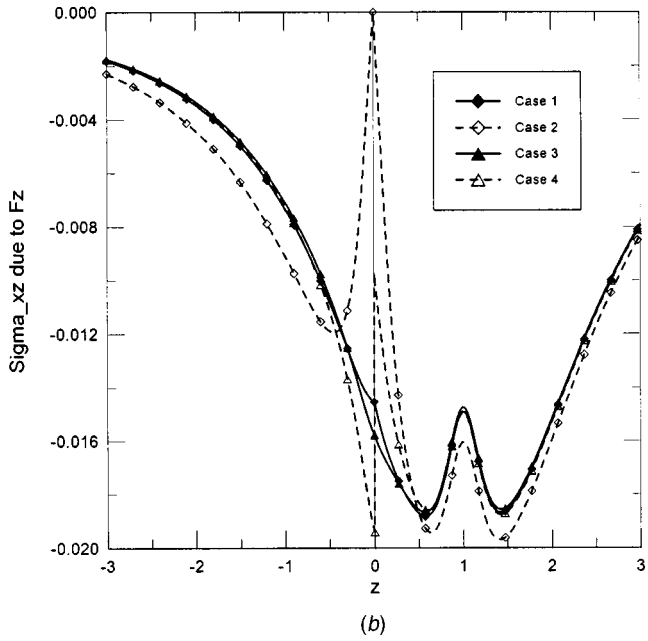

Fig. 4 Variation of the bimaterial Green's stress σ_{xz} with field point (1,1,$z\in[-3,3]$) due to a point force at d=(0,0,1) in the *x*-direction (*a*) and *z*-direction (*b*). Cases 1, 2, 3, and 4 correspond to models 1, 2, 3, and 4, respectively.

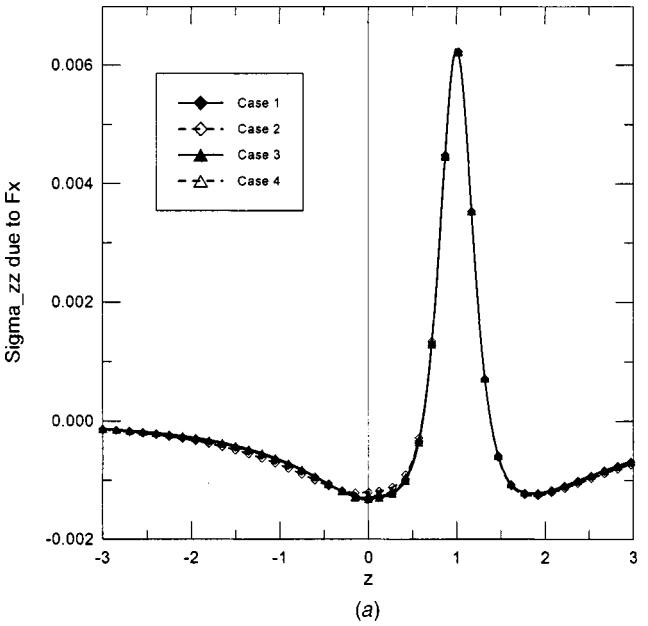

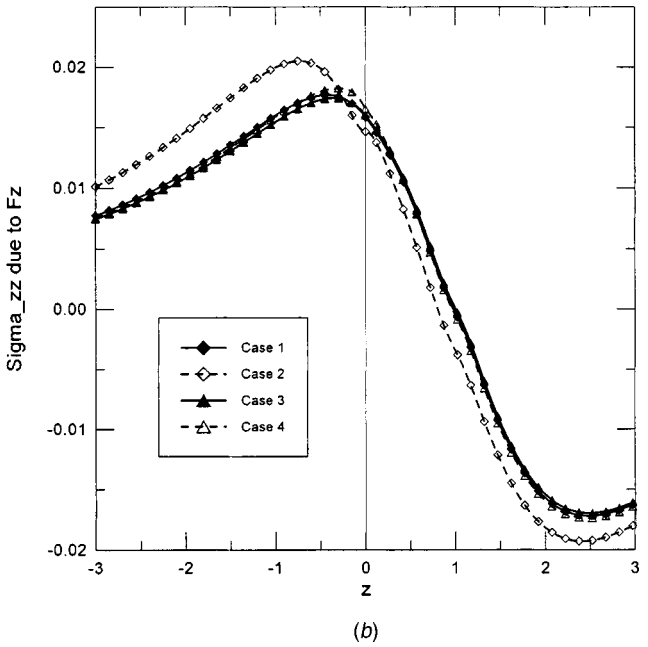

Fig. 5 Variation of the bimaterial Green's stress σ_{zz} with field point (1,1,$z\in[-3,3]$) due to a point force at d=(0,0,1) in the *x*-direction (*a*) and *z*-direction (*b*). Cases 1, 2, 3, and 4 correspond to models 1, 2, 3, and 4, respectively.

influence on this stress component when the point force is in *z*-direction. Furthermore, such an influence seems to extend to a larger region away from the interface.

Conclusions

We have derived the three-dimensional Green's functions in anisotropic bimaterials for four different interface models, namely, perfect-bond, smooth-bond, dislocation-like, and force-like. While the first model is for the perfect interface for which the corresponding bimaterial Green's functions were derived by Pan and Yuan [37], other three models are for the imperfect interface for which the corresponding bimaterial Green's functions are derived *for the first time* in this paper. A remarkable result is that for these imperfect interface models, the bimaterial Green's functions enjoy the same simple and concise structure as that for the prefect interface model. For the case of two-dimensional deformation, the corresponding bimaterial Green's functions are also derived analytically for the three imperfect interface models. We further mention that the methodology of deriving the bimaterial Green's functions with imperfect interface conditions is quite general. On the assumption that the interface displacement and traction vectors are uncoupled in the interface conditions, one needs only to construct the eigenmatrices for the given interface model in order to derive

the corresponding Green's functions. Therefore, the bimaterial Green's function corresponding to a more general interface model that combines the dislocation-like and force-like models together can be easily derived. However, it is also worthwhile to emphasize that should the interface displacement and traction vectors be coupled together, one will be unable to carry out the infinite integral over η exactly. Consequently, the bimaterial Green's function corresponding to such an interface condition would be very complicated even for the two-dimensional isotropic bimaterial case ([17]).

Numerical examples have been also carried out to study the dependence of the bimaterial Green's stresses on the interface matrices k_{ij}^u and k_{ij}^t and the effect of different interface models on the stress fields. It is observed that by varying the element values of the interface matrices k_{ij}^u and k_{ij}^t in models 3 and 4, various load transfers across the interface can be simulated. It is also shown that, among the three imperfect interface models with a middle interface value for the parameter $k(=0.5)$, the smooth-bond model shows the greatest influence on the bimaterial Green's stresses as compared to those for the perfect-bond interface. Since these bimaterial Green's functions can be obtained very efficiently and accurately, they can be easily implemented into a boundary integral formulism ([22]) to investigate the deformation, stress, and fracture problems in anisotropic and layered structures with imperfect interfaces.

Appendix

Two-Dimensional Bimaterial Green's Functions With Imperfect Interfaces. Similar to the three-dimensional bimaterial problem presented in the main text, we consider an anisotropic full-space made of two anisotropic half-spaces with interface at $z=0$. Here, however, we assume that the deformation is independent of the y-coordinate (i.e., the generalized plane-strain deformation in the (x,z) plane). We further let a line force $\mathbf{f}$ and a line dislocation with Burgers vector $\mathbf{b}$ be applied at $(x,z)=(0,d)$ with $d>0$ in material 1.

It is known that the general bimaterial Green's functions (displacements and stress functions) can be expressed as ([34,48])

$$\mathbf{u}^{(1)}=\frac{1}{\pi}\mathrm{Im}\{\mathbf{A}^{(1)}\langle\ln(z_*^{(1)}-p_*^{(1)}d)\rangle\mathbf{q}^{\infty}\}+\frac{1}{\pi}\mathrm{Im}\sum_{j=1}^{3}\{\mathbf{A}^{(1)}\langle\ln(z_*^{(1)}-\overline{p}_j^{(1)}d)\rangle\mathbf{q}_j^{(1)}\}$$
$$\boldsymbol{\phi}^{(1)}=\frac{1}{\pi}\mathrm{Im}\{\mathbf{B}^{(1)}\langle\ln(z_*^{(1)}-p_*^{(1)}d)\rangle\mathbf{q}^{\infty}\}+\frac{1}{\pi}\mathrm{Im}\sum_{j=1}^{3}\{\mathbf{B}^{(1)}\langle\ln(z_*^{(1)}-\overline{p}_j^{(1)}d)\rangle\mathbf{q}_j^{(1)}\} \tag{A1}$$

for $z>0$ (material 1), and

$$\mathbf{u}^{(2)}=\frac{1}{\pi}\mathrm{Im}\sum_{j=1}^{3}\{\mathbf{A}^{(2)}\langle\ln(z_*^{(2)}-p_j^{(1)}d)\rangle\mathbf{q}_j^{(2)}\}$$
$$\boldsymbol{\phi}^{(2)}=\frac{1}{\pi}\mathrm{Im}\sum_{j=1}^{3}\{\mathbf{B}^{(2)}\langle\ln(z_*^{(2)}-p_j^{(1)}d)\rangle\mathbf{q}_j^{(2)}\} \tag{A2}$$

for $z<0$ (material 2). In Eqs. (*A*1) and (*A*2), Im stands for the imaginary part, and the superscripts (1) and (2) denote, as in the text, the quantities in the material domain. $p_j^{(\alpha)}$ and $\mathbf{A}^{(\alpha)}$ and $\mathbf{B}^{(\alpha)}$ are the eigenvalues and the eigenmatrices similar to those given in the main text but depending upon the elastic stiffness coefficient only. Also in Eqs. (*A*1) and (*A*2),

$$\langle\ln(z_*^{(1)}-p_*^{(1)}d)\rangle=\mathrm{diag}[\ln(z_1^{(1)}-p_1^{(1)}d),\ln(z_2^{(1)}-p_2^{(1)}d),\ln(z_3^{(1)}-p_3^{(1)}d)]$$
$$\langle\ln(z_*^{(1)}-\overline{p}_j^{(1)}d)\rangle=\mathrm{diag}[\ln(z_1^{(1)}-\overline{p}_j^{(1)}d),\ln(z_2^{(1)}-\overline{p}_j^{(1)}d),\ln(z_3^{(1)}-\overline{p}_j^{(1)}d)] \tag{A3}$$
$$\langle\ln(z_*^{(2)}-p_j^{(1)}d)\rangle=\mathrm{diag}[\ln(z_1^{(2)}-p_j^{(1)}d),\ln(z_2^{(2)}-p_j^{(1)}d),\ln(z_3^{(2)}-p_j^{(1)}d)]$$

with the complex variable $z_j^{(\alpha)}$ being defined as

$$z_j^{(\alpha)}=x+p_j^{(\alpha)}z. \tag{A4}$$

It is seen that the first term in Eq. (*A*1) corresponds to the full-plane Green's functions (with material properties of material 1) with

$$\mathbf{q}^{\infty}=(\mathbf{A}^{(1)})^T\mathbf{f}+(\mathbf{B}^{(1)})^T\mathbf{b}. \tag{A5}$$

The second term in Eq. (*A*1) and the solution in material 2 (Eq. (*A*2)) are the complementary parts of the solution with the complex constant vectors $\mathbf{q}_j^{(\alpha)}$ $(\alpha=1,2;\ j=1,2,3)$ to be determined. For a perfect-bond interface at $z=0$, these constants are required to satisfy the following conditions ([34]) (for $j=1,2,3$):

$$\mathbf{A}^{(1)}\mathbf{q}_j^{(1)}+\overline{\mathbf{A}}^{(2)}\overline{\mathbf{q}}_j^{(2)}=\overline{\mathbf{A}}^{(1)}\mathbf{I}_j\overline{\mathbf{q}}^{\infty}$$
$$\mathbf{B}^{(1)}\mathbf{q}_j^{(1)}+\overline{\mathbf{B}}^{(2)}\overline{\mathbf{q}}_j^{(2)}=\overline{\mathbf{B}}^{(1)}\mathbf{I}_j\overline{\mathbf{q}}^{\infty} \tag{A6}$$

with

$$\mathbf{I}_1=\mathrm{diag}[1,0,0]$$
$$\mathbf{I}_2=\mathrm{diag}[0,1,0] \tag{A7}$$
$$\mathbf{I}_3=\mathrm{diag}[0,0,1].$$

Equation (*A*6) has a similar structure as Eq. (13a,b). Therefore, the solution for the involved complex constants are found to be ([34,48])

$$\mathbf{q}_j^{(1)}=(\mathbf{A}^{(1)})^{-1}(\mathbf{M}^{(1)}+\overline{\mathbf{M}}^{(2)})^{-1}(\overline{\mathbf{M}}^{(2)}-\overline{\mathbf{M}}^{(1)})\overline{\mathbf{A}}^{(1)}\mathbf{I}_j\overline{\mathbf{q}}^{\infty}$$
$$\mathbf{q}_j^{(2)}=(\mathbf{A}^{(2)})^{-1}(\overline{\mathbf{M}}^{(1)}+\mathbf{M}^{(2)})^{-1}(\mathbf{M}^{(1)}+\overline{\mathbf{M}}^{(1)})\mathbf{A}^{(1)}\mathbf{I}_j\mathbf{q}^{\infty} \tag{A8}$$

where $\mathbf{M}^{(\alpha)}$ are the impedance tensors (defined as Eq. (20)) with the eigenmatrices $\mathbf{A}$ and $\mathbf{B}$ dependent upon the material properties only.

Following the same procedure, the complex constants involved in the bimaterial Green's solutions (*A*1) and (*A*2) for the three imperfect interface models can also be determined. Similar to Eq. (*A*8), they are obtained as

$$\mathbf{q}_j^{(1)}=(\hat{\mathbf{A}}^{(1)})^{-1}(\hat{\mathbf{M}}^{(1)}+\overline{\hat{\mathbf{M}}^{(2)}})^{-1})(\overline{\hat{\mathbf{M}}^{(2)}}-\overline{\hat{\mathbf{M}}^{(1)}})\overline{\hat{\mathbf{A}}^{(1)}}\mathbf{I}_j\overline{\mathbf{q}}^{\infty}$$
$$\mathbf{q}_j^{(2)}=(\hat{\mathbf{A}}^{(2)})^{-1}(\overline{\hat{\mathbf{M}}^{(1)}}+\hat{\mathbf{M}}^{(2)})^{-1}(\hat{\mathbf{M}}^{(1)}+\overline{\hat{\mathbf{M}}^{(1)}})\hat{\mathbf{A}}^{(1)}\mathbf{I}_j\mathbf{q}^{\infty} \tag{A9}$$

where $\tilde{\mathbf{M}}^{(\alpha)}$ $(\alpha=1,2)$ are the modified impedance tensors defined by Eq. (20), and the modified eigenmatrices $\hat{\mathbf{A}}^{(\alpha)}$ and $\hat{\mathbf{B}}^{(\alpha)}$ $(\alpha=1,2)$ by Eqs. (22), (23), and (24) for the three imperfect interface models. The difference between the two-dimensional and three-dimensional expressions for the modified impedance tensors and eigenmatrices is that for the two-dimensional deformation, they are functions of the elastic stiffness tensor only $(\theta=0)$; for the three-dimensional deformation, however, they depend also on the Fourier transform variable θ. We further emphasize that, for both the two-dimensional and three-dimensional deformations, the modified eigenmatrices are used only in the process of determining the involved complex constants.

With the bimaterial Green's displacements and stress functions being given by Eqs. (*A*1) and (*A*2), their derivatives with respect to the field and source points can be analytically carried out and

the resulting Green's functions can then be applied to various problems involving bimaterial plane with imperfect interfaces. As for the corresponding three-dimensional deformation, the two-dimensional bimaterial Green's functions for the three imperfect interface models have not been reported in the literature.

References

[1] Dundurs, J., and Hetenyi, M., 1965, ''Transmission of Force Between Two Semi-infinite Solids,'' ASME J. Appl. Mech., **32**, pp. 671–674.

[2] Mura, T., and Furuhashi, R., 1984, ''The Elastic Inclusion With a Sliding Interface,'' ASME J. Appl. Mech., **51**, pp. 308–310.

[3] Benveniste, Y., 1984, ''The Effect of Mechanical Behavior of Composite Materials With Imperfect Contact Between the Constituents,'' Mech. Mater., **4**, pp. 197–208.

[4] Tsuchida, E., Mura, T., and Dundurs, J., 1986, ''The Elastic Field of an Elliptic Inclusion With Slipping Interface,'' ASME J. Appl. Mech., **52**, pp. 103–108.

[5] Achenbach, J. D., and Zhu, H., 1989, ''Effect of Interfacial Zone on Mechanical Behavior and Failure of Fiber-Reinforced Composites,'' J. Mech. Phys. Solids, **37**, pp. 381–393.

[6] Pagano, N. J., and Tandon, G. P., 1990, ''Modeling of Imperfect Bonding in Fiber Reinforced Brittle Matrix,'' Mech. Mater., **9**, pp. 49–64.

[7] Hashin, Z., 1990, ''Thermoelastic Properties of Fiber Composites With Imperfect Interface,'' Mech. Mater., **8**, pp. 333–348.

[8] Hashin, Z., 1991, ''The Spherical Inclusion with Imperfect Interface,'' ASME J. Appl. Mech., **58**, pp. 444–449.

[9] Kouris, D., 1993, ''Stress Concentration due to Interaction Between Two Imperfectly Bonded Fibers in a Continuous Fiber Composite,'' ASME J. Appl. Mech., **60**, pp. 203–206.

[10] Gao, Z., 1995, ''A Circular Inclusion With Imperfect Interface: Eshelby's Tensor and Related Problems,'' ASME J. Appl. Mech., **62**, pp. 860–866.

[11] Hanson, M. T., and Keer, L. M., 1995, ''Mechanics of Edge Effects on Frictionless Contacts,'' Int. J. Solids Struct., **32**, pp. 391–405.

[12] Meisner, M. J., and Kouris, D. A., 1995, ''Interaction of two Elliptic Inclusions,'' Int. J. Solids Struct., **32**, pp. 451–466.

[13] Zhong, Z., and Meguid, S. A., 1996, ''On the Eigenstrain Problem of a Spherical Inclusion With an Imperfectly Bonded Interface,'' ASME J. Appl. Mech., **63**, pp. 877–883.

[14] Yu, H. Y., 1998, ''A New Dislocation-Like Model for Imperfect Interfaces and Their Effect on Load Transfer,'' Composites, **29A**, pp. 1057–1062.

[15] Yu, H. Y., Wei, Y. N., and Chiang, F. P., 2002, ''Load Transfer at Imperfect Interfaces—Dislocation-Like Model,'' Int. J. Eng. Sci., **40**, pp. 1647–1662.

[16] Benveniste, Y., 1999, ''On the Decay of End Effects in Conduction Phenomena: A Sandwich Strip With Imperfect Interfaces of Low or High Conductivity,'' J. Appl. Phys., **86**, pp. 1273–1279.

[17] Shilkrot, L. E., and Srolovitz, D. J., 1998, ''Elastic Analysis of Finite Stiffness Bimaterial Interfaces: Application to Dislocation-Interface Interactions,'' Acta Mater., **46**, pp. 3063–3075.

[18] Shuvalov, A. L., and Gorkunova, A. S., 1999, ''Cutting-Off Effect at Reflection-Transmission of Acoustic Waves in Anisotropic Media With Sliding-Contact Interfaces,'' Wave Motion, **30**, pp. 345–365.

[19] Gharpuray, V. M., Dundurs, J., and Keer, L. M., 1991, ''A Crack Terminating at a Slipping Interface Between Two Materials,'' ASME J. Appl. Mech., **58**, pp. 960–963.

[20] Ru, C. Q., 1998, ''Interface Design of Neutral Elastic Inclusions,'' Int. J. Solids Struct., **35**, pp. 559–572.

[21] Ru, C. Q., 1998, ''A Circular Inclusion With Circumferentially Inhomogeneous Sliding Interface in Plane Elastosatics,'' ASME J. Appl. Mech., **65**, pp. 30–38.

[22] Pan, E., Yang, B., Cai, G., and Yuan, F. G., 2001, ''Stress Analyses Around Holes in Composite Laminates Using Boundary Element Method,'' Eng. Anal. Boundary Elem., **25**, pp. 31–40.

[23] Vijayakumar, S., and Cormack, D. E., 1987, ''Nuclei of Strain for Bi-Material Elastic Media With Sliding Interface,'' J. Elast., **17**, pp. 285–290.

[24] Yu, H. Y., and Sanday, S. C., 1991, ''Elastic Fields in Joined Half-spaces due to Nuclei of Strain,'' Proc. R. Soc. London, Ser. A, **434**, pp. 503–519.

[25] Yu, H. Y., Sanday, S. C., Rath, B. B., and Chang, C. I., 1995, ''Elastic Fields due to Defects in Transversely Isotropic Bimaterials,'' Proc. R. Soc. London, Ser. A, **449**, pp. 1–30.

[26] Davies, J. H., and Larkin, I. A., 1994, ''Theory of Potential Modulation in Lateral Surface Superlattices,'' Phys. Rev. B, **B49**, pp. 4800–4809.

[27] Larkin, I. A., Davies, J. H., Long, A. R., and Cusco, R., 1997, ''Theory of Potential Modulation in Lateral Surface Superlattices. II. Piezoelectric Effect,'' Phys. Rev. B, **B56**, pp. 15,242–15,251.

[28] Holy, V., Springholz, G., Pinczolits, M., and Bauer, G., 1999, ''Strain Induced Vertical and Lateral Correlations in Quantum Dot Superlattices,'' Phys. Rev. Lett., **83**, pp. 356–359.

[29] Ru, C. Q., 1999, ''Analytic Solution for Eshelby's Problem of an Inclusion of Arbitrary Shape in a Plane or Half-Plane,'' ASME J. Appl. Mech., **66**, pp. 315–322.

[30] Eshelby, J. D., 1957, ''The Determination of the Elastic Field of an Ellipsoidal Inclusion, and Related Problems,'' Proc. R. Soc. London, Ser. A, **241**, pp. 376–396.

[31] Mura, T., 1987, *Micromechanics of Defects in Solids*, 2nd Ed., Martinus Nijhoff Publishers, Dordrecht, The Netherlands.

[32] Stroh, A. N., 1958, ''Dislocations and Cracks in Anisotropic Elasticity,'' Philos. Mag., **3**, pp. 625–646.

[33] Stroh, A. N., 1962, ''Steady State Problems in Anisotropic Elasticity,'' J. Math. Phys., **41**, pp. 77–103.

[34] Ting, T. C. T., 1996, *Anisotropic Elasticity*, Oxford University Press, Oxford, UK.

[35] Ting, T. C. T., 2000, ''Recent Developments in Anisotropic Elasticity,'' Int. J. Solids Struct., **37**, pp. 401–409.

[36] Wu, K. C., 1998, ''Generalization of the Stroh Formalism to Three-Dimensional Anisotropic Elasticity,'' J. Elast., **51**, pp. 213–225.

[37] Pan, E., and Yuan, F. G., 2000, ''Three-Dimensional Green's Functions in Anisotropic Bimaterials,'' Int. J. Solids Struct., **37**, pp. 5329–5351.

[38] Mindlin, R. D., 1936, ''Force at a Point in the Interior of a Semi-Infinite Solid,'' Physica (Amsterdam), **7**, pp. 195–202.

[39] Tewary, V. K., 1995, ''Computationally Efficient Representation for Elastostatic and Elastodynamic Green's Functions,'' Phys. Rev. B, **51**, pp. 15,695–15,702.

[40] Ting, T. C. T., and Lee, V. G., 1997, ''The Three-Dimensional Elastostatic Green's Function for General Anisotropic Linear Elastic Solids,'' Q. J. Mech. Appl. Math., **50**, pp. 407–426.

[41] Sales, M. A., and Gray, L. J., 1998, ''Evaluation of the Anisotropic Green's Function and Its Derivatives,'' Comput. Struct., **69**, pp. 247–254.

[42] Tonon, F., Pan, E., and Amadei, B., 2001, ''Green's Functions and BEM Formulation for 3D Anisotropic Media,'' Comput. Struct., **79**, pp. 469–482.

[43] Walker, K. P., 1993, ''Fourier Integral Representation of the Green's Function for an Anisotropic Elastic Half-Space,'' Proc. R. Soc. London, Ser. A, **443**, pp. 367–389.

[44] Benveniste, Y., and Chen, T., 2001, ''On the Saint-Venant Torsion of Composite Bars With Imperfect Interfaces,'' Proc. R. Soc. London, Ser. A, **457**, pp. 231–255.

[45] Hashin, Z., 2001, ''Thin Interphase/Imperfect Interface in Conduction,'' J. Appl. Phys., **89**, pp. 2261–2267.

[46] Pan, E., 2003, ''Three-Dimensional Green's Functions in an Anisotropic Half Space With General Boundary Conditions,'' ASME J. Appl. Mech., **125**, pp. 101–110.

[47] Pan, E., 2002, ''Three-Dimensional Green's Functions in Anisotropic Magneto-Electro-Elastic Bimaterials,'' J. Appl. Math. Phys., **53**, pp. 815–838.

[48] Pan, E., and Amadei, B., 1999, ''Boundary Element Analysis of Fracture Mechanics in Anisotropic Bimaterials,'' Eng. Anal. Boundary Elem., **23**, pp. 683–691.

[49] Pan, E., and Yang, B., 2003, ''Three-Dimensional Interfacial Green's Functions in Anisotropic Bimaterials,'' Appl. Math. Model., in press.

The Initial Post-buckling Behavior of Face-Sheet Delaminations in Sandwich Composites

G. A. Kardomateas
Professor,
Fellow ASME

H. Huang[1]
Post-doctoral Fellow

School of Aerospace Engineering,
Georgia Institute of Technology,
Atlanta, GA 30332-0150

Should an interface crack between the layers of the composite face-sheet or between the core and the composite face-sheet of a sandwich beam/plate exists, local buckling and possible subsequent growth of this interface crack (delamination) may occur under compression. In this study, the buckling, and initial post-buckling behavior is studied through a perturbation procedure that is based on the nonlinear beam equations with transverse shear included. Closed-form solutions for the load and midpoint delamination deflection versus applied compressive strain during the initial postbuckling phase are derived. Illustrative results are presented for several sandwich construction configurations, in particular with regard to the effect of material system and transverse shear.
[DOI: 10.1115/1.1532320]

Introduction

Delaminations (layer interface cracks) constitute a common failure phenomenon in laminated composites and they are most easily introduced from impact loads. These delaminations may deteriorate the performance of the structure under compressive loading (e.g., Yin et al. [1] and Simitses et al. [2]). A large number of studies on the behavior of delamination buckling and post-buckling in composites have been carried out by many researchers, e.g., Chai et al. [3] by using a one-dimensional model, Whitcomb [4] and Shivakumar and Whitcomb [5] by using finite elements and Rayleigh-Ritz analysis, Kardomateas [6] by conducting monotonic compressive tests, Kardomateas [7] by using elastica theory to account for large deformations during post-buckling, Kardomateas et al. [8] by studying both experimentally and analytically the fatigue growth of delaminations during cyclic compression, etc.

Although the general principles are not very different, delamination failure in sandwich structures is just beginning to be explored in detail. In this regard, differences in the behavior of delamination buckling and post-buckling within a sandwich structure from that of a laminated composite structure arise due to the fact that the substrate in a delaminated sandwich structure includes a much different kind of material, namely a transversely flexible core made of foam or low strength honeycomb. To this extent, the contribution of the shear stresses and shear deformations of the core are expected to be noteworthy and therefore should be included in the formulation.

A typical sandwich structure is composed of two thin composite laminated faces and a thick soft core made of foam or low strength honeycomb. Due to its exceptional properties, mainly high stiffness and strength with little resultant weight penalty, sandwich structures have been used in aircraft, marine, and other types of structures. Research into sandwich structural behavior and failure modes can be traced following World War II in a rather sporadic fashion but intensified in the 1990s, especially with regard to proper modeling of the core through high-order theories (e.g., Kant and Patil [9], Hunt and Da Silva [10,11], Frostig [12], and Frostig and Baruch [13]). Recently, there have been many contributions presented at symposia dedicated to sandwich structures, e.g. Rajapakse et al. [14].

Although these high-order theories are expected to render most accurate results, they involve considerable effort in addressing the complexities of the formulation of the problem of post-buckling of delaminated beams, and therefore, in the present work, a nonlinear beam equation including transverse shear, properly formulated for an unsymmetric sandwich section (meaning face sheets not of the same geometry and/or material) is used to model the delaminated, substrate, and base parts. The same approach can be used to study either a delamination within the face sheet or a debond at the interface between the face sheet and the core.

Formulation

Governing Equations and Boundary Conditions. Let us consider a sandwich beam, of length $2L$, and width w, consisting of two face sheets of thickness f_1 and f_2, extensional moduli E_{f1} and E_{f2}, and shear moduli G_{f1} and G_{f2}, respectively. The core, of thickness c, has an extensional modulus, E_c, and shear modulus G_c (Fig. 1). The delamination, of length $2a$, is symmetrically located at a distance h from the top. Over the region of the delamination, the sandwich beam consists of two parts: the delaminated layer of the upper face sheet (referred to as the ''delaminated part,'' of thickness h) and the part below the delamination (''substrate part,'' of thickness $f_1-h+c+f_2$, which includes the core and the lower face sheet). The region outside the deamination is referred to as the ''base part'' and consists of the entire section of the sandwich beam, i.e., of thickness f_1+c+f_2. We shall also denote the base part with 1, the delaminated part with 2, and the substrate part with 3. Let us also assume that the beam is clamped-clamped.

The characteristic of sandwich construction is that the neutral axis for the base and the substrate parts is in general no longer at the middle of the corresponding sections. With respect to a reference axis x through the middle of the core, the neutral axis of the base section is defined at a distance e_1 (Fig. 2), as

$$e_1(E_{f1}f_1+E_cc+E_{f2}f_2)=E_{f2}f_2\left(\frac{f_2}{2}+\frac{c}{2}\right)-E_{f1}f_1\left(\frac{f_1}{2}+\frac{c}{2}\right), \tag{1a}$$

and that of the substrate part is at a distance e_3 given by

[1]Presently at Lucent Technologies.

Contributed by the Applied Mechanics Division of THE AMERICAN SOCIETY OF MECHANICAL ENGINEERS for publication in the ASME JOURNAL OF APPLIED MECHANICS. Manuscript received by the ASME Applied Mechanics Division, September 26, 2000; final revision, May 8, 2001. Associate Editor: T. E. Triantafyllijis. Discussion on the paper should be addressed to the Editor, Prof. Robert M. McMeeking, Department of Mechanical and Environmental Engineering University of California–Santa Barbara, Santa Barbara, CA 93106-5070, and will be accepted until four months after final publication of the paper itself in the ASME JOURNAL OF APPLIED MECHANICS.

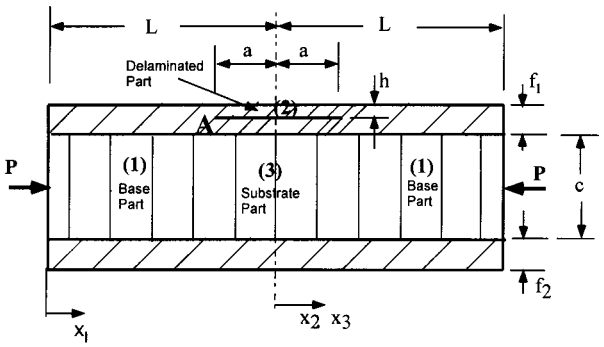

Fig. 1 Definition of the geometry for a delaminated sandwich beam/plate

$$e_3[E_{f1}(f_1-h)+E_c c+E_{f2}f_2]=E_{f2}f_2\left(\frac{f_2}{2}+\frac{c}{2}\right)-E_{f1}(f_1-h)\times\left(\frac{f_1-h}{2}+\frac{c}{2}\right). \quad (1b)$$

Moreover, while for the delaminated layer, which is homogeneous, the bending rigidity per unit width is

$$D_2=E_{f1}\frac{h^3}{12}, \quad (2a)$$

for the base part, the equivalent flexural rigidity of the sandwich section per unit width, is (Fig. 2)

$$D_1=E_{f1}\frac{f_1^3}{12}+E_{f1}f_1\left(\frac{f_1}{2}+\frac{c}{2}+e_1\right)^2+E_{f2}\frac{f_2^3}{12}+E_{f2}f_2\times\left(\frac{f_2}{2}+\frac{c}{2}-e_1\right)^2+E_c\frac{c^3}{12}+E_c c e_1^2, \quad (2b)$$

and for the substrate (again, per unit width),

$$D_3=E_{f1}\frac{(f_1-h)^3}{12}+E_{f1}(f_1-h)\left(\frac{f_1-h}{2}+\frac{c}{2}+e_3\right)^2+E_c\frac{c^3}{12}+E_c c e_3^2+E_{f2}\frac{f_2^3}{12}+E_{f2}f_2\left(\frac{f_2}{2}+\frac{c}{2}-e_3\right)^2. \quad (2c)$$

The nonlinear differential equations including transverse shear for the three parts of the sandwich beam-plate (Fig. 1), namely the base part (1), delaminated part (2), and substrate part (3), are (Huang and Kardomateas [15])

$$D_i\frac{d^2\theta}{ds^2}+P\left(\frac{\alpha_i P}{2A_i\bar{G}_i}\sin 2\theta+\sin\theta\right)=0,$$

which, after Taylor series expansion of the sin θ, becomes

$$D_i\frac{d^2\theta_i(x_i)}{dx_i^2}+\left(\frac{\alpha_i P_i^2}{A_i\bar{G}_i}+P_i\right)\theta_i(x_i)-\left(\frac{2\alpha_i P_i^2}{3A_i\bar{G}_i}+\frac{P_i}{6}\right)\theta_i^3(x_i)=0, \quad i=1,2,3 \quad (3a)$$

where $\theta_i(x)$ is the rotation of the normal to the cross section, D_i is the bending rigidity, α_i is the shear correction factor, P_i is the axial load, A_i are the cross-sectional areas and $\bar{G}_i$ is the "average" shear modulus of each part, calculated from the compliances of the constituent phases [15]

$$\frac{f_1+c+f_2}{\bar{G}_1}=\frac{f_1}{G_{f1}}+\frac{c}{G_c}+\frac{f_2}{G_{f2}};\quad \bar{G}_2=G_{f1};$$
$$A_1=(f_1+c+f_2)w;\quad A_2=hw \quad (3b)$$
$$\frac{f_1-h+c+f_2}{\bar{G}_3}=\frac{f_1-h}{G_{f1}}+\frac{c}{G_c}+\frac{f_2}{G_{f2}};$$
$$A_3=(f_1-h+c+f_2)w. \quad (3c)$$

The shear correction factors can be found in Huang and Kardomateas [15]. For the base part (1),

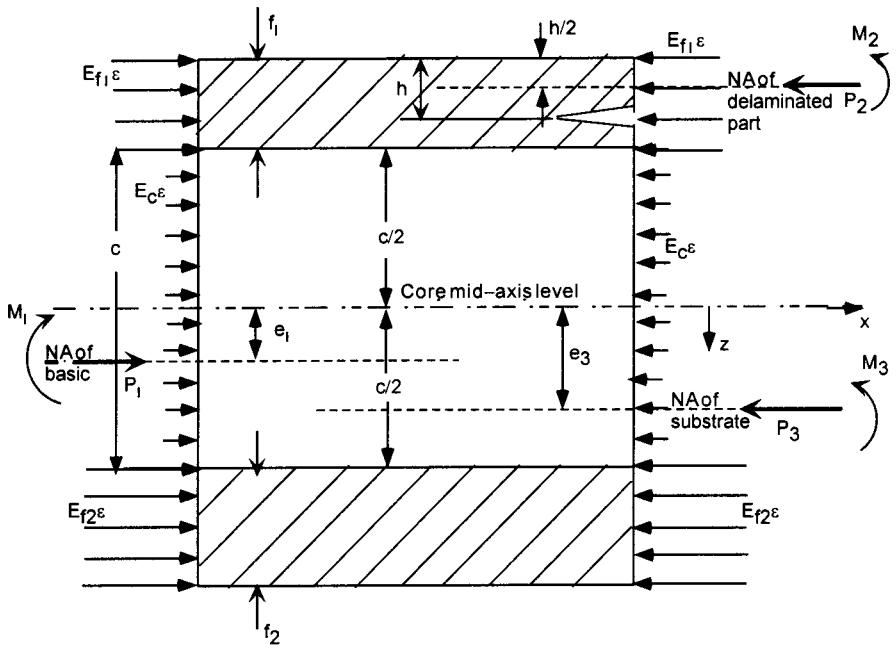

Fig. 2 Force and moment resultants at the tip of the delamination

$$\alpha_1=\bar{G}_1A_1w\sum_{i=1,2}\frac{E_{fi}^2}{4D_1^2G_{fi}}\left[a_i^4f_i-\frac{2}{3}a_i^2(a_i^3-b_i^3)+\frac{1}{5}(a_i^5-b_i^5)\right]$$
$$+\frac{E_{fi}^2}{D_1^2G_c}\left[f_i^2c_i^2b_i+\frac{2}{15}\frac{E_c^2}{E_{fi}^2}b_i^5+\frac{2}{3}\frac{E_c}{E_{fi}}f_ic_ib_i^3\right] \quad (3d)$$

where

$$a_i=f_i+\frac{c}{2}+(-1)^{i+1}e_1;\quad b_i=\frac{c}{2}+(-1)^{i+1}e_1;$$
$$c_i=\frac{f_i}{2}+\frac{c}{2}+(-1)^{i+1}e_1,\quad i=1,2. \quad (3e)$$

Notice that since the delaminated part is homogeneous, $\alpha_2=6/5$, and for the substrate part, α_3 is found from $(3d,e)$ by substituting f_1-h in place of f_1, and D_3, A_3, $\bar{G}_3$, e_3 in place of D_1, A_1, $\bar{G}_1$, e_1.

The way the geometry was configured, gives the following conditions at $x_i=0$:

$$\theta_i(0)=0,\quad i=1,2,3. \quad (4)$$

The above condition is valid for $i=1$ because of the clamped-end and for $i=2,3$ because of symmetry.

Furthermore, a kinematic condition of common slope between the different parts at the section where the delamination starts or ends reads

$$\theta_1(L-a)=\theta_2(-a)=\theta_3(-a)=\theta_A. \quad (5)$$

The force and moment (about the neutral axis of the base part) equilibrium conditions are (Fig. 2)

$$P_1=P_2+P_3, \quad (6)$$

$$M_1-M_2-M_3-P_2\left(f_1+\frac{c}{2}+e_1-\frac{h}{2}\right)+P_3(e_3-e_1)=0. \quad (7)$$

Finally the axial displacement continuity condition at the tip A (Fig. 1) is

$$u_2^A=u_3^A, \quad (8)$$

where

$$u_2^A=\frac{1}{2}\int_{-a}^{0}\theta_2^2dx_2+\frac{P_2a}{E_{f1}wh}+\theta_A\frac{h}{2}, \quad (9)$$

$$u_3^A=\frac{1}{2}\int_{-a}^{0}\theta_3^2dx_3+\frac{P_3a}{[E_{f1}(f_1-h)+E_cc+E_{f2}f_2]w}$$
$$-\theta_A\left(e_3+\frac{c}{2}+f_1-h\right). \quad (10)$$

Asymptotic Expansion. Now, let us expand P_i and θ_i as

$$P_i=P_i^{(0)}+\xi P_i^{(1)}+\xi^2P_i^{(2)}+\xi^3P_i^{(3)}+\ldots, \quad (11)$$

$$\theta_i(x_i)=\xi\theta_i^{(1)}(x_i)+\xi^2\theta_i^{(2)}(x_i)+\xi^3\theta_i^{(3)}(x_i)+\ldots, \quad (12)$$

where the (0) superscript corresponds to the pre-buckling state, the (1) to the buckling state and the (2), etc., to the post-buckling state. Also, let us set ξ to be the common slope of the section at the delamination tip A, i.e.,

$$\xi=\theta_A. \quad (13)$$

From (5) and (12), this gives the additional conditions

$$\theta_1^{(1)}(L-a)=1;\quad \theta_1^{(2)}(L-a)=\theta_1^{(3)}(L-a)=\ldots=0, \quad (14)$$

and

$$\theta_i^{(1)}(-a)=1;\quad \theta_i^{(2)}(-a)=\theta_i^{(3)}(-a)=\ldots=0,\quad i=2,3. \quad (15)$$

Substituting Eqs. (11) and (12) into Eq. (3) and (4)–(10) and rearranging the terms based on the order of ξ, we obtain separately the equations and boundary conditions for the pre-buckling, buckling, and initial post-buckling problem. The asymptotic expansion is an efficient way of deriving closed-form solutions for the initial post-buckling behavior and has also been used previously by Kardomateas [5] in the study of delaminations in monolithic composites in conjunction with the elastica theory.

Pre-buckling State, $O(\xi^0)$. The major characteristic of the pre-buckling state for a sandwich section is that under uniform compressive strain there are nonzero bending moments (as opposed to a monolithic one in which the bending moments are zero) but zero bending deflections.

Under a uniformly applied compressive strain, ϵ_0, the resultant forces (per unit width) for the base part (1), delaminated part (2), and substrate part (3), are (Fig. 2)

$$P_1^{(0)}=\epsilon_0(E_{f1}f_1+E_cc+E_{f2}f_2), \quad (16a)$$

$$P_2^{(0)}=\epsilon_0E_{f1}h;\quad P_3^{(0)}=\epsilon_0[E_{f1}(f_1-h)+E_cc+E_{f2}f_2]. \quad (16b)$$

The pre-buckling moments (per unit width) are then found as (Fig. 2)

$$M_1^{(0)}=\epsilon_0\left[E_{f1}f_1\left(\frac{f_1}{2}+\frac{c}{2}+e_1\right)+E_cce_1\right.$$
$$\left.-E_{f2}f_2\left(\frac{f_2}{2}+\frac{c}{2}-e_1\right)\right];\quad M_2^{(0)}=0, \quad (17a)$$

$$M_3^{(0)}=\epsilon_0\left[E_{f1}(f_1-h)\left(\frac{f_1-h}{2}+\frac{c}{2}+e_3\right)+E_cce_3\right.$$
$$\left.-E_{f2}f_2\left(\frac{f_2}{2}+\frac{c}{2}-e_3\right)\right]. \quad (17b)$$

These pre-buckling forces and moments satisfy identically the force and moment equilibrium equation (about the neutral axis of the base part), Eqs. (6) and (7). Furthermore, since a state of pure axial compressive strain exists without bending deflections, the compatibility of shortening, Eq. (8) is also satisfied.

Buckling (First-Order) Equations, $O(\xi^1)$. From (3) and (11,12), the first-order differential equation for the three parts is

$$D_i\frac{d^2\theta_i^{(1)}(x_i)}{dx_i^2}+\left(\frac{\alpha_iP_i^{(0)2}}{A_i\bar{G}_i}+P_i^{(0)}\right)\theta_i^{(1)}(x_i)=0,\quad i=1,2,3 \quad (18a)$$

and the corresponding boundary conditions from (4) are

$$\theta_i^{(1)}(0)=0,\quad i=1,2,3, \quad (18b)$$

and from (5),

$$\theta_1^{(1)}(L-a)=\theta_2^{(1)}(-a)=\theta_3^{(1)}(-a)=\theta_A^{(1)}=1. \quad (18c)$$

The first-order moment equilibrium from (7) is

$$D_1\left.\frac{d\theta_1^{(1)}}{dx_1}\right|_{x_1=L-a}-D_2\left.\frac{d\theta_2^{(1)}}{dx_2}\right|_{x_2=-a}-D_3\left.\frac{d\theta_3^{(1)}}{dx_3}\right|_{x_3=-a}$$
$$-P_2^{(1)}\left(f_1+\frac{c}{2}+e_1-\frac{h}{2}\right)+P_3^{(1)}(e_3-e_1)=0, \quad (18d)$$

and the first-order force equilibrium,

$$P_2^{(1)}+P_3^{(1)}=P_1^{(1)}. \quad (18e)$$

Finally, the first-order compatibility equation from (8) becomes, since $\theta_A^{(1)}=1$,

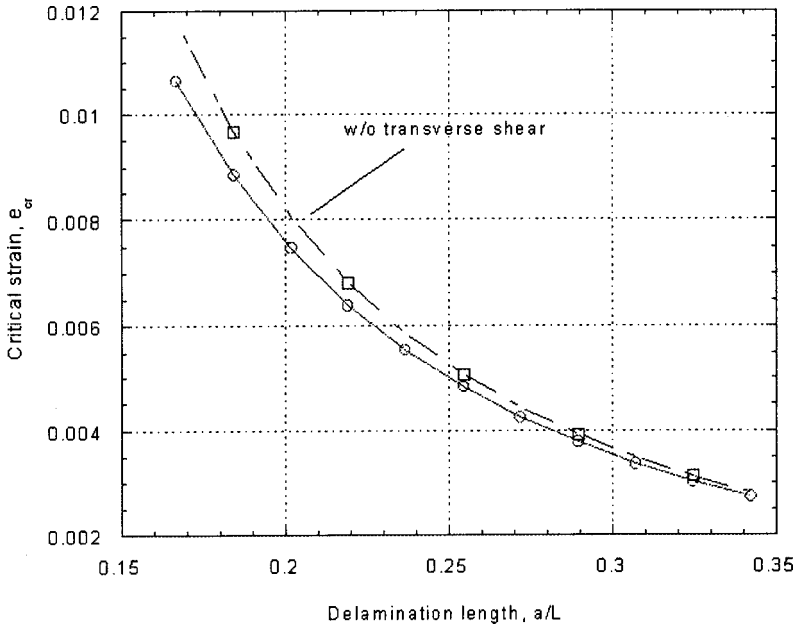

Fig. 3 Critical strain versus delamination length for the case of a glass-polyester/PVC sandwich composite

$$\frac{P_3^{(1)}a}{[E_{f1}(f_1-h)+E_c c+E_{f2}f_2]w}-\left(e_3+\frac{c}{2}+f_1-h\right)=\frac{P_2^{(1)}a}{E_{f1}hw}+\frac{h}{2}. \tag{18g}$$

Let's set

$$\lambda_i=\sqrt{\left(\frac{\alpha_i P_i^{(0)2}}{A_i\bar{G}_i}+P_i^{(0)}\right)\Big/ D_i},\quad i=1,2,3 \tag{19}$$

where $P_1^{(0)}$, $P_2^{(0)}$, and $P_3^{(0)}$ are given in (16) in terms of the uniform compressive strain ϵ_0. Then, the solutions for Eqs. (18*a*) that satisfies the boundary conditions (18*b*), is

$$\theta_i^{(1)}=C_i^{(1)}\sin(\lambda_i x_i),\quad i=1,2,3. \tag{20}$$

Now, the constants $C_1^{(1)}$, $C_2^{(1)}$, $C_3^{(1)}$ are determined from the common slope Eq. (18*c*), as

$$C_1^{(1)}=1/\sin\lambda_1(L-a);\quad C_2^{(1)}=-1/\sin\lambda_2 a;\quad C_3^{(1)}=-1/\sin\lambda_3 a. \tag{21}$$

The characteristic equation is found in terms of ϵ_0 by eliminating $P_1^{(1)}$, $P_2^{(1)}$, and $P_3^{(1)}$ from the previous equations. This is done as follows.

The moment equilibrium Eq. (18*d*), becomes

$$D_1\lambda_1\cot\lambda_1(L-a)+D_2\lambda_2\cot\lambda_2 a+D_3\lambda_3\cot\lambda_3 a =P_2^{(1)}\left(f_1+\frac{c}{2}+e_1-\frac{h}{2}\right)-P_3^{(1)}(e_3-e_1). \tag{22a}$$

By using the neutral axis definitions (1*a*) and (1*b*), we obtain

$$e_3-e_1=\left(f_1+\frac{c}{2}+e_1-\frac{h}{2}\right)\frac{E_{f1}h}{[E_{f1}(f_1-h)+E_c c+E_{f2}f_2]}, \tag{22b}$$

therefore (22*a*) becomes

$$P_2^{(1)}\frac{a}{E_{f1}hw}-P_3^{(1)}\frac{a}{[E_{f1}(f_1-h)+E_c c+E_{f2}f_2]w} =\frac{[D_1\lambda_1\cot\lambda_1(L-a)+D_2\lambda_2\cot\lambda_2 a+D_3\lambda_3\cot\lambda_3 a]a}{E_{f1}hw\left(f_1+\frac{c}{2}+e_1-\frac{h}{2}\right)}. \tag{23}$$

By comparing (18*g*) and (23), we can see that the left-hand side of (23) can be eliminated. Thus, we obtain the following characteristic equation:

$$\frac{[D_1\lambda_1\cot\lambda_1(L-a)+D_2\lambda_2\cot\lambda_2 a+D_3\lambda_3\cot\lambda_3 a]a}{E_{f1}hw\left(f_1+\frac{c}{2}+e_1-\frac{h}{2}\right)} +\left(e_3+\frac{c}{2}+f_1-\frac{h}{2}\right)=0. \tag{24}$$

Equation (24) is a nonlinear algebraic equation which can be solved numerically for the critical strain ϵ_0 (or critical load from (16)). In the numerical procedure, a solution is sought near the Euler buckling strain of the delaminated layer, which is $\epsilon_0=\pi^2h^2/(12a^2)$.

Initial Post-buckling, Second-order Equations, $O(\xi^2)$. From (3) and (11,12), we obtain the second-order differential equation

$$D_i\frac{d^2\theta_i^{(2)}(x_i)}{dx_i^2}+\left(\frac{\alpha_i P_i^{(0)2}}{A_i\bar{G}_i}+P_i^{(0)}\right)\theta_i^{(2)}(x_i) =-\left(\frac{2\alpha_i P_i^{(0)}P_i^{(1)}}{A_i\bar{G}_i}+P_i^{(1)}\right)\theta_i^{(1)}(x_i),\quad i=1,2,3 \tag{25}$$

and from (4) and (14,15),

$$\theta_i^{(2)}(0)=0,\quad i=1,2,3 \tag{26a}$$

$$\theta_1^{(2)}(L-a)=\theta_2^{(2)}(-a)=\theta_3^{(2)}(-a)=0. \tag{26b}$$

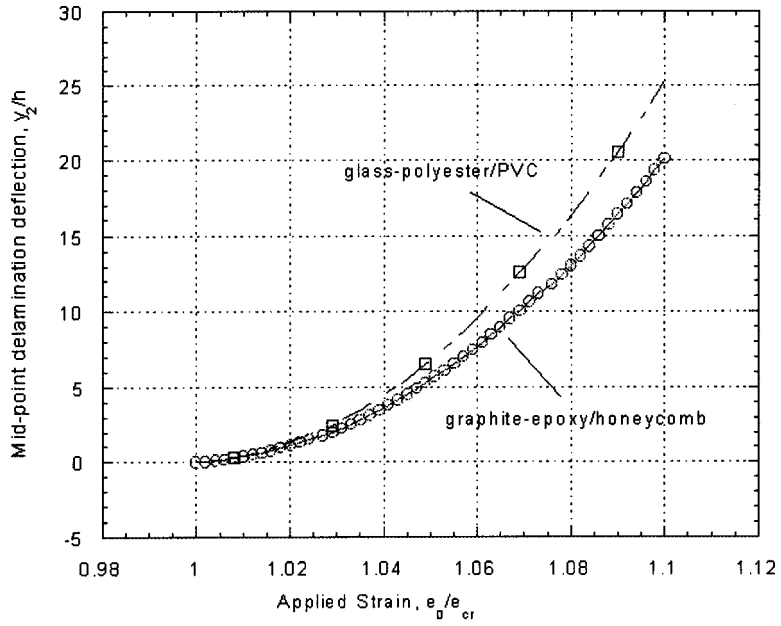

(*a*)

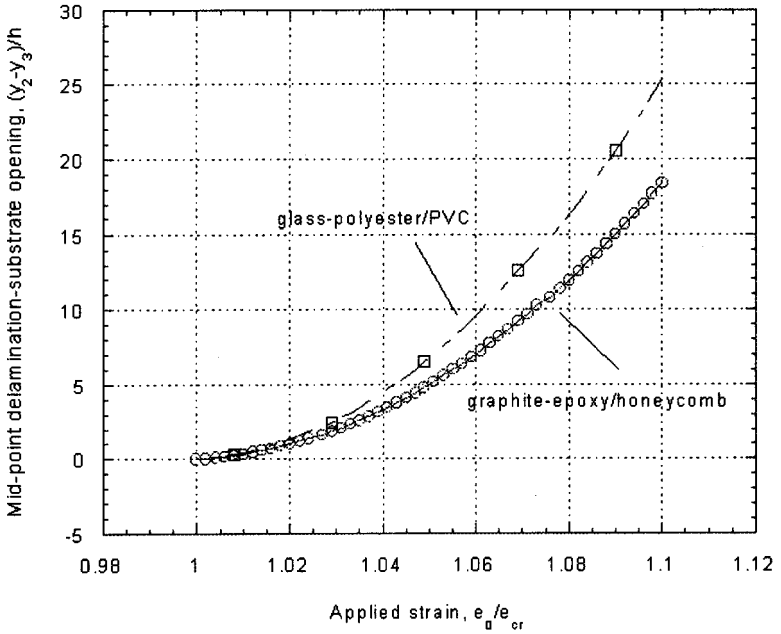

(*b*)

Fig. 4 (*a*) Comparison of the two material sandwich systems with regard to the delamination midpoint deflection during the initial post-buckling phase. (*b*) Comparison of the two material sandwich systems with regard to the midpoint delamination-substrate opening during the initial post-buckling phase.

The second-order moment equilibrium from (7) is

$$D_1\frac{d\theta_1^{(2)}}{dx_1}\bigg|_{x_1=L-a}-D_2\frac{d\theta_2^{(2)}}{dx_2}\bigg|_{x_2=-a}-D_3\frac{d\theta_3^{(2)}}{dx_3}\bigg|_{x_3=-a}$$
$$-P_2^{(2)}\left(f_1+\frac{c}{2}+e_1-\frac{h}{2}\right)+P_3^{(2)}(e_3-e_1)=0, \qquad (27)$$

and the second-order force equilibrium is

$$P_2^{(2)}+P_3^{(2)}=P_1^{(2)}. \qquad (28)$$

Finally, the second-order displacement compatibility from (8)–(10) and (11,12) is

$$\frac{1}{2}\int_{-a}^{0}\theta_3^{(1)^2}(x_3)dx_3+\frac{P_3^{(2)}a}{w[E_{f1}(f_1-h)+E_cc+E_{f2}f_2]}$$
$$=\frac{1}{2}\int_{-a}^{0}\theta_2^{(1)^2}(x_2)dx_2+\frac{P_2^{(2)}a}{E_{f1}wh}. \qquad (29)$$

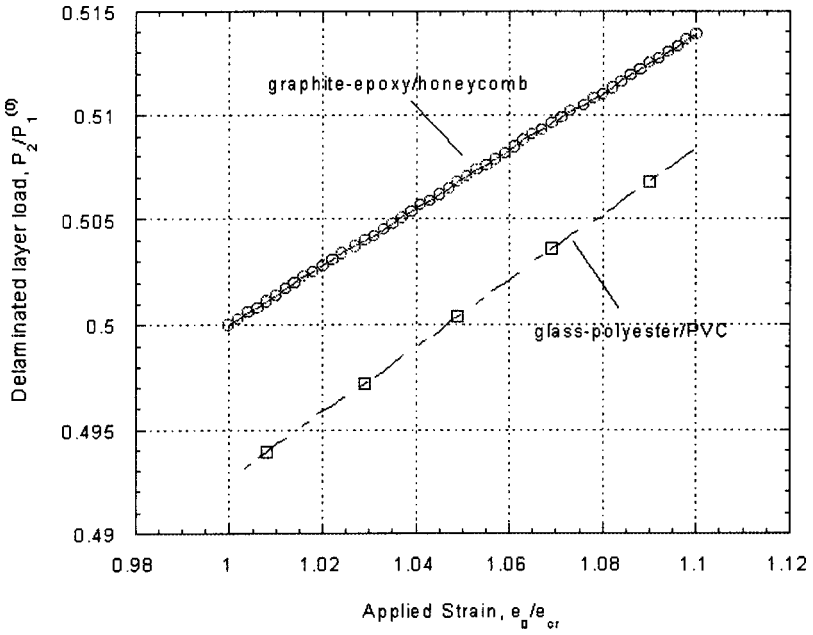

(*a*)

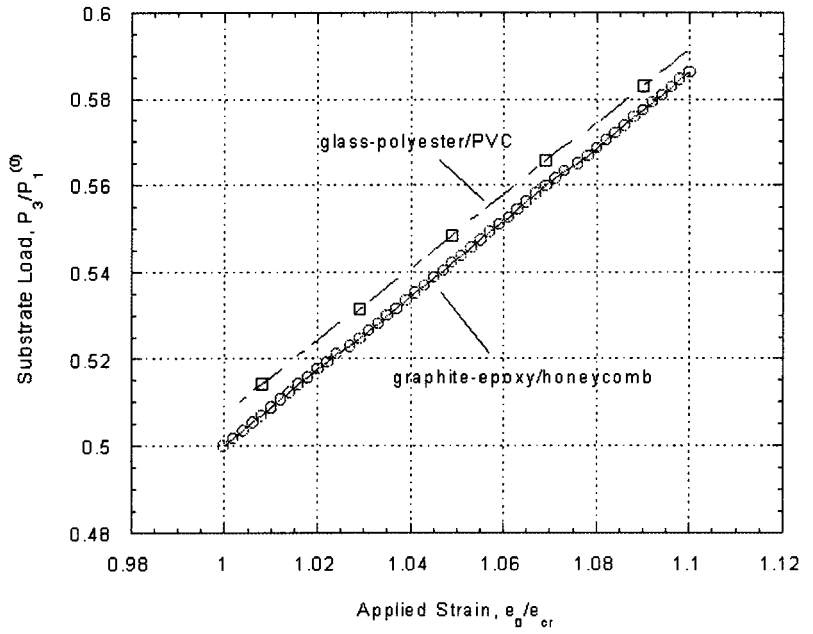

(*b*)

Fig. 5 (*a*) Comparison of the two material sandwich systems with regard to the delamination load during the initial post-buckling phase. (*b*) Comparison of the two material sandwich systems with regard to the substrate load during the initial post-buckling phase.

The general solution for the second-order differential Eq. (25) is

$$\theta_i^{(2)}(x_i) = C_i^{(2)} \sin \lambda_i x_i + B_i^{(2)} \cos \lambda_i x_i + \frac{P_i^{(1)}}{2\lambda_i D_i}\left(\frac{2\alpha_i P_i^{(0)}}{A_i \bar{G}_i} + 1\right) C_i^{(1)} x_i \cos \lambda_i x_i . \quad (30)$$

The constants $B_i^{(2)}$ are zeros due to the boundary conditions (26*a*),

$$B_i^{(2)} = 0, \quad i = 1,2,3. \quad (31)$$

Applying the conditions (26*b*), we can find the constants $C_i^{(2)}$ as

$$C_1^{(2)} = -\frac{P_1^{(1)}}{2\lambda_1 D_1} C_1^{(1)} (L-a) \cot \lambda_1 (L-a)\left(\frac{2\alpha_1 P_1^{(0)}}{A_1 \bar{G}_1} + 1\right), \quad (32a)$$

and

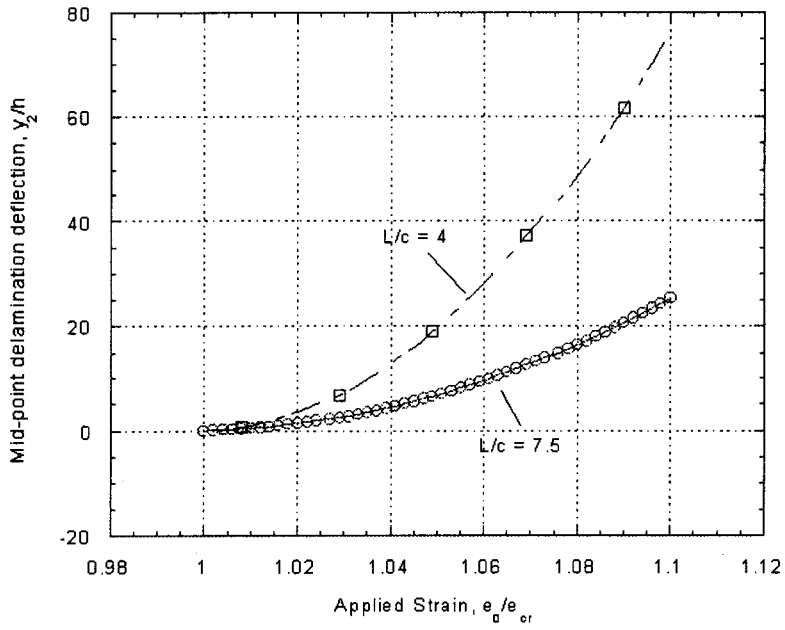

Fig. 6 Effect of the length over core thickness aspect ratio on the midpoint delamination deflection during the initial post-buckling phase for glass-epoxy/polyester

$$C_i^{(2)} = -\frac{P_i^{(1)}}{2\lambda_i D_i} C_i^{(1)} a \cot \lambda_i a \left(\frac{2\alpha_i P_i^{(0)}}{A_i \bar{G}_i} + 1 \right), \quad i = 2,3. \tag{32b}$$

Now the displacement compatibility Eq. (29), becomes

$$P_2^{(2)} \frac{a}{E_{f1} wh} - P_3^{(2)} \frac{a}{w[E_{f1}(f_1 - h) + E_c c + E_{f2} f_2]} = \frac{1}{4} \left[C_3^{(1)2} \left(a - \frac{\sin 2\lambda_3 a}{2\lambda_3} \right) - C_2^{(1)2} \left(a - \frac{\sin 2\lambda_2 a}{2\lambda_2} \right) \right]. \tag{33}$$

The moment equilibrium (27), by substituting the second-order deflections (30) and again the relationship for the neutral axes of the substrate and the base part (22*b*), becomes

$$\left[P_2^{(2)} \frac{a}{E_{f1} wh} - P_3^{(2)} \frac{a}{w[E_{f1}(f_1 - h) + E_c c + E_{f2} f_2]} \right] \times \frac{E_{f1} wh \left(f_1 + \frac{c}{2} + e_1 - \frac{h}{2} \right)}{a} = D_1 \left\{ C_1^{(2)} \lambda_1 \cos \lambda_1 (L - a) + \frac{C_1^{(1)} P_1^{(1)}}{2\lambda_1 D_1} \left(\frac{2\alpha_1 P_1^{(0)}}{A_1 \bar{G}_1} + 1 \right) \times [\cos \lambda_1 (L - a) - (L - a) \lambda_1 \sin \lambda_1 (L - a)] \right\} - \sum_{i=2,3} D_i \left[C_i^{(2)} \lambda_i \cos \lambda_i a + \frac{C_i^{(1)} P_i^{(1)}}{2\lambda_i D_i} \left(\frac{2\alpha_i P_i^{(0)}}{A_i \bar{G}_i} + 1 \right) \times (\cos \lambda_i a - a \lambda_i \sin \lambda_i a) \right]. \tag{34}$$

Comparing (34) and (33), we can eliminate the left-hand side of the latter equation, which contains the second-order forces, and, by using also (32), thus obtain one equation for the first-order forces, i.e.,

$$a_2 P_2^{(1)} + a_3 P_3^{(1)} = \frac{1}{4} \left[C_3^{(1)2} \left(a - \frac{\sin 2\lambda_3 a}{2\lambda_3} \right) - C_2^{(1)2} \times \left(a - \frac{\sin 2\lambda_2 a}{2\lambda_2} \right) \right] \frac{E_{f1} wh \left(f_1 + \frac{c}{2} + e_1 - \frac{h}{2} \right)}{a}, \tag{35}$$

where

$$a_i = \frac{C_1^{(1)}}{2\lambda_1} \left(\frac{2\alpha_1 P_1^{(0)}}{A_1 \bar{G}_1} + 1 \right) \left[\cos \lambda_1 (L - a) - \frac{(L - a)\lambda_1}{\sin \lambda_1 (L - a)} \right] + \frac{C_i^{(1)}}{2\lambda_i} \left(\frac{2\alpha_i P_i^{(0)}}{A_i \bar{G}_i} + 1 \right) \left(\frac{a \lambda_i}{\sin \lambda_i a} - \cos \lambda_i a \right), \quad i = 2,3.$$

The second equation for the first-order forces is the first-order compatibility Eq. (18*g*).

The system of these two linear equations, (35) and (18*g*), can be solved for the first-order forces, $P_2^{(1)}$ and $P_3^{(1)}$.

The solution for the higher-order terms can proceed in the same fashion.

The first-order applied load $P_1^{(1)}$ is in turn found from the second-order force equilibrium, Eq. (28). Notice that from (11), since $P_1^{(0)} = P_{cr}$, the perturbation parameter ξ can be found from the applied external load, $\bar{P}$, as

$$\xi = \frac{\bar{P} - P_{cr}}{P_1^{(1)}}. \tag{36}$$

This, of course, presumes that we only account for the first-order load terms.

Deflections. The deflections can be found by integrating the relationship (Huang and Kardomateas [15])

$$\frac{dy_i}{dx_i}=\sin\theta_i+\frac{\alpha_i P_i}{2A_i\overline{G}_i}\sin 2\theta_i\,. \tag{37a}$$

Introducing the asymptotic expansions (11) and (12) and the first and second-order expressions (20) and (30), gives

$$\frac{dy_i}{dx_i}=\xi\left(1+\frac{\alpha_i P_i^{(0)}}{\overline{G}_i A_i}\right)\theta_i^{(1)}+\xi^2\left[\left(1+\frac{\alpha_i P_i^{(0)}}{\overline{G}_i A_i}\right)\theta_i^{(2)}+\frac{\alpha_i P_i^{(1)}}{\overline{G}_i A_i}\theta_i^{(1)}\right]+O(\xi^3), \tag{37b}$$

and therefore by integrating with the boundary condition

$$y_1(0)=0;\quad \text{and } y_i(-a)=0;\quad i=2,3 \tag{37c}$$

gives the first-order deflections as

$$y_1^{(1)}=\frac{C_1^{(1)}}{\lambda_1}\left(1+\frac{\alpha_1 P_1^{(0)}}{\overline{G}_1 A_1}\right)(1-\cos\lambda_1 x_1), \tag{38a}$$

$$y_i^{(1)}=\frac{C_i^{(i)}}{\lambda_i}\left(1+\frac{\alpha_i P_i^{(0)}}{\overline{G}_i A_i}\right)(\cos\lambda_i a-\cos\lambda_i x_i);\quad i=2,3 \tag{38b}$$

and the second-order deflections as

$$y_1^{(2)}=\left(1+\frac{\alpha_1 P_1^{(0)}}{\overline{G}_1 A_1}\right)\left[\left(\frac{Q_1^{(1)}}{\lambda_1^2}-\frac{C_1^{(2)}}{\lambda_1}\right)(\cos\lambda_1 x_1-1)+\frac{Q_1^{(1)}}{\lambda_1}x_1\sin\lambda_1 x_1\right]+\frac{C_1^{(1)}}{\lambda_1}\frac{\alpha_1 P_1^{(1)}}{\overline{G}_1 A_1}(1-\cos\lambda_1 x_1), \tag{39a}$$

$$y_i^{(2)}=\left(1+\frac{\alpha_i P_i^{(0)}}{\overline{G}_i A_i}\right)\left[\left(\frac{Q_i^{(1)}}{\lambda_i^2}-\frac{C_i^{(2)}}{\lambda_i}\right)(\cos\lambda_i x_i-\cos\lambda_i a)+\frac{Q_i^{(1)}}{\lambda_i}(x_i\sin\lambda_i x_i-a\sin\lambda_i a)\right]+\frac{C_i^{(1)}}{\lambda_i}\frac{\alpha_i P_i^{(1)}}{\overline{G}_i A_i}(\cos\lambda_i a-\cos\lambda_i x_i);\quad i=2,3 \tag{39b}$$

where

$$Q_i^{(1)}=\frac{P_i^{(1)}C_i^{(1)}}{2\lambda_i D_i}\left(\frac{2\alpha_i P_i^{(0)}}{\overline{G}_i A_i}+1\right);\quad i=1,2,3. \tag{39c}$$

Discussion of Results

For an illustration of the results from the previous analysis, consider a sandwich beam with (in mm) $f_1=f_2=3$, $c=25$, $h=3$, $w=20$, and $L=150$. Two types of core were used: (a) a PVC core with (in MPa) $E_c=93$, $G_c=35$, and (b) an aluminum honeycomb core with $E_c=1$, $G_c=200$ (data from Gibson and Asby [16]). The corresponding face-sheets were (a) E-glass/polyester unidirectional with (in GPa) $E_{f1}=E_{f2}=26$ and $G_{f1}=G_{f2}=3$ and (b) graphite/epoxy unidirectional with $E_{f1}=E_{f2}=140$ and $G_{f1}=G_{f2}=5$. In the results presented, the case of no transverse shear effect corresponds to $\alpha_i=0$.

The shear correction factors for the case of glass-polyester/PVC system are $\alpha_1=1.215$, $\alpha_2=1.200$, and $\alpha_3=1.044$. More important are the corresponding ratios $\alpha_i/\overline{G}_i A_i$, as these represent the magnitude of the effect of transverse shear and these were, respectively, 0.453×10^{-4}, 0.667×10^{-5}, and 0.476×10^{-4}. The first and the last numbers are larger because they include the core, unlike the second number which is for the delaminated layer only. For the graphite-epoxy/honeycomb, the corresponding data are $\alpha_1=1.209$, $\alpha_2=1.200$, and $\alpha_3=0.482$, whereas the $\alpha_i/\overline{G}_i A_i$ ratios are 0.794×10^{-5}, 0.400×10^{-5}, and 0.386×10^{-5}. The last set of numbers shows the importance of the low extensional modulus of the honeycomb core.

Figure 3 shows the critical strain, ϵ_{cr} for a range of delamination lengths in the case of sandwich material system (a). It is seen that the critical strain decreases with longer delaminations, as expected, and that the effect of transverse shear is to lower the critical strain, again as expected.

The initial post-buckling results which follow are produced for delamination length $a=L/3$. This solution is an asymptotic solution, so accuracy is expected to be compromised as we move away from the critical point. Figure 4(a) shows the midpoint delamination deflection versus applied strain for the two material systems and Fig. 4(b) shows the midpoint delamination-substrate opening. Both deflections are higher for the glass-polyester/PVC case, which is expected due to the lower stiffness of the face sheet. The delamination load (normalized with the critical load) is shown in Fig. 5(a) and the substrate load is shown in Fig. 5(b). For both material systems the delamination load and the substrate load increases with applied strain, but no definite trend exists between the two material systems—the normalized (with P_{cr}) delamination load being higher in the material system (b) but the normalized substrate load being higher in the material system (a).

Finally, Fig. 6 shows the effect of the length over core thickness aspect ratio on the midpoint delamination deflection during the initial post-buckling phase for glass-epoxy/polyester material system. The face sheet thickness and delamination length was kept constant and the critical strain is essentially the same in both cases (slightly lower for the higher aspect ratio). But the case of a thicker core (lower aspect ratio) shows a higher delamination deflection.

Acknowledgments

The financial support of the Office of Naval Research, Ship Structures S & T Division, Grant N00014-90-J-1995, and of the Air Force Office of Scientific Research, Grant F49620-98-1-0384, and the interest and encouragement of the Grant Monitors, Dr. Y. D. S. Rajapakse, Dr. Brian Sanders, and Dr. Ozden Ochoa are both gratefully acknowledged. The authors would also like to acknowledge valuable discussions regarding sandwich material properties with Prof. Leif Carlsson, Florida Atlantic University.

References

[1] Yin, W. L., Sallam, S., and Simitses, G. J., 1986, "Ultimate Axial Load Capacity of a Delaminated Beam-Plate," AIAA J., **24**(1), pp. 123–128.
[2] Simitses, G. J., Sallam, S., and Yin, W. L., 1985, "Effect of Delamination on Axially Loaded Homogeneous Laminated Plates," AIAA J., **23**, pp. 1437–1444.
[3] Chai, H., Babcock, C. D., and Knauss, W. G., 1981, "One Dimensional Modeling of Failure in Laminated Plates by Delamination Buckling," Int. J. Solids Struct., **17**(11), pp. 1069–1083.
[4] Whitcomb, J. D., 1981, "Finite Element Analysis of Instability-Related Delamination Growth," NASA TM 81964, Mar.
[5] Shivakumar, K. N., and Whitcomb, J. D., 1985, "Buckling of a Sublaminate in a Quasi-Isotropic Composite Laminate," J. Compos. Mater., **19**, Jan., pp. 2–18.
[6] Kardomateas, G. A., 1990, "Postbuckling Characteristics in Delaminated Kevlar/Epoxy Laminates: An Experimental Study," J. Compos. Technol. Res., **12**(2), pp. 85–90.
[7] Kardomateas, G. A., 1993, "The Initial Postbuckling and Growth Behavior of Internal Delaminations in Composite Plates," ASME J. Appl. Mech., **60**, pp. 903–910.
[8] Kardomateas, G. A., Pelegri, A. A., and Malik, B., 1995, "Growth of Internal Delaminations Under Cyclic Compression in Composite Plates," J. Mech. Phys. Solids, **43**(6), pp. 847–868.
[9] Kant, T., and Patil, H. S., 1991, "Buckling Load of Sandwich Columns With a Higher-Order Theory," J. Reinf. Plast. Compos., **10**(1), pp. 102–109.

[10] Hunt, G. E., and Da Silva, L. S., 1990, ''Interaction Bending Behavior of Sandwich Beams,'' ASME J. Appl. Mech., **57**, pp. 189–196.
[11] Hunt, G. E., and Da Silva, L. S., 1990, ''Interactive Buckling in Sandwich Structures With Core Orthotropy,'' Int. J. Mech. Struct. Mech., **18**(3), pp. 353–372.
[12] Frostig, Y., 1992, ''Behavior of Delaminated Sandwich Beams With Transversely Flexible Core—High Order Theory,'' Composite Structures, **20**, pp. 1–16.
[13] Frostig, Y., and Baruch, M., 1993, ''Buckling of Simply-Supported Sandwich Beams With Transversely Flexible Core—A High Order Theory,'' J. Eng. Mech. Div., **119**(5), pp. 955–972.
[14] Rajapakse Y. D. S., Kardomateas G. A., and Birman V., eds, 2000, *Mechanics of Sandwich Structures*, AD-Vol. 62/AMD-Vol. 245, ASME, New York.
[15] Huang, H., and Kardomateas, G. A., 2002, ''Buckling and Postbuckling of Sandwich Beams Including Transverse Shear,'' AIAA J., **40**(11), pp. 2331–2335.
[16] Gibson, L. J., and Ashby, M. F., 1997, *Cellular Solids—Structure and Properties*, 2nd Ed., Cambridge University Press, Cambridge, UK.

J. C. Nadeau
Department of Civil and Environmental Engineering,
Duke University,
Durham, NC 27708-0287

M. Ferrari
Center for Biomedical Engineering and
Department of Mechanical Engineering,
The Ohio State University,
Columbus, OH 43210-1002

Bounds on Texture Coefficients

The orientation distribution function (ODF) is expanded in terms of generalized spherical harmonics and bounds on the resulting texture coefficients are derived. A necessary and sufficient condition for satisfaction of the normalization property of the ODF is also provided. These results are of significance in, for example, microstructural optimization of materials and predicting texture coefficients based on wave velocity measurements.
[DOI: 10.1115/1.1533808]

Introduction

A polycrystal, at a sufficiently large length scale, can appear macroscopically homogeneous and isotropic if the anisotropic single crystals which comprise the polycrystal are not preferentially distributed spatially nor orientationally. If a polycrystal exhibits a preferential orientation of its grains then it is said to exhibit texture. As a consequence of texture, a polycrystal will, in general, exhibit anisotropy which can be quantified regardless of material anisotropy, [1]. If the texture varies spatially then at that same length scale the polycrystal will be nonhomogeneous.

The texture of a polycrystal may be quantified by the orientation distribution function (ODF) which is, in essence, a probability distribution function; the random variable being the orientation of a single crystal. The texture of the polycrystal can be equivalently quantified by texture coefficients which are the coefficients of a harmonic expansion of the ODF. The terms of the expansion are the generalized spherical harmonics (GSH) and the expansion is termed the Viglin expansion, [2].

The use of ODFs and texture coefficients are not limited to polycrystals. The analysis of many modern composite materials necessitates the appropriate characterization of the composites texture by quantifying the orientation distribution of each constituent. Thus, texture, and its quantification, is important not only in polycrystals, [3–6], but also, more generally, in composite materials, [7–10].

Increasing technological interest in composite materials in the areas of, for example, thermal barrier coatings, [11], and functionally graded materials, [12,13], will lead ultimately to optimally designed microstructures of materials, [14,15]. If the texture of the material is taken as a design parameter then it would be conceivable to optimize the texture coefficients. As a result of the truncation theorem, [6], not all texture coefficients affect the effective properties. However, optimizing those texture coefficients which are relevant necessitates that only physically plausible texture coefficients be considered. For this reason bounds on the texture coefficients are significant. Bounds are also of relevance when using inversion techniques to estimate the texture coefficients based on wave velocity measurements, [16,17].

Preliminaries

The orientation distribution function (ODF) is denoted by $f(g)$ where $g := (\psi_1, \phi, \psi_2) \in SO(3)$ is the Euler triad and ψ_1, ϕ, and ψ_2 are the Euler angles and $SO(3)$ is the group of proper orthogonal rotations. Let x_i and x_i', $i \in \{1,2,3\}$, denote the Cartesian axes of the global and local coordinate frames, respectively, which are indistinguishable apart from a translation. The Euler angles ψ_1, ϕ, and ψ_2 are successive rotations about the x_3', x_1', and x_3' axes, respectively. For a graphical illustration see Fig. 1. The Euler triad g thus describes the orientation of the local coordinate frame relative to the global coordinate frame. The quantity $f(g)dg$ is the probability of an orientation within the "interval" $[g, g+dg)$ being achieved where $dg = 1/(8\pi^2)\sin\phi\, d\psi_1 d\phi d\psi_2$.

The ODF, being a probability density function, possess certain properties. Namely, (a) $f(g)$ is a real quantity; (b) $f(g)$ is strictly positive: $f(g)dg \geqslant 0$; and (c) $f(g)$ is normalized such that it integrates to unity: $\oint f(g)dg = 1$, where $\oint(\cdot)dg := 1/(8\pi^2)\int_0^{2\pi} \times \int_0^{\pi}\int_0^{2\pi}(\cdot)\sin\phi\, d\psi_1 d\phi d\psi_2$.

Generalized spherical harmonics (GSH) are the matrix elements of the irreducible representation of the three-dimensional rotation group. They are defined by (see, for example, Bunge [4])

$$T_l^{mn}(g) \equiv T_l^{mn}(\psi_1, \phi, \psi_2) := e^{im\psi_2} P_l^{mn}(\cos\phi) e^{in\psi_1} \tag{1}$$

where $P_l^{mn}(\cos\phi)$ are the generalized Legendre functions. We note that $P_0^{00}(\cos\phi) = 1$ and, thus, $T_0^{00}(g) = 1$. We also note that $T_l^{mn}(0,0,0) = \delta^{mn}$, $T_l^{mn}(0,\pi,0) = (-1)^l \delta^{m\hat{n}}$ and, finally,

$$\begin{aligned} P_l^{mn}(\cos\phi) &= P_l^{nm}(\cos\phi) \\ &= P_l^{\hat{m}\hat{n}}(\cos\phi) = (-1)^{l+m+n} P_l^{\hat{m}n}(-\cos\phi) \end{aligned} \tag{2}$$

where $\hat{m} := -m$.

The GSH form a complete set of orthonormal functions, ([4], p. 352), meaning that

$$\oint T_l^{mn}(g)\overline{T}_{l'}^{m'n'}(g)dg = \frac{1}{2l+1}\delta_{ll'}\delta^{mm'}\delta^{nn'} \tag{3}$$

where $\delta_{ij} \equiv \delta^{ij}$ is the Kronecker delta and an overbar denotes complex conjugation. We should remark that, throughout this paper, summation convention is *not* invoked.

A Viglin expansion, [2], of the ODF is now given in terms of the GSH

$$f(g) = \sum_{l=0}^{\infty}\sum_{m=-l}^{l}\sum_{n=-l}^{l} C_l^{mn} T_l^{mn}(g) \tag{4}$$

where C_l^{mn} are the coefficients of the expansion. These coefficients are termed texture coefficients and are given by the inverse relation

$$C_l^{mn} = (2l+1)\oint f(g)\overline{T}_l^{mn}(g)dg. \tag{5}$$

Bounds

As discussed above, the orientation distribution function (ODF) is a real-valued, strictly positive function which is normalized to unity. Thus, by means of Eq. (5), these properties of the ODF

Contributed by the Applied Mechanics Division of THE AMERICAN SOCIETY OF MECHANICAL ENGINEERS for publication in the ASME JOURNAL OF APPLIED MECHANICS. Manuscript received by the Applied Mechanics Division, June 5, 2002; final revision, July 26, 2002. Associate Editor: L. T. Wheeler. Discussion on the paper should be addressed to the Editor, Prof. Robert M. McMeeking, Chair, Department of Mechanics and Environmental Engineering, University of California–Santa Barbara, Santa Barbara, CA 93106-5070, and will be accepted until four months after final publication in the paper itself in the ASME JOURNAL OF APPLIED MECHANICS.

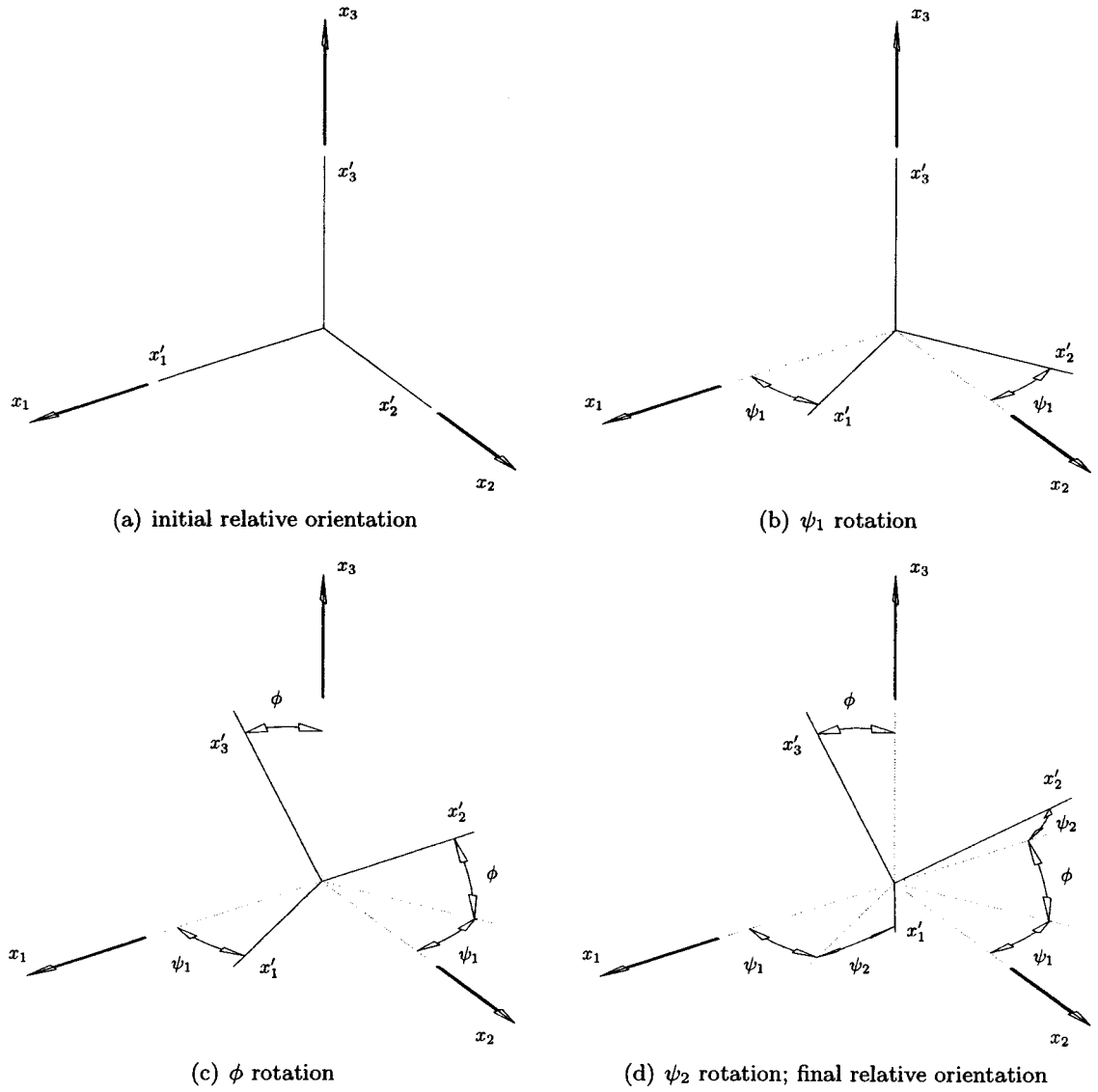

Fig. 1 The orientation of the local coordinate system $(x_1'x_2'x_3')$ with respect to the global coordinate system $(x_1x_2x_3)$, as shown in (*d*), is described in terms of a sequence of Euler angle $(g:=(\psi_1,\phi,\psi_2))$ rotations as illustrated in (*b*), (*c*), and (*d*) given the initial relative orientation of the coordinates systems in (*a*)

must imply constraints on the texture coefficients. For example, the requirement that the ODF be a real quantity implies that $C_l^{\hat{m}\hat{n}}=(-1)^{m+n}\overline{C}_l^{mn}$, [2,4]. We now present another constraint, namely, bounds on the texture coefficients.

The generalized spherical harmonics T_l^{mn}, for $-l\leqslant m,n\leqslant l$ form a unitary matrix. That is, $\Sigma_{s=-l}^{l}T_l^{ms}\overline{T}_l^{ns}=\delta^{mn}$. It follows that

$$1=\sum_{s=-l}^{l}T_l^{ms}(g)\overline{T}_l^{ms}(g)=\sum_{s=-l}^{l}|T_l^{ms}(g)|^2=\sum_{s=-l}^{l}|P_l^{ms}(\cos\phi)|^2 \tag{6}$$

which is a result that can be found in [[18], p. 89]. It follows that

$$|P_l^{ms}(\cos\phi)|\leqslant 1. \tag{7}$$

It follows from Eq. (5) that

$$|C_l^{mn}|=(2l+1)\left|\oint f(g)\overline{T}_l^{mn}(g)dg\right| \tag{8}$$

$$\leqslant(2l+1)\oint f(g)|\overline{T}_l^{mn}(g)|dg \tag{9}$$

$$=(2l+1)\oint f(g)|P_l^{mn}(\cos\phi)|dg \tag{10}$$

$$\leqslant(2l+1)\oint f(g)dg \tag{11}$$

$$=2l+1. \tag{12}$$

In arriving at Eq. (9) from Eq. (8) we made use of Hölder's inequality and the fact that $f(g)dg\geqslant 0$. Equation (11) follows from Eq. (10) by use of Eq. (7). This concludes the proof, however, details are given below for more rigorous bounds on some of the texture coefficients, namely, the coefficients C_l^{mn} for which $|m|\neq|n|$.

Further restrictive bounds on C_0^{00} can be achieved by making use of the normalization requirement of the ODF. In fact, the normalization requirement is satisfied if and only if $C_0^{00}=1$. This result has been recorded without proof in [5] so we shall provide the proof below.

To prove necessity, evaluate C_0^{00} using Eq. (5). This leads to $C_0^{00}=\oint f(g)dg=1$ because $\overline{T_0^{00}}(g)=1$. To prove sufficiency, we begin by noting that

$$\oint T_l^{mn}(g)dg=\begin{cases}1, & l=m=n=0\\ 0, & \text{otherwise}\end{cases} \tag{13}$$

which follows directly from the orthonormal property (3) of the generalized spherical harmonics (GSH). To complete the proof

$$1=\oint f(g)dg=\oint \sum_{l=0}^{\infty}\sum_{m=-l}^{l}\sum_{n=-l}^{l} C_l^{mn}T_l^{mn}(g)dg \tag{14}$$

$$=\sum_{l=0}^{\infty}\sum_{m=-l}^{l}\sum_{n=-l}^{l} C_l^{mn}\oint T_l^{mn}(g)dg \tag{15}$$

$$=C_0^{00}. \tag{16}$$

The last result follows from Eq. (13). This concludes the proof.

As mentioned above, more rigorous bounds can be ascertained on some of the texture coefficients. We investigate this issue now. Consider the unidirectional ODF $f(g)=k\,\delta(\psi_1)\,\delta(\phi)\,\delta(\psi_2)$ where δ is the Dirac delta function and k is a normalizing constant determined such that $\oint f(g)dg=1$. Substituting this ODF into Eq. (5) after evaluating the normalizing constant k, and recalling that $T_l^{mn}(0,0,0)=\delta^{mn}$, yields $C_l^{mn}=(2l+1)\,\delta^{mn}$. Thus, $C_l^{mm}=2l+1$ from which it follows that more restrictive bounds can *not* be determined on C_l^{mm} without additional information on the ODF. Similarly, by considering the unidirectional ODF $f(g)=k'\,\delta(\psi_1)\,\delta(\phi-\pi)\,\delta(\psi_2)$ and recalling that $T_l^{mn}(0,\pi,0)=(-1)^l\delta^{m\hat{n}}$ it can be determined that $C_l^{mn}=(-1)^l\delta^{m\hat{n}}$. Thus, $|C_l^{\hat{n}n}|=2l+1$ from which it follows that more restrictive bounds can *not* be determined on $C_l^{\hat{n}n}$, or, equivalently, $C_l^{n\hat{n}}$ since $-l\leqslant n\leqslant l$, without additional information on the ODF.

This leaves the remaining texture coefficients C_l^{mn} with $|m|\neq|n|$ for which we can *not* conclude that a maximum modulus of $2l+1$ can be achieved. In fact, more restrictive bounds are possible on these texture coefficients. We proceed by bounding the corresponding generalized Legendre function $P_l^{mn}(\cos\phi)$ and returning to Eq. (10) to yield the result

$$|C_l^{mn}|\leqslant\alpha_l^{mn}(2l+1),\quad 0\leqslant\alpha_l^{mn}\leqslant 1 \tag{17}$$

where α_l^{mn} is the least upper bound to $|P_l^{mn}(\cos\phi)|$. From the relations (2) we can conclude, for a given l, m, and n, that

$$\alpha_l^{mn}=\alpha_l^{\hat{m}\hat{n}}=\alpha_l^{\hat{m}n}=\alpha_l^{m\hat{n}}. \tag{18}$$

From those same relations we also conclude that $\alpha_l^{mn}=\alpha_l^{nm}$. From our previous results we know that $\alpha_l^{mn}=1$ for $|m|=|n|$. The result (17) yields the most restrictive bounds possible without additional information on the ODF.

For $l=1$ and $l=2$ we can consider the closed-form expressions for $P_l^{mn}(\cos\phi)$ given by Bunge ([4], pp. 352–353). For $l=1$ we have $P_1^{01}=-(i/\sqrt{2})\sin\phi$ where $i^2=-1$. Thus, $\alpha_1^{01}=1/\sqrt{2}$, and, with the assistance of Eq. (18), we tabulate the values of α_1^{mn} in Table 1. For $l=2$ the values of α_l^{mn} are presented in Table 2.

For $l\geqslant 3$ we proceed by considering a Fourier series expansion of $P_l^{mn}(\cos\phi)$ as given by Bunge [4, Section 14.3]. It is also necessary at this stage to implement a numerical procedure for determining the least upper bound to $|P_l^{mn}(\cos\phi)|$. Because we need only consider those cases for which $|m|\neq|n|$, and because of the relations (18), it is only necessary to find the least upper bound to $l(l+1)/2$ functions in distinction from the $(2l+1)^2$ generalized Legendre functions—for a given l. Results from implementing such a numerical procedure for $l=3$ and $l=4$ are presented in Tables 3 and 4, respectively.

Table 1 Bounding coefficients $\alpha_1^{mn}(|C_1^{mn}|\leqslant 3\alpha_1^{mn})$

	α_1^{mn}	
m	n	
	0	±1
0	1	$1/\sqrt{2}$
±1	$1/\sqrt{2}$	1

In closing, we make mention of two additional points. First, satisfaction of the bounds (17) is *not* a sufficient condition for a strictly positive ODF. Consider the set of texture coefficients, $C_0^{00}=1$, $C_2^{00}=-5$ and all other $C_l^{mn}=0$. These texture coefficients satisfy the bounds (17) but yield the function $f(g)=1-5[\frac{1}{4}+\frac{3}{4}\cos(2\phi)]$, for which, clearly, $f(g)dg$ takes on negative values. Secondly, if more information on the ODF is known, for example in terms of its symmetries, then relations among the texture coefficients may be deduced (see, for example, Ferrari and Johnson [9]).

Closure

This paper has derived bounds, namely, $|C_l^{mn}|\leqslant 2l+1$, on the texture coefficients C_l^{mn} as deduced from properties of the orientation distribution function (ODF). It has also been shown that more rigorous bounds can, in general, be proven when $|m|\neq|n|$. The form of the bounds on C_l^{mn} can then be written as $|C_l^{mn}|\leqslant\alpha_l^{mn}(2l+1)$ where α_l^{mn} is the least upper bound to the modulus of the generalized Legendre function $P_l^{mn}(\cos\phi)$. Results for α_l^{mn} have been tabulated for $l=1$, 2, 3, and 4. It has also been proven

Table 2 Bounding coefficients $\alpha_2^{mn}(|C_2^{mn}|\leqslant 5\alpha_2^{mn})$

	α_2^{mn}		
m	n		
	0	±1	±2
0	1	$\sqrt{6}/4$	$\sqrt{6}/4$
±1	$\sqrt{6}/4$	1	$3\sqrt{3}/8$
±2	$\sqrt{6}/4$	$3\sqrt{3}/8$	1

Table 3 Bounding coefficients $\alpha_3^{mn}(|C_3^{mn}|\leqslant 7\alpha_3^{mn})$

	α_3^{mn}			
m	n			
	0	±1	±2	±3
0	1	0.596285	0.527046	0.559017
±1	0.596285	1	0.601333	0.573775
±2	0.527046	0.601333	1	0.633938
±3	0.559017	0.573775	0.633938	1

Table 4 Bounding coefficients $\alpha_4^{mn}(|C_4^{mn}|\leqslant 9\alpha_4^{mn})$

	α_4^{mn}				
m	n				
	0	±1	±2	±3	±4
0	1	0.590337	0.508223	0.480326	0.522913
±1	0.590337	1	0.591869	0.516186	0.530690
±2	0.508223	0.591869	1	0.597026	0.558088
±3	0.480326	0.516186	0.597026	1	0.626655
±4	0.522913	0.530690	0.558088	0.626655	1

that $C_0^{00}=1$ is a necessary and sufficient condition for satisfaction of the normalization property of the ODF: $\oint f(g)dg=1$.

Acknowledgments

JCN was supported by the National Science Foundation (NSF) grant MSS-9215671 and MF gratefully acknowledges the support of the NSF through the National Young Investigator Award in the Mechanics and Materials program.

References

[1] Nadeau, J. C., and Ferrari, M., 2001, ''On Optimal Zeroth-Order Bounds With Application to Hashin-Shtrikman Bounds and Anisotropy Parameters,'' Int. J. Solids Struct., **38**, pp. 7945–7965.
[2] Viglin, A. S., 1961, ''A Quantitative Measure of the Texture of a Polycrystalline Material-Texture Function,'' Sov. Phys. Solid State, **2**(10), pp. 2195–2207.
[3] Morris, P. R., and Heckler, A. J., 1965, ''Crystallite Orientation Analysis for Rolled Cubic Materials,'' Adv. X-Ray Anal., **11**, pp. 454–472.
[4] Bunge, H.-J., 1982, *Texture Analysis in Materials Science*, Butterworths, London.
[5] Johnson, G. C., and Wenk, H. R., 1986, ''Elastic Properties of Polycrystals With Trigonal Crystal and Orthorhombic Specimen Symmetry,'' J. Appl. Phys., **60**(11), pp. 3868–3875.
[6] Ferrari, M., and Johnson, G. C., 1988, ''The Equilibrium Properties of a 6 mm Polycrystal Exhibiting Transverse Isotropy,'' J. Appl. Phys., **63**(9), pp. 4460–4468.
[7] Takao, Y., Chou, T. W., and Taya, M., 1982, ''Effective Longitudinal Young's Modulus of Misoriented Short Fiber Composites,'' ASME J. Appl. Mech., **49**(3), pp. 536–540.
[8] Advani, S. G., and Tucker, C. L., 1987, ''The Use of Tensors to Describe and Predict Fiber Orientation in Short Fiber Composites,'' J. Rheol., 31(8), pp. 751–784.
[9] Ferrari, M., and Johnson, G. C., 1989, ''Effective Elasticities of Short-Fiber Composites With Arbitrary Orientation Distribution,'' Mech. Mater., **8**, pp. 67–73.
[10] Marzari, N., and Ferrari, M., 1992, ''Textural and Micromorphological Effects on the Overall Elastic Response of Macroscopically Anisotropic Composites,'' ASME J. Appl. Mech., **59**, pp. 269–275.
[11] Taylor, R., Brandon, J. R., and Morrell, P., 1992, ''Microstructure, Composition and Property Relationships of Plasma-Sprayed Thermal Barrier Coatings,'' Surf. Coat. Technol., **50**(2), pp. 141–149.
[12] Lee, W. Y., Stinton, D. P., Berndt, C. C., Erdogan, F., Lee, Y.-D., and Mutasim, Z., 1996, ''Concept of Functionally Graded Materials for Advanced Thermal Barrier Coating Applications,'' J. Am. Ceram. Soc., **79**(12), pp. 3003–3012.
[13] Cherradi, N., Kawasaki, A., and Gasik, M., 1994, ''Worldwide Trends in Functionally Gradient Materials Research and Development,'' Composites Eng., **4**(8), pp. 883–894.
[14] Nadeau, J. C., and Ferrari, M., 1999, ''Microstructural Optimization of a Functionally Graded Transversely Isotropic Layer,'' Mech. Mater., **31**(10), pp. 637–652.
[15] Nadeau, J. C., and Meng, X. N., 2000, ''On the Response Sensitivity of an Optimally Designed Functionally Graded Layer,'' Composites, Part B, **31**, pp. 285–297.
[16] Kielczynski, P. J., Moreau, A., and Bussière, J. F., 1994, ''Determination of Texture Coefficients in Hexagonal Polycrystalline Aggregates With Orthorhombic Symmetry Using Ultrasounds,'' J. Acoust. Soc. Am., **95**(2), pp. 813–827.
[17] Clark, Jr., A. V., Reno, R. C., Thompson, R. B., Smith, J. F., Blessing, G. V., Fields, R. J., Delsanto, P. P., and Mignogna, R. B., 1988, ''Texture Monitoring in Aluminum Alloys: A Comparison of Ultrasonic and Neutron Diffraction Measurement,'' Ultrasonics, **26**, pp. 189–197.
[18] Gel'fand, I. M., Minlos, R. A., and Shapiro, Z. Ya., 1993, *Representations of the Rotation and Lorentz Groups and Their Applications*, MacMillan, New York.

Determination of the Local Stress-Strain Response of Foams

T. Wierzbicki

M. Doyoyo

Impact and Crashworthiness Laboratory,
Massachusetts Institute of Technology,
Cambridge, MA 02139

A new specimen for determining the local stress-strain response of foams under uniaxial compression is presented along with the corresponding theory. The drawback of using conventional cubic specimens is that average stresses and strains are calculated, which introduces size effects due to structural and material inhomogeneities of commercial foams. Under compression, foam cubes develop unstable regimes, which involve localized deformation. The instabilities cause difficulties in establishing the correct stress-strain response of the material. Tapering specimens can enable controlled motion of the boundary separating the unstable and stable regimes. This concept is exploited in the present paper in experiments on closed-cell aluminum foam trapezoids. A crushing front propagates down the tapered specimen during compression, while the deformed region develops a new lateral shape. The experimental results are used along with several assumptions to extract a more representative stress-strain response of foam. The response is characterized by the initial plateau stress, shape exponent and densification strain. The significant effect of the variable Poisson's ratio during crushing is also introduced. The results provide a basis for developing local constitutive behavior of foams.
[DOI: 10.1115/1.1546242]

1 Introduction

This paper deals with the determination of local stress-strain response of foams for finite element applications. In finite element modeling of three-dimensional bodies, decisions must be made on the size and constitutive equation governing a solid element. In continuum mechanics, the physical law is independent of the spatial discretization. However, for cellular materials such as foams, which are inhomogeneous, the mechanical properties are directly related to the size of the solid element.

The significant drop of the peak shear stress with the height of the foam specimen has been reported (see, e.g., Andrews et al. [1]). Wierzbicki [2] provided a qualitative explanation of this phenomenon in relation to honeycomb blocks in shear. Different failure modes were observed experimentally and numerically depending on block height. Short specimens developed uniform shear buckling patterns. Intermediate height blocks evolved diagonal shear bands. Higher specimens underwent nonuniform compression along loaded edges. Hanssen et al. [3] observed different stress-strain curves for slender and stocky foam cubes. A pronounced size effect was confirmed in a series of compression tests on ductile and brittle aluminum foam cubes (Wierzbicki et al. [4]). Depending on specimen size, different initial plateau stresses and different stress-strain curves were obtained. A typical stress-strain curve obtained from the compression of a regular foam cube is shown in Fig. 1. One can clearly distinguish an initial elastic regime up to the yield point, followed by the initial plateau stress and subsequent hardening all the way to densification and locking.

While the nature of size effect has not been clearly described and quantified in the literature, a recent study has contributed to the understanding of this phenomenon. Using digital image correlation analysis, Bastawros and Evans [5] detected formation of discrete bands of concentrated strain across sections of compressed foam cubes. These bands were spaced at a distance of three to four cells. The actual local strains in uniformly compressed cubes are thus different from the average strains obtained by dividing the end displacement by specimen height. Therefore, the question as to what is the proper reference size to measure strains in foams must be asked. The Bastawros and Evans' results suggest that this height must be equal to three to four cell diameters. But in finite element application, the size of the solid elements could be much smaller.

The situation becomes quite different for loading cases involving strain gradients. An example is indentation of a block of foam with a hemispherical punch. Deformation patterns under the punch show a clear interface between zones of fully crushed and uncrushed cells (Fig. 2). This interface propagates down the foam block with increasing punch displacement. Each collapsing cell develops increasing strains and enters the densification stage until the next row of cells starts to deform. The local crushing stress can be obtained by dividing the total resistive force by the projected cross-sectional area (Doyoyo and Wierzbicki [6]). However, the local strains cannot be measured easily in this type of test. Finite element codes require the correct true stress-strain curve of the material as an input. This information can be obtained neither from spherical punch indentation tests nor from uniaxial

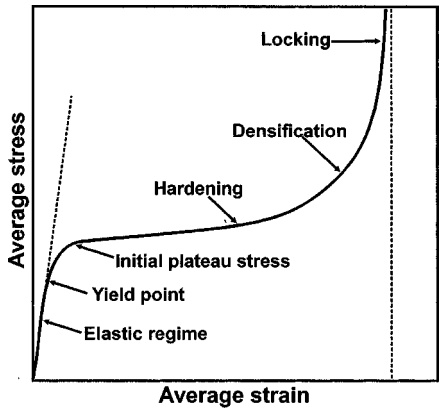

Fig. 1 A typical stress-strain curve of a closed-cell metallic foam cube under uniaxial compression. The plastic regime is characterized by a plateau stress, followed by a hardening region, which eventually leads to densification and locking.

Contributed by the Applied Mechanics Division of THE AMERICAN SOCIETY OF MECHANICAL ENGINEERS for publication in the ASME JOURNAL OF APPLIED MECHANICS. Manuscript received by the ASME Applied Mechanics Division, Sept. 27, 2001; final revision, Apr. 16, 2002. Associate Editor: K. Ravi-Chandar. Discussion on the paper should be addressed to the Editor, Prof. Robert M. McMeeking, Department of Mechanical and Environmental Engineering University of California–Santa Barbara, Santa Barbara, CA 93106-5070, and will be accepted until four months after final publication of the paper itself in the ASME JOURNAL OF APPLIED MECHANICS.

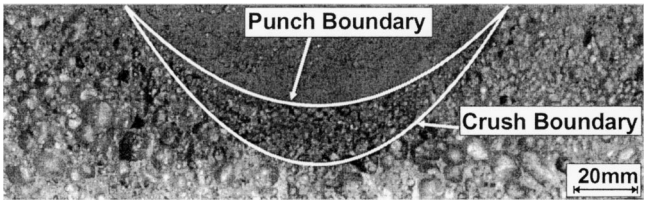

Fig. 2 A section through a block of Cymat aluminum alloy foam, which was indented by a hemi-spherical punch (Doyoyo and Wierzbicki [6]). A distinct boundary/interface separates the crushed and uncrushed regions.

compression of cubes. To overcome this difficulty, a new type of test is designed for foams and performed in our laboratory. The test involves crushing of tapered specimens (*foam trapezoids*). In the compressed specimen, stress at the smallest upper cross section is the largest so that a front of crushed cells propagates from the upper edge down the specimen. From the deformed lateral surface, local stresses and strains can be calculated and the local true stress-strain curve of the foam can be found.

The idea of inducing inhomogeneous stress and strain states to determine mechanical properties of solids is not new. Marciniak [7] proposed a method of calculating the stress-strain curve of copper from tensile testing of conical rods. McClintock and Zheng [8] used slightly tapered specimens to study initiation and propagation of necking and fracture in ductile metals. More recently, Doyoyo and Weirzbicki [9,10] used butterfly-shaped specimens to determine biaxial yield of brittle and ductile aluminum foams. The present scheme is a promising way of acquiring local compressive properties of foams, which can then be used directly in finite element modeling of complex boundary value problems.

2 Analysis of Nonuniform Crushing of a Foam

Several tests on closed-cell aluminum foam trapezoids (which will be reported fully in the next section) were performed and the following observations were made:

- There is always a clear boundary between the continually crushed and uncrushed regions.
- The front separating the above two regions is moving down the specimen as the load is increased.
- The material above the front continues to deform after the front has passed and higher stresses buildup in this region.
- Because of the boundary effect, the front is slightly curved but for the sake of simplicity, it is assumed to be flat.
- The width of the front is of the order of the average cell size but for strain calculation, it is assumed to be just a geometrical line.
- At some load level, the crushing front reaches the bottom of the specimen. The test should stop at this point or earlier because our analysis is not valid beyond this point.
- A unique feature of the present method is that the entire stress-strain curve is reconstructed from the final configuration. Therefore, there was no need to monitor the position of the traveling front. Various cross sections of the deformed specimen correspond to different stress and strain states.
- In the following analysis, we will determine the local stress-strain response of foams subjected to large crushing displacements. Thus, the elastic regime will be ignored and the analysis begins at the initial plateau stress.

We introduce a spatial coordinate system (x,y), which moves with the front where x is aligned with the front and y is perpendicular to it, Fig. 3(a). Consider three points on the original specimen; A, B, and C, Fig. 3(b). The point C defines the current position of the front. The width of the front is denoted by b. The current positions of the points A and B are denoted by A^1 and B^1, respectively. Consider the current cross section defined by the

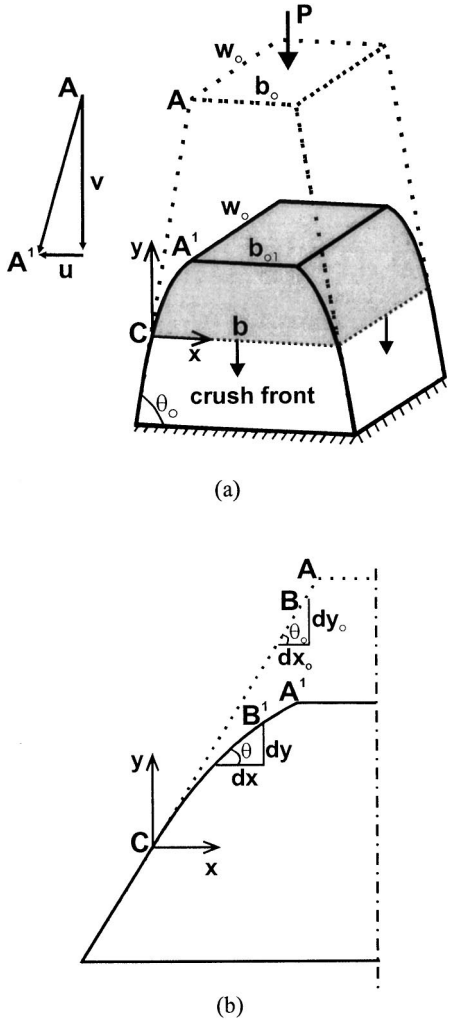

Fig. 3 (*a*) A schematic of the original tapered specimen (*dotted line*) and the deformed specimen (*solid line*). The crushing front propagates down the specimen, separating the crushed cells (shaded region) from the uncrushed cells ahead of the front. The effect of the plastic Poisson's ratio is shown when point *A* moves vertically (*v*) and horizontally (*u*) to point A^1 during loading. (*b*) A schematic showing how the original points *A* and *B* in the undeformed specimen travel to their current positions A^1 and B^1 in the deformed specimen during loading.

point B^1 and its mirror reflection of the other side of the symmetry axis. The width of this cross section is $(b-2x)$. The corresponding normal local true stress is

$$\sigma_{yy}=\frac{P}{w_o(b-2x)} \tag{1}$$

where w_o is the constant thickness of the trapezoid and $b=b(P)$. Note that the true stress σ_{yy} is equal to the engineering stress S_{yy}. Because the trapezoid is truncated, it follows from geometry that $b-b_o/2<x$. The normal yield stress should remain constant at the front, thus

$$\sigma_o=\frac{P_o}{w_o b_o}=\frac{P}{w_o b} \tag{2}$$

where P_o is the initial peak load. Eliminating b between Eqs. (1) and (2), then

$$\sigma_{yy}=P\left\{w_o\left(b_o\frac{P}{P_o}-2x\right)\right\}^{-1} \tag{3}$$

which is more convenient because P is readily measurable while b is not. From geometry of the deformed specimen, the local normal engineering strain E_{yy} is

$$E_{yy}=1-\frac{(1+\nu)y'}{(y')_o} \tag{4}$$

and the true (*logarithmic*) ε_{yy} strain is

$$\varepsilon_{yy}=\ln\frac{(1+\nu)y'}{(y')_o} \tag{5}$$

where $(y')_o=dy_o/dx_o=\tan\theta_o$ and $y'(x)=dy(x)/dx$, and ν is the local plastic Poisson's ratio. Equation (3) has a vertical asymptote when the normal strain reaches the densification strain $(E_{yy})_d$, thus

$$b_o\frac{P}{P_o}-2x\big|_{E_{yy}=(E_{yy})_d}=0. \tag{6}$$

The Poisson's ratio ν is defined as the negative ratio of the local lateral strain E_{xx} to the local normal strain E_{yy}

$$\nu=-\frac{E_{xx}}{E_{yy}} \tag{7}$$

this is not a constant, but varies with E_{yy} from the initial value ν_o to ν_L at full densification. The initial plastic Poisson's ratio ν_o is roughly zero for low-density foams. The variation of ν with E_{yy} has not been reported in the literature. Here, ν is assumed to follow the power law

$$\nu=\nu_o+\beta(E_{yy})^m \tag{8}$$

where the two material constants β and m are to be determined from the following two conditions. First, it is observed that at full densification the foam becomes a solid for which $\nu=\nu_L$

$$\nu_L=\nu_o+\beta[(E_{yy})_d]^m. \tag{9}$$

Secondly, what is measured at full densification is not the current plastic Poisson's ratio but the accumulated Poisson's ratio, given by

$$\nu_{\rm acc}=-\frac{(E_{xx})_d}{(E_{yy})_d}=\int_0^{(E_{yy})_d}[\nu_o+\beta(E_{yy})^m]dE_{yy}. \tag{10}$$

From Eqs. (9) and (10), the two unknown parameters can be expressed in terms of the measurable quantities $(E_{yy})_d$, $\nu_{\rm acc}$, and ν_o

$$m=\frac{\nu_L-\nu_o}{\nu_{\rm acc}-\nu_o}(E_{yy})_d \quad \text{and} \quad \beta=\frac{\nu_L-\nu_o}{[(E_{yy})_d]^m}. \tag{11}$$

Note that for foams made up of metallic alloys, which are incompressible, the plastic Poisson's ratio at full densification $\nu_L=0.5$, whereas it can lie between -1 and 0.5 for foams made up of compressible materials.

3 Testing of Tapered Foam Specimens Under Uniaxial Compression

In this section, the results of tests on two different foam trapezoids under uniaxial compression are reported. The following were the measurement objectives:

• The variation of the load P with displacement δ during specimen crushing had to be measured. The initial peak load P_o necessary to propagate the crushing front will be deduced from this variation.

• The lateral shape function $y(x)$ of the crushed specimen at the end of the test had to be measured. The final crushing front width b_L will be deduced from this function.

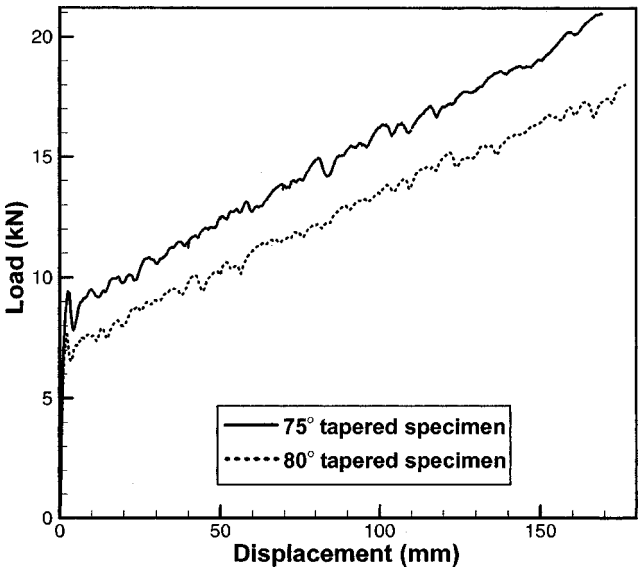

Fig. 4 The variation of load with crushing displacement during compression of foam trapezoids. The load increases linearly with crushing displacement beyond the initial plateau load.

• The accumulated plastic Poisson's ratio $\nu_{\rm acc}$ had to be measured.

The specimens were composed of ductile closed-cell aluminum foam of commercial name Alporas. Alporas was manufactured by the Shinko Wire Company, Amagasaki, Japan. The cell walls were made up of an aluminum alloy with small percentages of Ca and Ti. The nominal density of the foam was 257 kg/m^3 or 9.5 percent relative to solid aluminum ($\rho_{\rm Al}=2700$ kg/m^3). The specimens were extracted from foam blocks supplied by the manufacturers using EDM. The geometry and dimensions of the trapezoids are described in the schematic of Fig. 3(*a*).

Several foam trapezoids were tested in an MTS servo-hydraulic testing machine with a 200 kN load cell (Model 45G, MTS, Eden Prairie, MN). The specimens were placed between parallel platens and then compressed. Load and displacement were acquired with Testworks software (Sintec Division, MTS). The photographs of the specimens at different stages of crushing were taken with a digital camera.

It appeared during testing that the choice of the taper angle θ_o is important for producing reliable results. *In this study, the taper angle was not quantified or fully optimized*. Instead, only a conceptual definition of the ''optimum taper angle range'' is made. This angle should be large enough to override a tendency for developing localized deformation. At the same time, it cannot be too small because the propagating front ceases to be flat. For the above foam, specimens in taper angle range $\theta_o=75$ deg–80 deg evolved approximately flat crushing fronts. Two specimens of different sizes and different taper angles in this optimum range are now presented.

i. First specimen: This specimen had a taper angle $\theta_o=75$ deg with top width $b_o=100$ mm, height $h_o=300$ mm and thickness $w_o=100$ mm. It was compressed at 0.05 mm/s down to a height of 130 mm. The load-displacement curve for the specimen is shown in Fig. 4. The load increases linearly with displacement. If a best-fit line were to be drawn through the data points, the load at which the line intersects the load axis is the initial peak load $P_o=0.91$ kN, thus the corresponding initial plateau stress $\sigma_o=0.91$ MPa.

ii. Second specimen: This specimen had a taper angle $\theta_o=80$ deg with top width $b_o=75$ mm, height $h_o=300$ mm and thickness $w_o=100$ mm. It was compressed at 0.1 mm/s down to a

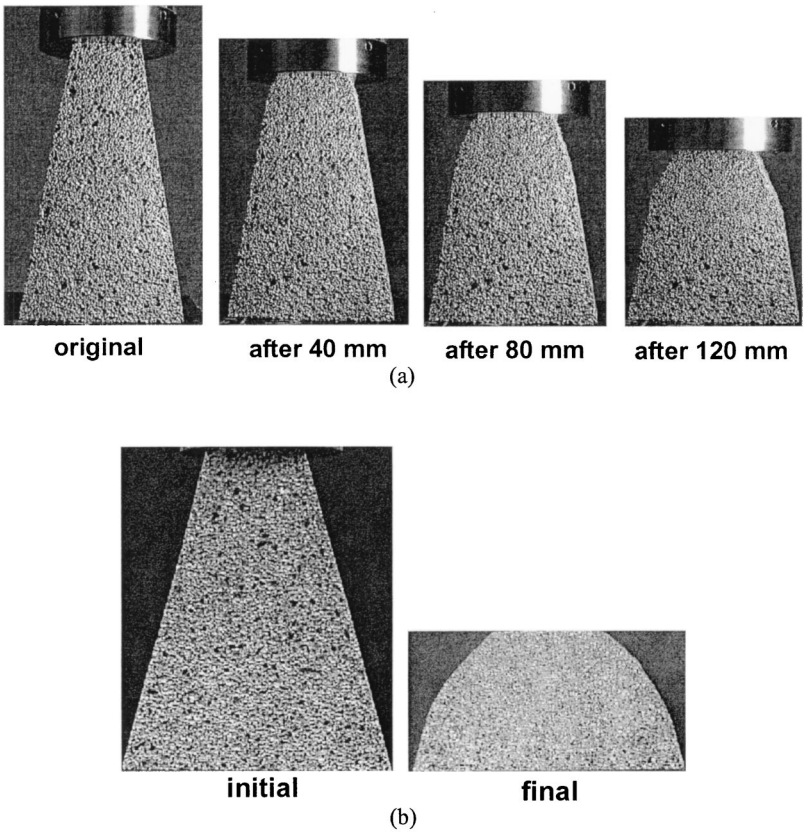

Fig. 5 (*a*) **Photographs of the 80 deg tapered specimen at subsequent stages of uniaxial compression.** (*b*) **The photograph of the original 75 deg tapered specimen and the deformed tapered specimen after compression down to a height of 130 mm. The specimen develops new lateral shapes during compression.**

height of 125 mm. Its load-displacement response is presented in Fig. 4 with initial peak load $P_o = 0.70$ kN and $\sigma_o = 0.93$ MPa.

The change of shape of the second specimen during compression is shown photographically in Fig. 5(*a*). The initial and final configurations of the first specimen are shown photographically in Fig. 5(*b*). The photographs of the final shapes are digitized and the points describing these shapes are plotted in Fig. 6(*a*). Points along and perpendicular to the crushing front are denoted by x and y, respectively. The point of reference is the position at which the front intersects the specimen surface. In the logarithmic scale plot of Fig. 6(*b*), the points lie in a straight line, suggesting a power-type shape function

$$y = \tan\theta_o x - \alpha x^n \tag{12}$$

where $n = 1.21$, $\alpha = 0.98$ and the final crushing front width $b_L = 240$ mm for the first specimen while $n = 1.21$, $\alpha = 1.65$, and $b_L = 163$ mm for the second specimen.

The parameters β and m defined in Eq. (11) are required in order to determine the variation of the local plastic Poisson's ratio with local normal strain. These parameters depend on local densification strain, initial and accumulated Poisson's ratios. For the low-density foam under consideration, the initial plastic Poisson's ratio is assumed to be zero. The local densification strain is calculated directly from the final specimen shape in the next section. Therefore, the accumulated plastic Poisson's ratio related to strains at full densification is the only unknown quantity. This quantity is obtained by crushing a foam block to full densification.

A foam block of height 27 mm and cross-sectional area 50 mm by 50 mm is extracted from the same block from which foam trapezoids were cut. The block is compressed at 0.05 mm/s until the load is about 80(!) times the initial plateau load. The photograph of the crushed and uncrushed blocks is shown in Fig. 7(*a*). The corresponding engineering stress-strain curve for the test is given in Fig. 7(*b*). The vertical asymptote of this curve is the average normal strain at full densification

$$(E_{yy})_d^{av} \approx 0.91. \tag{13}$$

The cross-sectional area of the crushed block is 54.5 mm by 54.5 mm. Therefore, the average lateral strain at full densification is

$$(E_{xx})_d^{av} = \frac{50\text{-}54.5}{50} \approx -0.09. \tag{14}$$

The accumulated plastic Poisson's ratio for the above foam is then

$$\nu_{\text{acc}} = -\frac{(E_{xx})_d^{av}}{(E_{yy})_d^{av}} = -\frac{(-0.09)}{(0.91)} \approx 0.1. \tag{15}$$

4 Determination of the Local Stress-Strain Response of Foams

In this section, the local stress-strain response of foams is determined for two different cases, namely; (i) the local plastic Poisson's ratio ν remains zero during deformation and (ii) the local plastic Poisson's ratio ν varies with deformation. Case (i) is typically assumed for low-density foams (see, e.g., Gibson and Ashby [11]). Although physically realistic, case (ii) is a new concept, which has been previously ignored for foams.

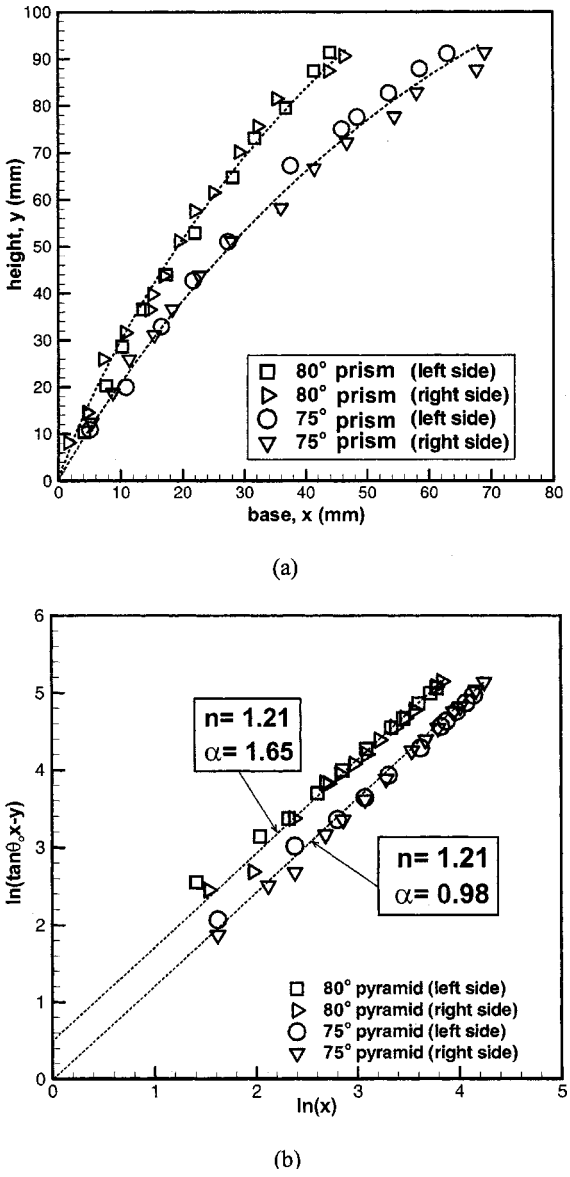

Fig. 6 (*a*) **Final shapes of the crushed regions of the tapered specimens obtained from digitized photographs.** (*b*) **The evaluation of the power-type function, which describes the lateral shape of the deformed specimens.**

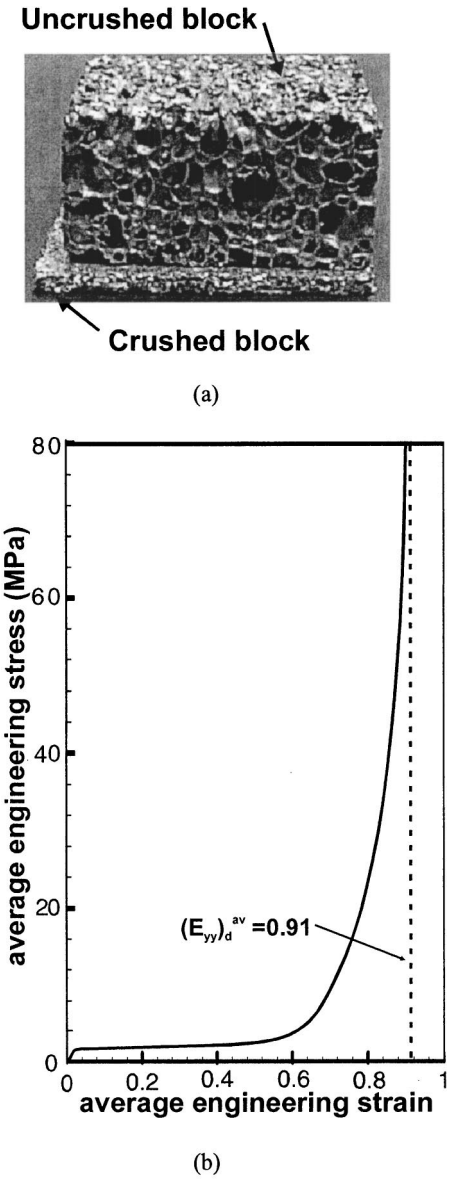

Fig. 7 (*a*) **Foam block crushed to 80 times the initial peak load is compared photographically to the uncrushed block.** (*b*) **The conventional stress-strain curve corresponding to the crushing of the foam block to densification and locking.**

(i) Local Stress-Strain Response of Foams for Zero Plastic Poisson's Ratio. When the local plastic Poisson's ratio remains zero during crushing, the local normal engineering strain, obtained by combining Eqs. (4) and (13) is

$$E_{yy}=E=\frac{\alpha}{\tan\theta_o}nx^{n-1}. \tag{16}$$

Eliminating x from Eq. (1) using the above expression, the local normal engineering stress becomes

$$S_{yy}=S=P\left\{w_o\left(b_o\frac{P}{P_o}-2\left(\frac{\tan\theta_o E}{\alpha n}\right)^{1/n-1}\right)\right\}^{-1}. \tag{17}$$

The above equation has a vertical asymptote when the normal strain reaches $(E_{yy})_d=E_d$ at full densification, so that

$$b_o\frac{P}{P_o}-2\left(\frac{\tan\theta_o E_d}{\alpha n}\right)^{1/n-1}=0. \tag{18}$$

Combining Eqs. (17) and (18) by eliminating b_oP/P_o, one gets the local engineering stress-strain response of foams

$$\frac{S}{S_o}=\left[1-\left(\frac{E}{E_d}\right)^{1/n-1}\right]^{-1} \tag{19}$$

where the normal local strain at full densification is also uniquely determined,

$$E_d=\frac{\alpha}{\tan\theta_o}nb_L^{n-1}. \tag{20}$$

The local true stress-strain curve is obtained by using the strain conjugate relation

$$E=1-\exp\{-\varepsilon\}. \tag{21}$$

Note that $\varepsilon_{yy}=\varepsilon$ and $(E,\varepsilon)\geqslant 0$. Recalling that $S_{yy}=\sigma_{yy}=\sigma$, then the local true stress-strain response is found by substituting Eq. (21) into Eq. (19)

Table 1 Stress-strain curve parameters assuming zero plastic Poisson's ratio for the 257 kg/m^3 dense Alporas foam. The thicknesses and heights: w_o=100 mm and h_o=300 mm are the same for the two specimens.

	First Specimen	Second Specimen
Taper angle θ_o (in degrees)	75	80
Top width b_o (mm)	100	75
Shape exponent n	1.21	1.21
Initial plateau stress σ_o (MPa)	0.91	0.93
Densification strain E_d	0.87	0.89

$$\frac{\sigma}{\sigma_o}=\left[1-\left(\frac{1-\exp\{-\varepsilon\}}{1-\exp\{-\varepsilon_d\}}\right)^{1/n-1}\right]^{-1} \tag{22}$$

and the local true strain at full densification is

$$\varepsilon_d=-\ln\left(1-\frac{\alpha}{\tan\theta_o}nb_L^{n-1}\right). \tag{23}$$

The measured stress-strain curve parameters (E_d,n,σ_o) for the two specimens are given in Table 1. The parameters are identical for the two specimens.

(ii) Local Stress-Strain Response for Variable Plastic Poisson's Ratio. When the local plastic Poisson's ratio varies with deformation, the local engineering strain is obtained by combining Eq. (4) with Eq. (14),

$$E=-\nu+(1+\nu)\frac{\alpha}{\tan\theta_o}nx^{n-1}. \tag{24}$$

After substituting x from the above equation into Eq. (3) and observing that the stress approaches infinity at full densification,

$$b_o\frac{P}{P_o}-2\left[\frac{(E_d+\nu_L)}{(1+\nu_L)}\frac{\tan\theta_o}{\alpha n}\right]^{1/n-1}=0. \tag{25}$$

Simplifying Eq. (3) by eliminating x and b_oP/P_o, it can be shown that the local engineering stress-strain response is

$$\frac{S}{S_o}=\left\{1-\left[\frac{E+\nu(E)}{E_d+\nu(E_d)}\right]^{1/n-1}\right\}^{-1} \tag{26}$$

where $\nu(E)$ is given by Eq. (7). The expression for the engineering densification strain becomes

$$E_d=-\nu_L+(1+\nu_L)\frac{\alpha}{\tan\theta_o}nb_L^{n-1}. \tag{27}$$

The local true stress-strain response is obtained by substituting Eq. (21) into the above equation

$$\frac{\sigma}{\sigma_o}=\left\{1-\left[\frac{1-\exp(-\varepsilon)+\nu_o+\beta(1-\exp(-\varepsilon))^m}{1-\exp(-\varepsilon_d)+\nu_d}\right]^{1/n-1}\right\}^{-1} \tag{28}$$

and the true densification strain is given by

$$\varepsilon_d=-\ln\left(1+\nu_L-(1+\nu_L)\frac{\alpha}{\tan\theta_o}nb_L^{n-1}\right). \tag{29}$$

The measured stress-strain curve parameters (E_d,n,σ_o,m,β) for the two specimens are given in Table 2. The parameters are identical for the two specimens. The variation of the plastic Poisson's ratio with strain for average values of $E_d,m,\beta\approx$0.83,4.10,1.13 deduced from Table 2 is plotted in Fig. 8.

5 Discussions

The analysis of the previous sections demonstrates that a simple local stress-strain response of foams can be obtained by testing foam trapezoids. The stress-strain curve depends on the initial peak stress σ_o, densification strain E_d, shape exponent n, first and second Poisson's ratio parameters m,β. These parameters can be determined from a single test and were identical for the tested foam trapezoids.

Table 2 Stress-strain curve parameters assuming variable Poisson's ratio for the 257 kg/m^3 dense Alporas foam

	First Specimen	Second Specimen
Taper angle θ_o (in degrees)	75	80
Top width b_o (mm)	100	75
Shape exponent n	1.21	1.21
Initial plateau stress σ_o (MPa)	0.91	0.93
Densification strain E_d	0.81	0.84
First Poisson's ratio parameter m	4.05	4.15
Second Poisson's ratio parameter β	1.17	1.08

Although the physical meanings of the initial peak stress and densification strain are known, it is not immediately obvious what the shape exponent represents. Figure 9 shows the dependence of the local stress-strain response on the shape exponent. It can be seen that foams that harden during crushing have higher values of

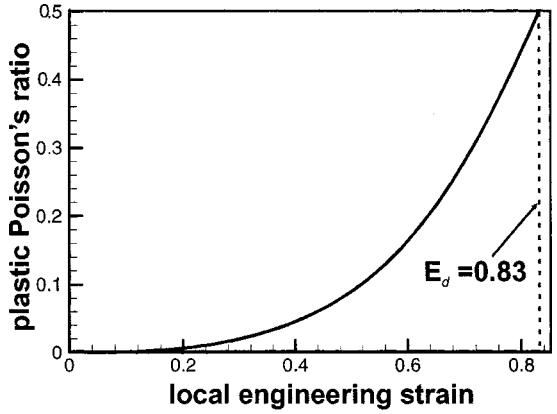

Fig. 8 The variation of local plastic Poisson's ratio with local engineering strain during crushing of the 257 kg/m^3 dense Alporas foam trapezoid

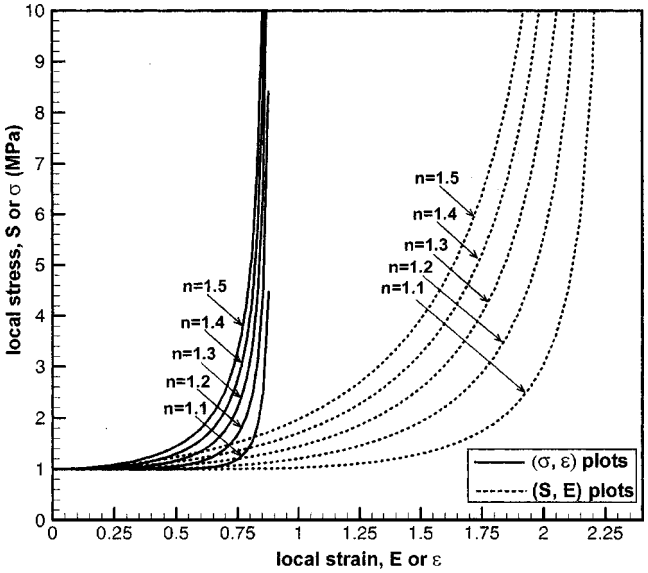

Fig. 9 Local stress-strain response in foams for different values of *n*, according to Eq. (17) for zero plastic Poisson's ratio. The pattern is similar for the variable Poisson's ratio case in Eq. (23) as the values of *n* are the same for the two cases.

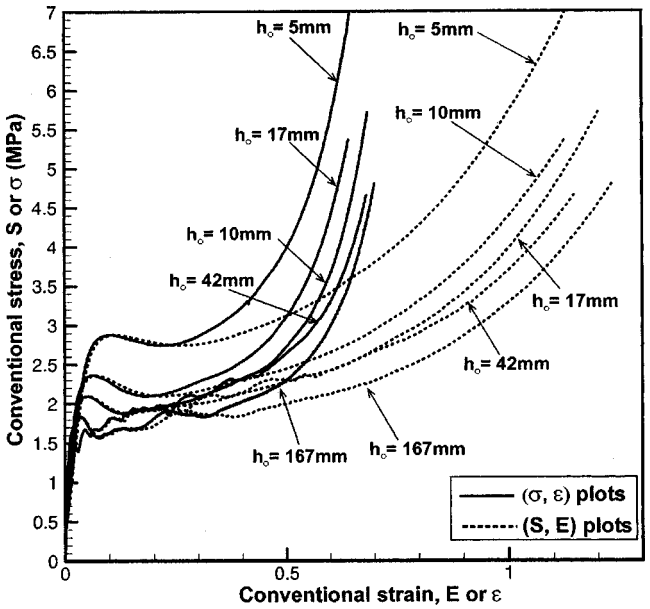

Fig. 10 The effect of specimen size in conventional stress-strain curves obtained by compressing the 257 kg/m^3 dense Alporas foam cubes

n than foams that crush at constant plateau stresses. Thus, the shape exponent is a measure of foam hardening during crushing beyond the initial plateau point.

Figure 10 gives the conventional stress-strain responses of the present foam cubes of cross-sectional area 50 mm by 50 mm and heights $h_o = 5-167$ mm. The responses are clearly dependent on specimen size. The above conventional stress-strain curves are compared with the present local stress-strain curves in Fig. 11. Note that the average values of the parameters for the two specimens in Tables 1 and 2 were used for the local stress-strain curves. The stresses for each specimen were normalized by the initial plateau stresses.

It can be seen in Fig. 11 that if a cubic specimen is used (with the same initial peak stress as the tapered specimen); then the foam would appear to absorb more energy than it is possible. Further, the foam material would appear to begin its densification phase at lower strains. Thus, the two methods already yield different results before size effect is considered (e.g., $\sigma_o \approx 0.91-0.93$ MPa for tapered specimens while $\sigma_o = 1.5-3.0$ MPa for cubic specimens). The local stress-strain responses for zero and variable plastic Poisson's ratios during crushing are also compared in Fig. 11. The energy absorption capacity for the foam is underestimated by neglecting the variation of the Poisson's ratio with strain.

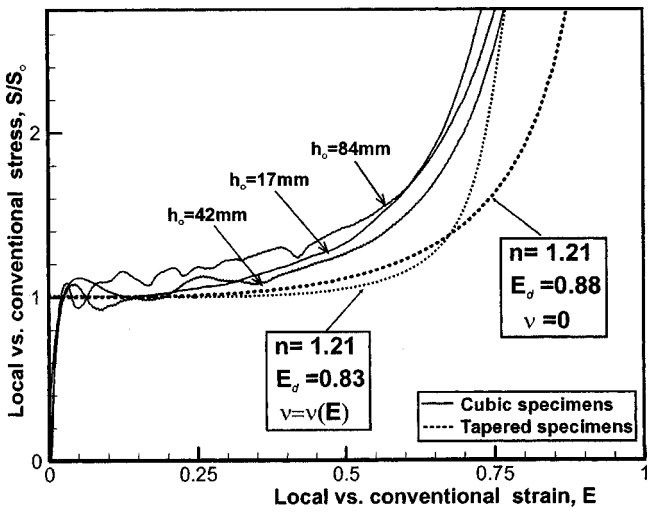

Fig. 11 The local versus conventional stress-strain responses in the 257 kg/m^3 dense Alporas foam

Finally, it should be mentioned that the optimum taper angle range is dependent on foam density and cellular structure. Indeed the taper angle range 75–80 deg obtained in this study is only valid for the 257 kg/m^3 dense Alporas foam tested.

Conventional Versus New Locally Based Densification Strain. Hanssen et al. [3] defined full densification strain for cubic specimens as

$$E_d^{av} = 1 - \frac{\rho_f}{\rho_s} \tag{30}$$

where ρ_f and ρ_s are the densities of the foam and solid, respectively. The superscript "av" is used to distinguish between conventional strain from cubic specimens and local strain from tapered specimens. This strain E_d^{av} corresponds to a complete closure of all cells so that the density of the foam becomes equal to that of the solid. For zero plastic Poisson's ratio during crushing, the above expression for the locking strain can be derived from the conservation of rate of energy per unit mass (*work conjugancy*) (Malvern [12])

$$\frac{1}{\rho_f}\sigma^{av} d\varepsilon^{av} = \frac{1}{\rho_s} S^{av} dE^{av}. \tag{31}$$

At full densification $\rho_f = \rho_s$ and $E^{av} = E_d^{av}$. Noting that the plastic Poisson's ratio is initially zero, and observing that $\sigma^{av} = S^{av}$ and using the strain conjugate relation in Eq. (21), then Eq. (30) is recovered. For the foam under consideration with $\rho_f/\rho_s = 0.095$, then $E_d^{av} \approx 0.9$. This strain compares closely with densification strains obtained from tapered specimens for zero plastic Poisson's ratio ($E_d = 0.87, 0.89$ in Table 1).

6 Conclusions

A new procedure to obtain the local compressive stress-strain response of foams has been presented. The method allows one to calculate local strains and stresses directly from the final shape of compressed foam trapezoid. Tests were conducted on specimens composed of ductile closed-cell aluminum foam. For the optimum taper angle range, a roughly flat crushing front evolved under uniaxial compression, separating crushed from uncrushed cells, while a new specimen shape was formed. The local stress-strain curve depends on several parameters: initial plateau stress, shape exponent, densification strain, and Poisson's ratio parameters, all obtained from a single test. These parameters were identical for the two specimens of different sizes and different taper angles. It was demonstrated that the constitutive behavior obtained from the present method is very different from that obtained from foam cubes. Further, the effect of the variable plastic Poisson's ratio with strain in the stress-strain curve was introduced. An assumed power-law variation illustrated that an incorrect constitutive response is obtained if this effect is neglected. The actual variation should be incorporated in the scheme. This can be done in two ways: by measuring lateral and normal strains during crushing with digital image correlation analysis; or by finding an analytical procedure and/or developing the specimen such that both strain components can be calculated directly from the final shape. Among future improvements, this scheme should be quantified and fully optimized with respect to specimen size and taper angle.

Acknowledgments

We are grateful for financial support of the Joint M.I.T./Industry Ultralight Consortium. We thank the Shinko Wire Company for supplying the Alporas foam tested in this study.

References

[1] Andrews, E. W., Gioux, G., Onck, P., and Gibson, L. J., 2001, ''Size Effects in Ductile Cellular Foams. Part II: Experimental Results,'' Int. J. Mech. Sci., **43**, p. 701.

[2] Wierzbicki, T., 1997, ''Experimental, Numerical and Analytical Study of Honeycomb Material,'' Report No. 1: Joint MIT/Industry Ultralight Consortium, Impact and Crashworthiness Laboratory, MIT, Cambridge, MA, Nov.

[3] Hanssen, A. G., Hopperstad, O. S., Langseth, M., and Ilstad, H., 2000, ''Validation of Constitutive Models Applicable to Aluminum Foams,'' Ph.D. thesis, Norwegian University of Science and Technology.

[4] Wierzbicki, T., Doyoyo, M., and Markaki, A., 2001, ''Redefining the Concept of Stress-Strain Curve for Foams,'' *Cellular Metals and Metal Foaming Technology*, Ed.: J. Banhart, M. Ashby, and N. Fleck, eds., Verlag MIT Publishing, Germany, pp. 449–453.

[5] Bastawros, A. F., and Evans, A. G., 2000, ''Deformation Heterogeneity in Cellular Al Alloys,'' Adv. Eng. Mat., **4**, p. 210.

[6] Doyoyo, M., and Wierzbicki, T., 2000, ''Fracture of Aluminum Honeycombs and Foams Under Hemi-spherical Punch Indentation,'' Report No. 38: Joint MIT/Industry Ultralight Consortium, Impact and Crashworthiness Laboratory, MIT, Cambridge, MA, June.

[7] Marciniak, 1965, private communication.

[8] McClintock, F. A., and Zheng, Z. M., 1993, ''Ductile Fracture in Sheets Under Transverse Strain Gradients,'' Int. J. Fract., **64**, p. 321.

[9] Doyoyo, M., and Wierzbicki, T., 2002, ''Measurement of the Failure Surface for Ductile and Brittle Foams,'' *Plasticity, Damage and Fracture at Macro, Micro and Nano Scales*, A. Khan and O. Lopez-Pamies, eds., Neat Press, pp. 114–116.

[10] Doyoyo, M., and Wierzbicki, T., 2002, ''Experimental Studies on Yield Behavior of Ductile and Brittle Aluminum Foams Under a Biaxial State of Stress,'' Int. J. Plast., in press.

[11] Gibson, L. J., and Ashby, M. F., 1997, *Cellular Solids: Structure and Properties*, 2nd Ed., Cambridge University Press, Cambridge, UK.

[12] Malvern, L. E., 1969, *Introduction to the Mechanics of a Continuous Media*, Prentice-Hall, Englewood Cliffs, NJ.

Comparison of Double-Shearing and Coaxial Models for Pressure-Dependent Plastic Flow at Frictional Boundaries

S. Alexandrov
Center for Mechanical Technology and Automation,
Department of Mechanical Engineering,
University of Aveiro,
3810-193 Averio, Portugal
e-mail: salexandrov@mec.ua.pt

and
Institute for Problems in Mechanics,
Russian Academy of Sciences,
101-1 Prospect Vernadskogo,
117526 Moscow, Russia

The qualitative difference in solution behavior in the vicinity of maximum friction surfaces is demonstrated for two distinct models of pressure-dependent plasticity (the double-shearing and coaxial models) using closed-form solutions for planar flow through an infinite wedge-shaped channel and plane-strain compression of an infinite block between parallel plates. Singular velocity fields (some components of the strain rate tensor approach infinity at the friction surface) occur in the solutions based on the double-shearing model. This is similar to behavior in the vicinity of maximum friction surfaces in classical plasticity of pressure-independent materials. A singular velocity field is also obtained in the solution based on the coaxial model for the problem of channel flow; but, in contrast to the double-shearing model and classical plasticity, sticking must occur at this friction surface. For the problem of compression of a material obeying the coaxial model, no solution based on conventional assumptions exists with the maximum friction law. This is quite different from both the corresponding solution based on the double-shearing model and the channel flow solution based on the coaxial model. [DOI: 10.1115/1.1532319]

1 Introduction

Models of pressure-dependent plasticity incorporating the incompressibility equation are applicable to soil, granular materials, and conventional metals. A brief review of such models has been given in Ostrowska-Maciejewska and Harris [1] where also a new model has been proposed. General properties of equations for different models have been investigated by Spencer [2,3], Ostrowska-Maciejewska and Harris [1], Hill and Wu [4,5], Harris [6], and Lubarda [7] among others. Most of these studies have dealt with the deformation of granular material or soil. However, pressure dependence of the yield criterion is also a feature of conventional metals (Yoshida et al. [8], Spitzig et al. [9], Spitzig [10], and Kao et al. [11]). For such materials, the angle of internal friction (in the terminology of soil mechanics) is very small and one would expect that its influence on solutions of classical plasticity is negligible. Nevertheless, this is not true in some cases. This paper concerns two models, the coaxial model and the double-shearing model (in Ostrowska-Maciejewska and Harris [1] these models are also referred to as Hill's model and Spencer's model, respectively) under plane-strain conditions and emphasizes the interaction between the constitutive laws and a modified Tresca frictional law. Note that the original Tresca frictional law is very popular in the modeling of metal forming processes (see, for example, Schey [12]). Using analytical solutions for flow through an infinite wedge-shaped channel and compression between two parallel plates, it is shown that the solutions may be qualitatively different for these two models and may not reduce to the corresponding solution of classical plasticity at the vanishing internal friction angle in the case of maximum friction. The reason for this is that the velocity fields in rigid/perfectly plastic materials are singular at the maximum friction surface. For smooth yield criteria, this result in most general form has been presented in Alexandrov and Richmond [13]. Also, such behavior of the velocity field has been found in the cases of Tresca's nonsmooth yield criterion (Alexandrov and Richmond [14]) and thermoplasticity (Alexandrov and Richmond [15]).

The double-shearing model has been discussed in detail in Spencer [2] and the solutions to the aforementioned problems for that model have been found by Pemberton [16] and Marshall [17]. A brief description of the equations of the coaxial model and the solutions based on this model are given in the present paper. Also, some features of the maximum frictional law (Tresca's frictional law with the friction factor $m=1$) are discussed for various constitutive models.

2 Coaxial Model and Frictional Boundary Condition

Constitutive Equations. A plane-strain yield criterion for pressure-dependent materials may be written in the form

$$\sqrt{4\sigma_{\alpha\beta}^2+(\sigma_{\alpha\alpha}-\sigma_{\beta\beta})^2}=2(k\cos\phi-\sigma\sin\phi) \tag{1}$$

where $\alpha\beta$ is an arbitrary plane orthogonal coordinate system; $\sigma_{\alpha\alpha}$, $\sigma_{\beta\beta}$, and $\sigma_{\alpha\beta}$ are the components of the stress tensor in these coordinates; $\sigma=(\sigma_{\alpha\alpha}+\sigma_{\beta\beta})/2$ is the mean stress; k is the cohesion; and ϕ is the angle of internal friction. (The terminology for k and ϕ is from the theory of granular materials.) For conventional metals ϕ is a very small parameter.

It is supposed that the principal axes of the stress and the strain rate tensors coincide. This gives

$$\frac{\sigma_{\alpha\alpha}-\sigma_{\beta\beta}}{2\sigma_{\alpha\beta}}=\frac{\xi_{\alpha\alpha}-\xi_{\beta\beta}}{2\xi_{\alpha\beta}} \tag{2}$$

where $\xi_{\alpha\alpha}$, $\xi_{\beta\beta}$, and $\xi_{\alpha\beta}$ are the components of the strain rate tensor. The material is assumed to be incompressible, therefore, these components should obey the following equation:

$$\xi_{\alpha\alpha}+\xi_{\beta\beta}=0. \tag{3}$$

Contributed by the Applied Mechanics Division of THE AMERICAN SOCIETY OF MECHANICAL ENGINEERS for publication in the ASME JOURNAL OF APPLIED MECHANICS. Manuscript received by the ASME Applied Mechanics Division, November 30, 1999; final revision, August 19, 2002. Associate Editor: B. M. Moran. Discussion on the paper should be addressed to the Editor, Prof. Robert M. McMeeking, Department of Mechanical and Environmental Engineering University of California–Santa Barbara, Santa Barbara, CA 93106-5070, and will be accepted until four months after final publication of the paper itself in the ASME JOURNAL OF APPLIED MECHANICS.

Since the yield criterion (1) depends on the hydrostatic stress, it is clear that the associated normality flow rule is not satisfied for this material model. To obtain a closed-form system, one needs to add two equilibrium equations to (1)–(3).

The yield criterion (1) is automatically satisfied by the substitution

$$\sigma_{\alpha\alpha}=\sigma+(k\cos\phi-\sigma\sin\phi)\cos 2\psi$$

$$\sigma_{\beta\beta}=\sigma-(k\cos\phi-\sigma\sin\phi)\cos 2\psi \tag{4}$$

$$\sigma_{\alpha\beta}=(k\cos\phi-\sigma\sin\phi)\sin 2\psi.$$

Then, (2) may be transformed to

$$\tan 2\psi=\frac{2\xi_{\alpha\beta}}{\xi_{\alpha\alpha}-\xi_{\beta\beta}}. \tag{5}$$

Frictional Law. One of the most popular frictional laws in the theory of metal forming is Tresca's which states that the friction stress is equal to a portion of the shear yield stress (see, for example, Schey [12] p. 16). A particular case of this law is called the maximum friction law if the friction stress is equal to the shear yield stress. This law is of special interest because its application may lead to such features of solutions as nonuniqueness, nonexistence, and singularities. In particular, in the case of rigid/perfectly plastic materials velocity fields are singular at the friction surface (Alexandrov and Richmond [13]). Such a singular behavior may cause computational difficulty and explain certain physical phenomena in subsurface layers. For other pressure-independent constitutive models, studies of solution behavior in the vicinity of maximum friction surfaces have been carried out by Alexandrov and Richmond [13,18], Alexandrov et al. [19], and Alexandrov and Alexandrova [20,21]. These studies show that the behavior of the solution is very sensitive to the constitutive model chosen. Computational difficulties with the application of the maximum frictional law have been reported by Rebelo and Kobayashi [22] and Appleby et al. [23].

A modification of the maximum friction law for pressure dependent materials has been proposed by Alexandrov and Druyanov [24]. This law states that a plane of maximum shear stress in the plastically deforming material is tangent to the friction surface. In the formulation of particular problems for the double-shearing model, another modification of the maximum friction law has been applied by Pemberton [16] and Marshall [17]. This law states that the friction surface coincides with an envelop of characteristics. In this case the plane of maximum shear stress is not tangent to the friction surface, but the frictional stress obtained by Pemberton [16] and Marshall [17] is the maximum possible among all solutions to the considered problems. This is an effect of the pressure dependence of the material. The reason for the latter formulation is that an envelop of characteristics is a natural boundary of the analytical solution. For pressure-independent materials both formulations of friction coincide with each other and with the classical formulation. However, for pressure-dependent materials several questions arise: (1) How can one formulate the second law of friction for nonhyperbolic equations? In general it may be possible since isolated characteristics and envelopes may exist even in the case of nonhyperbolic equations in bulk. The conditions for the existence of characteristic surfaces for the three-dimensional equations of classical plasticity based on Mises yield criterion have been derived by Craggs [25]. (2) How can one formulate the frictional law for models whose equations do not have the property, as in the double shearing model, that the characteristic fields for stress and velocity coincide? The present paper does not address these and other questions of the formulation of the maximum friction law for pressure dependent materials, but shows that both formulations coincide for the considered problems. Therefore, the difference in solutions is solely a consequence of distinctive features of the constitutive laws.

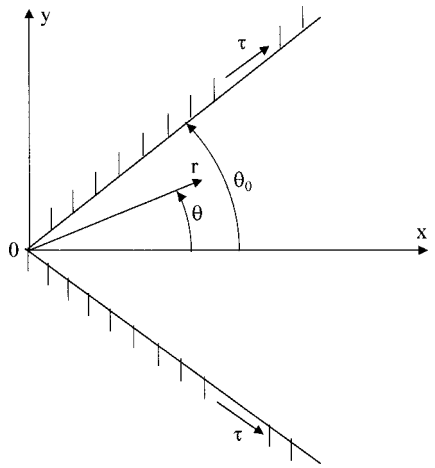

Fig. 1 Flow in wedge-shaped channel and coordinate systems

Assume a generalization of Tresca's frictional law for the material defined by (1) and (2) in the form

$$\tau=m(k\cos\phi-\sigma\sin\phi) \tag{6}$$

at the friction surface at sliding. Here τ is the frictional stress and m is the friction factor $(0\leqslant m\leqslant 1)$. At $m=1$ the maximum friction law for the material under consideration is obtained. At $\phi=0$ the frictional law (6) reduces to the corresponding law in classical plasticity. If an α (or β) line coincides with a friction surface then combining $(4)^3$ and (6) gives

$$|\sin 2\psi|=m. \tag{7}$$

At $m=1$ this equation corresponds to the formulation proposed by Alexandrov and Druyanov [24]. Coincidence of (7) at $m=1$ with the formulation proposed by Pemberton [16] and Marshall [17] is demonstrated for each problem separately.

3 Flow Through a Wedge-Shaped Channel

A solution to this problem for a pressure-independent rigid/perfectly plastic material has been found by Nadai and Hill (see Hill [26]) and modified by Durban and Budiansky [27] for a rigid/plastic linear-hardening material and by Alexandrov et al. [19] for a rigid/perfectly plastic three-layer material. Using the double shearing model, Pemberton [16] has solved the problem for a pressure-dependent material. As follows from the general theory (Alexandrov and Richmond [13]) singular velocity fields have been obtained in the solutions of classical plasticity. A singular velocity field also occurs in the solution for the pressure-dependent material. Since this has not been mentioned in Pemberton [16], this aspect of the solution is discussed in an Appendix. The solution for the rigid/plastic hardening material obtained for an arbitrary value of m is not valid for $m=1$. The reason for this is that there would have to be sticking with this frictional law (Alexandrov and Alexandrova, [21]), which is not possible due to the a priori assumptions. A solution for the coaxial model is given and discussed in this section.

It is convenient to introduce a polar coordinate system $r\theta$, instead of $\alpha\beta$, with its origin at the channel apex 0 (Fig. 1). Since the flow is converging, $\sigma_{\alpha\beta}>0$ at the channel wall and, therefore, $\psi>0$ and (7) should be written in the form

$$\sin 2\psi=m \tag{8}$$

at $\theta=\theta_0$ where θ_0 is half of the total angle of the channel. Moreover, due to symmetry,

$$\psi=0 \tag{9}$$

at $\theta=0$.

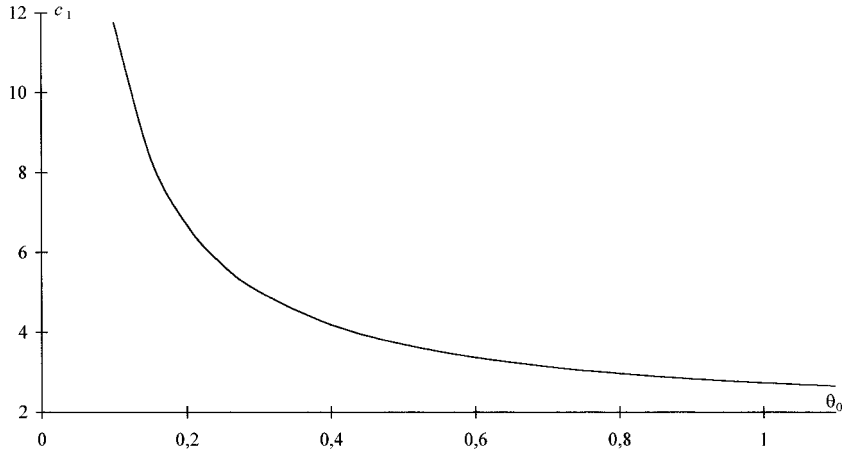

Fig. 2 Variation of the parameter c_1 with the angle θ_0 at $\phi=0.01$

The circumferential velocity is zero at the wall ($\theta=\theta_0$) and at the axis of symmetry ($\theta=0$). Therefore, it is reasonable to assume that this velocity is zero everywhere, as in the case of the aforementioned solutions (Hill [26], Pemberton [16], Durban and Budiansky [27], and Alexandrov et al. [19]). Then, the radial velocity v is determined from the incompressibility Eq. (3) as

$$v=u(\theta)/r \tag{10}$$

where $u(\theta)$ is an arbitrary function of θ. Using this solution, Eq. (5) may be transformed to

$$\tan 2\psi=-\frac{1}{2u}\frac{du}{d\theta}. \tag{11}$$

Substituting (4) into the equilibrium equations gives

$$\begin{aligned} &r(1-\sin\phi\cos 2\psi)\frac{\partial\sigma}{\partial r}-\sin 2\psi\sin\phi\frac{\partial\sigma}{\partial\theta}\\ &\quad+2\cos 2\psi(k\cos\phi-\sigma\sin\phi)\left(\frac{d\psi}{d\theta}+1\right)=0\\ &-r\sin\phi\sin 2\psi\frac{\partial\sigma}{\partial r}+(1+\cos 2\psi\sin\phi)\frac{\partial\sigma}{\partial\theta}\\ &\quad+2\sin 2\psi(k\cos\phi-\sigma\sin\phi)\left(\frac{d\psi}{d\theta}+1\right)=0 \end{aligned} \tag{12}$$

where we have taken into account that ψ is independent of r as follows from (11). It is convenient to introduce a new variable by the equation

$$q=\ln(k\cos\phi-\sigma\sin\phi). \tag{13}$$

It is important to mention that this variable can be introduced for any small value of ϕ, but not for $\phi=0$ (in this case $q=\text{const}$) which corresponds to the pressure-independent yield condition. Substituting (13) into (12) gives

$$\begin{aligned} &-r\frac{(1-\sin\phi\cos 2\psi)}{\sin\phi}\frac{\partial q}{\partial r}+\sin 2\psi\frac{\partial q}{\partial\theta}+2\cos 2\psi\left(1+\frac{d\psi}{d\theta}\right)=0\\ &r\sin 2\psi\frac{\partial q}{\partial r}-\frac{(1+\sin\phi\cos 2\psi)}{\sin\phi}\frac{\partial q}{\partial\theta}+2\sin 2\psi\left(1+\frac{d\psi}{d\theta}\right)=0. \end{aligned} \tag{14}$$

These equations are compatible if

$$q=c\ln r+p(\theta) \tag{15}$$

where c is constant and p is a function of θ. Combining (14) and (15), after some algebra we arrive at the following equations:

$$\frac{d\theta}{d\psi}=\frac{2(\cos 2\psi+\sin\phi)}{c_1-2(\cos 2\psi+\sin\phi)} \tag{16}$$

$$\frac{dp}{d\psi}=\frac{2c_1\cos^2\phi\sin\phi\sin 2\psi}{c_1-2(\cos 2\psi+\sin\phi)} \tag{17}$$

where $c_1=c\cos^2\phi/\sin\phi$. Using the boundary condition (9) the solution to (16) may be written as

$$\theta=2\int_0^{\psi}\frac{(\cos 2z+\sin\phi)}{[c_1-2(\cos 2z+\sin\phi)]}dz \tag{18}$$

where z is an auxiliary variable. Integration in (18) can be performed analytically, but it is actually easier to deal with the form of solution given in (18). The value of c_1 is determined from (8) and (18) in implicit form:

$$\theta_0=2\int_0^{(1/2)\arcsin m}\frac{(\cos 2\psi+\sin\phi)}{[c_1-2(\cos 2\psi+\sin\phi)]}d\psi. \tag{19}$$

At $m=1$, corresponding to the maximum friction law, the variation of c_1 with θ_0 is presented in Fig. 2 for $\phi=0.01$. This value of ϕ is typical for metals, for example for a low carbon steel investigated by Kao et al. [11]. Equation (17) may be integrated to give

$$p=(1/2)c_1\cos^2\phi\sin\phi\ln|2\sin\phi-c_1+2\cos 2\psi|+\ln p_0 \tag{20}$$

where p_0 is a constant but cannot be found for an infinite channel. Combining (13), (15), and (20) we obtain

$$\sigma\sin\phi=k\cos\phi-p_0r^c|c_1-2\sin\phi-\cos 2\psi|^b \tag{21}$$

where $b=c\cos^4\phi/2$. For the pressure-independent yield condition ($\phi=0$), the mean stress is proportional to $\ln r$ rather than to a power of r (Hill [26]). Such a dependence is obtainable from (21) as the limit as $\phi\to 0$ if $p_0=k$. A difference between the solutions for the pressure-dependent and pressure-independent yield conditions is that at $r=0$ the mean stress is bounded in the former case and is infinite in the latter case. All components of the stress tensor may be found from (4) and (21). Of special interest is the component $\sigma_{\theta\theta}$ which is given by

$$\sigma_{\theta\theta}=\frac{k\cos\phi}{\sin\phi}-p_0r^c|c_1-2\sin\phi-2\cos 2\psi|^b(1/\sin\phi+\cos 2\psi). \tag{22}$$

One can see that $\sigma_{\theta\theta}>0$ at $r=0$ and, therefore, in a vicinity of this point. This means that the solution is not valid in this vicinity since any frictional law requires a negative normal stress on the

friction surface. For a pressure-independent material such inconsistency has been mentioned by Alexandrov and Goldstein [28].

Using (16) the function $u(\theta)$ involved in (10) is determined from (11) as

$$\frac{u}{u_0}=-(\cos 2\psi)^t\left[\frac{c_1-2(1+\sin\phi)}{c_1-2(\cos 2\psi+\sin\phi)}\right]^n \tag{23}$$

where

$$t=\frac{2\sin\phi}{c_1-2\sin\phi}\quad\text{and}\quad n=\frac{c_1}{c_1-2\sin\phi} \tag{24}$$

and $u_0>0$ is constant which may be found if a flux, Q, is given. Then,

$$Q=2u_0\int_0^{(1/2)\arctan m}\frac{(\cos 2\psi+\sin\phi)(\cos 2\psi)^t}{[c_1-2(\cos 2\psi+\sin\phi)]}\times\left[\frac{c_1-2(1+\sin\phi)}{c_1-2(\cos 2\psi+\sin\phi)}\right]^n d\psi. \tag{25}$$

To demonstrate that the solution obtained satisfies the friction law used by Pemberton [16], we mention that the stress characteristics are defined by the following equations (Pemberton [16]):

$$r\frac{d\theta}{dr}=\tan\left(\psi\mp\frac{\pi}{4}\mp\frac{\phi}{2}\right) \tag{26}$$

whereas the velocity characteristics are defined by

$$r\frac{d\theta}{dr}=\tan\left(\psi\mp\frac{\pi}{4}\right). \tag{27}$$

Since ψ is independent of r, the envelopes of these characteristic curves are given by

$$\theta=\text{const} \tag{28}$$

at $\psi=\psi_s=\pi/4+\phi/2$ and $\psi=\psi_v=\pi/4$, respectively. We have taken into account that $\psi\geqslant 0$. But (7) at $m=1$ shows that $\psi=\pi/4$ at the wall and, therefore, (28) should be replaced by $\theta=\theta_0$ and this line is an envelope of the velocity characteristics. On the other hand, an envelop of the stress characteristics (26) is not reachable because ψ is a monotonically increasing function of θ, $\psi=0$ at $\theta=0$ and $\psi_v<\psi_s$. Thus, for the problem under consideration the only possible interpretation of the friction law used by Pemberton [16] is to assume that the friction surface coincides with the envelope of velocity characteristics. As we have just seen, this leads to condition (7) at $m=1$.

We have mentioned that in the case of pressure-independent perfectly plastic material the velocity fields are singular at the maximum friction surface. To check the possibility of such a behavior in the present solution, we note that it follows from (10) that a singularity in the velocity field may be involved in the function $u(\theta)$ only. Equations (24) and Fig. 2 show that $t>0$ and $n>0$. Therefore, $u=0$ and $v=0$ at $\psi=\pi/4$ (maximum friction surface) as follows from (10) and (23). Thus, there is sticking at this surface. Nevertheless, substituting (23) into (11) shows that the velocity field is singular (nondifferentiable) since

$$\frac{du}{d\theta}\sim 2u_0(\cos 2\psi)^{(t-1)}\left[\frac{c_1-2(1+\sin\phi)}{c_1-2(\cos 2\psi+\sin\phi)}\right]^n\sin 2\psi$$

as $\psi\to\dfrac{\pi}{4}$, (29)

and then

$$\lim_{\psi\to\pi/4}(du/d\theta)\to\infty. \tag{30}$$

We have here taken into account that $t-1<0$ as follows from Eq. (24)[1] and Fig. 2.

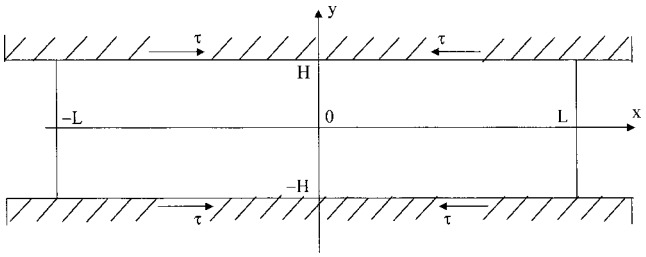

Fig. 3 Compression of block between parallel plates and coordinate system

Thus, in the vicinity of the maximum friction surface the solution obtained is qualitatively different (singular velocity field and sticking) from solutions based on other constitutive laws. In the case of the pressure-independent perfectly plastic material the velocity field is also singular, but sliding occurs. Moreover, the rate at which $du/d\theta$ tends to infinity in (30) is different from the rate for the pressure-independent material. In the latter case the rate is independent of the shape of the yield surface on the deviatoric plane and is $du/d\theta=O(1/\sqrt{\theta_0-\theta})$ for the problem under consideration, see Alexandrov and Richmond [13]. At $m=1$, it follows from (16) that in the vicinity of $\theta=\theta_0$ we have

$$\psi=\pi/4-\frac{(c_1-2\sin\phi)}{2\sin\phi}(\theta_0-\theta)+o(\theta_0-\theta)^2. \tag{31}$$

Therefore, $\cos 2\psi$ is expressible as

$$\cos(2\psi)=\frac{(c_1-2\sin\phi)}{\sin\phi}(\theta_0-\theta) \tag{32}$$

to leading order. Substituting (32) into (29) gives

$$du/d\theta=O(\theta_0-\theta)^{t-1}. \tag{33}$$

In the case of the pressure-independent hardening plastic material, sticking occurs but the velocity field is not singular. Actually, no solution has been found for radial flow through an infinite channel. It is easy to check by direct substitution that the solution proposed by Durban and Budiansky [27] fails for the maximum friction law. However, for many hardening laws it is possible to show that there is no sliding and that velocity fields are not singular at the maximum friction surface (see Alexandrov and Alexandrova, [21] for axisymmetric flow).

In the case of the double-shearing model the radial velocity is describable by nondifferential functions (see Appendix), but the rate at which its derivative with respect to θ tends to infinity is different from (33). In addition, this solution requires sliding at the friction surface. In general, the qualitative behavior of this solution is very similar to that of classical plasticity.

4 Compression of a Block Between Two Parallel Plates

A solution to this problem for a pressure-independent rigid/perfectly plastic material was found by Prandtl and Nadai (see Hill [26]) and modified by many authors to include various effects. For example, Collins and Mequid [29] have proposed solutions for hardening and anisotropic materials, Adams et al. [30] for a viscoplastic material, and Nepershin [31], for a thermoviscoplastic material. For the double-shearing model the problem has been solved by Marshall [17]. The singular behavior of the velocity field in this solution is discussed in the Appendix. A solution for the coaxial model is given in the present section. As in the case of flow through the wedge-shaped channel, the behavior of the solution in the vicinity of the maximum friction surface depends on the constitutive law.

Introduce a Cartesian coordinate system xy, instead of $\alpha\beta$, with its origin at the intersection of the axes of symmetry of the block (Fig. 3). Only a quarter of the block, $-L\leqslant x\leqslant 0$ and $0\leqslant y\leqslant H$,

needs to be considered due to symmetry. Moreover, as in other solutions to this problem, regions in the vicinity of $x=0$ and $x=-L$ are not covered by the solution and, therefore, the boundary conditions at those positions are not satisfied. Nevertheless, it is assumed that the material flows in the negative direction of the x-axis. Therefore, $\sigma_{\alpha\beta}>0$ and $\psi>0$ at the friction surface and (8) holds at $y=H$.

Assume the velocity field has the form

$$u_y=-u_0 y/H \quad \text{and} \quad u_x=w_0+u_0 x/H+u_0 f(y) \tag{34}$$

where $u_0>0$ is the velocity of the plates, w_0 is constant, and $f(y)$ is an arbitrary function of y. The velocity field (34) satisfies the incompressibility Eq. (3) and the boundary conditions for velocity at $y=0$ and $y=H$. Using this velocity field, Eq. (5) may be transformed to

$$\tan 2\psi=\frac{H}{2}\frac{df}{dy}. \tag{35}$$

It follows from this equation that ψ is independent of x. Then, substituting (4) into the equilibrium equations gives

$$\begin{aligned}&(1-\sin\phi\cos 2\psi)\frac{\partial\sigma}{\partial x}-\sin\phi\sin 2\psi\frac{\partial\sigma}{\partial y}\\&\quad+2\cos 2\psi(k\cos\phi-\sigma\sin\phi)\frac{d\psi}{dy}=0\\&(1+\sin\phi\cos 2\psi)\frac{\partial\sigma}{\partial y}+2\sin 2\psi(k\cos\phi-\sigma\sin\phi)\frac{d\psi}{dy}\\&\quad-\sin\phi\sin 2\psi\frac{\partial\sigma}{\partial x}=0.\end{aligned} \tag{36}$$

Assuming that

$$q=cx+p(y) \tag{37}$$

where q is defined by (13), c is constant and $p(y)$ is a function of y, Eqs. (36) reduce to

$$\frac{d\psi}{dy}=\frac{c_1}{2(\sin\phi+\cos 2\psi)} \tag{38}$$

$$\frac{dp}{dy}=\frac{c\sin 2\psi}{\sin\phi+\cos 2\psi} \tag{39}$$

where, as before, $c_1=c\cos^2\phi/\sin\phi$. Equation (38) may be integrated with the boundary condition $\psi=0$ at $y=0$ (zero shear stress at the axis of symmetry $y=0$) to give

$$yc_1=2\psi\sin\phi+\sin 2\psi. \tag{40}$$

The value of c_1 is determined from (8) and (40) as

$$c_1=\frac{\arcsin m\sin\phi+m}{H}. \tag{41}$$

Also, combining (38) and (39) and integrating we find

$$p=-\frac{\sin\phi}{\cos^2\phi}\cos 2\psi+p_0 \tag{42}$$

where p_0 is constant. Substituting (40) into (35) with the use of (41) and integrating gives

$$f=-\frac{2[\sin\phi\ln(\cos 2\psi)+\cos 2\psi]}{(\arcsin m\sin\phi+m)}. \tag{43}$$

Since the exact boundary condition for the velocity at $x=0$ cannot be fulfilled, the constant w_0 in (34) may be found from Eq. (3) integrated over the entire area of the block assuming the exact boundary conditions everywhere. This gives

$$w_0=-\frac{2u_0L}{H}-\frac{u_0}{H}\int_0^H f(y)dy.$$

Substituting (43) into this equation and using (38) and (41) we arrive at

$$\frac{w_0}{u_0}=\frac{4}{(\arcsin m\sin\phi+m)^2}\int_0^{(1/2)\arcsin m}[\sin\phi\ln(\cos 2\psi)+\cos 2\psi](\sin\phi+\cos 2\psi)d\psi. \tag{44}$$

In particular, for $m=1$ integration in (44) can be performed analytically to give

$$\frac{w_0}{u_0}=\frac{2(\pi+4\sin\phi)}{(\pi\sin\phi+2)^2}. \tag{45}$$

The components of the stress tensor may be obtained from (4), with the use of (13), (37), (41), and (42), in the form

$$\begin{aligned}\sigma_{xx}&=k\frac{\cos\phi}{\sin\phi}+\left(\cos 2\psi-\frac{1}{\sin\phi}\right)\\&\quad\times\exp\left\{\frac{\sin\phi}{\cos^2\phi}\left[(\arcsin m\sin\phi+m)\frac{x}{H}-\cos 2\psi\right]+p_0\right\}\\\sigma_{yy}&=k\frac{\cos\phi}{\sin\phi}-\left(\cos 2\psi+\frac{1}{\sin\phi}\right)\\&\quad\times\exp\left\{\frac{\sin\phi}{\cos^2\phi}\left[(\arcsin m\sin\phi+m)\frac{x}{H}-\cos 2\psi\right]+p_0\right\}\end{aligned} \tag{46}$$

$$\sigma_{xy}=\exp\left\{\frac{\sin\phi}{\cos^2\phi}\left[(\arcsin m\sin\phi+m)\frac{x}{H}-\cos 2\psi\right]+p_0\right\}\sin 2\psi.$$

The parameter p_0 may be found from the integral condition $\int_0^H\sigma_{xx}dy=0$ at $x=-L$ which replaces the exact condition $\sigma_{xx}=0$ at $x=-L$. Using $(46)^1$ and (38) we have

$$\begin{aligned}k/e^{p_0}&=\frac{2\exp\left[-\frac{\sin\phi}{\cos^2\phi}\frac{L}{H}(\arcsin m\sin\phi+m)\right]}{(\arcsin m\sin\phi+m)}\\&\quad\times\int_0^{(1/2)\arcsin m}(1-\sin\phi\cos 2\psi)(\sin\phi+\cos 2\psi)\\&\quad\times\exp\left(-\frac{\sin\phi\cos 2\psi}{\cos^2\phi}\right)d\psi.\end{aligned} \tag{47}$$

The solution for the pressure-independent material is obtainable from (46) as the limit as $\phi\to 0$ if

$$p_0=\ln k \quad \text{and} \quad dp_0/d\phi=\arcsin m/m+\sqrt{1-m^2}+mL/H \tag{48}$$

at $\phi=0$. It is easy to check by direct substitution that (47) results in (48). Thus, the solution for stress (46) approaches the solution for the pressure-independent material (Hill [26]) as $\phi\to 0$.

The situation with the solution for velocities is quite different. Of special interest is the distribution of the velocity u_x at $m=1$ which may be found from (34), (41), (43), and (45) as

$$\frac{u_x}{u_0}=\frac{x}{H}+\frac{2(\pi+4\sin\phi)}{(\pi\sin\phi+2)^2}-\frac{4[\sin\phi\ln(\cos 2\psi)+\cos 2\psi]}{(\pi\sin\phi+2)}. \tag{49}$$

It follows from (49) that the velocity field found by Nadai (see Hill [26]) is obtainable at $\phi=0$. However, at any small value of $\phi\neq 0$ the solution does not have a physical meaning since u_x approaches infinity at the friction surface ($\psi=\pi/4$). Moreover, u_x is positive there which contradicts the solution for stress. It is

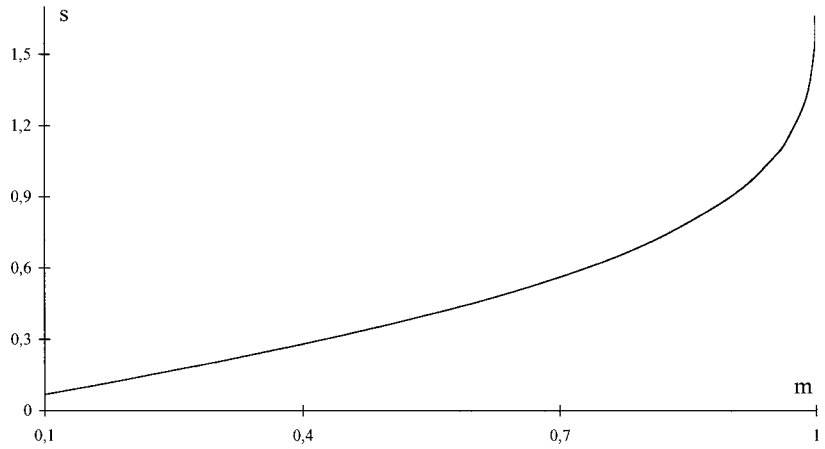

Fig. 4 Variation of the parameter *s*, which is involved in the condition of zero tangent velocity at the interface, with the friction factor *m*

clear that this contradiction should also appear for $m<1$. It follows from (34), (41), and (43) that u_x is positive at the interface if

$$s=\frac{w_0}{u_0}-\frac{\sin\phi\,\ln(1-m^2)+2\sqrt{1-m^2}}{\arcsin m\,\sin\phi+m}>\frac{x}{H} \tag{50}$$

for any x in the interval of interest. The value of w_0/u_0 in (50) is defined by (44). Variation of the parameter s with the friction factor m at $\phi=0.01$ is shown in Fig. 4. Because the solution under consideration may be in general acceptable for sufficiently large values of x/H, one can see from this figure that the contradiction occurs for values of m which are very close to 1. For example, for $x/H=1.5$, which is quite a small magnitude, $u_x>0$ at $m>0.999$. For larger values of x/H the value of m at which inequality (50) is satisfied is even closer to 1.

To demonstrate that the frictional law (7) at $m=1$ coincides with the law used by Marshall [17], we mention that the stress characteristics are defined by the following equations (Marshall [17]):

$$\frac{dy}{dx}=\tan\left(\psi\mp\frac{\pi}{4}\mp\frac{\phi}{2}\right) \tag{51}$$

whereas the velocity characteristics are defined by

$$\frac{dy}{dx}=\tan\left(\psi\mp\frac{\pi}{4}\right). \tag{52}$$

Since ψ is independent of x, the envelopes of these characteristic curves are given by

$$y=\text{const} \tag{53}$$

at $\psi=\psi_s=\pi/4+\phi/2$ and $\psi=\psi_v=\pi/4$, respectively. We here taken into account that $\psi\geqslant 0$. But (7) at $m=1$ shows that $\psi=\pi/4$ at the wall and, therefore, (53) should be replaced by $y=H$ and this line is an envelope of the velocity characteristics. On the other hand, an envelop of the stress characteristics (51) is not reachable because ψ is a monotonically increasing function of y, $\psi=0$ at $y=0$ and $\psi_v<\psi_s$. Thus, for the problem under consideration the only possible interpretation of the friction law used by Marshall [17] is to assume that the friction surface coincides with the envelope of velocity characteristics. As we have just seen, this leads to condition (7) at $m=1$.

The nonexistence of the found solution at $m=1$ and $\phi\neq 0$ is probably a consequence of the fact that the velocity field (34) assumes no sticking. For the same reason the solutions given by Collins and Mequid [29], Adams et al. [30], and Nepershin [31] fail at $m=1$. On the other hand, the solutions found by Nadai (see Hill [26]) and Marshall [17]) exist, but involve nondifferentiable functions. It is interesting that the solutions for both of the considered problems based on the same constitutive law show the same main features, but the solutions based on the coaxial model are quite different.

Conclusions

Two classical problems of plane-strain plasticity theory, flow through an infinite wedge-shaped channel and compression between parallel rough plates, have been solved analytically for pressure-dependent materials obeying the coaxial model. A comparison between these solutions and those found earlier for materials obeying the double-shearing model and pressure-independent materials has been made with the main emphasis on the solution behavior in the vicinity of the maximum friction surface. It has been demonstrated that the qualitative behavior of the solutions depends on the constitutive law chosen. In the case of flow through an infinite channel, the solutions are singular (some components of the strain rate tensor approach infinity), but sticking occurs for the coaxial model whereas the other models require sliding. Moreover, the rate at which the components of the strain rate tensor approach infinity depends on the specific constitutive law, but the same for the pressure-independent material and the double-shearing model. In the case of compression between parallel rough plates, no solution exists for the coaxial model at the maximum friction condition whereas the solutions for the other models exist, but are singular (some components of the strain rate tensor approach infinity) and the rate at which the components of the strain rate tensor approach infinity is the same.

Since the solutions for both of the considered problems based on the equations of classical plasticity and the double-shearing model show that same main features, it is expected that the use of the latter model with the maximum friction law should not lead to any difficulty other than the singularity of velocity field. On the other hand, a possibility of the use of the coaxial model with the maximum friction law may depend on specific problems.

It is believed that for successful applications, including numerical simulation, of both models it is necessary to perform a general study on the solution behavior in the vicinity of maximum friction surfaces and to clarify the formulation of this frictional law for pressure-dependent materials, as mentioned in Section 2.

Acknowledgment

The author wishes to thank Dr. Owen Richmond who initiated this work and contributed into it through many fruitful discussions.

Appendix

The solutions found by Pemberton [16] and Marshall [17] involve singular velocity fields with very large gradients in the vicinity of the maximum friction surface (some components of the strain rate tensor are infinite at the surface). This aspect of the solutions has not been mentioned by the authors, but has considerable theoretical and practical interest because such velocity fields may lead to computational difficulty and, on the other hand, are consistent with experimental data that show very large gradients of velocity near the friction surfaces.

Pemberton's Solution. The radial velocity is given by

$$v = -\frac{B}{r(\lambda - \cos 2\psi)} \tag{A1}$$

where $\lambda > 1$ and $B > 0$ are constant and ψ is defined by

$$\frac{d\theta}{d\psi} = \frac{\cos 2\psi + \sin\phi}{\lambda - \cos 2\psi}. \tag{A2}$$

The value of ψ at the maximum friction surface, ψ_w, is

$$\psi_w = \frac{\pi}{4} + \frac{\phi}{2}. \tag{A3}$$

It follows from this equation that

$$\cos 2\psi_w = -\sin\phi. \tag{A4}$$

Using (*A*1) and (*A*2) the derivative $\partial v/\partial\theta$ may be found in the form

$$\frac{\partial v}{\partial\theta} = -\frac{2B\sin 2\psi}{r(\lambda - \cos 2\psi)(\cos 2\psi + \sin\phi)}. \tag{A5}$$

The singularity of the velocity field now follows by inspection from (*A*4) and (*A*5).

To find the asymptotic behavior of the radial velocity in the vicinity of the maximum friction surface we expand the right in (A2) in the vicinity of $\psi = \psi_w$ as

$$\frac{d\theta}{d\psi} = -\frac{2\cos\phi}{(\lambda + \sin\phi)}(\psi - \psi_w) + O[(\psi - \psi_w)^2]. \tag{A6}$$

Using the boundary condition $\theta = \theta_0$ at $\psi = \psi_w$ Eq. (*A*6) may be integrated to give

$$\psi - \psi_w = -\sqrt{\frac{(\lambda + \sin\phi)}{\cos\phi}(\theta_0 - \theta)} \tag{A7}$$

to leading order. Substituting (*A*7) into (*A*5) gives

$$\partial v/\partial\theta = O(1/\sqrt{\theta_0 - \theta}) \quad \text{as} \quad \theta \to \theta_0 \tag{A8}$$

Marshall's Solution. The component of the velocity vector tangent to the friction surface is given by

$$\frac{u_x}{U} = \frac{x}{H} - \frac{2}{(\cos\phi + 2\psi_w \sin\phi)}\cos 2\psi + B \tag{A9}$$

where U and B are constant and ψ is defined by

$$\frac{y}{H} = \frac{\sin 2\psi + 2\psi\sin\phi}{\cos\phi + 2\psi_w \sin\phi}. \tag{A10}$$

The value of ψ at the maximum friction surface, ψ_w, is given by (*A*3). The derivative $\partial u_x/\partial y$ may be found from (*A*9) and (*A*10) in the form

$$\frac{\partial u_x}{\partial y} = \frac{U}{H}\frac{\sin 2\psi}{(\cos 2\psi + \sin\phi)}. \tag{A11}$$

The singularity of the velocity field now follows by inspection from (*A*4) and (*A*11). Using expansion of the right-hand side of Eqs. (*A*10) and (*A*11) in the vicinity of $\psi = \psi_w$ it is possible to show that

$$\partial u_x/\partial y = O(1/\sqrt{H - y}) \quad \text{as} \quad y \to H. \tag{A12}$$

Equations (*A*8) and (*A*12) show that in the considered problems the velocity tangent to the surface with maximum friction follows a square root law near such a surface. The same asymptotic behavior of the velocity has been found in classical plasticity (Alexandrov and Richmond [13]).

References

[1] Ostrowska-Maciejewska, J., and Harris, D., 1990, "Three-Dimensional Constitutive Equations for Rigid/Perfectly Plastic Granular Materials," Math. Proc. Cambridge Philos. Soc., **108**, pp. 153–169.

[2] Spencer, A. J. M., 1982, "Deformation of Ideal Granular Materials," *Mechanics of Solids, The Rodney Hill 60th Anniversary Volume*, H. G. Hopkins and M. J. Sewell, eds., Pergamon Press, Oxford, UK, pp. 607–652.

[3] Spencer, A. J. M., 1983, "Kinematically Determined Axially Symmetric Deformations of Granular Materials," *Mechanics of Granular Materials: New Models and Constitutive Relations*, J. T. Jenkins and M. Satake, eds., Elsevier, Amsterdam, pp. 245–253.

[4] Hill, J. M., and Wu, Y.-H., 1993, "Plastic Flows of Granular Materials of Shear Index *n*—I. Yield Functions," J. Mech. Phys. Solids, **41**, pp. 77–93.

[5] Hill, J. M., and Wu, Y.-H., 1993, "Plastic Flows of Granular Materials of Shear Index *n*—II. Plane and Axially Symmetric Problems for $n = 2$," J. Mech. Phys. Solids, **41**, pp. 95–115.

[6] Harris, D., 1993, "Constitutive Equations for Planar Deformations of Rigid-Plastic Materials," J. Mech. Phys. Solids, **41**, pp. 1515–1531.

[7] Lubarda, V. A., 1996, "Some Comments on Plasticity Postulates and Non-Associative Flow Rules," Int. J. Mech. Sci., **38**, pp. 247–258.

[8] Yoshida, S., Oguchi, A., and Nobuki, M., 1971, "Influence of High Hydrostatic Pressure on the Flow Stress of Copper Polycrystals," Trans. Jpn. Inst. Met., **12**, pp. 238–242.

[9] Spitzig, W. A., Sober, R. J., and Richmond, O., 1976, "The Effect of Hydrostatic Pressure on the Deformation Behavior of Maraging and HY-80 Steels and Its Implications for Plasticity Theory," Metall. Trans. A, **7A**, pp. 1703–1710.

[10] Spitzig, W. A., 1979, "Effect of Hydrostatic Pressure on Plastic-Flow Properties of Iron Single Crystals," Acta Metall., **27**, pp. 523–534.

[11] Kao, A. S., Kuhn, H. A., Spitzig, W. A., and Richmond, O., 1990, "Influence of Superimposed Hydrostatic Pressure on Bending Fracture and Formability of a Low Carbon Steel Containing Globular Sulfides," ASME J. Eng. Mater. Technol., **112**, pp. 26–30.

[12] Schey, J. A., 1984, *Tribology in Metalforming*, ASM International, Materials Park, OH.

[13] Alexandrov, S., and Richmond, O., 2001, "Singular Plastic Flow Fields Near Surfaces of Maximum Friction Stress," Int. J. Non-Linear Mech., **36**, pp. 1–11.

[14] Alexandrov, S., and Richmond, O., 1998, "Asymptotic Behavior of the Velocity Field in the Case of Axially Symmetric Flow of a Material Obeying the Tresca Condition," Dokl. Phys., **43**(6), pp. 362–364 (translated from Russian).

[15] Alexandrov, S., and Richmond, O., 1999, "Estimation of Thermomechanical Fields Near Maximum Shear Stress Tool/Workpiece in Metalforming Processes," *Proc of 3rd Int. Cong. on Thermal Stress*, J. J. Skrzypek and R. B. Hetnarski, eds., Cracow University of Technology, Cracow, pp. 153–156.

[16] Pemberton, C. S., 1965, "Flow of Imponderable Granular Materials in Wedge-Shaped Channels," J. Mech. Phys. Solids, **13**, pp. 351–360.

[17] Marshall, E. A., 1967, "The Compression of a Slab of Ideal Soil Between Rough Plates," Acta Mech., **3**, pp. 82–92.

[18] Alexandrov, S., and Richmond, O., 2001, "Couette Flows of Rigid/Plastic Solids: Analytical Examples of the Interaction of Constitutive and Frictional Laws," Int. J. Mech. Sci., **43**, pp. 653–665.

[19] Alexandrov, S., Mishuris, G., and Miszuris, W., 2000, "Planar Flow of a Three-Layer Plastic Material Through a Converging Wedge-Shaped Channel: Part 1—Analytical Solution," Eur. J. Mech. A/Solids, **19**, pp. 811–825.

[20] Alexandrov, S., and Alexandrova, N., 2000, "On the Maximum Friction Law in Viscoplasticity," Mech. Time-Depend. Mater., **4**, pp. 99–104.

[21] Alexandrov, S., and Alexandrova, N., 2000, "On the Maximum Friction Law for Rigid/Plastic, Hardening Materials," Meccanica, **35**, pp. 393–398.

[22] Rebelo, N., and Kobayashi, S., 1980, "A Coupled Analysis of Viscoplastic Deformation and Heat Transfer—II," Int. J. Mech. Sci. **22**, pp. 707–718.

[23] Appleby, E. J., Lu, C. Y., Rao, R. S., Devenpeck, M. L., Wright, P. K., and Richmond, O., 1984, "Strip Drawing: A Theoretical-Experimental Comparison," Int. J. Mech. Sci., **26**, pp. 351–362.

[24] Alexandrov, S. E., and Druyanov, B. A., 1992, "Friction Conditions for Plastic Bodies," Mech. Solids, **27**(4), pp. 110–115 (translated from Russian).

[25] Craggs, J. W., 1954, "Characteristic Surfaces in Ideal plasticity in Three Dimensions," Q. J. Mech. Appl. Math., **7**, Pt. 1, pp. 35–39.

[26] Hill, R., 1950, *The Mathematical Theory of Plasticity*, Oxford University Press, Oxford, UK.
[27] Durban, D., and Budiansky, B., 1979, ''Plane-Strain Radial Flow of Plastic Materials,'' J. Mech. Phys. Solids, **26**, pp. 303–324.
[28] Alexandrov, S., and Goldstein, R., 1993, ''Flow of a Plastic Substance Through a Convergent Channel: Characteristics of the Solution,'' Sov. Phys. Dokl., **38**(9), pp. 370–372 (translated from Russian).
[29] Collins, I. F., and Meguid, S. A., 1977, ''On the Influence of Hardening and Anisotropy on the Plane-Strain Compression of Thin Metal Strip,'' ASME J. Appl. Mech., **44**, pp. 271–278.
[30] Adams, M. J., Briscoe, B. J., Corfield, G. M., Lawrence, C. J., and Papathanasiou, T. D., 1997, ''An Analysis of the Plane-Strain Compression of Viscoplastic Materials,'' ASME J. Appl. Mech., **64**, pp. 420–424.
[31] Nepershin, R. I., 1997, ''Non-Isothermal Plane Plastic Flow of a Thin Layer Compressed by Flat Rigid Dies,'' Int. J. Mech. Sci., **39**, pp. 899–912.

A. Cochard
Laboratoire de Détection Géophysique, CEA,
B. P. 12,
91680 Bruyères-le-Châtel, France
and
Laboratoire de Géologie (UMR 8538),
École Normale Supérieure,
24, rue Lhomond,
75231 Paris, Cedex 05, France

L. Bureau

T. Baumberger[1]
e-mail: tristan@gps.jussieu.fr

UMR 7588,
Université Denis Diderot (Paris 7),
2, place Jussieu,
75251 Paris, Cedex 05, France

Stabilization of Frictional Sliding by Normal Load Modulation

This paper presents the stability analysis of a system sliding at low velocities (<100 $\mu m \cdot s^{-1}$) under a periodically modulated normal load, preserving interfacial contact. Experiments clearly evidence that normal vibrations generally stabilize the system against stick-slip oscillations, at least for a modulation frequency much larger than the stick-slip one. The mechanical model of L. Bureau, T. Baumberger, and C. Caroli validated on the steady-state response of the system, is used to map its stability diagram. The model takes explicitly into account the finite shear stiffness of the load-bearing asperities, in addition to a classical state and rate-dependent friction force. The numerical results are in excellent quantitative agreement with the experimental data obtained from a multicontact frictional system between glassy polymer materials. Simulations at larger amplitude of modulation (typically 20 percent of the mean normal load) suggest that the nonlinear coupling between normal and sliding motion could have a destabilizing effect in restricted regions of the parameter space. [DOI: 10.1115/1.1546241]

1 Introduction

It is well known that nonlinearities in the constitutive laws of dry friction may lead to the instability of steady frictional sliding against stick-slip oscillations, even for a single degree-of-freedom system driven at nominal constant velocity through a compliant stage. Sliding instability is an important issue in mechanical engineering since it is an ultimate limitation to the positioning accuracy for precision structures and machine tools. When designing a sliding mechanism, it is therefore of primary importance to characterize accurately the variations of the friction coefficient with, e.g., sliding velocity, keeping in mind that even slight variations may have a destabilizing effect. This requires to go beyond Amontons-Coulomb's law which assumes a constant friction coefficient. It might be legitimately feared that a more detailed constitutive law would have a restricted scope, e.g., in terms of materials and range of sliding velocities. It is thus remarkable that in the limit of low velocities (typically lower that 100 $\mu m \cdot s^{-1}$), and light enough loads so that the interface is made of a sparse set of microcontacts between load-bearing asperities, a relatively material-independent frictional behavior is found which can be accounted for by a simple set of nonlinear constitutive equations. Such studies have been initiated in the field of rock mechanics by Dieterich [1] and Rice and Ruina [2], motivated by the need for low velocity friction models to investigate fault dynamics and earthquake nucleation. They have put on a firm phenomenological basis the idea, already suggested by the work of Rabinowicz [3], that friction does not depend only on the instantaneous sliding velocity v but also on the whole sliding history. An experimental signature is the hysteretic frictional response of the interface when the slider is driven at a nonsteady rate. Rice and Ruina [2] proposed a family of dynamical equations coupling the sliding velocity to a set of state variables. Subsequent experimental investigations have shown that a single state variable ϕ is sufficient for most purposes. These experimental studies were performed on a wide range of materials, such as granite, [1], paper, [4], polymer glasses, [5], and elastomers, [6]. The friction force in this model is $F = W\mu(v,\phi)$ with W the normal load and μ the friction coefficient. Moreover, it has been possible, [7,8], to give a physical interpretation of ϕ as the average "age" of the microcontacts which grow while the material creeps under normal load, until sliding interrupts the process by renewing the load-bearing contact population. The dynamical model is closed by specifying a differential equation coupling v to ϕ so as to account for the renewal of the microcontact population after a slip length D_0 of micrometric order. This length is of order the mean radius of the microcontacts between surfaces of micrometric roughness, [9]. The resulting state-dependent and rate-dependent friction laws will be hereafter referred to as SRF. Among several SRF expressions proposed originally, the one that we use in this paper are

$$\mu(v,\phi) = \mu_0 + A \ln\left(\frac{v}{V_0}\right) + B \ln\left(1 + \frac{V_{sat}\phi}{D_0}\right) \tag{1}$$

for the friction coefficient and

$$\frac{d\phi}{dt} = 1 - \frac{v\phi}{D_0} \tag{2}$$

for the evolution of the state variable, where μ_0, A, B, V_{sat}, and V_0 are constants.

This SRF model has been extensively validated by testing against numerous experimental situations involving transient dynamical responses of the system. The most stringent test relies upon the nonlinear characteristics of the bifurcation from steady-sliding to stick-slip oscillations, [10]. The model can be understood as resulting from two distinct physical mechanisms, the effect of which can be summarized in the following decomposition of the friction force, proposed by Bowden and Tabor [11], in terms of the real area of contact Σ_r, and an interfacial shear strength σ_s:

$$F(v,\phi) = \sigma_s(v)\Sigma_r(\phi). \tag{3}$$

Here, the real area of contact depends on the interfacial age because it grows due to the creep of the load-bearing asperities, [7]. The velocity-dependent interfacial shear strength has been ascribed to the adhesivè, nanometer thick junctions between mi-

[1]To whom correspondence should be addressed.

Contributed by the Applied Mechanics Division of THE AMERICAN SOCIETY OF MECHANICAL ENGINEERS for publication in the ASME JOURNAL OF APPLIED MECHANICS. Manuscript received by the ASME Applied Mechanics Division, Aug. 24, 2001; final revision, Apr. 24, 2002. Associate Editor: K. T. Ramesh. Discussion on the paper should be addressed to the Editor, Prof. Robert M. McMeeking, Department of Mechanical and Environmental Engineering University of California–Santa Barbara, Santa Barbara, CA 93106-5070, and will be accepted until four months after final publication of the paper itself in the ASME JOURNAL OF APPLIED MECHANICS.

croasperities. A simple microscopic model has been proposed for the elastoviscoplastic rheology of the junctions, compatible with the existence of a finite friction threshold, [5].

Recently, attention has been paid to the effect of a time-dependent normal load on the response of a single degree-of-freedom sliding system. This situation is of practical interest when the mechanical design allows cross-talking between the normal (loading) and the tangential (driving) forces, [12], or when external vibrations contribute to the loading of the interface, as it may be the case for seismic faults, [13–15], or bolts and threaded fastners, [16]. The response of the system is not intuitive. First, since the friction force is directly proportional to the normal load, the sliding velocity is dynamically coupled to the normal load modulation, hence feeds back the friction force, [17]. Moreover, it has been shown that more subtle interplays must be taken into account. Linker and Dieterich [13] have interpreted the transient response to a step in normal load by coupling directly the time variations of ϕ and W, thus adding a term $-\text{const}\,\phi d\ln(W)/dt$ in Eq. (2). The physical motivation for this extension of the SRF aging equation is the fact that, according to [9], a change in normal force creates fresh load-bearing contact area. This certainly influences directly the age ϕ, though probably in a weaker measure than proposed by Linker and Dieterich [13], as briefly discussed in [18]. More recently, Bureau et al. [18] have studied the response of a sliding system to a periodically modulated normal load $W(t)=W_0[1+\epsilon\cos(\omega t)]$ with $\epsilon<1$. They found that the friction force, averaged on a modulation period, is significantly lowered with respect to the situation under constant load W_0. The oscillating part of the force, primarily harmonic at ω in the limit of vanishing ϵ, becomes quickly anharmonic as ϵ is increased while still remaining much smaller than 1. They have shown that the SRF equations can fit accurately all their results provided that the model is modified to account for the finite interfacial shear stiffness κ resulting from the elastic deformation of the load-bearing asperities. This means that the sliding velocity differs from the velocity of the center of mass of the slider, a statement which is clearly illustrated in the static state, i.e., for tangential forces well below the static threshold, where the interface responds elastically without sliding, [19,20]. Under constant normal load and constant driving velocity V, this ''hidden'' interfacial degree-of-freedom manifests itself only for nonsteady motion, and plays no significant role at the circular frequency $\Omega_c\sim V/D_0$ of the oscillations at the onset of the stick-slip instability.

However, under a modulated load at $\omega\gg\Omega_c$, one must take the finite interfacial compliance κ into account, all the more so since the latter is known to be itself proportional to W, [20]. This results in a nontrivial and efficient coupling between the normal load and the sliding velocity.

Of particular interest is the effect of load modulation on the sliding stability of the system. Dupont and Bapna [12] have computed the critical stiffness of the drive below which stick-slip occurs for a slider-spring system loaded at a constant angle with respect to the sliding plane. This configuration would provide a direct test for the coupling between ϕ and W proposed by Linker and Dieterich [13], but the experimental study has not been performed so far.

The present paper addresses the problem of the stability of a slider-spring system under an externally and harmonically modulated normal load. The experimental arrangement is described in Section 2 and it is shown that for a circular frequency $\omega\gg\Omega_c$ the modulation generally stabilizes the system against stick-slip.

Though the role of vibrations is seemingly part of the empirical culture in mechanical engineering, [16], it is, to our knowledge, the first time that the stabilization effect is investigated experimentally. This spectacular effect is accounted for by the SRF model with modulated interfacial stiffness, as shown by the numerical study of the bifurcation which is detailed in Section 3.

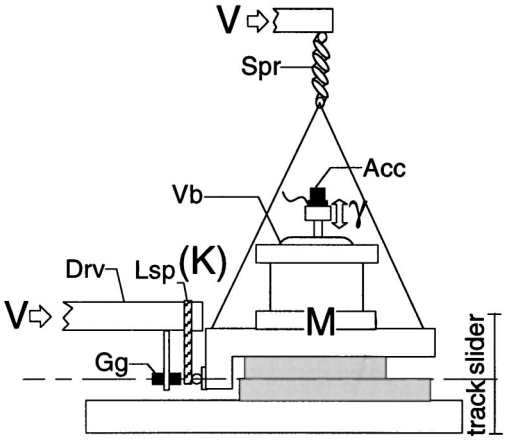

Fig. 1 Main elements of the experimental setup: translation stage (Drv); loading leaf spring (Lsp); displacement gauge (Gg); vibration exciter (Vb); weighting spring (Spr); accelerometer (Acc). The labeled parameters (K, V, M, γ) are defined in the text.

2 Experiments

2.1 Apparatus. The apparatus (Fig. 1) consists of a slider of mass M driven along a track through a loading spring of stiffness $K=0.21\ \text{N}\cdot\mu\text{m}^{-1}$. The loading end of the spring is moved at constant velocity V in the range 1–100 $\mu\text{m}\cdot\text{s}^{-1}$ by means of a translation stage driven by a stepping motor. The spring elongation is measured by an inductive probe (Electro, sensor 4937, module PBA200), with a 0.1 μm resolution over the 10 kHz bandwidth. The average normal load W_0 can be set in the range 3–23 N with the help of a vertical spring attached to a remote point, itself translated horizontally at the pulling velocity V through a second translation stage in order to prevent any tangential coupling. The normal load modulation is achieved by means of a vibration exciter (LDS, model V100) rigidly attached to the slider: A harmonic voltage input of given amplitude and frequency f results in a harmonic vertical motion of the moving element of the exciter on which an accelerometer (Brüel & Kjær, type 4371 V) is fixed. An acceleration of amplitude γ of this moving element of mass m induces a normal load modulation on the slider of amplitude $m\gamma$ at frequency f. We thus obtain a normal load $W(t)=W_0[1+\epsilon\cos(\omega t)]$ with $\omega=2\pi f$ and $\epsilon=m\gamma/W_0$ in the range 0.01–0.5. A fixed frequency $f=120$ Hz has been used for the whole study. Two poly(methylmethacrylate) (PMMA) samples are glued, respectively, on the slider and the track. They have nominally flat surfaces which have been lapped together with 400-grit SiC powder and water to obtain a rms roughness $R_q=1.3\ \mu$m, [20]. The interface between the two blocks is made of a sparse set of load-bearing microcontacts, [20]. An air layer of micrometric thickness is therefore trapped between the surfaces and acts as a viscoelastic element, in parallel with the microcontacts, which partially bears the normal load. This effect has been studied in details in Bureau et al. [18] who concluded that the remaining effect of the load modulation on the asperities can be described by an effective amplitude $\epsilon_{\text{eff}}=\rho\epsilon$, with ρ a constant close to 0.5, taken in the following as $\rho=0.43$, a value which will be justified in Section 3.3.

2.2 Localization of the Stick-Slip Bifurcation, Effect of the Modulation. The bifurcation between steady sliding and stick-slip oscillations under constant load ($\epsilon=0$) has been extensively described (see, e.g., [4]). When K and V are kept constant, steady sliding occurs for values of the remaining control parameter $W_0<W_0^c(V)$ where the K-dependency has been omitted here since the value of K is fixed in this study. The bifurcation is of the direct Hopf kind, which means that while the circular frequency of the

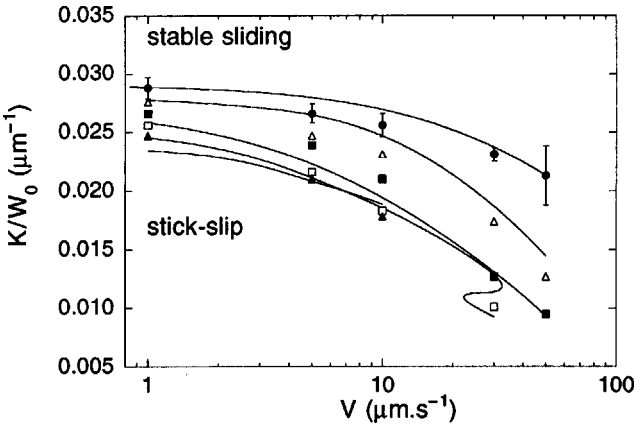

Fig. 2 Stability diagram for different values of the modulation amplitude. For given V and ϵ_{eff}, bifurcation from stick-slip to stable sliding occurs when the control parameter K/W_0 overcomes the plotted critical value: $\epsilon_{eff}=0$ (●); 0.045 (△); 0.09 (■); 0.13 (□); 0.18 (▲). For the sake of clarity, typical standard deviations are plotted as error bars only for $\epsilon_{eff}=0$. The solid line curves are the output of the numerical study (see Section 3.3). The larger ϵ_{eff} the lower the curve at $V=1$ μm·s^{-1}.

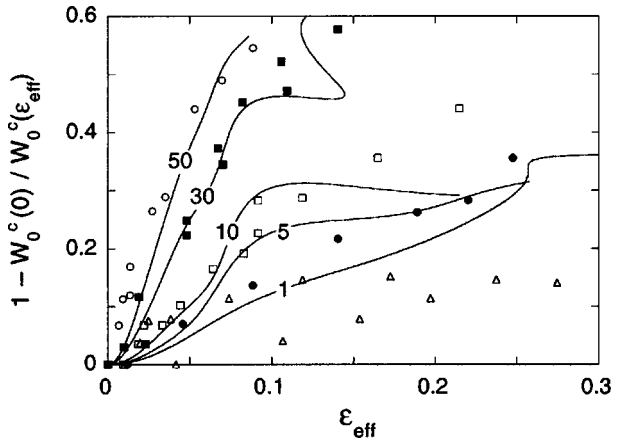

Fig. 4 Reduced critical load versus ϵ_{eff} for different driving velocities: $V(\mu$m·s$^{-1})=1$ (△); 5 (●); 10 (□); 30 (■); 50 (○). The curves are the output of the numerical study (see Section 3.3) labeled with the corresponding velocities in μm·s^{-1}.

slider velocity oscillations tends to a finite value Ω_c, their amplitude goes continuously to zero[2] on approaching the bifurcation locus from the stick-slip region of the dynamic phase diagram (Fig. 2). In addition, the characteristic time of the oscillating transients following an external perturbation diverges on approaching the bifurcation locus from the steady sliding region. A practical consequence is that in the close vicinity of the bifurcation it becomes difficult to distinguish between established steady stick-slip oscillations of small amplitude and long transient relaxation towards steady sliding (see Fig. 3), resulting from the perturbating effect of friction force fluctuations along the track. This is the main source of uncertainty in the localization of the bifurcation.

For $\epsilon=0$, the ratio K/W_0 is the relevant control parameter, at least in the low velocity region where inertia of the slider oscillating at the circular frequency Ω_c can be neglected, [4]. Henceforth, although the external stiffness K is kept constant for the whole set of experiments reported in this paper, we will keep on representing the stability domain of the system in the parameter plane $(K/W_0, V)$ where it is bounded by the experimental bifurcation curve (Fig. 2). The experimental uncertainty on the critical value K/W_0^c, determined from the standard deviation over at least ten measurements at a given velocity V, is indicated by the error bars in Fig. 2. It is typically ± 3 percent, except at the larger velocity, since the results are more sensitive to long wavelength irregularities along the track for large sliding distances.

When a harmonic modulation at ω is superimposed to a value of W_0 corresponding to steady sliding at V, the velocity of the slider oscillates about V, possibly in a anharmonic way, with a fundamental component at ω. The motion of the slider, when averaged over a period $2\pi/\omega$ is therefore steady. For given V and K, one has now to consider two control parameters, namely W_0 and ϵ_{eff}.

When the DC load W_0 is increased while keeping constant ϵ_{eff}, the motion of the slider, averaged over a period $2\pi/\omega$, is found to become of the stick-slip kind above a critical value, $W_0^c(V,\epsilon_{eff}) > W_0^c(V)$ (Fig. 2). A normal load modulation of even very small effective amplitude may therefore *stabilize* the system against stick-slip as illustrated directly in Fig. 3 where a modulation with $\epsilon_{eff}=4.5\times10^{-2}$ is enough to suppress well developed, strongly anharmonic, large-amplitude and low-frequency stick-slip oscillations (the force signal then only shows the remaining small amplitude modulation at the forcing frequency).

The effect of ϵ_{eff} on the critical value of $K/W_0(V)$ is characterized in Fig. 4. The higher the velocity, the stronger the stabilizing effect of the normal load modulation. The effect is spectacular when described in terms of the velocity domain corresponding to steady sliding at constant K/W_0. For instance, the critical velocity at $K/W_0=0.026$ μm^{-1} is decreased by more than a factor of ten by applying a modulation with $\epsilon_{eff}=0.09$.

The empirical study indicates that, as a rule of thumb, steady-sliding is promoted by high velocity, high amplitude of normal load modulation, low average normal load, and large stiffness. This is tested in the following against a numerical study of the SRF model including normal load modulation.

[2]Note that the term "stick-slip" is therefore a misnomer since the sliding velocity does not reach zero, i.e., the slider does not "stick" during an oscillation period.

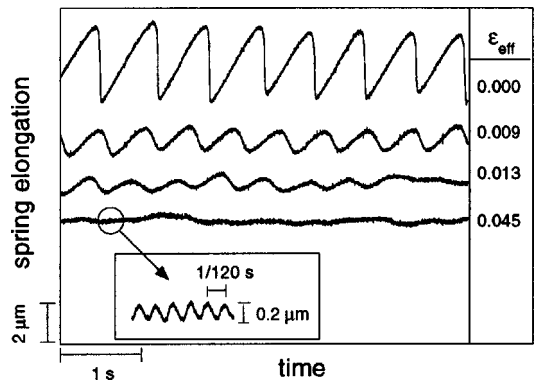

Fig. 3 Time evolution of the loading spring elongation for $V=8$ μm·s^{-1} and different modulation amplitudes ϵ_{eff} indicated at the right end of each trace. A vertical offset has been added to each trace in order to display clearly the bifurcation sequence from stick-slip to stable sliding. The inset is a blow up of the stable sliding trace showing the remaining oscillating response at the frequency of the load modulation ($f=120$ Hz, much higher than the stick-slip frequency).

3 Numerical Study

3.1 The State and Rate-Dependent Friction (SRF) Model Equations. The SRF laws (Eqs. (1), (2)) are incorporated into the equation of motion of the slider, according to the simple model sketched in Fig. 5. The proportionality constant between the nor-

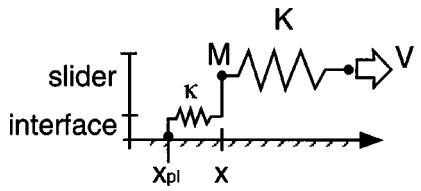

Fig. 5 Equivalent mechanical circuit of the slider/track system. *K* is the stiffness of the loading spring, κ is the one of the interface.

Table 1 Values of the SRF parameters

Parameter	Trial Value	Optimized Value
K ($\mathrm{N}\cdot\mu\mathrm{m}^{-1}$)	0.21	
M (kg)	2.37	
$\mu_0(V_0=1\ \mu\mathrm{m}\cdot\mathrm{s}^{-1})$	0.33	
A	0.012 ± 0.002	0.0126
B	0.023 ± 0.002	0.0241
D_0 (μm)	0.40 ± 0.04	0.402
V_{sat} ($\mu\mathrm{m}\cdot\mathrm{s}^{-1}$)	280 ± 70	256
λ (μm)	0.62 ± 0.15	0.56
$\rho=\epsilon_{eff}/\epsilon$	0.48 ± 0.10	0.43

mal load W and the interfacial stiffness κ is a length λ of micrometric order: $\kappa=W/\lambda$, [20]. The equation of motion of the slider thus reads

$$Mx''=K(Vt-x)-\kappa(x-x_{pl}) \tag{4}$$

where here and henceforth the prime denotes time derivative. Taking a massless interfacial zone (a reasonable assumption, see appendix), we also have, according to Eq. (1),

$$\frac{W}{\lambda}(x-x_{pl})=W\left[\mu_0+A\ln\left(\frac{v}{V_0}\right)+B\ln\left(1+\frac{V_{sat}\phi}{D_0}\right)\right], \tag{5}$$

where $v=x'_{pl}$ is the relative sliding velocity at the interface and ϕ follows the evolution law (2) rewritten here for the sake of clarity[3]:

$$\phi'(t)=1-\frac{v\,\phi(t)}{D_0}. \tag{6}$$

For numerical purposes, we wish to recast those equations in the form of a system of first-order ordinary differential equations (ODEs). Noting $z=x'$, $u=Vt-x$, further differentiating $x-x_{pl}$ with respect to time in (5) using the explicit expression for $W(t)=W_0[1+\epsilon_{eff}\cos(\omega t)]$ and solving for v', we get the following ODE system, which we will use for the numerical bifurcation analysis:

$$u'=V-z \tag{7}$$

$$z'=\frac{K}{M}u-\frac{W_0(1+\epsilon_{eff}\cos(\omega t))}{M}\left[\mu_0+A\ln\left(\frac{v}{V_0}\right)+B\ln\left(1+\frac{V_{sat}\phi}{D_0}\right)\right] \tag{8}$$

$$v'=\frac{v}{\lambda A}\left[z-v-\frac{\lambda BV_{sat}(1-v\,\phi/D_0)}{D_0(1+V_{sat}\phi/D_0)}\right] \tag{9}$$

$$\phi'=1-\frac{v\,\phi}{D_0}. \tag{10}$$

3.2 Determination of the SRF Parameters. In order to analyze the data within the SRF framework, we need to determine a set of values for the relevant parameters of the model. This is performed under constant normal load, according to a well-established procedure. The values, which will be used in the numerical analysis, some of them as trial ones, are gathered in Table 1. The useful formulas are established in the Appendix.

1. First, the steady sliding friction coefficient $\mu_d(V)$ is measured to be velocity-weakening with an almost constant logarithmic slope over the 1–100 $\mu\mathrm{m}\cdot\mathrm{s}^{-1}$ range. This indicates that V_{sat}, above which $\mu_d(V)$ increases with increasing V according to Eqs. (1), (2), is certainly larger than 100 $\mu\mathrm{m}\cdot\mathrm{s}^{-1}$ and allows to extract a value for $B-A$ and μ_0 at $V_0=1\ \mu\mathrm{m}\cdot\mathrm{s}^{-1}$, i.e., far below the saturation of the aging term.

2. Next, the critical value of K/W_0, here taken at midrange (10 $\mu\mathrm{m}\cdot\mathrm{s}^{-1}$) where inertial terms can be neglected in Eq. (21), yields a determination of the memory length D_0.

3. From the value of the critical stick-slip period at 10 $\mu\mathrm{m}\cdot\mathrm{s}^{-1}$ (Eq. (22)), we obtain a value for A.

4. A determination of V_{sat} is finally obtained by a best fit of the whole bifurcation curve in the plane $(K/W_0,V)$ for V in the 1–50 $\mu\mathrm{m}\cdot\mathrm{s}^{-1}$ range, treating the inertial term in Eq. (21) as a perturbative one. Since the value of V_{sat} is out of the experimental velocity window, this determination is not very accurate. Treating several data set corresponding to different runs yields an uncertainty as large as ±25 percent on the value of V_{sat}.

5. The value of the length λ, defined by the ratio of the load W_0 and the interfacial shear stiffness κ, has been obtained in [18] from a best fit of the AC response of the slider position to the normal load modulation.

It is clear that this procedure, though systematic, generates cumulative errors which are difficult to evaluate (the uncertainties on A, B, and D_0 given in Table 1 are conservative values). In view of the high sensitivity of the bifurcation to small variations of the parameters, we have chosen in the following numerical analysis to use the set determined above as a trial one. Namely, the parameters which are left free are A, B, D_0, λ, V_{sat}, and the ratio $\rho=\epsilon_{eff}/\epsilon$.

3.3 Bifurcation Analysis. Technically, the transition from steady sliding to stick-slip, both states being modulated by the forcing (when $\epsilon\neq0$), is a Neimark-Saker bifurcation (also called secondary Hopf), which corresponds to two complex conjugate values of the fundamental matrix of the ODE system crossing the unit circle. The fundamental matrix H is defined as $dH/dt=J(x(t))H$ with $H(x,0)=I$, with J the Jacobian matrix of the ODE system and I the identity. The numerical software CANDYS/QA, [21], has been used to track this bifurcation. For a given parameter set, a bifurcation curve like in Fig. 2 can be obtained as follows: For a given driving velocity, one starts from a low enough normal load W_0 in order to be in the steady sliding regime. Once such a ''first point'' is indeed found by the software, one varies W_0 only (one-parameter continuation) until a bifurcation is detected ($W_0=W_0^c$); one then follows this bifurcation curve by further varying the driving velocity too (two-parameter continuation).

The procedure to detect the bifurcation has been automated. Starting from the parameter values determined in Section 3.2, the critical values W_0^c are determined and compared to the experimental ones $W_{0_{exp}}^c$. A systematic procedure (Powell's method, as described in [22]) is then used that attempts to minimize $\Sigma_{V,\epsilon}[W_0^c(\rho\epsilon)-W_{0_{exp}}^c]^2$, with $\rho=\epsilon_{eff}/\epsilon$, for a representative set of

[3]This equation, including the actual sliding velocity v in place of x' is consistent with our physical understanding of the age ϕ. It has been checked that mistaking x' for v, as in [18], has no significant effect on their results, at least for the modulation frequencies much larger than V/D_0 used in their study.

experimental data. The set of parameters hence determined, which corresponds to a local minimum of the cost function, reducing it by a factor of fifteen[4], is given in Table 1.

The full bifurcation curves are then determined as described above, by a two-parameter continuation. The results are shown in Figs. 2 and 4 together with experimental data covering a range of ϵ_{eff} values wider than the one involved in the adjustment procedure.

4 Discussion

The curves displayed in Figs. 2 and 4 have been calculated with the optimized set of parameters. However, it is worth noting that the trial set yields numerical results in good qualitative agreement with the experimental data as well. Namely, the main effect of normal load modulation, at least for moderate values of ϵ_{eff}, which is to stabilize sliding against stick-slip oscillations, is well reproduced by the SRF model. Moreover, the enhanced efficiency of the modulation on increasing the sliding velocity is correctly accounted for.

The set of optimized data differs from the trial set essentially for three parameters, namely the elastic length λ, the saturation velocity V_{sat}, and the ratio $\rho=\epsilon_{\text{eff}}/\epsilon$ accounting for the air-cushion effect.

The final value for λ lies within the error bars estimated in [18].

As already mentioned in Section 3.2 the large variation of V_{sat} during the optimization procedure is attributable to the fact that the crossover from a velocity-weakening regime to a strengthening one for steady sliding friction lies well above the upper experimental velocity, whence the goodness of the fit is only weakly sensitive to V_{sat}.

The ratio $\rho=\epsilon_{\text{eff}}/\epsilon$ was determined in [18] by comparison of the experimental shift of the steady friction level $\Delta\mu_0$ at 120 Hz and the value predicted by the SRF model. The value taken in this reference was $\rho=0.48$. Taking into account the error bars on $\Delta\mu_0$ one finds that the relative uncertainty on ρ is about ± 20 percent. The optimized value for this parameter lies therefore within this range.

Thus, the SRF model with its set of parameters as determined from the dynamical study of the system under constant normal load is fully predictive as regards the sliding stability of the system under modulated load, at least for the values of ϵ_{eff} probed by the data of Fig. 2. In turn, the sensitivity of this experiment enabled us to refine the determination of the parameters.

The quantitative overall agreement between the experimental data and the numerical curves in Fig. 4 is excellent for, say, $\epsilon_{\text{eff}}<0.15$. Above this value the calculated curves tend to fold and correspond to a re-entrent stability diagram; namely, for given ϵ_{eff} and V, increasing K/W_0 yields successive bifurcations from stick-slip to steady sliding then back to steady-sliding, etc. No experimental evidence of such an unexpected behavior has been encountered so far. It is clearly the result of the nonlinear coupling between the normal load modulation and the stick-slip oscillations. As such, it is expected to depend drastically on the *details* of the SRF laws. The importance of the terms which ultimately cut-off the logarithmic variations in the SRF laws has been stressed in several studies, [10,23]. The existence of V_{sat}, which accounts for a short time cut-off in the creep deformation of the load-bearing asperities, [7], yields one of these terms. It should be kept in mind that the SRF constitutive law (1) retains only the leading terms in the expansion of the friction force in powers of $\ln(v)$. For instance, Eq. (3) with physically sounded expressions for $\sigma_s(v)$ and $\Sigma_r(\phi)$ would lead to terms of order $AB\ln(v)\ln(\phi)$ which, though negligible for most purposes, would probably affect the critical behavior of the system under a strongly modulated load. For these reasons, we think that a full quantitative agreement between the experimental bifurcation at large[5] ϵ_{eff} and the SRF model predictions would be illusive.

In addition, we have investigated numerically the effect of the extra term in Eq. (2) proposed by Linker and Dieterich [13] and already discussed in [18]. No significant effect has been found at 120 Hz, where we conclude that this term, if it exists as such, is not relevant to the present relatively high frequency study.

5 Conclusion

The stability of a sliding system with a few degrees-of-freedom, submitted to a periodically modulated normal load, has been studied experimentally. The study clearly evidences the role of load modulation, even at moderate amplitude, as a stabilizer against stick-slip oscillations. The results have been compared to the numerical predictions of a model of the SRF type, relevant to multicontact friction at low velocities and low loads, including finite interfacial shear stiffness as a key parameter. Excellent quantitative agreement has been found as long as the amplitude of load modulation is restricted to about 10 percent of the dead load.

Although, as discussed above, the main effect of the normal load modulation is stabilization, the numerical study strongly suggests that *destabilization* may also occur, due to the highly nonlinear features of the model which also gives rise to re-entrent stability diagram in Fig. 2. More precisely, it can be seen in this figure that the $\epsilon_{\text{eff}}=0.18$ curve crosses the $\epsilon_{\text{eff}}=0.13$ one around $V=7\ \mu\text{m}\cdot\text{s}^{-1}$. For a $(V,K/W_0)$ point slightly on the right of this crossing, in between the two curves, increasing ϵ_{eff} would result in a bifurcation from stable sliding to stick-slip. This effect has not been observed directly so far, probably because it corresponds to small regions of the parameter space, strongly dependent on the value of the parameters. Clearly, this point would deserve further experimental study.

Appendix

Linear Stability Analysis for $\epsilon=0$. The linear stability analysis of the SRF equations has been performed previously, [2,4]. However, difference between sliding velocity and the velocity of the center of mass of the slider was disregarded in these works. Since the interfacial stiffness is of paramount importance when the normal load is modulated at relatively high frequency, it is necessary to evaluate its role on the location of the bifurcation under constant load. Moreover, we will derive in this appendix expressions for the critical stiffness and the critical pulsation that hold for any state and rate-dependent friction force.

Let us consider a general expression:

$$F=W_0\mu(v,\phi). \tag{11}$$

The time evolution of the age variable ϕ is ruled by

$$\phi'=1-\frac{v\phi}{D_0}. \tag{12}$$

When the slider is driven at constant velocity V, the steady sliding values of the dynamical variables are $v=V$ and $\phi=D_0/V$. We define

$$\begin{cases} \mu_v=\dfrac{\partial\mu}{\partial\ln v}(V,D_0/V)>0 \\ \mu_\phi=\dfrac{\partial\mu}{\partial\ln\phi}(V,D_0/V)>0 \end{cases}. \tag{13}$$

The position of the center of mass of the slider is $x(t)$ so that the elongation of the loading spring is $x-Vt$. At frequencies of interest the interfacial zone can be assumed massless and essentially elastic with a frequency independent, real stiffness κ, [19]. The following relation holds:

[4]When several critical values for W_0 can be detected, the one retained in the evaluation of the cost function is the closest chosen among the odd ones (first, third, etc.), corresponding to a transition from steady sliding to stick-slip when increasing W_0, while even ones correspond to a transition from steading sliding to stick-slip.

[5]It has been shown in [18] that the relevant perturbation parameter is actually $\mu_0\epsilon_{\text{eff}}/A\gg\epsilon_{\text{eff}}$ which is already larger than 1 for $\epsilon_{\text{eff}}=0.1$.

$$v = x' + \frac{d}{dt}\left(\frac{Mx'' - K(Vt-x)}{\kappa}\right). \tag{14}$$

We will make use in the following of the ratio η of the loading spring stiffness K to the equivalent stiffness of the loading spring in parallel with the interface $K \| \kappa$:

$$\eta = \frac{K}{K\|\kappa} = \frac{K+\kappa}{\kappa}. \tag{15}$$

Finally, the dynamical equation for the motion of the slider reads

$$Mx'' = K(Vt-x) - W_0\mu(v,\phi). \tag{16}$$

The set of dynamical Eqs. (12), (14), (16) is closed and can be linearized about the steady sliding state, setting

$$\begin{cases} x = Vt - F(V,D_0/V)/K + \delta x, & |\delta x| \ll F(V,D_0/V)/K \\ \phi = D_0/V + \delta\phi, & |\delta\phi| \ll D_0/V \end{cases}. \tag{17}$$

The linearized system becomes

$$\begin{cases} M\delta x'' = -K\delta x - W_0\left[(\mu_v/V)\left(\eta\delta x' + \dfrac{M}{\kappa}\delta x'''\right) + (\mu_\phi V/D_0)\delta\phi\right] \\ \delta\phi' = -\eta\delta x'/V - \dfrac{M}{K}\delta x'''/V - \delta\phi V/D_0 \end{cases}. \tag{18}$$

The solutions are the real parts of the complex $\tilde{\delta x} = \tilde{\delta}x_0 \exp(i\Omega t)$ and $\tilde{\delta\phi} = \tilde{\delta}\phi_0 \exp(i\Omega t)$ with Ω a complex number. Replacing into Eq. (18) and writing the condition for nontrivial amplitudes $\tilde{\delta}x_0$ and $\tilde{\delta}\phi_0$, one finds the dispersion relationship

$$C_4\Omega^4 + C_3\Omega^3 + C_2\Omega^2 + C_1\Omega + C_0 = 0 \tag{19}$$

with

$$\begin{cases} C_0 = \dfrac{KV}{D_0} \\ C_1 = i\dfrac{W_0}{D_0}\left[\dfrac{KD_0}{W_0} - \eta(\mu_\phi - \mu_v)\right] \\ C_2 = -\left(\dfrac{MV}{D_0} + \dfrac{\eta\mu_v W_0}{V}\right) \\ C_3 = -iM\dfrac{W_0}{\kappa D_0}\left[\dfrac{\kappa D_0}{W_0} + (\mu_v - \mu_\phi)\right] \\ C_4 = M\mu_v\dfrac{W_0}{\kappa V} \end{cases}. \tag{20}$$

The critical value of the control parameters and the critical pulsation Ω_c are obtained by expressing that at the Hopf bifurcation (at least) one root of Eq. (19) crosses the imaginary axis. Setting that Ω is purely imaginary and extracting the real and imaginary components from Eq. (19) yield the requested values.

Let us first solve for an infinitely stiff interface, i.e., for $\eta = 1$ and $\kappa \to \infty$. It is then straightforward to find

$$\frac{KD_0}{W_0^c} = (\mu_\phi - \mu_v)\left(1 + \frac{MV^2}{W_0^c D_0 \mu_v}\right) \tag{21}$$

and

$$\frac{D_0\Omega_c}{V} = \sqrt{\frac{\mu_\phi - \mu_v}{\mu_v}}. \tag{22}$$

These relations make sense only for $\mu_\phi - \mu_v > 0$, i.e., when the steady sliding friction coefficient $\mu^{ss}(V)$ is velocity weakening: $\partial\mu^{ss}/\partial \ln V < 0$. For the particular expression of $\mu(v,\phi)$ used in the numerical analysis, this reads

$$-\frac{\partial\mu^{ss}}{\partial \ln V} = \mu_\phi - \mu_v = \frac{B}{1+V/V_{sat}} - A > 0. \tag{23}$$

Now, let us evaluate the contribution of the finite interfacial stiffness κ to Eq. (19) by estimating the order of magnitude of $c = |C_4\Omega_c^4/C_0|$ with Ω_c given by Eq. (22), i.e., $\Omega_c \simeq V/D_0$. This reads

$$c \simeq \mu_v \frac{MV^2}{KD_0^2} \tag{24}$$

where we have expressed that $W_0/(\kappa D_0) = \lambda/D_0 \simeq 1$. One can estimate $c < 10^{-3}$ within the experimental velocity range, hence the fourth-order term in Eq. (19) can be safely discarded. Next, a finite κ introduces perturbative terms in C_3 which are of order μ_v, $\mu_\phi \simeq 10^{-2}$, still well below the relative uncertainty on the experimental determination of the critical parameters. Since the correction to the drive stiffness due to the interfacial elastic element is of order $\eta - 1 = K/\kappa \simeq 10^{-2}$, it can be concluded that for the purpose of calculating the values of the critical parameters, the finite interfacial stiffness has no practical effect, and one can make use of Eqs. (21) and (22).

Acknowledgments

The authors would like to thank Christiane Caroli and Jim Rice for discussions and encouragement, as well as Wolfgang Jansen for prompt assistance with CANDYS/QA.

References

[1] Dieterich, J. H., 1979, "Modeling of Rock Friction 1. Experimental Results and Constitutive Equations," J. Geophys. Res., **84**, pp. 2161–2168.
[2] Rice, J. R., and Ruina, A. L., 1983, "Stability of Steady Frictional Slipping," ASME J. Appl. Mech., **105**, pp. 343–349.
[3] Rabinowicz, E., 1965, *Friction and Wear of Materials*, John Wiley and Sons, New York.
[4] Heslot, F., Baumberger, T., Perrin, B., Caroli, B., and Caroli, C., 1994, "Creep, Stick-Slip, and Dry Friction Dynamics: Experiments and a Heuristic Model," Phys. Rev. E, **49**, pp. 4973–4988.
[5] Baumberger, T., Berthoud, P., and Caroli, C., 1999, "Physical Analysis of the State- and Rate-Dependent Friction Law: II. Dynamic Friction," Phys. Rev. B, **60**, pp. 3928–3939.
[6] Ronsin, O., and Labastie-Coueyrehourcq, K., 2001, "State, Rate and Temperature-Dependent Sliding Friction of Elastomers," Proc. R. Soc. London, Ser. A, **457**, pp. 1277–1294.
[7] Berthoud, P., Baumberger, T., G'Sell, C., and Hiver, J.-M., 1999, "Physical Analysis of the State- and Rate-Dependent Friction Law: Static Friction," Phys. Rev. B, **59**, pp. 14,313–14,327.
[8] Dieterich, J. H., and Kilgore, D., 1994, "Direct Observation of Frictional Contacts: New Insights for State-Dependent Properties," Pure Appl. Geophys., **43**, pp. 283–302.
[9] Greenwood, J. A., and Williamson, J. B. P., 1966, "Contact of Nominally Flat Surfaces," Proc. R. Soc. London, Ser. A, **295**, pp. 300–319.
[10] Baumberger, T., Caroli, C., Perrin, B., and Ronsin, O., 1995, "Nonlinear Analysis of the Stick-Slip Bifurcation in the Creep-Controlled Regime of Dry Friction," Phys. Rev. E, **51**, pp. 4005–4010.
[11] Bowden, F. P., and Tabor, D., 1950, *Friction and Lubrication of Solids*, Clarendon, Oxford, UK.
[12] Dupont, P. E., and Bapna, D., 1994, "Stability of Sliding Frictional Surfaces With Varying Normal Force," ASME J. Vibr. Acoust., **116**, pp. 237–242.
[13] Linker, M., and Dieterich, J. H., 1992, "Effects of Variable Normal Stress on Rock Friction: Observations and Constitutive Equations," J. Geophys. Res., **124**, pp. 445–485.
[14] Perfettini, H., Schmittbuhl, J., Rice, J. R., and Cocco, M., 2001, "Frictional Response Induced by Time-Dependent Fluctuations of the Normal Loading," J. Geophys. Res., **106**(B7), pp. 13,455–13,472.
[15] Richardson, E., and Marone, C., 1999, "Effects of Normal Stress Vibrations on Frictional Heating," J. Geophys. Res., **104**, pp. 28,859–28,878.
[16] Akay, A., 2002, "Acoustics of Friction," J. Acoust. Soc. Am., **111**, pp. 1525–1548, and references therein.
[17] Polycarpou, A. A., and Soom, A., 1995, "Boundary and Mixed Friction in the Presence of Dynamic Normal Loads: Part II—Friction Transients," ASME J. Tribol., **117**, pp. 261–266.
[18] Bureau, L., Baumberger, T., and Caroli, C., 2000, "Shear Response of a Frictional Interface to a Normal Load Modulation," Phys. Rev. E, **62**, pp. 6810–6820.
[19] Baumberger, T., Bureau, L., Busson, M., Falcon, E., and Perrin, B., 1998, "An Inertial Tribometer for Measuring Microslip Dissipation at a Solid-Solid Multicontact Interface," Rev. Sci. Instrum., **69**, pp. 2416–2420.

[20] Berthoud, P., and Baumberger, T., 1998, ''Shear Stiffness of a Solid-Solid Multicontact Interface,'' Proc. R. Soc. London, Ser. A, **454**, pp. 1615–1634.
[21] Feudel, U., and Jansen, W., 1992, ''CANDYS/QA—A Software System for the Qualitative Analysis of Nonlinear Dynamical Systems,'' Int. J. Bifurcation Chaos Appl. Sci. Eng., **2**, pp. 773–794. See also http://www.agnld.uni-potsdam.de/wolfgang/wolfgang.html
[22] Press, W. H., Teukolsky, S. A., Vetterling, W. T., and Flannery, B. P., 1992, *Numerical Recipes*, Cambridge University Press, Cambridge, UK.
[23] Baumberger, T., and Gauthier, L., 1996, ''Relaxation at the Interface Between Rough Solids Under Shear,'' J. Phys. I, **6**, pp. 1021–1025.

Transient Study of Mode III Fracture in an Elastic Solid With a Single Plane of Material Symmetry

L. M. Brock
Fellow ASME
Mechanical Engineering,
University of Kentucky,
Lexington, KY 40506
e-mail: brock@engr.uky.edu

Diffraction of a plane SH-wave causes semi-infinite mode III crack extension in an unbounded linear elastic solid. The solid is nonorthotropic, with a single plane of material symmetry that is perpendicular to the crack edge. The crack plane itself lies at an arbitrary angle to the axes of material symmetry, the SH-wave direction is largely arbitrary, and extension is not necessarily instantaneous or at a constant speed. An exact transient study produces the fracture energy release rate, and uses a full-field analytical solution to derive the dynamic stress intensity factor on any plane radiating from the moving crack edge. A crack path stability analysis of the factor indicates that crack extension in the original plane can occur in directions associated with maximum and minimum values of the shear wave speed. The energy release rate for such extensions shows that, if an isotropic solid subjected to the same type of loading has the same specific fracture energy, then the nonorthotropic solid may fracture first. [DOI: 10.1115/1.1533807]

Introduction

The classical theory of anisotropic elasticity, [1], and its application to wave propagation, [2–4], are well developed. Studies of rapid (dynamic) fracture in anisotropic elastic solids also exist and have, in general, focused on crack extension parallel to a principal axis of material symmetry, and upon orthotropic or transversely isotropic materials, e.g., [5,6]. More recently, [7], rapid Mode III semi-infinite crack growth in an unbounded solid with only a single plane of material symmetry, [8], was considered. Crack extension in any direction with respect to the principal material axes in the symmetry plane was allowed, and conditions examined for which such extension might be likely. The fracture process was driven by forces moving on the crack faces, and a dynamic steady-state assumed, i.e., the forces and crack extend at the same constant speed.

In this article, a transient study of a similar situation is made. Fracture is now triggered by diffraction of a plane horizontally polarized shear (SH) wave, and is not necessarily instantaneous or at a constant speed. Orientations of the crack plane and principal material axes are again arbitrary, and crack path stability conditions are again examined. In addition, comparison with isotropic results, [9–11], is made on the basis of fracture energy release rate. Indeed, the same solution methods are used.

The study begins with introduction of basic equations and the problem statement. The solution process gives first the crack-plane quantities required for calculating the energy release rate. The full-field solution is then examined for crack path stability requirements. Consistent with the steady-state study, [7], these suggest that crack extension in the original plane might well occur when that plane coincides with the directions of extremal shear wave speeds. Crack path stability in directions of maximum shear wave speed, however, could be precluded when the degree of nonorthotropy of the solid is increased sufficiently. Results also suggest that, if the specific fracture energy is the same for an isotropic and a nonorthotropic solid, fracture initiation would occur first in the nonorthotropic material.

Contributed by the Applied Mechanics Division of THE AMERICAN SOCIETY OF MECHANICAL ENGINEERS for publication in the ASME JOURNAL OF APPLIED MECHANICS. Manuscript received by the Applied Mechanics Division, Mar. 17, 2002; final revision, July 26, 2002. Associate Editor: K. Ravi-Chandar. Discussion on the paper should be addressed to the Editor, Prof. Robert M. McMeeking, Chair, Department of Mechanics and Environmental Engineering, University of California–Santa Barbara, Santa Barbara, CA 93106-5070, and will be accepted until four months after final publication in the paper itself in the ASME JOURNAL OF APPLIED MECHANICS.

Basic Equations

A homogeneous linearly elastic solid has only the x_1x_2-plane as a plane of material symmetry, where (x_1,x_2,x_3) are Cartesian coordinates. Hooke's law, [12], is, therefore,

$$\begin{bmatrix}\sigma_{11}\\ \sigma_{22}\\ \sigma_{33}\\ \sigma_{32}\\ \sigma_{13}\\ \sigma_{21}\end{bmatrix}=\begin{bmatrix}c_{11} & c_{12} & c_{13} & 0 & 0 & c_{16}\\ c_{21} & c_{22} & c_{23} & 0 & 0 & c_{26}\\ c_{31} & c_{32} & c_{33} & 0 & 0 & c_{36}\\ 0 & 0 & 0 & c_{44} & c_{45} & 0\\ 0 & 0 & 0 & c_{54} & c_{55} & 0\\ c_{61} & c_{62} & c_{63} & 0 & 0 & c_{66}\end{bmatrix}\begin{bmatrix}\varepsilon_{11}\\ \varepsilon_{22}\\ \varepsilon_{33}\\ 2\varepsilon_{32}\\ 2\varepsilon_{13}\\ 2\varepsilon_{21}\end{bmatrix}. \quad (1)$$

The c_{ik} are the elastic constants, $c_{ik}=c_{ki}$, and discussions of their relation to crystallographic properties is found in [13,14]. The form of (1) shows that x_k define the principal material axes. The strains ε_{ik} and stresses σ_{ik} satisfy, in the absence of body forces, the standard equations

$$2\varepsilon_{ik}=2\varepsilon_{ki}=u_{i,k}+u_{k,i}, \quad \sigma_{ik,k}=\rho\ddot{u}_i, \quad \sigma_{ik}=\sigma_{ki}. \quad (2)$$

Here ρ is the mass density, u_i is the displacement in the x_i-direction, $(\ )_{,i}=\partial(\ )/\partial x_i$, and $(\cdot)$ denotes time differentiation. Equations (1) and (2) support the antiplane state

$$u_1=u_2=0, \quad u_{3,3}=0, \quad \sigma_{11}=\sigma_{22}=\sigma_{33}=\sigma_{21}=0 \quad (3)$$

and reduce to the system

$$\sigma_{32}=c_{44}u_{3,2}+c_{45}u_{3,1}, \quad \sigma_{13}=c_{55}u_{3,1}+c_{45}u_{3,2} \quad (4a)$$

$$\sigma_{13,1}+\sigma_{32,2}=\rho\ddot{u}_3 \quad (4b)$$

under the positive definiteness, c.f. [3,4], requirements

$$(c_{44},c_{55})>0, \quad c_{44}c_{55}-c_{45}^2>0. \quad (5)$$

No preference is given to either c_{44} or c_{55}, and $c_{45}=0$ in the orthotropic limit, [12]. It is convenient, therefore, to introduce the parameters

$$\bar{\mu}=\frac{1}{2}(c_{44}+c_{55}),\quad \bar{v}=\sqrt{\frac{\bar{\mu}}{\rho}} \tag{6}$$

and the dimensionless ratios

$$\alpha=\frac{c_{55}}{\bar{\mu}},\quad \beta=\frac{c_{44}}{\bar{\mu}},\quad \gamma=\frac{c_{45}}{\bar{\mu}}. \tag{7}$$

Equation (5) does not restrict the sign of c_{45}, and (6) defines an average shear modulus $\bar{\mu}$ and shear wave speed $\bar{v}$ in the plane of material symmetry. In the isotropic limit, (6) then gives the single modulus and wave speed, [15]. In view of (5) and (6),

$$\alpha+\beta=2,\quad (\alpha-1)^2+\gamma^2=(\beta-1)^2+\gamma^2=1-\Gamma \tag{8}$$

where the dimensionless quadratic

$$\Gamma=\alpha\beta-\gamma^2\quad (0<\Gamma<1) \tag{9}$$

is useful in characterizing material behavior. The quantities (Γ,γ) control, in effect, the degree of nonorthotropy: the upper bound in (9) arises because (α,β,γ) must be real and, indeed, occurs only when $\gamma=0$, $\alpha=\beta=1$, i.e., the isotropic limit $c_{45}=0$, $c_{44}=c_{55}$.

Problem Formulation

An unbounded solid of such a material contains a semi-infinite crack, defined in terms of the Cartesian coordinates (x,y,z) as the region $y=0,x<0$. The xy-plane coincides with the x_1x_2-plane of material symmetry, but the x-axis, i.e., crack plane, makes an arbitrary angle ϕ with the x_1-principal axis. In view of this rotation, the field equations

$$\frac{1}{\bar{\mu}}\sigma_{yz}=C\frac{\partial w}{\partial x}+B\frac{\partial w}{\partial y},\quad \frac{1}{\bar{\mu}}\sigma_{xz}=A\frac{\partial w}{\partial x}+C\frac{\partial w}{\partial y} \tag{10a}$$

$$A\frac{\partial^2 w}{\partial x^2}+2C\frac{\partial^2 w}{\partial x\partial y}+B\frac{\partial^2 w}{\partial y^2}=\frac{\partial^2 w}{\partial s^2},\quad s=\bar{v}\times\text{time} \tag{10b}$$

emerge from (4)–(9). Here s, with its dimension of length, is the temporal variable, $w(x,y,s)$ corresponds to u_3, and

$$A=1+\tfrac{1}{2}(\alpha-\beta)\cos 2\phi+\gamma\sin 2\phi \tag{11a}$$

$$B=1+\tfrac{1}{2}(\beta-\alpha)\cos 2\phi-\gamma\sin 2\phi \tag{11b}$$

$$C=\tfrac{1}{2}(\beta-\alpha)\sin 2\phi+\gamma\cos 2\phi \tag{11c}$$

define the array (A,B,C) that represents the tensor transformation of array (α,β,γ) due to the aforementioned rotation, c.f., [8]. The formulas

$$\frac{dA}{d\phi}=-\frac{dB}{d\phi}=2C,\quad \frac{dC}{d\phi}=B-1=1-A \tag{12a}$$

$$A+B=2,\quad AB-C^2=\Gamma \tag{12b}$$

are also useful, and it is noted that Γ is an invariant of the transformation.

This cracked solid is at rest when a plane horizontally polarized shear (SH) wave, characterized by the displacement,

$$w^i=\int_0^{s_\psi}U(t)dt,\quad s_\psi=s+k_\psi x\cos\psi+k_\psi y\sin\psi>0 \tag{13}$$

is for $s<0$ incident upon the crack with attack angle ψ $(0<\psi<90$ deg), as depicted schematically in Fig. 1(a). The dimensionless function $U\equiv 0(t\leqslant 0)$ and is bounded above and piecewise continuous for finite $t>0$. The dimensionless parameters

$$c_\psi=\frac{1}{k_\psi}=\sqrt{1+\frac{1}{2}(\alpha-\beta)\cos 2(\phi+\psi)+\gamma\sin 2(\phi+\psi)} \tag{14}$$

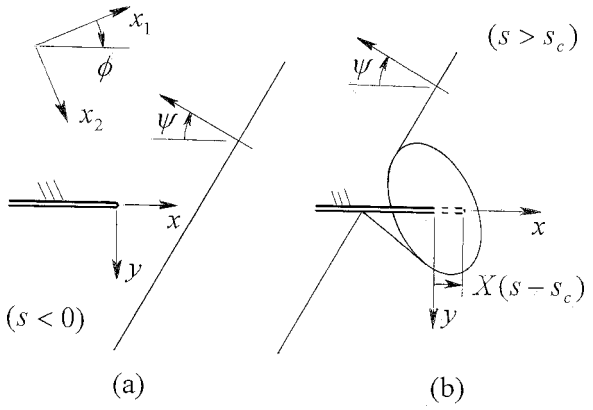

Fig. 1 (*a*) Schematic of SH-wave incident upon crack; (*b*) schematic of wave diffraction and crack extension

define the plane wave speed $c_\psi\bar{v}$, and $s=s_\psi$ locates the wave front for all s. Form (13) satisfies (10b) and, in light of (10a), gives the traction

$$\sigma^i_{yz}=\bar{\mu}A_\psi U(s+k_\psi x\cos\psi),\quad c_\psi s+x\cos\psi>0 \tag{15a}$$

$$c_\psi A_\psi=\sin\psi+\tfrac{1}{2}(\beta-\alpha)\sin(2\phi+\psi)+\gamma\cos(2\phi+\psi) \tag{15b}$$

that is induced on the crack plane $(y=0)$. This wave reaches the crack edge at $s=0$, and is diffracted. At $s=s_c>0$ the crack begins to extend in the positive x-direction, so that its edge is located at $y=0$, $x=X(s-s_c)$, where

$$X\equiv 0(s<s_c), \tag{16a}$$

$$0<X'<c(s\geqslant s_c) \tag{16b}$$

and $(\,)'$ signifies differentiation with respect to the argument. The dimensionless parameters

$$c=\frac{1}{k}=\sqrt{\frac{\Gamma}{B}} \tag{17}$$

define the shear wave speed $c\bar{v}$ along the crack plane; thus, (16b) precludes supersonic crack growth and crack retreat. In addition, the crack edge location function X is finite and continuous for finite $s>s_c$. The incident/scattered wave field and crack extension is depicted schematically in Fig. 1(b). In light of (10), the expanding elliptical region

$$s\geqslant k\sqrt{\left(x-\frac{C}{B}y\right)^2+\frac{\Gamma}{B^2}y^2} \tag{18}$$

is formed by the scattered waves. Its semi-major and semi-minor axes tilt with respect to the crack plane due to the ϕ-dependent slope parameter C/B. Scattered waves also occur in the wedge-shaped region whose apex moves with the incident wave/crack plane intersection, and whose plane fronts form tangents with the elliptical region. As seen in Fig, 1(b), the part of this wedge-shaped region in $y>0$ represents incident wave reflection from the crack; the part $y<0$ creates a shadow zone through incident wave cancellation.

Linearity of (10) allows the superposition

$$w=w^i+w^s. \tag{19}$$

Here w^s is the displacement field engendered by the scattered waves. It satisfies in addition to (10) the initial condition $w^s\equiv 0(s\leqslant 0)$ and, in view of (15), the condition

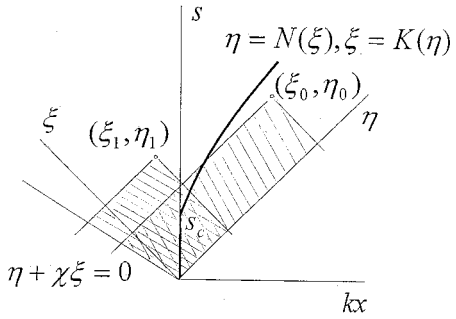

Fig. 2 Schematic of integration region ($y=y_0=0$)

$$\sigma^s_{yz} = -\bar{\mu}A_\psi U(s + k_\psi x\cos\psi) \quad \left(y=0, -\frac{c_\psi s}{\cos\psi} < x < X\right). \tag{20}$$

It should also be finite for finite $s \geqslant 0$, and continuous everywhere except perhaps the region defined in (20). Its gradient, however, may be discontinuous along the wave fronts depicted in Fig. 1(b), and singular at the crack edge $y=0, x=X$.

Scattered Field Solution

The scattered wave, in addition to (20), produces a crack plane stress $\tau(x,s)(y=0, X<x<\bar{v}s)$ ahead of the crack edge. If τ were known, and the complete scattered wave traction along $y=0$ denoted as $T(x,s)$, standard Green's function techniques would give the scattered wave displacement field for a given (x_0, y_0, s_0) as

$$w^s = \frac{\pm 1}{2\pi\bar{\mu}\sqrt{\Gamma}} \int_s\int \frac{T(x,s)dxds}{\sqrt{(s_0-s)^2 - k^2R_0^2}},$$

$$R_0 = \sqrt{\left(x_0 - \frac{C}{B}y_0 - x\right)^2 + \frac{\Gamma}{B^2}y_0^2} \tag{21}$$

for $y_0 > 0(+)$ and $y_0 < 0(-)$. The integration region S in the xs-plane is the intersection of a wedge-shaped area $-c_\psi s/\cos\psi < x < \mathbf{v}s$ due to $T(x,s)$ with the cone $s_0 - s > kR_0$ of elliptical cross section. Equation (21) does not have the antisymmetry with respect to $y_0 = 0$ of the corresponding isotropic case, [9–11].

The unknown portion $\tau(x,s)$ of the field $T(x,s)$ follows by requiring that (21) be continuous in the plane ahead of the crack edge. That is

$$[w^s]^+_- = \frac{1}{\pi\bar{\mu}\sqrt{\Gamma}} \int_s\int \frac{T(x,s)dxds}{\sqrt{(s_0-s)^2 - k^2(x_0-x)^2}} = 0 \tag{22}$$

for $y_0 = 0$, $x > X_0$, where $X_0 = X(s_0 - s_c)$ and $[\ ]^+_-$ signifies the jump as the x-axis is crossed in the positive y-direction. The intersection now passes through the cone axis and S can, as shown in Fig. 2, be described simply in terms of the characteristic variables

$$\xi = \frac{s-kx}{\sqrt{2}}, \quad \eta = \frac{s+kx}{\sqrt{2}} \tag{23}$$

as the shaded trapezoid $(-\chi\xi < \eta < \eta_0, 0 < \xi < \xi_0)$, where

$$\chi = \frac{c_\psi - c\cos\psi}{c_\psi + c\cos\psi} (0 < \chi < 1). \tag{24}$$

In Fig. 2 the crack edge trajectory $s > 0, x = X$ can be expressed as $\xi > 0, \eta = N(\xi)$ or $\eta > 0, \xi = K(\eta)$, where (N, K) are obtained from the formulas

$$N(\xi) = \xi + \sqrt{2}kX\left(\frac{\xi + N(\xi)}{\sqrt{2}} - s_c\right),$$

$$K(\eta) = \eta - \sqrt{2}kX\left(\frac{\eta + K(\eta)}{\sqrt{2}} - s_c\right). \tag{25}$$

These functions are, in view of the requirements on X, also piecewise smooth, with $N'(\xi) \leqslant 1, K'(\eta) \geqslant 1$. For $0 < s < s_c$, (25) reduce to the explicit forms

$$N(\xi) = \xi\left(0 < \xi < \frac{s_c}{\sqrt{2}}\right), \quad K(\eta) = \eta < \left(0 < \eta < \frac{s_c}{\sqrt{2}}\right). \tag{26}$$

When $(s_0 > 0, x_0 > X_0)$ we have, as seen in Fig. 2, $(\xi_0 > 0, \eta_0 > N(\xi_0))$. Thus, S has regions $(\xi > 0, -\chi\xi < \eta < N(\xi))$ and $(\xi > 0, \eta > N(\xi))$ in which, respectively, $T = -\bar{\mu}A_\psi\hat{U}(\xi,\eta)$ and $T = \hat{\tau}(\xi,\eta)$, where, in light of (23),

$$\hat{U}(\xi,\eta) = U\left(\frac{\eta+\xi}{\sqrt{2}} + \frac{\eta-\xi}{k\sqrt{2}}k_\psi\cos\psi\right),$$

$$\hat{\tau}(\xi,\eta) = \tau\left(\frac{\eta-\xi}{k\sqrt{2}}, \frac{\eta+\xi}{\sqrt{2}}\right). \tag{27}$$

Equation (23) also shows that $(s_0-s)^2 - k^2(x_0-x)^2 = 2(\xi_0-\xi)\times(\eta_0-\eta)$, so that (22) can be written as

$$\frac{1}{\pi k\sqrt{2\Gamma}} \int_0^{\xi_0} \frac{d\xi}{\sqrt{\xi_0-\xi}} \left[-A_\psi \int_{-\chi\xi}^{N(\xi)} \frac{\hat{U}(\xi,\eta)}{\sqrt{\eta_0-\eta}} d\eta + \frac{1}{\bar{\mu}} \int_{N(\xi)}^{\eta_0} \frac{\hat{\tau}(\xi,\eta)}{\sqrt{\eta_0-\eta}} d\eta \right] = 0. \tag{28}$$

Setting the term in brackets to zero gives a standard Abel integral equation, [9–11,16], whose solution is, c.f., [9–11],

$$\hat{\tau}(\xi,\eta) = \frac{\bar{\mu}A_\psi}{\pi\sqrt{\eta - N(\xi)}} \int_{-\chi\xi}^{N(\xi)} \frac{\hat{U}(\xi,u)}{\eta-u} \sqrt{N(\xi)-u}\, du$$
$$(\xi > 0, \eta > N(\xi)). \tag{29}$$

In light of (13), (19), (21), (23), and (29), the scattered field and the complete solution has been obtained. Its properties are now examined in view of classical fracture mechanics, [11,17].

Crack Edge Stress Field, Energy Release Rate

An integration variable change in (29) gives in view of (23) and (25)–(27)

$$\tau(x,s) = \frac{\bar{\mu}A_\psi}{\pi\sqrt{k}} \int_{-u_\psi(x,s)}^{kX^*} U\left(u + s - kx + \frac{uk_\psi}{k}\cos\psi\right) \frac{\sqrt{kX^*-u}}{kx-u} du \tag{30}$$

where $X^* = X(s^* - s_c)$ and

$$u_\psi(x,s) = \frac{c_\psi(s-kx)}{c_\psi + c\cos\psi}, \tag{31a}$$

$$s^* - kX^* = s - kx. \tag{31b}$$

We choose $s > s_c$ and a point x ahead of but very near the crack edge at s, i.e., $x - X \to 0+$, $X = X(s - s_c)$. Then for $s^* \to s$ one can write in view of (31b)

$$s^* \approx s - \frac{\partial s^*(kX)}{\partial(kx)}k(x-X), \quad x - X^* \approx -\frac{\partial s^*(kX)}{\partial(kx)}(x-X). \tag{32}$$

Performing the differentiation and combining with (30) gives

$$\tau(x,s)\approx \frac{\overline{\mu}A_\psi}{\pi}\frac{\sqrt{c-X'}}{\sqrt{x-X}}\int_{-u_\psi(X,s)}^{kX} U\Big(u+s-kX + \frac{uk_\psi}{k}\cos\psi\Big)\frac{du}{\sqrt{kX-u}} \tag{33}$$

for $(s>s_c, x\to X+)$, c.f., [9–11]. The corresponding result for $(0<s<s_c, x\to 0+)$ follows by setting $(X,X')=0$.

On the newly formed crack surface we have $(x=x_1,\ y=0,\ s=s_1)$, where $(s_1>s_c, 0<x<X(s_1-s_c))$. In light of the discussion of (22), these values correspond to the point (ξ_1,η_1) in Fig. 2. Region S is again a trapezoid, but it now has the parts $(-\chi\xi<\eta<\eta_1, 0<\xi<K(\eta_1))$ and $(-\chi\xi<\eta<\eta_1, K(\eta_1)<\xi<\xi_1)$. In view of (28) the contribution from the first part vanishes, so that (21) gives, c.f., [9–11],

$$[w^s]_-^+ = -\frac{cA_\psi}{\pi\sqrt{2\Gamma}}\int_{K(\eta_1)}^{\xi_1}\frac{d\xi}{\sqrt{\xi_1-\xi}}\int_{-\chi\xi}^{\eta_1}\frac{\hat{U}(\xi,\eta)}{\sqrt{\eta_1-\eta}}d\eta. \tag{34}$$

The corresponding particle velocity discontinuity (crack slip speed) for $(s>s_c, x\to X-)$, i.e., just behind the moving crack edge, follows by differentiation and a similar limiting process:

$$\left[\frac{\partial w^s}{\partial s}\right]_-^+ \approx -\frac{2A_\psi}{\pi\sqrt{\Gamma}}\frac{cX'}{\sqrt{c+X'}}\frac{1}{\sqrt{X-x}}\int_{-u_\psi(X,s)}^{kX} U\Big(u+s-kX + \frac{k_\psi u}{k}\cos\psi\Big)\frac{du}{\sqrt{kX-u}}. \tag{35}$$

With (33) and (35) available, the (fracture) energy release rate (per unit length of crack edge) can be obtained, [7,9–11], as the positive quantity

$$\dot{\mathcal{J}} = \frac{2\overline{\mu}}{\pi}A_\psi^2\frac{c_\psi\overline{v}}{\sqrt{\Gamma}}X'\sqrt{\frac{c-X'}{c+X'}}I^2,$$

$$I = \frac{\sqrt{c}}{\sqrt{c_\psi + c\cos\psi}}\int_0^{s+k_\psi X\cos\psi}\frac{U(u)du}{\sqrt{s+k_\psi X\cos\psi-u}} \tag{36}$$

where an integration variable change, c.f., [9], is introduced for simplification.

The coefficient of $1/\sqrt{x-X}$ in (33) is the dynamic stress intensity factor. Both it and (36) are derived on the assumption that the crack extends in its original plane. For some insight into the validity of this assumption, the scattered field and the traction that it develops on planes radiating from the crack edge is considered.

Full Scattered Field

Consider (21) for the more general situation $(x_0, y_0>0, s_0)$. The intersection of the region filled by $T(x,s)$ and the elliptical cone does not include the cone axis, and S is now the region bounded by the lines $\eta+\chi\xi=0$, $C_0(\xi,\eta)=0$ and range $0<\xi<\xi_\chi$ depicted in Fig. 3. There $(\xi_0+C\zeta_0, \eta_0-C\zeta_0)$ correspond to $(x_0, y_0>0, s_0)$ where, c.f., (23),

$$\xi_0 = \frac{s_0-kx_0}{\sqrt{2}},\quad \eta_0=\frac{s_0+kx_0}{\sqrt{2}},\quad \zeta_0=\frac{ky_0}{B\sqrt{2}} \tag{37}$$

and are the intersection of hyperbolic asymptotes. The hyperbola branch $C_0(\xi,\eta)=0$ defines one boundary of S, where

$$C_0(\xi,\eta) = (\xi_0+C\zeta_0-\xi)(\eta_0-C\zeta_0-\eta)-\Gamma\zeta_0^2. \tag{38}$$

The intersection $(\xi_N, N(\xi_N))$ of this curve and the crack edge trajectory is given by the implicit formulas

$$(\xi_0+C\zeta_0-\xi_N)(\eta_0-C\zeta_0-N(\xi_N))-\Gamma\zeta_0^2=0 \tag{39a}$$

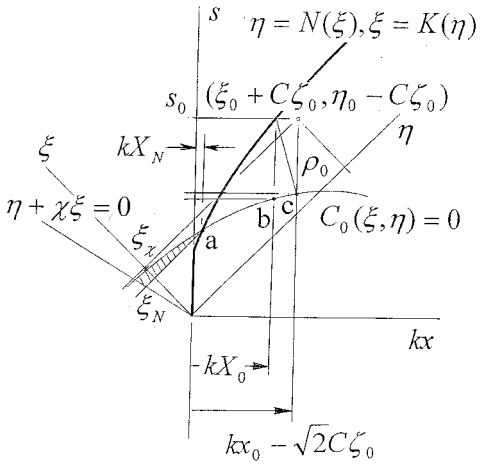

Fig. 3 Schematic of integration region ($y=y_0>0$)

$$N(\xi_N) = \xi_N+\sqrt{2}kX_N,\quad X_N=X(s_N-s_c),\quad s_N=\frac{\xi_N+N(\xi_N)}{\sqrt{2}}. \tag{39b}$$

The intersection $(\xi_\chi, -\chi\xi_\chi)$ of the curves $(C_0, \eta+\chi\xi)=0$ is obtained explicitly as

$$\xi_\chi = \frac{P_-}{2\chi}+Q,\quad 2\chi Q=\sqrt{P_-^2+4\chi C_0(0,0)}=\sqrt{P_+^2-4\chi\Gamma\zeta_0^2} \tag{40a}$$

$$P_\pm = \chi(\xi_0+C\zeta_0)\pm(\eta_0-C\zeta_0). \tag{40b}$$

It is noted that $\xi_\chi \gtrless \xi_N$, even when $(\xi_0+C\zeta_0, \eta_0-C\zeta_0)$ lies on the other side of the crack edge trajectory than the one depicted in Fig. 3. Thus, S can be broken into the two regions $(0<\xi<\xi_N,\ -\chi\xi<\eta<L(\xi))$ and $(\xi_N<\xi<\xi_\chi, -\chi\xi<\eta<L(\xi))$, where $\eta=L(\xi)$ is the relevant solution of the equation $C_0(\xi,\eta)=0$. Equation (21) gives

$$w^s = \frac{c}{2\pi\sqrt{\Gamma}}\int_0^{\xi_N}d\xi\Big[-A_\psi\int_{-\chi\xi}^{N(\xi)}\frac{\hat{U}(\xi,\eta)d\eta}{\sqrt{2C_0(\xi,\eta)}} + \frac{1}{\overline{\mu}}\int_{N(\xi)}^{L(\xi)}\frac{\hat{\tau}(\xi,\eta)d\eta}{\sqrt{2C_0(\xi,\eta)}}\Big] - \frac{cA_\psi}{2\pi\sqrt{\Gamma}}\int_{\xi_N}^{\xi_\chi}d\xi\int_{-\chi\xi}^{L(\xi)}\frac{\hat{U}(\xi,\eta)d\eta}{\sqrt{2C_0(\xi,\eta)}}. \tag{41}$$

In light of (29), the bracketed term can be written as

$$A_\psi\int_{-\chi\xi}^{N(\xi)}\hat{U}(\xi,u)du\Big[\frac{-1}{\sqrt{2C_0(\xi,u)}} + \frac{1}{\pi}\sqrt{N(\xi)-u}\int_{N(\xi)}^{L(\xi)}\frac{d\eta}{\sqrt{2C_0(\xi,\eta)}\sqrt{\eta-N(\xi)}}\frac{1}{\eta-u}\Big]. \tag{42}$$

By use of the Cauchy residue theory, the second integration yields

$$\frac{\pi}{\sqrt{2C_0(\xi,u)}\sqrt{N(\xi)-u}} \tag{43}$$

whereupon (42) vanishes. Thus, only the second term in (41) arises, whose integration involves the shaded area in Fig. 3—a result that is consistent with (34). The step-stress pulse $U=\tau_i/\overline{\mu}$ is now examined, and standard tables, [18], give for (41)

$$w^s=\frac{cA_\psi\tau_i}{\pi\bar{\mu}}\sqrt{2}\left[\zeta_0\cos^{-1}\left(\frac{e_\chi(e_+-e_N)}{Qe_N}-1\right)-\frac{P_+}{2\sqrt{\chi\Gamma}}\cos^{-1}\left(1+\frac{e_\chi-e_N}{Q}\right)\right]-\frac{cA_\psi\tau_i}{\pi\bar{\mu}}\sqrt{\frac{2\chi}{\Gamma}}\sqrt{e_N-e_\chi}\sqrt{e_+-e_N} \quad (44a)$$

$$e_\chi=\frac{P_+}{2\chi}-Q,\quad e_+=\frac{P_+}{2\chi}+Q,\quad e_N=\xi_0+C\zeta_0-\xi_N \quad (44b)$$

when $(y_0>0, e_N>e_\chi)$. If, in the limit as $\zeta_0\to 0$ the point (ξ_0,η_0) remains on the positive side of the crack edge trajectory, then $e_N\to e_\chi$ as $C_0(\xi,\eta)=0$ collapses onto the asymptotes $(\xi=\xi_0,\eta=\eta_0)$. If the point lies on the other side as $\zeta_0\to 0$, however, then $e_N>e_\chi$ even as collapse occurs—unless $\xi_0\to K(\eta_0)$ as well. This behavior is consistent with that in Fig. 2.

Traction on Planes Radiating From Crack Edge

Envision in Fig. 1(*b*) the polar coordinates (r,θ) affixed to the moving crack so that $r>0$ defines radial planes from the edge, and $0<\theta<180$ deg corresponds to the region $y>0$. In light of (10*a*) the traction on a given radial plane is

$$\frac{1}{\bar{\mu}}\sigma_{\theta z}=(C\cos\theta-A\sin\theta)\frac{\partial w}{\partial x}+(B\cos\theta-C\sin\theta)\frac{\partial w}{\partial y}. \quad (45)$$

Because it is likely to be singular at the crack edge, only the scattered wave contribution to (45) need be considered. For $(x_0,y_0>0,s_0)$ differentiation of (44*a*) can be performed in terms of $(\xi_0,\eta_0,\zeta_0>0)$ by using (37), so that

$$\frac{2\pi}{A_\psi\tau_i}\sigma^s_{\theta z}=-\sqrt{\frac{\chi}{\Gamma}}\sqrt{e_N-e_\chi}\sqrt{e_+-e_n}\frac{1}{e_N}\partial_0 e_N-\frac{1}{4\chi^2}\sqrt{\frac{\chi}{\Gamma}}\frac{1}{\zeta_0}\cos^{-1}\left[\frac{e_\chi(e_+-e_N)}{Qe_N}-1\right]\partial_0(P_+^2-2\chi\Gamma\zeta_0^2)+\frac{1}{2\chi\sqrt{\chi}}\cos^{-1}\left(1+\frac{e_\chi-e_N}{Q}\right)\partial_0 P_+ \quad (46)$$

for $e_N>e_\chi$, where the gradient operator

$$\partial_0\equiv(C\cos\theta-A\sin\theta)\left(\frac{\partial}{\partial\eta_0}-\frac{\partial}{\partial\xi_0}\right)+\left(\cos\theta-\frac{C}{B}\sin\theta\right)\frac{\partial}{\partial\zeta_0}. \quad (47)$$

From (39) and (44*b*) follow the results

$$\sqrt{2}e_N=k(X_N-x_0)+\sqrt{2}C\zeta_0+\sqrt{[k(X_N-x_0)+\sqrt{2}C\zeta_0]^2+2\Gamma\zeta_0^2} \quad (48a)$$

$$\frac{\partial e_N}{\partial\eta_0}-\frac{\partial e_N}{\partial\xi_0}=\frac{-\sqrt{2}e_N}{(1-kX_N')[k(x_0-X_N)-\sqrt{2}C\zeta_0]+\sqrt{2}e_N} \quad (48b)$$

$$\frac{\partial e_N}{\partial\zeta_0}=\sqrt{2}\frac{ce_N+\Gamma(1-kX_N')\zeta_0}{(1-kX_N')[k(x_0-X_N)-\sqrt{2}C\zeta_0]+\sqrt{2}e_N}. \quad (48c)$$

The other operations with (47) are readily performed, and (46) becomes

$$\frac{2\pi}{A_\psi\tau_i}\sigma^s_{\theta z}=\frac{-\sqrt{2\chi\Gamma}\sqrt{e_N-e_\chi}\sqrt{e_+-e_N}}{k(x_0-X_N)+\frac{\sqrt{2}e_N}{1-kX_N'}-\sqrt{2}C\zeta_0}\left[\frac{\zeta_0}{e_N}\left(\cos\theta-\frac{C}{B}\sin\theta\right)+\frac{\sin\theta}{B(1-kX_N')}\right]+\frac{\sqrt{\chi}}{2\chi^2}\cos^{-1}\left[\frac{e_\chi(e_+-e_N)}{Qe_N}-1\right]\times\left[(1-\chi)\frac{P_+}{\zeta_0}\sin\theta+2\chi(B\cos\theta-C\sin\theta)\right]+\frac{\sqrt{\Gamma}}{2\chi}(1-\chi)\sin\theta\cos^{-1}\left(1+\frac{e_\chi-e_N}{Q}\right) \quad (49)$$

for $e_N>e_\chi$. Now consider the three points (a,b,c) in Fig. 3: Point (a) is the intersection of the curves $C_0=0$ and $\eta=N(\xi)$; its coordinates in the (kx,s)-plane are, therefore, (kX_N,s_N). Point (b) is the intersection of the curve $C_0=0$ and the crack edge location line $kx=kX_0=kX(s_0-s_c)$, while point (c) is the intersection of the curve $C_0=0$ and the line $kx=kx_0$. Their coordinates are then (kX_0,s_b) and $(kx_0-\sqrt{2}C\zeta_0,s_0-\sqrt{2}\zeta_0)$, respectively. In Fig. 3 ρ_0 is the distance between the crack edge location (kX_0,s_0) and point (c). The polar coordinates for a given (x_0,y_0,s_0) are

$$x_0-X_0=r\cos\theta,\quad y_0=r\sin\theta \quad (50)$$

and it follows that

$$\zeta_0=\frac{k}{B\sqrt{2}}r\sin\theta, \quad (51a)$$

$$\rho_0=kr\sqrt{\left(\cos\theta-\frac{C}{B}\sin\theta\right)^2+\frac{\Gamma}{B^2}\sin^2\theta}. \quad (51b)$$

As $r\to 0$, therefore, the points (a,b,c) and (kX_0,s_0) collapse onto each other. Then, one can write in view of Fig. 3 that

$$kX_N=kX_0-k\int_{s_N}^{s_0}X'ds\approx kX_0-kX_0'(s_0-s_N) \quad (52a)$$

$$\frac{s_b-s_N}{k(X_0-X_N)}\approx\frac{\partial s(kX_0)}{\partial(kx)}=\frac{\partial s_b}{\partial(kx)}. \quad (52b)$$

The function $s=s(kx)$ follows from $C_0=0$ as, c.f., (51*b*),

$$s=s_0-kr\lambda,\quad \lambda=\sqrt{\left(\cos\theta-\frac{C}{B}\sin\theta\right)^2+\frac{\Gamma}{B^2}\sin^2\theta}. \quad (53)$$

Its differentiation allows (52) to be solved for (s_h,s_N), and (52*b*) then yields

$$X_N-X_0\approx-k\Omega X_0'r, \quad (54a)$$

$$\Omega=\frac{\lambda^2}{\lambda-kX_0'\left(\cos\theta-\frac{C}{B}\sin\theta\right)}. \quad (54b)$$

Use of (50) and (54) in (49) then gives for $r\to 0$ the asymptotic result

$$\sigma^s_{\theta z}\approx\frac{\tau_i A_\psi}{2\pi}\sqrt{\chi(cs_0-X_0)+cs_0+X_0}\frac{K(\theta)}{\sqrt{r}} \quad (55)$$

where $K(\theta)$ is the dimensionless dynamic stress intensity factor coefficient

$$K(\theta)=\sqrt{p+q}\left[1-\frac{\Omega kX_0'(1-kX_0')}{p-qkX_0'}\right] \quad (56a)$$

$$p=\sqrt{q^2+\frac{\Gamma}{B^2}\sin^2\theta},\quad q=\cos\theta-\frac{C}{B}\sin\theta+\Omega kX_0'. \tag{56b}$$

Examination of (21) for $y_0<0$ gives the same results. For $\theta=0$ it can be shown that

$$K(0)=\sqrt{2(1-kX_0')} \tag{57a}$$

$$\frac{dK(0)}{d\theta}=-\frac{C}{B\sqrt{2}}\sqrt{1-kX_0'} \tag{57b}$$

$$\frac{d^2K(0)}{d\theta^2}=\frac{1}{2B^2\sqrt{2}}\sqrt{1-kX_0'}\Bigg[C^2(4kX_0'-1)-2+\frac{2\Gamma kX_0'}{1-kX_0'}+\Gamma(1-kX_0')^2\Bigg]. \tag{57c}$$

The results prior to crack extension ($0<s<s_c$) follow by setting $X_0'=0$. Absenting a branching study, insight into whether or not crack extension proceeds in the original plane is possible by finding when (57*a*) is a local maximum with respect to θ, i.e., (57*b*) vanishes and (57*c*) is negative. Clearly, the former occurs for $C=0$, whereupon (57*c*) gives the stability condition

$$\Gamma(1-kX_0')^3+2\Gamma kX_0'-2(1-kX_0')<0. \tag{58}$$

In view of (12) and (17), $C=0$ implies that crack growth in the original plane occurs when the principal material axes form one of the four angles ($\phi_\pm,\phi_+-180$ deg, ϕ_-+180 deg) with the crack plane, where for $\gamma\geqslant 0$

$$\phi_\pm=\tan^{-1}\frac{1}{\gamma}\left[\frac{1}{2}(\beta-\alpha)\pm\sqrt{1-\Gamma}\right]. \tag{59}$$

Corresponding to these orientations are the extremal shear wave speeds $c_\pm\bar{v}$, where

$$c_\pm=\sqrt{1\pm\sqrt{1-\Gamma}},\quad c_+^2+c_-^2=2. \tag{60}$$

In view of (59) and (60), the path stability requirement (58) is satisfied for $\gamma\geqslant 0$ when the crack speed $X_0'\bar{v}$ at $s_0>s_c$ is limited by

$$\phi=\phi_-,\phi_-+180\ \text{deg};\quad c=c_-:0<X_0'<X_-'\ \ (0<\Gamma<1) \tag{61a}$$

$$\phi=\phi_+,\phi_+-180\ \text{deg};$$

$$c=c_+:0<X_0'<X_+'<\left(\frac{8}{9}<\Gamma<1\right),\quad X_0'=0\ \ \left(0<\Gamma<\frac{8}{9}\right) \tag{61b}$$

Here $X_\pm'$ are the relevant cubic roots, [19], of (58):

$$X_-'=c_--\frac{4}{\sqrt{3}}\cos\frac{1}{3}\left(\pi+\tan^{-1}\sqrt{\frac{64}{27c_-^3}-1}\right)\ \ (0<\Gamma<1) \tag{62a}$$

$$X_+'=c_+-\frac{4}{\sqrt{3}}\cos\frac{1}{3}\left(\pi+\tan^{-1}\sqrt{\frac{64}{27c_+^3}-1}\right)\ \ \left(\frac{8}{9}<\Gamma<1\right). \tag{62b}$$

In the isotropic limit there is no restriction on ϕ, and (63) give ($X_\pm'=0.4608$, $c_\pm=1$).

These results indicate that, in general, crack extension in the original plane might not occur. It can occur when the crack plane shear wave speed is a minimum ($c_-\bar{v}$), but only for crack speeds below a subsonic value $X_-'\bar{v}$. It might also occur when the crack plane shear wave speed is a maximum, but the limiting subsonic speed $X_+'\bar{v}$ vanishes unless $8/9<\Gamma<1$. That is, increasing the nonorthotropy $|\gamma|$ beyond a certain value precludes path stability for a maximum crack plane shear wave speed.

Table 1 Parameters for maximum/minimum shear wave speeds and path stability limit speeds

Γ	c_-	X_-'	X_-'/c_-	c_+	X_+'	X_+'/c_+
0	0	0	1.0	1.4142	0	0
0.1	0.2265	0.1726	0.762	1.396	0	0
0.2	0.325	0.2322	0.7145	1.3764	0	0
0.3	0.4041	0.2751	0.6808	1.3552	0	0
0.4	0.4748	0.3101	0.6531	1.3321	0	0
0.5	0.5412	0.3401	0.6284	1.3066	0	0
0.6	0.6062	0.3668	0.6051	1.2777	0	0
0.7	0.6725	0.3912	0.5817	1.2441	0	0
0.8	0.7435	0.414	0.5568	1.203	0	0
0.9	0.8269	0.436	0.5273	1.1473	0.447	0.3896
1.0	1.0	0.4608	0.4608	1.0	0.4608	0.4608

In Table 1 values of $c_\pm$ for all Γ and values of ($X_\pm'$, $X_\pm'/c_\pm$) for (allowable) Γ are given. The entries for $c_\pm$ show that the maximum shear wave speed exceeds the isotropic value ($c=1$), and increases as the degree of nonorthotropy is increased, ($c_+\to\sqrt{2},\Gamma\to 0$). Those for c_- show that the minimum shear wave speeds lie below the isotropic value, and vanish in the limit as $\Gamma\to 0$. For the minimum-speed case, not only does a finite path stability speed always exist; decreasing Γ increases the ratio X_-'/c_-. That is, path stability is possible for a larger portion of the subsonic speed range as nonorthotropy is increased. It should be noted, finally, that although a steady-state analysis is approximate, the conclusions drawn in [7] are essentially the same.

An Isotropic/Nonorthotropic Comparison

For the step-stress pulse case, (36) gives the energy release rate

$$\dot{\mathfrak{J}}=\frac{8\tau_i^2\bar{v}}{\pi\bar{\mu}\sqrt{B}}A_\psi^2\frac{c_\psi s+X\cos\psi}{c_\psi+c\cos\psi}X'\sqrt{\frac{c-X'}{c+X'}}\ (s>s_c). \tag{63}$$

During fracture, the surface energy (per unit of crack edge length)

$$E_s=2\int_{s_c}^{s}f(\phi)X'ds\ \ (s>s_c) \tag{64}$$

is produced, where $f(\phi)$ is the specific fracture energy. A classical, [9], theory of fracture maintains that fracture proceeds so long as $\dot{\mathfrak{J}}=\dot{E}_s$. If the specific fracture energy is a pure material property, then this condition gives in view of (63) and (64) the differential equation

$$\sqrt{\frac{c+X'}{c-X'}}-\frac{4\tau_i^2A_\psi^2}{\pi\bar{\mu}f(\phi)}\frac{c_\psi s+X\cos\psi}{c_\psi+c\cos\psi}=0\ \ (s>s_c) \tag{65}$$

for the crack edge trajectory, c.f., [9–11]. Equation (65) cannot support instantaneous fracture ($s_c=0$). For smooth crack growth ($X'=0$, $s=s_c$) it gives

$$s_c=\frac{\pi\bar{\mu}}{4\tau_i^2}\frac{f(\phi)\sqrt{B}}{A_\psi^2}\left(1+\frac{c}{c_\psi}\cos\psi\right). \tag{66}$$

In the isotropic limit (66) reduces to the result derived in [9]. As an illustration, we consider (66) under the restrictions for crack path stability found above, and assume that fracture for given (τ_i,ψ) initiates at the same instant in a nonorthotropic and an isotropic material. In view of (10*b*) and (66), the dimensionless ratio

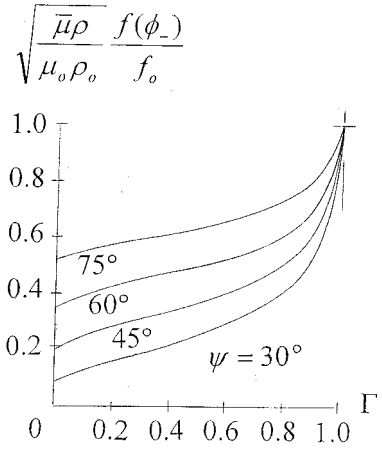

Fig. 4 Ratio of specific fracture energies for various incident wave directions

$$\sqrt{\frac{\bar{\mu}\rho}{\mu_o\rho_o}}\frac{f(\phi_\pm)}{f_o} = \sqrt{1 \pm \sqrt{1-\Gamma}\cos 2\psi} \times \frac{\sqrt{1 \pm \sqrt{1-\Gamma}\cos 2\psi} + \sqrt{1 \pm \sqrt{1-\Gamma}}\cos\psi}{(1+\cos\psi)(1 \mp \sqrt{1-\Gamma})^{3/2}} \tag{67}$$

emerges, where (μ_o, ρ_o, f_o) are the corresponding isotropic values of shear modulus, mass density, and specific fracture energy. It is noted that nonorthotropy enters the ratio only in the form of the dimensionless invariant Γ.

A plot of (67) in Fig. 4 for the less-restrictive minimum shear wave speed case shows that the ratio is always less than unity, that it decreases rapidly as nonorthotropy is increased ($\Gamma \to 0$), and that its deviation from unity for a given Γ decreases as $\psi \to 90$ deg. This behavior suggests that, when nonorthotropic and isotropic materials match in the sense that $\bar{\mu}\rho = \mu_o\rho_o$, fracture initiation at a given instant requires a greater specific fracture energy in the isotropic material. Conversely, if the specific fracture energies are equal, then fracture occurs earlier in the nonorthotropic material. Matching automatically occurs, of course, when the densities are identical and $c_{44} + c_{55} = 2\mu_o$.

Figure 4 and Eqs. (65) and (67) are based on the assumption that specific fracture energy is purely a material property, i.e., independent of location, time, or dependent variables. As noted in fracture literature, [11,17], it might actually also vary with crack speed. In any event, specific fracture energy must at present be found by experiment, under clearly defined and parameterized conditions, [20].

Some Comments

This article examined the mode III fracture of an unbounded solid with a single plane of material symmetry, [8], due to the diffraction of a plane SH-wave by a semi-infinite crack. The crack plane formed an arbitrary angle with the principal material axes in the single plane, and the travel direction of the plane wave was largely arbitrary. Crack extension was not necessarily instantaneous, and acceleration was allowed.

A transient analysis, similar in approach to those used in isotropic studies, [7,9–11], yielded exact expressions for the traction and crack surface slip velocity very near the crack edge, and the energy release rate. A closed-form expression for the full-field scattered wave displacement in the case of an incident step-stress pulse was also derived, and used to examine the dynamic stress intensity factor on any plane radiating from the moving crack edge. The factor achieved a local maximum on the original crack plane when that plane coincided with the directions for extremal values of the shear wave speed in the material symmetry plane, and a related crack path stability speed was not exceeded. However, the maximum and minimum shear wave speed cases differed: The maximum shear wave speed exceeded the isotropic value, and increased as the degree of nonorthotropy increased. Moreover, the corresponding subsonic stability speed vanished when the degree exceeded a critical level. The minimum shear wave speed fell below the isotropic value, and a subsonic stability speed always existed. These results agree with those obtained in a steady-state dynamic analysis, [7].

The fracture energy release rate for these two cases was examined in light of a classical fracture criterion, [9]. For the less-restrictive minimum shear wave speed case, comparison of the fracture initiation time with the isotropic limit value indicated that, if the specific fracture energy in the two types of materials were the same, then the nonorthotropic material might fracture first under the same diffraction process. This particular result was based on the assumption that the specific fracture energies are pure material constants. As noted, these quantities might also depend on both independent and dependent variables, e.g., location, crack speed. In any case, their determination requires careful experimentation, [20].

Moreover, the relative tractability of mode III fracture studies also limits their applicability. Nevertheless, they are useful for general insight. It is hoped, therefore, that the present results, and their steady-state counterpart, [7], do demonstrate the sensitivity of the dynamic fracture process in a nonorthotropic solid to both its properties and its orientation. In particular, the relative crack path stability in the direction of minimum shear wave speed might provide insight into the design of structures that must withstand dynamic loading.

References

[1] Lekhnitskii, S. G., 1963, *Theory of Elasticity of an Anisotropic Elastic Body*, Holden-Day, San Francisco.
[2] Ting, T. C. T., 1996, *Anisotropic Elasticity*, Oxford Science, New York.
[3] Kraut, E. A., 1963, "Advances in the Theory of Anisotropic Wave Propagation," Rev. Geophys., **1**, pp. 401–488.
[4] Payton, R. G., 1983, *Elastic Wave Propagation in Transversely Isotropic Media*, Martinus Nijhoff, The Hague.
[5] Burridge, R., and Willis, J. R., 1969, "The Self-Similar Problem of the Expanding Elliptical Crack in an Anisotropic Solid," Proc. Cambridge Philos. Soc., **66**, pp. 443–468.
[6] Broberg, K. B., 1999, "Intersonic Crack Propagation in an Orthotropic Material," Int. J. Fract., **99**, pp. 1–11.
[7] Brock, L. M., 2002, "Dynamic Anti-Plane Fracture in Arbitrary Directions in the Single Plane of Material Symmetry of an Anisotropic Solid," submitted for publication.
[8] Eshelby, J. D., Read, W. T., and Shockley, W., 1953, "Anisotropic Elasticity With Applications to Dislocation Theory," Acta Metall., **1**, pp. 251–259.
[9] Achenbach, J. D., 1970, "Extension of a Crack by a Shear Wave," ZAMP, **21**, pp. 887–900.
[10] Brock, L. M., 1974, "Quasi-Sudden Brittle Fracture at Both Edges of a Finite Crack," Int. J. Eng. Sci., **12**, pp. 553–568.
[11] Freund, L. B., 1993, *Dynamic Fracture Mechanics*, Cambridge University Press, Cambridge, UK.
[12] Sokolnikoff, I. S., 1956, *Mathematical Theory of Elasticity*, McGraw-Hill, New York.
[13] Nye, J. F., 1957, *Physical Properties of Crystals, Their Representation by Tensors and Matrices*, Clarendon Press, Oxford, UK.
[14] Theocaris, P. S., and Sokolis, D. P., 2000, "Invariant Elastic Constants and Eigentensors of Orthorhombic, Hexagonal and Cubic Crystalline Materials," Acta Crystallogr., **56**, pp. 310–331.
[15] Achenbach, J. D., 1973, *Wave Propagation in Elastic Solids*, North-Holland, Amsterdam.
[16] Courant, R., and Hilbert, D., 1966, *Methods of Mathematical Physics*, Vol. I, John Wiley and Sons, New York.
[17] Ewalds, H. L., and Wanhill, R. J. H., 1985, *Fracture Mechanics*, Edward Arnold, London.
[18] Peirce, B. O., and Foster, R. M., 1956, *A Short Table of Integrals*, Blaisdell, Waltham, MA.
[19] Abramowitz, M., and Stegun, I. A., 1972, *Handbook of Mathematical Functions*, Dover, New York.
[20] Brace, W. F., and Walsh, J. B., 1962, "Some Direct Measurements of the Surface Energy of Quartz and Orthoclase," Am. Mineral., **47**, pp. 1111–1122.

Multiple Surface Cracking and Its Effect on Interface Cracks in Functionally Graded Thermal Barrier Coatings Under Thermal Shock

S. Rangaraj

K. Kokini
Fellow ASME

School of Mechanical Engineering,
Purdue University,
West Lafayette, IN 47907-1288

The thermal fracture behavior in functionally graded yttria stabilized zirconia–NiCoCrAlY bond coat alloy thermal barrier coatings was studied using analytical models. The response of three coating architectures of similar thermal resistance to laser thermal shock tests was considered. Mean field micromechanics models were used to predict the effective thermoelastic and time-dependent (viscoplastic) properties of the individual layers of the graded thermal barrier coatings (TBCs). These effective properties were then utilized in fracture mechanics analyses to study the role of coating architecture on the initiation of surface cracks. The effect of the surface crack morphology and coating architecture on the propensity for propagation of horizontal delamination cracks was then assessed. The results of the analyses are correlated with previously reported experimental results. Potential implications of the findings on architectural design of these material systems for enhanced thermal fracture resistance are discussed.
[DOI: 10.1115/1.1533809]

1 Introduction

Thermal barrier coatings (TBCs) are increasingly being used in power generation and propulsion applications such as gas turbines, diesel and jet engines to protect metallic components from high-temperature environments, [1]. They offer avenues for enhancing the durability of metallic components, improving fuel economy, efficiency, and reducing cooling requirements, [2]. A plasma sprayed yttria partially stabilized zirconia (YSZ) layer with a intermetallic NiCoCrAlY bond coat on a substrate made of nickel-based superalloy is a common superalloy/TBC system.

TBCs deposited by electron beam physical vapor deposition (EBPVD) are relatively thin ($\sim$50–100 μm thick) and provide a temperature protection of about 100–300°C [3] due to their lower thermal resistance. These coatings have excellent strain tolerance due to their columnar structure, [4,5]. However, the bond coat itself, when subjected to a high temperature, causes the Al in the bond coat to oxidize with time and become Al_2O_3. This thermally grown oxide (TGO) has been identified as a critical reason for failure of these thinner coatings, [3,4,6–10].

On the other hand, for applications such as diesel engines and combustion chambers, thicker ($\sim$500–2000 μm) coatings provide a better thermal insulation. These coatings are usually plasma sprayed and have lower thermal conductivities due to their laminar structure and porosity, [5]. Being thicker and having lower conductivities, these TBCs have higher thermal resistances. In these coatings, the bond coat remains at lower temperatures and hence no significant TGO layer forms. Yet, even though the *TGO does not form*, these *thick TBCs still experience thermomechanical fracture*.

Contributed by the Applied Mechanics Division of THE AMERICAN SOCIETY OF MECHANICAL ENGINEERS for publication in the ASME JOURNAL OF APPLIED MECHANICS. Manuscript received by the ASME Applied Mechanics Division, February 26, 2002; final revision, July 26, 2002. Associate Editor: K. Ravi-Chandar. Discussion on the paper should be addressed to the Editor, Prof. Robert M. McMeeking, Department of Mechanical and Environmental Engineering University of California–Santa Barbara, Santa Barbara, CA 93106-5070, and will be accepted until four months after final publication of the paper itself in the ASME JOURNAL OF APPLIED MECHANICS.

Thick TBCs are known to crack, delaminate and spall under the application of high temperatures and temperature gradients. Previous studies have shown that the stress relaxation process, occurring in TBCs at high temperatures, was a significant cause of crack initiation and propagation, [11]. Briefly, when the surface of the coating is subjected to a heat flux, a temperature gradient exists in the coating. This gradient causes the surface of the coating to experience a compressive stress during heating due to the constraint to its thermal expansion offered by the significantly cooler bond coat layer and substrate. At high enough temperatures and stresses, the layers near the surface of the coating experience a time-dependent deformation, which consists of sintering, consolidation, and creep-like behavior, [12]. This causes the large compression to relax with time. Subsequent cooling of the coating causes the surface to experience a tensile stress leading to surface cracking. This mechanism was shown to occur at relatively low surface temperatures (800–900°C) over two hours, [12], at high surface temperatures (1300–1500°C) in four seconds [13].

Thus, due to the aforementioned stress-relaxation effects, the TBC experiences tensile stresses at the end of a heating-cooling cycle. Further, there is a gradient in tensile stresses through the TBC thickness that causes a bending moment to act on the coating, [14]. The action of this moment on the TBC creates significantly high tensile normal stresses along the thermal barrier coating–bond coat (TBC–BC) interface, [11,14]. Further, there is a mismatch in thermomechanical properties at the thermal barrier coating–bond coat interface that creates shear stresses along this interface. Thus, the combined effect of the normal and shear stresses along this interface lead to the development of thermal barrier coating–bond coat interface cracks, [15]. Repeated application of thermal loads can cause the growth of the surface cracks. As will be shown later, the growth of the surface cracks leads to an increased driving force for interface crack propagation. This is due to increased tensile stresses along the TBC–BC interface and a reduction in the area resisting the bending moment acting on the coating.

TBCs comprised of monolithic ceramics have been the subject of many investigations, [12,16,17]. However, owing to the large

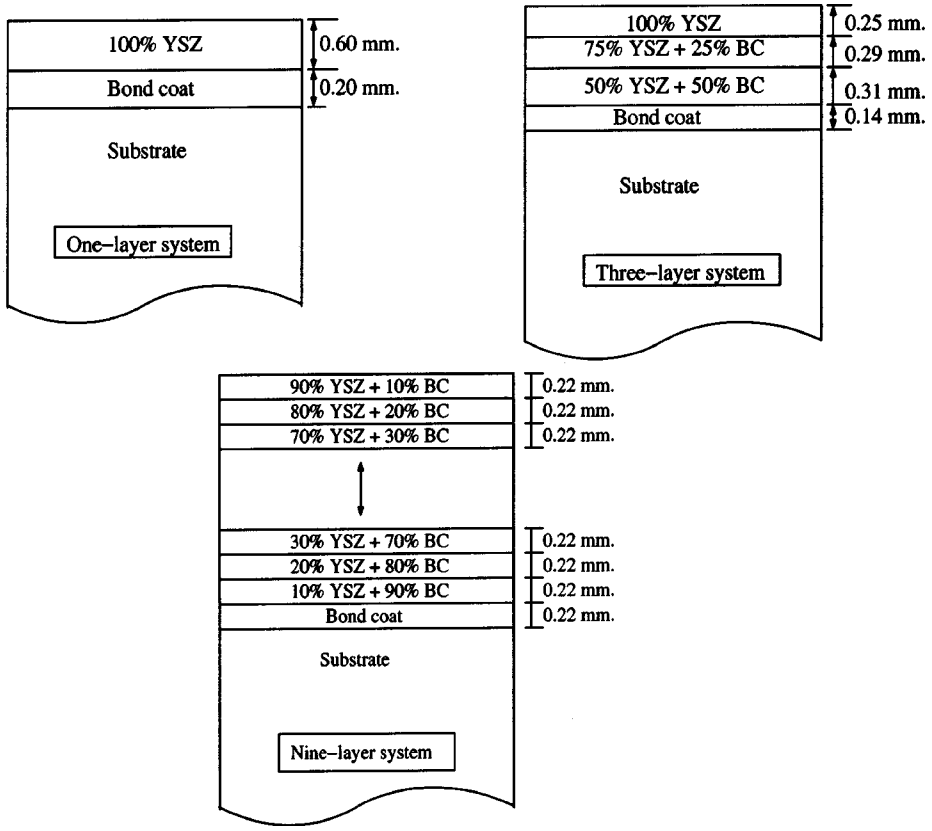

Fig. 1 Architectural layup of functionally graded yttria stabilized zirconia (YSZ)–bond coat alloy (BC) thermal barrier coating (TBC) systems. (All lengths in mm, each layer in nine-layer system is 0.22 mm thick with compositions varying linearly in 10% steps.)

mismatch between the thermomechanical properties of the ceramic and the bond coat layer, these coatings have been found to be susceptible to fracture and delamination at the yttria partially stabilized zirconia–bond coat (YSZ–BC) interface, [11,15]. Using functionally graded material systems as TBCs offers an excellent alternative to reduce the driving force for delamination. FGMs provide a gradual transition in properties through the coating thickness, [18,19]. For ease and economy of fabrication, such systems are comprised of a finite number of layers each having a certain ceramic bond coat alloy proportion. The composition changes through the TBC thickness. The topmost layer is ceramic-rich and the layer closest to the bond coat has the highest bond coat alloy proportion. The coating architectures for graded TBCs used in this study are illustrated in Fig. 1.

In the past ten years, functionally graded materials have opened new avenues for optimizing material and component structures to achieve high performance and material efficiency. At the same time, they post many challenging mechanics problems, including the prediction and measurement of their effective properties, thermal stress distribution and unusual fracture behavior. Many of these issues have been brought to light in biennial symposia on functionally graded materials, [20–21]. Thermomechanical fracture in graded materials has drawn significant attention in the recent past in a quest for developing durable functionally graded TBCs.

A fracture mechanics investigation into the development of multiple surface cracks in functionally graded ceramic-metal coatings have been studied previously in Bao and Wang [22]. The metallic substrate and the ceramic-metal FGM were all assumed to be *linearly elastic*. The FGM was modeled as a sequence of layers (of ceramic-metal mixtures) with different compositions. Parallel and equally spaced model I cracks on the surface of the FGM along the direction of compositional gradation were considered in this study. The response of a representative unit cell to a remotely applied uniform strain perpendicular to the gradation direction as well as to a *constant temperature* (greater than the stress-free temperature) was considered. For the loading considered, it was found that compared to a pure ceramic coating, gradation of the coating can significantly reduce the crack driving force under thermo-mechanical loading.

Bao and Cai [23] presented a micromechanics analysis of delamination cracking in functionally graded ceramic metal composite coating substrate system. Based on *linear fracture mechanics* analyses, the energy release rate of the delamination crack was determined as a function of coating gradation, crack location, and elastic properties of the ceramic and metal phase. It was found that functionally grading the coating reduces the force driving crack growth for both edge-delamination and buckle-driven delamination.

Erdogan and Wu [24] considered the response of an unconstrained *elastic FGM layer* to statically self-equilibrating thermal and mechanical residual stresses. The thermomechanical properties were assumed to be continuous functions through the thickness of this FGM layer. Thus, properties such as Young's modulus, thermal expansion coefficient, and thermal conductivity were expressed as exponential functions. Embedded and surface cracks perpendicular to the layer boundaries were considered. Results of the distribution of thermal stresses and stress intensity factors for surface and embedded cracks were presented.

Lee and Erdogan [25] considered the plain-strain *thermoelastic* problem of a crack at the interface between a homogeneous superalloy substrate and a FGM coating. The composition of the FGM coating was taken to vary continuously from 100% zirconia at the surface to 100% superalloy at the coating-substrate interface. Thermal loading involving exposure of the surface of the coating to a high-temperature environment, forced cooling of the

substrate and natural convection at the ends of the specimen were considered. The crack surfaces were assumed to be partially insulated and a heat conductivity index was used to describe this insulation condition. The thermal stress problem was solved for various composition profiles in the coating, including 100% ceramic, and for various values of the heat conductivity index. The normalized strain energy release rates at the interface crack was shown to decrease with increasing metal content in the coating.

The mechanism of multiple crack formation at the surface of graded mullite thermal barrier coatings subjected to transient heating and cooling loads was studied in Kokini and Takeuchi [26]. Here, an experimental setup was used to apply concentrated transient thermal loads on beam-shaped mullite-CoCrAlY (bond coat alloy) functionally graded TBCs plasma sprayed on steel substrates. The formation of multiple surface cracks on these specimens was observed. A corresponding analytical model was developed to study the fracture process. Since mullite is significantly more resistant to high-temperature creep and time-dependent deformation, [27], compared to YSZ that is more widely used in TBCs, its response was assumed to be *elastic* due to the *relatively lower temperatures* (800°C) considered in this study. It was shown that the location of the surface cracks may be estimated with reasonable accuracy by calculating the thermal stresses generated by the temperature gradients in the coating. It was also shown that the formation of multiple surface cracks reduces the propensity for growth of the horizontal delamination cracks thereby delaying final failure of the coating.

The above studies suggest that the present understanding of thermomechanical fracture in graded ceramic-metal systems is *limited to thermoelastic response under somewhat simplified loading and boundary conditions*. However, when such graded ceramic-metal systems (Fig. 1) are used as TBCs, under the typical service environments, [1,2], their response is not likely to remain elastic. Under the influence of high temperatures and gradients, the layers of a graded TBC (comprised of ceramic-bond coat alloy composites) are expected to experience significant *time-dependent* (viscoplastic) *deformations*. It becomes important then to model the effective time-dependent (viscoplastic) response and high temperature thermomechanical properties of graded TBC systems. These models can then be used to analyze the response of graded TBCs to loading conditions that more closely emulate their service environments. Such studies are vital for designing TBCs with enhanced durability.

The present study is motivated by experimental observations from laser thermal shock tests on functionally graded yttria partially stabilized zirconia–bond coat (YSZ–BC) (NiCoCrAlY) TBCs presented in Kokini et al. [28]. In what follows, these experimental results are briefly reviewed. Analytical models are then developed to help understand the observed thermal fracture behavior. Micromechanics models for the time-dependent behavior and effective thermoelastic properties of YSZ–BC alloy composites that constitute the layers of a graded TBC are discussed. These models are then utilized in fracture mechanics analyses to assess the response of the various TBC architectures used in the experiments to thermal loading and boundary conditions that simulate the laser thermal shock tests. The driving force for initiation of surface cracks and propagation of TBC-bond coat interface cracks in graded TBCs is then analyzed. Finally, the analytical models are correlated with the experimental findings.

2 Background and Motivation

For thick thermal barrier coating (TBCs) used in diesel engines applications, thermal fracture correlates with highly localized heating caused by the combustion of fuel plumes from the injection nozzle. This produces local steep temperature gradients through the coating thickness, [5,13]. Laser thermal shock experiments provide a means to recreate in a precisely controlled manner such high heat flux thermal loading conditions resulting in high surface temperatures and large temperature gradients through the TBC thickness. The thermal loads used in this study represent an upper bound of the loading that can be applied on such coatings. They may also represent situations such as overloads and transients during startup.

The results of thermal shock experiments performed using a high power laser on functionally graded YSZ–BC alloy TBCs were recently reported, [28]. The three TBC architectures (one, three, and nine-layer) that were considered in this study are illustrated in Fig. 1. The coatings were designed to have similar thermal resistances, [28], and hence offered comparable thermal protection to their substrates. The thermal shock experiments were performed by applying a concentrated CO_2 laser heat flux at the center of the top surface of the coating for four seconds, followed by ambient cooling. Surface cracks on the TBC as well as horizontal cracks near the TBC-BC interface were observed after the tests. These have been schematically illustrated in Fig. 2. The key observations from the thermal shock tests, [28], are reviewed:

1. Under similar thermal loads, most of the one-layer specimen showed single surface cracks, while most of the three and nine-layer specimen show multiple surface cracks. The average number of surface cracks per specimen increased with coating gradation as shown in Table 1.
2. For a given maximum surface temperature during thermal shock, the final length of horizontal cracks after the test, were observed to be shorter with increased coating gradation. Thus, the one and nine-layer specimens had the longest and shortest horizontal cracks, respectively, for similar surface temperatures. The measured horizontal crack lengths reported in Kokini et al. [28] are shown in Fig. 3.

Thus, there is a *greater tendency to form multiple surface cracks with increased level of coating gradation. A greater resistance to horizontal cracking* is also observed with *increasing coating gradation*. The analytical models presented in this paper help understand:

1 the effective thermo-elastic and time-dependent behavior of the individual layers.
2 response of the various TBC architectures to the applied thermal shock loading.
3 increased propensity for surface crack formation with increased coating gradation.
4 effects of coating architecture and surface crack configuration on the driving force for the horizontal crack growth.

3 Micromechanics Models for Effective Properties

3.1 Linear Elastic Properties of Ceramic-Bond Coat Alloy Mixtures. The thermoelastic properties of the ceramic (YSZ) and bond coat alloy were measured by the manufacturer of these coatings (Caterpillar, Inc., Peoria, IL, U.S.A.) over a range of temperatures between 25°C and 1500°C. Their average values at three of these temperatures are shown in Table 2 below. Using the properties of YSZ and bond coat alloy, the properties of the YSZ–BC alloy composites that comprise the layers of the graded TBC systems were computed using mean field micromechanics methods such as the self-consistent, Mori-Tanaka, Voigt (upper-bound) and Reuss (lower-bound) models, [29,30].

A comparison between the thermal conductivity at 25°C of YSZ–BC alloy composites predicted by the self-consistent, Mori-Tanaka, Voigt (upper-bound), and Reuss (lower-bound) models are shown in Fig. 4 for various ceramic volume fractions. These are also compared with the measured thermal conductivities of these composites at 25°C provided by the manufacturer, [28]. Similarly, the model predictions and experimental data of elastic modulus at 25°C are shown in Fig. 5. A detailed discussion of the correlation between the model predictions and experimental data for the thermoelastic properties is presented in Rangaraj and Kokini [31].

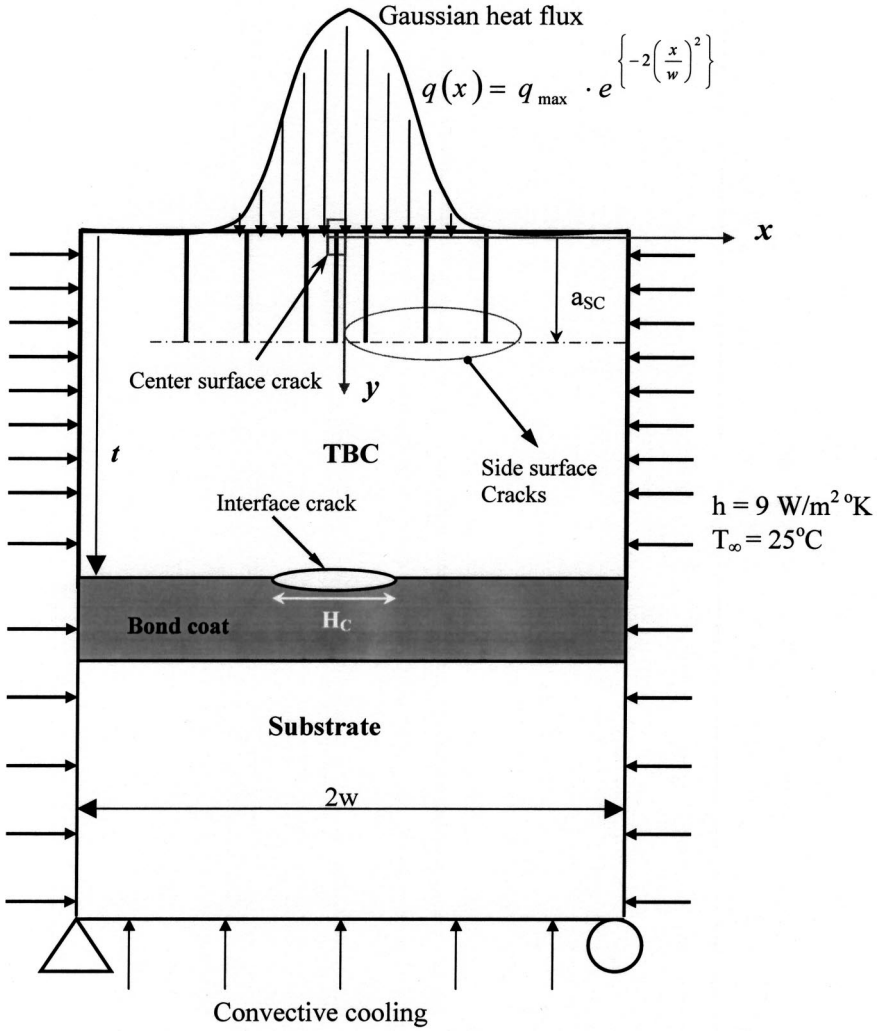

Fig. 2 Surface and interface cracks in the TBC systems and boundary conditions, thermal loads for analyses

Experimental measurements of thermoelastic properties for the YSZ–BC alloy composites at higher temperatures are currently unavailable. Hence, the high-temperature properties of YSZ and BC alloy (Table 2) may be utilized to predict those of the composite using the micromechanics models. This enables the computation of the effective thermoelastic properties of each layer of the graded TBCs (Fig. 1) over the range of temperatures (25–1300°C) considered here.

3.2 Time-Dependent Response of Ceramic-Bond Coat Alloy Composites. In graded TBCs, the temperature in layers below the relatively thin ceramic-rich top layer may also be significantly high. There are hence, likely to be significant time-dependent (viscoplastic) effects in these layers which are comprised of YSZ–BC alloy *composites*. An estimation of the effective viscoplastic properties of these composites is therefore essential in order to understand the response of graded TBCs to thermal shock loading.

The time-dependent behavior of YSZ and bond coat alloy can be described by the Norton-Hoff creep equation, [32,33]. This equation, describes the relation between the equivalent strain-rate and flow stress in YSZ (ceramic) and bond coat alloy (denoted by subscripts "*c*" and "*b*" respectively) as

$$\dot{\mathcal{E}}_C = A_c \exp\left(\frac{-\Delta H_c}{R \cdot T}\right) \sigma_c^{n_c} \tag{2}$$

$$\dot{\mathcal{E}}_b = A_b \exp\left(-\frac{\Delta H_b}{R \cdot T}\right) \sigma_b^{n_b}. \tag{3}$$

Table 1 Summary of surface thermal fracture data

Architecture	Samples Tested	Number of Samples Showing Particular Number of Surface Cracks (SC)				Average SCs per Specimen
		1 SC	2 SC	3 SC	4 SC	
One layer	19	14	5	0	0	1.25
Three layer	17	2	10	2	3	2.35
Nine layer	14	2	4	4	4	2.78

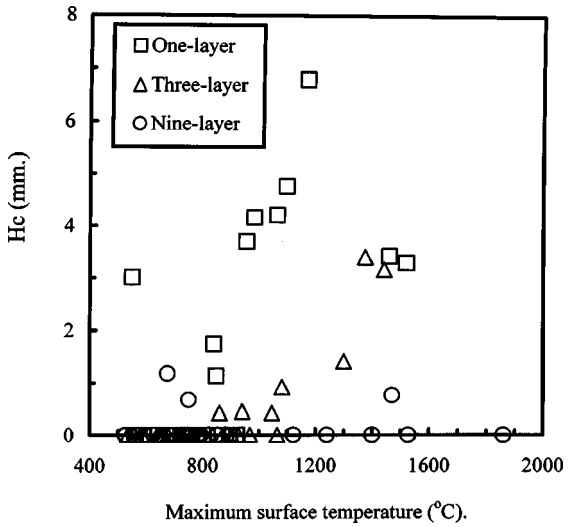

Fig. 3 Horizontal crack length (Hc) for the three TBC architectures. (Reproduced from Kokini et al. [28].)

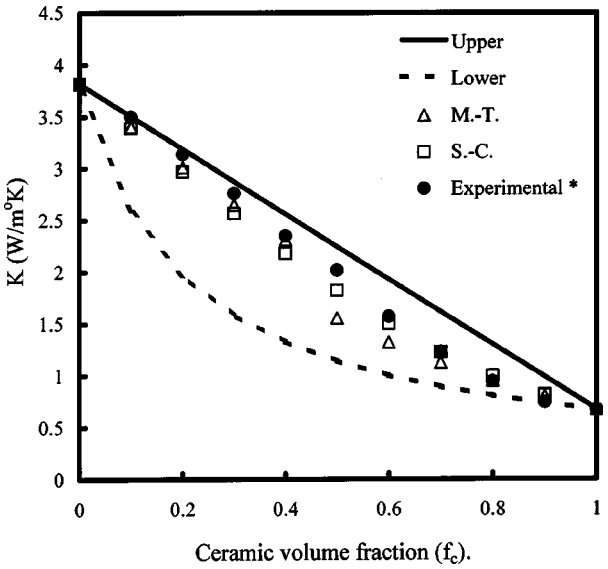

Fig. 4 Thermal conductivity of YSZ–BC alloy composites. (*Experimental data, as received from Caterpillar Inc., Peoria, IL.)

The constants A_c, ΔH_c, A_b, ΔH_b are the prefactors and creep activation energies for the ceramic and bond coat alloy, respectively, R and T denote the universal gas constant and absolute temperature, respectively. These properties for YSZ, [32], and BC alloy, [33], are shown in Table 3.

Rangaraj and Kokini [31] presented a model for effective time-dependent response of ceramic-bond coat alloy composites under typical TBC service temperatures. The model was based on a self-consistent micromechanics formulation, [34,35]. Briefly, the effective flow-stress in each phase was related to its strain rate through its nonlinear (strain-rate dependent) creep viscosity. Strain-rate averaging and self-consistent localization relations between the two phases were then used to compute the strain-rate-dependent creep viscosity of the composite as a function of the creep viscosity and volume fraction of the two phases. This model enabled the computation of stress versus strain-rate response, effective stress exponent (n), activation energy (ΔH), and prefactor (A) of the composite for various compositions. Sample results of stress exponent and activation energy of the YSZ–BC alloy composites for various YSZ volume fractions are shown in Fig. 6. The stress exponents and activation energies shown here have been normalized by the corresponding properties of the NiCoCrAlY BC alloy.

Since the effective time-dependent response and thermoelastic properties of the individual layers of a graded TBC are now available (Fig. 4–6), the previously discussed thermal shock experiments on the three TBC architectures (Fig. 1) can be simulated.

4 Simulation of the Laser Thermal Shock Test

4.1 Model, Boundary Conditions, and Materials. The finite element method was used to model the response of the functionally graded TBC systems (Fig. 1) to transient thermal loading that closely emulates the thermal shock tests, [28]. The thermal shock experiment consisting of subjecting the surface of the specimen to a laser beam for four seconds and subsequent cooling in air was simulated. The effect of the laser beam was modeled by applying a heat flux with a Gaussian spatial distribution about the center of the top surface of the TBC. Since the deformations did not affect the temperatures, the problem was modeled as a quasi-steady-state thermomechanical problem. First, the nodal temperatures were calculated by solving the transient heat transfer problem. All of these temperatures were entered into a transient structural analysis model to compute the resulting displacements and stresses. Since beam-shaped specimens had been used in the experiments, plane-stress finite element analyses were performed.

The structural and thermal boundary conditions, [36], placed on the model were chosen to simulate the experimental setup and are illustrated in Fig. 2. Due to symmetry of the loading and geometry, a half-symmetric model was considered. The top edge was subjected to a gaussian heat flux distribution and a boundary condition of ambient convection. The side and bottom edges were assigned boundary conditions of ambient convection as well. The applied heat flux intensity was varied with changing coating architectures to keep the same surface temperature (1300°C) in order to assess the response of coatings of similar thermal resistance to the same surface temperatures.

The different areas in the finite element model were assigned their respective thermomechanical properties. The TBC and bond coat were modeled as elastic-viscoplastic materials. Temperature-dependent (between 25–1300°C) thermomechanical properties were used for each layer of the TBC as well as for the bond coat using previously discussed experimental data (for YSZ and BC

Table 2 Temperature-dependent thermomechanical properties of yttria partially stabilized zirconia and bond coat alloy

Material	T°C	Thermal Conductivity K (W/mK)	Specific Heat, °C (J/mol.K)	Density ρ (Kg/m^3)	Elastic Modulus E (GPa)	Poisson's Ratio ν	Thermal Expn. Coeff. $\alpha\times10^5$ (/K)
BC	25	3.88	460	6290	64.5	0.30	1.03
alloy	725	7.93	617	6290	53.0	0.30	1.10
	1300	9.86	620	6290	43.0	0.30	1.14
YSZ	25	0.67	420	5600	13.6	0.25	0.75
	725	0.58	547	5600	10.4	0.25	0.90
	1300	0.56	569	5600	8.0	0.25	0.97

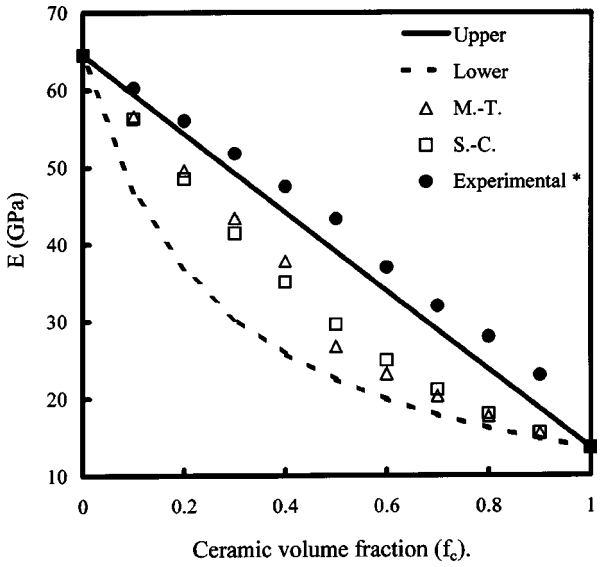

Fig. 5 Elastic stiffness of YSZ–BC alloy composites. (*Experimental data, as received from Caterpillar, Inc., Peoria IL.)

alloy) and micromechanics models (for YSZ–BC alloy composites). The layer of pure YSZ and the BC layer were assigned their respective viscoplastic (time-dependent) properties as shown in Table 3. The viscoplastic properties for layers of the TBC comprised of YSZ–BC alloy composites were computed from the previously discussed (Fig. 6) self-consistent model. The steel substrate was considered to be linear elastic in view of the fact that the temperatures here remain comparatively low. All the computations were performed with ABAQUS® developed by Hibbit, Karlsson & Sorensen, Inc., using eight-noded plane-stress elements.

Table 3 Properties for time-dependent behavior of ceramic and bond coat alloy

Material	Pre-factor A $(N/m^2)(sec^{-n})$	Stress Exponent n	Activation Energy ΔH (kJ/Kg)
Bond coat alloy	9.05×10^{-12}	2.7	150
Zirconia (YSZ)	5×10^{-7}	1.8	217

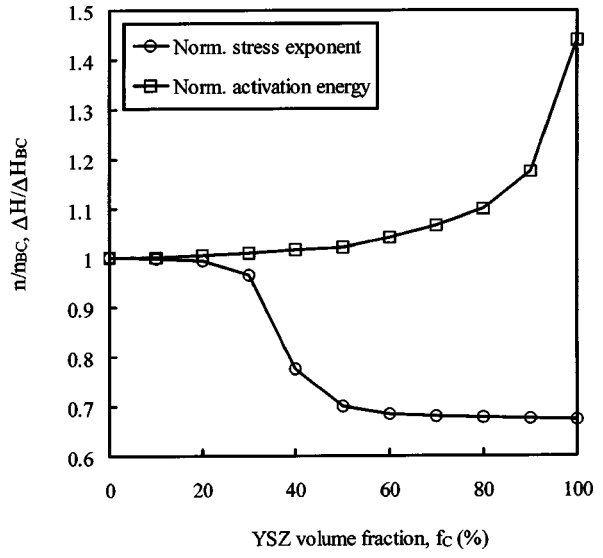

Fig. 6 Normalized stress exponent (n/n_{BC}) and activation energy ($\Delta H/\Delta H_{BC}$) for YSZ–BC alloy composites

4.2 Crack-Tip Finite Elements and Strain Energy Release Rates. In order the assess the driving force for surface and interface crack initiation, models with short surface cracks on the TBC and horizontal cracks at the TBC–bond coat interface were considered. The size and location of these cracks are discussed below in more detail. In order to compute the strain energy release rates and *J*-integrals accurately from these cracks, refined meshes were employed in the vicinity of the crack tips. A mesh size of around 0.5% of the crack length for the interface cracks and 0.75% of the crack length for the surface cracks, in general, yielded convergent results. Hence, the size of the elements near the crack tip was rather small in comparison to the TBC and more significantly the substrate thickness. To contain the size of the finite element model within reasonable limits, highly graded meshes were employed. A uniform element size (0.5% of crack length) was used in a small square area around the crack tip. The element size was then gradually increased with increasing distance from the crack tip. The models typically had 12,000 to 15,000 nodes and a total of 4000 to 5000 plane-stress elements.

To prevent the interpenetration of the crack surfaces due to the crack closure that results during heating, a contact boundary condition was used at the crack surfaces. This was facilitated by the use of six-noded interface elements between the edges of the eight-noded elements on either crack face. A smooth (coefficient of friction, $\mu=0$) contact between the crack faces was assumed in all cases. Following McDonald et al. [37], the gap conductance (k_G) across the crack faces is directly proportional to the conductivity (k) of the medium between the crack faces (air in the present study, $k_{air}=0.025$ W/m K) and inversely proportional to the crack-opening displacement (δ), i.e., $k_G=k_{air}/\delta$, [37]. In the present analyses, short cracks are being considered. The resulting crack-opening displacements (δ) are hence small. A relatively high gap conductance ($k_G\sim10^4$ W/m^2°K) was hence prescribed across the crack faces.

As shown later, the surface and interface cracks experience *no opening* and rather *small sliding displacements* during heating when time-dependent deformations and high-temperature stress relaxation effects occur in the TBC layers. The faces of the surface as well as the interface cracks were in contact only during heating. After the stress relaxation, during cooling, they experience significant opening displacements. However, this opening results due to the nonreversible viscoplastic deformations and stress-relaxation effects that occurred during heating. Thus, during cooling the crack faces were not in contact. Hence, only small sliding displacements occurred during heating when the crack faces were in contact.

As discussed later, the strain-energy release rates for the interface cracks were computed using the crack flank displacement method developed by Smelser [38] from the relative opening and sliding displacements between the two crack surfaces obtained from the finite element analyses. The calculated strain energy release rates agreed well with the *J*-integral computed from ABAQUS®. The driving force for growth of the surface cracks was assessed from the calculated *J*-integral values.

5 Temperature Distribution in the Thermal Barrier Coatings (TBCs)

As mentioned earlier, the heat flux applied to the TBC top surface (Fig. 2) was adjusted so as to yield a maximum surface temperature of 1300°C. The temperature history at the center of the top surface ($x=0$, $y=0$ in Fig. 2) for the three architectures is shown in Fig. 7. The coating is initially at uniform room temperature (298 K). The temperature at the center of the top surface increases to 1573 K at the end of the heating period ($t=4$ sec.) and subsequently cools back to nearly room temperature in the

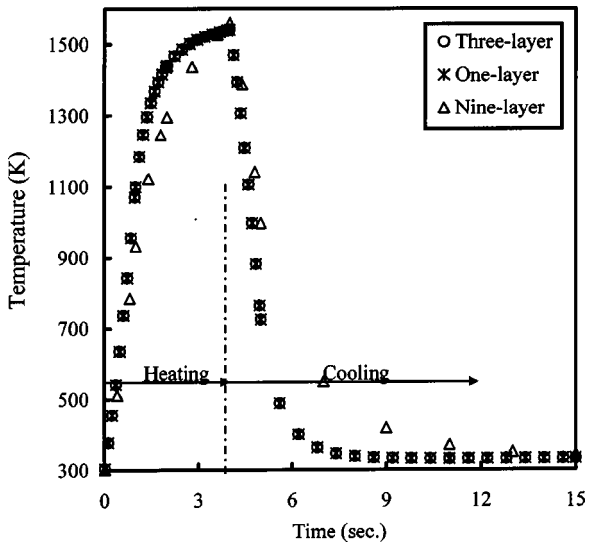

Fig. 7 Temperature history at the center of the top surface of the TBC

next 11 seconds after the heat flux is removed. The temperature histories on the surface of the one and three layer architectures were similar since they had similar thermal resistances of 8 and 7.8 K/W, respectively, [28]. Since the nine-layer system had a slightly higher thermal resistance (10 K/W), its surface heated and cooled at a slower rate.

The temperature distribution through the thickness of the coating along its center ($x=0$) at the end of the heating period ($t=4$ sec.) is shown in Fig. 8 for the three architectures studied. Here, the distance from the top surface of the coating (y) has been normalized with respect to the total TBC thickness (t) for each of the architectures. Since the coatings have similar thermal resistances, the bond coat temperatures are similar in all cases and range between 110–180°C. The small differences in the bond coat temperatures in the three architectures are consistent with their respective thermal resistances, i.e., the bond coat is coolest and hottest for the nine ($R=10$°K/W) and three-layer ($R=7.8$ K/W) systems, respectively. It is observed from Fig. 8 that as the content of bond coat alloy (which has a much higher thermal diffusivity than YSZ) in the coating is increased, the temperature at a given fraction of distance (y/t) from the TBC surface decreases. Thus the coating architecture has a significant influence on this temperature distribution.

6 Location of Surface Cracks

The region near the coating surface experiences high temperatures during heating (Fig. 7). A steep temperature gradient exists through the coating thickness (Fig. 8). The lower layers of the TBC, the bond coat layer and substrate are significantly cooler. This causes compressive stresses to develop near the coating surface due to its constrained thermal expansion. The combined effect of these compressive stresses and high temperatures cause thermally activated time-dependent deformations in the coating, [12,13]. The compressive stresses then relax with time during heating and the subsequent cooling gives rise to tensile stresses. These tensile stresses lead to formation of surface cracks (SC) in the coating.

The coatings used in the present study showed multiple surface cracks under transient thermal loading, [28]. A methodology developed in Kokini and Takeuchi [26] was used to analytically estimate the location of the surface cracks. At first, a transient thermal stress analysis of the TBC systems without any surface cracks is carried out. This analysis predicts the maximum tensile stress (σ_{xx}), to occur at the center of the top surface. The first surface crack would therefore form at this location and is hence is referred to as the center surface crack (Fig. 2). The transient thermal and structural analyses are again carried out with one short center surface crack (5% of TBC thickness) to determine the stress distribution along the TBC top surface. The second surface crack would then be located at the new peak of this stress profile. A similar procedure can be repeated with additional surface cracks in the model to estimate the locations of the subsequent surface cracks. The stress profiles along the coating top surface for the right half (symmetric model) of the nine-layer architecture with no surface cracks, one surface crack and two surface cracks are shown in Fig. 9. Here, the distance x is normalized with respect to half the coating width, w (Fig. 2). An important observation made from Fig. 9 is that the magnitude of the maximum stress decreases as an additional cracks forms on the surface. Multiple surface crack formation relieves the tensile stresses in the TBC. This is to be expected since the presence of additional surface cracks makes the TBC more compliant.

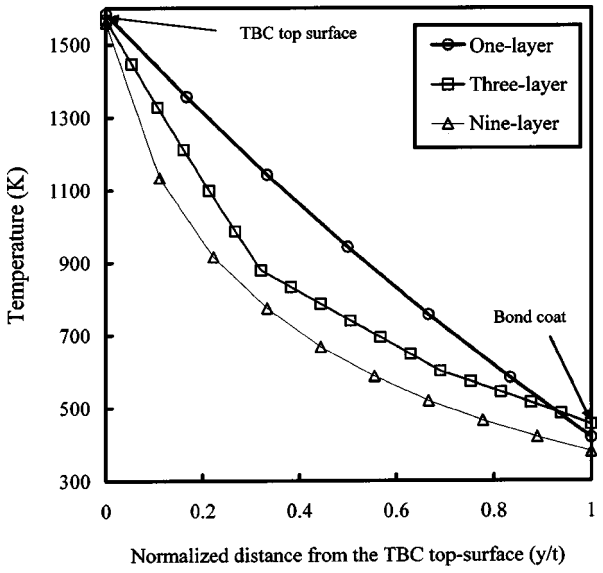

Fig. 8 Temperature distribution through the TBC thickness at the end of heating ($t=4$ sec)

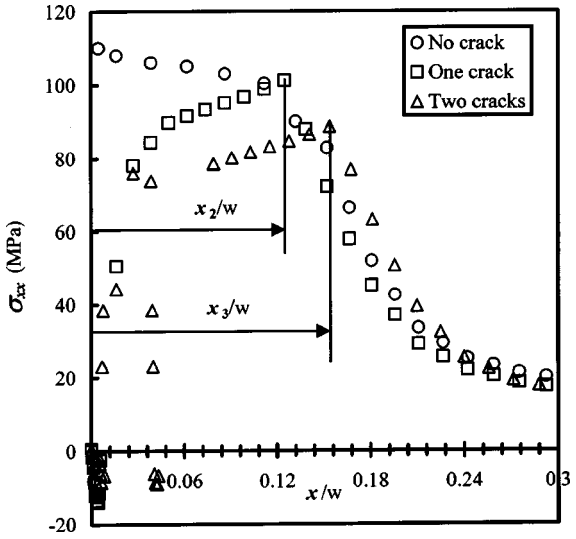

Fig. 9 Stress distribution along the top surface ($y=0$) of the nine-layer TBC

Table 4 Estimated location of surface cracks (SC)

Architecture	Location of *n*th SC as a fraction of half coating width (x_n/w)%			
	SC1	SC2	SC3	SC4
One layer	0	1.06	2.13	3.33
Three layer	0	4.25	12.2	16
Nine layer	0	12.5	15.4	18.2

The locations of up to four surface cracks in the symmetric model (that correspond to 7 on the TBC surface) were determined by the above procedure and the results for the three architectures are shown in Table 4. Here, the location of each surface crack (x_n) in the three architectures as a percentage of half the coating width (w in Fig. 2) is presented. The estimated locations of these surface cracks were verified with some of the micrographs presented in Kokini et al. [28] and a reasonable agreement was found. For instance, a nine-layer specimen subjected to a thermal shock test with a maximum surface temperature comparable to that in the present analysis (1300°C) exhibited a second surface crack (SC2) at a distance of 2000 μm from the center of the TBC, [28]. The corresponding analytically estimated distance in Table 4 is 1875 μm.

As the gradation of the coating increases, the surface cracks form further away from the center. This is a combined effect of temperature gradients, coating thickness and time-dependent deformations in the lower layers of the graded TBCs. To assess the effect of time-dependent behavior in the lower layers on the locations of the surface cracks, the calculations were performed without including the time-dependent behavior of the lower layers. In the nine-layer architecture, when time-dependent behavior in only the top layer is considered, the estimated locations of the second (SC2), third (SC3), and fourth (SC4) surface cracks reduce to 9, 11.6 and 14.3% of the coating width (w), respectively.

To estimate the role of total TBC thickness on the surface crack locations, the thickness of the one-layer TBC was varied between 0.6 mm. (its original thickness) and 2.2 mm. (thickness of the nine-layer TBC) and the location of the second surface crack (SC2) was calculated for each case. The estimated locations (as a percentage of coating width) of SC2 for one-layer TBC thickness of 0.6, 0.85 (thickness of three-layer TBC), 1.6 and 2.2 mm. were 1.06, 3.84, 11, and 11.8%, respectively. Comparing these estimates with those in Table 4 for the location of SC2 in the three and nine-layer TBCs, it is evident that the formation of the surface cracks further away from the center in a more graded TBC is mainly due to its increased thickness.

7 Surface Crack Initiation

As seen from the experimental observations, [28], there was an increased tendency for the formation of multiple surface cracks with increasing coating gradation. To understand this, the relative magnitudes of the forces driving the surface crack initiation in the three architectures must be compared. The response to the previously described thermal shock loading of models with pre-existing surface cracks was therefore considered. The location of the surface cracks for each of the architectures was as previously discussed (Table 4). To study the initiation of these cracks, short surface cracks (5% of the TBC thickness, crack ratio $a_{SC}/t = 0.05$) were considered. For a particular architecture, all the surface cracks in the model had the same length. The surface cracks were all contained in the top layer of the TBC.

The relative opening (dv) and sliding (du) displacements between the faces of the surface cracks in the one, three and nine-layer TBCs during the heating-cooling cycle are shown in Fig. 10. Models with four short ($a_{SC}/t = 0.05$) surface cracks have been considered in Fig. 10. The displacements are shown for the second surface crack (SC2), which is a side surface crack. The opening (normal) and sliding (tangential) displacements are represented by solid and dashed lines, respectively.

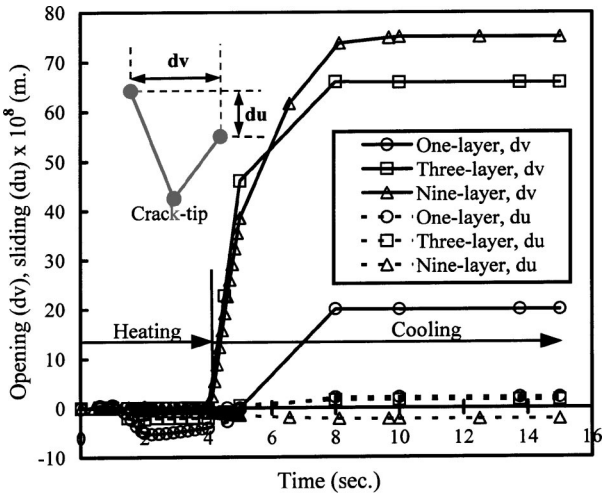

Fig. 10 Opening (dv) and sliding (du) displacements for the side surface crack (SC2) in coatings with four surface cracks, each 5% of the TBC thickness in length ($a_{SC}/t = 0.05$)

It is clear from Fig. 10 that the surface cracks experience *no opening* and rather *small sliding displacements* during heating ($t < 4$ sec). During heating, the TBC experiences compressive stresses and the time-dependent (viscoplastic) deformations and stress-relaxation effects occur. Thus, *when the viscoplastic deformations occur in the coating, the surface cracks experience very small sliding deformations*. During subsequent cooling, the coating experiences tensile stresses, [27]. These tensile stresses result due to the stress relaxation that occurred during heating. However, during cooling ($t > 4$ sec) *no additional viscoplastic strains* develop in the TBC. The surface cracks open during cooling when the TBC experiences tensile stresses. During cooling, the opening (normal) displacements between the surface crack faces increase and attain their maximum steady-state values by the end of the heating-cooling cycle. Furthermore, as seen from Fig. 10, the *crack opening that results during cooling is much larger in magnitude than the sliding that occurred during heating*. It can also be noted from Fig. 10 that with an increase in the gradation of the TBC, the crack opening increases and the nine-layer TBC has the highest crack opening.

The J-integral during the heating-cooling cycle for the same side surface crack (SC2) from Fig. 10 is shown in Fig. 11 for the three TBC architectures. For these surface cracks, it is clear from Fig. 11 that the J-integral follows the same trend as the relative displacements between the crack faces, i.e.; the J-integral remains negligibly small ($\sim 10^{-1}$ J/m^2) during heating when the surface cracks experience small sliding displacements. The J-integral increases during cooling when the TBC experiences tensile stresses and the surface cracks open. The J-integral attains a maximum steady-state value by the end of the heating-cooling cycle. Accordingly, this *maximum steady-state* magnitude of the J-integral, [39], was used to characterize the driving force for surface crack initiation. The J-integral was computed from ABAQUS® which uses the domain integral method to evaluate J-integral, [40].

For a crack growing in a nonlinear viscous material, the C^*-integral, [41–42], obtained by replacing the strains and displacements in the J-integral [39] by their corresponding rates is commonly used to assess the crack driving force. However, in the present case, the sliding displacements that occur during heating (when the viscoplastic deformations occur in the TBC) are rather small in comparison to the opening displacements that result during cooling (when the TBC experiences no additional time-

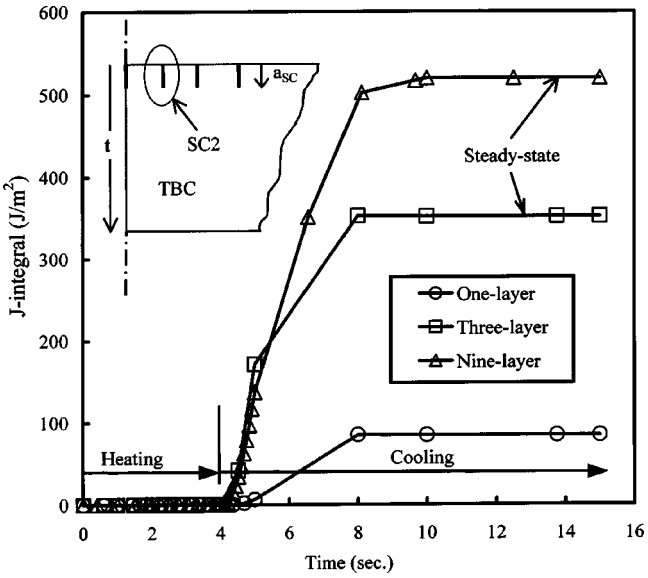

Fig. 11 *J*-integral for the side surface crack (SC2) during the heating-cooling cycle (model with four surface cracks, length of each surface crack was 5% of the TBC thickness, $a_{SC}/t = 0.05$)

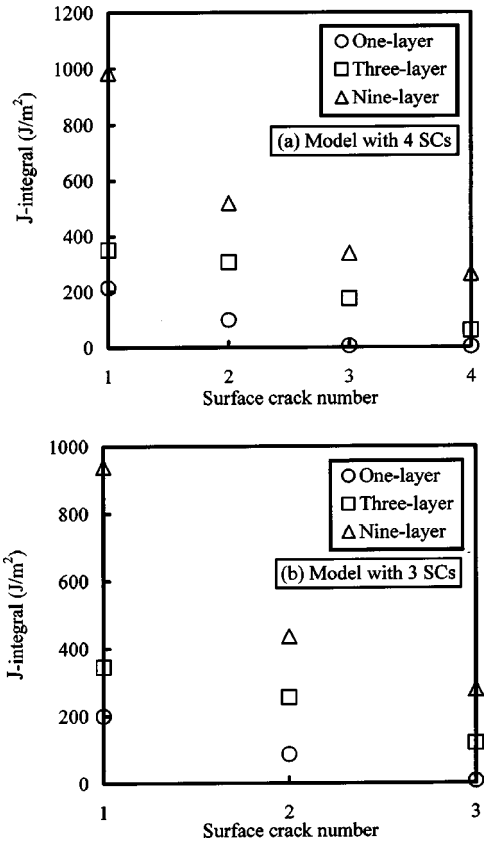

Fig. 12 Steady-state *J*-integrals for the surface cracks in models with multiple 5% ($a_{SC}/t = 0.05$) surface cracks (SCs)

dependent deformations). Hence, the *J*-integral, [39], was used to characterize the driving force for surface crack extension.

The *J*-integral values at the end of the thermal loading cycle (heating and cooling) after the system has cooled back to steady-state ($t = 15$ sec.) are shown in Fig. 12. The cases of four surface cracks and three surface cracks in the symmetric model were considered. In Fig. 12, the *J*-integral values for each of the surface cracks for the three coating architectures are shown. It can be noted that the *J*-integral values increase with coating gradation. At a given surface crack, the nine-layer coating has the highest *J*-integral value whereas the one-layer coating has the lowest. Thus, with increasing compositional gradation of the TBC, there is an increased driving force for surface crack initiation.

This is related to the temperature distribution through the coating thickness (Fig. 8) and its effect on the time-dependent deformation in the coating layers. The three coating architectures have similar thermal resistances, but they are of different compositional gradations. The distributions of thermomechanical and viscoplastic properties through the TBC thickness hence change with TBC architecture (Figs. 4–6). The bond coat alloy has a significantly higher stress exponent and lower activation energy (Table 3) compared to the ceramic and therefore experiences a higher amount of viscoplasticity. In a graded TBC, the layers below the ceramic-rich top layer contain significant volume fractions of bond coat alloy (Fig. 1). These layers are also subjected to elevated temperatures (Fig. 8). The resulting time-dependent deformations (stress relaxation) in these layers causes the surface cracks in the functionally graded TBCs to have higher *J*-integral values.

Further, the total TBC thickness and, the thickness of the top ceramic-rich layers are different (Fig. 1) in the three architectures. Previous studies on monolithic single layer YSZ coatings, [13], have shown that as the thickness of the coating was reduced, the density of surface cracks on the coating increased. It is believed that in the present study, as the gradation of the coating increases, and the top ceramic-rich layer becomes thinner, this top layer starts behaving in a manner similar to the previously studied thin monolithic zirconia TBCs, [13], and develops multiple surface cracks.

8 Effect of Top-Layer Thickness on Surface Cracking

To assess the role of the top ceramic-rich layer on surface crack initiation, the thickness of this top layer in the three and nine-layer architectures was varied in the models. The total thickness of the TBC and its thermal resistance were, however, kept constant. This was achieved by mutually adjusting the individual thickness of the lower layers in order to accommodate the changes (in resistance and thickness) brought about by varying the top-layer thickness. The boundary conditions and thermal loads were the same.

The steady-state *J*-integral values for each of the side surface cracks (Fig. 2) on the three-layer architecture, containing three surface cracks, as a function of its top-layer thickness are shown in Fig. 13. The top-layer thickness was varied between 0.125 mm and 0.375 mm. For each value of top-layer thickness, at least two surface crack lengths were considered. The lengths of the surface cracks varied between 5 and 18% of the total TBC thickness. Again, these surface cracks were all contained within the top layer. It is clear from Fig. 13 that the *J*-integral values are significantly higher for coatings with thinner top layers. This may be expected considering the fact that with a thinner top layer, the lower layers (comprised of ceramic-bond coat alloy composites) experience higher temperatures and this would lead to greater amount thermally activated time-dependent deformation in these layers. These time-dependent effects influence the deformations in the top layer as well and hence lead to the observed increase in the *J*-integrals for the surface cracks.

The effects of the top-layer thickness on the *J*-integral for each of the side surface cracks in the nine-layer architecture are shown in Fig. 14. Again, a model with three short surface cracks (5% of the TBC thickness) was considered and the *J*-integrals for the two side surface cracks are shown in Fig. 14. The results are similar to those in Fig. 13. Figures 12–14 suggest that an important factor responsible for the increased driving force for multiple surface

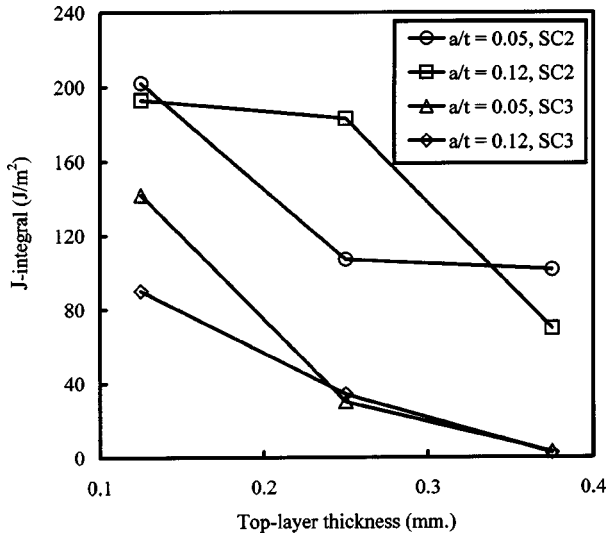

Fig. 13 Effect of top-layer thickness on *J*-integral for side-surface cracks in the three-layer TBC

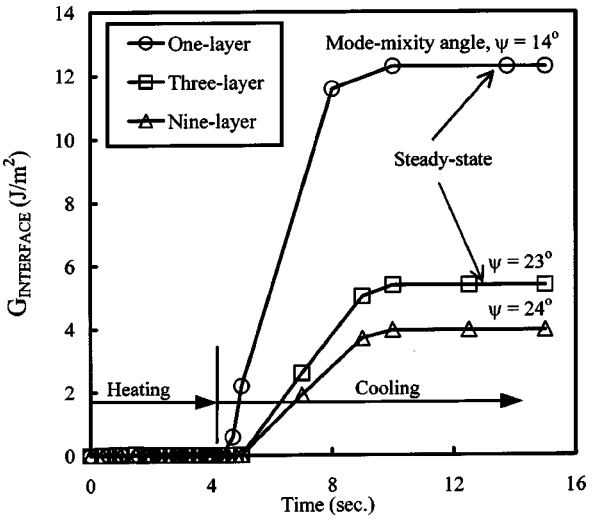

Fig. 15 Strain energy release rate for the TBC–bond coat interface crack during the heating-cooling cycle in coatings with one 50% ($a_{SC}/t=0.5$) center surface crack

cracking with increasing coating gradation at constant thermal resistance is the *reduced thickness of the ceramic-rich top layer*.

9 Effect of Surface Cracks on the Horizontal Cracks

As discussed earlier, the TBC experiences tensile stresses at the end of a heating-cooling cycle. The gradient in tensile stresses through the coating thickness causes a moment to act on the TBC. This moment creates tensile normal stresses along the TBC–BC interface leading to initiation of horizontal cracks near this interface, [14,15]. These cracks grow to cause final delamination and loss of structural integrity of the coating. As seen in Fig. 3, the coating architecture (gradation) and applied thermal loading can have a significant effect on the length of these horizontal cracks. Further, the presence of surface cracks in the coating may have an influence on the force driving the growth of these horizontal cracks.

To assess the influence of coating gradation as well as the number and size of the surface cracks on the force driving the growth of the horizontal cracks, models with horizontal cracks in addition to the previously described surface cracks were considered (Fig. 2). The horizontal cracks were assumed to be located at the interface between the TBC and bond coat layers. The surface crack locations for each of the TBC architectures were as shown in Table 4. To assess the force driving interface crack initiation in the three architectures, a short interface crack that was 12% of the thinnest (one-layer) coating was considered. The *J*-integral and strain energy release rate were used to characterize the force driving the growth of this interface crack. The layers near the TBC–BC interface do not experience elevated temperatures (Fig. 8). Hence, these layers do not experience any significant time-dependent effects and their response tends to remain elastic. The strain-energy release rates for the interface cracks were calculated following Smelser [38] from the relative opening and sliding displacements near the interface crack tip. The computed strain energy release rates agreed very closely with the *J*-integral estimated from ABAQUS®.

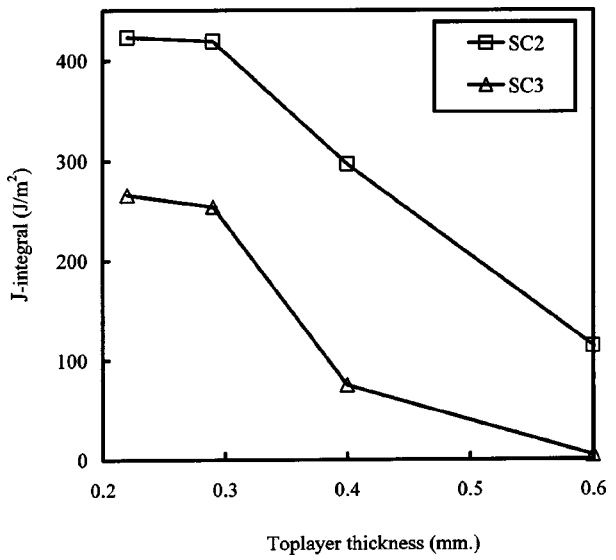

Fig. 14 Effect of top-layer thickness on *J*-integral for side-surface cracks in the nine-layer TBC

Figure 15 shows the strain energy release rate (*J*-integral) for the interface crack during the heating cooling cycle. One, three, and nine-layer TBCs with a single center surface crack that was half the TBC thickness ($a_{SC}/t=0.5$) have been considered here. Similar to the surface cracks (Fig. 10), the interface cracks experience no opening and rather small sliding displacements during heating and their energy release rates remain negligibly small during heating as seen in Fig. 15. During subsequent cooling, the interface cracks open and their energy release rate increases and attains a steady-state value. This maximum steady-state value of the energy release rate is used to characterize the driving force for interface crack extension.

The phase angle $\psi=\tan^{-1}(K_{II}/K_I)$, where K_I and K_{II} are the mode I (opening) and mode II (shear) stress intensity factors, respectively, may be used to assess the mode mixity for the interface cracks. For such a bimaterial interface crack, the phase angle (ψ) can be computed from the ratio of the crack-opening (dv) to the sliding (du) displacement and the elastic constants of the two materials across the interface, [43]. Accordingly, the ratios of the opening to the sliding displacements (dv/du) at steady state ($t=15$ sec) were used to compute the phase angle (ψ). The computed phase angles for the TBC–BC interface cracks in the one, three, and nine-layer TBCs were 14, 23, and 24 deg, respectively, and have been indicated in Fig. 15. Thus, the mode mixity is comparable in all three cases and there is a dominance of mode I (opening).

The steady-state ($t=15$ sec) strain energy release rates for the

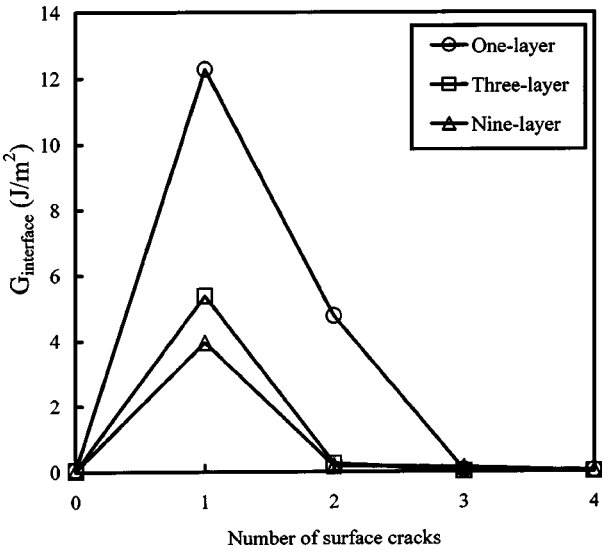

Fig. 16 Steady-state strain energy release rates for the interface cracks in coatings with 50% ($a_{SC}/t=0.50$) surface cracks

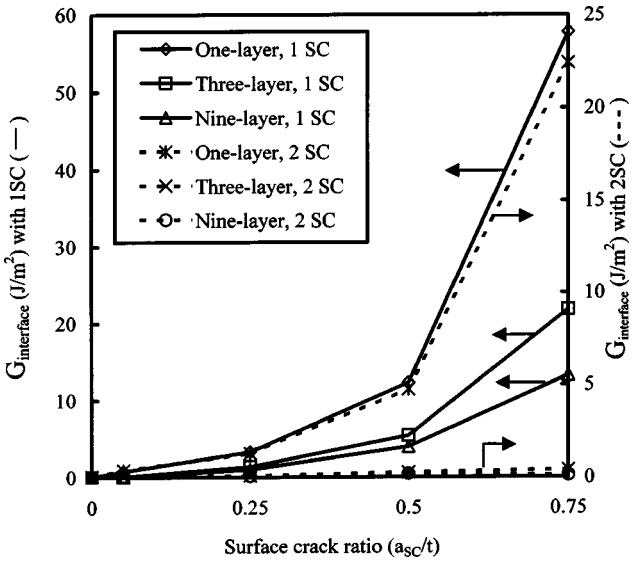

Fig. 17 Effect of surface crack length on the strain energy release rates for the interface cracks (arrows indicate pertinent *y*-axis)

interface cracks in the three architectures are shown in Fig. 16. Here, the lengths of all the surface cracks were 50% of the total TBC thickness ($a_{SC}/t=0.5$) in each of the three architectures. The case where no surface cracks are present as well as cases where one, two, three, and four surface cracks are present in the symmetric model have been shown in Fig. 16. Figure 16 shows that, for a given number of surface cracks, with a certain surface crack ratio (a_{SC}/t), the strain energy release rate for the interface crack reduces with increased coating gradation. Thus the force driving the interface crack growth is highest in the one-layer and lowest in the nine-layer architecture.

Figure 16 also shows that if no surface cracks were present on the TBC, the strain energy release rate for the interface cracks is negligibly small. Thus, if no surface cracks formed on the TBC, the driving force for interface cracking would be negligible. However, owing to the thermally activated time-dependent effects in YSZ based TBCs, the formation of these surface cracks are inevitable as evidenced by the previously presented experimental results, [28], as well as earlier investigations, [11,27]. With one relatively long ($a_{SC}/t=0.5$) surface crack in the model, the energy release rate for the interface crack is quite high. The reasons for the same are discussed below (Fig. 17). Given that these surface cracks do form, the strain energy release rate for the interface cracks decrease with an increase in the number of surface cracks. Thus, for a given architecture, with surface cracks of a certain length, as the number of surface cracks in the model is increased from one to four, a significant reduction in the driving force for interface crack growth is seen.

The interface cracks tend to open during cooling ($t>4$ sec) when the TBC experiences tensile stresses. It was seen from Fig. 9 that an increase in the number of surface cracks makes the coating more compliant (strain-tolerant) and relieves some of the tensile stresses (σ_{xx}) in the TBC. The interface cracks tend to open during cooling under the action of the bending moment acting on the TBC. This moment arises due to the gradient in tensile stresses through the coating thickness. With an increase in the number of surface cracks, the tensile stresses in the TBC and hence the moment acting on the TBC reduce significantly. Therefore, the relative opening displacements between the faces of the interface cracks as well as their energy release rates were found to reduce with an increase in the number of surface cracks on the TBC. Furthermore, the presence of these surface cracks does not change the temperature at the TBC–bond coat layer interface, and hence the insulating effects of the coating are preserved.

The effect of increasing surface crack lengths on the strain-energy release rates for the interface cracks is shown in Fig. 17. Here, the cases where one surface crack and two surface cracks (of equal length) were present in the symmetric model have been considered for each of the three architectures. Figure 17 shows that when there is no surface crack ($a_{SC}/t=0$), the energy release rate for the interface crack is negligibly small ($\sim 10^{-2}$ J/m^2). Further, for a given number of surface cracks, the energy release rate for the interface cracks increase as these surface cracks become longer. Again, the gradient in tensile stresses through the coating thickness after the heating-cooling cycle creates a bending moment. This moment causes the interface cracks to open during cooling. As the surface cracks become longer, the area of the TBC resisting this moment reduces and hence the effective bending (flexural) stiffness of the TBC becomes lower. This leads to higher opening displacements for the interface cracks. Hence, for a given number of surface cracks on the TBC, the strain energy release rate for the interface crack increases as these surface cracks become longer.

From the experimental data in Kokini et al. [28], it was seen that a one-layer coating would typically develop one surface crack approximately 75% of its thickness ($a_{SC}/t=0.75$) in a laser thermal shock test where the maximum surface temperature was 1300°C. The three-layer coating would develop three surface cracks, to reach about 70% of its thickness. In a similar test, the nine-layer coating would develop three surface cracks less than 30% of its total thickness. With these surface crack configurations, the strain energy release rate for the interface cracks in the three architectures can be compared from Fig. 17. It is found that the strain energy release rate for the interface crack in a one-layer TBC is *two orders of magnitude* greater than the corresponding value in the three-layer TBC and *three orders of magnitude* as that in the nine-layer TBC. This illustrates the combined effect of an increased number of surface cracks and coating architecture in reducing the driving force for interface crack growth with increased compositional gradation.

10 Summary and Conclusions

The response of functionally graded YSZ–bond coat alloy TBCs to transient thermal loading simulating previously reported

laser thermal shock tests was modeled. The effects of time-dependent (viscoplastic) deformations in the coating layers were incorporated in the analyses.

The results indicate that the tendency for multiple surface cracking with increased coating gradation may be attributed to the time-dependent effects of the lower layers and even more critically, to the decrease in thickness of the ceramic rich top layer. The thermal shock tests, [28], showed that the nine-layer specimens on an average had the highest number of surface cracks while the one-layer specimens predominantly had single surface cracks.

A more graded TBC develops more number of surface cracks. Multiple surface cracks make the TBC more compliant, relieve the tensile stresses in the TBC and consequently reduce the bending moment acting on the coating. This is mainly responsible for the decreased driving force for TBC–BC interface crack growth with increased compositional gradation. This correlates with the fact that for a given maximum surface temperature in the thermal shock tests, the nine-layer coatings had the shortest interface cracks while the one-layer coatings had the longest.

For a given number of surface cracks, the driving force for interface crack propagation increases with the length of these surface cracks due to a reduction in the area resisting the moment acting on the TBC. For surface cracks of a given length, an increase in their number reduces the driving force for interface crack growth. These two effects mutually compete and therefore having a TBC with a sufficiently high population of short surface cracks can enhance its resistance to delamination. A plasma-sprayed TBC with a dense population of short surface cracks then develops a strain tolerance similar to an EBPVD TBC while retaining its primary advantage of superior thermal resistance.

Acknowledgments

Support for this research from the National Science Foundation (Grant No. NSF-CMS-0201287) and from Purdue Research Foundation are gratefully acknowledged.

References

[1] Geiger, G., 1992, ''Ceramic Coatings Enhance Material Performance,'' Am. Ceram. Soc. Bull., **71**(10), Oct.
[2] Bennett, A., 1984, ''Rolls-Royce Experience with Thermal Barrier Coatings,'' Rolls-Royce Report No. PNR 90222.
[3] Mumm, D. R., and Evans, A. G., 2000, ''On the Role of Imperfections in the Failure of a Thermal Barrier Coating Made by Electron Beam Deposition,'' Acta Mater., **48**(8), pp. 1815–1827.
[4] Evans, A. G., Mumm, D. R., and Hutchinson, J. W., 2001, ''Mechanisms Controlling the Durability of Thermal Barrier Coatings,'' Prog. Mater. Sci., **46**, pp. 505–553.
[5] Beele, W., Marijnissen, G., and van Lieshout, A., 1999, ''The Evolution of Thermal Barrier Coatings—Status and Upcoming Solutions for Today's Key Issues,'' Surf. Coat. Technol., **120–121**, pp. 61–67.
[6] Mumm, D. R., Evans, A. G., and Spitsberg, I. T., 2001, ''Characterization of a Cyclic Displacement Instability for a Thermally Grown Oxide in a Thermal Barrier System,'' Acta Mater., **49**(12), pp. 2329–2340.
[7] Zhou, Y. C., and Hashida, T., 2001, ''Coupled Effects of Temperature Gradient and Oxidation on Thermal Stress in Thermal Barrier Coating System,'' Int. J. Solids Struct., **38**(24–25), pp. 4235–4264.
[8] Nusier, S. Q., and Newaz, G. M., 2000, ''Growth of Interfacial Cracks in a TBC/Superalloy System due to Oxide Volume Induced Internal Pressure and Thermal Loading,'' Int. J. Solids Struct., **37**(15), pp. 2151–2166.
[9] Rabiei, A., and Evans, A. G., 2000, ''Failure Mechanisms Associated With the Thermally Grown Oxide in Plasma-Sprayed Thermal Barrier Coatings,'' Acta Mater., **48**(15), pp. 3963–3976.
[10] Ali, M. Y., Nusier, S. Q., and Newaz, G. M., 2001, ''Mechanics of Damage Initiation and Growth in a TBC/Superalloy System,'' Int. J. Solids Struct., **38**, pp. 3329–3340.
[11] Kokini, K., and Takeuchi, Y. R., 1994, ''Initiation of Surface Cracks in Multilayer Ceramic Thermal Barrier Coatings Under Thermal Loads,'' Mater. Sci. Eng., A, **A189**, pp. 301–309.
[12] Zhu, D., and Miller, R. A., 1998, ''Sintering and Creep Behavior of Plasma-Sprayed Zirconia and Hafnia Based Thermal Barrier Coatings,'' Surf. Coat. Technol., **108**, pp. 114–120.
[13] Choules, B. D., and Kokini, K., and Taylor, T. A., 2001, ''Thermal Fracture of Ceramic Thermal Barrier Coatings Under High Heat Flux With Time-Dependent Behavior—Part I: Experimental Results,'' Mater. Sci. Eng., A, **A299**, pp. 296–304.
[14] Takeuchi, Y. R., and Kokini, K., 1994, ''Thermal Fracture of Multilayer Ceramic Thermal Barrier Coatings,'' ASME J. Eng. Gas Turbines Power, **116**, pp. 266–271.
[15] Choules, B. D., and Kokini, K., 1997, ''Interface Thermal Fracture of Ceramic Coatings in a High Heat Flux Environment,'' *Thermal Stress '97*, Rochester Institute of Technology, Rochester, NY.
[16] Rejda, F., Socie, D. F., and Itoh, T., 1999, ''Deformation Behavior of Plasma Sprayed Thick Thermal Barrier Coatings,'' Surf. Coat. Technol., **113**, pp. 218–226.
[17] Thurn, G., Schneider, G. A., and Aldinger, F., 1997, ''High-Temperature Deformation of Plasma-Sprayed ZrO_2 Thermal Barrier Coatings,'' Mater. Sci. Eng., A, **A233**, pp. 176–182.
[18] Khor, K. A., Dong, Z. L., and Gu, Y. W., 1999, ''Plasma Sprayed Functionally Graded Thermal Barrier Coatings,'' Mater. Lett., **38**, pp. 437–444.
[19] Dong, Z. L., Khor, K. A., and Gu, Y. W., 1999, ''Microstructure Formation in Plasma Sprayed Functionally Graded NiCoCrAlY/yttria-Stabilized Zirconia Coatings,'' Surf. Coat. Technol., **114**, pp. 181–186.
[20] Yamanouchi, M., Koizumi, M., Hirai, T., and Shiota, I., 1990, *Proceedings of the First International Symposium on Functionally Graded Materials (FGM'90)* Functionally Graded Materials Forum, Tokyo, Japan.
[21] Reimanis, I., Bowman, K., Sampath, S., and Trumble, K., 2003, *Proceedings of the Sixth International Symposium on Functionally Graded Materials (FGM' 2000)* American Ceramic Society, Westerville, OH, in press.
[22] Bao, G., and Wang, L., 1995, ''Multiple Cracking in Functionally Graded Ceramic/Metal Coatings,'' Int. J. Solids Struct., **32**(19), pp. 2853–2871.
[23] Bao, G., and Cai, H., 1997, ''Delamination Cracking in Functionally Graded Coating/Metal Substrate System,'' Acta Mater., **45**(4), pp. 1055–1066.
[24] Erdogan, F., and Wu, B. H., 1996, ''Crack Problems In FGM Layers Under Thermal Stresses,'' J. Therm. Stresses, **19**, pp. 237–265.
[25] Lee, Yi-Der, and Erdogan, F., 1998, ''Interface Cracking of FGM Coating Under Steady-State Heat Flow,'' Eng. Fract. Mech., **59**(3), pp. 361–380.
[26] Kokini, K., and Takeuchi, Y. R., 1998, ''Multiple Surface Thermal Fracture of Graded Ceramic Coatings,'' J. Therm. Stresses, **21**, pp. 715–725.
[27] Kokini, K., Takeuchi, Y. R., and Choules, B. D., 1996, ''Surface Thermal Cracking Owing to Stress Relaxation: Zirconia vs. Mullite,'' Surf. Coat. Technol., **82**, pp. 77–82.
[28] Kokini, K., DeJonge, J., Rangaraj, S. V., and Beardesly, B., 2002, ''Thermal Fracture in Functionally Graded Thermal Barrier Coatings With Similar Thermal Resistance,'' Surf. Coat. Technol., **154**, pp. 223–231.
[29] Nemat-Nasser, Sia, and Hori, M., 1999, *Micromechanics: Overall Properties of Heterogeneous Materials*, Elsevier, New York.
[30] Mori, T., and Tanaka, K., 1973, ''Average Stress in Matrix and Average Elastic Energy of Materials With Misfitting Inclusions,'' Acta Metall., **21**, pp. 571–574.
[31] Rangaraj, S. V., and Kokini, K., 2002, ''Time-Dependent Behavior of Ceramic (Zirconia)-Metal (NiCoCrAlY) Particulate Composites,'' Mech. Time-Depend. Mater., **6**, pp. 171–191.
[32] Banerjee, A., 1999, ''Thermal Fracture of Precracked Thermal Barrier Coatings,'' M. S. Thesis, Purdue University, West Lafayette, IN.
[33] Wereszczak, A. A., Hemrick, J. G., Kirkland, T. P., Haynes, J. A., Fitzgerald, T. J., and Junkin, J. E., 1998, ''Stress Relaxation of MCrAlY Bond Coat Alloys as a Function of Temperature and Strain,'' ASME Paper No. 98-GT-403.
[34] Hershey, A. V., 1954, ''The Elasticity of an Isotropic Aggregate of Anisotropic Cubic Crystals,'' ASME J. Appl. Mech., **21**, pp. 236.
[35] Hill, R., 1965, ''Continuum micromechanics of elastoplastic polycrystals,'' J. Mech. Phys. Solids, **13**, pp. 89.
[36] Choules, B. D., 1998, 'Thermal fracture of ceramic coatings under high heat flux with time dependent behavior,' Ph.D. Thesis, Purdue University, West Lafayette, IN.
[37] McDonald, K. R., Dryden, J. R., Majumdar, A., and Zok, F. W., 2000, ''Thermal Conductance of Delamination Cracks in a Fiber Reinforced Ceramic Composite,'' J. Am. Ceram. Soc., **83**(3), pp. 553–562.
[38] Smelser, R. E., 1979, ''Evaluation of Stress Intensity Factors for Bimaterial Bodies Using Numerical Crack Flank Displacement Data,'' Int. J. Fract., **15**(2), pp. 135–143.
[39] Rice, J. R., 1968, ''A Path Independent Integral and the Approximate Analysis of Strain Concentration by Notches and Cracks,'' ASME J. Appl. Mech., **35**, pp. 379–386.
[40] *ABAQUS®/Standard User's Manual*, 2001, Hibbitt, Karlsson and Sorenson, Inc.
[41] Landes, J. D., and Begley, J. A., 1976, ''Mechanics of Crack Growth,'' ASTM STP 590, American Society for Testing and Materials, pp. 128–148.
[42] Nikbin, K. M., Webster, G. A., and Turner, C. E., 1976, *Cracks and Fracture*, ASTM STP 601, ASTM, Philadelphia, pp. 47–62.
[43] Sun, C. T., and Qian, W., 1997, ''The Use of Finite Extension Strain Energy Release Rates in Fracture of Interfacial Cracks,'' Int. J. Solids Struct., **34**(2), pp. 2595–2609.

On Global Energy Release Rate of a Permeable Crack in a Piezoelectric Ceramic

S. Li
Department of Civil and Environmental Engineering,
University of California,
Berkeley, CA 94720-1710

A permeable crack model is proposed to analyze crack growth in a piezoelectric ceramic. In this model, a permeable crack is modeled as a vanishing thin, finite dimension, rectangular slit with dielectric medium inside. A first-order approximation solution is derived in terms of the slit height, h_0. The main contribution of this paper is that the newly proposed permeable crack model reveals that there exists a realistic leaky mode for electrical field, which allows applied electric field passing through the dielectric medium inside a crack. By taking into account the leaky mode effect, a correct estimation of electrical and mechanical fields in front of a crack tip in a piezoelectric ceramic is obtained. To demonstrate this new finding, a closed-form solution is obtained for a mode III permeable crack under both mechanical as well electrical loads. Both local and global energy release rates are calculated based on the permeable crack solution obtained. It is found that the global energy release rate derived for a permeable crack is in a broad agreement with some known experimental observations. It may be served as a fracture criterion for piezoelectric materials. This contribution reconciles the outstanding discrepancy between experimental observation and theoretical analysis on crack growth problem in piezoelectric materials. [DOI: 10.1115/1.1544539]

1 Introduction

Fracture mechanics of piezoelectric solids has been an active research area since early 1990s due to the widespread use of smart materials and smart structures. Many research works have been published in the past decade, e.g., Pak [1,2], Li et al. [3], Sosa [4,5], Suo et al. [6,7], Dunn [8], Dascalu and Maugin [9,10], Park and Sun [11,12], Gao and Barnett [13], and Gao et al. [14], Lynch et al. [15,16], Zhang and Hack [17], Fulton and Gao [18], Ru [19,20], Yang and Zhu [21–23], Zhang et al. [24,25], McMeeking [26,27], Yang [21,22] among others. A recent article by Zhang et al. [28] provides an excellent review.

A major challenge in fracture mechanics of piezoelectric materials has been how to resolve an outstanding discrepancy between experimental observation and theoretic analysis. In a landmark experimental work by Park and Sun [11], it was found that the experimental observation contradicts with some basic aspects of fracture mechanics theory of linear piezoelectric materials. For instance, the experimental results obtained by Park and Sun [11] show that there is a decrease in the critical stress of a cracked piezoelectric body if the electric field is applied along the direction of poling axis, and there is an increase in critical stress if the electric field is applied to the opposite direction, whereas according to linear fracture mechanics theory, the applied electric field does not induce any nonzero stress intensity factor (e.g., Pak [1,2] and Suo et al. [6]), and it always predicts a negative definite energy release rate regardless the directions of the applied electric fields, which implies that the applied electric field always retards crack growth.

Using micromechanics concepts related to domain switching, Gao and his co-workers [13,14,18] argued that crack growth in a piezoelectric solid is a multiscale phenomenon, and the local energy release rate may be a critical factor in fracture process. A local energy release rate criterion was subsequently proposed to measure the fracture toughness of piezoelectric materials. The local energy release rate criterion is based on the so-called saturation-strip model, or equivalently an electric dipole distribution model, which is basically a domain switch strip-zone model that is taking into account the nonlinearity induced by the overall effect of domain switching. The saturation-strip model is the direct analogous of Dugdale crack in a cohesive elastic medium of classical fracture mechanics.

The local energy release rate criterion was an immediate success, because it provides a plausible explanation on Park-Sun's empirical formula of energy release rate, [11,12]. However, the dissipative nature of saturation-strip model seems to be a nuisance, e.g., [27].

In this work, a permeable crack model is carefully crafted to render a tractable solution for mode III crack, while retaining all the main features of a permeable crack. By doing so, it provides an opportunity to systematically reexamine the permeable crack solution of a piezoelectric ceramic.

2 Formulation of the Problem

Consider a crack with finite dimension in the middle of a transversely isotropic piezoelectric solid under the antiplane mechanical load and the in-plane electrical load. Let $x_1=X$ and $x_2=Y$. The relevant field variables are

$$u_1=u_2\equiv 0, \quad u_3=:w(X,Y);$$

$$E_3\equiv 0, \quad \mathbf{E}=-\frac{\partial \phi}{\partial X}\mathbf{e}_1-\frac{\partial \phi}{\partial Y}\mathbf{e}_2.$$

For the symmetry class of 6 mm piezoelectric crystal, or general piezoelectric composite possessing the same symmetry, the relevant constitutive equations are as follows (Auld [29]):

$$\sigma_{XZ}=c_{44}^{E}\frac{\partial w}{\partial X}+e_{15}\frac{\partial \phi}{\partial X} \tag{1}$$

$$\sigma_{YZ}=c_{44}^{E}\frac{\partial w}{\partial Y}+e_{15}\frac{\partial \phi}{\partial Y} \tag{2}$$

Contributed by the Applied Mechanics Division of THE AMERICAN SOCIETY OF MECHANICAL ENGINEERS for publication in the ASME JOURNAL OF APPLIED MECHANICS. Manuscript received by the ASME Applied Mechanics Division, Mar. 28, 2002; final revision, Aug. 26, 2002. Associate Editor: H. Gao. Discussion on the paper should be addressed to the Editor, Prof. Robert M. McMeeking, Department of Mechanical and Environmental Engineering University of California–Santa Barbara, Santa Barbara, CA 93106-5070, and will be accepted until four months after final publication of the paper itself in the ASME JOURNAL OF APPLIED MECHANICS.

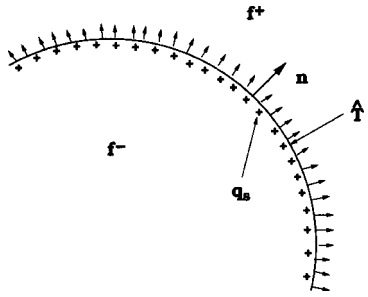

Fig. 1 Convention for boundary conditions

$$D_X = e_{15}\frac{\partial w}{\partial X} - \epsilon_{11}^s \frac{\partial \phi}{\partial X} \tag{3}$$

$$D_Y = e_{15}\frac{\partial w}{\partial Y} - \epsilon_{11}^s \frac{\partial \phi}{\partial Y}. \tag{4}$$

Subsequently, the Euler and Maxwell equations take the form

$$c_{44}^E \nabla^2 w + e_{15}\nabla^2 \phi = 0 \tag{5}$$

$$e_{15}\nabla^2 w - \epsilon_{11}^s \nabla^2 \phi = 0 \tag{6}$$

where

$$\nabla^2 := \frac{\partial^2}{\partial X^2} + \frac{\partial^2}{\partial Y^2}.$$

Since the determinant

$$\Delta_i := -\begin{vmatrix} c_{44}^E & e_{15} \\ e_{15} & -\epsilon_{11}^s \end{vmatrix} \neq 0 \tag{7}$$

one can decouple the system of governing equations

$$\begin{cases} \nabla^2 w = 0, & \forall (X,Y) \in \mathbb{R}^2/\Omega_h, \quad (8a) \\ \nabla^2 \phi = 0, & \forall (X,Y) \in \mathbb{R}^2/\Omega_h, \quad (8b) \end{cases}$$

where Ω_h is the void space inside the crack.

Note that the coupling between mechanical and electrical variables still exists in boundary conditions. For permeable cracks, there is a nonzero electrical field in the free space inside the void, and the electrical potential inside the crack, $\tilde{\phi}$, satisfies the equation

$$\nabla^2 \tilde{\phi} = 0, \quad \mathbf{x} \in \Omega_h \tag{9}$$

which interacts with both the mechanical field as well as the electrical field outside the crack along the crack surfaces. To capture this interaction, one has to employ the exact boundary conditions of both continuum mechanics and electromagnetics to solve the crack problem.

Instead of imposing various combinations of boundary conditions to show the coupling between the primary variables and their conjugate pairs, only standard mixed boundary value problems are considered here (Malvern [30] and Jackson [31]). The boundary conditions or interface conditions for two different dielectric media are

- mechanical boundary conditions

$$\mathbf{n}\cdot[|\boldsymbol{\sigma}|] = -\hat{\mathbf{T}} \quad \text{on } S_\sigma; \quad \mathbf{u} = \hat{\mathbf{u}} \text{ on } S_u; \tag{10}$$

- electrical boundary conditions

$$\mathbf{n}\cdot[|\mathbf{D}|] = q_s \quad \text{on } S_D \quad \text{and} \quad \mathbf{n}\times[|\mathbf{E}|] = 0 \quad \text{on } S_E \tag{11}$$

where S_σ, S_u identify appropriate subsets of the domain boundary and $S = S_\sigma \cup S_u$. Note that the notation $[|f|] := f^+ - f^-$, and the normal vector $\mathbf{n}$ is pointing from medium $-$ to medium $+$ as shown in Fig. 1. In electrostatics, condition (11) can sometimes be replaced by the continuity condition of electric potential, i.e., $[|\phi|] = 0$. It should be noted that $S_\sigma \cap S_u = 0$, but $S_D \cap S_E \neq 0$.

In this paper, a planar permeable crack is modeled as a vanishing thin, finite dimension, rectangular-shaped slit with height $2h_0$ and width $2a$ as shown in Fig. 2.

As $h_0 \to 0$, the permeable crack becomes a conventional mathematical crack. One may write the crack height as the function of X,

$$h(X) = \begin{cases} h_0, & |X| < a \\ 0, & |X| > a. \end{cases} \tag{12}$$

The interior region of the crack is denoted as the set Ω_h,

$$\Omega_h := \{(X,Y) | -a < X < a, \quad \text{and} \quad -h_0 < Y < h_0\}. \tag{13}$$

Adjacent to the slit, there are two semi-infinite strips, which are denoted as Ω_s,

$$\Omega_s := \{(X,Y) | a < |X|, \quad \text{and} \quad -h_0 < Y < h_0\}. \tag{14}$$

3 Crack Solution

Consider a mode III permeable crack that is perpendicular to the poling direction (out plane), and it is subjected to remote traction and charge distribution at remote boundary (see Fig. 2).

Let $\hat{\mathbf{T}} = \tau_\infty \mathbf{e}_Y$ and $q_s = -q_\infty$.

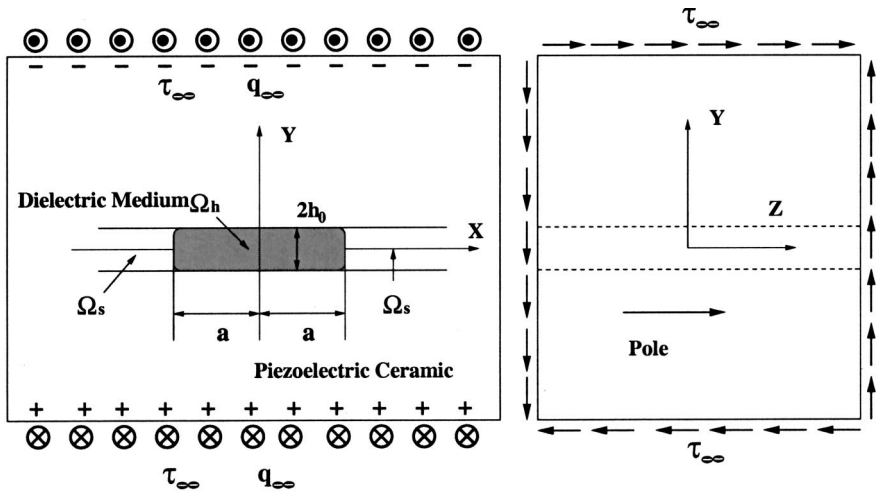

Fig. 2 A permeable crack with remote traction and charge distribution and surface charge distribution at the corner of the crack

$$\mathbf{n}\cdot[|\boldsymbol{\sigma}|]=-\hat{\mathbf{T}}\rightarrow\sigma_{YZ}=\tau_\infty,\quad \forall Y\rightarrow\infty \tag{15}$$

$$\mathbf{n}\cdot[|\mathbf{D}|]=q_s\rightarrow D_Y=q_\infty,\quad \forall Y\rightarrow\infty \tag{16}$$

where $q_s=-q_\infty$.

The boundary conditions on the crack surfaces

$$\mathbf{n}\cdot[|\boldsymbol{\sigma}|]=0,\quad \forall Y=\pm h_0 \quad \text{and} \quad |X|\leqslant a \tag{17}$$

$$\mathbf{n}\cdot[|\mathbf{D}|]=q_s,\quad \forall Y=\pm h_0 \quad \text{and} \quad |X|\leqslant a \tag{18}$$

$$\mathbf{n}\times[|\mathbf{E}|]=0,\quad \forall Y=\pm h_0 \quad \text{and} \quad |X|\leqslant a \tag{19}$$

take the form

$$\sigma_{YZ}(X,\pm h_0)=0,\quad \forall |X|\leqslant a \tag{20}$$

$$D_Y(X,\pm h_0)-D_Y^a(X,\pm h_0)=0,\quad \forall |X|\leqslant a \tag{21}$$

$$E_X(X,\pm h_0)-E_X^a(X,\pm h_0)=0,\quad \forall |X|\leqslant a. \tag{22}$$

The following symmetry conditions will be useful as well,

$$w(X,0)=0,\quad \forall |X|>a \tag{23}$$

$$\phi(X,0)=0,\quad \forall |X|>a \tag{24}$$

$$\phi^a(X,0)=0,\quad \forall 0<|X|<a \tag{25}$$

or

$$E_X(X,0)=0,\quad \forall |X|>a \tag{26}$$

$$E_X^a(X,0)=0,\quad \forall 0<|X|<a. \tag{27}$$

In the dielectric medium inside the crack, $D_i^a=\epsilon_0 E_i^a$ and $E_i^a=-\phi_{,i}^a$, $i=X,Y$.

Separate the displacement and electric potential fields into two parts: a uniform part due to the remote boundary conditions and a disturbance part due to the presence of the crack.

$$w=w_0+\tilde{w} \tag{28}$$

$$\phi=\phi_0+\tilde{\phi} \tag{29}$$

and choose

$$w_0=\gamma_\infty Y,\quad \phi_0=-E_\infty Y \tag{30}$$

and

$$\sigma_\infty=c_{44}^E\gamma_\infty-e_{15}E_\infty \tag{31}$$

$$q_\infty=e_{15}\gamma_\infty+\epsilon_{11}^S E_\infty \tag{32}$$

such that $\tilde{w},\ \tilde{\phi}\rightarrow 0$ as $Y\rightarrow\infty$.

It is convenient to write the inverse relationship among key physical variables on the remote boundary,

$$\gamma_\infty=\frac{1}{\Delta_i}(\epsilon_{11}^S\tau_\infty+e_{15}q_\infty) \tag{33}$$

$$E_\infty=\frac{1}{\Delta_i}(-e_{15}\tau_\infty+c_{44}^E q_\infty), \tag{34}$$

where $\Delta_i:=c_{44}^E\epsilon_{11}^S+e_{15}^2$.

Extend the definition domain of ϕ^a into $\Omega_h\cup\Omega_s$ and let

$$\tilde{\phi}^a=\begin{cases}\phi^a-\phi_0^a, & \forall (X,Y)\in\Omega_h\\ 0, & \forall (X,Y)\in\Omega_s\end{cases} \tag{35}$$

where the uniform part of the electric potential is the leaky mode, which is chosen as $\phi_0^a:=-q_\infty/\epsilon_0 Y$.

Introduce the Fourier cosine transform

$$\begin{cases}F^*(\zeta,Y)=\sqrt{\dfrac{2}{\pi}}\displaystyle\int_0^\infty F(X,Y)\cos(\zeta X)dX\\ F(X,Y)=\sqrt{\dfrac{2}{\pi}}\displaystyle\int_0^\infty F^*(\zeta,Y)\cos(\zeta X)d\zeta\end{cases} \tag{36}$$

where $F(X,Y)=\tilde{w}(X,Y)$, $\tilde{\phi}(X,Y)$, and $\tilde{\phi}^a(X,Y)$, and $F^*(\zeta,Y)=\tilde{w}^*(\zeta,Y)$, $\tilde{\phi}^*(\zeta,Y)$, and $\tilde{\phi}^{a*}(\zeta,Y)$.

The transformed governing equations become

$$\frac{d^2}{dY^2}F^*+\zeta^2F^*=0. \tag{37}$$

Within the piezoelectric ceramic,

$$\tilde{w}^*(\zeta,Y)=A(\zeta)\exp(-\zeta Y),\quad \forall Y>0 \tag{38}$$

$$\tilde{\phi}^*(\zeta,Y)=B(\zeta)\exp(-\zeta Y),\quad \forall Y>0. \tag{39}$$

Inside the permeable crack,

$$\tilde{\phi}^{a*}(\zeta,Y)=C(\zeta)\sinh(\zeta Y),\quad \forall Y>0 \tag{40}$$

which satisfies the symmetry condition $\tilde{\phi}^a(X,0)=0$.

Consider the boundary condition

$$E_X(X,\pm h_0)-E_X^a(X,\pm h_0)=0,\quad |X|<a \tag{41}$$

and the symmetry condition

$$E_X(X,0)=0,\quad |X|>a, \tag{42}$$

and in the extended domain

$$\tilde{E}_X^a(X,0)=0,\quad |X|>a. \tag{43}$$

Combining Eqs. (41)–(43), one may find that

$$\tilde{E}_X(X,\pm h(X))-\tilde{E}_X^a(X,\pm h(X))=0,\quad \forall -\infty<X<+\infty \tag{44}$$

where function $h(X)$ is defined in Eq. (12).

In transformed space (ζ,Y), the condition (44) reads as

$$\tilde{E}_X^*(\zeta,\pm h^*(\zeta))-\tilde{E}_X^{a*}(\zeta,\pm h^*(\zeta))=0,\quad \forall 0<\zeta<+\infty \tag{45}$$

where

$$h^*(\zeta)=h_0\frac{\sin(a\zeta)}{\zeta}. \tag{46}$$

Considering Eqs. (39) and (40), one has

$$\begin{aligned}B(\zeta)&=C(\zeta)\frac{1}{2}(\exp(2\zeta h^*(\zeta))-1)\\&=C(\zeta)\left(h_0\sin(a\zeta)+h_0^2\sin^2(a\zeta)+\frac{2}{3}h_0^3\sin^3(a\zeta)+\ldots\right).\end{aligned} \tag{47}$$

Let

$$A(\zeta)=A_1(\zeta)+h_0A_2(\zeta)+h_0^2A_3(\zeta)+\ldots \tag{48}$$

$$B(\zeta)=B_1(\zeta)+h_0B_2(\zeta)+h_0^2B_3(\zeta)+\ldots. \tag{49}$$

By virtue of Eq. (47),

$$B_1(\zeta)=C(\zeta)h_0\sin(a\zeta) \tag{50}$$

$$B_2(\zeta)=C(\zeta)h_0\sin^2(a\zeta) \tag{51}$$

$$B_3(\zeta)=C(\zeta)\frac{2h_0}{3}\sin^3(a\zeta) \tag{52}$$

$$\ldots. \tag{53}$$

After the Fourier transform, the boundary condition (21) becomes

$$\sqrt{\frac{2}{\pi}}\int_0^\infty \zeta\{[e_{15}A(\zeta)-\epsilon_{11}^S B(\zeta)]\exp(-h_0\zeta) - \epsilon_0 C(\zeta)\cosh(\zeta h_0)\}\cos(\zeta X)d\zeta=0, \quad \forall 0<X<a. \tag{54}$$

Note the subtlety in terms of crack surface position between Eq. (45) and Eq. (54). In the physical plane, the upper crack surface is at $Y=h_0$ for $|X|<a$, whereas in the transformed plane, $Y=h^*(\zeta)$, $0<\zeta<\infty$.

Consider the series expansion

$$[e_{15}A(\zeta)-\epsilon_{11}^S B(\zeta)]=[e_{15}A_1(\zeta)-\epsilon_{11}^S B_1(\zeta)]+h_0[e_{15}A_2(\zeta) - \epsilon_{11}^S B_2(\zeta)]+h_0^2[e_{15}A_3(\zeta)-\epsilon_{11}^S B_3(\zeta)] + \ldots \tag{55}$$

$$\exp(-h_0\zeta)=1-h_0\zeta+\frac{(h_0\zeta)^2}{2!}-\frac{(h_0\zeta)^3}{3!}+\ldots \tag{56}$$

$$\cosh(h_0\zeta)=1+\frac{(h_0\zeta)^2}{2!}+\ldots. \tag{57}$$

Assume that the permittivity constant, ϵ_0, is very small and comparable to h_0. The following asymptotic series integral equations may be derived:

$$\sqrt{\frac{2}{\pi}}\int_0^\infty \zeta\left\{e_{15}A_1(\zeta)-\left(\epsilon_{11}^S+\frac{\epsilon_0}{h_0\sin(a\zeta)}\right)B_1(\zeta)\right\}\cos(\zeta X)d\zeta =0, \quad \forall 0<X<a \tag{58}$$

$$\sqrt{\frac{2}{\pi}}\int_0^\infty \{-\zeta^2([e_{15}A_1(\zeta)-\epsilon_{11}^S B_1(\zeta)]+\zeta[e_{15}A_2(\zeta) - \epsilon_{11}^S B_2(\zeta)]\}\cos(\zeta X)d\zeta=0, \quad \forall 0<X<a \tag{59}$$

$$\ldots. \tag{60}$$

In the remainder of this paper, only the first-order approximation is considered. Moreover, when $h_0\to 0$, $\sin(a\zeta)$ is always bounded. To render a tractable solution, we adopt the following average approximation:

$$h_0\sin(a\zeta)\approx h_0\overline{\sin(a\zeta)}\to 0 \tag{61}$$

where

$$\overline{\sin(a\zeta)}:=\sqrt{\frac{\pi}{2}}\int_0^\infty \sin(a\zeta)d\zeta=\sqrt{\frac{\pi}{2}}\frac{1}{a}. \tag{62}$$

The identity (62) is in the sense of a generalized function (see Erdélyi et al. [32] or Lighthill [33], p. 33).

Let

$$r:=\sqrt{\frac{2}{\pi}}\frac{a}{h_0}. \tag{63}$$

Equation (54) becomes

$$\sqrt{\frac{2}{\pi}}\int_0^\infty \zeta(e_{15}A_1(\zeta)-(\epsilon_{11}^S+\epsilon_0 r)B_1(\zeta))\cos(\zeta X)d\zeta=0, \quad \forall 0<X<a. \tag{64}$$

The first-order approximation of boundary condition (20) provides the additional integral equation

$$\sqrt{\frac{2}{\pi}}\int_0^\infty \zeta(c_{44}^E A_1(\zeta)+e_{15}B_1(\zeta))\cos(\zeta X)d\zeta=\tau_\infty, \quad \forall 0<X<a. \tag{65}$$

Considering the symmetry conditions $w(X,0)=\phi(X,0)=0$, $\forall |X|>a$. Two sets of standard dual integral equations may be derived;

$$\begin{cases} \sqrt{\frac{2}{\pi}}\int_0^\infty \zeta A_1(\zeta)\cos(\zeta X)d\zeta=S, & |X|<a \\ \int_0^\infty A_1(\zeta)\cos(\zeta X)d\zeta=0, & |X|>a \end{cases} \tag{66}$$

and

$$\begin{cases} \sqrt{\frac{2}{\pi}}\int_0^\infty \zeta B_1(\zeta)\cos(\zeta X)d\zeta=T, & |X|<a \\ \int_0^\infty B_1(\zeta)\cos(\zeta X)d\zeta=0, & |X|>a \end{cases} \tag{67}$$

where

$$S:=\frac{(\epsilon_{11}^S+\epsilon_0 r)\tau_\infty}{\Delta} \tag{68}$$

$$T:=\frac{e_{15}\tau_\infty}{\Delta} \tag{69}$$

and $\Delta=c_{44}^E(\epsilon_{11}^S+\epsilon_0 r)+e_{15}^2$.

Let

$$A_1(\zeta)=\sqrt{\frac{\pi}{2}}\frac{Sa}{\zeta}J_1(a\zeta) \tag{70}$$

$$B_1(\zeta)=\sqrt{\frac{\pi}{2}}\frac{Ta}{\zeta}J_1(a\zeta). \tag{71}$$

Consequently, one may find that

$$w(X,Y)=\gamma_\infty Y+\frac{(\epsilon_{11}^S+\epsilon_0 r)\tau_\infty}{\Delta}a\int_0^\infty \zeta^{-1}J_1(a\zeta)\cos(\zeta X) \times\exp(-\zeta Y)d\zeta \tag{72}$$

$$\phi(X,Y)=-E_\infty Y+\frac{e_{15}\tau_\infty}{\Delta}a\int_0^\infty \zeta^{-1}J_1(a\zeta)\cos(\zeta X)\exp(-\zeta Y)d\zeta \tag{73}$$

and

$$w(X,0)=\frac{(\epsilon_{11}^S+\epsilon_0 r)\tau_\infty}{\Delta}\begin{cases}\sqrt{a^2-X^2}, & |X|<a \\ 0, & |X|>a\end{cases} \tag{74}$$

$$\phi(X,0)=\frac{e_{15}\tau_\infty}{\Delta}\begin{cases}\sqrt{a^2-X^2}, & |X|<a \\ 0, & |X|>a\end{cases}. \tag{75}$$

4 Intensity Factors

Let $Y=0$. The asymptotic fields of both mechanical and electric variables in front of the crack tip are found as follows:

$$\epsilon_{YZ}=\frac{(\epsilon+\epsilon_0 r)\tau_\infty}{\Delta}\frac{X}{\sqrt{X^2-a^2}}+\left(\gamma_\infty-\frac{(\epsilon+\epsilon_0 r)\tau_\infty}{\Delta}\right) + \text{higher order terms} \tag{76}$$

$$E_Y=-\frac{e_{15}\tau_\infty}{\Delta}\frac{X}{\sqrt{X^2-a^2}}+\left(E_\infty+\frac{e_{15}\tau_\infty}{\Delta}\right)+\text{higher order terms} \tag{77}$$

$$\sigma_{YZ}=\frac{\tau_\infty X}{\sqrt{X^2-a^2}}+\text{higher order terms} \tag{78}$$

$$D_Z=\frac{e_{15}\epsilon_0 r\tau_\infty}{\Delta}\frac{X}{\sqrt{X^2-a^2}}+\left(q_\infty-\frac{e_{15}\epsilon_0 r\tau_\infty}{\Delta}\right)$$

$$+\text{higher order terms.} \tag{79}$$

The relevant field intensity factors can be found as follows:

$$K_{III}^{\gamma}=\lim_{X\to a^+}\sqrt{2\pi(X-a)}\epsilon_{YZ}(X,0)=\frac{(\epsilon_{11}^S+\epsilon_0 r)\tau_\infty\sqrt{\pi a}}{\Delta} \tag{80}$$

$$K_{III}^{E}=\lim_{X\to a^+}\sqrt{2\pi(X-a)}E_Y(X,0)=-\frac{e_{15}\tau_\infty\sqrt{\pi a}}{\Delta} \tag{81}$$

$$K_{III}^{\tau}=\lim_{X\to a^+}\sqrt{2\pi(X-a)}\sigma_{YY}(X,0)=\tau_\infty\sqrt{\pi a} \tag{82}$$

$$K_{I}^{D}=\lim_{X\to a^+}\sqrt{2\pi(X-a)}D_Y(X,0)=\frac{e_{15}\epsilon_0 r\tau_\infty\sqrt{\pi a}}{\Delta}. \tag{83}$$

Assume that the permittivity inside the crack is very small, $\epsilon_0 \ll h_0$, or $\epsilon_0\to 0$, we may recover all the results obtained by Zhang and Hack [17] for a mode III crack.

$$K_{III}^{\gamma}=\frac{\epsilon}{\Delta_i}\tau_\infty\sqrt{\pi a} \tag{84}$$

$$K_{III}^{E}==-\frac{e_{15}}{\Delta_i}\tau_\infty\sqrt{\pi a} \tag{85}$$

$$K_{III}^{\tau}=\tau_\infty\sqrt{\pi a} \tag{86}$$

$$K_{III}^{D}=0 \tag{87}$$

Let $h_0=0$ and consequently $r\to\infty$. That is, the slit has zero height. The physical interpretation of this limit is that the upper and lower crack surfaces are constantly in close contact during fracture process, there is no dielectric medium inside the crack. The intensity factors become

$$K_{III}^{\gamma}=\frac{\epsilon_{11}^S}{c_{44}^E}\tau_\infty\sqrt{\pi a} \tag{88}$$

$$K_{III}^{E}=0 \tag{89}$$

$$K_{III}^{\tau}=\tau_\infty\sqrt{\pi a} \tag{90}$$

$$K_{III}^{D}=0. \tag{91}$$

This recovers the solution obtained by Yang and Kao [34] for a zero-height crack in piezoelectric medium.

5 Energy Release Rate

It is generally believed that energy release rate, or *J*-integral, is a better criterion for crack growth than stress intensity factors. The *J*-integral in a piezoelectric medium is given by Cherepanov [35],

$$J=\int_\Gamma (Hn_1-\sigma_{ij}n_i u_{j,1}-n_i D_i\phi_{,1})dS \tag{92}$$

where H is the electric enthalpy density.

On the surface of a permeable crack, both the normal component of electric displacement as well as the electric potential are not zero, consequently, the contribution in the contour integral, *J*, along crack surfaces is not zero. Therefore, for permeable cracks, two types of *J*-integrals can be defined: *local energy release rate* and *global energy release rate*. The global energy release rate consists of two parts: (1) *local energy release rate* and (2) the energy release rate due to interaction between dielectric medium inside the crack and piezoelectric matrix along crack surfaces. The local energy release rate is defined as the contour integral, *J*, along an infinitesimal circle around the crack tip, Γ_l. The global energy release rate may be defined as any contour integral, *J*, starting at the center of the lower part of the crack surface and ending at the center of upper part of the crack surface (see Fig. 3). Therefore, the global energy release rate is the sum of the local energy release rate and the contour integral contribution along the crack surfaces, i.e.,

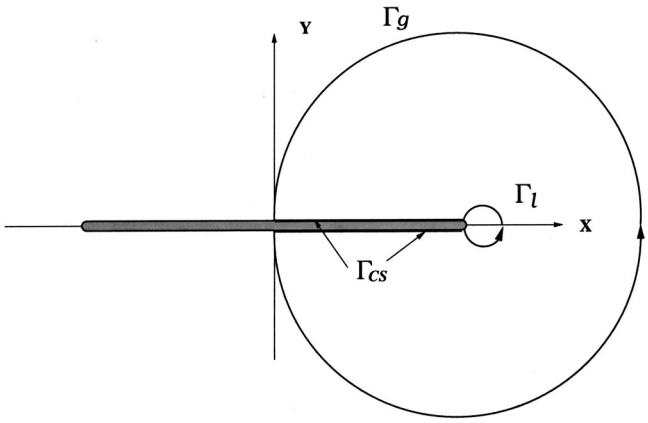

Fig. 3 ***J*-integral contours for evaluating local and global energy release rates**

$$J_g=J_l+J_{cs} \tag{93}$$

where J_{cs} denote the energy release rate contribution from crack surfaces, which can be calculated by

$$J_{cs}=-\int_{cs} n_i D_i\phi_{,x}dS. \tag{94}$$

5.1 Local Energy Release Rate. We first consider the so-called *local energy release rate*. Consider the following electromechanical boundary conditions:

$$\sigma_{YY}=\tau_\infty,\quad D_Y=q_\infty,\quad \forall Y\to\infty. \tag{95}$$

The corresponding local energy release rate of the present permeable crack model is

$$J_l^{NEW}=\frac{1}{2}(K_{III}^{\tau}K_{III}^{\gamma}-K_{III}^{E}K_{III}^{D})=\frac{\pi a}{2}\frac{\tau_\infty^2}{\Delta^2}(\Delta(\epsilon_{11}^S+\epsilon_0)+e_{15}^2\epsilon_0 r). \tag{96}$$

Letting $\epsilon_0=0$ in (96), one recovers the result obtained by Zhang and Hack [17], i.e.,

$$J_l^{NEW}\Rightarrow\frac{\pi a}{2}\frac{\epsilon_{11}^S}{\Delta_i}\tau_\infty^2. \tag{97}$$

Let $h_0=0$ or $r\to\infty$ in Eq. (96). The result obtained by Yang and Kao [34] may be recovered,

$$J_l^{NEW}\Rightarrow\frac{\pi a}{2}\frac{\tau_\infty^2}{c_{44}^E}. \tag{98}$$

Equation (98) is the purely elastic energy release rate, since there is no dielectric medium inside the crack.

5.2 Global Energy Release Rate. When a permeable crack grows, energy release is not only consumed in supplying the surface energy for newly formed crack surfaces, but also consumed by supplying the electrostatic energy to the dielectric medium inside the crack. In fact, if the surface charge is absent on the crack surfaces, the normal component of electric displacement in piezoelectric medium may be equal to the normal component of electric displacement in the dielectric medium inside the crack. This suggests that the crack surface contribution to the *J*-integral

is the part of energy release rate that goes directly into supplying the electrostatic energy increase in the dielectric medium inside the crack.

If the surface charge is present on crack surfaces, which may either enhance or reverse the direction of the energy-moment flux, an additional energy release rate may be created that will influence crack growth process.

In order the evaluate J_g, we first evaluate J_{cs}. Consider the normal component of the electric displacement on the crack surfaces.

$$\begin{aligned} D_Y(X,h_0) &\approx D_y(X,0) \\ &= e_{15}\frac{\partial w}{\partial Y} - \epsilon_{11}^S \frac{\partial \phi}{\partial Y} \\ &= q_\infty - \frac{e_{15}\epsilon_0 r \tau_\infty}{\Delta} a \int_0^\infty J_1(a\zeta)\cos(\zeta X)\, d\zeta \\ &= q_\infty - \frac{e_{15}\epsilon_0 r \tau_\infty}{\Delta} \begin{cases} 1, & |X|<a \\ 1-\dfrac{X}{\sqrt{X^2-a^2}}, & |X|>a \end{cases} \end{aligned} \tag{99}$$

Substituting Eq. (99) and Eq. (75) into Eq. (94) yields

$$\begin{aligned} J_{cs} &= D_Y(0,0^+)(\phi(0,0^+)-\phi(0,0^-)) \\ &= \left(q_\infty - \frac{\epsilon_0 e_{15} r \tau_\infty}{\Delta}\right)\left(\frac{2e_{15}\tau_\infty a}{\Delta}\right). \end{aligned} \tag{100}$$

Hence the global energy release has the form

$$\text{I:}\quad J_{cr}^g = \left(\frac{\pi a}{2\Delta}\right)\left\{\left[(\epsilon_{11}^S+\epsilon_0 r)+\frac{e_{15}^2\epsilon_0 r}{\Delta}\left(1-\frac{4}{\pi}\right)\right]\tau_\infty^2 + \frac{4}{\pi}e_{15}\tau_\infty q_\infty\right\}. \tag{101}$$

Let $\epsilon_0 = 0$. The global energy release rate becomes

$$\text{II:}\quad J_{cr1}^g = \left(\frac{\pi a}{2c_{44}^E}\right)\left(\frac{c_{44}^E\epsilon_{11}^S+\frac{4}{\pi}e_{15}^2}{c_{44}^E\epsilon_{11}^S+e_{15}^2}\tau_\infty^2 + \frac{4}{\pi}e_{15}^2\tau_\infty E_\infty\right). \tag{102}$$

If $h_0 \to 0$, the global energy release rate becomes

$$J_{cr2}^g = \left(\frac{\pi a}{2}\right)\frac{\tau_\infty^2}{c_{44}^E} \tag{103}$$

which was previously found by Yang and Kao [34].

Since $4/\pi = 1.273238 \approx 1.0$, the newly derived results (101) and (102) are very close to the empirical result proposed by Park and Sun [11,12].

$$J_{PS} = \frac{\pi a}{2(c_{44}^E\epsilon_{11}^S+e_{15}^2)}(\epsilon_{11}^S\tau_\infty^2 + e_{15}\tau_\infty q_\infty) \tag{104}$$

This result also agrees with the result obtained by Mao et al. [36] in analyzing a mode I crack by considering toughening under polarization switching.

6 Closure

The analysis presented in this work reveals that the interaction between a crack and its permeable environment can be crucial to crack growth in a piezoelectric ceramic. This interaction may be quantified through a *J*-integral along permeable crack surfaces. A global energy release rate that taking into account this effect may serve better as the fracture toughness for piezoelectric ceramics.

It has been an outstanding problem regarding the energy release rate of a piezoelectric crack. The impermeable crack solution always gives the negative energy release rate, presenting a false impression that the applied electric field will prohibit crack growth. The fallacy of impermeable approximation is that it shields, and may even reverse the direction of energy-momentum flux on the crack surface. The permeable crack model presented in this paper provides a leaky mode for an electrical field, allowing the applied electric field pass through the dielectric medium inside the crack. An in-depth analysis for a mode I permeable crack is presented in a recent paper by Li [37].

Based on the asymptotic analysis, a first-order approximation solution is obtained for a mode III crack in a permeable environment. The control parameters of the asymptotic analysis are the crack height, h_0, dielectric permittivity inside the crack, ϵ_0, and the crack width, a.

It has been found that the global energy release rate derived for a permeable crack is in broad agreement with the known experimental observations (e.g., [11,12]), which is in contrast with the local energy release rate criterion proposed by Gao et al. [13,14] according to the saturation-strip model. Nevertheless, for all practical purposes, it may be a good estimate that

$$J_l < J < J_g, \quad \text{or} \quad J_g < J < J_l \tag{105}$$

since the actual contour integral may has a path between Γ_l and Γ_g (see Fig. 3).

The global energy release rate derived here may be served as a fracture criterion for piezoelectric materials in general. This contribution reconciles the discrepancy between experimental observations and theoretic analyses without invoking any nonlinear theory, and it explains, by rigorous analysis, how an applied electric field affects crack growth in a piezoelectric ceramic through its interaction with the permeable environment surrounding the crack.

Acknowledgments

The author would like to acknowledge the support from the Senate Committee of Research at University of California (Berkeley) through the fund of BURNL-07427-11503-EGSLI.

References

[1] Pak, Y. E., 1990, "Crack Extension Force in a Piezoelectric Material," ASME J. Appl. Mech., **57**, pp. 647–653.
[2] Pak, Y. E., 1992, "Linear Electro-Elastic Fracture Mechanics of Piezoelectric Materials," Int. J. Fract., **54**, pp. 79–100.
[3] Li, S., Cao, W., and Cross, L. E., 1990, "Stress and Electric Displacement Distribution Near Griffith's Type III Crack Tips in Piezoceramics," Mater. Lett., **10**, pp. 219–222.
[4] Sosa, H. A., 1990, "Three-Dimensional Eigenfunction Analysis of a Crack in a Piezoelectric Material," Int. J. Solids Struct., **26**, pp. 1–15.
[5] Sosa, H. A., 1991, "Plane Problems in Piezoelectric Media With Defects," Int. J. Solids Struct., **28**, pp. 491–505.
[6] Suo, Z., Kuo, C.-M., Barnett, D. M., and Willis, J. R., 1992, "Fracture Mechanics for Piezoelectric Ceramics," J. Mech. Phys. Solids, **40**, pp. 739–765.
[7] Suo, Z., 1993, "Models for Breakdown-Resistant Dielectric and Ferroelectric Ceramics," J. Mech. Phys. Solids, **41**, pp. 1155–1176.
[8] Dunn, M. L., 1994, "The Effects of Crack Face Boundary Conditions on the Fracture Mechanics of Piezoelectric Solids," Eng. Fract. Mech., **48**, pp. 25–39.
[9] Dascalu, C., and Maugin, G. A., 1994, "Energy-Release Rates and Path-Independent Integrals in Electroelastic Crack Propagation," Int. J. Eng. Sci., **32**, pp. 755–765.
[10] Dascalu, C., and Maugin, G. A., 1995, "On the Electroelastic Fracture," ZAMP, **46**, pp. 355–365.
[11] Park, S., and Sun, C. T., 1995, "Fracture Criteria for Piezoelectric Ceramics," J. Am. Ceram. Soc., **78**, pp. 1475–1480.
[12] Park, S., and Sun, C. T., 1995, "Effect of Electric Field on Fracture of Piezoelectric Ceramics," Int. J. Fract., **70**, pp. 203–216.
[13] Gao, H., and Barnett, D. M., 1996, "An Invariance Property of Local Energy Release Rates in a Strip Saturation Model of Piezoelectric Fracture," Int. J. Fract., **44**, pp. R25–R29.
[14] Gao, H., Zhang, T.-Y., and Tong, P., 1997, "Local and Global Energy Release Rates for an Electrically Yielded Crack in a Piezoelectric Ceramic," J. Mech. Phys. Solids, **45**, pp. 491–510.
[15] Lynch, C. S., Yang, W., Suo, Z., and McMeeking, R. M., 1995, "Electric Field Induced Cracking in Ferroelectric Ceramics," Ferroelectrics, **166**, pp. 11–30.
[16] Lynch, C. S., Chen, L., Suo, Z., McMeeking, R. M., and Yang, W., 1995, "Crack Growth in Ferroelectric Ceramics Driven by Cyclic Polarization Switching," J. Intell. Mater. Syst. Struct., **6**, pp. 191–198.

[17] Zhang, T.-Y., and Hack, J. E., 1992, ''Mode-III Crack in Piezoelectric Materials,'' J. Appl. Phys., **71**, pp. 5865–5870.
[18] Fulton, C. C., and Gao, H., 2001, ''Effect of Local Polarization Switching on Piezoelectric Fracture,'' J. Mech. Phys. Solids, **49**, pp. 927–952.
[19] Ru, C. Q., Mao, X., and Epstein, M., 1998, ''Electric-Field Induced Interfacial Cracking in Multilayer Electrictive Actuators,'' J. Mech. Phys. Solids, **46**, pp. 1301–1318.
[20] Ru, C. Q., 1999, ''Effect of Electrical Polarization Saturation on Stress Intensity Factors in a Piezoelectric Ceramic,'' Int. J. Solids Struct., **36**, pp. 869–883.
[21] Yang, W., and Zhu, T., 1998, ''Fracture and Fatigue of Ferroelectric Under Electric and Mechanical Loading,'' Fatigue Fract. Eng. Mater. Struct., **21**, pp. 1361–1369.
[22] Yang, W., and Zhu, T., 1998, ''Switch-Toughening of Ferroelectric Subjected to Electric Field,'' J. Mech. Phys. Solids, **46**, pp. 291–311.
[23] Zhu, T., and Yang, W., 1997, ''Toughness Variation of Ferroelectrcs by Polarization Switch Under Non-uniform Electric Field,'' Acta Mater., **45**, pp. 4695–4702.
[24] Zhang, T.-Y., and Tong, P., 1996, ''Fracture Mechanics for a Mode III Crack in a Piezoelectric Material,'' Int. J. Solids Struct., **33**, pp. 343–359.
[25] Zhang, T.-Y., Qian, C.-F., and Tong, P., 1998, ''Linear Electro-Elastic Analysis of a Cavity or a Crack in a Piezoelectric Material,'' Int. J. Solids Struct., **35**, pp. 2121–2149.
[26] McMeeking, R. M., 1999, ''Crack Tip Energy Release Rate for a Piezoelectric Compact Tension Specimen,'' Eng. Fract. Mech., **64**, pp. 217–244.
[27] McMeeking, R. M., 2001, ''Towards a Fracture Mechanics for Brittle Piezoelectric and Dielectric Materials,'' Int. J. Fract., **108**, pp. 25–41.
[28] Zhang, T.-Y., Zhao, M., and Tong, P., 2001, ''Fracture of Piezoelectric Ceramics,'' *Advances in Applied Mechanics*, E. vsn der Giessen and T. Y. Wu, eds., Academic Press, San Diego, CA, **38**, pp. 147–289.
[29] Auld, B. A., 1973, *Acoustic Fields and Waves in Solids*, Vols. I and II. John Wiley and Sons, New York.
[30] Malvern, L. E., 1969, *Introduction to the Mechanics of af a Continuous Medium*, Prentice-Hall, Englewood Cliffs, NJ.
[31] Jackson, J. D., 1974, *Classical Electrodynamics*, John Wiley and Sons, New York.
[32] Erdély, A., Oberhettinger, F., Magnus, W., and Tricomi, F. G., 1954, *Tables of Integral Transforms. Based, in Part, on Notes Left by Harry Bateman*, Vols. 1–2, McGraw-Hill, New York.
[33] Lighthill, M. J., 1958, *Introduction to Fourier Analysis and Generalized Functions*, Cambridge University Press, Cambridge, UK.
[34] Yang, F., and Kao, I., 1999, ''Crack Problem in Piezoelectric Materials: General Anti-Plane Mechanical Loading,'' Mech. Mater., **31**, pp. 395–406.
[35] Cherepanov, G. P., 1979, *Mechanics of Brittle Fracture*, McGraw-Hill, New York.
[36] Mao, S. X., Li, X., and Han, X., 2000, ''Toughening of Ferroelectric Ceramics Under Polarization Switching,'' Mater. Sci. Eng., **A292**, pp. 66–73.
[37] Li, S., 2002, ''On Permeable Cracks in a Piezoelectric Ceramic. I. Global Energy Release Rate,'' submitted for publication.

The Bending of Curved Pipes With Variable Wall Thickness

V. P. Cherniy
Department of Strength and
Stability of Pipelines,
Scientific Research Institute of Natural Gases
and Gas Technologies,
VNIIGAZ,
Russian Joint Stock Company "GAZPROM",
Moscow 142085, Russia

A general solution is presented for the in-plane bending of short-radius curved pipes (pipe bends) which have variable wall thickness. Using the elastic thin-shell theory, the actual radius of curvature of the pipe's longitudinal fibers and displacement of the neutral line of the cross section under bending are taken into account. The pipe's wall thickness is assumed to vary smoothly along the contour of the pipe's cross section, and is a function of an angular coordinate. The solution uses the minimization of the total energy, and is compared to our previous solution for curved pipes with constant wall thickness.
[DOI: 10.1115/1.1546262]

Introduction

The classical theory for bending of curved pipes was developed by von Kármán [1] and by Clark and Reissner [2]. These works assumed that the actual curvature of longitudinal fibers of a curved pipe should not be taken into account, instead, this curvature was considered to be equal to the center line curvature. This assumption leads to an error in results if applied to pipes with a small radius of curvature. A solution taking the actual curvature of longitudinal fibers into account was developed by Cheng and Thailer [3,4].

All investigations of the bending of curved pipes rely on the assumption of constant wall thickness along the contour of the pipe's cross section. However, the majority of short-radius curved pipes are made using a forming process, and, as a result, have variable wall thickness along the contour of the pipe's cross section. The pipe wall is thinner than nominal on the convex side and is thicker on the concave one.

The problem of in-plane bending of curved short-radius pipe bends is solved in the present paper for pipes with variable wall thickness. The wall thickness is assumed to be a function of the angular coordinate of the pipe's cross section. The pipe has a plane of symmetry, and all aspects of the pipe are symmetric with respect to this plane, including the cross-sectional geometry. The actual curvature of longitudinal fibers of a curved pipe and displacement of the neutral line of cross section under bending are taken into account. The solution is based on the approach developed by the present author for pipes with constant wall thickness (Cherniy [5]). Relations familiar from the theory of thin elastic shells are used for the displacements, strains, and stresses. The solution uses the minimization of the total energy in the manner of Rayleigh-Ritz. The analysis applies to pipes which are made of an isotropic material and have a constant mean cross-sectional radius and a constant curvature of the center line. The obtained results for displacements, strains, and rigidity of these pipes are compared to the corresponding results for the similar pipes with constant wall thickness.

The presented solution is very important in terms of its practical applications. It presents a useful tool for evaluation of strain and rigidity of short-radius curved pipes with variable wall thickness as such pipes frequently arise during manufacture. Besides, it enables the development of new choices of cross sections for curved pipes allowing for their strength.

Contributed by the Applied Mechanics Division of THE AMERICAN SOCIETY OF MECHANICAL ENGINEERS for publication in the ASME JOURNAL OF APPLIED MECHANICS. Manuscript received by the ASME Applied Mechanics Division, Oct. 23, 2001; final revision, Sept. 25, 2002. Associate Editor: O. O'Reilly. Discussion on the paper should be addressed to the Editor, Prof. Robert M. McMeeking, Department of Mechanical and Environmental Engineering, University of California–Santa Barbara, Santa Barbara, CA 93106-5070, and will be accepted until four months after final publication of the paper itself in the ASME JOURNAL OF APPLIED MECHANICS.

Formulation of Problem

Figure 1 shows a curved, circular thin-walled pipe with a center line radius of curvature R and a mean cross-sectional radius r. Under pure in-plane bending of the pipe by the moments M, the central angle ψ has a change $\Delta\psi$. We assume that the pipe wall thickness is variable and depends on an angular coordinate β:

$$t(\beta)=(1-\gamma\cos\beta)t \qquad \gamma\geqslant 0. \tag{1}$$

In (1), γ represents the wall thickness variability factor. We assume that the maximum value of γ is considerably smaller than 1:

$$1\pm(1+\gamma)\frac{t}{r}\approx 1. \tag{2}$$

If Eq. (2) holds then the pipe obeys the assumptions of the theory of thin shells. Consequently, we consider the range $0\leqslant\gamma\leqslant 0.20$. This range of γ matches the tolerances for wall thickness of pipe bends as determined by existing standards (see [6]).

If we put $\gamma=0$ in (1), we obtain a curved pipe with constant wall thickness: $t=\text{const}$. This pipe is useful for comparison purposes. As for our pipe with variable wall thickness, it is only points with angular coordinates $\beta=\pm\pi/2$ (see (1)) that have wall thickness equal to t.

It is also worth noticing that this curved pipe with variable wall thickness has the same parameter of curved pipes $h=Rt/r^2$ as does a curved pipe with constant wall thickness (von Kármán [1]). It is necessary to say that the curved pipes of both types being compared have identical cross-sectional areas and identical moments of inertia relative to the axis going through the geometrical center of pipe cross section (assuming the wall thickness variation (1)).

The points on the middle line of the pipe's cross section are specified by the radius r and angular coordinate β. The OY vertical axis lies in the plane of the pipe's axis of curvature and goes through the middle-line cross-sectional curvature center O. The vertical coordinate of points on the middle line of the cross section is

$$y=r\cos\beta. \tag{3}$$

The deformation of a cross section is accompanied by a radial displacements w and tangential displacements v of points on the cross section's middle line (Fig. 1) as well as by vertical displacements (parallel to the OY-axis) w_y of the same points. The following geometrical formula describes their relationship:

$$w_y=w\cos\beta-v\sin\beta. \tag{4}$$

Further, we determine the displacements, strains, and rigidity of the curved pipe in question.

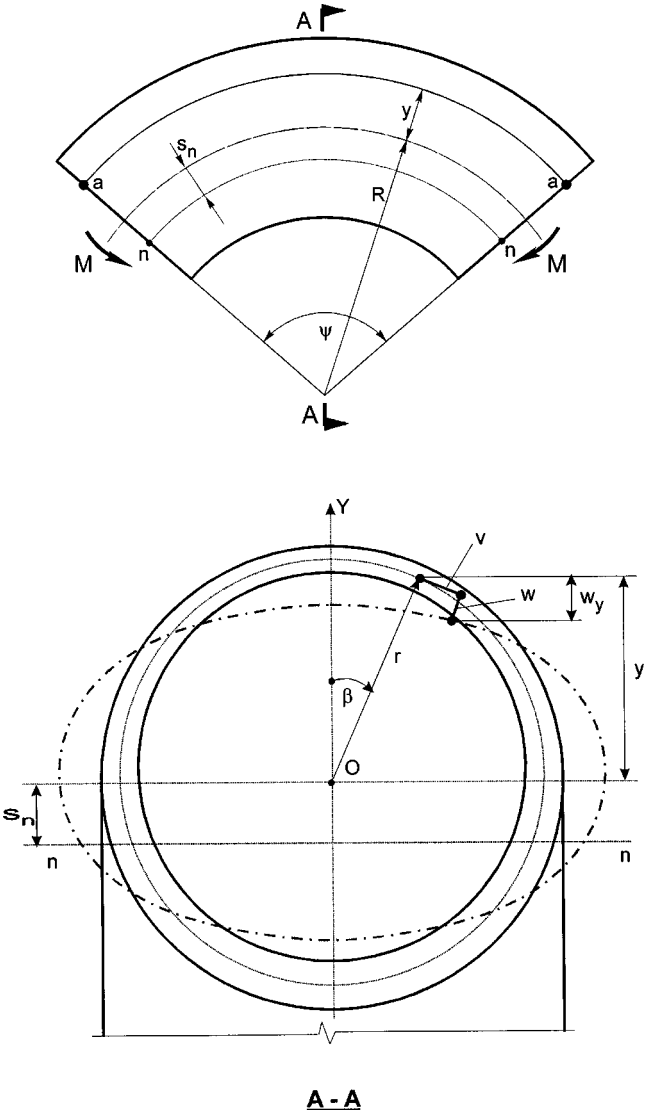

Fig. 1 Bending of a curved circular pipe with variable wall thickness

Longitudinal Strains

Here, we write down formulas for longitudinal strains and rigidity factor so that a straight pipe with the same radius of cross section r and with constant wall thickness t is used for comparison. Both pipes (curved and straight) are assumed to have identical lengths.

In [5], it was shown that the longitudinal strain ε_1 of any filament $a-a$ which lies on the median surface of a curved pipe and has an angular coordinate β (see Fig. 1) may be represented as a sum:

$$\varepsilon_1=\frac{1}{K}\frac{s_n+y}{R+y}(\kappa_0 r)+\frac{w_y}{R+y}; \tag{5}$$

where

$$\kappa_0=M/EI, \tag{6}$$

and EI, κ_0 are the straight pipe's rigidity under bending and curvature change of the straight pipe, respectively; K is rigidity factor of the curved pipe, and s_n is the displacement of the neutral line $n-n$ from the central line of the cross section (see Fig. 1).

The first part of formula (5) is the so-called "bar" component of the longitudinal strains. The second part of formula (5) is the strain caused by the flattening of cross-sectional contours of the curved pipe. It is necessary to point out that the neutral line used here refers to the bar component of the longitudinal strains.

The rigidity factor K of the curved pipe is determined as the ratio of the angle change $(\Delta\psi)_0$ in the straight pipe to the central angle change $(\Delta\psi)$ in the curved pipe under bending by identical moments M:

$$K=\frac{(\Delta\psi)_0}{\Delta\psi}. \tag{7}$$

The radial components w of displacements are assumed to have a power series expansion:

$$w=(\kappa_0 r^2)\sum_{n=2}^{\infty} X_n\cos n\beta, \tag{8}$$

where X_n are unknown coefficients.

The expression for tangential displacements v may be obtained using the thin-shell theory hypothesis of inextensibility of the middle surface in the meridional direction:

$$\frac{\partial v}{\partial\beta}+w\approx 0. \tag{9}$$

From (8) and (9), it follows that

$$v=-(\kappa_0 r^2)\sum_{n=2}^{\infty} n^{-1}X_n\sin n\beta. \tag{10}$$

Using (4), (8), and (10), the representation (5) for longitudinal strains may be rewritten as

$$\varepsilon_1=(1+\lambda\cos\beta)^{-1}\left[\frac{1}{K}(s+\cos\beta)+\frac{1}{2}\frac{r}{R}\sum_{n=2}^{\infty} X_n w_n^*\right](\kappa_0 r), \tag{11}$$

where

$$\lambda=r/R,\quad s=s_n/r, \tag{12}$$

$$w_n^*=\frac{n+1}{n}\cos(n-1)\beta+\frac{n-1}{n}\cos(n+1)\beta. \tag{13}$$

A relative displacement of the neutral line s and rigidity factor K can be found from the static equilibrium conditions:

$$N=Ert\int_0^{2\pi}(1-\gamma\cos\beta)\varepsilon_1 d\beta=0, \tag{14}$$

$$M=Ert\int_0^{2\pi}(1-\gamma\cos\beta)\varepsilon_1 y\,d\beta. \tag{15}$$

Using the following formula (see [5])

$$\int_0^{2\pi}\frac{\cos n\beta}{1+\lambda\cos\beta}d\beta=(-1)^n\frac{2e^n}{a}\pi,\quad n=0,1,2,3,\ldots;\quad \lambda<1, \tag{16}$$

where

$$e=\frac{1}{\lambda}(1-\sqrt{1-\lambda^2}),\quad (\lambda<1), \tag{17}$$

$$a=1-\lambda e, \tag{18}$$

and also using (14) and (15), we obtain formulas for the relative displacements s of the neutral line and the rigidity factor K, correspondingly,

$$s=K_{1\gamma}\left(1+\frac{1}{2}K\frac{r}{R}\sum_{n=2}^{\infty} C_n X_n\right), \tag{19}$$

$$K=\left(aK_{2\gamma}-\frac{1}{2}\frac{r}{R}\sum_{n=2}^{\infty} D_nX_n\right)^{-1}. \tag{20}$$

The following designations are used in (19) and (20):

$$C_n=(-1)^n\frac{1}{n}e^{n-2}[(n+1)+(n-1)e^2], \tag{21}$$

$$D_n=K_{2\gamma}(K_{3\gamma}C_n-\gamma I_{1n}), \tag{22}$$

$$K_{1\gamma}=\frac{2e+\gamma(1+e^2)}{2(1+\gamma e)}, \tag{23}$$

$$K_{2\gamma}=\left\{(1+e^2-2eK_{1\gamma})-\gamma\left[(1+e^2)K_{1\gamma}-\frac{1}{2}e(3+e^2)\right]\right\}^{-1}, \tag{24}$$

$$K_{3\gamma}=(1+e^2)(1-\gamma K_{1\gamma})-2eK_{1\gamma}, \tag{25}$$

$$I_{1n}=-\frac{e}{a}C_n-(-1)^n\frac{1}{2an}[(n+1)(e^{n+1}+e^{|n-3|}) +(n-1)(e^{n+3}+e^{n-1})]. \tag{26}$$

Then, we obtain the following formula for the longitudinal strain ε_1:

$$\varepsilon_1=(1+\lambda\cos\beta)^{-1}\left\{aK_{2\gamma}(K_{1\gamma}+\cos\beta) +\frac{1}{2}\frac{r}{R}\sum_{n=2}^{\infty}[(E_n-D_n\cos\beta+w_n^*)X_n]\right\}, \tag{27}$$

where

$$E_n=K_{1\gamma}(C_n-D_n). \tag{28}$$

The result (27) is used below in the solution of the problem. If we put $\gamma=0$ for all the coefficients in (27), we arrive at the expression for strains which is obtained in paper [5] for curved pipes with constant wall thickness.

Determination of the Unknown Coefficients X_n

The coefficients X_n of the series (8) are determined through the minimization of the total energy V

$$V=U-W, \tag{29}$$

where U is strain energy, and W is the work done by the end moments.

The strain energy is

$$U=\int_F\left(\frac{1}{2}N_1\varepsilon_1+\frac{1}{2}M_2\kappa_2\right)dF =\frac{1}{2}r(R\psi)\int_0^{2\pi}(1+\lambda\cos\beta) \times[E(1-\gamma\cos\beta)t\varepsilon_1^2+(1-\gamma\cos\beta)^3D\kappa_2^2]d\beta, \tag{30}$$

where $N_1=(1-\gamma\cos\beta)tE\varepsilon_1$ and $M_2=(1-\gamma\cos\beta)^3D\kappa_2$ are the longitudinal force and bending moment in a meridional direction accordingly in a curved pipe as in a shell, $D=Et^3/12(1-\nu^2)$ is the flexural rigidity of the shell with the constant wall thickness t, F is the area of the median surface of a curved pipe, ε_1 is the longitudinal strain, κ_2 is the curvature change of the middle line of pipe cross section, and ν is Poisson's ratio.

To determine the work done by the end moments, we take into account the relationship between the central angle of the curved pipe and the central angle change (this relationship was obtained in [5]):

$$\frac{\Delta\psi}{\psi}=\frac{R}{r}\frac{1}{K}(\kappa_0 r). \tag{31}$$

Then, in view of (20), we obtain

$$W=-M*\Delta\psi=-\kappa_0^2EI(R\psi)\left(aK_{2\gamma}-\frac{1}{2}\frac{r}{R}\sum_{n=2}^{\infty}D_nX_n\right). \tag{32}$$

The curvature change of the middle line κ_2 is determined using the theory of shells, as in von Kármán's work, [1],

$$\kappa_2=-\frac{1}{r^2}\left(\frac{d^2}{d\beta^2}+1\right)w. \tag{33}$$

If (8) is taken into account then

$$\kappa_2=\kappa_0\sum_{n=2}^{\infty}(n^2-1)X_n\cos n\beta. \tag{34}$$

The minimum of the total energy may be obtained in the Rayleigh-Ritz manner if

$$\frac{\partial V}{\partial X_n}=0. \tag{35}$$

Substituting (30) and (32) into (29), integrating it, and meeting the requirements (35), we get an infinite system of linear equations which describes the unknown coefficients:

$$a_{n,n}X_n+\sum_{\substack{i=2\\ i\neq n}}^{\infty}a_{n,i}X_i=b_n, \quad n=2,3,4,\ldots. \tag{36}$$

We used the formula (16) for while integrating (29). The coefficients $a_{n,n}$, $a_{n,i}$, and free terms b_n in the set of Eq. (36) are determined by the following expressions:

$$a_{n,n}=4\left\langle U_{n,n}^*+\left\{1-\frac{3}{2}\gamma\left[(\lambda-\gamma)+\frac{1}{4}\lambda\gamma^2\right]-\frac{9}{16}\lambda\gamma^3\delta_{2n}\right\} \times\frac{(n^2-1)^2}{3(1-\nu^2)}h^2\right\rangle,$$

$$a_{n,i}=4U_{n,i}^*+\frac{2}{3(1-\nu^2)}(n^2-1)(i^2-1)h^2\sum_{k=1}^{4}A_{\lambda\gamma k}\delta_{i(n\pm k)}, \tag{37}$$

$$b_n=-8\frac{R}{r}(U_{bn}^*+D_n)\cong-8\frac{R}{r}D_n.$$

The following designations are used in (37):

$$U_{n,n}^*=a^{-1}\left\{I_{2n}-2eC_nE_n-2(1+e^2)C_nD_n+2E_n^2+4eE_nD_n +(1+e^2)D_n^2-\gamma\left[I_{3n}-2D_nI_{1n}+2(1+e^2)K_{1\gamma}^{-1}E_n^2 -2e\left(E_n^2+\frac{3+e^2}{4}D_n^2\right)\right]\right\}, \tag{38}$$

$$U_{n,i}^*=a^{-1}\left\langle A_{ni}+2(1-2eK_{1\gamma}^{-1})E_nE_i -(1+e^2)(K_{1\gamma}^{-1}D_nE_i-C_nD_i) -\gamma\left\{B_{ni}+2[(1+e^2)K_{1\gamma}^{-1}-e]E_nE_i -\frac{1}{2}e(3+e^2)D_nD_i-I_{1n}D_i-D_nI_{1i}\right\}\right\rangle, \tag{39}$$

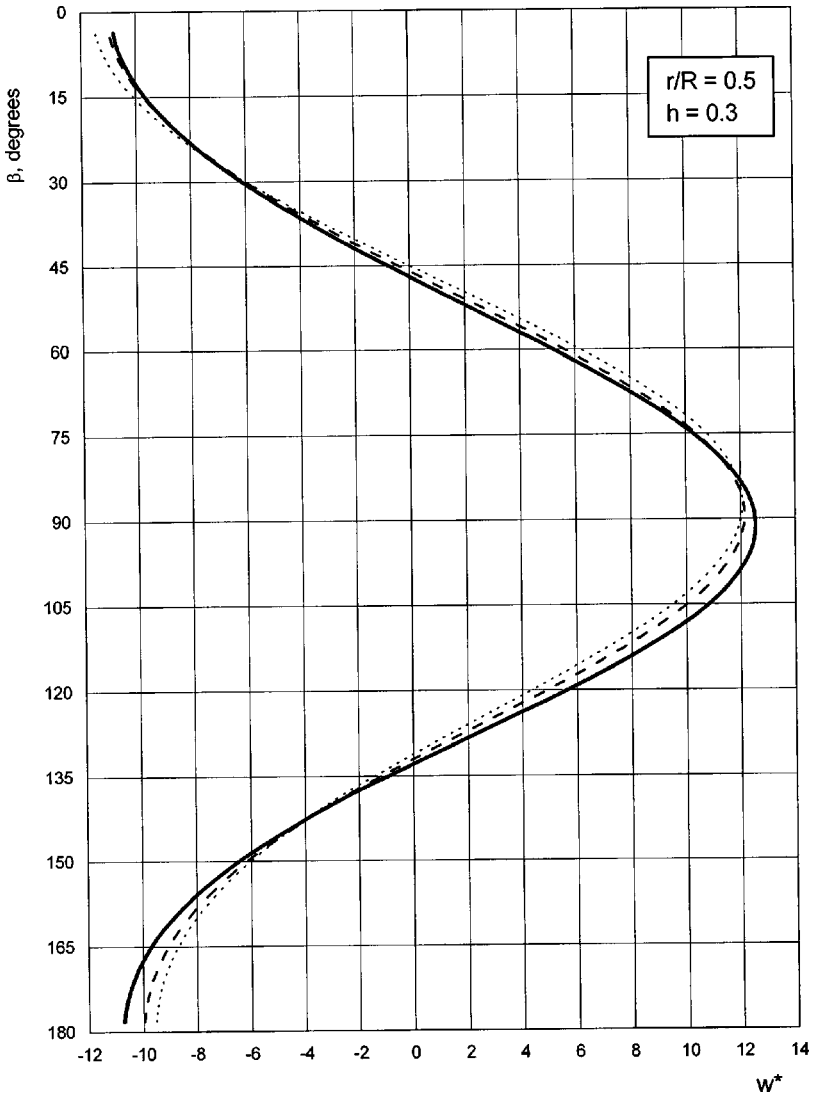

Fig. 2 Radial displacements distribution; (*a*) γ=0 (solid line), (*b*) γ=0.1 (dashed line), (*c*) γ=0.2 (dotted line)

$$U^*_{bn}=K_{2\gamma}\left\{[2K_{1\gamma}+(1+e^2)K^{-1}_{1\gamma}-4e]E_n - \gamma\left(\frac{3+e^2}{2}D_n-2eK_{1\gamma}E_n+I_{1n}\right)\right\}\approx 0, \tag{40}$$

$$\delta_{2n}=\begin{cases}1 & (n=2)\\ 0 & (n\neq 2)\end{cases} \qquad \delta_{i(n\pm k)}=\begin{cases}1 & (i=n\pm k)\\ 0 & (i\neq n\pm k)\end{cases}. \tag{41}$$

In (38) and (39), the designation a is used as it was defined in (18).

The coefficients $A_{\lambda\gamma k}(k=\overline{1,4})$ are determined by the following expressions:

$$\begin{aligned} A_{\lambda\gamma 1}&=\lambda-3\gamma\left[1-\frac{3}{4}\gamma(\lambda-\gamma)\right],\\ A_{\lambda\gamma 2}&=-\frac{1}{2}\gamma[\lambda\gamma^2+3(\lambda-\gamma)],\\ A_{\lambda\gamma 3}&=\frac{3}{4}\gamma^2(\lambda-\gamma),\\ A_{\lambda\gamma 4}&=-\frac{1}{8}\lambda\gamma^3. \end{aligned} \tag{42}$$

The following designations are used in (38):

$$I_{2n}=(1+e^{2n-2})\left(1+2\frac{n-1}{n+1}e^2\right)\left(\frac{n+1}{n}\right)^2+(1+e^{2n+2})\left(\frac{n-1}{n}\right)^2, \tag{43}$$

$$I_{3n}=-\frac{e}{2n^2}\langle[2+(1+e^2)e^{2n-4}](n+1)^2+(1+e^2)(1+e^{2n-2}) \times(n^2-1)+[2+(1+e^2)e^{2n}](n-1)^2\rangle. \tag{44}$$

The results for D_i, E_i, I_{1i} are made according to the corresponding formulas for D_n, E_n, I_{1n} where n is replaced with i.

There are also formulas for other members of (39):

$$A_{ni}=\frac{(-1)^{n-i}}{ni}\sum_{k=1}^{2}(K_A)_{nk}(u_A)_{nik}, \tag{45}$$

$$(K_A)_{nk}=n-2k+3, \tag{46}$$

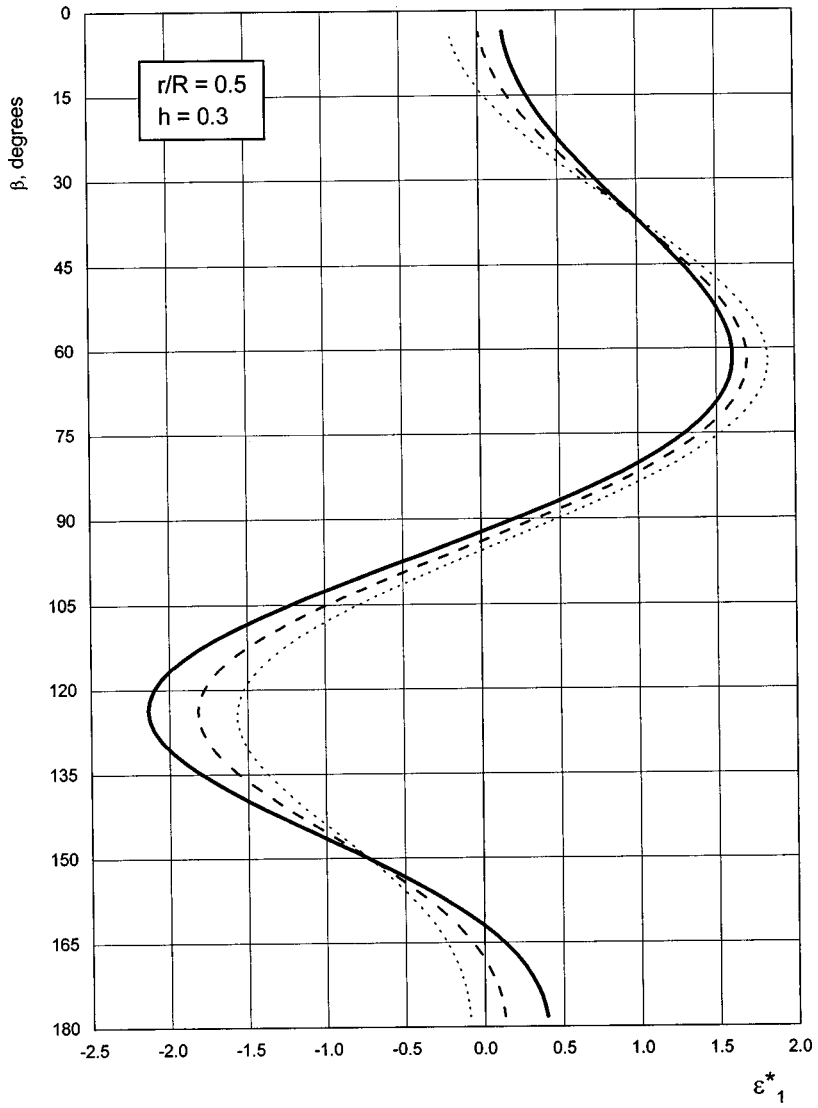

Fig. 3 Longitudinal strain distribution; (*a*) $\gamma=0$ (solid line), (*b*) $\gamma=0.1$ (dashed line), (*c*) $\gamma=0.2$ (dotted line)

$$(u_A)_{nik}=(i+1)\lfloor e^{n+i+2(k-2)}+e^{|n-i+2(k-1)|}\rfloor + (i-1)\lfloor e^{n+i+2(k-1)}+e^{|n-i+2(k-2)|}\rfloor, \quad (47)$$

$$B_{ni}=\frac{(-1)^{n-i}}{2ni}\sum_{k=1}^{2}(K_B)_{nk}(u_B)_{nik}, \quad (48)$$

$$(K_B)_{nk}=-2(n-1)+(4n-1)k-nk^2, \quad (49)$$

$$(u_B)_{nik}=(i+1)\lfloor e^{n+i+(2k-5)}+e^{|n-i+(2k-3)|}\rfloor + (i-1)\lfloor e^{n+i+(2k-3)}+e^{|n-i+(2k-5)|}\rfloor. \quad (50)$$

The infinite system of linear Eq. (36) was solved by the method of sections. In the infinite series (8), a finite number of terms was omitted. Then, the infinite system of linear Eq. (36) was solved as a finite system using Cramer's Rule.

Results and Discussion

The results of the solution for curved pipes with variable wall thickness are presented below. The diagrams are drawn for the basic parameters of curved pipe bending. All diagrams are plotted for curved pipes with $h=0.3$, $\lambda=0.5$. The calculations are made for three values of the parameter γ: $\gamma=0$ (curved pipe with constant wall thickness), $\gamma=0.1$, and $\gamma=0.2$. In the infinite series (8) eight terms with $n=\overline{2,9}$ have been left. To estimate the preciseness of the calculations, the change in cross-sectional middle line curvature is used (34). A ratio of absolute values of the last term in the series (34) to the first term does not exceed 0.1 percent for the presented calculations.

The radial displacements in cross section of the curved pipe are presented in Fig. 2. Dimensionless parameter of the radial displacement is obtained from (8):

$$w^*=\frac{w}{\kappa_0 r^2}=\sum_{n=2}^{\infty}X_n\cos n\beta. \quad (51)$$

The general relationship of changes in radial displacements remains the same for the three values of γ which are given above. However, the increase of displacements in the thinner cross section zone (at $\beta\approx 0$), as well as the decrease of displacements in the thicker zone (at $\beta\approx\pi$), is observed when γ increases. The differences in values of the radial displacements for curved pipes with various γ are small. The maximum difference is observed when the value of angular coordinate $\beta=\pi$. In this case, the difference is equal to 13%.

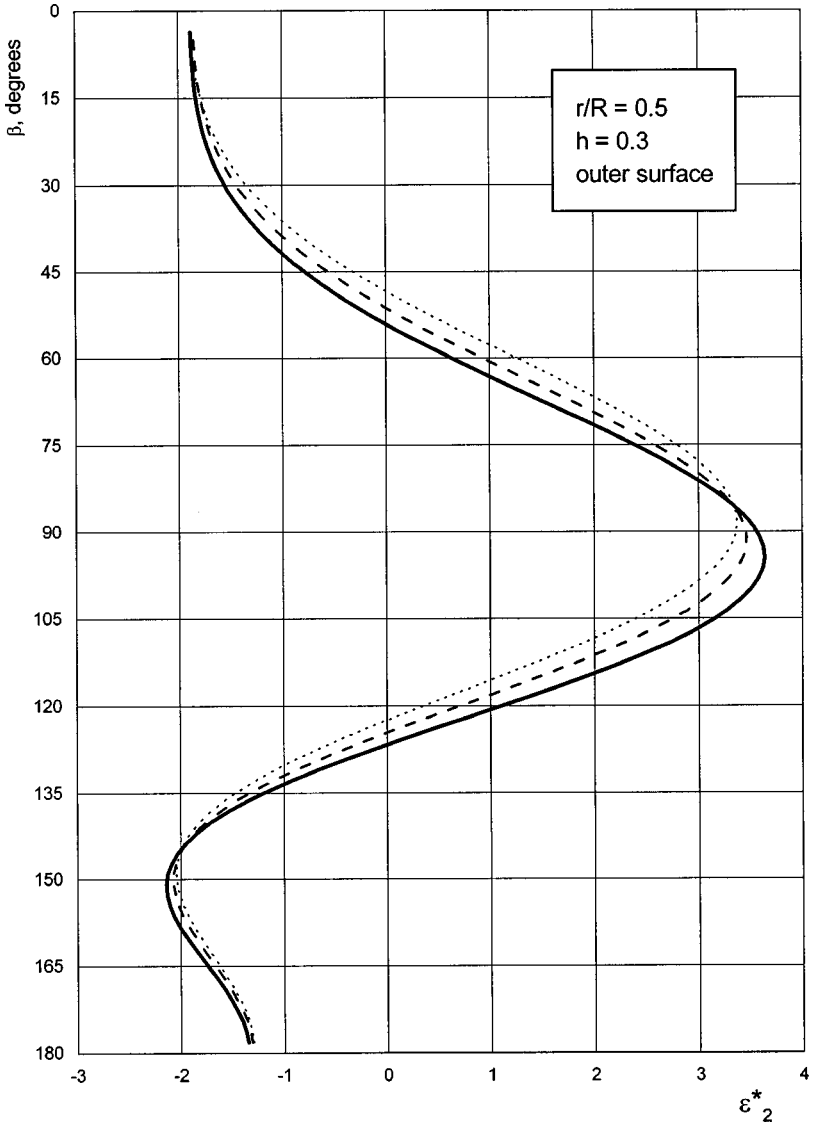

Fig. 4 Meridional bending strain distribution; (*a*) γ=0 (solid line), (*b*) γ=0.1 (dashed line), (*c*) γ=0.2 (dotted line)

More substantial differences are observed for the longitudinal strains. Figure 3 presents the distributions for the parameter ε_1^* of longitudinal strains:

$$\varepsilon_1^* = \frac{\varepsilon_1}{\kappa_0 r}. \tag{52}$$

The longitudinal strain ε_1 in (52) is calculated using (26).

The graphs in Fig. 3 demonstrate that the convex (thinner) part of the cross section (under the bending of curved pipe with variable wall thickness) is deformed more and the concave (thicker) part of the cross section is deformed less when compared with a curved pipe of constant wall thickness. At the extreme points of the cross section (β=0 and $\beta=\pi$), even a change in sign for the values of the longitudinal strain is observed. An increase of the neutral line displacement is also observed as γ increases.

The meridional bending strains are determined according to the expression for the curvature change of the middle-line of the cross section (34):

$$\varepsilon_2 = \pm\frac{1}{2}(1-\gamma\cos\beta)h\frac{r}{R}\kappa_0 r\sum_{n=2}^{\infty}(n^2-1)X_n\cos n\beta. \tag{53}$$

The top mark in (53) refers to the outer surface of the pipe, and the bottom mark refers to the inner surface.

Results for the meridional bending strain $\varepsilon_2^* = \varepsilon_2/\kappa_0 r$ (for the outer surface of the pipe's cross section) are presented in Fig. 4. In the same way, the meridional strains increase in the thinner zone and decrease in the thicker zone (in comparison with the curved pipe with constant wall thickness).

Figure 5 demonstrates the change in the relative values of the basic parameters of curved pipe depending on the wall thickness variability factor (γ). These parameters describe the stress and strain state of curved pipes. The graphs for radial displacements and meridional strains show their maximum (in magnitude) values. The diagrams for longitudinal strains present the maximum (in magnitude) values of longitudinal strains in the concave part of curved pipes. The corresponding values of these parameters in the curved pipe with constant wall thickness (γ=0) are used as datum values (representing 100%).

The relative displacement of the neutral line *s* and the rigidity factor *K* are determined according to (19) and (20). The analysis of the graphs in Fig. 5 reveals that the parameter γ mostly influ-

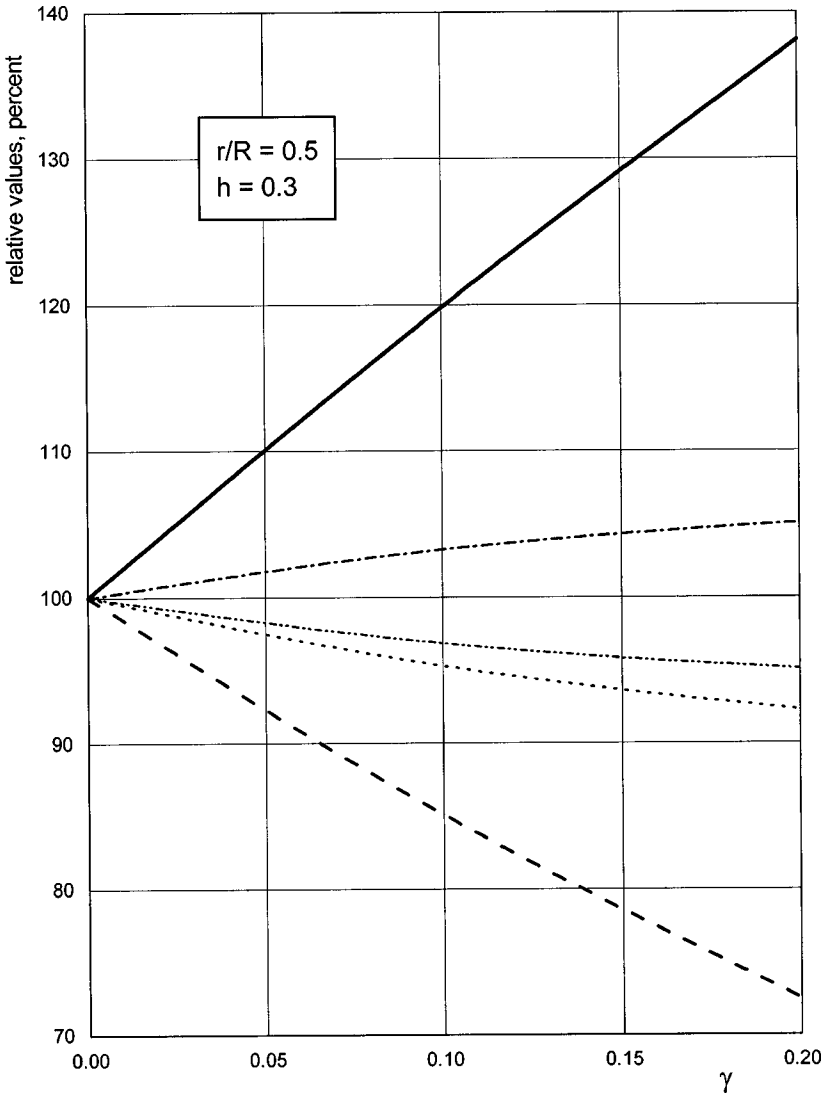

Fig. 5 Diagrams of change in the relative values of basic parameters of a curved pipe depending on the wall thickness variability factor γ; (*a*) *s* (solid line), (*b*) $|\varepsilon_1|_{max}$ (in the concave part of the curved pipe) (dashed line), (*c*) $|\varepsilon_2|_{max}$ (dotted line), (*d*) *K* (dash-dot line), (*e*) $|w|_{max}$ (dash-dot-dot line)

ences the neutral line displacements and longitudinal strains. The meridional strains, rigidity factor and radial displacements are less influenced by γ.

The wall thickness variability in short-radius curved pipes is determined by the technology of pipe production. In the design of pipeline systems, this circumstance is considered as a constructional shortcoming. The analysis of the diagrams in Fig. 5 shows that under bending, a curved pipe with variable wall thickness is a somewhat more rational structure than a curved pipe with constant wall thickness. The curved pipe with variable wall thickness has substantially smaller longitudinal strains while its rigidity is increasing insignificantly.

It should be pointed out that the results of the presented solution for curved pipes with $\gamma=0$ are completely consistent with the solution for curved pipe with constant wall thickness given in paper [5] where the actual radius of curvature of longitudinal fibers and the displacement of the neutral line are taken into account.

Conclusions

The general solution is presented for in-plane bending of short-radius curved pipes (pipe bends) with variable wall thickness. Using elastic thin-shell theory, the actual curvature radius of longitudinal fibers of the pipe as well as the displacement of the neutral line of cross section under bending are taken into account.

Results are presented for the basic parameters which describe the stress and strain state of curved pipes as functions of wall thickness variability factor γ. Increasing γ considerably influences the values of longitudinal strains and displacement of the neutral line. While, the displacements of points on the middle line of the cross section, the meridional strains and rigidity of curved pipe under bending are influenced to a lesser extent.

References

[1] Von Kármán, Th., 1911, "Über die Formänderung dünnwandiger Rohre, insbesondere federnder Ausgleichrohre," Z. Ver. Deut. Ing., **55**, pp. 1889–1895.

[2] Clark, R. A., and Reissner, E., 1951, "Bending of Curved Tubes," *Advances in Applied Mechanics*, Vol. II, Academic Press, San Diego, pp. 93–122.

[3] Cheng, D. H., and Thailer, H. J., 1968, "In-Plane Bending of Curved Circular Tubes," J. Eng. Ind., **90**(4), pp. 666–670.

[4] Cheng, D. H., and Thailer, H. J., 1970, "On Bending of Curved Circular Tubes," J. Eng. Ind., Series B, **92**(1), pp. 62–66.

[5] Cherniy, V. P., 2001, "Effect of Curved Bar Properties on Bending of Curved Pipes," ASME J. Appl. Mech., **68**, pp. 650–655.

[6] ASME B16.28. Wrought Steel Butt-Welding Short Radius Elbows and Returns.

Green's Functions for Infinite and Semi-infinite Anisotropic Thin Plates

Z.-Q. Cheng
Research Associate

J. N. Reddy
Distinguished Professor,
Fellow ASME

Department of Mechanical Engineering,
Texas A&M University,
College Station, TX 77843-3123

This paper presents fundamental solutions of an anisotropic elastic thin plate within the context of the Kirchhoff theory. The plate material is inhomogeneous in the thickness direction. Two systems of problems with non-self-equilibrated loads are solved. The first is concerned with in-plane concentrated forces and moments and in-plane discontinuous displacements and slopes, and the second with transverse concentrated forces. Exact closed-form Green's functions for infinite and semi-infinite plates are obtained using the recently established octet formalism by the authors for coupled stretching and bending deformations of a plate. The Green functions for an infinite plate and the surface Green functions for a semi-infinite plate are presented in a real form. The hoop stress resultants are also presented in a real form for a semi-infinite plate. [DOI: 10.1115/1.1533806]

Introduction

A plate is one of the most common type of structural elements encountered in mechanical, civil, and aerospace engineering structures. Among numerous existing two-dimensional theories for modeling deformations of a thin plate element, the Kirchhoff plate theory is the most classic and celebrated model in which a transverse normal before deformation remains normal to the midplane of the plate during deformation, [1–3]. In many cases stretching and bending deformations are coupled, an important example is a laminated plate with unsymmetric lay-up, [4].

Green's functions are useful, for example, in constructing a general solution and in boundary element and boundary integral equation methods. Study on Green's functions has been one of the important topics in structural mechanics. The complex function method was used to study the fundamental solutions for anisotropic laminates with coupled bending and stretching under concentrated loads, [5,6], and under discontinuous in-plane displacements and slopes, [7], respectively. Their studies considered an infinitely extended plate and the solutions were given in a complex form and needed further numerical evaluations.

Based on the work of Eshelby et al. [8], Stroh [9,10] developed a sextic formalism for generalized plane-strain deformations of an anisotropic elastic material. The Stroh formalism is mathematically elegant and technically power. Ting [11,12] has made an extensive review of the Stroh sextic formalism and its applications. Recently, a new octet formalism has been proposed by Cheng and Reddy [13] for the Kirchhoff anisotropic plates. This formalism symbolically preserves extensive elegant properties and identities that have been established in the Stroh sextic formalism.

As one of powerful applications of the new octet formalism for an anisotropic thin plate, the problem of Green's functions is addressed in this investigation. As was done in [5,6], the problem is first classified into three systems according to the types of concentrated loads and discontinuous displacements and slopes. We then define the three systems of problems in terms of stress functions. The first two are solved for an infinite plate by using the new formalism. Although the second system of problem we have defined is different from the one defined by Becker [5] and Zakharov and Becker [6], we are able to show that our fundamental solution also satisfies the system of equations defined therein. This is helpful for clarifying the equivalency of the solutions to two systems of problems that are posed differently. The solutions for an infinitely plate are modified to give new exact fundamental solutions for a semi-infinite plate with a rigidly clamped edge or a free edge. The surface Green's functions are obtained in a special case. Using some elegant properties established in the formalism, the Green functions for infinite plates, surface Green functions and hoop stress resultants for a semi-infinite plate are converted into a real and closed form without solving for the eigenvalues and eigenvectors. Unlike the previous work, [5–7], that were developed only for an infinite plate made of a nondegenerate material, the present real form results apply to plates made of a degenerate material as discussed in Ref. [13], including an isotropic material as well.

Contributed by the Applied Mechanics Division of THE AMERICAN SOCIETY OF MECHANICAL ENGINEERS for publication in the ASME JOURNAL OF APPLIED MECHANICS. Manuscript received by the Applied Mechanics Division, Jan. 29, 2002; final revision, July 23, 2002. Associate Editor: D. A. Kouris. Discussion on the paper should be addressed to the Editor, Prof. Robert M. McMeeking, Chair, Department of Mechanics and Environmental Engineering, University of California–Santa Barbara, Santa Barbara, CA 93106-5070, and will be accepted until four months after final publication in the paper itself in the ASME JOURNAL OF APPLIED MECHANICS.

Octet Formulation for Anisotropic Thin Plates

In this section, we first recapitulate the basic Kirchhoff plate theory and the new formalism for an anisotropic plate. Let an undeformed plate of uniform thickness h be considered in a Cartesian coordinate system $\{x_i\}$ $(i=1,2,3)$ and its midplane is at $x_3=0$. The plate is composed of an anisotropic, linearly elastic material that can be inhomogeneous in the thickness direction. Accordingly, it includes the important special cases of laminated cross-ply and angle-ply plates. A comma followed by a subscript α denotes the partial derivative with respect to x_α. A repeated index implies, unless otherwise specified, summation over the range of the index with Greek indices ranging from 1 to 2, lowercase Latin indices from 1 to 3, and uppercase Latin indices from 1 to 4.

The displacement field in the Kirchhoff plate theory is assumed as

$$\tilde{u}_\alpha(x_i)=u_\alpha+x_3\vartheta_\alpha, \quad \tilde{u}_3(x_i)=w, \tag{1}$$

where u_α, w and $\vartheta_\alpha=-w_\alpha$ are independent of x_3. The strain and stress components are obtained from

$$e_{\alpha\beta}=\tfrac{1}{2}(\tilde{u}_{\alpha,\beta}+\tilde{u}_{\beta,\alpha}), \quad \sigma_{\alpha\beta}=\tilde{C}_{\alpha\beta\omega\rho}e_{\omega\rho}, \tag{2}$$

where the reduced elasticity tensor is

$$\tilde{C}_{\alpha\beta\omega\rho}=C_{\alpha\beta\omega\rho}-C_{\alpha\beta33}C_{33\omega\rho}/C_{3333}. \tag{3}$$

The membrane stress resultants $\mathcal{N}_{\alpha\beta}$, bending moments $\mathcal{M}_{\alpha\beta}$, and transverse shearing forces $\mathcal{R}_\beta$ are defined by

$$\mathcal{N}_{\alpha\beta}=\mathcal{Q}\sigma_{\alpha\beta}, \quad \mathcal{M}_{\alpha\beta}=\mathcal{Q}x_3\sigma_{\alpha\beta}, \quad \mathcal{R}_\beta=\mathcal{M}_{\alpha\beta,\alpha}, \tag{4}$$

"with the integral operator

$$\mathcal{Q}(\cdots)=\int_{-h/2}^{h/2}(\cdots)dx_3. \tag{5}$$

The modified Kirchhoff transverse shearing forces that exclusively apply to free edges are

$$\mathcal{V}_1=\mathcal{R}_1+\mathcal{M}_{12,2},\quad \mathcal{V}_2=\mathcal{R}_2+\mathcal{M}_{21,1}. \tag{6}$$

In the absence of external loads on the top and bottom surfaces of the plate, the equilibrium equations are given by

$$\mathcal{N}_{\alpha\beta,\beta}=0,\quad \mathcal{R}_{\beta,\beta}=0. \tag{7}$$

If the displacements on the midplane of the plate are assumed in the following form

$$u_\alpha=a_\alpha f(z),\quad w=-a_3\int f(z)dz, \tag{8}$$

where f is an arbitrary function of $z=x_1+px_2$, and p and a_i are unknown constants to be determined, the equilibrium equations in (7) can be reduced to, [13],

$$\begin{bmatrix}\mathcal{Q}\mathcal{C} & \mathcal{Q}x_3\mathcal{C}\tilde{\mathbf{p}}\\ \tilde{\mathbf{p}}^T\mathcal{Q}x_3\mathcal{C} & \tilde{\mathbf{p}}^T\mathcal{Q}x_3^2\mathcal{C}\tilde{\mathbf{p}}\end{bmatrix}\begin{bmatrix}a_1\\a_2\\a_3\end{bmatrix}=\begin{bmatrix}0\\0\\0\end{bmatrix}, \tag{9}$$

where

$$\tilde{\mathbf{p}}^T=[1\ \ p],\quad \mathcal{C}=\tilde{\mathbf{Q}}+p(\tilde{\mathbf{R}}+\tilde{\mathbf{R}}^T)+p^2\tilde{\mathbf{T}}, \tag{10}$$

the components of the 2×2 matrices $\tilde{\mathbf{Q}}$, $\tilde{\mathbf{R}}$, and $\tilde{\mathbf{T}}$ are

$$\tilde{Q}_{\alpha\omega}=\tilde{C}_{\alpha1\omega1},\quad \tilde{R}_{\alpha\omega}=\tilde{C}_{\alpha1\omega2},\quad \tilde{T}_{\alpha\omega}=\tilde{C}_{\alpha2\omega2}. \tag{11}$$

$\tilde{\mathbf{Q}}$ and $\tilde{\mathbf{T}}$ are symmetric and positive definite. For a nontrivial solution of $[a_1\ a_2\ a_3]^T$, the vanishing determinant of the coefficient matrix of (9) provides four pairs of complex conjugates for the eigenvalue p.

Let us introduce

$$\hat{\mathbf{a}}=\begin{bmatrix}a_1\\a_2\end{bmatrix},\quad \check{\mathbf{a}}=\begin{bmatrix}a_3\\a_4\end{bmatrix},\quad \hat{\mathbf{b}}=\begin{bmatrix}b_1\\b_2\end{bmatrix},\quad \check{\mathbf{b}}=\begin{bmatrix}b_3\\b_4\end{bmatrix}, \tag{12}$$

such that

$$\begin{bmatrix}-p\hat{\mathbf{b}}\\ \hat{\mathbf{b}}\end{bmatrix}=\begin{bmatrix}\mathcal{Q}(\tilde{\mathbf{Q}}+p\tilde{\mathbf{R}}) & \mathcal{Q}x_3(\tilde{\mathbf{Q}}+p\tilde{\mathbf{R}})\\ \mathcal{Q}(\tilde{\mathbf{R}}^T+p\tilde{\mathbf{T}}) & \mathcal{Q}x_3(\tilde{\mathbf{R}}^T+p\tilde{\mathbf{T}})\end{bmatrix}\begin{bmatrix}\hat{\mathbf{a}}\\ \check{\mathbf{a}}\end{bmatrix}, \tag{13a}$$

$$\begin{bmatrix}-p\check{\mathbf{b}}+\begin{bmatrix}0\\c\end{bmatrix}\\ \check{\mathbf{b}}-\begin{bmatrix}c\\0\end{bmatrix}\end{bmatrix}=\begin{bmatrix}\mathcal{Q}x_3(\tilde{\mathbf{Q}}+p\tilde{\mathbf{R}}) & \mathcal{Q}x_3^2(\tilde{\mathbf{Q}}+p\tilde{\mathbf{R}})\\ \mathcal{Q}x_3(\tilde{\mathbf{R}}^T+p\tilde{\mathbf{T}}) & \mathcal{Q}x_3^2(\tilde{\mathbf{R}}^T+p\tilde{\mathbf{T}})\end{bmatrix}\begin{bmatrix}\hat{\mathbf{a}}\\ \check{\mathbf{a}}\end{bmatrix}, \tag{13b}$$

with

$$a_4=pa_3,\quad c\equiv\tfrac{1}{2}(b_3+pb_4)=\tfrac{1}{2}\tilde{\mathbf{p}}^T\check{\mathbf{b}}. \tag{14}$$

The first and second equilibrium equations in (9) are thus satisfied in terms of (13*a*) and the third is satisfied by (13*b*). We now have seven new relations (13*a*,*b*) with four additional unknowns b_K $(K=1,2,3,4)$ in replacement of the three equilibrium equations.

Furthermore, four stress functions are defined by

$$\varphi_\alpha=b_\alpha f(z),\quad \psi_\alpha=b_{\alpha+2}f(z). \tag{15}$$

Equations (4) and (6) can be rewritten as

$$\mathcal{N}_{\alpha1}=-\varphi_{\alpha,2},\quad \mathcal{N}_{\alpha2}=\varphi_{\alpha,1}, \tag{16a}$$

$$\mathcal{M}_{\alpha1}=-\psi_{\alpha,2}-\tfrac{1}{2}\varepsilon_{\alpha1}\psi_{\omega,\omega},\quad \mathcal{M}_{\alpha2}=\psi_{\alpha,1}-\tfrac{1}{2}\varepsilon_{\alpha2}\psi_{\omega,\omega}, \tag{16b}$$

$$\mathcal{R}_1=-\tfrac{1}{2}\psi_{\omega,\omega2},\quad \mathcal{R}_2=\tfrac{1}{2}\psi_{\omega,\omega1}, \tag{16c}$$

$$\mathcal{V}_1=-\psi_{2,22},\quad \mathcal{V}_2=\psi_{1,11}, \tag{16d}$$

where $\varepsilon_{\alpha\beta}$ is the two-dimensional permutation tensor. Thus all of the stress resultants can be obtained by differentiating the four stress functions with respect to x_α.

In terms of (8) and (15), we can define the generalized displacement vector and the stress function vector as

$$\mathbf{u}\equiv\begin{bmatrix}u_1\\u_2\\\vartheta_1\\\vartheta_2\end{bmatrix}=\mathbf{a}f(z),\quad \boldsymbol{\phi}\equiv\begin{bmatrix}\varphi_1\\\varphi_2\\\psi_1\\\psi_2\end{bmatrix}=\mathbf{b}f(z), \tag{17}$$

in which $\mathbf{a}$ and $\mathbf{b}$ are eigenvectors defined by, [13],

$$\mathbf{a}=\begin{bmatrix}a_1\\a_2\\a_3\\a_4\end{bmatrix},\quad \mathbf{b}=\begin{bmatrix}b_1\\b_2\\b_3\\b_4\end{bmatrix}. \tag{18}$$

Because there are four pairs of complex conjugates for p, the associated eigenvectors are also four pairs of complex conjugates. We denote

$$p_{K+4}=\overline{p_K},\quad (\mathrm{Im}\,p_K>0),\quad \mathbf{a}_{K+4}=\overline{\mathbf{a}}_K,\quad \mathbf{b}_{K+4}=\overline{\mathbf{b}}_K,\quad (K=1,2,3,4), \tag{19}$$

where Im refers to the imaginary part and the overbar denotes the complex conjugate. If p_K $(K=1,2,3,4)$ are distinct, the general solution for the generalized displacements and stress functions are obtained by superposing eight solutions of the form (17) as

$$\mathbf{u}=\sum_{K=1}^{4}\{\mathbf{a}_Kf_K(z_K)+\overline{\mathbf{a}}_Kf_{K+4}(\overline{z_K})\},$$

$$\boldsymbol{\phi}=\sum_{K=1}^{4}\{\mathbf{b}_Kf_K(z_K)+\overline{\mathbf{b}}_Kf_{K+4}(\overline{z_K})\}, \tag{20}$$

where f_K and f_{K+4} are eight arbitrary functions of their arguments and $z_K=x_1+p_Kx_2$. For a given boundary value problem, the unknown functions $f_K(z_K)$ and $f_{K+4}(\overline{z_K})$ remain to be sought to satisfy the given boundary conditions.

Equations (13*a*,*b*) and (14) can be reduced to the following standard eigenrelation

$$\mathbf{N}\boldsymbol{\xi}=p\boldsymbol{\xi}, \tag{21}$$

where

$$\mathbf{N}=\begin{bmatrix}\mathbf{N}_1 & \mathbf{N}_2\\ \mathbf{N}_3 & \mathbf{N}_1^T\end{bmatrix},\quad \boldsymbol{\xi}=\begin{bmatrix}\mathbf{a}\\\mathbf{b}\end{bmatrix}. \tag{22}$$

$\mathbf{N}$ is real and called as the *fundamental elastic plate matrix* in Ref. [13]; $\mathbf{N}_2$ and $\mathbf{N}_3$ are symmetric. By denoting

$$\mathbf{A}=[\mathbf{a}_1\ \mathbf{a}_2\ \mathbf{a}_3\ \mathbf{a}_4],\quad \mathbf{B}=[\mathbf{b}_1\ \mathbf{b}_2\ \mathbf{b}_3\ \mathbf{b}_4], \tag{23}$$

the *orthogonality* relations of the formalism are

$$\mathbf{B}^T\mathbf{A}+\mathbf{A}^T\mathbf{B}=\mathbf{I}=\overline{\mathbf{B}}^T\overline{\mathbf{A}}+\overline{\mathbf{A}}^T\overline{\mathbf{B}}, \tag{24a}$$

$$\mathbf{B}^T\overline{\mathbf{A}}+\mathbf{A}^T\overline{\mathbf{B}}=\mathbf{0}=\overline{\mathbf{B}}^T\mathbf{A}+\overline{\mathbf{A}}^T\mathbf{B}. \tag{24b}$$

The *closure* relations of the formalism are

$$\mathbf{A}\mathbf{B}^T+\overline{\mathbf{A}\mathbf{B}}^T=\mathbf{I}=\mathbf{B}\mathbf{A}^T+\overline{\mathbf{B}\mathbf{A}}^T, \tag{25a}$$

$$\mathbf{A}\mathbf{A}^T+\overline{\mathbf{A}\mathbf{A}}^T=\mathbf{0}=\mathbf{B}\mathbf{B}^T+\overline{\mathbf{B}\mathbf{B}}^T. \tag{25b}$$

It is clear from (25*a*) that the real part of $2\mathbf{A}\mathbf{B}^T$ is $\mathbf{I}$ and from (25*b*) that both $\mathbf{A}\mathbf{A}^T$ and $\mathbf{B}\mathbf{B}^T$ are purely imaginary. Hence, the following three real matrices $\mathbf{S}$, $\mathbf{H}$, and $\mathbf{L}$ can be defined as

$$\mathbf{S}=i(2\mathbf{A}\mathbf{B}^T-\mathbf{I}),\quad \mathbf{H}=2i\mathbf{A}\mathbf{A}^T,\quad \mathbf{L}=-2i\mathbf{B}\mathbf{B}^T. \tag{26}$$

Their counterparts in Stroh's sextic formalism for generalized plane strain elasticity are called the Barnett-Lothe tensors, [14]. An indirect proof will be given in Section 6 that **H** and **L** are positive definite matrices. Thus **A** and **B** are nonsingular matrices.

Green's Functions for an Infinite Plate

Assume that the concentrated forces $\hat{\mathcal{N}}_i$ and concentrated moments $\hat{\mathcal{M}}_i$ are applied at the origin of the Cartesian coordinate system. The force and moment equilibrium conditions of an arbitrary plane subregion of the plate enclosing the origin require that

$$\hat{\mathcal{N}}_\alpha+\oint_\Gamma \mathcal{N}_{\alpha\beta}n_\beta ds=0, \tag{27}$$

$$\hat{\mathcal{N}}_3+\oint_\Gamma \mathcal{R}_\alpha n_\alpha ds=0, \tag{28}$$

$$\hat{\mathcal{M}}_1-\oint_\Gamma \mathcal{M}_{2\alpha}n_\alpha ds+\oint_\Gamma \mathcal{R}_\alpha n_\alpha x_2 ds=0, \tag{29}$$

$$\hat{\mathcal{M}}_2+\oint_\Gamma \mathcal{M}_{1\alpha}n_\alpha ds-\oint_\Gamma \mathcal{R}_\alpha n_\alpha x_1 ds=0, \tag{30}$$

$$\hat{\mathcal{M}}_3+\oint_\Gamma (\mathcal{N}_{2\alpha}x_1-\mathcal{N}_{1\alpha}x_2)n_\alpha ds=0, \tag{31}$$

where s is the arc-length measured along the contour Γ, and the enclosed material lies on the left-hand side while increasing s. The components of the unit outward normal vector to the curve are

$$n_1=\frac{dx_2}{ds},\quad n_2=-\frac{dx_1}{ds}. \tag{32}$$

Denote $(\cdots)|_{\partial\Gamma}$ as a jump in $(\cdots)$ when moving along the curve Γ counterclockwise from one point to the same point. Substituting (16*a*,*b*,*c*) and (32) into (27)–(31) yields

$$\varphi_\alpha|_{\partial\Gamma}=\hat{\mathcal{N}}_\alpha, \tag{33}$$

$$\tfrac{1}{2}\psi_{\omega,\omega}|_{\partial\Gamma}=\hat{\mathcal{N}}_3, \tag{34}$$

$$(\psi_2-\tfrac{1}{2}x_2\psi_{\omega,\omega})|_{\partial\Gamma}=-\hat{\mathcal{M}}_1, \tag{35}$$

$$(\psi_1-\tfrac{1}{2}x_1\psi_{\omega,\omega})|_{\partial\Gamma}=\hat{\mathcal{M}}_2, \tag{36}$$

$$(x_\omega\chi_{,\omega}-\chi)|_{\partial\Gamma}=\hat{\mathcal{M}}_3, \tag{37}$$

where χ in (37) is the Airy function defined by $\varphi_1=-\chi_{,2}$ and $\varphi_2=\chi_{,1}$ in order to satisfy $\mathcal{N}_{21}=\mathcal{N}_{12}$, i.e., $\varphi_{1,1}+\varphi_{2,2}=0$. Note that if the concentrated loads are not applied at the origin, saying x_α^0, Eqs. (29)–(31) and (35)–(37) must be modified to replace x_α by $x_\alpha-x_\alpha^0$.

Assume that there are jumps in in-plane displacements of magnitude $\hat{u}_\alpha$, in deflection of magnitude $\hat{w}$, and in slopes of magnitude $\hat{\vartheta}_\alpha$, of the midplane of the plate across the negative x_1-axis. The physical meaning of $\hat{\vartheta}_\alpha$ represents a plastic hinge, [15]. The discontinuous in-plane displacements and deflection are analogous to the edge dislocation and screw dislocation in a three-dimensional solid, where $\hat{u}_\alpha$ and $\hat{w}$ are the components of the corresponding Burgers vector. If $(\cdots)|_{\partial\Gamma}$ is designated as a jump across the negative x_1-axis, we have

$$u_\alpha|_{\partial\Gamma}=\hat{u}_\alpha, \tag{38}$$

$$w|_{\partial\Gamma}=\hat{w}, \tag{39}$$

$$\vartheta_\alpha|_{\partial\Gamma}=\hat{\vartheta}_\alpha. \tag{40}$$

The original problem for finding Green's functions can be separated into three systems of problems. We will examine later whether they are equivalent to the original problem. The first system of problem consists of Eqs. (33), (35), (36), (38), and (40), i.e.,

$$\mathbf{u}^{(1)}|_{\partial\Gamma}=\hat{\mathbf{U}},\quad \boldsymbol{\phi}^{(1)}|_{\partial\Gamma}=\hat{\boldsymbol{\Phi}}^{(1)}, \tag{41}$$

while the second system of problem results from Eq. (34),

$$\mathbf{u}^{(2)}|_{\partial\Gamma}=\mathbf{0},\quad \boldsymbol{\phi}^{(2)}|_{\partial\Gamma}=x_1\hat{\boldsymbol{\Phi}}^{(2)}, \tag{42}$$

where we have used the notations

$$\hat{\mathbf{U}}\equiv\begin{bmatrix}\hat{u}_1\\ \hat{u}_2\\ \hat{\vartheta}_1\\ \hat{\vartheta}_2\end{bmatrix},\quad \hat{\boldsymbol{\Phi}}^{(1)}\equiv\begin{bmatrix}\hat{\mathcal{N}}_1\\ \hat{\mathcal{N}}_2\\ \hat{\mathcal{M}}_2\\ -\hat{\mathcal{M}}_1\end{bmatrix},\quad \hat{\boldsymbol{\Phi}}^{(2)}\equiv\begin{bmatrix}0\\ 0\\ \hat{\mathcal{N}}_3\\ 0\end{bmatrix}. \tag{43}$$

The third system of problem contains (37) and (39). However, the two conditions are not sufficient for a complete solution of the third problem. It is of a higher-order singularity and needs additional knowledge of double forces and double moments to give a complete solution. We will not study it in this work.

The eight arbitrary functions in (20) are assumed to have the same function form as

$$f_K(z_K)=f(z_K)q_K,\quad f_{K+4}(\overline{z_K})=\overline{f}(\overline{z_K})\overline{q_K}, \tag{44}$$

where q_K are arbitrary complex constants. Thus (20) can be written in a real form as

$$\mathbf{u}=2\,\mathrm{Re}\{\mathbf{A}\langle f(z_*)\rangle\mathbf{q}\},\quad \boldsymbol{\phi}=2\,\mathrm{Re}\{\mathbf{B}\langle f(z_*)\rangle\mathbf{q}\}, \tag{45}$$

where $\langle f(z_*)\rangle$ is the diagonal matrix given by

$$\langle f(z_*)\rangle=\mathrm{diag}[f(z_1)\ \ f(z_2)\ \ f(z_3)\ \ f(z_4)]. \tag{46}$$

When replacing $\mathbf{q}$ by $-i\mathbf{q}$, (45) leads to the alternate form

$$\mathbf{u}=2\,\mathrm{Im}\{\mathbf{A}\langle f(z_*)\rangle\mathbf{q}\},\quad \boldsymbol{\phi}=2\,\mathrm{Im}\{\mathbf{B}\langle f(z_*)\rangle\mathbf{q}\}. \tag{47}$$

In the polar coordinate system

$$x_1=r\cos\theta,\quad x_2=r\sin\theta, \tag{48}$$

the function $\ln z$ is a multivalued function which increases its value by $2\pi i$ each time θ increases by 2π in the x_1Ox_2-plane. In order for the multivalued function to maintain a unique value, we introduce a branch cut along the negative x_1-axis so that the range of θ is limited to $-\pi\leqslant\theta\leqslant\pi$. The function $\ln z$ is now continuous in the x_1Ox_2 plane except across the negative x_1-axis. Because

$$\ln z=\ln r\pm i\pi,\quad \text{at}\ \ \theta=\pm\pi, \tag{49}$$

we have

$$(\ln z)|_{\partial\Gamma}=2\pi i. \tag{50}$$

The solution for the first system of problem is assumed as

$$\mathbf{u}^{(1)}=\frac{1}{\pi}\,\mathrm{Im}\{\mathbf{A}\langle\ln z_*\rangle\mathbf{q}^{(1)}\},\quad \boldsymbol{\phi}^{(1)}=\frac{1}{\pi}\,\mathrm{Im}\{\mathbf{B}\langle\ln z_*\rangle\mathbf{q}^{(1)}\}. \tag{51}$$

Substitution of (51) into (41) gives

$$2\,\mathrm{Re}(\mathbf{A}\mathbf{q}^{(1)})=\hat{\mathbf{U}},\quad 2\,\mathrm{Re}(\mathbf{B}\mathbf{q}^{(1)})=\hat{\boldsymbol{\Phi}}^{(1)}, \tag{52}$$

or

$$\begin{bmatrix}\mathbf{A} & \overline{\mathbf{A}}\\ \mathbf{B} & \overline{\mathbf{B}}\end{bmatrix}\begin{bmatrix}\mathbf{q}^{(1)}\\ \overline{\mathbf{q}}^{(1)}\end{bmatrix}=\begin{bmatrix}\hat{\mathbf{U}}\\ \hat{\boldsymbol{\Phi}}^{(1)}\end{bmatrix}. \tag{53}$$

Use of the orthogonality relations (24*a*,*b*) leads to

$$\begin{bmatrix}\mathbf{q}^{(1)}\\ \overline{\mathbf{q}}^{(1)}\end{bmatrix}=\begin{bmatrix}\mathbf{B}^T & \mathbf{A}^T\\ \overline{\mathbf{B}}^T & \overline{\mathbf{A}}^T\end{bmatrix}\begin{bmatrix}\hat{\mathbf{U}}\\ \hat{\boldsymbol{\Phi}}^{(1)}\end{bmatrix}, \tag{54}$$

or

$$\mathbf{q}^{(1)}=\mathbf{A}^T\hat{\boldsymbol{\Phi}}^{(1)}+\mathbf{B}^T\hat{\mathbf{U}}. \tag{55}$$

Therefore, the solution for the first system of problem (41) is given by substituting (55) into (51) as

$$\begin{bmatrix}\mathbf{u}^{(1)}\\ \boldsymbol{\phi}^{(1)}\end{bmatrix}=\frac{1}{\pi}\mathrm{Im}\begin{bmatrix}\mathbf{A}\langle\ln z_*\rangle\mathbf{B}^T & \mathbf{A}\langle\ln z_*\rangle\mathbf{A}^T\\ \mathbf{B}\langle\ln z_*\rangle\mathbf{B}^T & \mathbf{B}\langle\ln z_*\rangle\mathbf{A}^T\end{bmatrix}\begin{bmatrix}\hat{\mathbf{U}}\\ \hat{\boldsymbol{\Phi}}^{(1)}\end{bmatrix}. \tag{56}$$

Similarly, we assume the solution for the second system of problem to be of the form

$$\mathbf{u}^{(2)}=\frac{1}{\pi}\mathrm{Im}\{\mathbf{A}\langle z_*\ln z_*\rangle\mathbf{q}^{(2)}\},\quad \boldsymbol{\phi}^{(2)}=\frac{1}{\pi}\mathrm{Im}\{\mathbf{B}\langle z_*\ln z_*\rangle\mathbf{q}^{(2)}\}. \tag{57}$$

The conditions (42) are used to give

$$\mathbf{q}^{(2)}=\mathbf{A}^T\hat{\boldsymbol{\Phi}}^{(2)}, \tag{58}$$

and thus,

$$\begin{bmatrix}\mathbf{u}^{(2)}\\ \boldsymbol{\phi}^{(2)}\end{bmatrix}=\frac{1}{\pi}\mathrm{Im}\begin{bmatrix}\mathbf{A}\langle z_*\ln z_*\rangle\mathbf{A}^T\\ \mathbf{B}\langle z_*\ln z_*\rangle\mathbf{A}^T\end{bmatrix}\hat{\boldsymbol{\Phi}}^{(2)}. \tag{59}$$

Because we are not studying the third system of problem, the total solution is obtained by superposing (56) and (59), i.e.,

$$\begin{bmatrix}\mathbf{u}\\ \boldsymbol{\phi}\end{bmatrix}=\begin{bmatrix}\mathbf{u}^{(1)}\\ \boldsymbol{\phi}^{(1)}\end{bmatrix}+\begin{bmatrix}\mathbf{u}^{(2)}\\ \boldsymbol{\phi}^{(2)}\end{bmatrix}. \tag{60}$$

Now we need to check whether (33)–(40) are satisfied upon setting $\hat{\mathcal{M}}_3=0$ and $\hat{w}=0$. In terms of (50), (56), (59), and (60), we have

$$\begin{bmatrix}\mathbf{u}\\ \boldsymbol{\phi}\end{bmatrix}\Big|_{\partial\Gamma}=2\,\mathrm{Re}\begin{bmatrix}\mathbf{A}\mathbf{B}^T & \mathbf{A}\mathbf{A}^T\\ \mathbf{B}\mathbf{B}^T & \mathbf{B}\mathbf{A}^T\end{bmatrix}\begin{bmatrix}\hat{\mathbf{U}}\\ \hat{\boldsymbol{\Phi}}^{(1)}+x_1\hat{\boldsymbol{\Phi}}^{(2)}\end{bmatrix},$$

$$\begin{bmatrix}\mathbf{u}_{,1}\\ \boldsymbol{\phi}_{,1}\end{bmatrix}\Big|_{\partial\Gamma}=2\,\mathrm{Re}\begin{bmatrix}\mathbf{A}\mathbf{A}^T\\ \mathbf{B}\mathbf{A}^T\end{bmatrix}\hat{\boldsymbol{\Phi}}^{(2)}, \tag{61}$$

and furthermore, using the closure relations (25*a*,*b*),

$$\begin{bmatrix}\mathbf{u}\\ \boldsymbol{\phi}\end{bmatrix}\Big|_{\partial\Gamma}=\begin{bmatrix}\hat{\mathbf{U}}\\ \hat{\boldsymbol{\Phi}}^{(1)}+x_1\hat{\boldsymbol{\Phi}}^{(2)}\end{bmatrix},\quad \begin{bmatrix}\mathbf{u}_{,1}\\ \boldsymbol{\phi}_{,1}\end{bmatrix}\Big|_{\partial\Gamma}=\begin{bmatrix}\mathbf{0}\\ \hat{\boldsymbol{\Phi}}^{(2)}\end{bmatrix}. \tag{62}$$

From Eq. (21), we may obtain

$$\begin{bmatrix}\mathbf{u}_{,2}\\ \boldsymbol{\phi}_{,2}\end{bmatrix}=\mathbf{N}\begin{bmatrix}\mathbf{u}_{,1}\\ \boldsymbol{\phi}_{,1}\end{bmatrix}, \tag{63}$$

and thus, using $(22)_1$ and $(62)_2$,

$$\begin{bmatrix}\mathbf{u}_{,2}\\ \boldsymbol{\phi}_{,2}\end{bmatrix}\Big|_{\partial\Gamma}=\begin{bmatrix}\mathbf{N}_2\\ \mathbf{N}_1^T\end{bmatrix}\hat{\boldsymbol{\Phi}}^{(2)}. \tag{64}$$

As shown in (*A*8) in the Appendix that

$$(\mathbf{N}_2)_{K3}=0,\ \ (\mathbf{N}_1^T)_{K3}=\delta_{K4},\quad (K=1,2,3,4), \tag{65}$$

thus we have

$$\begin{bmatrix}\mathbf{u}_{,2}\\ \boldsymbol{\phi}_{,2}\end{bmatrix}\Big|_{\partial\Gamma}=\begin{bmatrix}\mathbf{0}\\ \mathbf{i}_4\hat{\mathcal{N}}_3\end{bmatrix}, \tag{66}$$

where the following notations are adopted:

$$\mathbf{i}_3=[0\ \ 0\ \ 1\ \ 0]^T,\quad \mathbf{i}_4=[0\ \ 0\ \ 0\ \ 1]^T. \tag{67}$$

It is easily seen, according to (43), (62), and (66), that Eqs. (33)–(40) are satisfied by the solution (60) provided that $\hat{\mathcal{M}}_3=0$ and $\hat{w}=0$. Moreover, the following conditions are also satisfied:

$$u_{\alpha,\beta}|_{\partial\Gamma}=0,\quad w_{,\alpha\beta}|_{\partial\Gamma}=0. \tag{68}$$

They are nothing but the single-valued conditions for three plane strains and three curvatures on the midplane and for the rotation angle about the x_3-axis. Instead of (42), the seven conditions (68) as well as (28) have been used in Refs. [5,6] for obtaining the solution for the second system of problem. Although Eqs. (42) were not explicitly shown to be valid in Refs. [5,6] we have demonstrated herein that the solution (59) for Eqs. (42) is also a solution for (68). This provides a clear explanation of the equivalency of the two approaches for finding Green's function. Because a Green function is a particular solution for a differential equation, the present Green function is not necessarily the same as that given in Refs. [5,6] and the difference would be the homogeneous solution for the differential equation.

The Green functions given in Refs. [5,6] for concentrated forces and moments and in Ref. [7] for discontinuous in-plane displacements and slopes, respectively, appeared to be in an analytical complex form and required numerical calculations. By contrast, with the help of the octet formalism, [13], our fundamental solutions are given in an exact closed form. Moreover, the present Green's functions can be converted into a real form and there is no need for the calculation of the eigenvalues and eigenvectors.

In terms of $(43)_3$ and (65), we have

$$(x_1\mathbf{I}+x_2\mathbf{N})\begin{bmatrix}\mathbf{0}\\ \hat{\boldsymbol{\Phi}}^{(2)}\end{bmatrix}=\begin{bmatrix}\mathbf{0}\\ (x_1\mathbf{i}_3+x_2\mathbf{i}_4)\hat{\mathcal{N}}_3\end{bmatrix}. \tag{69}$$

According to Eq. (*A*27) in the Appendix, the fundamental solutions (56) and (59) can be rewritten as

$$\begin{bmatrix}\mathbf{u}^{(1)}\\ \boldsymbol{\phi}^{(1)}\end{bmatrix}=-\frac{1}{2\pi}\{(\ln r)\mathbf{I}+\pi\tilde{\mathbf{N}}(\theta)\}\tilde{\mathbf{N}}\begin{bmatrix}\hat{\mathbf{U}}\\ \hat{\boldsymbol{\Phi}}^{(1)}\end{bmatrix}, \tag{70}$$

$$\begin{bmatrix}\mathbf{u}^{(2)}\\ \boldsymbol{\phi}^{(2)}\end{bmatrix}=-\frac{1}{2\pi}\{(\ln r)\mathbf{I}+\pi\tilde{\mathbf{N}}(\theta)\}\tilde{\mathbf{N}}\begin{bmatrix}\mathbf{0}\\ (x_1\mathbf{i}_3+x_2\mathbf{i}_4)\hat{\mathcal{N}}_3\end{bmatrix}, \tag{71}$$

where $\tilde{\mathbf{N}}(\theta)$ and $\tilde{\mathbf{N}}$ are defined by (*A*22) and (*A*26) in the Appendix.

Green's Functions for a Semi-Infinite Plate

In the Kirchhoff plate theory, the boundary condition for a rigidly clamped edge at $x_2=0$ is given by

$$u_1=0,\quad u_2=0,\quad w=0,\quad \vartheta_2=0, \tag{72}$$

which give

$$\mathbf{u}=\mathbf{0},\quad \text{at } x_2=0. \tag{73}$$

The boundary condition for a free edge at $x_2=0$ is given by

$$\mathcal{N}_{12}=0,\quad \mathcal{N}_{22}=0,\quad \mathcal{V}_2=0,\quad \mathcal{M}_{22}=0, \tag{74}$$

which reduce to, [13],

$$\boldsymbol{\phi}=\mathbf{0},\quad \text{at } x_2=0. \tag{75}$$

Having found the Green functions for an infinite anisotropic plate, now we are able to modify them to give the Green functions for a semi-infinite anisotropic plate. The approach is similar to that for finding the Green functions for an anisotropic elastic half-space, [11,16].

The semi-infinite anisotropic plate is located at $x_2>0$, and the concentrated forces, moments and discontinuous displacements and slopes are located at

$$(x_1,x_2)=(0,d),\quad d>0. \tag{76}$$

In correspondence to the first system of problem for an infinite plate, we assume the solution for the semi-infinite plate as

$$\mathbf{u}^{(1)}=\frac{1}{\pi}\mathrm{Im}\{\mathbf{A}\langle\ln(z_*-p_*d)\rangle\mathbf{q}^{(1)}\}+\frac{1}{\pi}\mathrm{Im}\sum_{J=1}^{4}\{\mathbf{A}\langle\ln(z_*-\overline{p}_Jd)\rangle\mathbf{q}_J^{(1)}\}, \tag{77a}$$

$$\boldsymbol{\phi}^{(1)}=\frac{1}{\pi}\,\mathrm{Im}\{\mathbf{B}\langle\ln(z_*-p_*d)\rangle\mathbf{q}^{(1)}\}$$
$$+\frac{1}{\pi}\,\mathrm{Im}\sum_{J=1}^{4}\{\mathbf{B}\langle\ln(z_*-\overline{p}_Jd)\rangle\mathbf{q}_J^{(1)}\},\qquad(77b)$$

where $\mathbf{q}^{(1)}$ is given by (55) and $\mathbf{q}_J^{(1)}$ $(J=1,2,3,4)$ are unknown vectors to be determined. The second term on the right-hand side of (77*a*) or (77*b*) represents four image singularities because the singularity points are located on the lower-half plane.

Consider first the rigidly clamped edge at $x_2=0$. Substituting (77*a*) into (73) leads to

$$\mathrm{Im}\{\mathbf{A}\langle\ln(x_1-p_*d)\rangle\mathbf{q}^{(1)}\}+\mathrm{Im}\sum_{J=1}^{4}\{\mathbf{A}\langle\ln(x_1-\overline{p}_Jd)\rangle\mathbf{q}_J^{(1)}\}=\mathbf{0}.\qquad(78)$$

Using the equalities

$$\mathrm{Im}\{\mathbf{A}\langle\ln(x_1-p_*d)\rangle\mathbf{q}^{(1)}\}=-\mathrm{Im}\{\overline{\mathbf{A}}\langle\ln(x_1-\overline{p}_*d)\rangle\overline{\mathbf{q}}^{(1)}\},\qquad(79a)$$

$$\langle\ln(x_1-\overline{p}_*d)\rangle=\sum_{J=1}^{4}\ln(x_1-\overline{p}_Jd)\mathbf{I}_J,\qquad(79b)$$

in which

$$\mathbf{I}_1=\mathrm{diag}[1,0,0,0],\quad \mathbf{I}_2=\mathrm{diag}[0,1,0,0],$$
$$\mathbf{I}_3=\mathrm{diag}[0,0,1,0],\quad \mathbf{I}_4=\mathrm{diag}[0,0,0,1],\qquad(80)$$

Eq. (78) reduces to

$$\mathrm{Im}\sum_{J=1}^{4}\ln(x_1-\overline{p}_Jd)\{-\overline{\mathbf{A}}\mathbf{I}_J\overline{\mathbf{q}}^{(1)}+\mathbf{A}\mathbf{q}_J^{(1)}\}=\mathbf{0},\qquad(81)$$

which gives

$$\mathbf{q}_J^{(1)}=\mathbf{A}^{-1}\overline{\mathbf{A}}\mathbf{I}_J\overline{\mathbf{q}}^{(1)}.\qquad(82)$$

If the boundary $x_2=0$ is free, i.e., (75), following the same procedure gives

$$\mathbf{q}_J^{(1)}=\mathbf{B}^{-1}\overline{\mathbf{B}}\mathbf{I}_J\overline{\mathbf{q}}^{(1)}.\qquad(83)$$

Similarly, we can construct the solution for the second system of problem of a semi-infinite plate as

$$\mathbf{u}^{(2)}=\frac{1}{\pi}\,\mathrm{Im}\{\mathbf{A}\langle(z_*-p_*d)\ln(z_*-p_*d)\rangle\mathbf{q}^{(2)}\}$$
$$+\frac{1}{\pi}\,\mathrm{Im}\sum_{J=1}^{4}\{\mathbf{A}\langle(z_*-\overline{p}_Jd)\ln(z_*-\overline{p}_Jd)\rangle\mathbf{q}_J^{(2)}\},\qquad(84a)$$

$$\boldsymbol{\phi}^{(2)}=\frac{1}{\pi}\,\mathrm{Im}\{\mathbf{B}\langle(z_*-p_*d)\ln(z_*-p_*d)\rangle\mathbf{q}^{(2)}\}$$
$$+\frac{1}{\pi}\,\mathrm{Im}\sum_{J=1}^{4}\{\mathbf{B}\langle(z_*-\overline{p}_Jd)\ln(z_*-\overline{p}_Jd)\rangle\mathbf{q}_J^{(2)}\},\qquad(84b)$$

where, for the rigidly clamped edge at $x_2=0$,

$$\mathbf{q}_J^{(2)}=\mathbf{A}^{-1}\overline{\mathbf{A}}\mathbf{I}_J\overline{\mathbf{q}}^{(2)},\qquad(85)$$

and, for the free edge at $x_2=0$,

$$\mathbf{q}_J^{(2)}=\mathbf{B}^{-1}\overline{\mathbf{B}}\mathbf{I}_J\overline{\mathbf{q}}^{(2)}.\qquad(86)$$

The hoop membrane stress resultants, bending moments, and transverse shear forces at the edge $x_2=0$ are of particular interest. In terms of (16*a–d*), we have

$$\begin{bmatrix}\mathcal{N}_{11}\\ \mathcal{N}_{21}\\ \mathcal{M}_{11}\\ 2\mathcal{M}_{21}\end{bmatrix}=-\boldsymbol{\phi}_{,2}+\begin{bmatrix}0\\0\\0\\ \psi_{1,1}\end{bmatrix}=-\boldsymbol{\phi}_{,2}+\mathbf{I}_{43}\boldsymbol{\phi}_{,1},\qquad(87a)$$

$$\begin{bmatrix}\mathcal{R}_1\\ \mathcal{V}_1\end{bmatrix}=-\begin{bmatrix}\frac{1}{2}&\frac{1}{2}\\0&1\end{bmatrix}\begin{bmatrix}\psi_{1,12}\\ \psi_{2,22}\end{bmatrix}=-\begin{bmatrix}\frac{1}{2}&\frac{1}{2}\\0&1\end{bmatrix}\begin{bmatrix}\mathbf{i}_3^T\boldsymbol{\phi}_{,12}\\ \mathbf{i}_4^T\boldsymbol{\phi}_{,22}\end{bmatrix},\qquad(87b)$$

where $\mathbf{I}_{43}$ is a 4×4 matrix whose elements are $(\mathbf{I}_{43})_{KL}=\delta_{K4}\delta_{L3}$ and the notations (67) have been used. Furthermore, with the help of $(22)_1$ and (63),

$$\begin{bmatrix}\mathcal{N}_{11}\\ \mathcal{N}_{21}\\ \mathcal{M}_{11}\\ 2\mathcal{M}_{21}\end{bmatrix}=-\mathbf{N}_3\mathbf{u}_{,1}+(\mathbf{I}_{43}-\mathbf{N}_1^T)\boldsymbol{\phi}_{,1},\qquad(88a)$$

$$\begin{bmatrix}\mathcal{R}_1\\ \mathcal{V}_1\end{bmatrix}=-\begin{bmatrix}\frac{1}{2}&\frac{1}{2}\\0&1\end{bmatrix}\begin{bmatrix}\mathbf{i}_3^T[\mathbf{N}_3\ \ \mathbf{N}_1^T]\\ \mathbf{i}_4^T[\mathbf{N}_3\ \ \mathbf{N}_1^T]\mathbf{N}\end{bmatrix}\begin{bmatrix}\mathbf{u}_{,11}\\ \boldsymbol{\phi}_{,11}\end{bmatrix}.\qquad(88b)$$

For a semi-infinite plate with a rigidly clamped edge at $x_2=0$, (73) is used to give

$$\begin{bmatrix}\mathcal{N}_{11}\\ \mathcal{N}_{21}\\ \mathcal{M}_{11}\\ 2\mathcal{M}_{21}\end{bmatrix}=(\mathbf{I}_{43}-\mathbf{N}_1^T)\boldsymbol{\phi}_{,1}(x_1,0),\qquad(89a)$$

$$\begin{bmatrix}\mathcal{R}_1\\ \mathcal{V}_1\end{bmatrix}=-\begin{bmatrix}\frac{1}{2}&\frac{1}{2}\\0&1\end{bmatrix}\begin{bmatrix}\mathbf{i}_3^T\mathbf{N}_1^T\\ \mathbf{i}_4^T(\mathbf{N}_3\mathbf{N}_2+\mathbf{N}_1^T\mathbf{N}_1^T)\end{bmatrix}\boldsymbol{\phi}_{,11}(x_1,0).\qquad(89b)$$

For a semi-infinite plate with a free edge at $x_2=0$, (75) is used to give

$$\begin{bmatrix}\mathcal{N}_{11}\\ \mathcal{N}_{21}\\ \mathcal{M}_{11}\\ 2\mathcal{M}_{21}\end{bmatrix}=-\mathbf{N}_3\mathbf{u}_{,1}(x_1,0),\qquad(90a)$$

$$\begin{bmatrix}\mathcal{R}_1\\ \mathcal{V}_1\end{bmatrix}=-\begin{bmatrix}\frac{1}{2}&\frac{1}{2}\\0&1\end{bmatrix}\begin{bmatrix}\mathbf{i}_3^T\mathbf{N}_3\\ \mathbf{i}_4^T(\mathbf{N}_3\mathbf{N}_1+\mathbf{N}_1^T\mathbf{N}_3)\end{bmatrix}\mathbf{u}_{,11}(x_1,0).\qquad(90b)$$

It is seen from (89*a*,*b*) and (90*a*,*b*) that the first and second derivatives of $\boldsymbol{\phi}(x_1,0)$ and $\mathbf{u}(x_1,0)$ with respect to x_1 are needed for calculating the hoop stress resultants. We now derive these expressions at the boundary $x_2=0$. Using the procedure similar to (79*a*,*b*), the solution (77*b*) at $x_2=0$ for a clamped semi-infinite plate can be reduced to

$$\boldsymbol{\phi}^{(1)}(x_1,0)=\frac{1}{\pi}\,\mathrm{Im}\{(\mathbf{B}\mathbf{A}^{-1}-\overline{\mathbf{B}\mathbf{A}}^{-1})\mathbf{A}\langle\ln(x_1-p_*d)\rangle\mathbf{q}^{(1)}\}.\qquad(91)$$

The following identities can be derived from (24*a*,*b*) and (26)

$$-i\mathbf{B}\mathbf{A}^{-1}=\mathbf{H}^{-1}+i\mathbf{H}^{-1}\mathbf{S},\quad i\mathbf{A}\mathbf{B}^{-1}=\mathbf{L}^{-1}-i\mathbf{S}\mathbf{L}^{-1}.\qquad(92)$$

With $(92)_1$, Eq. (91) is rewritten as

$$\boldsymbol{\phi}^{(1)}(x_1,0)=\frac{2}{\pi}\mathbf{H}^{-1}\,\mathrm{Re}\{\mathbf{A}\langle\ln(x_1-p_*d)\rangle\mathbf{q}^{(1)}\},\qquad(93)$$

or, in a real form,

$$\boldsymbol{\phi}^{(1)}(x_1,0)=\mathbf{H}^{-1}\left\{\frac{1}{\pi}(\ln\hat{r})\hat{\mathbf{U}}+\mathbf{S}(\hat{\theta})\hat{\mathbf{U}}+\mathbf{H}(\hat{\theta})\hat{\boldsymbol{\Phi}}^{(1)}\right\},\qquad(94)$$

where

$$\hat{r}\cos\hat{\theta}=x_1,\quad \hat{r}\sin\hat{\theta}=-d,\qquad(95)$$

and use have been made of (55) and (*A*27) in the Appendix.

In a same way, we can write the generalized displacement vector at $x_2=0$ in a real form for the first system of problem of a semi-infinite plate with a free edge at $x_2=0$. The result can be written, together with (94), in a compact form

$$\begin{bmatrix} \mathbf{H}\boldsymbol{\phi}^{(1)}(x_1,0) \\ -\mathbf{L}\mathbf{u}^{(1)}(x_1,0) \end{bmatrix} = \frac{1}{\pi}\{(\ln \hat{r})\mathbf{I} + \pi\tilde{\mathbf{N}}(\hat{\theta})\}\begin{bmatrix} \hat{\mathbf{U}} \\ \hat{\mathbf{\Phi}}^{(1)} \end{bmatrix}. \tag{96}$$

The expressions for the second system of problem are similarly given as

$$\begin{bmatrix} \mathbf{H}\boldsymbol{\phi}^{(2)}(x_1,0) \\ -\mathbf{L}\mathbf{u}^{(2)}(x_1,0) \end{bmatrix} = \frac{1}{\pi}\{(\ln \hat{r})\mathbf{I} + \pi\tilde{\mathbf{N}}(\hat{\theta})\}\begin{bmatrix} \mathbf{0} \\ (x_1\mathbf{i}_3 - d\mathbf{i}_4)\hat{\mathcal{N}}_3 \end{bmatrix}. \tag{97}$$

Using the relation

$$\frac{\partial}{\partial x_1} = \cos\hat{\theta}\frac{\partial}{\partial \hat{r}} - \frac{\sin\hat{\theta}}{\hat{r}}\frac{\partial}{\partial \hat{\theta}}, \tag{98a}$$

$$\frac{\partial^2}{\partial x_1^2} = \cos^2\hat{\theta}\frac{\partial^2}{\partial \hat{r}^2} + \sin^2\hat{\theta}\left(\frac{1}{\hat{r}}\frac{\partial}{\partial \hat{r}} + \frac{1}{\hat{r}^2}\frac{\partial^2}{\partial \hat{\theta}^2}\right) + \sin 2\hat{\theta}\left(\frac{1}{\hat{r}^2}\frac{\partial}{\partial \hat{\theta}} - \frac{1}{\hat{r}}\frac{\partial^2}{\partial \hat{r}\partial \hat{\theta}}\right), \tag{98b}$$

we can derive the first and second derivatives of (96) with respect to x_1. The detailed derivation is omitted for brevity, only final results are given as follows:

$$\begin{bmatrix} \mathbf{H}\boldsymbol{\phi}^{(1)}_{,1}(x_1,0) \\ -\mathbf{L}\mathbf{u}^{(1)}_{,1}(x_1,0) \end{bmatrix} = \frac{1}{\pi\hat{r}}\{\cos\hat{\theta}\mathbf{I} - \sin\hat{\theta}\mathbf{N}(\hat{\theta})\}\begin{bmatrix} \hat{\mathbf{U}} \\ \hat{\mathbf{\Phi}}^{(1)} \end{bmatrix}. \tag{99}$$

$$\begin{bmatrix} \mathbf{H}\boldsymbol{\phi}^{(2)}_{,1}(x_1,0) \\ -\mathbf{L}\mathbf{u}^{(2)}_{,1}(x_1,0) \end{bmatrix} = \frac{1}{\pi\hat{r}}\{\cos\hat{\theta}\mathbf{I} - \sin\hat{\theta}\mathbf{N}(\hat{\theta})\}\begin{bmatrix} \mathbf{0} \\ (x_1\mathbf{i}_3 - d\mathbf{i}_4)\hat{\mathcal{N}}_3 \end{bmatrix} + \frac{1}{\pi}\{(\ln \hat{r})\mathbf{I} + \pi\tilde{\mathbf{N}}(\hat{\theta})\}\begin{bmatrix} \mathbf{0} \\ \mathbf{i}_3\hat{\mathcal{N}}_3 \end{bmatrix}. \tag{100}$$

$$\begin{bmatrix} \mathbf{H}\boldsymbol{\phi}^{(1)}_{,11}(x_1,0) \\ -\mathbf{L}\mathbf{u}^{(1)}_{,11}(x_1,0) \end{bmatrix} = -\frac{1}{\pi\hat{r}^2}\left\{\cos 2\hat{\theta}\mathbf{I} - \frac{d}{d\hat{\theta}}(\sin^2\hat{\theta}\mathbf{N}(\hat{\theta}))\right\}\begin{bmatrix} \hat{\mathbf{U}} \\ \hat{\mathbf{\Phi}}^{(1)} \end{bmatrix}. \tag{101}$$

$$\begin{bmatrix} \mathbf{H}\boldsymbol{\phi}^{(2)}_{,11}(x_1,0) \\ -\mathbf{L}\mathbf{u}^{(2)}_{,11}(x_1,0) \end{bmatrix} = -\frac{1}{\pi\hat{r}^2}\left\{\cos 2\hat{\theta}\mathbf{I} - \frac{d}{d\hat{\theta}}(\sin^2\hat{\theta}\mathbf{N}(\hat{\theta}))\right\} \times \begin{bmatrix} \mathbf{0} \\ (x_1\mathbf{i}_3 - d\mathbf{i}_4)\hat{\mathcal{N}}_3 \end{bmatrix} + \frac{2}{\pi\hat{r}}\{\cos\hat{\theta}\mathbf{I} - \sin\hat{\theta}\mathbf{N}(\hat{\theta})\} \times \begin{bmatrix} \mathbf{0} \\ \mathbf{i}_3\hat{\mathcal{N}}_3 \end{bmatrix}. \tag{102}$$

With these expressions, the hoop stress resultants (89*a*,*b*) and (90*a*,*b*) are readily obtained in a real form. Once again, one must keep in mind that the stress function vector and the generalized displacement vector given in (96), (97), and (99)–(102) are for a semi-infinite plate with a rigidly clamped edge and a free edge, respectively.

Surface Green's Functions for a Semi-Infinite Plate

Let a semi-infinite anisotropic plate is located at $x_2>0$, and the concentrated forces and moments are applied at the origin of the Cartesian coordinate system. The edge $x_2=0$ is otherwise traction-free. The surface Green functions can be reduced from the solutions for a semi-infinite plate by taking $\hat{\mathbf{U}}=\mathbf{0}$ and $d=0$. From (55) and (83),

$$\mathbf{q}^{(1)} = \mathbf{A}^T\hat{\mathbf{\Phi}}^{(1)}, \quad \mathbf{q}^{(1)}_J = \mathbf{B}^{-1}\overline{\mathbf{B}}\mathbf{I}_J\overline{\mathbf{q}}^{(1)}. \tag{103}$$

The solution given in (77*a*,*b*) reduces to

$$\mathbf{u}^{(1)} = \frac{1}{\pi}\mathrm{Im}\{\mathbf{A}\langle \ln z_*\rangle(\mathbf{A}^T + \mathbf{B}^{-1}\overline{\mathbf{B}\mathbf{A}}^T)\}\hat{\mathbf{\Phi}}^{(1)}, \tag{104a}$$

$$\boldsymbol{\phi}^{(1)} = \frac{1}{\pi}\mathrm{Im}\{\mathbf{B}\langle \ln z_*\rangle(\mathbf{A}^T + \mathbf{B}^{-1}\overline{\mathbf{B}\mathbf{A}}^T)\}\hat{\mathbf{\Phi}}^{(1)}, \tag{104b}$$

Using the closure relation (25*a*) and Eq. $(26)_3$, the solution (104*a*,*b*) can be rewritten as

$$\mathbf{u}^{(1)} = -\frac{2}{\pi}\mathrm{Re}\{\mathbf{A}\langle \ln z_*\rangle\mathbf{B}^T\}\mathbf{L}^{-1}\hat{\mathbf{\Phi}}^{(1)}, \tag{105a}$$

$$\boldsymbol{\phi}^{(1)} = -\frac{2}{\pi}\mathrm{Re}\{\mathbf{B}\langle \ln z_*\rangle\mathbf{B}^T\}\mathbf{L}^{-1}\hat{\mathbf{\Phi}}^{(1)}. \tag{105b}$$

Similarly, from (58) and (86),

$$\mathbf{q}^{(2)} = \mathbf{A}^T\hat{\mathbf{\Phi}}^{(2)}, \quad \mathbf{q}^{(2)}_J = \mathbf{B}^{-1}\overline{\mathbf{B}}\mathbf{I}_J\overline{\mathbf{q}}^{(2)}. \tag{106}$$

The solution given in (84*a*,*b*) reduces to

$$\mathbf{u}^{(2)} = -\frac{2}{\pi}\mathrm{Re}\{\mathbf{A}\langle z_* \ln z_*\rangle\mathbf{B}^T\}\mathbf{L}^{-1}\hat{\mathbf{\Phi}}^{(2)}, \tag{107a}$$

$$\boldsymbol{\phi}^{(2)} = -\frac{2}{\pi}\mathrm{Re}\{\mathbf{B}\langle z_* \ln z_*\rangle\mathbf{B}^T\}\mathbf{L}^{-1}\hat{\mathbf{\Phi}}^{(2)}. \tag{107b}$$

Using Eq. (*A*24) in the Appendix, the solutions (105*a*,*b*) and (107*a*,*b*) can be converted into a real form as

$$\begin{bmatrix} \mathbf{u}^{(1)} \\ \boldsymbol{\phi}^{(1)} \end{bmatrix} = \begin{bmatrix} -\frac{1}{\pi}(\ln r)\mathbf{I} - \mathbf{S}(\theta) \\ \mathbf{L}(\theta) \end{bmatrix}\mathbf{L}^{-1}\hat{\mathbf{\Phi}}^{(1)}, \tag{108}$$

$$\begin{bmatrix} \mathbf{u}^{(2)} \\ \boldsymbol{\phi}^{(2)} \end{bmatrix} = (x_1\mathbf{I} + x_2\mathbf{N})\begin{bmatrix} -\frac{1}{\pi}(\ln r)\mathbf{I} - \mathbf{S}(\theta) \\ \mathbf{L}(\theta) \end{bmatrix}\mathbf{L}^{-1}\hat{\mathbf{\Phi}}^{(2)}. \tag{109}$$

Strain Energy

The strain energy for a classical anisotropic thin plate on the area Λ is given by

$$\mathcal{U} = \tfrac{1}{2}\int_\Lambda (\mathcal{N}_{\alpha\beta}e^0_{\alpha\beta} + \mathcal{M}_{\alpha\beta}\kappa^0_{\alpha\beta})d\Lambda, \tag{110}$$

where the components of the plane strain and curvature on the midplane are

$$e^0_{\alpha\beta} = \frac{1}{2}(u_{\alpha,\beta} + u_{\beta,\alpha}), \quad \kappa^0_{\alpha\beta} = -w_{,\alpha\beta}. \tag{111}$$

Integrating (110) by parts and using the equilibrium Eqs. (7) yields

$$\mathcal{U} = \frac{1}{2}\oint_\Gamma (\mathcal{N}_{\alpha\beta}u_\alpha + \mathcal{M}_{\alpha\beta}\vartheta_\alpha + \mathcal{R}_\beta w)n_\beta ds, \tag{112}$$

where Γ is the contour of the area Λ on the x_1Ox_2-plane and n_β is its unit outward normal vector. The strain energy can be rewritten, after substitution of (16*a*–*c*), as

$$\mathcal{U} = -\frac{1}{2}\oint_\Gamma \left\{u_\alpha d\varphi_\alpha + \vartheta_\alpha d\psi_\alpha + \frac{1}{2}d(w\psi_{\omega,\omega})\right\}. \tag{113}$$

For the annulus region $0<r_1\leqslant r\leqslant r_2$ shown in Fig. 1, Γ consists of two circles of radii r_1 and r_2 and the lines above and below the branch cut on the negative x_1-axis between $r=r_1$ and r_2. The generalized displacement vector and stress function vector are continuous inside Γ. Thus the strain energy can be reduced to

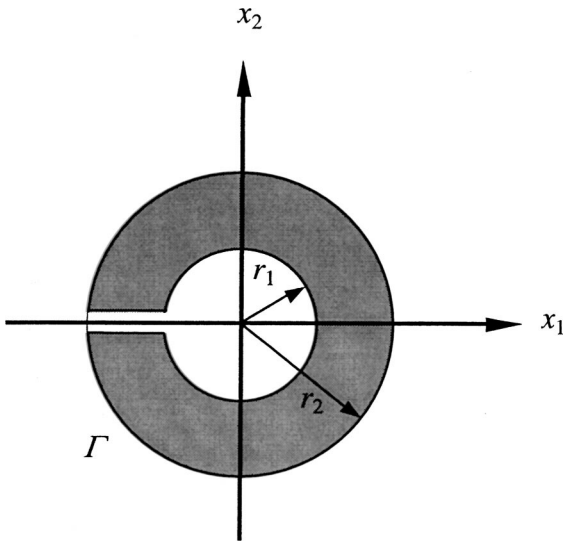

Fig. 1 Geometry and coordinate system used

$$\mathcal{U}=-\frac{1}{2}\oint_{\Gamma}\mathbf{u}^T d\boldsymbol{\phi}, \quad \text{or} \quad \mathcal{U}=\frac{1}{2}\oint_{\Gamma}\boldsymbol{\phi}^T d\mathbf{u}. \tag{114}$$

The calculation of the strain energy for an infinite anisotropic plate is based on the solutions given by (70) and (71). For the case of vanishing $\hat{\mathcal{N}}_3$, only solution in (70) for the first system of problem is needed. This solution is symbolically the same as the counterpart of the generalized plane-strain elasticity, [11,17,18]. We do not duplicate the detailed calculation but give the final result as

$$\mathcal{U}=\frac{1}{4\pi}\ln\left(\frac{r_2}{r_1}\right)(\hat{\boldsymbol{\Phi}}^{(1)T}\mathbf{H}\hat{\boldsymbol{\Phi}}^{(1)}+\hat{\mathbf{U}}^T\mathbf{L}\hat{\mathbf{U}}). \tag{115}$$

The strain energy caused by $\hat{\mathbf{U}}$ is obtained from the integrals on two lines above and below the branch cut, while the strain energy caused by $\hat{\boldsymbol{\Phi}}^{(1)}$ is obtained from the integrals on the two circles. Equation (115) shows that there is no interaction of strain energy between $\hat{\mathbf{U}}$ and $\hat{\boldsymbol{\Phi}}^{(1)}$. As used by Ref. [18], Eq. (115) also gives an indirect proof for the plate case that $\mathbf{H}$ and $\mathbf{L}$ must be positive definite if the strain energy is positive.

If $\hat{\mathbf{U}}$ is only concerned, then the integrals on the two circles contribute zero strain energy. This point was not provable in Ref. [7] analytically but confirmed in their numerical evaluation for a specific example.

For the case of the addition of the transverse force $\hat{\mathcal{N}}_3$, it seems there is interaction of strain energy between $\hat{\mathbf{U}}$, $\hat{\boldsymbol{\Phi}}^{(1)}$, and $\hat{\mathcal{N}}_3$ for an infinite anisotropic plate.

Conclusions

This work has presented an application of the new formalism for anisotropic thin plates. The exact Green functions for an infinite plate and surface Green functions for a semi-infinite plate have been given in a real form. The exact fundamental solutions for a semi-infinite plate with a clamped or free edge are also obtained by modifying the solutions for an infinite plate. The hoop stress resultants are presented in a real form. An indirect proof that $\mathbf{H}$ and $\mathbf{L}$ are positive definite matrices is provided under consideration of the strain energy.

Acknowledgment

The research presented herein was supported by the Oscar S. Wyatt Endowed Chair.

Appendix

Fundamental Elastic Plate Matrix. The standard eigenrelation in the Cartesian coordinate system $\{x_i\}$ is

$$\mathbf{N}\boldsymbol{\xi}=p\boldsymbol{\xi}, \tag{A1}$$

where, [13],

$$\mathbf{N}=(\mathbf{Y}_1+\mathbf{Y}_2)^{-1}(\mathbf{X}_1+\mathbf{X}_2), \quad \boldsymbol{\xi}=\begin{bmatrix}\mathbf{a}\\ \mathbf{b}\end{bmatrix}, \tag{A2}$$

with

$$\mathbf{X}_1=\begin{bmatrix}-\mathbf{Q} & \mathbf{0}\\ -\mathbf{R}^T & \mathbf{I}\end{bmatrix}, \quad \mathbf{Y}_1=\begin{bmatrix}\mathbf{R} & \mathbf{I}\\ \mathbf{T} & \mathbf{0}\end{bmatrix}, \tag{A3}$$

$$\mathbf{X}_2=\begin{bmatrix}\alpha\mathbf{I}_{44} & \frac{1}{2}\mathbf{I}_{43}\\ \beta\mathbf{I}_{34} & -\frac{1}{2}\mathbf{I}_{33}\end{bmatrix}, \quad \mathbf{Y}_2=\begin{bmatrix}\alpha\mathbf{I}_{43} & -\frac{1}{2}\mathbf{I}_{44}\\ \beta\mathbf{I}_{33} & \frac{1}{2}\mathbf{I}_{34}\end{bmatrix}, \tag{A4}$$

$$\mathbf{Q}=\begin{bmatrix}\mathcal{Q}\tilde{\mathbf{Q}} & \mathcal{Q}x_3\tilde{\mathbf{Q}}\\ \mathcal{Q}x_3\tilde{\mathbf{Q}} & \mathcal{Q}x_3^2\tilde{\mathbf{Q}}\end{bmatrix}, \quad \mathbf{R}=\begin{bmatrix}\mathcal{Q}\tilde{\mathbf{R}} & \mathcal{Q}x_3\tilde{\mathbf{R}}\\ \mathcal{Q}x_3\tilde{\mathbf{R}} & \mathcal{Q}x_3^2\tilde{\mathbf{R}}\end{bmatrix},$$

$$\mathbf{T}=\begin{bmatrix}\mathcal{Q}\tilde{\mathbf{T}} & \mathcal{Q}x_3\tilde{\mathbf{T}}\\ \mathcal{Q}x_3\tilde{\mathbf{T}} & \mathcal{Q}x_3^2\tilde{\mathbf{T}}\end{bmatrix}, \tag{A5}$$

and $\mathbf{I}_{33}$, $\mathbf{I}_{34}$, $\mathbf{I}_{43}$, and $\mathbf{I}_{44}$ are 4×4 matrices whose elements are

$$(\mathbf{I}_{33})_{KL}=\delta_{K3}\delta_{L3}, \quad (\mathbf{I}_{34})_{KL}=\delta_{K3}\delta_{L4},$$
$$(\mathbf{I}_{43})_{KL}=\delta_{K4}\delta_{L3}, \quad (\mathbf{I}_{44})_{KL}=\delta_{K4}\delta_{L4}. \tag{A6}$$

It can be easily shown that both $\mathbf{X}_1+\mathbf{X}_2$ and $\mathbf{Y}_1+\mathbf{Y}_2$ are reversible when $\alpha\neq\beta$.

The following equations are resulted from $(A2)_1$:

$$(\mathbf{Y}_1+\mathbf{Y}_2)_{KL}(\mathbf{N})_{L7}=(\mathbf{X}_1+\mathbf{X}_2)_{K7}, \quad (K,L=1,\ldots,8). \tag{A7}$$

We may view (A7) as a set of linear equations with respect to the eight unknowns $(\mathbf{N})_{L7}$. We do not have to solve the set of equation but can easily confirm that

$$(\mathbf{N})_{L7}=\delta_{L8} \tag{A8}$$

is a solution of (A7) in view of (A3) and (A4). Because $\mathbf{Y}_1+\mathbf{Y}_2$ is nonsingular when $\alpha\neq\beta$, the set of Eqs. (A7) have a unique solution for $(\mathbf{N})_{L7}$, which is (A8).

Fundamental Elastic Plate Matrix in a Rotated Coordinate System. Consider a rotated coordinate system $\{x_i^*\}$, obtained by rotating an angle θ about x_3-axis, i.e.,

$$x_\alpha^*=\Omega_{\alpha\beta}x_\beta, \quad \boldsymbol{\Omega}=\begin{bmatrix}\cos\theta & \sin\theta\\ -\sin\theta & \cos\theta\end{bmatrix}. \tag{A9}$$

Denoting $\mathbf{n}$ and $\mathbf{m}$ as the unit vectors along the positive x_1^* and x_2^*-axes, we have

$$\mathbf{n}^T=[\cos\theta \ \ \sin\theta], \quad \mathbf{m}^T=[-\sin\theta \ \ \cos\theta]. \tag{A10}$$

The standard eigenrelation in a rotated coordinate system $\{x_i^*\}$ can be derived as

$$\mathbf{N}(\theta)\boldsymbol{\xi}=p(\theta)\boldsymbol{\xi}, \tag{A11}$$

where

$$p(\theta)=\frac{p\cos\theta-\sin\theta}{p\sin\theta+\cos\theta}, \tag{A12}$$

$$\mathbf{N}(\theta)=(\mathbf{Y}_1(\theta)+\mathbf{Y}_2(\theta))^{-1}(\mathbf{X}_1(\theta)+\mathbf{X}_2(\theta)), \tag{A13}$$

with

$$\mathbf{X}_1(\theta)=\begin{bmatrix}-\mathbf{Q}(\theta) & \mathbf{0}\\ -\mathbf{R}^T(\theta) & \mathbf{I}\end{bmatrix},\quad \mathbf{Y}_1(\theta)=\begin{bmatrix}\mathbf{R}(\theta) & \mathbf{I}\\ \mathbf{T}(\theta) & \mathbf{0}\end{bmatrix}, \tag{A14}$$

$$\mathbf{X}_2(\theta)=\boldsymbol{\Theta}^T\mathbf{X}_2\boldsymbol{\Theta},\quad \mathbf{Y}_2(\theta)=\boldsymbol{\Theta}^T\mathbf{Y}_2\boldsymbol{\Theta},\quad \boldsymbol{\Theta}=\mathrm{diag}[\boldsymbol{\Omega},\boldsymbol{\Omega},\boldsymbol{\Omega},\boldsymbol{\Omega}]. \tag{A15}$$

$$\mathbf{Q}(\theta)=\begin{bmatrix}\mathcal{Q}\tilde{\mathbf{Q}}(\theta) & \mathcal{Q}x_3\tilde{\mathbf{Q}}(\theta)\\ \mathcal{Q}x_3\tilde{\mathbf{Q}}(\theta) & \mathcal{Q}x_3^2\tilde{\mathbf{Q}}(\theta)\end{bmatrix},$$

$$\mathbf{R}(\theta)=\begin{bmatrix}\mathcal{Q}\tilde{\mathbf{R}}(\theta) & \mathcal{Q}x_3\tilde{\mathbf{R}}(\theta)\\ \mathcal{Q}x_3\tilde{\mathbf{R}}(\theta) & \mathcal{Q}x_3^2\tilde{\mathbf{R}}(\theta)\end{bmatrix},$$

$$\mathbf{T}(\theta)=\begin{bmatrix}\mathcal{Q}\tilde{\mathbf{T}}(\theta) & \mathcal{Q}x_3\tilde{\mathbf{T}}(\theta)\\ \mathcal{Q}x_3\tilde{\mathbf{T}}(\theta) & \mathcal{Q}x_3^2\tilde{\mathbf{T}}(\theta)\end{bmatrix}, \tag{A16}$$

and

$$\begin{bmatrix}\tilde{\mathbf{Q}}(\theta) & \tilde{\mathbf{R}}(\theta)\\ \tilde{\mathbf{R}}^T(\theta) & \tilde{\mathbf{T}}(\theta)\end{bmatrix}=\begin{bmatrix}\cos\theta\mathbf{I} & \sin\theta\mathbf{I}\\ -\sin\theta\mathbf{I} & \cos\theta\mathbf{I}\end{bmatrix}\begin{bmatrix}\tilde{\mathbf{Q}} & \tilde{\mathbf{R}}\\ \tilde{\mathbf{R}}^T & \tilde{\mathbf{T}}\end{bmatrix}\times\begin{bmatrix}\cos\theta\mathbf{I} & -\sin\theta\mathbf{I}\\ \sin\theta\mathbf{I} & \cos\theta\mathbf{I}\end{bmatrix}, \tag{A17}$$

or

$$\tilde{Q}_{\alpha\omega}(\theta)=\tilde{C}_{\alpha\beta\omega\rho}n_\beta n_\rho,\quad \tilde{R}_{\alpha\omega}(\theta)=\tilde{C}_{\alpha\beta\omega\rho}n_\beta m_\rho,\quad \tilde{T}_{\alpha\omega}(\theta)=\tilde{C}_{\alpha\beta\omega\rho}m_\beta m_\rho. \tag{A18}$$

Identities Converting *A*, *B*, and $f(z)$ Into Real Matrices. From (*A*1), we have

$$(x_1\mathbf{I}+x_2\mathbf{N})\boldsymbol{\xi}=(x_1+px_2)\boldsymbol{\xi}=z\boldsymbol{\xi}, \tag{A19}$$

and thus,

$$(x_1\mathbf{I}+x_2\mathbf{N})^n\boldsymbol{\xi}=z^n\boldsymbol{\xi}. \tag{A20}$$

Integrating (*A*11) with respect to θ yields

$$\pi\tilde{\mathbf{N}}(\theta)\boldsymbol{\xi}=\ln(\cos\theta+p\sin\theta)\boldsymbol{\xi}=(\ln z-\ln r)\boldsymbol{\xi}, \tag{A21}$$

where

$$\tilde{\mathbf{N}}(\theta)\equiv\begin{bmatrix}\mathbf{S}(\theta) & \mathbf{H}(\theta)\\ -\mathbf{L}(\theta) & \mathbf{S}^T(\theta)\end{bmatrix}=\frac{1}{\pi}\int_0^\theta\mathbf{N}(\theta)d\theta. \tag{A22}$$

In terms of (*A*21), we have

$$((\ln r)\mathbf{I}+\pi\tilde{\mathbf{N}}(\theta))^s\boldsymbol{\xi}=(\ln z)^s\boldsymbol{\xi}. \tag{A23}$$

Combining (*A*20) and (*A*23) for $p=p_1,\ p_2,\ p_3,\ p_4$ gives

$$\begin{bmatrix}\mathbf{A}\langle z_*^n(\ln z_*)^s\rangle\mathbf{B}^T & \mathbf{A}\langle z_*^n(\ln z_*)^s\rangle\mathbf{A}^T\\ \mathbf{B}\langle z_*^n(\ln z_*)^s\rangle\mathbf{B}^T & \mathbf{B}\langle z_*^n(\ln z_*)^s\rangle\mathbf{A}^T\end{bmatrix}=\tfrac{1}{2}(x_1\mathbf{I}+x_2\mathbf{N})^n\{(\ln r)\mathbf{I}+\pi\tilde{\mathbf{N}}(\theta)\}^s(\mathbf{I}-i\tilde{\mathbf{N}}), \tag{A24}$$

and use has been made of the following identity:

$$\begin{bmatrix}\mathbf{A}\mathbf{B}^T & \mathbf{A}\mathbf{A}^T\\ \mathbf{B}\mathbf{B}^T & \mathbf{B}\mathbf{A}^T\end{bmatrix}=\frac{1}{2}(\mathbf{I}-i\tilde{\mathbf{N}}), \tag{A25}$$

where

$$\tilde{\mathbf{N}}=\begin{bmatrix}\mathbf{S} & \mathbf{H}\\ -\mathbf{L} & \mathbf{S}^T\end{bmatrix}. \tag{A26}$$

Because $\mathbf{N}$ and $\mathbf{N}(\theta)$ share the same eigenvectors, they are commutative matrices. So are $\mathbf{N}$, $\tilde{\mathbf{N}}(\theta)$, and $\tilde{\mathbf{N}}$. Sometimes, it is convenient to use an alternative form of (*A*24) as

$$\begin{bmatrix}\mathbf{A}\langle z_*^n(\ln z_*)^s\rangle\mathbf{B}^T & \mathbf{A}\langle z_*^n(\ln z_*)^s\rangle\mathbf{A}^T\\ \mathbf{B}\langle z_*^n(\ln z_*)^s\rangle\mathbf{B}^T & \mathbf{B}\langle z_*^n(\ln z_*)^s\rangle\mathbf{A}^T\end{bmatrix}=\tfrac{1}{2}\{(\ln r)\mathbf{I}+\pi\tilde{\mathbf{N}}(\theta)\}^s(\mathbf{I}-i\tilde{\mathbf{N}})(x_1\mathbf{I}+x_2\mathbf{N})^n. \tag{A27}$$

References

[1] Timoshenko, S. P., and Woinowsky-Krieger, S., 1959, *Theory of Plates and Shells*, McGraw-Hill, New York.
[2] Reddy, J. N., 1999, *Theory and Analysis of Elastic Plates*, Taylor and Francis, Philadelphia.
[3] Reddy, J. N., 2002, *Energy Principles and Variational Methods in Applied Mechanics*, John Wiley, and Sons, New York.
[4] Reddy, J. N., 1997, *Mechanics of Laminated Composite Plates: Theory and Analysis*, CRC Press, Boca Raton, FL.
[5] Becker, W., 1995, "Concentrated Forces and Moments on Laminates With Bending Extension Coupling," Compos. Struct. , **30**, pp. 1–11.
[6] Zakharov, D. D., and Becker, W., 2000, "Singular Potentials and Double-Force Solutions for Anisotropic Laminates With Coupled Bending and Stretching," Arch. Appl. Mech., **70**, pp. 659–669.
[7] Zakharov, D. D., and Becker, W., 2000, "Unsymmetric Composite Laminate With a Discontinuity of the In-Plane Displacement or of the Slope," Acta Mech., **144**, pp. 127–135.
[8] Eshelby, J. D., Read, W. T., and Shockley, W., 1953, "Anisotropic Elasticity With Applications to Dislocation Theory," Acta Metall., **1**, pp. 251–259.
[9] Stroh, A. N., 1958, "Dislocations and Cracks in Anisotropic Elasticity," Philos. Mag., **3**, pp. 625–646.
[10] Stroh, A. N., 1962, "Steady State Problem in Anisotropic Elasticity," J. Math. Phys., **41**, pp. 77–103.
[11] Ting, T. C. T., 1996, *Anisotropic Elasticity: Theory and Applications*, Oxford University Press, New York.
[12] Ting, T. C. T., 2000, "Recent Developments in Anisotropic Elasticity," Int. J. Solids Struct., **37**, pp. 401–409.
[13] Cheng, Z. Q., and Reddy, J. N., 2002, "Octet Formalism for Kirchhoff Anisotropic Plates," Proc. R. Soc. London, Ser. A, **458**, pp. 1499–1517.
[14] Barnett, D. M., and Lothe, J., 1973, "Synthesis of the Sextic and the Integral Formalism for Dislocations, Greens Functions and Surface Waves in Anisotropic Elastic Solids," Phys. Norv., **7**, pp. 13–19.
[15] Qin, S. W., Fan, H., and Mura, T., 1991, "The Eigenstrain Formulation for Classical Plates," Int. J. Solids Struct., **28**, pp. 363–372.
[16] Ting, T. C. T., 1992, "Image Singularities of Green's Functions for Anisotropic Elastic Half-Spaces and Bimaterials," Q. J. Mech. Appl. Math., **45**, pp. 119–139.
[17] Eshelby, J. D., 1956, "The Continuum Theory of Lattice Defects," Solid State Phys., **3**, pp. 79–144.
[18] Chadwick, P., and Smith, G. D., 1997, "Foundations of the Theory of Surface Waves in Anisotropic Elastic Materials," Adv. Appl. Mech., **17**, pp. 303–376.

An Acoustic-Microwave Method for the Study of the Mechanical Influence of Moisture Content in Materials

C. Bacon

E. Guilliorit

B. Hosten

Laboratoire de Mécanique Physique,
Université Bordeaux, 1,
UMR 5469 CNRS,
351, cours de la Libération,
33405 Talence Cedex, France

A one-dimensional theoretical model is developed to predict the acoustic waves generated by rapid thermal expansion caused by electromagnetic microwave absorption in viscoelastic rods. The theoretical acceleration at the end of the irradiated rod is predicted. The comparison between the experimental and the theoretical accelerations leads to the evaluation of viscoelastic characteristics. Parameters related to the electromagnetic absorption can be also obtained. A procedure to find approximate values of the different parameters is developed. Since it is considered in the model that the distribution of the temperature rise along the rod is exponential, very absorbing materials can be tested. Consequently, the influence of the moisture content on viscoelastic properties of a porous material can be investigated. The method is applied to study the influence of the moisture content on viscoelastic characteristics of medium density fiberboard materials.
[DOI: 10.1115/1.1545783]

1 Introduction

The mechanical properties of materials made from wood are particularly influenced by their moisture content. For such materials, a good knowledge of their mechanical properties needs to evaluate their viscoelastic properties for several moisture contents. This is useful, for instance, in order to perform numerical simulations.

A lot of experimental methods permit the determination of viscoelastic properties of materials. The most famous method involves classical creep or relaxation tests which are time-consuming and leads to the viscoelastic characteristics of the tested material at very low frequency only. Higher frequencies can be reached by dynamic tests. A comprehensive review of the experimental techniques is out of the scope of this paper. The reader is referred to the reviews of Nolle [1], McSkimin [2], Ferry [3], and Nowick and Berry [4]. Among these dynamic methods, some papers have been devoted to the determination of viscoelastic characteristics by means of a dynamically loaded slender rod. The rod specimen can be loaded harmonically, [5–11], by means of a shaker or impacted, [12–15]. In the latter case, the viscoelastic properties are evaluated by studying the change in shape of a stress pulse as it travels back and forth along a viscoelastic rod. In both cases, the wave generation requires the contact of a shaker or a projectile.

The present paper deals with a new method where the specimen rod is loaded by a rapid electromagnetic microwave irradiation, [16]. Contrary to the above techniques, this method does not require a mechanical contact for the wave generation. Consequently, the tests are very reproducible. The acoustic generation is caused by the electromagnetic absorption of the irradiated material. Indeed, the microwave energy is absorbed and converted into thermal energy, which caused the irradiated material to expand in accord with its thermoelastic properties. Thus the acoustical waves are produced by a sudden heating of the irradiated material. In a previous paper, [17], since the electromagnetic absorption was low, it was assumed that the profile of the temperature rise in the irradiated rod was uniform or linear. In the present paper, the electromagnetic absorption due to a high moisture content may be significant. Thus the assumption of a linear profile is not appropriate in this case and an exponential profile must be assumed, as already applied to composite materials, [18].

The aim of this paper is to develop an experimental method which permits the determination of the viscoelastic properties by means of the acoustic waves generated by electromagnetic absorption of pulsed microwaves. Contrary to the method described in a previous paper for low absorbing materials, [17], the presented method must be available for very absorbing materials when a linear profile of the temperature rise is not appropriate any more. A high moisture content may indeed increase the electromagnetic absorption significantly. Consequently, it must be considered that the profile of the temperature rise in the irradiated rod is exponential. A one-dimensional model will be developed to predict the acceleration at the end of the specimen. The comparison between the experimental and the theoretical accelerations will allow one to evaluate the viscoelastic properties of the specimen but also other parameters, such as its absorption coefficient or the temperature rise reached after the irradiation by a microwave pulse. A procedure will be presented to estimate approximate values of these parameters.

The method will be used for the study of the moisture content influence on the viscoelastic properties of medium density fiberboard (MDF) rods.

2 Experimental Setup

The experimental setup with the instrumented specimen rod is presented in Fig. 1.

The microwaves are produced by a time-gated electromagnetic generator at 9.41 GHz. The maximum power of the incident electromagnetic wave is 5.5 kW, and the maximum pulse width is 1 μs. To increase the amplitude of the acoustic waves generated, a burst of 10 pulses with a repetition rate of 500 kHz is used. The wave is delivered by a circular waveguide having a diameter of 24 mm that permits only the fundamental waveguide mode TE_{11} to propagate (no electric field in the propagation direction). To ob-

Contributed by the Applied Mechanics Division of THE AMERICAN SOCIETY OF MECHANICAL ENGINEERS for publication in the ASME JOURNAL OF APPLIED MECHANICS. Manuscript received by the Applied Mechanics Division, July 18, 2000; final revision, Aug. 1, 2002. Associate Editor: V. K. Kinra. Discussion on the paper should be addressed to the Editor, Prof. Robert M. McMeeking, Chair, Department of Mechanics and Environmental Engineering, University of California–Santa Barbara, Santa Barbara, CA 93106-5070, and will be accepted until four months after final publication in the paper itself in the ASME JOURNAL OF APPLIED MECHANICS.

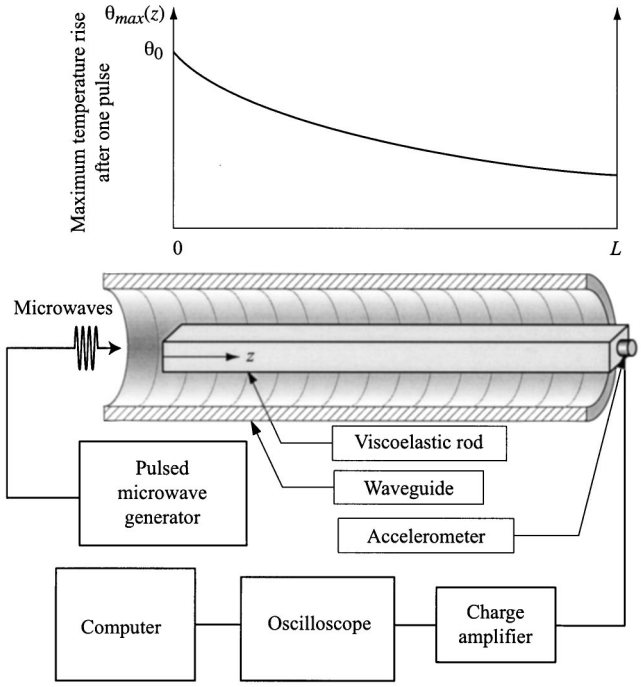

Fig. 1 Experimental setup

tain the maximum power from the generator, a hybrid tee impedance adaptor (tee associated to two sliding short circuits) is inserted into the circuit and adjusted to achieve a minimum voltage standing wave ratio (VSWR), as measured by a wattmeter. Then, the specimen can receive the maximum electromagnetic energy and the measured signals are increased.

The viscoelastic rod sample is held vertically inside the waveguide by means of a piece of foam put at the end of the waveguide. A piezoelectric miniature accelerometer (Brüel & Kjaer 4374) is attached to the end of the rod by means of a very thin layer of couplant. The accelerometer mass m is 0.65 g and its charge sensitivity is 0.129 pC/m·s^{-2}. Its dynamic frequency range lies between about 1 Hz and 20 kHz. The signal from the accelerometer is amplified by a charge amplifier (Brüel & Kjaer 2525), and recorded on a digital oscilloscope (Lecroy 9310) that is, in turn, linked to a computerized data acquisition system. The waveforms are averaged in the scope during ten sweeps in order to minimize the electronic noise and the environmental vibrations, and transferred to a computer for further processing.

3 Theory

The aim of this section is to find a one-dimensional model which can predict the theoretical acceleration at the end of a viscoelastic irradiated rod.

Let us consider a viscoelastic rod put in a waveguide (z is the axial coordinate, see Fig. 1). The length of the rod is L. Its mechanical characteristics, its mass density ρ and its cross-sectional area A are uniform. The free surface at $z=0$ is irradiated uniformly by an electromagnetic pulsed microwave. Owing to the electromagnetic absorption, a temperature rise $\theta(z,t)$ occurs inside the body (t is the time).

The Fourier transforms, $\tilde{\sigma}(z,\omega)$ and $\tilde{u}(z,\omega)$, of the normal stress $\sigma(z,t)$ and the axial displacement $u(z,t)$, respectively, are related by

$$\frac{\partial}{\partial z}\tilde{\sigma}(z,\omega)=-\rho\omega^2\tilde{u}(z,\omega) \tag{1}$$

where the angular frequency ω is related to the frequency ν by $\omega=2\pi\nu$. The stress state can be considered uniaxial in the rod if the lateral dimensions are much smaller than the wavelengths. According to the classical theory of thermoviscoelasticity, the normal stress and the axial displacement are connected through the convolution relation

$$\sigma(z,t)=\int_{-\infty}^{t}E(t-\tau)\frac{\partial}{\partial\tau}[\varepsilon(z,\tau)-\beta\theta(z,\tau)]d\tau$$

$$=\frac{\partial E(t)}{\partial t}*[\varepsilon(z,t)-\beta\theta(z,t)] \tag{2}$$

where $E(t)$ is the tensile relaxation modulus, $\varepsilon(z,t)$ the longitudinal strain, β the coefficient of linear thermal expansion in the z-direction, and $\theta(z,t)$ the temperature rise above the initial temperature. This linear viscoelastic constitutive law can be expressed in the frequency domain as

$$\tilde{\sigma}(z,\omega)=E^*\tilde{\varepsilon}(z,\omega)-E^*\beta\tilde{\theta}(z,\omega) \tag{3}$$

where $E^*=E'+iE''$ is the complex Young's modulus in the z-direction with E' the storage modulus and E'' the loss modulus, $\tilde{\varepsilon}(z,\omega)$ and $\tilde{\theta}(z,\omega)$ the Fourier transforms of the longitudinal strain and the temperature rise above the initial temperature, respectively.

Since it will be seen that the temperature rise is very low, the temperature distribution will be assumed to be independent of the mechanical state of the material. From Eqs. (1) and (3), it can be demonstrated that the Fourier transforms of the axial displacement can be calculated if the longitudinal strain and the temperature rise are known, i.e.,

$$\tilde{u}(z,\omega)=\frac{1}{(\omega S^*)^2}\left[\beta\frac{\partial\tilde{\theta}(z,\omega)}{\partial z}-\frac{\partial\tilde{\varepsilon}(z,\omega)}{\partial z}\right] \tag{4}$$

where the complex slowness $S^*=S'-iS''$ is given by

$$S^{*2}=\frac{\rho}{E^*}. \tag{5}$$

Equation (3) becomes

$$\tilde{\sigma}(z,\omega)=\frac{\rho}{S^{*2}}[\tilde{\varepsilon}(z,\omega)-\beta\tilde{\theta}(z,\omega)]. \tag{6}$$

The axial particle velocity $\tilde{v}(z,\omega)$ and the axial acceleration $\tilde{a}(z,\omega)$ are given by

$$\tilde{v}(z,\omega)=i\omega\tilde{u}(z,\omega),\tilde{a}(z,\omega)=-\omega^2\tilde{u}(z,\omega). \tag{7}$$

In the hypothesis of small strains, the longitudinal strain is related to the axial displacement by $\varepsilon(z,t)=\partial u(z,t)/\partial z$. Consequently, Eq. (1) becomes

$$\frac{\partial^2\tilde{\varepsilon}(z,\omega)}{\partial z^2}+\omega^2S^{*2}\tilde{\varepsilon}(z,\omega)-\beta\frac{\partial^2\tilde{\theta}(z,\omega)}{\partial z^2}=0. \tag{8}$$

For short microwave pulses, the heat conduction can be neglected. Owing to the electromagnetic absorption, it can be assumed with sufficient accuracy that the temperature rise profile in the irradiated rod is exponential, i.e.,

$$\theta(z,t)=[\theta_0e^{-az}]\cdot r(t)\ \text{ with }\ r(t)=\begin{cases}0 & \text{for } t\leqslant 0\\ t/\tau & \text{for } 0<t<\tau\\ 1 & \text{for } t\geqslant\tau\end{cases} \tag{9}$$

where τ is the duration of the microwave pulse and θ_0 is the temperature rise after one pulse at $z=0$. The temporal evolution of the temperature rise is explained by the fact that, during the electromagnetic pulse ($0<t<\tau$), the temperature increases linearly since the heat conduction can be neglected owing to the short

duration of the microwave pulses. The spatial decreasing exponential profile is caused by the electromagnetic absorption when the wave propagates along the specimen.

With this exponential temperature profile, the general solution of Eq. (8) can be written as

$$\tilde{\varepsilon}(z,\omega)=\tilde{P}(\omega)e^{-i\omega S^* z}+\tilde{N}(\omega)e^{i\omega S^* z}+\frac{\beta\theta_0 a^2}{a^2+\omega^2 S^{*2}}\tilde{r}(\omega)e^{-az} \tag{10}$$

where the functions $\tilde{P}(\omega)$ and $\tilde{N}(\omega)$ are two functions depending on the boundary conditions at both ends of the rod.

At this stage, the purpose is to find the relationship between the normal force and the acceleration at cross section $z=0$ and these two quantities at cross section $z=L$. By writing the normal force $\tilde{F}(z,\omega)$ and the acceleration $\tilde{a}(z,\omega)$ at $z=0$ and $z=L$ with the help of Eqs. (4), (6), (7), and (10), $\tilde{P}(\omega)$ and $\tilde{N}(\omega)$ can be eliminated. Then, we obtain

$$\begin{bmatrix}\tilde{F}(L,\omega)\\ \tilde{a}(L,\omega)\end{bmatrix}=P\begin{bmatrix}\tilde{F}(0,\omega)\\ \tilde{a}(0,\omega)\end{bmatrix}+G \tag{11}$$

where the components of the matrix P and the vector G are defined by

$$P=\begin{bmatrix} c & \dfrac{\rho A}{\omega S^*}s \\ -\dfrac{\omega S^*}{\rho A}s & c \end{bmatrix}, \tag{12}$$

$$G=\frac{\beta\theta_0\tilde{r}\omega^2}{a^2+\omega^2 S^{*2}}\begin{bmatrix} A\rho\left(c-\dfrac{as}{\omega S^*}-e^{-aL}\right) \\ -\omega S^* s+ae^{-aL}-ac \end{bmatrix} \tag{13}$$

where $c=\cos(\omega S^* L)$ and $s=\sin(\omega S^* L)$. It can be noticed that the matrix P is related to the wave propagation whereas the vector G is related to the wave generation due to the thermal expansion. Only G depends on the spatial profile of the temperature rise in the irradiated rod.

Then, the determination of the acceleration at $z=L$ (for instance) involves the knowledge of the boundary conditions. The end at $z=0$ is free. Consequently, the normal force at $z=0$ must be zero, i.e., $\tilde{F}(0,\omega)=0$. The rod is instrumented with an accelerometer having a mass m at the end $z=L$. Thus, the normal force at this end is related to the axial velocity by

$$\tilde{F}(L,\omega)=-Z_a\tilde{v}(L,\omega) \tag{14}$$

where Z_a is the mechanical impedance of the accelerometer. At low frequencies, the accelerometer can be assumed to be a rigid mass. Then, its mechanical impedance is given by $Z_a=im\omega$. With the help of these boundary conditions and Eq. (11), the acceleration at $z=L$ is

$$\tilde{a}(L,\omega)=\frac{P_{22}G_1-P_{12}G_2}{\dfrac{iZ_a}{\omega}P_{22}-P_{12}}. \tag{15}$$

In the forward problem, the viscoelastic mechanical properties, the mass density, the dimensions of the irradiated rod, the product $\beta\theta_0$ of the coefficient of thermal expansion by the maximum temperature reached after one pulse, the electromagnetic absorption a and the temporal function $r(t)$ are known. Thus, the acceleration measured by the accelerometer can be predicted theoretically. The function $r(t)$ is assumed to be given by Eq. (9). In the inverse problem, the acceleration is measured at the end of the irradiated rod. By comparing the measured signal to the theoretical one, it may be possible to evaluate the real part and the imaginary part of the complex slowness, S' and S'', the electromagnetic absorption a, and the product $\beta\theta_0$. To solve this inverse problem, we need to implement a numerical procedure using the theoretical Eq. (15).

4 Determination of the Different Parameters

In order to evaluate experimentally the set of the four parameters $\mathbf{p}=(S',S'',a,\beta\theta_0)$, the difference between the moduli of the Fourier transforms of the experimental and the theoretical accelerations in the accelerometer frequency range can be minimized by a numerical procedure. The minimization allows one to find the optimal set of parameters $\mathbf{p}$ that fits the experimental and the theoretical acceleration spectra at best. To simplify the minimization procedure, it must be assumed that the variation of the complex slowness with frequency is small in the frequency range of the accelerometer. The function to minimize is given by

$$J(\mathbf{p})=\sum_{\nu}\left\|\tilde{a}_{\exp}(\nu)|-|\tilde{a}(\nu,\mathbf{p})\right\| \tag{16}$$

where $|\tilde{a}_{\exp}(\nu)|$ and $|\tilde{a}(\nu,\mathbf{p})|$ are the moduli of the Fourier transforms of the experimental and the theoretical accelerations, respectively. The values reached by this procedure may be false if the initial values used to start the numerical minimization are too far from the real values. Consequently, it is important to develop a method that can provide approximate values close to the real ones. The method will be based on the shape of the acceleration spectrum measured at the end $z=L$. This spectrum has been calculated theoretically and plotted in Fig. 2 in the case of a PVC rod having a length $L=20$ cm ($S'=600$ μs/m, $S''=10$ μs/m). It is characterized by the presence of peaks (only the first and the second ones are represented in Fig. 2). The frequency of the nth peak is called ν_n and its amplitude is a_n. The characteristics of the two first peaks at frequencies ν_1 and ν_2 will allow one to evaluate the approximate values of some parameters.

First, it can be noticed that the frequencies ν_n are related to the real part of the complex slowness by

$$\nu_n\approx\frac{n}{2LS'}. \tag{17}$$

This relation is an approximation because the presence of the accelerometer reduces the value of the peak frequency slightly. As an example, for a PVC rod of 20 cm, the error made by using relation (17) with an accelerometer lighter than 2 g would be less than 3.2%. With an accelerometer having a mass of 0.65 g (accelerometer used in the experimental setup), the error would be less than 1%. The value of the real part of the complex slowness is found without knowing the spatial profile of the temperature rise. Moreover, the parameter S' can be obtained independently at each frequency ν_n of the measured acceleration peaks. This fact allows to verify whether the real part of the slowness depends on the frequency.

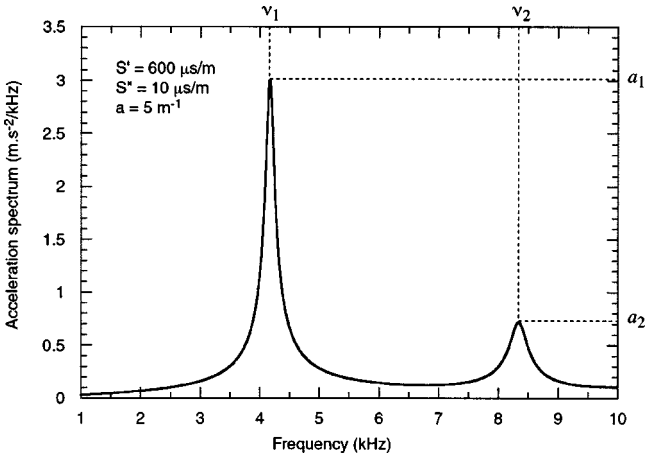

Fig. 2 Theoretical acceleration spectrum for a PVC rod

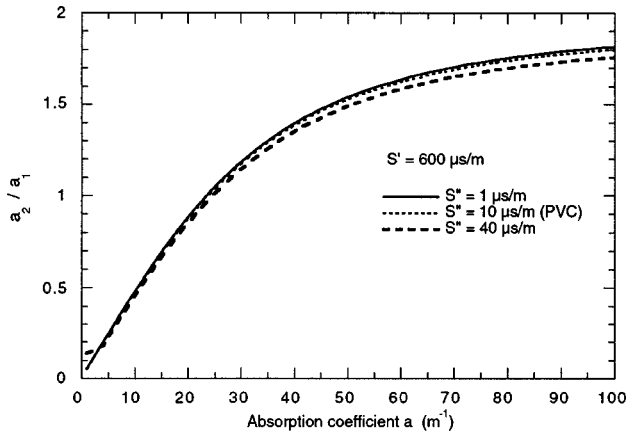

Fig. 3 Ratios a_2/a_1 for different imaginary parts of the complex slowness ($L=20$ cm)

Once the parameter S' is evaluated thanks to Eq. (17), the electromagnetic absorption coefficient a can be determined even if the imaginary part of the complex slowness is unknown. To prove that, the curve corresponding to the ratio a_2/a_1 (where a_1 and a_2 are the amplitudes of the two first peaks of the acceleration spectrum, see Fig. 2) is plotted in Fig. 3 for very different values of the imaginary part S'' of the complex slowness (the other characteristics used in the calculation are the characteristics of a PVC rod having a length of 20 cm). From Fig. 3, it can be noticed that, compared to the amplitude of the first peak, the amplitude of the second peak increases with the absorption coefficient. This curve permits the determination of the absorption coefficient a with a quite good accuracy by measuring the ratio a_2/a_1 of the amplitudes of the two first peaks. It can be plotted automatically in a few seconds when S' is known.

The imaginary part S'' of the complex slowness is more difficult to obtain. As shown in Fig. 4, this parameter is related to the widths of the spectrum peaks. The normalized acceleration spectra have been plotted in Fig. 4 for three different values of S''. Each normalized acceleration spectrum corresponds to the ratio between the acceleration spectra and the maximum amplitude a_1 of the first peak. The parameters S' and a evaluated by the methods described above are used for the calculations. The normalized spectra does not depend on the last parameter $\beta\theta_0$.

Consequently, the value of S'' can be obtained by a numerical minimization procedure using one parameter. In this case, the function to minimize is given by

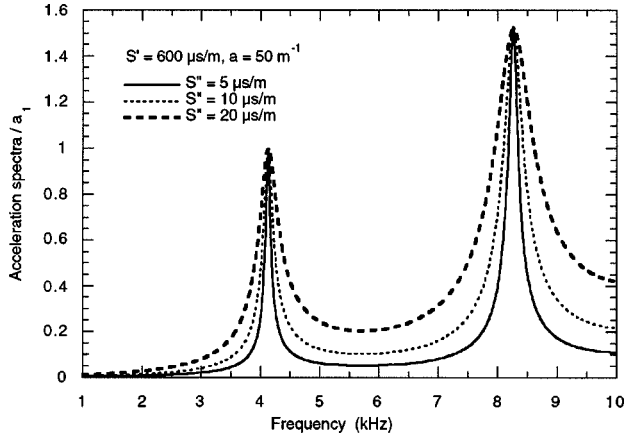

Fig. 4 Normalized acceleration spectra for different imaginary parts of the complex slowness ($L=20$ cm)

$$J(S'')=\sum_{\nu}\left|\frac{|\tilde{a}_{\exp}(\nu)|}{a_{1\,\exp}}-\frac{|\tilde{a}(\nu,S'')|}{a_1(S'')}\right|. \tag{18}$$

A trick to evaluate an approximate value of S'' is to measure the amplitude of the normalized spectrum in the central area between the two first peaks. Indeed, this value is almost proportional to the value of S''. This fact has been verified for very different values of the other parameters S' and a. Then, in the central area between the two frequencies ν_1 and ν_2, the ratio between the experimental normalized spectrum and a theoretical normalized spectrum, calculated with an arbitrary reference value S''_{ref} of S'', gives directly the ratio between the approximate actual value of S'' and the chosen reference value:

$$\frac{S''}{S''_{\text{ref}}}\approx\left.\frac{|\tilde{a}(\nu,S'')|/a_1(S'')}{|\tilde{a}(\nu,S''_{\text{ref}})|/a_1(S''_{\text{ref}})}\right|_{\nu\approx\nu_1+\nu_2/2}. \tag{19}$$

At this stage, approximate values of the three parameters S', S'', and a have been obtained. Only the product $\beta\theta_0$ remains unknown. Since the acceleration spectrum is proportional to $\beta\theta_0$, the simplest way to evaluate its approximate value is to use the following equation:

$$\beta\theta_0=\frac{\Sigma_\nu|\tilde{a}_{\exp}(\nu)|}{\Sigma_\nu|\tilde{a}(\nu,\beta\theta_0=1)|} \tag{20}$$

where $|\tilde{a}(\nu,\beta\theta_0=1)|$ corresponds to the theoretical acceleration spectrum calculated with the values of S', S'', and a obtained above and $\beta\theta_0=1$.

Once all the approximate values of the four parameters have been evaluated by the methods described above, these values can be used as initial values in the numerical minimization procedure of the function given by Eq. (16) in order to increase their accuracy.

5 Experimental Results for Medium Density Fiberboard (MFD) Rods

MDF is an engineered wood product composed of fine wood fibers combined with a synthetic resin or other bonding system and joined together under heat and pressure to form large panels. The influence of the moisture content on the viscoelastic properties of this kind of material may be significant. The aim of this section is to apply the method described above for the study of different MDF materials. The effect of the moisture content will be particularly analyzed.

Three different MDF materials with different densities were tested. They are denoted MDF A, MDF B, and MDF C. The material A comes from a manufacturer, the materials B and C come from another one. For each material, one rod specimen was cut in the machine direction. The lengths are 19 cm for MDF A and 21 cm for MDF B and C. The cross sections are rectangular with lateral dimensions 10×20 mm^2.

In order to increase their moisture content, the three specimens were put in a box with saturated air (humidity of 100%) during 72 hours approximately at room temperature. Afterward, the specimens were dried progressively at ambient humidity and temperature. During this stage, microwave tests, dimensions, and mass measurements were performed regularly for the three specimens. When the mass of the rods became stable, they were put in an oven at a temperature of 80°C during about ten hours in order to dry them completely. The mass of the dry specimen is used for the calculation of the moisture content. Indeed, the moisture content of a specimen is defined as the difference between its mass and its dry mass divided by its dry mass. The densities calculated from these dry masses are 510 kg/m^3, 570 kg/m^3, and 700 kg/m^3 for MDF A, B, and C, respectively.

The data collected from the previous tests were treated with the method described above in order to determinate the four parameters S', S'', a, and $\beta\theta_0$ at each moisture content for the three

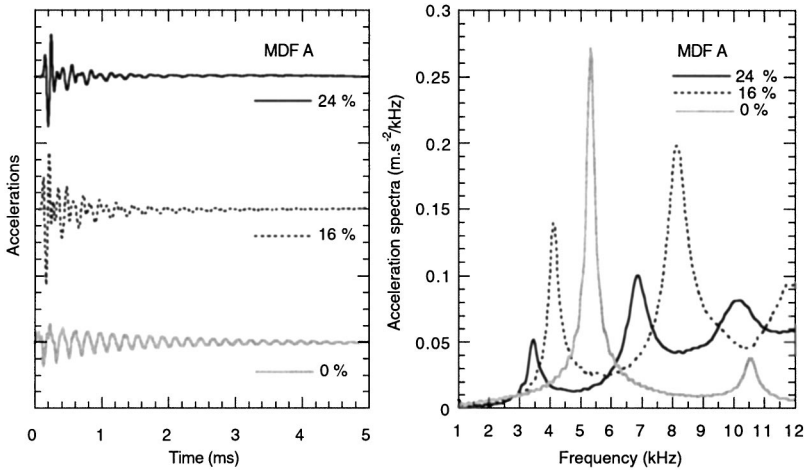

Fig. 5 Experimental acceleration signals and experimental acceleration spectra for three moisture contents (MDF A)

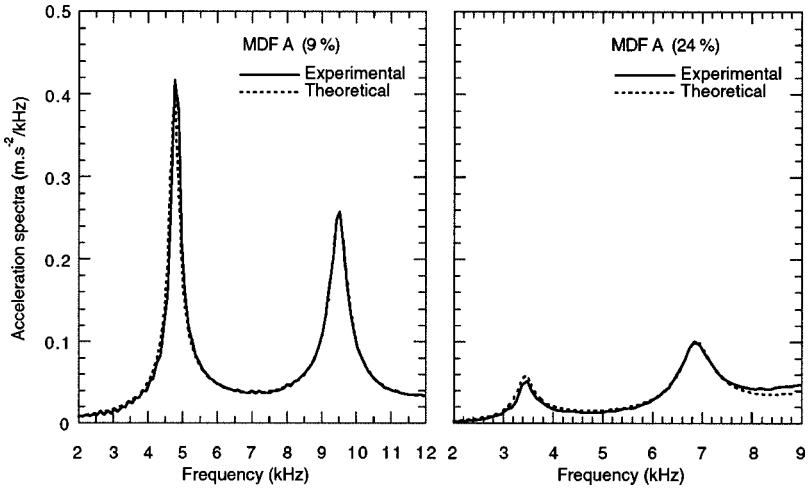

Fig. 6 Experimental and theoretical acceleration spectra for two moisture contents (MDF A)

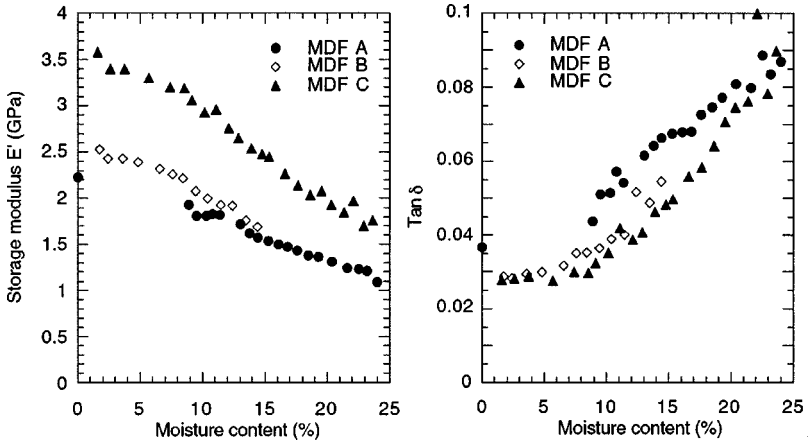

Fig. 7 Storage modulus and loss angle versus moisture content

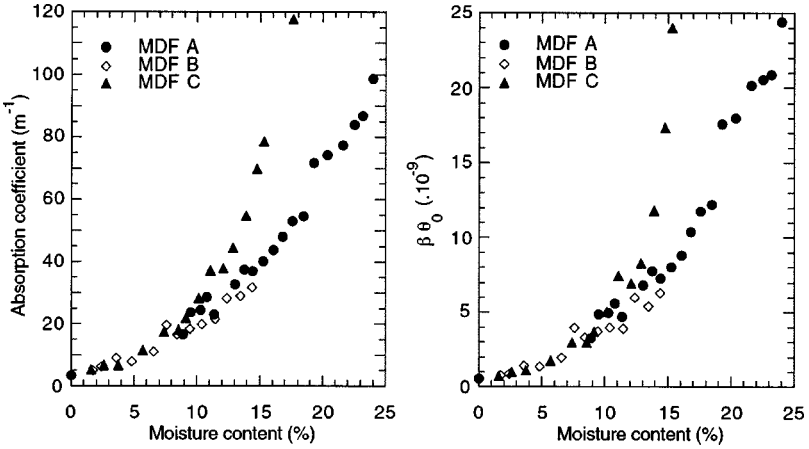

Fig. 8 Absorption coefficient and product of the maximum temperature rise by the thermal expansion coefficient versus moisture content

specimens. The moisture contents tested are less than 25% for MDF A and C. They are less than 15% for MDF B. The specimen A was not tested between 0% and 9%. Some examples of experimental acceleration signals are given in Fig. 5 for three different moisture contents. These waveforms come from the tests performed for MDF A. The corresponding experimental acceleration spectra are also plotted in Fig. 5 for the same moisture contents.

It is well known that the electromagnetic absorption of microwaves by water is quite significant. Consequently, since the electromagnetic absorption of the irradiated body will increase with its moisture content, the temperature rise will increase too. The result of the data processing will show that this statement is true although it can be shown in Fig. 5 that the amplitude of the first peak in the acceleration spectra decreases when the moisture content increases for the plotted spectra.

The method presented in the last section has been used to determinate the experimental values of the four parameters for each specimen rod and for each tested moisture content. From the results obtained by the minimization procedure, the theoretical acceleration spectra have been calculated and compared to the experimental acceleration spectra in the case of the material MDF A and for two different moisture contents (see Fig. 6).

The experimental curve and the theoretical curve obtained from the evaluated set of parameters are very close. This fact tends to demonstrate the validity of the theoretical model. The results obtained for the four parameters are presented in Figs. 7 and 8. From the evaluated complex slowness, the complex viscoelastic modulus has been calculated by means of Eq. (5). The real part, the storage modulus, and the tangent of the loss angle δ ($\tan\delta = E''/E'$) have been plotted in Fig. 7.

Concerning the storage modulus, it can be noticed that the ones of MDF A and B are very close even if the densities of both materials are different. The storage modulus of MDF C is higher. This fact can be explained by a higher density of this last material. On the other hand, the loss angles are quite close for the three materials but the one of MDF A seems to be a little higher. From Fig. 7, it can be shown that the increase of the moisture content leads to a decrease of the specimen rigidity and an increase of the viscoelastic damping effect. As it has been predicted above, it is shown in Fig. 8 that the electromagnetic absorption and thus the temperature rise increase for the three material when the moisture content increases. In order to give an order of magnitude for the temperature rise reached in the irradiated materials, the coefficient of thermal expansion must be known. If the coefficient of thermal expansion is estimated on the order of $10^{-5}/°C$ (that is generally the case for most materials, particularly for wood), it can be deduced that the temperature rise θ_0 reached after one pulse of 1 μs varies between $0.5\cdot10^{-4}°C$ and $25\cdot10^{-4}°C$ approximately. This temperature rise is extremely low but it is sufficient to generate acoustic waves which are measurable with the accelerometer. For the absorption coefficient as well as for the product $\beta\theta_0$ shown in Fig. 8, it can be noticed the fact that the results are very close up to about 10% or 12% of moisture content. Beyond, there is a discrepancy between MDF A and C. It is out of the scope of this paper to explain these effects. It can be just concluded here that the absorption coefficient and the maximum temperature rise (or rather the product $\beta\theta_0$) are some better indicators of the moisture content than the mechanical properties evaluated by the method since the variations of these parameters with the moisture content seem to be identical for the three tested materials, at least up to 10% or 12% of moisture content.

6 Conclusions

A new method to determine the viscoelastic properties of materials in a frequency range between 1 kHz to 20 kHz has been presented. This method uses a theoretical one-dimensional model developed in order to predict the acoustic waves generated in viscoelastic rods by electromagnetic microwave pulses. The phenomenon of acoustic generation is thermoviscoelastic. Besides the viscoelastic characteristics, parameters related to the electromagnetic absorption can be evaluated. These parameters are the electromagnetic absorption coefficient and the product of the coefficient of thermal expansion by the maximum temperature reached after one microwave pulse. Finally, four parameters can be obtained (two mechanical ones and two electromagnetic ones). Contrary to a previous paper where it was considered that the electromagnetic absorption in the irradiated material was low, [17], very absorbing materials can be tested with the present method since the profile of the temperature rise in the rod is assumed to be exponential, which is more realistic than a linear or uniform profile. This fact allows one to investigate the influence of the moisture content on the viscoelastic properties of a porous material. The presence of the accelerometer mass at the end of the rod is taken into account in the model. Moreover, a procedure has been proposed to find approximate values of the different parameters to be measured. Once these approximate values have been evaluated, a numerical minimization procedure allows to increase their accuracy.

Next, the method has been applied to the study of the influence of the moisture content on the viscoelastic characteristics of medium density fiberboard (MFD) materials. Three specimens having different densities have been tested. The comparisons between experimental spectra and theoretical spectra calculated with the evaluated parameters have demonstrated the validity of the theoretical one-dimensional model. The results obtained for the me-

chanical parameters have confirmed that the moisture content has a significant influence on viscoelastic properties of MDF materials. An important observation is that the evaluated absorption coefficient and maximum temperature rise are some good indicator of the moisture content in the tested material. In a future study, we could imagine an extension of this method, directly implemented in the production line, to control moisture content and viscoelastic characteristics during the manufacturing process.

Acknowledgment

The authors are indebted to the Conseil Régional d'Aquitaine and the Délégation Régionale à la Recherche et à la Technologie d'Aquitaine for their financial support.

References

[1] Nolle, A. W., 1948, ''Methods for Measuring the Dynamic Mechanical Properties of Rubber-Like Materials,'' J. Appl. Phys., **19**, pp. 753–774.
[2] McSkimin, H. J., 1964, ''Ultrasonic Methods for Measuring the Mechanical Properties of Liquids and Solids,'' Phys. Acoust., E. P. Mason, ed, **1A**, pp. 271–334.
[3] Ferry, J. D., 1970, *Viscoelastic Properties of Polymers*, John Wiley and Sons, New York.
[4] Nowick, A. S., and Berry, B. S., 1972, Anelastic Relaxation in Crystalline Solids, Academic Press, New York.
[5] Hillier, K. W., and Kolsky, H., 1949, ''An Investigation of the Dynamic Mechanical Properties of Some High Polymers,'' Proc. Phys. Soc. London, **B62**, pp. 111–121.
[6] Hillier, K. W., 1949, ''A Method of Measuring Some Dynamic Elastic Constants and Its Application to the Study of High Polymers,'' Proc. Phys. Soc. London, **B62**, pp. 701–713.
[7] Kolsky, H., 1957, ''The Propagation of Stress Pulses in Viscoelastic Solids,'' Philos. Mag., **1**(8), pp. 693–711.
[8] Norris, D. M., and Young, W. C., 1970, ''Complex Modulus Measurement by Longitudinal Vibration Testing,'' Exp. Mech., **10**, pp. 93–96.
[9] Madigosky, W. M., and Lee, G. F., 1983, ''Improved Resonance Technique for Materials Characterization,'' J. Acoust. Soc. Am., **73**(4), pp. 1374–1377.
[10] Pritz, T., 1982, ''Transfer Function Method for Investigating the Complex Modulus Acoustical Materials: Rod-Like Specimen,'' J. Sound Vib., **81**, pp. 359–376.
[11] Buchanan, J. L., 1987, ''Numerical Solution for the Dynamic Moduli of a Viscoelastic Bar,'' J. Acoust. Soc. Am., **81**, pp. 1775–1786.
[12] Blanc, R. H., 1971, ''Détermination de l'équation de comportement des corps viscoélastiques linéaires par une méthode d'impulsion,'' Ph.D. thesis, Université d'Aix-Marseille.
[13] Lundberg, B., and Blanc, R. H., 1988, ''Determination of Mechanical Material Properties From the Two-Point Response of an Impacted Linearly Viscoelastic Rod Specimen,'' J. Sound Vib., **126**(1), pp. 97–108.
[14] Trendafilova, I. N., Ödeen, S., and Lundberg, B., 1994, ''Identification of Viscoelastic Materials From Electro-Optical Displacement Measurements at Two Sections of an Impacted Rod Specimen,'' Eur. J. Mech. A/Solids, **13**(6), pp. 793–802.
[15] Ödeen, S., and Lundberg, B., 1993, ''Determination of Complex Modulus From Measured End-Point Accelerations of an Impacted Rod Specimen,'' J. Sound Vib., **165**(1), pp. 1–8.
[16] Hosten, B., and Bernard, P. A., 1998, ''Ultrasonic Wave Generation by Time-Gated Microwaves,'' J. Acoust. Soc. Am., **104**(2), pp. 860–866.
[17] Bacon, C., Hosten, B., and Bernard, P. A., 1999, ''Acoustic Wave Generation in Viscoelastic Rods by Time-Gated Microwaves,'' J. Acoust. Soc. Am., **106**(1), pp. 195–201.
[18] Hosten, B., and Bacon, C., 2000, ''Measurement of Complex Young Moduli of Composite Materials by Time-Gated Microwaves,'' *Review of Progress in Quantitative Non Destructive Evaluation*, D. O. Thompson and D. E. Chimenti, eds., Plenum Press, New York, **19**(1), pp. 1113–1120.

E. M. Beunder
Research Assistant

P. C. Rem[1]
Senior Researcher
e-mail: p.c.rem@ta.tudelft.nl

Delft University of Technology,
Mijnbouwstraat 120,
2628 RX Delft, The Netherlands

The Motion of a Rolling Polygon

Galileo was the first to analyze the motion of spheres rolling down an inclined surface. Since then, Coulomb's law of dry friction has covered the case of sliding particles. However, a particle that is not round can still roll, although in a way that is essentially different from the motion studied by Galileo. Instead of keeping contact with the surface, such particles will start bouncing after reaching a certain angular velocity. This motion is a combination of flying and colliding. It is shown that the acceleration of a bouncing particle is always bounded by the accelerations for perfect rolling and sliding. In order to describe the motion of a not perfectly round particle, the polygon is used as a model. The aim of the model is to predict the trajectories of particles that cannot be covered by the models for perfect rolling and sliding. [DOI: 10.1115/1.1481893]

1 Introduction

Galileo studied the motion of spheres rolling down an inclined plane, and concluded that ''the distances, then, from the beginning of motion are as the squares of the times'' (see Galileo, translation by Drabkin and Drake [1] and Drake [2]). Sliding motion, on the other hand, can be described by Coulomb's law of dry friction. Only one empirical constant, the coefficient of friction, is needed. For sliding, the distance traveled is also proportional to the square of time.

The descriptions of sliding and perfect rolling do not cover all possible particle motions, however. In practice, a lot of particles have the ability to roll, but their rolling is dissipative, unlike that of a sphere. The energy dissipation, in this case, originates from collisions with the surface, rather than from forces of friction. At some point, such particles may lose contact with the surface and start bouncing.

Shinohara [3] attempted to describe the motion of granular particles by treating particles as ellipsoids, without taking into account bouncing due to impact at the moment of landing. Azzoni et al. [4] studied rock fall trajectories in order to determine accurate risk zoning and construct adequate defense systems. Their model uses fitted values for the restitution and roll friction coefficients. Variation in slope and irregularities of the slope are the important parameters, rather than the irregularities of the shape of the rocks. Hacar Benitez et al. [5] did a similar study on bodies falling down from various slopes: Again, the irregularities of the slope are the main parameters. For roughly round particles, that are moving on a smooth slope, the approaches mentioned above are inadequate.

In particle technology, the effect of shape on particle motion is used for separation. (see Furuuchi and Gotoh [6] for an overview). Modeling these separations requires a theory that accounts for irregularly shaped particles. In this paper, a model is presented which deals with alternative rolling behavior by treating particles as polygons and including impact effects. The number of edges of the polygon is a measure for the energy loss due to collisions, comparable to the friction coefficient used in the theory of sliding. The coefficient of friction also plays a role in the description of a rolling polygon, in determining which type of collision occurs.

The rolling behavior of irregularly shaped particles can be studied on the scale of individual particle collisions as well as macroscopically, i.e., by considering the average behavior of a large number of similar particles, or alternatively, by considering a single particle over time intervals containing many collisions. For particle separation models, the macroscopic view is the most helpful, and therefore this view is adopted here. The purpose of these models is to predict the trajectories of particles on the basis of parameters which can be easily measured or estimated, so as to tell how particles of a different nature, in terms of material or shape, segregate into different streams while moving down a (usually curved) surface.

In order to simplify the calculations, the model that is presented here is restricted to two dimensions and the supporting surface is represented by a straight line. The particles on the surface are subject to the acceleration g' of a constant external force, which is at some angle θ with the normal into the surface. Collisions between the particles and the surface are modeled by the theory of Keller [7] more in particular by the method developed by Wang and Mason [8] for two dimensions. This theory treats the collision of solid bodies as an infinitesimally short process governed by two parameters, the coefficient of dry friction, μ, and the coefficient of restitution e. Apart from the external force and the interaction with the surface, no other forces, such as, for example, air drag, are taken into account.

The choice for a regular polygon as a model for particles of irregular shapes is motivated by the fact that this choice reduces the shape parameter to a single number, i.e., the number of edges n, while at the same time providing flat and round particles as limiting cases.

2 Limits of Rolling and Sliding

The speed of a rolling or bouncing particle, starting from rest, is bounded by the motion of sliding and rolling particles with the same physical properties, but with an appropriate change of shape. In order to show this, consider a two-dimensional particle of arbitrary shape that is subject to a constant acceleration g', such as gravity, while constrained by a surface, here the positive x'-axis, that acts on the particle with a timedependent support force F'_n and a friction force F'_f, which are normal and parallel to the surface, respectively. The gravity force makes an angle θ with the normal into the surface, so as to accelerate the particle towards the right (see Fig. 1). During its flight, the particle is described by its mass m' and moment of inertia I'_c, its linear velocity (v'_x, v'_y) and angular velocity Ω'. (The primes are used here to distinguish the original physical quantities from their dimensionless counterparts introduced later on.)

We now consider two consecutive points in time at which the particle has a zero velocity component normal to the surface while it is in contact with the surface. Integrating for the change of momentum in this time-interval $\Delta t'$, we get

[1]To whom correspondence should be addressed.

Contributed by the Applied Mechanics Division of THE AMERICAN SOCIETY OF MECHANICAL ENGINEERS for publication in the ASME JOURNAL OF APPLIED MECHANICS. Manuscript received by the ASME Applied Mechanics Division, December 12, 1999; final revision, December 21, 2001. Associate Editor: A. A. Ferri. Discussion on the paper should be addressed to the Editor, Prof. Robert M. McMeeking, Department of Mechanical and Environmental Engineering University of California–Santa Barbara, Santa Barbara, CA 93106-5070, and will be accepted until four months after final publication of the paper itself in the ASME JOURNAL OF APPLIED MECHANICS.

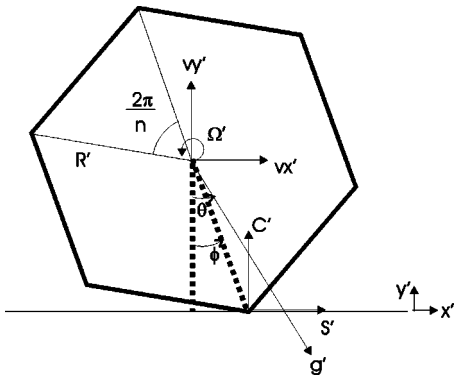

Fig. 1 Problem definition

$$m'\Delta v_x' = m'g'\sin\theta\Delta t' - \int_{t'} F_f' \tag{1}$$

$$m'\Delta v_y' = \int_{t'} F_n' - m'g'\cos\theta\Delta t'. \tag{2}$$

Since $v_y' = 0$ both at the start and at the end of the time interval, it follows that

$$\Delta v_x' = g'\cos\theta\Delta t'\left(\tan\theta - \int_{t'} F_f' \Big/ \int_{t'} F_n'\right). \tag{3}$$

From Coulomb's law of dry friction we know that all times $F_f' \leqslant \mu F_n'$, and consequently $\int_{t'} F_f' \leqslant \mu \int_{t'} F_n'$. This means that $\Delta v_x'$ is at a minimum for a particle with a shape that implies sliding motion ($F_f' = \mu F_n'$).

By integrating for the change of kinetic energy over the same time interval, we get

$$\Delta\left(\frac{1}{2}I_c'\Omega'^2 + \frac{1}{2}m'v_x'^2\right) = \int_{t'} m'v_x'g'\sin\theta - L_f - L_p - \Delta\Phi \tag{4}$$

with $L_f, L_p \geqslant 0$ the losses due to friction and inelastic collisions. The difference in potential energy $\Delta\Phi$ at the times of contact is due to small, random variations of the height y' of the center of mass of the particle above the surface (as a consequence of the irregular shape of the particle) and the difference of the elastic energy stored in the particle-surface contact. Since the particle is accelerating, it seems fair to assume that the elastic energy is growing with time and so $\Delta\Phi \geqslant 0$ as well.

From this point on, two different cases emerge from the analysis. One possibility is that the particle structurally slips in collisions with the surface, because its rotation lags essentially behind the condition of perfect rolling $v_x' + \Omega' y' = 0$ and hence the velocity at the point of contact is consistently positive. In this case, we get back to the previous case with $F_f' = \mu F_n'$. The second possibility is that the condition of perfect rolling (or even $v_x' + \Omega' y' < 0$) is regularly satisfied. In that case, the rotation of the particle remains close to the condition of perfect rolling and on average $v_x' = |\Omega'|R'$ for some effective particle radius R'. The latter case implies

$$\left(\frac{I_c'}{R'^2} + m'\right)\Delta\frac{v_x'^2}{2} \leqslant m'g'\sin\theta\int_{t'} v_x'. \tag{5}$$

By replacing the integral with the trapezoidal rule

$$\int_{t_1'}^{t_2'} v_x' \simeq ((v_x')_1 + (v_x')_2)\Delta t'/2 \tag{6}$$

and observing that

Table 1 Factors that are used to make dimensionless quantities.

Variable	Dimension	Dividing Factor
Force	kg m/s^2	$m'g'$
Torque	kg m^2/s^2	$m'g'R'$
Velocity	m/s	$\sqrt{g'R'}$
Angular velocity	1/s	$\sqrt{g'/R'}$
Time	s	$\sqrt{R'/g'}$
Distance	m	R'
Moment of inertia	kg m^2	$m'R'^2$

$$\Delta\frac{v_x'^2}{2} = ((v_x')_1 + (v_x')_2)\Delta v_x'/2 \tag{7}$$

it then follows that

$$\left(\frac{I_c'}{R'^2} + m'\right)\frac{\Delta v_x'}{\Delta t'} \leqslant m'g'\sin\theta. \tag{8}$$

Note that the equal sign corresponds to the case of perfect rolling of a particle with radius R'. Therefore, the particle acceleration is bounded from above by the maximum of sliding and rolling.

3 The Polygon Model

In order to arrive at equations of motion for particles of an irregular shape, we now turn to a polygon with n edges (see Fig. 1). Whenever a polygon is in continuous contact with the surface, it will either slide or stick. If it slides, Coulomb's law of dry friction can be applied. If it sticks and the particle rolls, the point of contact changes, every time the next edge of the polygon touches the surface. This change of point of contact is accompanied by a collision. At a certain angular velocity, the particle will start to jump from the surface and its motion will become a combination of flying and colliding.

The motion of a polygon is essentially defined by a number of dimensionless parameters, such as the angle θ between the normal into the surface and the external acceleration, the number of edges of the polygon, n, the moment of inertia to mass ratio $I_c'^2/m'R'^2$ and two material properties: the friction coefficient μ, and the restitution coefficient of the collision with the surface e. In order to make this more apparent, the equations of motion are made dimensionless using the magnitude of the external acceleration g', the particle radius R', and the particle mass m'. Table 1 shows the factors that are used for the various quantities.

3.1 Modeling Assumptions. In general, a polygon has, next to sliding and standing still, two possible modes of interaction with the surface: rolling and bouncing. In rolling mode, the polygon is continuously in contact with the surface. In this paper, only the case when the polygon sticks at the point of contact is considered for rolling. This corresponds to the assumption that the friction coefficient is sufficiently high. If the particle has a small number of edges, it will only take a few collisions before it starts bouncing. The number of collisions before this point increases with an increasing number of edges. However, the energy loss per collision decreases with an increasing number of edges. For this reason, it is assumed that collisions play a minor role in rolling mode and they are therefore ignored during this mode. Rolling is modeled with an average rotation axis, by taking an average value for the orientation ϕ, instead of a function of time, $\phi(t)$, in accordance with the macroscopic character of the model.

Bouncing mode is when the polygon is free from the surface except for collisions. It is assumed that the horizontal velocity at the point of contact is always positive before collision. This is a consequence of the horizontal component of the external force that accelerates the polygon while traveling through the air. The external force will result in a linear velocity that exceeds the sur-

face velocity of the particle. In accordance with this assumption, only two possibilities are considered for the horizontal contact velocity after collision: zero or positive. The collisions themselves are modeled by Routh's graphical method, using Poisson's model of restitution, and are assumed to be perfectly plastic: $e=0$ (a restitution coefficient of 1 corresponds to a perfectly elastic collision). This latter assumption is not obvious and will be supported by results from numerical simulations for a number of values of e (see Section 4).

3.2 Collision Model. Wang and Mason [8] showed that all two-dimensional collisions can be described by five impact modes, each mode representing a different microscopic transfer of momentum. The five modes are bounded by relations between the coefficient of friction, the coefficient of restitution, and the contact velocities before collision. As a result of the assumption $e=0$, two of the five impact modes cannot occur. The assumption of a positive horizontal velocity at the point of contact before the collision rules out a third impact mode (see the Appendix).

For ease of notation, subscript 1 and 2 will refer to the state of the polygon just before and just after the collision, respectively. (Subscript 0 will be used later and represents the state just after the previous collision.) Following the notation of Wang and Mason, S and C refer to the x-component and y-component of the velocity of the polygon at the point of contact, respectively:

$$S=v_x+\Omega\cos\phi \tag{9}$$

$$C=v_y+\Omega\sin\phi\,. \tag{10}$$

A collision with the surface delivers an impulse (P_x,P_y) to the polygon:

$$v_{x2}=v_{x1}+P_x \tag{11}$$

$$v_{y2}=v_{y1}+P_y \tag{12}$$

$$\Omega_2=\Omega_1+(P_x\cos\phi+P_y\sin\phi)/I_c\,. \tag{13}$$

The two remaining impact modes result into different expressions for (P_x,P_y). The first mode, called *sticking in compression phase* (collision 1) is described by

$$P_x=-\frac{P_y\sin\phi\cos\phi+S_1}{1+\cos^2\phi} \tag{14}$$

$$P_y=(1+e)\frac{S_1\sin\phi\cos\phi-C_1(1+\cos^2\phi)}{2}. \tag{15}$$

The second contact mode called *sliding* (collision 2), is described by

$$P_x=-\mu P_y \tag{16}$$

$$P_y=-(1+e)\frac{C_1}{1+\sin^2\phi-\mu\sin\phi\cos\phi}. \tag{17}$$

The conditions for all contact modes are given in the Appendix.

In order to arrive at macroscopic values for the impulse delivered by a collision, a representative value is needed for the orientation parameter ϕ. To this end, we consider the flight of the polygon between two subsequent collisions. Immediately after a collision, the state of the polygon is defined by a set of values $(v_{x0},v_{y0},\Omega_0,\phi_0)$ that define its motion until it hits the surface again in a precollision state $(v_{x1},v_{y1},\Omega_1=\Omega_0,\phi_1)$. Since the velocity of the point of contact after the first collision is strictly horizontal, we have $v_{y0}=-\Omega_0\sin\phi_0$. During its flight between the collisions, the y-coordinates of the n vertices of the polygon are given by

$$y^i=\cos\phi_0-\cos\left(\phi_0+\frac{2i\pi}{n}+\Omega_0 t\right)-\Omega_0\sin\phi_0 t-\frac{t^2\cos\theta}{2};$$
$$i=1,.,n. \tag{18}$$

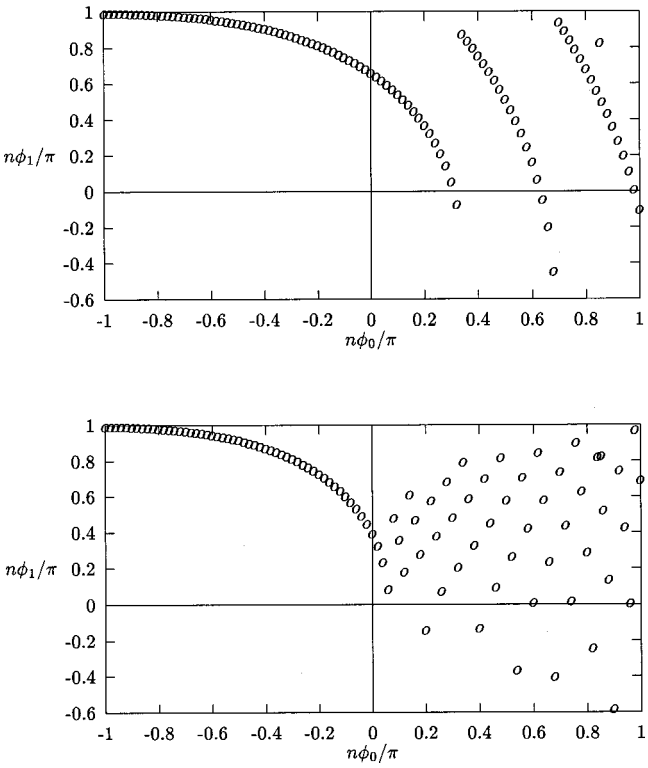

Fig. 2 Relation between values of ϕ in subsequent collisions for $n=6$ and $\Omega/\sqrt{\cos\theta}=2$ (top) and $\Omega/\sqrt{\cos\theta}=4$ (bottom)

ϕ_1 is found as the solution for $\phi_0+(2i\pi/n)+\Omega_0 t$ at the first zero of $\min_i y^i$. The formula shows that ϕ_1 depends only on n, $\Omega_0/\sqrt{\cos\theta}$ and ϕ_0. Figure 2 shows diagrams of ϕ_1 against ϕ_0 for $n=6$ and two different values of $\Omega/\sqrt{\cos\theta}$. The diagrams show that the relationship is such that any negative values of ϕ_0 result in positive values of ϕ_1, whereas most initially positive values of ϕ are randomly thrown into the interval $[0,\pi/n]$ for increasing values of Ω. This behavior suggests $\bar{\phi}=\pi/2n$ as an appropriate value for the macroscopic model.

3.3 Equations of Motion. The time-averaged dimensionless equations of motion for a polygon contain both terms due to the external force and friction as well as terms resulting from collisions with the surface. The latter are averaged in time by dividing their effect by Δt, the dimensionless time between two collisions:

$$F_{xc}=\frac{v_{x2}-v_{x1}}{\Delta t} \tag{19}$$

$$F_{yc}=\frac{v_{y2}-v_{y1}}{\Delta t} \tag{20}$$

$$T_c=I_c\frac{\Omega_2-\Omega_1}{\Delta t}. \tag{21}$$

3.3.1 Motion Without Rotation. A polygon will not move when the torque and the sum of forces are zero, which is the case when

$$\tan\theta<\mu<\tan\frac{\pi}{n}. \tag{22}$$

A polygon will only slide (and not roll) when the torque is zero and the sum of forces is positive, which is the case when

$$\mu < \min\left(\tan\theta, \tan\frac{\pi}{n}\right). \tag{23}$$

In this case, the acceleration of the polygon is given by

$$\dot{v}_x = \cos\theta(\tan\theta - \mu). \tag{24}$$

In all other cases, the polygon will start rolling.

3.3.2 Rolling. If the polygon rolls, its corners remain in contact with the surface at all times. In particular, if the orientation of the polygon is ϕ, the acceleration of its center of gravity towards the surface is $\Omega^2 \cos\phi$. Since this acceleration cannot exceed that of the external acceleration for any value of ϕ, rolling motion implies

$$\Omega^2 \leqslant \cos\theta. \tag{25}$$

Otherwise, the polygon will start bouncing. To come to macroscopic equations of motion, it is further assumed that ϕ can be approximated by the average value $\overline{\phi} = \pi/2n$. Ignoring losses from collisions and sliding, we get

$$\dot{\Omega} = -\frac{\cos\overline{\phi}\sin\theta}{I_c + \cos^2\overline{\phi}} \tag{26}$$

$$v_x = -\Omega\cos\overline{\phi}. \tag{27}$$

The solution for $\Omega(t)$ is a simple linear function of t.

3.3.3 Bouncing. The particle starts bouncing when the support force needs to be negative in order to keep the polygon in contact with the surface. All energy losses during bouncing result from collisions.

During bouncing the following general relations apply between the velocities v_x, Ω of two consecutive after-collision states:

$$v_{x2} = v_{x0} + \sin\theta\Delta t + P_x \tag{28}$$

$$\Omega_2 = \Omega_0 + (P_x\cos\overline{\phi} + P_y\sin\overline{\phi})/I_c \tag{29}$$

with Δt the time between collisions. Note that the results for both impact modes express P_x in terms of P_y and P_y in terms of S_1 and C_1. Regardless of the type of collision,

$$C_1 = v_{y0} + \Omega_0\sin\overline{\phi} - \cos\theta\Delta t \tag{30}$$

$$= -\cos\theta\Delta t. \tag{31}$$

For *sticking in compression phase* (collision 1), there is the additional relation

$$S_1 = v_{x0} + \Omega_0\cos\overline{\phi} + \sin\theta\Delta t \tag{32}$$

$$= \sin\theta\Delta t \tag{33}$$

since this type of collision ends with sticking. Inserting the expressions for P_x and P_y and using the relations above, we find for collision 1.

$$\dot{v}_x = (v_{x2} - v_{x0})/\Delta t \tag{34}$$

$$= \frac{\cos^2\overline{\phi}\sin\theta - \sin\overline{\phi}\cos\overline{\phi}\cos\theta}{2} \tag{35}$$

$$\dot{\Omega} = (\Omega_2 - \Omega_0)/\Delta t \tag{36}$$

$$= \frac{\sin\overline{\phi}\cos\theta - \cos\overline{\phi}\sin\theta}{2I_c} \tag{37}$$

and for collision 2

$$\dot{v}_x = \sin\theta - \frac{\mu\cos\theta}{1 + \sin^2\overline{\phi} - \mu\sin\overline{\phi}\cos\overline{\phi}} \tag{38}$$

$$\dot{\Omega} = \frac{(\sin\overline{\phi} - \mu\cos\overline{\phi})\cos\theta}{I_c(1 + \sin^2\overline{\phi} - \mu\sin\overline{\phi}\cos\overline{\phi})}. \tag{39}$$

Collision 1 occurs as long as the condition below is satisfied (see the Appendix).

$$\mu > \frac{\sin\theta + \sin\overline{\phi}\cos\overline{\phi}\cos\theta + \sin\theta\sin^2\overline{\phi}}{\cos\theta + \cos\theta\cos^2\overline{\phi} + \sin\overline{\phi}\cos\overline{\phi}\sin\theta} \tag{40}$$

Otherwise, collision 2 occurs.

4 Numerical Calculations

The moment of inertia I_c' of a polygon can be approximated by the average of the moments of inertia of the inscribed and outscribed cylinder.

$$I_c' \approx \frac{\frac{1}{2}m'\left(R'^2 + R'^2\cos^2\left(\frac{\pi}{n}\right)\right)}{2} \tag{41}$$

and the dimensionless moment of inertia is then approximated by

$$I_c = \frac{I_c'}{m'R'^2} \approx 0.5. \tag{42}$$

This value is used in both the model calculations and the numerical calculations presented here.

Numerical calculations were performed to verify the assumptions used in the macroscopic model, in particular the assumption $e = 0$. The ODE-solver DASSL (see Petzold [9] and Brenan et al. [10]) was used to integrate the detailed microscopic equations of motion between collisions:

$$\dot{\phi} = \Omega \tag{43}$$

$$\dot{v}_x = \sin\theta - F_f \tag{44}$$

$$\dot{v}_y = \cos\theta + F_n \tag{45}$$

$$I_c\dot{\Omega} = F_n\sin\phi - F_f\cos\phi. \tag{46}$$

For rolling mode, F_n and F_f are computed from the constraints of the point of contact with the surface and for bouncing mode, $F_n = F_f = 0$. The transition from rolling to bouncing is triggered by the change of sign of F_n.

When ϕ reaches $-(\pi/n)$, corresponding to another rotation of $-(2\pi/n)$, ϕ is reset to π/n. In rolling mode, a collision occurs at this point, which is calculated using the full method by Wang and Mason (see the Appendix). In bouncing mode, a collision is carried out when the nearest edge of the polygon touches the surface.

4.1 The Assumption $e = 0$. An important contribution of the numerical results from the detailed microscopic model is to show the effect of variations of the coefficient of restitution e, which is assumed to be zero in the macroscopic model. Table 2 shows the tangential velocity v_x at time $t = 100$ for various combinations of e and μ. The coefficient of restitution e is varied from 0.0 to 1.0, covering the entire possible range. The friction μ is varied from 0.0 to 1.0, which is a typical range of values occurring in practice.

For low values of the friction, the particle will slide. In this case, the friction force is not sufficiently large to make the particle rotate. For higher values of μ, the particle will rotate. At the given combination of n and θ, a further increase of the coefficient of friction will make the particle keep still. In general, the values of the friction at the transitions from sliding to rolling and from rolling to keeping still depend on the number of edges as well as on the angle of the slope.

For low coefficients of restitution we observe that the coefficient of friction, rather than the coefficient of restitution determines the tangential velocity. This is fortunate because high val-

Table 2 Horizontal velocity for various combinations of e and μ, for $n=10$ and $\theta=40$ deg at dimensionless time $t=100$

μ,e	0.0	0.2	0.4	0.6	0.8	1.0
0.0	64	64	64	64	64	64
0.2	49	49	49	49	49	49
0.4	32	33	35	36	33	31
0.6	26	26	27	31	27	32
0.8	0	0	0	0	0	0
1.0	0	0	0	0	0	0

ues of restitution are rare and the exact value of e may depend on the orientation of the colliding object with respect to the surface, [11]. These results support the assumption $e=0$ for a macroscopic model for computing the tangential velocity. For higher values of e, changes of the coefficient of restitution do affect the resulting tangential velocity, the effect being of the same order of magnitude as resulting from variations of the coefficient of friction.

4.2 Comparison of Numerical and Model Calculations. As a further check on the modeling assumptions involved in the macroscopic model, the results of the model are compared to numerical calculations for various values of the friction, slope, and the number of edges of the polygon around the central case $\theta=40$ deg, $\mu=0.5$, $n=20$.

Figure 3 shows that the motion of the polygon is bounded by the cases of perfect rolling (top dark line) and sliding (bottom dark line), as the number of surfaces n is varied from 10 to 100. Continuous lines show the results of numerical calculations and dotted lines represent the macroscopic model. Notice that even a perfect sphere or cylinder will start to bounce as soon as it meets an irregularity of the surface. It can therefore be questioned whether the limit of perfect rolling could be observed in practice for such an extent of time. Figure 3 shows a good resemblance between the model and numerical calculations, apart from fluctuations in the numerical velocity that are caused by individual collisions. Figures 4 and 5 compare the model and numerical calculations for various values of μ and different slopes. At $\mu=0.1$ the polygon slides without collisions. Table 3 shows the impact modes for all the presented results. All cases show good resemblance between the model and numerical calculations.

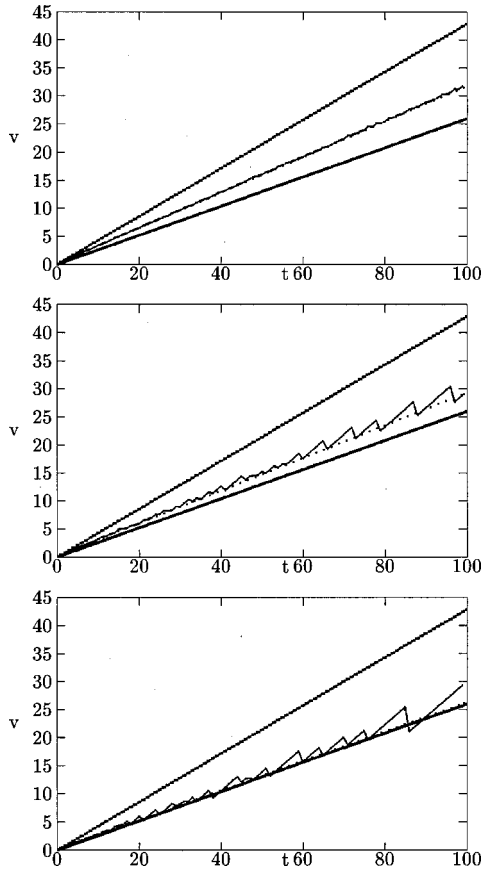

Fig. 3 $\theta=40$ deg, $\mu=0.5$, $n=100$ (top), $n=20$ (middle), $n=10$ (bottom) with the dotted line the macroscopic model and the continuous line the numerical calculations. The top and bottom line represent, respectively, perfectly rolling and perfectly sliding

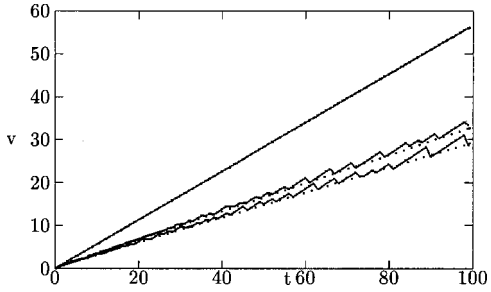

Fig. 4 Effect of the friction coefficient. $\theta=40$ deg, $n=20$. From top to bottom: $\mu=0.1$, $\mu=0.4$, and $\mu=0.7$, with the dotted line the macroscopic model and the continuous line the numerical calculations.

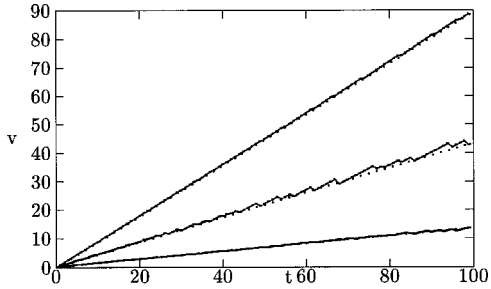

Fig. 5 Effect of the slope. $\mu=0.5$, $n=20$. From top to bottom $\theta=80$ deg, $\theta=50$ deg, and $\theta=20$ deg, with the dotted line the macroscopic model and the continuous line the numerical calculations.

Table 3 Impact modes of the macroscopic model for the conditions of Figs. 3, 4, and 5. Sticking means sticking in compression phase; none means the particle slided without collisions.

n	μ	θ (degrees)	Impact Mode
10	0.5	40	sticking
20	0.5	40	sticking
100	0.5	40	sticking
20	0.5	20	sticking
20	0.5	50	sliding
20	0.5	80	sliding
20	0.1	40	none
20	0.4	40	sticking
20	0.7	40	sliding

5 Conclusions

The motion of a polygon can be used as a model for the nonperfect rolling of bodies of irregular shape. The number of surfaces n of the polygon is a measure for the roundness of the particle and the energy loss due to collisions with the surface. The

larger the number of edges of the polygon, the lower the energy loss due to collisions, and the faster it will roll. For practical applications, a macroscopic model based on time-averaged equations of motion is developed. This model shows very good resemblance to detailed numerical calculations and is a powerful and fast tool to describe the motion of polygons, without having to perform numerical calculations. It gives a good insight in the way particle shape relates to energy losses during rolling.

Acknowledgments

The authors wish to thank the TNO Institute of Environmental Sciences, Energy Research and Process Innovation for their financial support for this project. We are indebted to the referee for carefully reading the manuscript and useful suggestions.

Appendix

Impact Modes: Boundary Conditions. The collisions are computed by the two-dimensional model described by Wang and Mason [8]. Their model is based on Routh's graphical method to describe an impact process and to determine the frictional impulse. They distinguish two directions for impulses due to impact, i.e., normal P_y and tangential P_x. For an oblique impact, five impact modes can be identified, and the impulses due to collision depend on the impact mode. The impact modes have to do with the order in which sticking and maximal compression take place during the collision and whether the point of contact sticks or starts reversed sliding.

The conditions that define the impact modes of the collision use the following definitions:

$$\mu_s = \frac{-\sin\phi\cos\phi}{1+\cos^2\phi} \tag{47}$$

$$P_d = (1+\sin^2\phi - \mu\sin\phi\cos\phi)S_1 \tag{48}$$

$$P_q = (\mu(1+\cos^2\phi) - \sin\phi\cos\phi)(-C_1). \tag{49}$$

For a polygon colliding with a surface of infinite mass, the impact modes and impulses after collision are described by (with $s=\mathrm{sgn}(S_0)$, $B_1 = 1+\cos^2\phi$, $B_2 = 1+\sin^2\phi$, $B_3 = -\sin\phi\cos\phi$):

1 Sliding

$$P_d > (1+e)P_q$$

$$P_x = -s\mu P_y$$

$$P_y = -(1+e)\frac{C_0}{B_2 + s\mu B_3}$$

2 Sticking in compression phase (C-sticking)

$$P_d < P_q \quad \text{and} \quad \mu > |\mu_s|$$

$$P_x = \frac{B_3 P_y - S_0}{B_1}$$

$$P_y = -(1+e)\frac{B_1 C_0 + B_3 S_0}{B_1 B_2 - B_3^2}$$

3 Sticking in restitution phase (R-sticking)

$$P_q < P_d < (1+e)P_q \quad \text{and} \quad \mu > |\mu_s|$$

$$P_x = \frac{B_3 P_y - S_0}{B_1}$$

$$P_y = -(1+e)\frac{C_0}{B_2 + s\mu B_3}$$

4 Reversed sliding in compression phase (C-reversed sliding)

$$P_d < P_q \quad \text{and} \quad \mu < |\mu_s|$$

$$P_x = s\mu\left[P_y - \frac{2S_0}{B_3 + s\mu B_1}\right]$$

$$P_y = -\frac{1+e}{B_2 - s\mu B_3}\left[C_0 + \frac{2s\mu B_3 S_0}{B_3 + s\mu B_1}\right]$$

5 Reversed sliding in restitution phase (R-reversed sliding)

$$P_q < P_d < (1+e)P_q \quad \text{and} \quad \mu < |\mu_s|$$

$$P_x = s\mu\left[P_y - \frac{2S_0}{B_3 + s\mu B_1}\right]$$

$$P_y = -(1+e)\frac{C_0}{B_2 + s\mu B_3}$$

The third and the fifth mode do not occur in the macroscopic model, due to the choice of $e=0$. If $\mu < |\mu_s|$, it follows that $P_q < -cC_1$ and $P_d > (2(1+\cos^2\phi))S_1$, with c a negative constant. As C_1 is always negative before collision, and S_1 is always positive, it follows that if $\mu < |\mu_s|$, then $P_d > P_q$, and thus the fourth impact mode never occurs in the polygon model either.

References

[1] Drake, S., 1978, *Galileo at Work, His Scientific Biography*, University of Chicago Press, Chicago, IL.

[2] Galileo, G., (ca., 1590 and ca. 1600), 1960, *On Motion and on Mechanics*, The University of Wisconsin Press, Translation by Drakbin and Drake.

[3] Shinohara, K., 1986, "Fundamental Analysis on Gravitational Separation of Differently Shaped Particles on Inclined Plates," Powder Technol., **48**, pp. 151–159.

[4] Azzoni, A., La Barbera, G., and Zaninetti, A., 1995, "Analysis and Prediction of Rockfall Using a Mathematical Model," Int. J. Rock Mech. Min. Sci. Geomech. Abstr., **32**(7), pp. 709–724.

[5] Hacar Benitez, M. A., Bollo, MI. F., and Hacar Rodrigues, M. P., 1977, "Bodies Falling Down on Different Slopes—Dynamic Study," *Proceedings of the 9th International Conference on Soil Mechanics and Foundation Engineering*, MAA Publishing, pp. 91–95.

[6] Furuuchi, M., and Gotoh, K., 1992, "Shape Separation of Particles," Powder Technol., **73**, pp. 1–9.

[7] Keller, J. B., 1986, "Impact With Friction," ASME J. Appl. Mech., **53**, pp. 1–4.

[8] Wang, Y., and Mason, M. T., 1992, "Two-Dimensional Rigid-Body Collisions With Friction," ASME J. Appl. Mech., **59**, pp. 635–642.

[9] Petzold, L. R., 1982, "A Description of DASSL: Differential Algebraic System Solver," SAND82-8637, Sandia National Laboratories, Sept.

[10] Brenan, K. E., Campbell, S. L., and Petzold, L. R., 1989, *Numerical Solution of Initial Value Problems in Differential-Algebraic Equations*, Elsevier, New York.

[11] Stoianovici, D., and Hurmuzlu, Y., 1996, "A Critical Study of the Applicability of Rigid-Body Collision Theory," ASME J. Appl. Mech., **63**, pp. 307–316.

Forced Vibration of Cylindrical Helical Rods Subjected to Impulsive Loads

B. Temel[1]
e-mail: btemel@mail.cu.edu.tr

F. F. Çalim

Department of Civil Engineering,
University of Çukurova,
01330 Balcali-Adana, Turkey

In this study, the forced vibration of cylindrical helical rods subjected to impulsive loads is theoretically investigated in the Laplace domain. The free vibration is then taken into account as a special case of forced vibration. The governing equations for naturally twisted and curved space rods obtained using Timoshenko beam theory are rewritten for cylindrical helical rods. The material of the rod is assumed to be homogeneous, linear elastic, and isotropic. The axial and shear deformations are also taken into account in the formulation. Ordinary differential equations in scalar form obtained in the Laplace domain are solved numerically using the complementary functions method to calculate exactly the dynamic stiffness matrix of the problem. The desired accuracy is obtained by taking only a few elements. The solutions obtained are transformed to the real space using the Durbin's numerical inverse Laplace transform method. The free and forced vibrations of cylindrical helical rods are analyzed through various example. The results obtained in this study are found to be in a good agreement with those available in the literature.
[DOI: 10.1115/1.1554413]

1 Introduction

As is known, a closed-form solution of a curved, initially twisted space rod problem using the three-dimensional elasticity theory is not available. An approximation in the formulation of the problem is adopted by introducing Bernoulli-Euler and Timoshenko beam theories. Thus, mathematically tractable equations without introducing a significant error in practical engineering problems are obtained. Moreover, the finite element, finite difference, and energy methods are employed. It is quite difficult to obtain the element stiffness matrix with these methods, and the results are inevitably approximate.

Massoud [1] has used D'Alambert's principle to derive the equation of motion in vectorial form for slender spatial bar taking into account both axial and shear deformations and has given the expressions of the scalar equations for the free vibrations of the cylindrical helice.

Wittrick [2], using the Timoshenko beam theory, has obtained the differential equations for a large step of unit angle of helix and has studied the wave propagation in semi-infinite springs and obtained approximate solutions by neglecting the axial and shear deformations.

Kiral and Ertepinar [3,4] obtained governing equations of the free and forced vibration of curved space rod in the canonical form using the Timoshenko beam theory. They solved the free-vibration problem by the transfer matrix method and concluded that a more efficient method is needed for general forced-vibration analysis.

Mottershead [5], using the equations given by Wittrick [2] for the static case, computed the natural frequencies by the finite element method and compared his results with the values measured at his own experiments.

Pearson [6] extended the dynamic equations given by Wittrick [2] to the analysis of behavior of compressed circular cross-sectioned cylindrical helical springs and has studied the problem of free vibrations by the transfer matrix method.

Pearson and Wittrick [7] have determined the dynamic stiffness matrix based on the Bernoulli-Euler hypothesis, where the effect of shear deformation is not considered, for the free vibrations of a helical spring.

Nagaya, Takeda, and Nakata [8] have determined the natural frequencies of noncircular helical springs with circular cross sections both experimentally and by the method of equivalence transfer matrix method. They used the static element transfer matrix that was deduced in closed form taking into account only the axial deformations.

Lin and Pisano [9,10] derived the general dynamic equations of helical springs with circular cross section, variable pitch angle, and variable helix radius.

Tabarrok et al. [11] have studied free vibrations of spatially curved and twisted rods with the aid of a finite element model and have obtained displacement modes of a problem.

Haktanir [12] examined only static behavior of a helical spring under arbitrary distributed loads and has computed the element stiffness matrix using complementary functions.

Yildirim [13] has studied free vibrations of helical springs with the help of the transfer matrix method. In a separate work, Yildirim [14] studied the free-vibration problem of cylindrical helical springs, where the actual helical element stiffness matrix and the concentrated element mass matrix are used in the formulation of the problem.

Lee and Thompson [15] have recently studied the dynamic stiffness formulation for free vibration and wave motion of helical springs. They have used Wittrick-Williams algorithm to determine the free-vibration frequencies with the dynamic stiffness matrix and have compared the results of the dynamic stiffness matrix with those of the transfer matrix and the finite element methods.

As Lee and Thompson [15] pointed out, Jiang et al. [16] obtained nonlinear equations of motion and from them linearized equations for the vibration of a spring. They studied the coupling between axial and torsional motion in more detail then Wittrick, deriving the complex form of the oscillations of the spring in the time domain due to the interaction and superposition of the component waves. Sinha and Costello [17] used a finite difference technique and the method of nonlinear characteristics to solve

[1]To whom correspondence should be addressed.

Contributed by the Applied Mechanics Division of THE AMERICAN SOCIETY OF MECHANICAL ENGINEERS for publication in the ASME JOURNAL OF APPLIED MECHANICS. Manuscript received by the ASME Applied Mechanics Division, March 3, 2002; final revision, August 16, 2002. Associate Editor: N. C. Perkins. Discussion on the paper should be addressed to the Editor, Prof. Robert M. McMeeking, Department of Mechanical and Environmental Engineering University of California–Santa Barbara, Santa Barbara, CA 93106-5070, and will be accepted until four months after final publication of the paper itself in the ASME JOURNAL OF APPLIED MECHANICS.

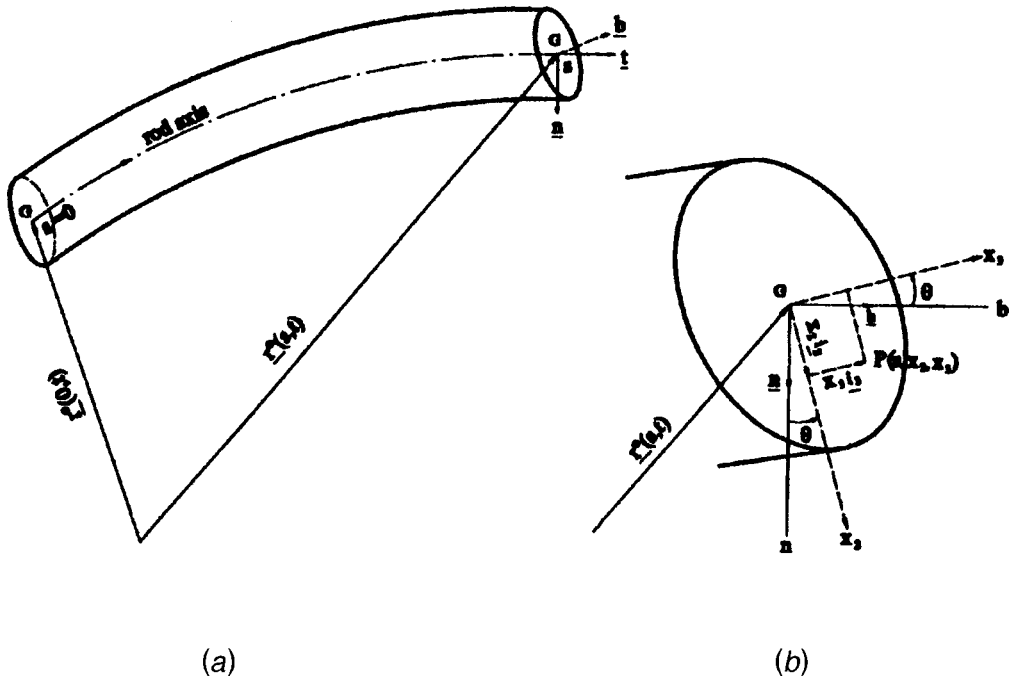

Fig. 1 The rod geometry

numerically the nonlinear partial differential equations in the time domain. This study too is limited to axial and torsional motion of the spring.

Berdichevsky and Sutyrin [18] have studied the problem of an equivalent rod in nonlinear theory of springs. In a separate work, Berdichevsky and Starosel'skii [19] studied the theory of curvilinear Timoshenko-type rods. Cesnik et al. [20] have studied an advanced beam theories include the effects of initial twist and curvature. Borri et al. [21] have studied linear analysis of naturally curved and twisted anisotropic beams Yu et al. [22] examined Timoshenko-like modeling of initially curved and twisted composite beams with oblique cross sections.

Although there are numerous studies on the free vibration of helical spatial rods, research pertaining to the analysis of forced vibration under dynamic loads of helical spatial rods is scarce.

In this study, an efficient method is introduced for the analysis of the forced vibration of cylindrical helical rods and springs under arbitrary time-dependent and impulsive loads in the Laplace domain. In this method, the governing equations for naturally twisted and curved spatial rods obtained using the Timoshenko beam theory are rewritten for cylindrical helical rods. The curvature of the rod axis, effect of rotary inertia, and shear and axial deformations are considered in the formulation. The element dynamic stiffness matrix is calculated in the Laplace transform space by applying the complementary functions method to the differential equations in canonical form. This provides great convenience in the solution of the problems having general boundary conditions as the desired accuracy is obtained by taking only a few elements as opposed to high number of elements (in the order of 100) needed in finite element analysis. Ordinary differential equations with variable coefficients can also be solved exactly in Laplace domain by using the complementary functions method. The complementary functions method given for only static loads in Haktanir [12] is used in the Laplace domain with the addition of dynamic loads. The solutions obtained in the Laplace transform space are then transformed to the time space using the Durbin's inverse Laplace transform method, [23–25].

2 The Rod Geometry

Consider a naturally curved and twisted spatial slender rod. The trajectory of geometric center G of the rod is defined as the rod axis and its position vector at $t=0$ is given by $\mathbf{r}^0=\mathbf{r}^0(s,0)$ where s is measured from an arbitrary reference point $s=0$ on the axis (Fig. 1(a)). Let, at any time t, a reference frame defined by the unit vectors **t, n, b** with the origin of the axis of the rod, be chosen such that

$$\mathbf{t}=\frac{\partial \mathbf{r}^0(s,t)}{\partial s} \tag{1}$$

which indicates that **t** is in the direction of increasing s. **n** is normal to the axis and in the osculating plane, directed toward the center of curvature. The binormal vector **b** is given by $\mathbf{b}=\mathbf{t}\times\mathbf{n}$. The following differential relations among the unit vectors **t, n, b** can be obtained with the aid of the Frenet formulas, [26]:

$$\partial\mathbf{t}/\partial s=\chi\mathbf{n}, \quad \partial\mathbf{n}/\partial s=\tau\mathbf{b}-\chi\mathbf{t}, \quad \partial\mathbf{b}/\partial s=-\tau\mathbf{n} \tag{2}$$

where χ and τ are the curvature and the natural twist of the axis, respectively. It is noted that χ is always positive and that τ is positive, in the right-hand sense, about **t** when advanced in the increasing s-direction. They are expressed in terms of the spatial derivatives of the position vector $\mathbf{r}^0(s,t)$:

$$\chi=\left|\frac{\partial^2\mathbf{r}^0}{\partial s^2}\right|, \quad \tau=-\frac{\dfrac{\partial\mathbf{r}^0}{\partial s}\cdot\dfrac{\partial^2\mathbf{r}^0}{\partial s^2}\times\dfrac{\partial^3\mathbf{r}^0}{\partial s^3}}{\chi^2}. \tag{3}$$

For planar rods $\tau=0$, and for straight rods $\chi=\tau=0$.

In order to take into account the initial twist of the cross section, a second rectangular Cartesian frame (x_1,x_2,x_3) is defined such that the x_1-axis is in the direction of **t**, and x_2, x_3 are the principal axes of the cross section (Fig. 1(b)). Let $\mathbf{i}_1$, $\mathbf{i}_2$, and $\mathbf{i}_3$ be the unit vectors along x_1, x_2, and x_3. From Fig. 1(b) Eq. (4) can be written:

$$\mathbf{t}=\mathbf{i}_1, \quad \mathbf{n}=\mathbf{i}_2\cos\theta-\mathbf{i}_3\sin\theta, \quad \mathbf{b}=\mathbf{i}_2\sin\theta+\mathbf{i}_3\cos\theta. \tag{4}$$

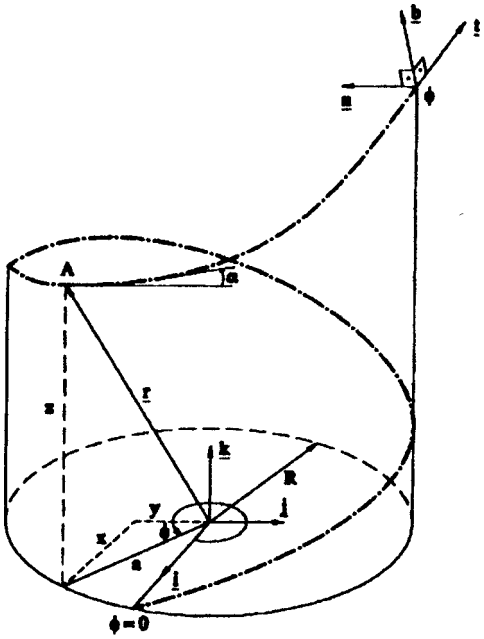

Fig. 2 Geometry of a cylindrical helix

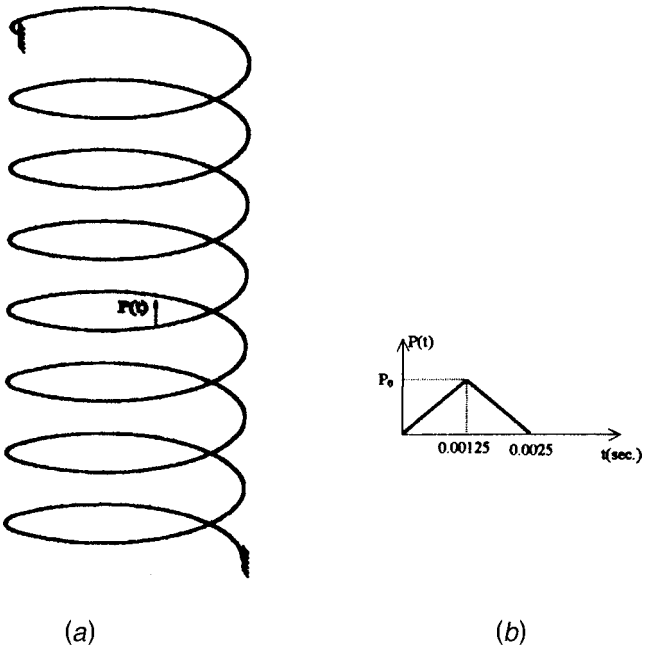

(a) (b)

Fig. 3 (*a*) Cylindrical helical spring; (*b*) a triangular impulsive load

3 The Governing Equations

Let us denote the displacement of any point on the rod axis by $\mathbf{U}^0(s,t)$, the rotation of the cross section about an axis passing through the geometric center G by $\mathbf{\Omega}^0(s,t)$, and the relative extension and the relative rotation of the unit length on the axis by $\boldsymbol{\gamma}^0(s,t)$ and $\boldsymbol{\omega}^0(s,t)$, respectively. Assuming the displacements and the deformations are infinitesimal, the equations of geometric compatibility and the equations of motion are, respectively, given by, [4,13],

$$\boldsymbol{\gamma}^0=\frac{\partial \mathbf{U}^0}{\partial s}+\mathbf{t}\times\mathbf{\Omega}^0, \quad \boldsymbol{\omega}^0=\frac{\partial \Omega^0}{\partial s} \tag{5}$$

and

$$\frac{\partial \mathbf{T}^0}{\partial s}+\mathbf{p}^{(ex)}=\mathbf{p}^{(in)}, \quad \frac{\partial \mathbf{M}^0}{\partial s}+\mathbf{t}\times\mathbf{T}^0+\mathbf{m}^{(ex)}=\mathbf{m}^{(in)} \tag{6}$$

where the inertia force vector is $\mathbf{T}^0$, the inertia moment vector is $\mathbf{M}^0$ and $\mathbf{p}^{(ex)}$ and $\mathbf{m}^{(ex)}$ are the external distributed load and external distributed moment vectors per unit length of axis, respectively. The mass density ρ, the inertia force $\mathbf{p}^{(in)}$ and the inertia moment $\mathbf{m}^{(in)}$, per unit length of the rod axis are given by, [4],

$$p_i^{(in)}=-\rho A\frac{\partial^2 U_i^0}{\partial t^2}, \quad m_i^{(in)}=-\rho I_i\frac{\partial^2 \Omega_i^0}{\partial t^2} \quad (i=t,n,b). \tag{7}$$

Assuming that the centroid and the shear center of cross section coincide; the normal and binormal axes are the principal axes; the effect of warping is ignored; the material of the rod is homogeneous, linear elastic, and isotropic, the constitutive equations are given by, [13],

$$T_i^0=A_{ij}\gamma_j^0, \quad M_i^0=D_{ij}\omega_j^0 \quad (i,j=t,n,b) \tag{8}$$

where A_{ij} and D_{ij} are defined as

$$[A]=\begin{bmatrix} EA & 0 & 0 \\ 0 & GA/\alpha_n & 0 \\ 0 & 0 & GA/\alpha_b \end{bmatrix} \tag{9}$$

$$[D]=\begin{bmatrix} GI_t & 0 & 0 \\ 0 & EI_n & 0 \\ 0 & 0 & EI_b \end{bmatrix} \tag{10}$$

where A is area of cross section, E and G are elastic constants, α_n and α_b are shear coefficients, I_t is torsional, and I_n, I_b are bending moments of inertia.

4 Governing Equations in Canonical Form for Free and Forced Vibrations

The free-vibration problem could be studied as a special case of forced vibrations. Therefore, the forced vibration analysis will be presented here.

4.1 Forced Vibrations. For the case of forced vibrations, a column matrix $\mathbf{Y}(s,t)$ is introduced as

$$\mathbf{Y}(s,t)=\{U_t^0,\ U_n^0,\ U_b^0,\ \Omega_t^0,\ \Omega_n^0,\ \Omega_b^0,\ T_t^0,\ T_n^0,\ T_b^0,\ M_t^0,\ M_n^0,\ M_b^0\}^t. \tag{11}$$

Laplace transform of Eq. (11) with respect to time $L[\mathbf{Y}(s,t)]=\overline{\mathbf{Y}}(s,z)$, for $t>0$ is defined as

$$\overline{\mathbf{Y}}(s,z)=\int_0^\infty \mathbf{Y}(s,t)e^{-zt}dt \tag{12}$$

where Laplace transform parameter z is a complex number. With the aid of these definitions, Eqs. (5) and (6) are reduced to a set of 12 first-order nonhomogeneous ordinary differential equations

$$\frac{d\overline{\mathbf{Y}}(s,z)}{ds}=\overline{\mathbf{F}}(s,z)\overline{\mathbf{Y}}(s,z)+\overline{\mathbf{B}}(s,z). \tag{13}$$

Some of the elements of $\overline{\mathbf{F}}(s,z)$ are obtained by applying Laplace transform of the following second derivatives:

Table 1 Natural frequencies in Hertz (FEM: the finite element method, TMM: the transfer matrix method, CFM: the complementary functions method, N/A: not available)

	1	2	3	4	5	6	7	8	9	10
Mottershead [5]^{Experimental}	391.0	391.0	459.0	528.0	878.0	878.0	906.0	N/A	1282.0	1386.0
Mottershead [5]^{FEM}	396.0	397.0	469.0	532.0	887.0	900.0	N/A	N/A	N/A	N/A
Pearson [6]^{TMM}	394.9	397.6	456.4	518.3	859.7	874.7	902.2	1023.7	1293.4	1351.9
Yildirim [13]^{TMM}	393.5	395.9	462.8	525.5	864.0	876.8	914.3	1037.0	1310.5	1363.8
Yildirim [14]	393.4	396.0	462.7	525.6	863.7	876.6	N/A	N/A	N/A	N/A
ANSYS [28]$^{(80\ elements)\ FEM}$	400.2	402.9	481.5	545.2	886.3	898.1	949.3	1075.2	1360.7	1408.8
ANSYS [28]$^{(200\ elements)\ FEM}$	394.5	397.1	465.7	528.7	867.3	880.2	919.1	1043.2	1318.4	1371.3
ANSYS [28]$^{(500\ elements)\ FEM}$	393.6	396.2	463.2	526.1	864.2	877.3	914.4	1038.2	1311.4	1365.4
Present Study ^{CFM}	393.4	395.9	462.7	525.6	863.6	876.8	913.5	1037.2	1310.4	1364.3

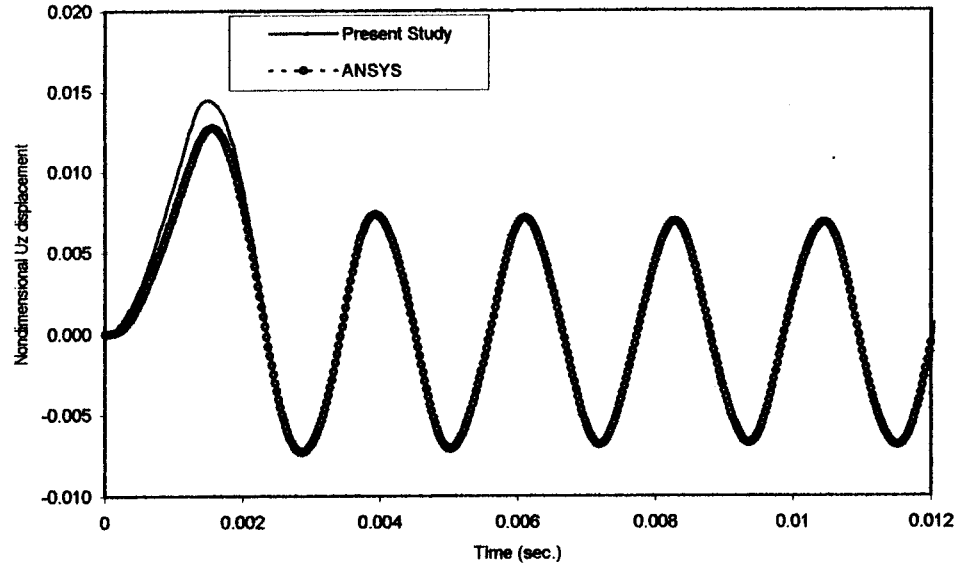

(*a*)

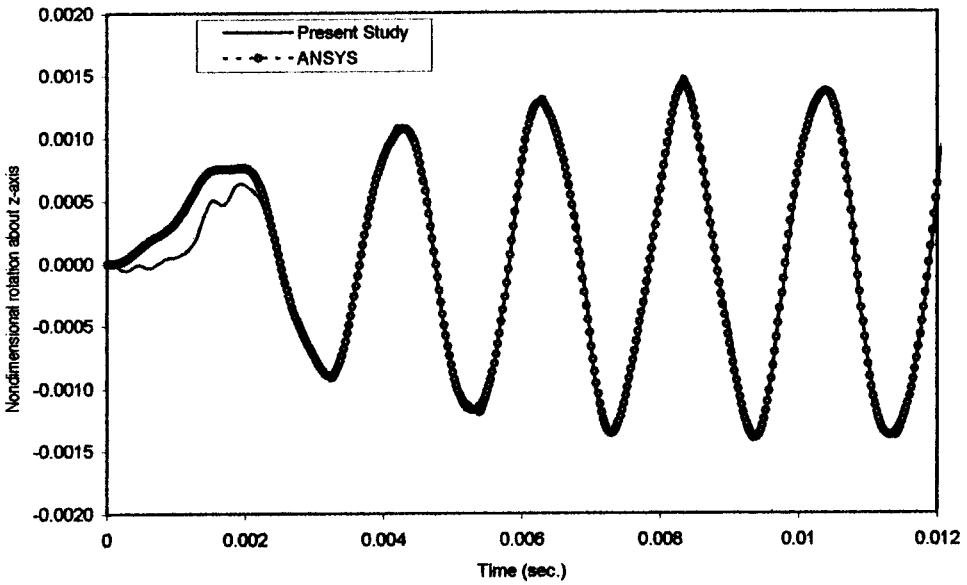

(*b*)

Fig. 4 (*a*) Vertical displacement versus time at the arc-length midpoint, (*b*) rotation versus time at the arc-length midpoint, (*c*) vertical shear force versus time at the fixed end, (*d*) moment versus time at the fixed end

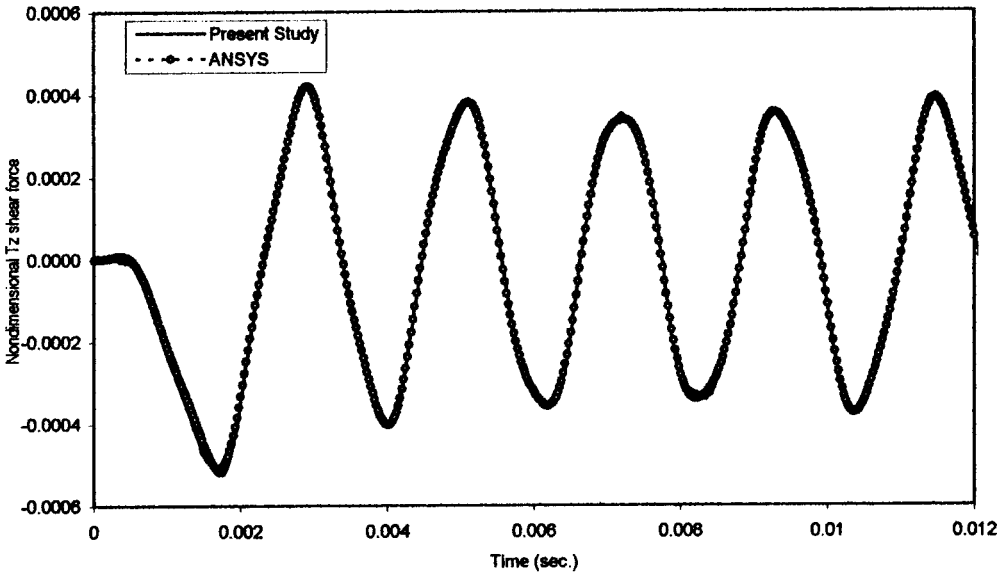

(*c*)

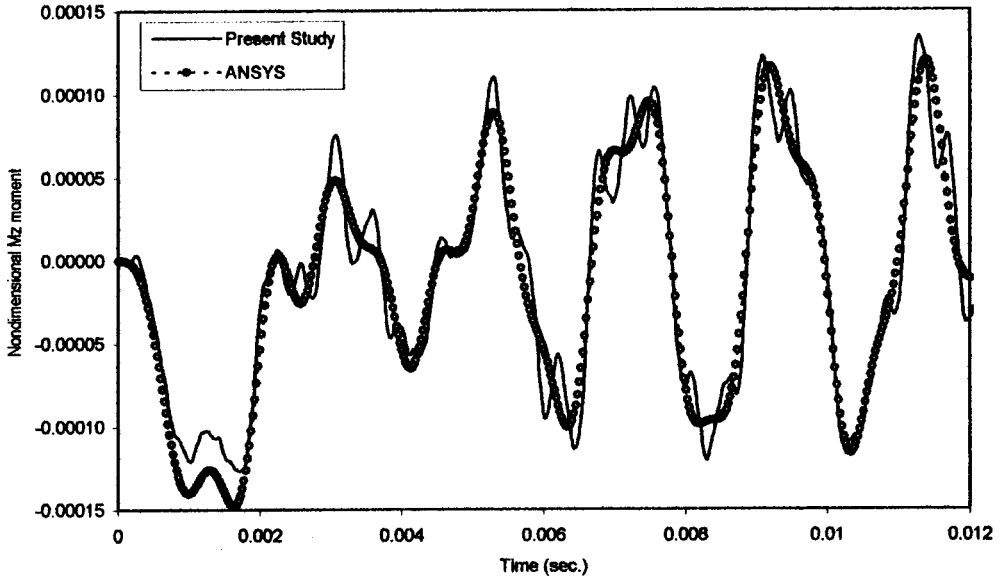

(*d*)

Fig. 4 (***continued***)

$$L\left[\rho A\frac{\partial^2 U_k^0}{\partial t^2}\right]=\rho A\left[z^2\overline{U}_k^0-zU_k^0(s,0)-\frac{\partial U_k^0(s,0)}{\partial t}\right]$$
$$L\left[\rho I_k\frac{\partial^2 \Omega_k^0}{\partial t^2}\right]=\rho I_k\left[z^2\overline{\Omega}_k^0-z\Omega_k^0(s,0)-\frac{\partial \Omega_k^0(s,0)}{\partial t}\right]\quad(k=t,n,b). \tag{14}$$

The second and third terms on the right-hand side of the Eq. (14) are the initial conditions given at $t=0$. The elements of the column matrix $\overline{\mathbf{B}}(s,z)$ are

$$\overline{B}_i(s,z)=0\qquad(i=1,2,\ldots,6)$$
$$\overline{B}_{6+j}(s,z)=-(\overline{p}_k^{(ex)})-\rho A\left[zU_k^0(s,0)+\frac{\partial U_k^0(s,0)}{\partial t}\right]\quad(j=1,2,3) \tag{15}$$
$$\overline{B}_{9+j}(s,z)=-(\overline{m}_k^{(ex)})-\rho I_k\left[z\Omega_k^0(s,0)+\frac{\partial \Omega_k^0(s,0)}{\partial t}\right]\quad(k=t,n,b).$$

Note that the initial conditions shown in Eqs. (14) are now included in the load vector $\overline{\mathbf{B}}(s,z)$.

4.2 Free Vibrations. For the vibration analysis, we set $p_i^{(ex)}=0$ and $m_i^{(ex)}=0$ with $(i=t,n,b)$. Assuming harmonic motion, $\mathbf{U}^0$, $\mathbf{\Omega}^0$, $\mathbf{T}^0$, and $\mathbf{M}^0$ take the form

$$\mathbf{U}^0(s,t)=\mathbf{U}^*(s)\mathbf{e}^{i\omega t}$$
$$\mathbf{\Omega}^0(s,t)=\mathbf{\Omega}^*(s)\mathbf{e}^{i\omega t}$$
$$\mathbf{T}^0(s,t)=\mathbf{T}^*(s)\mathbf{e}^{i\omega t} \tag{16}$$
$$\mathbf{M}^0(s,t)=\mathbf{M}^*(s)\mathbf{e}^{i\omega t}$$

and substituting (16) into (6), a set of 12 first-order linear, homogeneous ordinary differential equations is obtained. If the generalized displacements U_t^*, U_n^*, U_b^*, Ω_t^*, Ω_n^*, Ω_b^* and corresponding generalized resultant forces T_t^0, T_n^0, T_b^0, M_t^0, M_n^0, M_b^0

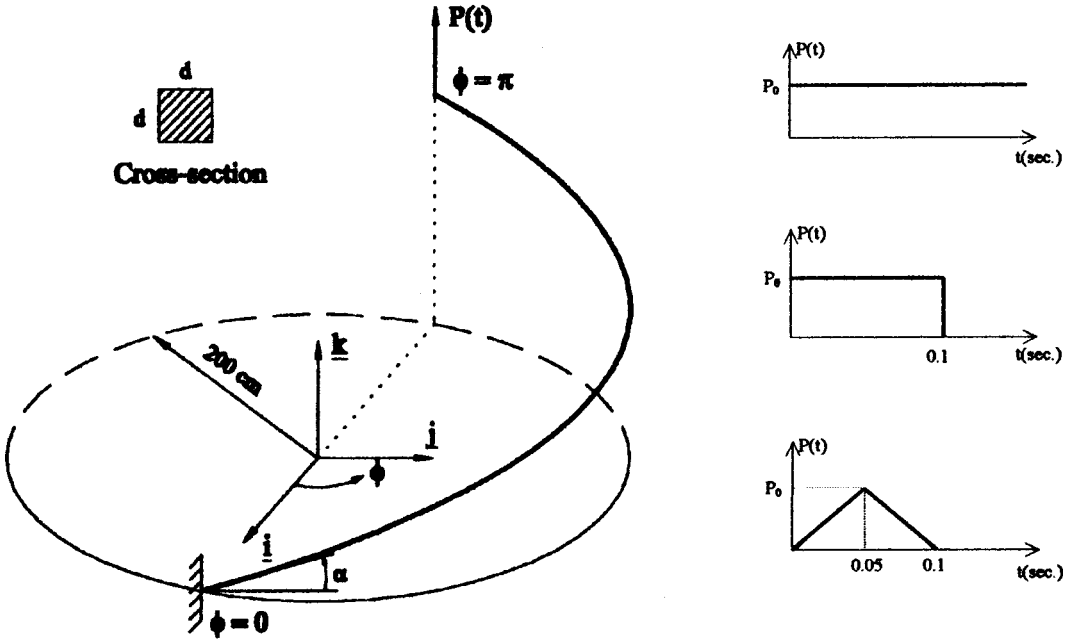

(*a*) (*b*)

Fig. 5 (*a*) A cantilever helical rod; (*b*) type of the dynamic loads

are considered as the components, in the indicated order, of a column matrix $\mathbf{Y}^*(s)$, these 12 equations can be rewritten in the matrix form as

$$\frac{dY^*(s)}{ds} = F(s,\omega)Y^*(s). \tag{17}$$

The values of ω which make the determinant of the system dynamic stiffness matrix zero are the natural frequencies of the problem. For the case of free vibrations the dynamic stiffness matrix is obtained by applying the complementary functions method described in Section 6.

5 Special Cases

The spatially curved system is examined as a free-vibration problem in Yildirim [13]. Forced vibration problem with time-dependent loading will be considered here. The parametric equation of a helix is (Fig. 2)

$$x = a\cos\phi, \quad y = a\sin\phi, \quad z = h\phi \tag{18}$$

where ϕ is the horizontal angle of the helix. The infinitesimal length element of the helix is defined as

$$c = \sqrt{a^2+h^2}, \quad ds = c\,d\phi, \quad \cos\alpha = a/c, \quad \sin\alpha = h/c \tag{19}$$

where α and a are pitch angle and centreline radius of the helix, respectively. The curvatures of a cylindrical helical spring are

$$\chi = a/c^2 = \text{constant}, \quad \tau = h/c^2 = \text{constant}. \tag{20}$$

The relationship between the moving axis (**t**, **n**, **b**) and the fixed reference frame (**i**, **j**, **k**) is

$$\{V\}^t_{tnb} = [B]\{V\}^t_{ijk}$$

$$\begin{Bmatrix} V_i \\ V_n \\ V_b \end{Bmatrix} = \begin{bmatrix} -(a/c)\sin\phi & (a/c)\cos\phi & (h/c) \\ -\cos\phi & -\sin\phi & 0 \\ (h/c)\sin\phi & -(h/c)\cos\phi & (a/c) \end{bmatrix} \begin{Bmatrix} V_i \\ V_j \\ V_k \end{Bmatrix}. \tag{21}$$

The scalar equations governing the forced vibration behavior of helical bars are obtained by using Eqs. (6), (19), and (20). Nondimensional parameters in the Laplace domain are defined as

$$\overline{U}_i = \frac{1}{c}U_i^0, \quad \overline{\Omega}_i = \Omega_i^0, \quad \overline{T}_i = \frac{c^2}{EI_n}T_i^0,$$

$$\overline{M}_i = \frac{c}{EI_n}M_i^0 \quad (i = t,n,b). \tag{22}$$

Finally, the nondimensional forced vibration equations in canonical form are as follows:

$$\frac{d\overline{U}_t}{d\phi} = \frac{a}{c}\overline{U}_n + \frac{I_n}{Ac^2}\overline{T}_t \tag{23a}$$

$$\frac{d\overline{U}_n}{d\phi} = -\frac{a}{c}\overline{U}_t + \frac{h}{c}\overline{U}_b + \overline{\Omega}_b + \frac{\alpha_n EI_n}{GAc^2}\overline{T}_n \tag{23b}$$

$$\frac{d\overline{U}_b}{d\phi} = -\frac{h}{c}\overline{U}_n - \overline{\Omega}_n + \frac{\alpha_b EI_n}{GAc^2}\overline{T}_b \tag{23c}$$

$$\frac{d\overline{\Omega}_t}{d\phi} = \frac{a}{c}\overline{\Omega}_n + \frac{EI_n}{GI_t}\overline{M}_t \tag{23d}$$

$$\frac{d\overline{\Omega}_n}{d\phi} = -\frac{a}{c}\overline{\Omega}_t + \frac{h}{c}\overline{\Omega}_b + \overline{M}_n \tag{23e}$$

$$\frac{d\overline{\Omega}_b}{d\phi} = -\frac{h}{c}\overline{\Omega}_n + \frac{I_n}{I_b}\overline{M}_b \tag{23f}$$

$$\frac{d\overline{T}_t}{d\phi} = \frac{\rho Ac^4 z^2}{EI_n}\overline{U}_t + \frac{a}{c}\overline{T}_n + \overline{B}_7 \tag{23g}$$

$$\frac{d\overline{T}_n}{d\phi} = \frac{\rho Ac^4 z^2}{EI_n}\overline{U}_n - \frac{a}{c}\overline{T}_t + \frac{h}{c}\overline{T}_b + \overline{B}_8 \tag{23h}$$

$$\frac{d\overline{T}_b}{d\phi} = \frac{\rho A c^4 z^2}{EI_n}\overline{U}_b - \frac{h}{c}\overline{T}_n + \overline{B}_9 \tag{23i}$$

$$\frac{d\overline{M}_t}{d\phi} = \frac{\rho I_t c^2 z^2}{EI_n}\overline{\Omega}_t + \frac{a}{c}\overline{M}_n + \overline{B}_{10} \tag{23j}$$

$$\frac{d\overline{M}_n}{d\phi} = \frac{\rho c^2 z^2}{E}\overline{\Omega}_n + \overline{T}_b - \frac{a}{c}\overline{M}_t + \frac{h}{c}\overline{M}_b + \overline{B}_{11} \tag{23k}$$

$$\frac{d\overline{M}_b}{d\phi} = \frac{\rho I_b c^2 z^2}{EI_n}\overline{\Omega}_b - \overline{T}_n - \frac{h}{c}\overline{M}_n + \overline{B}_{12}. \tag{23l}$$

6 Solutions of the Differential Equations With the Complementary Functions Method

Equations (23*a–l*) make up a set of 12 simultaneous differential equations with constant coefficients. Each one of these equations involves first-order derivatives with respect to position. The relationships given for only the static case in Haktanir [12] were used in the Laplace domain with the addition of dynamic loads. In matrix notation, Eqs. (23*a–l*) can be expressed as

$$\frac{d\overline{\mathbf{Y}}(\phi,z)}{d\phi} = \overline{\mathbf{F}}(\phi,z)\overline{\mathbf{Y}}(\phi,z) + \overline{\mathbf{B}}(\phi,z). \tag{24}$$

For the case of spatial bar, the elements of state vector are defined as

$$\overline{\mathbf{Y}}(\phi,z) = \{\overline{\mathbf{U}}(\phi,z),\ \overline{\mathbf{\Omega}}(\phi,z),\ \overline{\mathbf{T}}(\phi,z),\ \overline{\mathbf{M}}(\phi,z)\}^t. \tag{25}$$

The complementary functions method is based on the principle of solving Eq. (25) with the aid of initial conditions. This method of the complementary functions method is basically the reduction of two-point boundary value problems to the numerical solution of initial-value problems which are much more suitable for programming. The general solution of the governing differential Eq. (25), is given by

$$\overline{\mathbf{Y}}(\phi,z) = \sum_{m=1}^{12} C_m(\overline{\mathbf{U}}^{(m)}(\phi,z)) + \overline{\mathbf{V}}(\phi,z) \tag{26}$$

where $\overline{\mathbf{U}}^{(m)}(\phi,z)$ is the complementary solution such that its mth component is equal to 1, whereas all the others are zero. $\overline{\mathbf{V}}(\phi,z)$

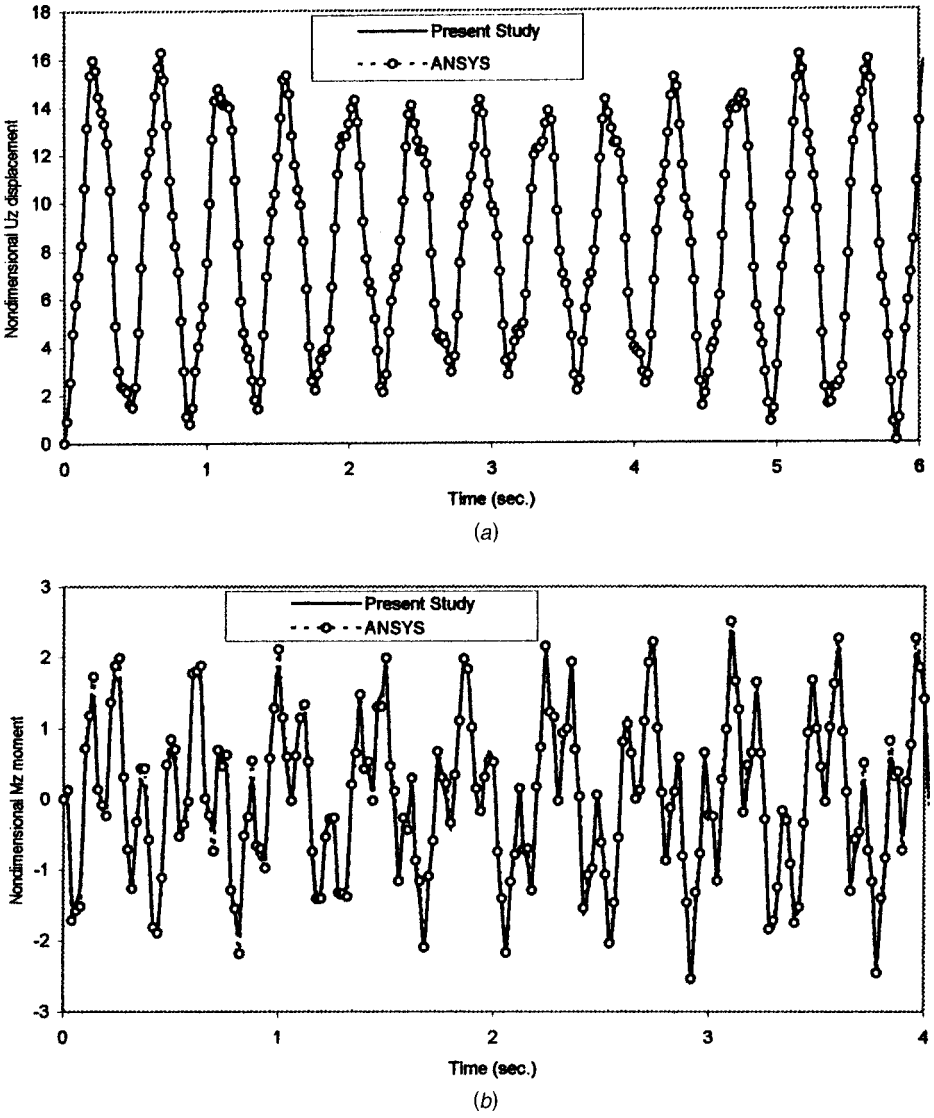

Fig. 6 (***a***) **Vertical displacement versus time at the free end for the step load,** (***b***) **bending moment versus time at the fixed end for the step load**

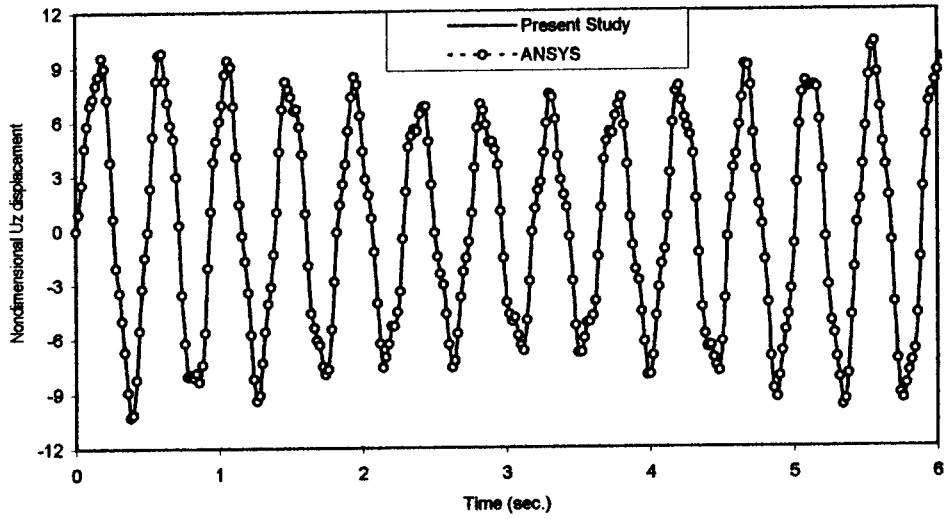

(*a*)

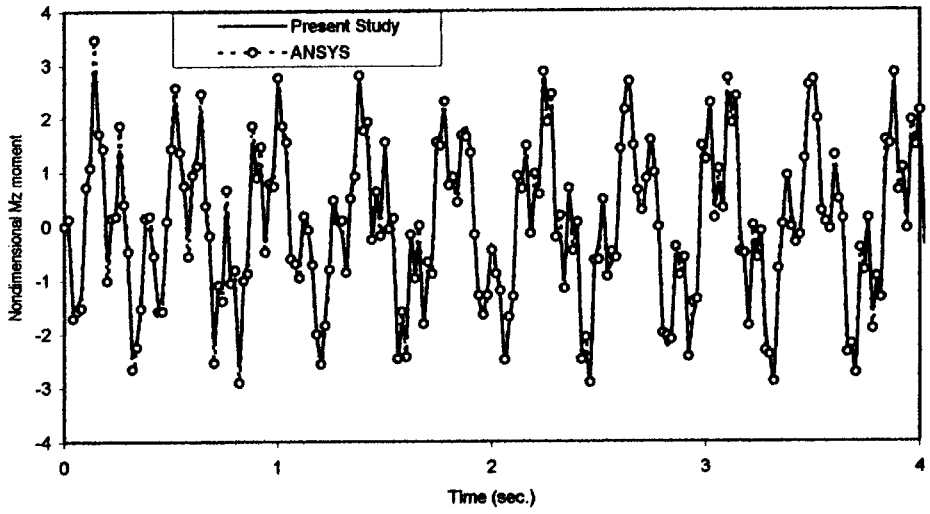

(*b*)

Fig. 7 (*a*) Vertical displacement versus time at the free end for the rectangular impulsive load, (*b*) bending moment versus time at the fixed end for the rectangular impulsive load

is the inhomogeneous solution with all zero initial conditions, the integration constants C_m will be determined from the boundary conditions at both ends.

7 Determination of the Dynamic Stiffness Matrix

The element equation is given in the Laplace domain by

$$\{\overline{p}\}=[\overline{k}]\{\overline{d}\}+\{\overline{f}\}. \tag{27}$$

There are six degrees-of-freedom at each node, three of these six are translations and others are rotations. Letting *i* stand for the beginning and *j* for the end of an element, the end displacements and the end forces are given in Eqs. (28) and (29).

$$\{\overline{d}\}^t=\{\overline{\mathbf{U}}(\phi_i,z),\ \overline{\mathbf{\Omega}}(\phi_i,z),\ \overline{\mathbf{U}}(\phi_j,z),\ \overline{\mathbf{\Omega}}(\phi_j,z)\} \tag{28}$$

$$\{\overline{p}\}^t=\{\overline{\mathbf{T}}(\phi_i,z),\ \overline{\mathbf{M}}(\phi_i,z),\ \overline{\mathbf{T}}(\phi_j,z),\ \overline{\mathbf{M}}(\phi_j,z)\} \tag{29}$$

In order to determine the element stiffness matrix, the end displacements of the element as defined in (28) are equated to unity for any one of the 12 directions while keeping the others zero. This is done 12 times using each equation. From the homogeneous solution of the system (23), the element end forces are obtained, and these forces are incorporated into the element dynamic stiffness matrix appropriately.

The fixed-end forces are computed from (23) by taking all the end displacements to be equal to zero.

$$\{\overline{f}\}^t=\{-\overline{\mathbf{T}}(\phi_i,z),\ -\overline{\mathbf{M}}(\phi_i,z),\ \overline{\mathbf{T}}(\phi_j,z),\ \overline{\mathbf{M}}(\phi_j,z)\} \tag{30}$$

For the transformation to the common reference system, the following equations are used:

$$[\overline{k}]_{ijk}=[T]^T[\overline{k}]_{tnb}[T] \tag{31}$$

$$\{\overline{f}\}_{ijk}=[T]^t\{\overline{f}\}_{tnb} \tag{32}$$

where the transformation matrix $[T]$ is given by

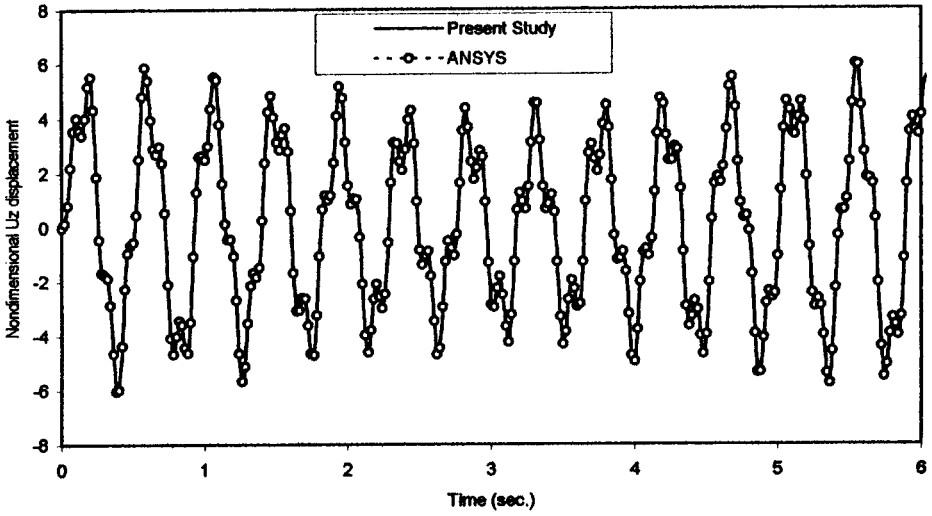

(*a*)

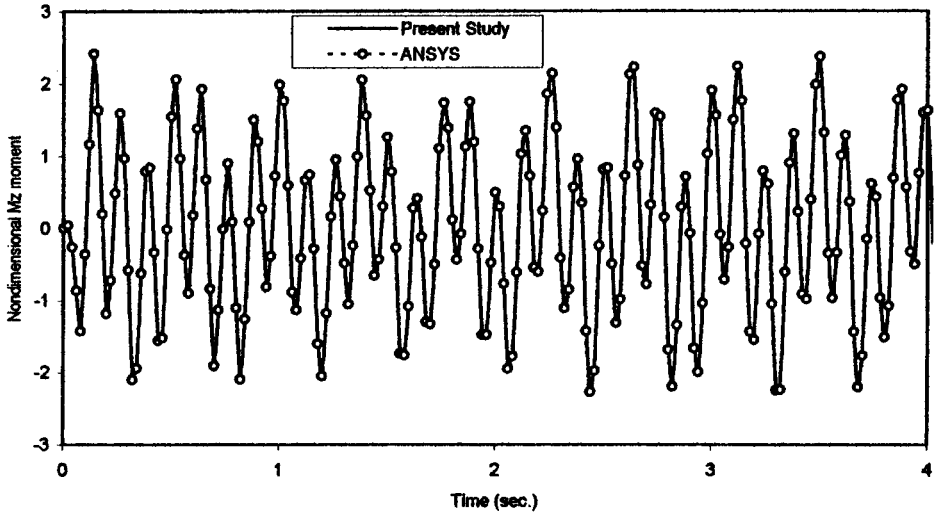

(*b*)

Fig. 8 (*a*) Vertical displacement versus time at the free end for the triangular impulsive load, (*b*) bending moment versus time at the fixed end for the triangular impulsive load

$$[T]=\begin{bmatrix} [B(\phi_i)] & [0] & [0] & [0] \\ [0] & [B(\phi_i)] & [0] & [0] \\ [0] & [0] & [B(\phi_j)] & [0] \\ [0] & [0] & [0] & [B(\phi_j)] \end{bmatrix}_{12\times 12} \tag{33}$$

and $[B]$ is defined in Eq. (21).

In this study, both the element dynamic stiffness matrix $[\overline{k}]$ and the fixed-end forces $\{\overline{f}\}$, are determined by solving Eq. (23) by the method of the complementary functions method in the Laplace domain. The system equation of motion can then be assembled from the element dynamic stiffness matrices and end forces as

$$[\mathbf{K}(\mathbf{z})]\{\mathbf{D}\}=\{\mathbf{P}(\mathbf{z})\} \tag{34}$$

where $[\mathbf{K}(\mathbf{z})]$ and $\{\mathbf{P}(\mathbf{z})\}$ are the system dynamic stiffness matrix and load vector. $\{\mathbf{D}\}$ is the vector of unknown displacements of the system.

For the free-vibration case, the system load vector is equal to zero and the Laplace parameter "z" is replaced with "$i\omega$." The eigenvalues in this case give the natural frequencies.

8 Numerical Examples

In this study, a general-purpose computer program is coded in FORTRAN77 for time-dependent loading to analyze forced vibration of cylindrical helical rods. As a special case, free-vibration analysis can also be done by simply removing the applied loads and replacing the Laplace parameter "z" with "$i\omega$." Butcher's fifth-order Runge-Kutta algorithm, [27], is used for the solution of the initial value problem based on the complementary functions method. Forty steps of integration are used in the analysis. The Durbin's inverse Laplace transform, [23,24], is applied for the transformation from the Laplace domain to the time domain.

In this section, two sample problems are presented. First, in order to validate the developed computer program, the free-vibration frequencies of a helical spring that is fixed at two ends are compared with the results available in the literature. In addition, this system is also analyzed under an impulsive load. Second, a cantilever helical rod is considered. Various dynamic loads are applied on the free end of the rod, then the analysis is done by using the present computer program and ANSYS [28]. Displacement values and the element forces are compared in the graphics.

Example 1. The helical spring fixed at the both ends shown in Fig. 3 is considered. The spring is made of steel and has a circular cross section with the diameter $d=1$ mm. The pitch angle, radius of the helix circle and the number of active turns are chosen as $\alpha=8.5744°$, $a=5$ mm, and $n=7.6$, respectively. The material properties are $E=2.06\times10^{11}$ N/m^2, $\rho=7900$ kg/m^3, and $\nu=0.3$. Free-vibration frequencies calculated by using the present computer program are given in Table 1 with the theoretical and experimental data given in the literature for a comparison. It can be seen from Table 1 that the result of the present model demonstrates a good agreement with the previous results. Table 1 shows the results obtained from ANSYS are also in accord with the results of the present study. It should be noted that, in the present method, only two elements were used to achieve the desired accuracy as opposed to 500 straight-beam elements needed in ANSYS.

After having tested the validity of the present model on the free-vibration problem, the forced vibration analysis is presented. A triangular impulsive load (Fig. 3(*b*)) with the amplitude $P_0=0.25$ N is applied vertically at the arc-length midpoint of the spring. A time increment Δt of 25 μs is used in the calculations. Six and 2994 active degrees-of-freedom were present in this study and the ANSYS model, respectively. Vertical displacement and rotation at the arc-length midpoint of the spring and vertical shear force and moment at the fixed end of the spring are compared with the results of the ANSYS (in Fig. 4(*a–d*)). Results obtained in this study with two elements agree well with ANSYS using the 500-element mesh. The computation time for the solutions obtained by using the program coded in this study is approximately one tenth of that of ANSYS.

Example 2. A cantilever helical rod is now considered. Material and geometrical properties are $d=12$ cm, $\alpha=25.522834°$, $a=200$ cm, $E=2.06\times10^{11}$ N/m^2, $\rho=7850$ kg/m^3, and $\nu=0.3$ (see Fig. 5(*a*)). Various dynamic loads as shown in Fig. 5(*b*) with the amplitude $P_0=10^6$ N are applied vertically at the free end of the rod. A time increment Δt of 20 ms is used in the calculations. Identical cross-sectional stiffness constants are used for both the present model and the ANSYS. Six and 486 active degrees-of-freedom were present in this study and the ANSYS model, respectively. Using the present computer program and ANSYS carries out a transient analysis.

Vertical displacement at the free end and bending moment at the fixed end are compared with the results of ANSYS (see Figs. 6–8). Results obtained by the present formulation with only one element agree quite well with those obtained from ANSYS using 81 straight-beam elements. The computation time is reduced approximately five times with the present model.

9 Discussions and Conclusions

The formulation to analyze the forced vibration of cylindrical helical rods and springs subjected to time-dependent loads is presented in this study. A general-purpose computer program is coded in FORTRAN77 to perform the analysis in the Laplace domain. As a special case, it is shown that free vibration analysis can also be done by simply removing the applied loads and replacing the Laplace parameter "z" with "$i\omega$." Butcher's fifth-order RK method is used for the solution of the initial value problem based on the complementary functions method.

In the present work, the dynamic stiffness matrix has been calculated in the Laplace domain by applying the complementary functions method to the differential equations in canonical form. This provides great convenience in the solution of the physical problems having general boundary conditions. Another advantage of using the complementary functions method-based solution is that the helical rods with variable cross section and geometry, which yield ordinary differential equations having variable coefficients, can also be considered. The differential equations can be solved by using the complementary functions method as accurate as required with an appropriate integration step-size. In the present method, only one or two elements were used to achieve the desired accuracy as opposed to high number of elements (in the order of 100) needed in ANSYS.

Free-vibration frequencies calculated to validate the developed computer program are compared with the theoretical and experimental data given in the literature. It is seen that the results of the present model demonstrate a good agreement with the results of other independent methods and ANSYS.

After having tested the validity of the present model on the free-vibration problem, the results of forced vibration analysis is compared with those of ANSYS in graphic form, and close agreement has been observed. The computation time is also significantly reduced with the present model.

Acknowledgments

The authors are greatly indebted to Dr. Erhan Kiral, Professor at the Department of Civil Engineering at Çukurova University, for his valuable help. The authors would also like to thank Çukurova University Scientific Research Projects Directorate (FBE2002 D-178) for supporting this study.

References

[1] Massoud, M. F., 1965, "Vectorial Derivation of the Equations for Small Vibrations of Twisted Curved Beams," ASME J. Appl. Mech., **32**, pp. 439–440.
[2] Wittrick, W. H., 1966, "On Elastic Wave Propagation in Helical Spring," Int. J. Mech. Sci., **8**, pp. 25–47.
[3] Kiral, E., and Ertepinar, A., 1974, "Studies on Elastic Rods Subject to Diverse External Agencies—Part I: Derivation of Governing Equations," METU J. Pure Appl. Sci., **7**(1), pp. 23–40.
[4] Kiral, E., and Ertepinar, A., 1974, "Studies on Elastic Rods Subject to Diverse External Agencies—Part III: Vibrational Analysis of Space Rods," METU J. Pure Appl. Sci., **7**(1), pp. 55–69.
[5] Mottershead, J. E., 1980, "Finite Elements for Dynamical Analysis of Helical Rods," Int. J. Mech. Sci., **22**, pp. 267–283.
[6] Pearson, D., 1982, "The Transfer Matrix Method for the Vibration of Compressed Helical Springs," Int. J. Mech. Sci., **24**, pp. 163–171.
[7] Pearson, D., and Wittrick, W. H., 1986, "An Exact Solution for the Vibration of Helical Spring Using a Bernoulli-Euler Model," Int. J. Mech. Sci., **28**, pp. 83–96.
[8] Nagaya, K., Takeda, S., and Nakata, Y., 1986, "Free Vibrations of Coil Springs of Arbitrary Shape," Int. J. Numer. Methods Eng., **23**, pp. 1081–1099.
[9] Lin, Y., and Pisano, A. P., 1987, "General Dynamic Equations of Helical Springs With Static Solution and Experimental Verification," ASME J. Appl. Mech., **54**, pp. 910–916.
[10] Lin, Y., and Pisano, A. P., 1988, "The Differential Geometry of the General Helix as Applied to Mechanical Spring," ASME J. Appl. Mech., **55**, pp. 831–835.
[11] Tabarrok, B., Sinclair, A. N., Farshad, M., and Yi, H., 1988, "On the Dynamics of Spatially Curved and Twisted Rods: A Finite Element Formulation," J. Sound Vib., **123**(2), pp. 315–326.
[12] Haktanir, V., 1995, "The Complementary Functions Method for the Element Stiffness Matrix of Arbitrary Spatial Bars of Helicoidal Axes," Int. J. Numer. Methods Eng., **38**, pp. 1031–1056.
[13] Yildirim, V., 1996, "Investigation of Parameters Affecting Free Vibration Frequency of Helical Spring," Int. J. Numer. Methods Eng., **39**, pp. 99–114.
[14] Yildirim, V., 1999, "An Efficient Numerical Method for Predicting the Natural Frequencies of Cylindrical Helical Springs," Int. J. Mech. Sci., **41**, pp. 919–939.
[15] Lee, J., and Thompson, D. J., 2001, "Dynamic Stiffness Formulation, Free Vibration and Wave Motion of Helical Springs," J. Sound Vib., **239**(2), pp. 297–320.
[16] Jiang, W., Jones, W. K., Wang, T. L., and Wu, K. H., 1991, "Free Vibration of Helical Springs," Trans. ASME, **58**, pp. 222–228.
[17] Sinha, S. K., and Costello, G. A., 1978, "The Numerical Solution of the Dynamic Response of Helical Springs," Int. J. Numer. Methods Eng., **12**, pp. 949–961.
[18] Berdichevsky, V. L., and Sutyrin, V. G., 1984, "Problem of an Equivalent Rod in Nonlinear Theory of Springs," Prikl. Mat. Mekh., **47**(2), pp. 197–205.
[19] Berdichevsky, V. L., and Starosel'skii, L. A., 1983, "On the Theory of Curvilinear Timoshenko-Type Rods," Prikl. Mat. Mekh., **47**(6), pp. 809–817.
[20] Cesnik, C. E. S., Hodges, D. H., and Sutyrin, V. G., 1996, "Cross-Sectional Analysis of Composite Beams Including Large Initial Twist and Curvature Effects," AIAA J., **34**(9), pp. 1913–1920.
[21] Borri, M., Ghiringhelli, G. L., and Merlini, T., 1992, "Linear Analysis of Naturally Curved and Twisted Anisotropic Beams," Composites Eng., **2**(5–7), pp. 433–456.

[22] Yu, W., Hodges, D. H., Volovoi, V. V., and Cesnik, C. E. S., 2000, ''Timoshenko-Like Modelling of Initially curved and Twisted Composite Beams With Oblique Cross Section,'' *Proceedings of the 41st Structures, Structural Dynamics and Materials Conference*, AIAA Paper No. 2000-1405.
[23] Durbin, F., 1974, ''Numerical Inversion of Laplace Transforms: An Efficient Improvement to Dubner and Abate's Method,'' Comput. J., **17**, pp. 371–376.
[24] Narayanan, G. V., 1979, ''Numerical Operational Methods in Structural Dynamics,'' Ph.D. thesis, University of Minnesota, Minneapolis, MN.
[25] Yerli, H. Y., Temel, B., and Kiral, E., 1998, ''Transient Infinite Elements for 2D Soil-Structure Interaction Analysis,'' J. Geotech. Eng., **124**(10), pp. 976–988.
[26] Sokolnikoff, I. S., and Redheffer, R. M., 1958, *Mathematics of Physics and Modern Engineering*, McGraw-Hill, Tokyo.
[27] Chapra, S. C., and Canale, R. P., 1998, *Numerical Methods for Engineers*, 3rd Ed., McGraw-Hill, New York.
[28] ANSYS Swanson Analysis System, Inc., 201 Johnson Road, Houston, PA 15342–1300.

Vibration of Thick Circular Disks and Shells of Revolution

A. V. Singh

L. Subramaniam

Department of Mechanical and Materials Engineering,
The University of Western Ontario,
London, ON N6A 5B9, Canada

A fully numerical and consistent method using the three-dimensional theory of elasticity is presented in this paper to study the free vibrations of an axially symmetric solid. The solid is defined in the cylindrical coordinates (r,θ,z) by a quadrilateral cross section in the r-z plane bounded by four straight and/or curved edges. The cross section is then mapped using the natural coordinates (ξ,η) to simplify the mathematics of the problem. The displacement fields are expressed in terms of the product of two simple algebraic polynomials in ξ and η, respectively. Boundary conditions are enforced in the later part of the solution by simply controlling coefficients of the polynomials. The procedure setup in this paper is such that it was possible to investigate the free axisymmetric and asymmetric vibrations of a wide range of problems, namely; circular disks, cylinders, cones, and spheres with considerable success. The numerical cases include circular disks of uniform as well as varying thickness, conical/cylindrical shells and finally a spherical shell of uniform thickness. Convergence study is also done to examine the accuracy of the results rendered by the present method. The results are compared with the finite element method using the eight-node isoparametric element for the solids of revolution and published data by other researchers. [DOI: 10.1115/1.1544542]

Introduction

Vibrations of circular annular plates and shells of revolution have been the focus of study for a very large number of researchers for nearly a century. The problem of vibrating solid cylinders was considered by many researchers from the three-dimensional theory of elasticity. Different solution types were introduced by incorporating in the analysis some simplifying assumptions and cases of slender rods and relatively thick circular disks were examined as special cases. McMahon [1] deduced equations for some special cases of the free vibration analysis of circular cylinders. He continued to verify his analytical results by performing some experiments on the free vibrations of solid cylinders. Mirsky [2] deduced an approximate theory of vibrations of orthotropic thick cylindrical shells in which the effect of transverse normal stress was retained. Hutchinson [3–5] published a series of papers on axisymmetric and asymmetric vibrations of solids of revolution. For example, he studied axisymmetric vibrations of a stress-free rod, [3], using Bessel functions in the solution. The vibration of solid cylinders using three-dimensional equations of linear elasticity was also investigated in his paper of 1980, [4]. This work was further extended to consider the vibration of thick circular plates (Hutchinson, [5]). A detailed survey paper dealing with the dynamic analysis of cylinders and open cylindrical panels made of an arbitrary number of anistropic linearly elastic layers perfectly bonded together, was published by Soldatos [6]. Leissa and So [7] compared the natural frequencies for rods and beams from one-dimensional and three-dimensional theories using the Rayleigh Ritz method. After establishing the advantage of three-dimensional analysis, they continued with the free vibration analysis of circular cylinders (Leissa and So, [8]) and presented results for free-free and clamped-free boundary conditions. The Rayleigh-Ritz method was used by Young and Dickinson [9,10] to study a class of homogeneous solids including several solids of revolution. Using the same method, Singh and Saxena [11] studied the axisymmetric vibrations of a circular plate with double linear variable thickness. In their paper, the thickness of each of the core and the outer annular region was considered to be linearly varying. Numerical results were given for the clamped as well as the simply supported cases and compared with other published sources. Recently, So and Leissa [12] investigated the free vibration of thick circular and annular plates and compared their results with those obtained by others using Mindlin plate theory. Majority of the researchers mentioned above focussed their attention on the analysis of circular plates and cylinders.

This paper presents a consistent numerical method for the free vibration analysis of solids of revolution. The method is unified in a way that a varied class of problems with respect to axisymmetric and asymmetric vibrations, can be studied. The solid is defined in the cylindrical coordinates (r,θ,z) by revolving around the z-axis a quadrilateral cross section bounded by four straight and/or curved edges. The cross section is then mapped using the natural coordinates (ξ,η) to simplify the mathematics of the problem. Such a mapping is routinely carried out for the formulation of isoparametric quadrilateral finite elements. The solution algorithm is developed on the basis of the Ritz method, which requires predefined admissible displacement fields, which are constructed by multiplying two simple algebraic polynomials in the ξ and η directions, respectively. The present formulation is different from those by other researchers, because it is entirely numerical and has a significantly wider range of applicability. It is very similar to the formulation of Leissa and So [7,8], but more general in the sense that it can accommodate various other geometries, such as spherical and conical shells having uniform or variable thicknesses. Through the convergence study, numerical scheme is found to be robust and stable. The results are obtained first for uniform as well as variable thickness circular disks and then compared with those obtained from the classical method using Mindlin plate theory and finite element method using eight-node isoparametric axisymmetric ring elements. Although the mode shapes were generated for these cases, due to lack of space, they are not included in this paper. Still, it is worthwhile to mention that an interesting pattern was observed from the mode shapes of the vibrating thick circular disks. Some modes were found to be predominantly flexural type, whereas the others were the in-plane stretching type. They coexist independently. Numerical examples for solid cylinder and thick

Contributed by the Applied Mechanics Division of THE AMERICAN SOCIETY OF MECHANICAL ENGINEERS for publication in the ASME JOURNAL OF APPLIED MECHANICS. Manuscript received by the Applied Mechanics Division, June 24, 1999; final revision, Aug. 29, 2002. Associate Editor: V. K. Kinra. Discussion on the paper should be addressed to the Editor, Prof. Robert M. McMeeking, Chair, Department of Mechanics and Environmental Engineering, University of California–Santa Barbara, Santa Barbara, CA 93106-5070, and will be accepted until four months after final publication in the paper itself in the ASME JOURNAL OF APPLIED MECHANICS.

conical and spherical shells are also presented and discussed in this study. Frequencies of the circular disks and thick shells of revolution are plotted versus the thickness.

Formulation

To begin with a general formulation, it is assumed that the solid is made of a linearly elastic isotropic material. Figure 1 shows the sectional view in the r-z plane and the solid is formed by revolving the shown area about the z-axis. The area is bounded by four curved edges. The coordinates (r,z) of the four corner points 1 through 4 and also of the additional middle points 5 through 8 of the four edges are prescribed. The natural coordinate system $(\xi$-$\eta)$ is used to map this area into a square. The relationship between the $(r$-$z)$ and $(\xi$-$\eta)$ systems is well known, as this type of mapping is routinely used in the formulation of an eight-node isoparametric finite element. Consider a point inside the area shown in Fig. 1. The coordinates of this point can be represented by

$$r(\xi,\eta)=\sum_{i=1}^{\infty} N_i(\xi,\eta)r_i$$
$$z(\xi,\eta)=\sum_{i=1}^{\infty} N_i(\xi,\eta)z_i\,. \tag{1}$$

Here, $N_i(\xi,\eta)$ and (r_i,z_i); for $i=1,2,3,\ldots,8$ are, respectively, the shape functions and the coordinates of the eight points defining the geometry. According to this notation, the infinitesimal volume dV can be written as

$$dV=r\,d\theta\,dr\,dz=r(\xi,\eta)|J(\xi,\eta)|\,d\xi\,d\eta\,d\theta. \tag{2}$$

The cross-sectional area is not divided into smaller regions, as is done to generate the mesh in the finite element method. In the following, the basic equations from the theory of elasticity for axisymmetric solids are presented briefly in the (r,θ,z) coordinate system. These equations include strain displacement relations, stress strain relations, and energy expressions.

Elasticity Equations

Assume that the translations along the r, z, and θ directions are denoted by u, v, and w, respectively. The strain-displacement relationships in this system are given by

$$\varepsilon_r=\frac{\partial u}{\partial r}$$
$$\varepsilon_z=\frac{\partial v}{\partial z}$$
$$\varepsilon_\theta=\frac{u}{r}+\frac{1}{r}\frac{\partial w}{\partial \theta}$$
$$\gamma_{rz}=\frac{\partial u}{\partial z}+\frac{\partial v}{\partial r} \tag{3}$$
$$\gamma_{z\theta}=\frac{1}{r}\frac{\partial v}{\partial \theta}+\frac{\partial w}{\partial z}$$
$$\gamma_{r\theta}=\frac{1}{r}\frac{\partial u}{\partial \theta}+\frac{\partial w}{\partial r}-\frac{w}{r}.$$

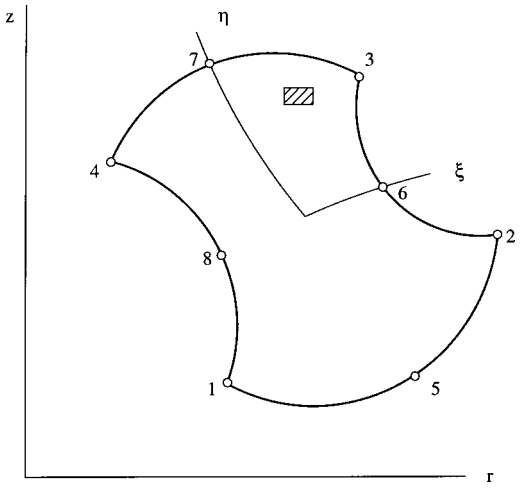

Fig. 1 Cross section of a solid of revolution

The matrix form of Eq. (3) is

$$\{\varepsilon\}=[d]\{u\} \tag{4}$$

where $\{\varepsilon\}^T=\{\varepsilon_r\ \varepsilon_z\ \varepsilon_\theta\ \gamma_{rz}\gamma_{z\theta}\gamma_{r\theta}\}$, $\{u\}^T=\{u v w\}$ and $[d]$ is called for convenience the matrix of differential operator. It is given by

$$[d]=\begin{bmatrix} \frac{\partial}{\partial r} & 0 & 0 \\ 0 & \frac{\partial}{\partial z} & 0 \\ \frac{1}{r} & 0 & \frac{1}{r}\frac{\partial}{\partial \theta} \\ \frac{\partial}{\partial z} & \frac{\partial}{\partial r} & 0 \\ 0 & \frac{1}{r}\frac{\partial}{\partial \theta} & \frac{\partial}{\partial z} \\ \frac{1}{r}\frac{\partial}{\partial \theta} & 0 & \frac{\partial}{\partial r}-\frac{1}{r} \end{bmatrix}. \tag{5}$$

The next important equation to consider here is the stress-strain relationship. By denoting the transpose of the stress vector as $\{\sigma\}^T=\{\sigma_r\sigma_z\sigma_\theta\tau_{rz}\tau_{z\theta}\tau_{r\theta}\}$, one can write the following relationship:

$$\{\sigma\}=[E]\{\varepsilon\}. \tag{6}$$

If the material is isotropic with r, z, and θ as the principal directions, the stress-strain operator matrix $[E]$ can be written as follows:

$$[E]=\frac{E}{(1+\nu)e_2}\begin{bmatrix} e_1 & \nu & \nu & 0 & 0 & 0 \\ \nu & e_1 & \nu & 0 & 0 & 0 \\ \nu & \nu & e_1 & 0 & 0 & 0 \\ 0 & 0 & 0 & e_3 & 0 & 0 \\ 0 & 0 & 0 & 0 & e_3 & 0 \\ 0 & 0 & 0 & 0 & 0 & e_3 \end{bmatrix} \tag{7}$$

where, $e_1=1-\nu$, $e_2=1-2\nu$, $e_3=e_4=e_5=e_2/2$ and E=modulus of elasticity of the material. Orthotropic material can also be treated with some minor alteration in Eq. (7). The strain energy is given by

$$U=\frac{1}{2}\int_{\text{volume}}\{\sigma\}^T\{\varepsilon\}dV=\frac{1}{2}\int_{\text{volume}}\{\varepsilon\}^T[E]\{\varepsilon\}dV. \tag{8}$$

Similarly, the kinetic energy for the continuum is given by

$$K=\frac{1}{2}\int_{\text{volume}}\rho\{\partial u/\partial t\}^T\{\partial u/\partial t\}dV. \tag{9}$$

Here, $\{\partial u/\partial t\}^T=\{\partial u/\partial t\ \partial v/\partial t\ \partial w/\partial t\}$ and ρ=mass density of the material. The strain and kinetic energy expressions given by Eqs.

(8) and (9) are left in the above form and will be revisited, when the solution procedure is discussed in the subsequent section.

Method of Solution

As said earlier, the solution procedure developed herein is based on the Ritz method. The original Rayleigh-Ritz method requires predefined displacement fields with fully satisfied essential boundary conditions. To define the displacement fields, the following form of the simple algebraic polynomial is chosen:

$$f(\xi)=a_0(1-\xi)^n+a_1(1-\xi)^{n-1}(1+\xi)+a_2(1-\xi)^{n-2}(1+\xi)^2 + \ldots + a_{n-1}(1-\xi)(1+\xi)^{n-1}+a_n(1+\xi)^n. \quad (10)$$

The advantages of considering such a polynomial in the solution procedure are as follows. First, if the polynomial is complete (i.e., none of the intermediate terms has been removed), there is no mathematical constraint imposed to the solution. Second, the enforcement of the geometric boundary conditions is very simple and straightforward. For example, by examining the above polynomial in Eq. (10), it is observed that $f(\xi)=0$ at $\xi=-1$ and $\xi=+1$, if a_0 and a_n are set to zero. Similarly, the derivative $\partial f(\xi)/\partial\xi$ is zero at the two extreme values of ξ, when the condition of $a_0=a_1=a_{n-1}=a_n=0$ is applied. The boundary conditions are applied prior to the eigenvalue calculation.

The admissible displacement fields are generated by multiplying the polynomial $f(\xi)$ by its counterpart $f(\eta)$. The coefficients resulting from the product of the polynomials are denoted by a set of two-dimensional arrays: a_{jk}, b_{jk} and c_{jk} for u, v, and w, respectively. Therefore, the displacement components are represented using the following double summation series in which n represents the Fourier harmonic mode of vibration:

$$u=\sum_{k=1}^{p}\sum_{j=1}^{q} a_{jk}f_j(\xi)f_k(\eta)\cos n\theta$$

$$v=\sum_{k=1}^{p}\sum_{j=1}^{q} b_{jk}f_j(\xi)f_k(\eta)\cos n\theta \quad (11)$$

$$w=\sum_{k=1}^{p}\sum_{j=1}^{q} c_{jk}f_j(\xi)f_k(\eta)\sin n\theta.$$

In a matrix form, the above series equations can be written as

$$\{u\}=[F]\{q\} \quad (12)$$

where $[F]$ is a $(3\times 3pq)$ matrix and constructed as follows. For the row one, the first $(p\times q)$ terms are made of $f_j(\xi)f_k(\eta)$ and the remaining terms are zero. Similarly, the second row is formed with the first and the last $(p\times q)$ terms being zero and the middle $(p\times q)$ terms constructed from the products of the two polynomial functions. The values of j and k are assigned to be 1,2,3 . . . q and 1,2,3, . . . p, where $(q-1)$ and $(p-1)$ represent the orders of the polynomials $f_j(\xi)=(1-\xi)^{q-j}(1+\xi)^{j-1}$ and $f_k(\eta)=(1-\eta)^{p-k}(1+\eta)^{k-1}$, respectively. When Eq. (12) is substituted into Eq. (4), the strain vector is obtained and written as

$$\{\varepsilon\}=[d][F]\{q\}=[B]\{\delta\}. \quad (13)$$

In this equation, the size of matrix $[B]$ is $(6\times 3pq)$ and its terms are made of functions $f_j(\xi)$ and $f_k(\eta)$, their derivatives with respect to ξ and η and also the function as such multiplied by a factor of $(1/r)$. The relationship between the two sets of coordinate parameters is well understood in the field of finite element methods and the terms of the inverse of the Jacobian matrix $[J(\xi,\eta]$ are to be used for this purpose. The vector $\{\delta\}$, the size of which is $3pq$, contains all the unknown coefficients of the double summation series given by Eq. (11). The values of these coefficients are determined during the eigensolution of the equation. Also, the infinitesimal volume for an area $drdz$ located at point (r,z) is written as $dV=r(\xi,\eta)|J(\xi,\eta)|d\xi d\eta d\theta$.

Now, Eqs. (12) and (13) are substituted into the energy expressions given by Eqs. (8) and (9), respectively, to obtain the following:

$$U=\tfrac{1}{2}\{\delta\}^T\left(\pi\int_{-1}^{+1}\int_{-1}^{+1}[B]^T[E][B]r(\xi,\eta)|J(\xi,\eta)|d\xi d\eta\right)\{\delta\}$$

$$K=\tfrac{1}{2}\{\dot\delta\}^T\left(\pi\rho\int_{-1}^{+1}\int_{-1}^{+1}[F]^T[F]r(\xi,\eta)|J(\xi,\eta)|d\xi d\eta\right)\{\dot\delta\}.$$

Finally,

$$U=\tfrac{1}{2}\{\delta\}^T[k]\{\delta\} \quad \text{and} \quad K=\tfrac{1}{2}\{\dot\delta\}^T[m]\{\dot\delta\}. \quad (14)$$

In the above, $[k]$ and $[m]$ are the stiffness and mass matrices of the system and an overdot denotes the time derivative. From these energy equations, one can use standard procedure to obtain the following equation of motion for the free symmetric and asymmetric vibrations of the solid of revolution:

$$[m]\{\ddot\delta\}+[k]\{\delta\}=0. \quad (15)$$

Also, for simple harmonic motion, one can write $\{\delta\}=\{\Delta\}\cos(\omega t+\phi)$. Further, E and ρ can be taken out of the stiffness and mass matrices and then the final eigenequation is

$$([k]-\Omega^2[m])\{\Delta\}=0. \quad (16)$$

Here, $\Omega^2=(\rho/E)\omega^2a^2$. The symbol Ω=the dimensionless frequency parameter of the system, ρ=mass density of the material, ω=natural frequency in radian/second, and a=a length parameter which is typically a prominent dimension depending upon the type of the problem. The computational algorithm is written such that numerical results are obtained in nondimensional form. It is noted here that the displacement components u, v, and w and coordinates are normalized with respect to the length parameter a of the solid of revolution.

Numerical Results

Although the analysis is valid for more general solids of revolution, numerical investigations in this paper are carried out only for solids of revolution formed by revolving areas bounded by four straight or curved edges around the z-axis. The orientation of this quadrangular shaped region determines the type of the problem we need to solve. By changing the parameters, it is possible to analyze problems having a wide range of shapes and sizes. To illustrate the versatility of the present formulation, three types of axisymmetric solids are investigated in this study. They are: thick circular disks of variable thickness, conical shells, and spherical shells. In addition, cylindrical configuration is considered as a special case of the conical one. Numerical values obtained for the frequency parameter Ω are also compared with results available through other sources in the literature. The value of the Poisson's ratio ν is taken to be 0.3 in the computation of all the results that follow. (See Fig. 2.)

In the calculations using the Ritz method, the accuracy of the results depends upon the number of terms used in the polynomials $f_j(\xi)$ and $f_k(\eta)$ which are complete functions in the sense that

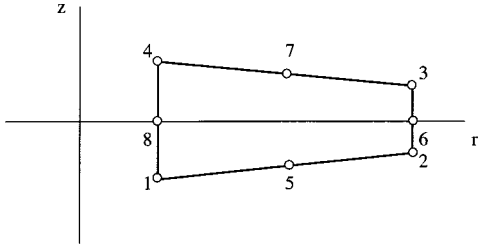

Fig. 2 Area to be revolved around *z*-axis to form a variable thickness circular disk

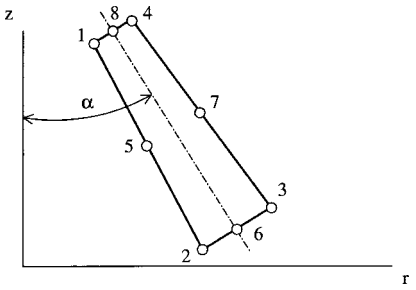

Fig. 3 Representation of a thick conical shell

there are no terms that are missing between the first and the last terms. If a sufficiently large number (theoretically it is ∞) of terms is used in the calculation, the method will yield exact solution. However, by increasing the number of terms in the polynomials, one is bound to encounter numerical complications. If the computer is not powerful enough, the computer code will not render successful runs. To ensure the degree of accuracy of the results as well as the validity of the polynomial form used in this study, it is appropriate to conduct a convergence study.

Convergence Study. For this, a conical shell with cone angle=30 deg and clamped at the lower end shown by point 2-6-3 in Fig. 3 is analyzed. The number of terms in $f_k(\eta)$ is kept at 4 which is reasonable as it represents solution part associated with the thickness of the shell. (See Fig. 4.) The number of terms in $f_j(\xi)$, which represents variation along the axis generating the conical surface, is varied from 4 to 9. Figure 5 shows the first five natural frequencies corresponding to the asymmetric modes with $n=1$. Two cases with thickness $h/a=0.05$ and 0.10, respectively, are analyzed and the results are plotted using symbols "o" and "x," respectively. Clearly, the convergence is seen to be monotonic for the first four modes. For the fifth mode of vibration, some peculiarity is observed for both cases. Especially, with the mode corresponding to $h/a=0.10$, for which two curves appear to be intersecting at $j=5$. This can be explained by considering the fact that this type of formulation includes all kinds of behaviors: namely flexural, thickness-shear and purely extensional, of the shell structure. For extensional modes, the frequency does not vary with the thickness (Kalnins [13]). It is also seen here that the values of the frequency are the same for both $h/a=0.05$ and 0.10. By considering eight or more terms in $f_j(\xi)$, it is reasonable to say that the values of the natural frequencies are expected to be within 3 to 5 percent of the correct value. One should realize that the exact solution based on the three-dimensional theory of elasticity may not be simple (if not impossible) for the shell types considered in this study. For additional numerical investigation, generally thick circular disks and shells of revolution are taken as example problems. The computation is carried out with eight terms (i.e., $q=8$) in $f_j(\xi)$ and four term (i.e., $p=4$) in $f_k(\eta)$.

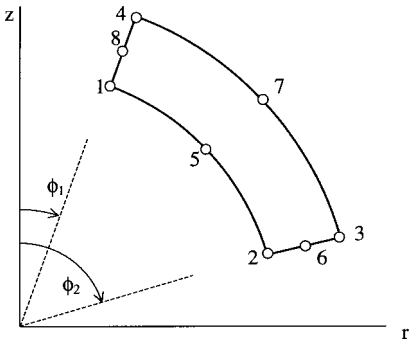

Fig. 4 Representation of a thick spherical shell

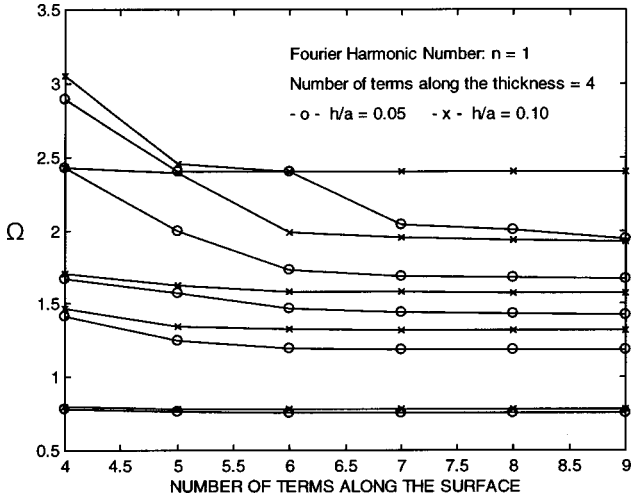

Fig. 5 Convergence study for a conical shell clamped at the lower open end

With these polynomials the order of each of the stiffness and mass matrices is 96. The stiffness and the mass matrices are computed numerically by Gaussian quadrature, with eight and four integration points in ξ and η directions, respectively.

Case 1. Analysis of Circular Disks. A thick circular disk of varying thickness as shown in Fig. 2, is considered. It is symmetrical about the z-axis and the detailed dimension of this disk is described as follows:

$$h_1=z_4-z_1, \quad h_2=z_3-z_2, \quad a=r_2=r_3=r_6 \quad \text{and} \quad b=r_1=r_4=r_8. \tag{17}$$

Here, (r_i, z_i) for $i=1$ through 8 represent the coordinates of the eight nodes. The inside edge contains nodes 1, 8, and 4 and the outside edge is defined by nodes 2, 6, and 3.

For further validation of the numerical method presented in this paper, a circular disk of uniform thickness, clamped at the inside edge and free at the outside, is analyzed so that the results obtained can be compared with those from the work by Irie et al. [14]. By using the Mindlin plate theory for solving the differential equation of motion in terms of the Bessel functions, they published an extensive set of data pertaining to the natural frequencies of thick annular plate of uniform thickness. The comparison as seen in Table 1 is generally very good for relatively thin annular plates. But for thick disks, the discrepancy between the numerical results from the two sources is expected as the work by Irie et al. [14] is based on the first-order shear deformation theory of plates. It is further noticed is that there are some blank cells in columns B of Table 1. The present formulation is capable of providing the results of both the bending and in-plane stretching modes, whereas the results based on the Mindlin plate theory yields frequencies for the flexural vibration only. Irie et al. did not publish results with a thickness ratio (h/a) of 0.4 and higher for the annular plate with $b/a=0.3$. Because of this, the last column of the second half of Table 1 is blank.

Table 2 is included in this study to illustrate how the Ritz method fairs with the standard finite element method. Again a disk of variable thickness clamped at the inside edge and free at the outside is considered. The variables for which the frequency calculation corresponding to the first five axisymmetric $(n=0)$ modes of vibration was carried out, are given as follows:

$$b/a=0.3,0.4 \quad \text{and} \quad 0.5; \qquad h_2/a=1.0,\ 0.50 \text{ and } 0.05; \quad \text{and} \quad h_1/a=1.0. \tag{18}$$

Table 1 Natural frequency parameter Ω for a thick annular plate clamped at the inner edge and free at the outer. *S*=Wave number in the radial direction. A–present analysis and B–Irie et al. [14].

		$b/a=0.2$							
		$h/a=0.1$		$h/a=0.2$		$h/a=0.3$		$h/a=0.4$	
n	S	A	B	A	B	A	B	A	B
	1	0.1547	0.1537	0.2941	0.2911	0.4095	0.4031	0.5003	0.4902
0	2	0.8961	0.8867	1.4628	1.4380	1.7676	1.7267	1.9376	1.8860
	3	2.3904	⋯	2.3156	⋯	2.3146	⋯	2.3115	⋯
	1	0.1408	0.1395	0.2574	0.2536	0.3478	0.3414	0.4186	0.4091
1	2	0.9530	0.9440	0.9655	⋯	0.9660	⋯	0.9665	⋯
	3	0.9650	⋯	1.5680	1.5445	1.9256	1.8883	2.1372	2.0880
	1	0.1873	0.1861	0.3498	0.3480	0.4911	0.4884	0.6134	0.6101
2	2	1.1507	1.1427	1.6179	⋯	1.6184	⋯	1.6189	⋯
	3	1.6174	⋯	1.9172	1.8956	2.3850	2.3468	2.6614	2.6085
		$b/a=0.3$							
		$h/a=0.1$		$h/a=0.2$		$h/a=0.3$		$h/a=0.4$	
n	S	A	B	A	B	A	B	A	B
	1	0.1987	0.1973	0.3756	0.3716	0.5200	0.5120	0.6321	⋯
0	2	1.1591	1.1466	1.8348	1.8012	2.1657	2.1125	2.3327	⋯
	3	2.5278	⋯	2.5297	⋯	2.5298	⋯	2.5275	⋯
	1	0.1927	0.1910	0.3553	0.3504	0.4815	0.4730	0.5778	⋯
1	2	1.2090	1.1965	1.1399	⋯	1.1402	⋯	1.1405	⋯
	3	1.2330	⋯	1.9212	1.8883	2.2882	2.2360	2.4806	⋯
	1	0.2300	0.2285	0.4208	0.4170	0.5765	0.5701	0.7064	⋯
2	2	1.3686	1.3566	1.8093	⋯	1.8102	⋯	1.1811	⋯
	3	1.8084	⋯	2.1916	2.1595	2.6436	2.5919	2.8710	⋯

The boundary condition at the inside edge is given by $u=v=0$. The Ritz solution used 8 terms in the series in each of ξ and η directions. This order of the polynomial translates into working with 128×128 matrices. An eight-node quadrilateral solid of revolution element is used in the finite element analysis. The finite element mesh consists of 10 elements in the *r*-direction and 8 in the *z*-direction. The 80-element model consists of 277 nodes, each node having two degrees-of-freedom. Hence, there is a total of 554 known (through the given boundary conditions) and unknown degrees-of-freedom. The results from the two methods are found to be in very good agreement. The Ritz method consistently yields lower values for the natural frequency than the finite element method and hence is more accurate.

A solid circular disk of variable thickness is further analyzed here. The dimensionless parameters taken for this case are $b/a=0.0$, $h_1/a=0.5$ and h_2/a is varied from 0.05 to 0.50. The variation of the frequency parameter Ω versus the thickness ratio h_2/a is presented in Fig. 6 for the tapered disk clamped at the inside and free at the outside. The value of $h_2/a=0.05$ represents a disk almost shaped like a wedge, i.e., thick at the inside edge where it is clamped and nearly a sharp point at $r=a$. The first five modes for each of the axisymmetric (line with "o" for $n=0$) and asymmetric (line with "x" for $n=1$) cases are presented in this figure. Frequency distribution shows no distinct pattern. Both the flexural/thickness-shear and in-plane stretching modes are present here.

Case 2. Analysis of Conical/Cylindrical Shells. The second solid of revolution investigated herein is described by Fig. 3, in which a frustum of a cone of variable thickness is shown. The

Table 2 Comparison of the frequencies obtained from the Ritz and finite element method (FEM) for the axisymmetric circular disk of varying thickness, clamped at the inside edge

	$h_2/a=1.0$		$h_2/a=0.5$		$h_2/a=0.05$	
Mode	Present	FEM	Present	FEM	Present	FEM
			$b/a=0.3$			
1	0.9115	0.9126	0.8733	0.8759	1.0708	1.1723
2	2.4273	2.4282	2.3143	2.3422	2.1581	2.4031
3	2.5337	2.5338	2.7258	2.7288	3.2760	3.2815
4	3.1673	3.1679	4.1896	4.1914	4.5165	4.6448
5	3.7296	3.7298	4.5865	4.5954	5.5833	5.5953
			$b/a=0.4$			
1	1.1452	1.1465	1.0808	1.0843	1.2971	1.4256
2	2.7059	2.7071	2.7412	2.7418	2.5757	2.8275
3	2.9242	2.9243	3.0531	3.0569	3.6438	3.6517
4	3.3640	3.3645	4.2172	4.2189	3.3591	5.4806
5	3.9186	3.9190	5.0815	5.0935	5.9965	6.0082
			$b/a=0.5$			
1	1.4705	1.4720	1.3744	1.3791	1.5970	1.7608
2	3.0510	3.0523	3.2454	3.2454	3.1046	3.3617
3	3.4566	3.4571	3.4805	3.4850	4.1521	4.1600
4	3.7373	3.7375	4.3262	4.3285	6.4578	6.4662
5	4.2491	4.2495	5.7099	5.7171	6.5154	6.5295

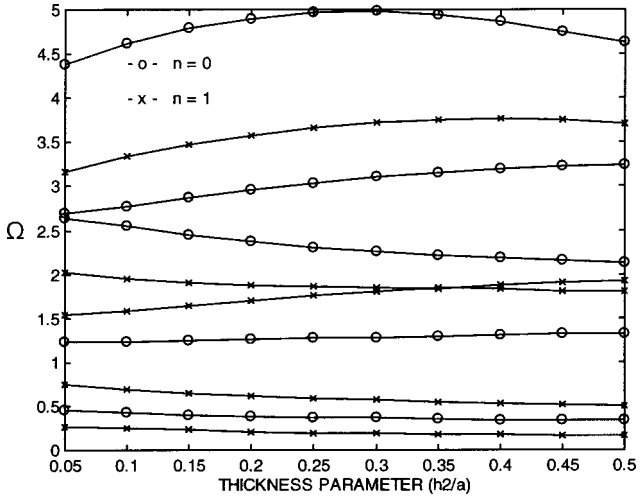

Fig. 6 Frequency Ω versus thickness ratio h_2/a for a clamped-free tapered disk. Parameters used are $b/a=0.0$, $h_1/a=0.50$ and $\nu=0.30$.

Table 3 Comparison of the frequencies obtained from the present analysis and Leissa and So [8]. Cylindrical solid clamped at the bottom. A–present analysis, B–Leissa and So [8].

	$L/a=2.0$							
	$n=0$		$n=1$		$n=2$		$n=3$	
Mode	A	B	A	B	A	B	A	B
1	0.7980	0.7975	0.3140	0.3138	1.3410	1.3408	2.0234	2.0205
2	1.8365	1.8357	0.8958	0.8955	1.5628	1.5616	2.2961	2.2934
3	1.9660	1.9653	1.6069	1.6050	2.1424	2.1400	2.6657	2.6600
4	2.5951	2.5936	1.7702	1.7700	2.3352	2.3320	2.8923	2.8844
5	2.6719	2.6650	2.0770	2.0751	2.7103	2.6960	3.3396	3.3180

Table 4 Comparison of the frequencies obtained from the present analysis and Singh and Mirza [15]. Thick spherical shell clamped at the open edge ϕ=60 deg. A–present analysis, B–Singh and Mirza [15].

	$h/R=0.05$							
	$n=1$		$n=2$		$n=3$		$n=4$	
Mode	A	B	A	B	A	B	A	B
1	0.9007	0.8990	1.0916	1.0790	1.2264	1.2140	1.3998	1.3931
2	1.2071	1.2092	1.4750	1.4756	1.7741	1.7657	2.2122	2.1028
3	1.7884	1.7596	2.2329	2.1842	2.7676	2.6141	3.3418	3.0760
4	2.2592	2.2397	3.2212	3.0864	4.1377	3.6792	5.0005	4.2431
5	3.0291	2.7194	3.8304	3.3194	4.5975	4.1620	5.5276	5.0022

generator of the middle surface of the shell is shown by a chain line joining nodes 6 and 8. The cylindrical shell can also be described by this geometry, if the chain line is made parallel to the z-axis. To calculate the natural frequencies we define the following geometric parameters.

$$a=r_6, \quad b=r_8, \quad L=z_8-z_6, \quad h_1=\text{length of side 2-6-3,}$$
$$\text{and} \quad h_2=\text{length of side 1-8-4.} \tag{19}$$

From the given numerical values of a, b, L, h_1, h_2, cone angle (α), etc., the coordinates of the eight-nodal point defining the shell geometry can be easily obtained and used in the computer program.

Leissa and So [7,8] published accurate data for the first 20 frequencies of completely free-elastic cylinders. Also included in their study is a table containing the frequencies of a clamped-free solid circular cylinder having the following parameters:

$$b/a=1.0; \quad h_1/a=h_2/a=1.0; \quad L/a=2.0 \quad \text{and} \quad \alpha=0. \tag{20}$$

The numerical results for the shell with parameters given in Eq. (20) is pertinent to the present investigation. To compare the results, therefore, a cylindrical solid clamped at the bottom (i.e., along the edge 2-6-3) is analyzed using the present method by taking 8 terms along ξ and 4 along η directions. Table 3 shows a very good comparison of the results from the two sources. It is to be noted here that the excellent agreement here is not due to a mere chance. The analysis by Leissa and So is also based on the Ritz method similar to the present work.

The variation of the frequency parameter Ω versus the thickness parameter h/a is examined for a uniform conical shell free (at the inner edge 1-8-4) and clamped at the other edge 2-6-3. Parameters used for this case are given by cone angle $\alpha=30$ deg, $L/a=1.0$, and $0.05\leqslant h/a\leqslant 0.50$. This range of thickness ratio covers both thin and thick shells. Figure 7 shows the plot of the frequencies, both axisymmetric ($n=0$) and asymmetric ($n=1$), versus h/a. As can be expected, the frequency Ω generally increases with the thickness.

Case 3. Analysis of Spherical Shells. An attempt is also made in this present work to analyze a thick spherical shell for which very limited amount of result is available in the literature. First, a case is run to compare results with those from an earlier publication by Singh and Mirza [15] which is based on the Reissner-Naghdi theory of thin shells. The shell parameter taken for this purpose are $\phi_1=0$ deg, $\phi_2=60$ deg, $h/a=0.05$, and $\nu=0.3$. The shell is clamped at the open edge 2-6-3. This boundary condition is simulated by substituting $u=v=w=0$. Numerical results for the dimensionless frequency parameter $\Omega=\omega a\sqrt{(\rho/E)}$ is presented in Table 4 for asymmetric modes of vibration corresponding to $n=1$ through 4. Frequencies in the first two rows compare reasonably well. But the agreement is not very good as the mode number and/or circumferencial wave number n increase. The main reason for the difference can be attributed to the two different theories that are used to obtain the results. The Reissner-Naghdi theory of shell is valid only for thin to moderately thick shells. Using the present formulation, some additional results are calculated with $n=0$ (axisymmetric mode of vibration) and $n=1$ (asymmetric mode of vibration) and pre-

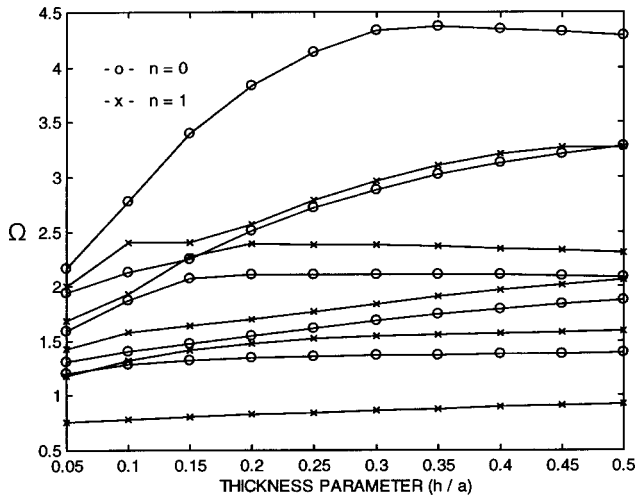

Fig. 7 Frequency Ω versus thickness ratio h/a for a conical shell free at the top opening and clamped at the bottom. Parameters used are cone angle α=30 deg, L/a=1.0 and ν=0.30.

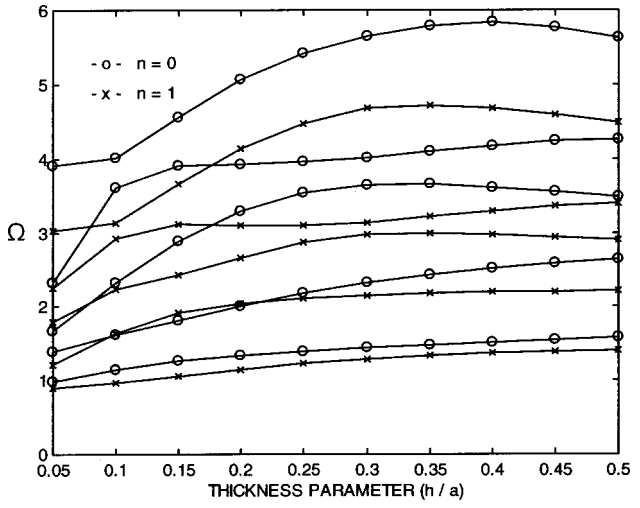

Fig. 8 Frequency Ω versus thickness ratio h/a for a spherical shell clamped at the open end. Parameters used are ϕ_1 =0 deg, ϕ_2=60 deg, and ν=0.30.

sented in Fig. 8 showing the variation of Ω against the thickness to radius ratio h/a. A uniform thickness spherical shell clamped at $\phi_2 = 60$ deg is considered for the results. Generally, the frequency parameter increases with the thickness for all cases shown in this figure.

Concluding Remarks

In this paper a numerical method to examine the free axially symmetric and antisymmetric vibrations of solids of revolution is presented. The numerical method is based on the Ritz method and utilizes a mapping technique from the formulation of quadrilateral finite elements. By using the natural coordinates, it is possible to define the cross section of the solid of revolution in terms of four curved boundaries. The energy expressions are derived by selecting displacement fields made of simple algebraic polynomials in ξ and η. It is well known that individually the Ritz and finite element methods are well established in this area. However, the combination of the two in the present context does bring in considerable novelty. The unified approach presented herein is capable of solving various types of free vibration problems involving solids of revolution. Cases dealing with a thick circular disk of uniform as well as varying thickness, thick conical, cylindrical, and spherical solids of revolution are investigated as numerical examples. Very good comparison of results from the present method and other published sources is also established. Using the case of axially symmetric thick circular disks of variable thickness, it is shown that the present method and the finite element method yield basically the same results. However, the order of the matrix solved for the frequencies and mode shapes is 128 and 554, respectively. The Ritz method, generally, gives lower and more accurate values of the natural frequencies than those obtained by the finite element method.

When the values of the natural frequencies are plotted against the thickness parameter of the disk, no distinct pattern is found. This, possibly, can be attributed to two very distinct types of modal behaviors, namely bending and stretching. The low frequency vibrational modes are predominantly the bending type. However, there are some in between modes of vibration which are completely of the stretching (or breathing) type. The formulation presented in this paper is very general, consistent, and truly numerical.

References

[1] McMahon, G. W., 1964, ''Experimental Study of the Vibrations of Solid Isotropic Cylinders,'' J. Acoust. Soc. Am., **36**, pp. 85–92.

[2] Mirsky, I., 1964, ''Vibrations of Orthotropic, Thick Cylindrical Shells,'' J. Acoust. Soc. Am., **36**(01), pp. 41–51.

[3] Hutchinson, J. R., 1972, ''Axisymmetric Vibrations of a Free Finite Length Rod,'' J. Acoust. Soc. Am., **51**, pp. 233–240.

[4] Hutchinson, J. R., 1980, ''Vibrations of Solid Cylinders,'' ASME J. Appl. Mech., **47**, pp. 901–907.

[5] Hutchinson, J. R., 1984, ''Vibrations of Thick Free Circular Plates, Exact Versus Approximate Solutions,'' ASME J. Appl. Mech., **51**, pp. 581–585.

[6] Soldatos, K. P., 1994, ''Review of Three Dimensional Dynamic Analyses of Circular Cylinders and Cylindrical Shells,'' Appl. Mech. Rev., **47**, pp. 501–516.

[7] Leissa, A. W., and So, J., 1995, ''Comparison of Vibration Frequencies for Rods and Beams From One Dimensional and Three Dimensional Analyses,'' J. Acoust. Soc. Am., **98**, pp. 2122–2134.

[8] Leissa, A. W., and So, J., 1995, ''Accurate Vibration Frequencies of Circular Cylinders From Three Dimensional Analysis,'' J. Acoust. Soc. Am., **98**, pp. 2316–2141.

[9] Young, P. G., and Dickinson, S. M., 1994, ''Free Vibration of a Class of Solids With Cavities,'' Int. J. Mech. Sci., **36**(12), pp. 1099–1107.

[10] Young, P. G., and Dickinson, S. M., 1995, ''Free Vibration of a Class of Homogeneous Isotropic Solids,'' ASME J. Appl. Mech., **62**, pp. 706–708.

[11] Singh, B., and Saxena, V., 1995, ''Axisymmetric Vibration of a Circular Plate With Double Linear Thickness,'' J. Sound Vib., **179**, pp. 879–889.

[12] So, J., and Leissa, A. W., 1998, ''Three Dimensional Vibrations of Thick Circular and Annular Plates,'' J. Sound Vib., **209**(1), pp. 15–41.

[13] Kalnins, A., 1964, ''Effect of Bending on Vibrations of Spherical Shells,'' J. Acoust. Soc. Am., **36**(01), pp. 74–81.

[14] Irie, T., Yamada, G., and Takagi, K., 1982, ''Natural Frequencies of Thick Annular Plate,'' ASME J. Appl. Mech., **49**, pp. 633–638.

[15] Singh, A. V., and Mirza, S., 1985, ''Asymmetric Modes and Associated Eigenvalues for Spherical Shells,'' ASME J. Pressure Vessel Technol., **107**, pp. 77–82.

Journal of Applied Mechanics

Brief Notes

A Brief Note is a short paper that presents a specific solution of technical interest in mechanics but which does not necessarily contain new general methods or results. A Brief Note should not exceed 2500 words *or equivalent* (a typical one-column figure or table is equivalent to 250 words; a one line equation to 30 words). Brief Notes will be subject to the usual review procedures prior to publication. After approval such Notes will be published as soon as possible. The Notes should be submitted to the Editor of the JOURNAL OF APPLIED MECHANICS. Discussions on the Brief Notes should be addressed to the Editorial Department, ASME International, Three Park Avenue, New York, NY 10016-5990, or to the Editor of the JOURNAL OF APPLIED MECHANICS. Discussions on Brief Notes appearing in this issue will be accepted until two months after publication. Readers who need more time to prepare a Discussion should request an extension of the deadline from the Editorial Department.

Rocking Vibration of Rotating Disk and Spindle Systems With Asymmetric Bearings

J. S. Park
Graduate Student

I. Y. Shen
Professor

Department of Mechanical Engineering,
University of Washington, Seattle, WA 98195-2600

C.-P. R. Ku
R&D Director, Western Digital Corporation,
San Jose, CA 95138

This note presents how bearing asymmetry affects natural frequencies and mode shapes of a rotating disk/spindle system through a perturbation analysis. The analysis will focus on rocking motion of the disk/spindle system that consists of rigid-body rocking of the spindle, one-nodal-diameter modes of each disk, and deformation of spindle bearings. [DOI: 10.1115/1.1544537]

Consider a rotating disk/spindle system consisting of N identical elastic circular disks, a rigid spindle hub, a rigid housing (or stator), and a pair of ball bearings. The rotational speed is ω_3. According to [1], the motion of the rotating disk pack can be described by

$$\mathbf{q}_r=(\theta_x,\theta_y,R_x,R_y,q_{01}^{(1)},q_{0,-1}^{(1)},q_{01}^{(2)},q_{0,-1}^{(2)},\ldots,q_{01}^{(N)},q_{0,-1}^{(N)})^T \tag{1}$$

where $R_x(t)$ and $R_y(t)$ are translation of the disk pack centroid in the disk plane, $\theta_x(t)$ and $\theta_y(t)$ are the rocking of the disk pack, $q_{01}^{(i)}(t)$ and $q_{0,-1}^{(i)}(t)$ are generalized coordinates associated with the one-nodal-diameter cosine and sine modes of the ith disk. With these generalized coordinates, equation of motion of the spindle system will take the form of

$$\mathbf{M}_r\ddot{\mathbf{q}}_r+\mathbf{G}_r\dot{\mathbf{q}}_r+[\mathbf{K}_r^{(0)}+\epsilon\mathbf{K}_r^{(1)}]\mathbf{q}_r=\mathbf{0} \tag{2}$$

where $\mathbf{K}_r^{(0)}$ is the stiffness matrix of the unperturbed system (i.e., axisymmetric bearings) and $\epsilon\mathbf{K}_r^{(1)}$ is the stiffness matrix resulting from bearing asymmetry. The physics of the rocking motion governed by (2) depends on the spin speed. At low spin speed, the gyroscopic effect and bearing asymmetry are equally important. At high spin speed, the gyroscopic effect becomes dominant. For perturbation analysis, these two cases need to be considered separately.

For the low-speed perturbation approach, the unperturbed system is the *stationary* disk/spindle system with symmetric bearings. The perturbation is the bearing asymmetry. Also note that the unperturbed system has repeated natural frequencies for rocking motion. To formulate the eigenvalue problem, assume that $\mathbf{q}_r(t)=\mathbf{v}e^{j\mu t}$, where μ and $\mathbf{v}$ are the natural frequencies and mode shapes of the perturbed system. Then (2) becomes

$$[\mathbf{K}_r^{(0)}-\mu^2\mathbf{M}_r]\mathbf{v}=-[j\mu\mathbf{G}_r+\epsilon\mathbf{K}_r^{(1)}]\mathbf{v}. \tag{3}$$

Note that $[j\mu\mathbf{G}_r+\epsilon\mathbf{K}_r^{(1)}]$ is a Hermitian matrix; therefore, μ will be real but $\mathbf{v}$ could be complex. The solution of (3) is

$$\mathbf{v}=-\mathbf{H}(\mu)[j\mu\mathbf{G}_r+\epsilon\mathbf{K}_r^{(1)}]\mathbf{v} \tag{4}$$

where $\mathbf{H}(\mu)$ is the frequency response function of the unperturbed system. Moreover,

$$\mathbf{H}(\mu)=\sum_{k=1}^{2N+4}\frac{\mathbf{u}_k\overline{\mathbf{u}}_k^T}{\omega_k^2-\mu^2} \tag{5}$$

where ω_k and $\mathbf{u}_k$ are natural frequencies and mode shapes of the unperturbed system. Also in (5), the overbar denotes the complex conjugation, and the mode shapes satisfy the orthonormality conditions

$$\overline{\mathbf{u}}_i^T\mathbf{M}_r\mathbf{u}_j=\delta_{ij},\quad \overline{\mathbf{u}}_i^T\mathbf{K}_r^{(0)}\mathbf{u}_j=\delta_{ij}\omega_i^2 \tag{6}$$

where δ_{ij} is the Kronecker delta. To facilitate a perturbation solution through contraction mapping, substitution of (5) into (4) results in

$$\mathbf{v}=\sum_{k=1}^{2N+4}\left\{\frac{\overline{\mathbf{u}}_k^T[j\mu\mathbf{G}_r+\epsilon\mathbf{K}_r^{(1)}]\mathbf{v}}{\mu^2-\omega_k^2}\right\}\mathbf{u}_k. \tag{7}$$

Note that $\mathbf{G}_r$ and $\epsilon\mathbf{K}_r^{(1)}$ are both small quantities in (7). Therefore, (7) takes the standard form of contraction mappings. Consecutive iterations of (7) result in a perturbation solution.

Let $\mathbf{u}_1$ and $\mathbf{u}_2$ be two orthonormal rocking modes of the unperturbed system. In addition, they have repeated natural frequency

Contributed by the Applied Mechanics Division of THE AMERICAN SOCIETY OF MECHANICAL ENGINEERS for publication in the ASME JOURNAL OF APPLIED MECHANICS. Manuscript received by the ASME Applied Mechanics Division, Feb. 1, 2001; final revision, Sept. 27, 2002. Associate Editor: A. A. Ferri.

$\omega_1=\omega_2$, because the unperturbed system is axisymmetric and stationary. To obtain μ_1 and $\mathbf{v}_1$, one can normalize (7) so that the coefficient of $\mathbf{u}_1$ is one, i.e.,

$$\mu_1^2=\omega_1^2+\overline{\mathbf{u}}_1^T[j\mu_1\mathbf{G}_r+\epsilon\mathbf{K}_r^{(1)}]\mathbf{v}_1. \tag{8}$$

Then (7) becomes

$$\mathbf{v}_1=\mathbf{u}_1+\sum_{k=2}^{2N+4}\left\{\frac{\overline{\mathbf{u}}_k^T[j\mu_1\mathbf{G}_r+\epsilon\mathbf{K}_r^{(1)}]\mathbf{v}_1}{\mu_1^2-\omega_k^2}\right\}\mathbf{u}_k. \tag{9}$$

To perform the contraction mapping, replacing μ_1 and $\mathbf{v}_1$ of the right side of (8) by ω_1 and $\mathbf{u}_1$ results in

$$\mu_1^2\approx\omega_1^2+\overline{\mathbf{u}}_1^T[j\omega_1\mathbf{G}_r+\epsilon\mathbf{K}_r^{(1)}]\mathbf{u}_1. \tag{10}$$

In replacing μ_1 and $\mathbf{v}_1$ of the right side of (9) by ω_1 and $\mathbf{u}_1$ to obtain the mode shape $\mathbf{v}_1$, one finds that the denominator of $\mathbf{u}_2$ in (9) is vanishing because $\omega_1=\omega_2$. To maintain the contraction mapping, $\mathbf{u}_1$ and $\mathbf{u}_2$ cannot be chosen arbitrarily. Instead, they have to satisfy

$$\overline{\mathbf{u}}_2^T[j\omega_1\mathbf{G}_r+\epsilon\mathbf{K}_r^{(1)}]\mathbf{u}_1=0. \tag{11}$$

In this case, the perturbed mode shape is

$$\mathbf{v}_1\approx\mathbf{u}_1+\sum_{k=3}^{2N+4}\left\{\frac{\overline{\mathbf{u}}_k^T[j\omega_1\mathbf{G}_r+\epsilon\mathbf{K}_r^{(1)}]\mathbf{u}_1}{\omega_1^2-\omega_k^2}\right\}\mathbf{u}_k. \tag{12}$$

Similarly, μ_2 and $\mathbf{v}_2$ can be derived as

$$\mu_2^2\approx\omega_2^2+\overline{\mathbf{u}}_2^T[j\omega_2\mathbf{G}_r+\epsilon\mathbf{K}_r^{(1)}]\mathbf{u}_2 \tag{13}$$

$$\mathbf{v}_2\approx\mathbf{u}_2+\sum_{k=3}^{2N+4}\left\{\frac{\overline{\mathbf{u}}_k^T[j\omega_2\mathbf{G}_r+\epsilon\mathbf{K}_r^{(1)}]\mathbf{u}_2}{\omega_2^2-\omega_k^2}\right\}\mathbf{u}_k \tag{14}$$

with $\mathbf{u}_1$ and $\mathbf{u}_2$ satisfy

$$\overline{\mathbf{u}}_1^T[j\omega_2\mathbf{G}_r+\epsilon\mathbf{K}_r^{(1)}]\mathbf{u}_2=0. \tag{15}$$

To determine $\mathbf{u}_1$ and $\mathbf{u}_2$ satisfying (11) and (15), let's consider two simplest repeated rocking mode shapes

$$\mathbf{w}_1=A_1(\theta_x^{(1)},0,0,R_y^{(1)},0,1,0,1,\ldots,0,1)^T \tag{16}$$

and

$$\mathbf{w}_2=A_2(0,\theta_y^{(2)},R_x^{(2)},0,1,0,1,0,\ldots,1,0)^T \tag{17}$$

where $\theta_x^{(1)}=-\theta_y^{(2)}$, $R_y^{(1)}=R_x^{(2)}$, and A_1 and A_2 are normalization constants satisfying (6). Note that, however,

$$\overline{\mathbf{w}}_2^T[j\omega_1\mathbf{G}_r+\epsilon\mathbf{K}_r^{(1)}]\mathbf{w}_1\neq 0. \tag{18}$$

Therefore, the mode shapes $\mathbf{u}_1$ and $\mathbf{u}_2$ in (10) and (13) must be linear combinations of $\mathbf{w}_1$ and $\mathbf{w}_2$, i.e.,

$$[\mathbf{u}_1,\mathbf{u}_2]=[\mathbf{w}_1,\mathbf{w}_2]\mathbf{T} \tag{19}$$

where $\mathbf{T}$ is an orthogonal matrix satisfying

$$\mathbf{T}^T\mathbf{T}=\mathbf{I} \tag{20}$$

because $\mathbf{u}_1$ and $\mathbf{u}_2$ are orthonormal with respect to $\mathbf{M}_r$. To determine $\mathbf{T}$, consider the following matrix:

$$\mathbf{A}_r\equiv[\overline{\mathbf{u}}_1,\overline{\mathbf{u}}_2]^T[j\omega_1\mathbf{G}_r+\epsilon\mathbf{K}_r^{(1)}][\mathbf{u}_1,\mathbf{u}_2]. \tag{21}$$

According to (10), (11), (13), and (15), the matrix $\mathbf{A}_r$ in (21) must be a diagonal matrix. In addition, the diagonal elements of $\mathbf{A}_r$ are the perturbation to ω_1^2 and ω_2^2. Substitute (19) into (21) and recall (20) to obtain

$$\mathbf{A}_r=\mathbf{T}^{-1}\mathbf{B}_r\mathbf{T} \tag{22}$$

where

$$\mathbf{B}_r\equiv[\overline{\mathbf{w}}_1,\overline{\mathbf{w}}_2]^T[j\omega_1\mathbf{G}_r+\epsilon\mathbf{K}_r^{(1)}][\mathbf{w}_1,\mathbf{w}_2]. \tag{23}$$

Since $\mathbf{A}_r$ is diagonal, $\mathbf{T}$ is the modal matrix of $\mathbf{B}_r$ and the perturbed terms in (10) and (13) are the eigenvalues of $\mathbf{B}_r$.

For the high-speed perturbation approach, the unperturbed system is the *rotating* disk/spindle system with symmetric bearings. To reduce the size of equations of motion, one can define the following complex representations: $\theta\equiv\theta_x+j\theta_y$, $R\equiv R_x+jR_y$, and $Q_{01}^{(i)}\equiv q_{0,-1}^{(i)}-jq_{01}^{(i)}$. Under this complex formulation, the equation of motion becomes

$$\mathbf{M}\ddot{\mathbf{q}}+\mathbf{G}\dot{\mathbf{q}}+\mathbf{K}\mathbf{q}+\epsilon\mathbf{K}_1\overline{\mathbf{q}}=\mathbf{0} \tag{24}$$

where the overbar denotes complex conjugation, and $\mathbf{q}=(\theta,R,Q_{01}^{(1)},Q_{01}^{(2)},\ldots,Q_{01}^{(N)})^T$. Moreover, let $\mathbf{p}$ be an eigenvector associated with (24). Since the eigenvalue problem of (24) is not self-adjoint, the adjoint system will have a different eigenvector $\mathbf{h}$. Explicit expression of $\mathbf{p}$ and $\mathbf{h}$ can be found in [2].

Now consider the unperturbed system subjected to sinusoidal excitations governed by

$$\mathbf{M}\ddot{\mathbf{q}}(t)+\mathbf{G}\dot{\mathbf{q}}(t)+\mathbf{K}\mathbf{q}(t)=\mathbf{f}e^{j\Omega t} \tag{25}$$

where $\mathbf{f}$ is the excitation vector and Ω is the excitation frequency. The complex response $\mathbf{q}(t)$ is

$$\mathbf{q}(t)=\mathbf{H}(j\Omega)\mathbf{f}e^{j\Omega t} \tag{26}$$

where $\mathbf{H}(j\Omega)$ is the transfer function of the unperturbed system. When the excitation frequency Ω coincides with a natural frequency of the rocking modes, the system may or may not have a finite response depending on $\mathbf{f}$. According to Fredholm alternative theorem, the solvability condition is $\mathbf{h}^T\mathbf{f}=0$. Moreover, the solvability condition implies that secular terms are eliminated and periodic solutions are maintained in perturbation analysis.

Now we can apply Lindsted-Poncaré approach to find natural frequency of the perturbed system. First, let's define a new time scale $\tau=\omega t$, where ω is the natural frequency of the perturbed system. Therefore,

$$\omega=\omega(\epsilon)=\omega_0+\epsilon\omega_1+\epsilon^2\omega_2+\ldots \tag{27}$$

where ω_0 is the natural frequency of the unperturbed system, and ω_1 and ω_2 are the first and second-order perturbation. The corresponding perturbed response is

$$\mathbf{q}(\tau)=\mathbf{q}_0(\tau)+\epsilon\mathbf{q}_1(\tau)+\epsilon^2\mathbf{q}_2(\tau)+\ldots. \tag{28}$$

Substitution of (27) and (28) into (24) results in

$$\left(\omega_0^2\mathbf{M}\frac{d^2}{d\tau^2}+\omega_0\mathbf{G}\frac{d}{d\tau}+\mathbf{K}\right)\mathbf{q}_0(\tau)=0 \tag{29}$$

for ϵ^0 terms,

$$\left(\omega_0^2\mathbf{M}\frac{d^2}{d\tau^2}+\omega_0\mathbf{G}\frac{d}{d\tau}+\mathbf{K}\right)\mathbf{q}_1(\tau)=-\left(2\omega_0\omega_1\mathbf{M}\frac{d^2}{d\tau^2}+\omega_1\mathbf{G}\frac{d}{d\tau}\right)\mathbf{q}_0(\tau)-\mathbf{K}_1\overline{\mathbf{q}}_0(\tau) \tag{30}$$

for ϵ^1 terms, and

$$\left(\omega_0^2\mathbf{M}\frac{d^2}{d\tau^2}+\omega_0\mathbf{G}\frac{d}{d\tau}+\mathbf{K}\right)\mathbf{q}_2(\tau)=-\left[(\omega_1^2+2\omega_0\omega_2)\mathbf{M}\frac{d^2}{d\tau^2}+\omega_2\mathbf{G}\frac{d}{d\tau}\right]\mathbf{q}_0(\tau)-\left(2\omega_0\omega_1\mathbf{M}\frac{d^2}{d\tau^2}+\omega_1\mathbf{G}\frac{d}{d\tau}\right)\mathbf{q}_1(\tau)-\mathbf{K}_1\overline{\mathbf{q}}_1(\tau) \tag{31}$$

for ϵ^2 terms.

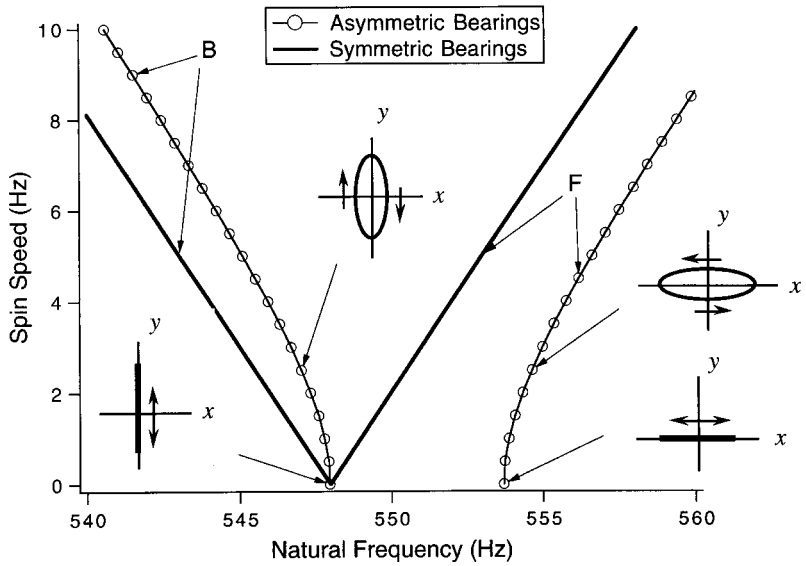

Fig. 1 Eigenvalue with respect to ω_3 from 0 to 10 Hz

The nontrivial solution from (29) is $\mathbf{q}_0(\tau)=\mathbf{p}e^{j\tau}$. Therefore, (30) results in

$$\left(\omega_0^2\mathbf{M}\frac{d^2}{d\tau^2}+\omega_0\mathbf{G}\frac{d}{d\tau}+\mathbf{K}\right)\mathbf{q}_1(\tau) = \omega_1(2\omega_0\mathbf{M}-j\mathbf{G})\mathbf{p}e^{j\tau}-\mathbf{K}_1\overline{\mathbf{p}}e^{-j\tau}. \quad (32)$$

Note that the term with $e^{j\tau}$ in (32) is the secular term. To eliminate the secular term, $\omega_1=0$. According to (26), the solution of (32) is $\mathbf{q}_1(\tau)=-\mathbf{u}_1e^{-j\tau}$, where $\mathbf{u}_1\equiv\mathbf{H}(-j\omega_0)\mathbf{K}_1\overline{\mathbf{p}}$. Finally, (31) becomes

$$\left(\omega_0^2\mathbf{M}\frac{d^2}{d\tau^2}+\omega_0\mathbf{G}\frac{d}{d\tau}+\mathbf{K}\right)\mathbf{q}_2(\tau) = [\omega_2(2\omega_0\mathbf{M}-j\mathbf{G})\mathbf{p}+\mathbf{K}_1\overline{\mathbf{u}}_1]e^{j\tau}. \quad (33)$$

Note that the terms with $e^{j\tau}$ in (33) are secular terms. To eliminate these secular term, the solvability condition requires that

$$\omega_2=-\frac{\mathbf{h}^T\mathbf{K}_1\overline{\mathbf{u}}_1}{\mathbf{h}^T(2\omega_0\mathbf{M}-j\mathbf{G})\mathbf{u}_0}. \quad (34)$$

As a numerical example, consider the axisymmetric spindle system used in [1]. (The major dimensions and properties can be found in [1].) The two bearings are identical and symmetric. Now consider the case with both bearings being 10 percent stiffer in one direction than the other Exact solutions can be found by solving eigenvalue problem of (2) numerically. Figures 1 and 2 plot the natural frequencies and mode shapes, when the spin speed is from 0 to 10 Hz, and above 10 Hz, respectively. When the disk/spindle system is stationary, the bearing asymmetry splits a pair of repeated rocking modes into two modes with distinct frequencies. When the rotational speed increases from zero, the low-frequency rocking mode evolves into backward precession and the high-frequency rocking mode evolves into forward precession. The precession orbits are elliptical. Figure 3 shows the low-speed perturbation. When the rotational speed varies from 0 Hz to 10 Hz, the

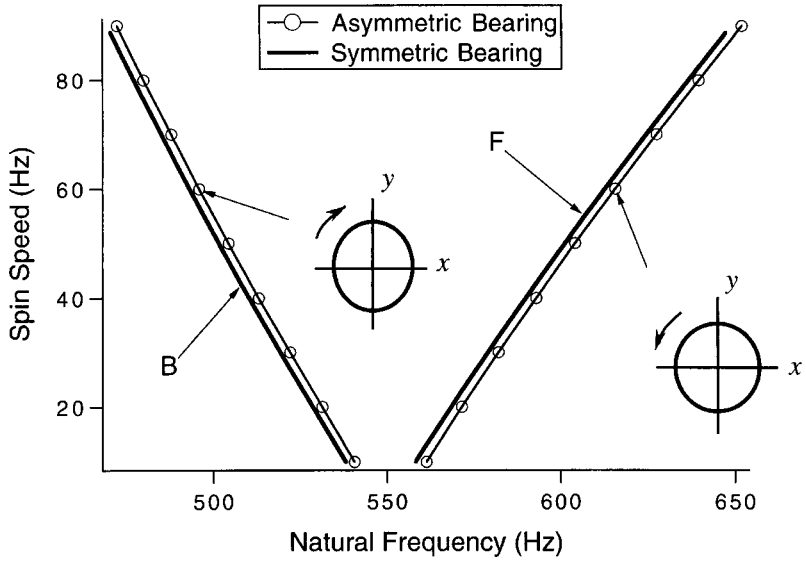

Fig. 2 Frequency split for spindles with and without bearing asymmetry from 10 to 90 Hz

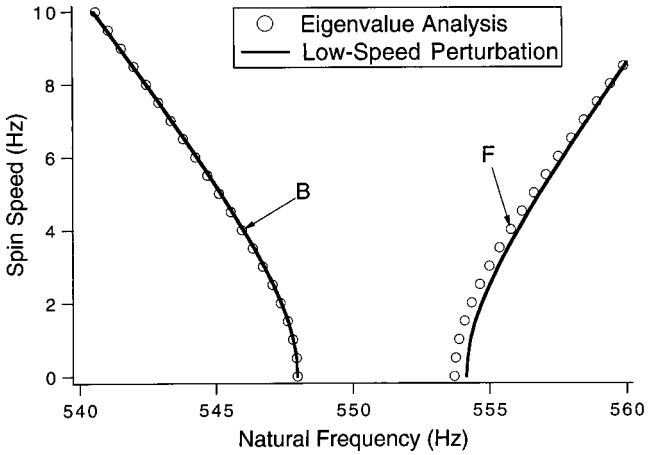

Fig. 3 Natural frequencies obtained from numerical simulation and low-speed perturbation, when the rotational speed varies from 0 to 10 Hz

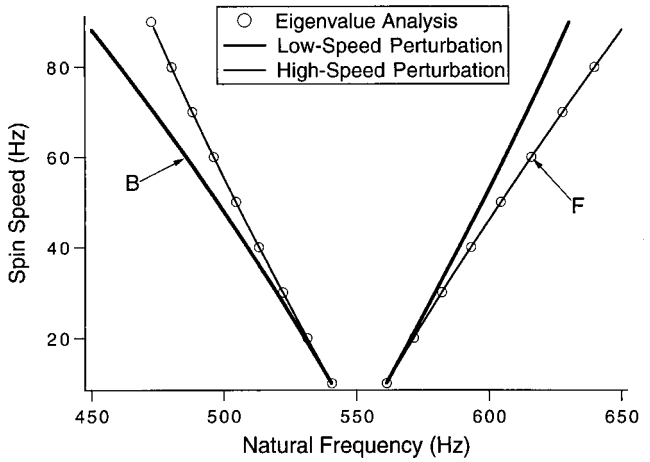

Fig. 4 Natural frequencies obtained from numerical simulation, low-speed perturbation, and high-speed perturbation, when the rotational speed exceeds 10 Hz

low-speed perturbation approximates the exact results very well including the veering of the frequency splitting. When the rotational speed exceeds 30 Hz (see Fig. 4), the low-speed perturbation (the thick solid lines in Fig. 4) loses its accuracy and deviates from the exact solution (the markers in Fig. 4). Figure 4 also compares the frequencies predicted from high-speed perturbation (thin solid lines) and the exact frequencies (markers), when the spin speed varies from 10 Hz to 90 Hz. The high-speed perturbation approximates the exact results from the numerical simulation very well as opposed to the low-speed perturbation.

Acknowledgment

The paper is based on work supported by National Science Foundation under grant CMS-9820745 and a gift from Western Digital Corporation.

References

[1] Shen, I. Y., and Ku, C.-P. Roger, 1997, ''A Non-Classical Vibration Analysis of Multiple Rotating Disks/Spindle Assembly,'' ASME J. Appl. Mech., **64**, pp. 165–174.

[2] Shen, I. Y., 1997, ''Closed-Form Forced Response of a Damped, Rotating, Multiple Disk/Spindle System,'' ASME J. Appl. Mech., **64**, pp. 343–352.

Analytically Approximate Solutions for Vibrations of a Long Discrete Chain

W. Lee
Department of Physics, Chung Yuan Christian University, Chung-Li, Taiwan 32023, ROC
e-mail: wlee@phys.cycu.edu.tw

This brief note studies small transverse vibrations of a long hanging chain of discrete links. Analytical approximate solutions are obtained when the number of links is considered large while they still possess nontrivial rotary inertia. The results imply that the rotary inertia becomes more significant for higher modes of vibration. [DOI: 10.1115/1.1526120]

1 Introduction

Previous attempts have been made to investigate the problem of small transverse vibrations of a uniform chain hanging vertically from one end. Treating such a chain as a continuous system, Bernoulli first found that the natural frequencies of the chain are related to the zeros of a power series (Watson [1]) that was later known as the Bessel function of order zero (Routh [2] and Spiegel [3]). Historically, earlier literature adopted the terms ''chain,'' ''string,'' and ''cable'' synonymously, inferring a continuous slender flexible material without any bending resistance (Wang [4]).

Small-amplitude transverse vibrations of a hanging chain with *finite* number of discrete links have been analyzed (Timoshenko, Young, and Weaver [5], McCreech, Goodfellow, and Seville [6] and Levinson [7]). Generally speaking, for a fixed chain length, a chain of fewer links possesses a slightly shorter oscillatory period. While the effect of the number of links is essential, numerical comparisons of natural frequencies indicate that the continuum model, especially for the lower modes, yields very accurate results for a given chain of a large number of one-dimensional links (McCreech, Goodfellow, and Seville [6] and Levinson [7]). Sujith and Hodges [8] discussed exact solutions for the free vibration of a hanging cord with a tip mass. Triantafyllou and Howell [9] studied the ill-posed problem of a perfectly flexible cable when the tension becomes negative. They found that the ill-posed problem can be resolved through the inclusion of additional dynamics, based on physical or theoretical grounds. The relationship between a discrete chain and a continuous cable of equal length has been revealed by Weng and Lee [10], who carried out a straightforward derivation of the differential equation of motion of a hanging cable as a special case of a hanging chain of one-dimensional links. It is shown that the natural frequencies of a hanging cable can be obtained from the resulting differential equation that is deduced from the coupled differential equations describing the motion of a hanging chain of infinitesimal links. The present note studies theoretically another extreme case of small transverse vibrations of a hanging chain of discrete links, where the number of links is considered to be large while they still possess nontrivial rotary inertia. The motivation of including the effect of link inertia is clear if one considers the ill-posed problem of a string with zero tension at an end (Triantafyllou and Howell [9]). Instead of making simplifying assumptions initially to treat the system a hanging massive string with rotary inertia and directly generate a differential equation, this brief note intends to

Contributed by the Applied Mechanics Division of THE AMERICAN SOCIETY OF MECHANICAL ENGINEERS for publication in the ASME JOURNAL OF APPLIED MECHANICS. Manuscript received by the ASME Applied Mechanics Division, June 19, 2001; final revision, July 26, 2002. Associate Editor: A. A. Ferri.

present explicit derivation steps, beginning from the coupled equations of motion that govern the behaviors of all links in a chain system, to reveal the relationships between a hanging string with rotary inertia and a hanging chain of two-dimensional links.

2 Analysis

Consider a chain of length L supported at one end in a uniform gravitational field and oscillating about stable equilibrium in a vertical plane. The chain is assumed to have N identical, rectangular links, each of length h, mass m, and moment of inertia I, connected by light pins at their ends as shown in Fig. 1. If the links, lying on the x-axis in equilibrium, are numbered $1,2,\ldots,N$ beginning at the free end of the chain, then, for the general nonequilibrium case, the equation of motion for the jth link may be expressed as

$$-2m\sum_{i=1}^{j}\ddot{Y}_i=(2I/h)\ddot{\theta}_j+(2j-1)mg\theta_j-m\ddot{Y}_j,\quad j=1,2,\ldots,N, \tag{1}$$

where θ_j and Y_j represent the angular displacement and transverse displacement of the center of mass of the jth link, respectively. Because each rectangular link is considered to be a rigid body, one is entitled to write

$$\theta_j=(y_{j-1}-y_j)/h \tag{2}$$

and

$$Y_j=(y_{j-1}+y_j)/2, \tag{3}$$

where y_j denotes the transverse displacement of the top pivot of the jth link. (Note that y_0 denotes the transverse displacement of the free end and that $y_N=0$ at the point of suspension, $x=L=Nh$.) Substitution of these expressions into Eq. (1) leads to the following equations of motion:

$$(m/2)(\ddot{y}_0+\ddot{y}_1)+(2I/h^2)(\ddot{y}_0-\ddot{y}_1)+(mg/h)(y_0-y_1)=0, \tag{4}$$

and

$$-m\left(\ddot{y}_0+2\sum_{i=1}^{j-1}\ddot{y}_i+\ddot{y}_j\right)=(2I/h^2)(\ddot{y}_{j-1}-\ddot{y}_j)+[(2j-1)mg/h]\times(y_{j-1}-y_j)-(m/2)(\ddot{y}_{j-1}+\ddot{y}_j),\quad j=2,3,\ldots,N. \tag{5}$$

As N becomes very large or h approaches zero, the term on the left side of Eq. (5), based upon the trapezoidal rule of integration, may be approximated as

$$-m\left(\ddot{y}_0+2\sum_{i=1}^{j-1}\ddot{y}_i+\ddot{y}_j\right)\approx-2\lambda\int_{x_0}^{x_j}\ddot{y}dx=-2\lambda\int_0^x\ddot{y}dx, \tag{6}$$

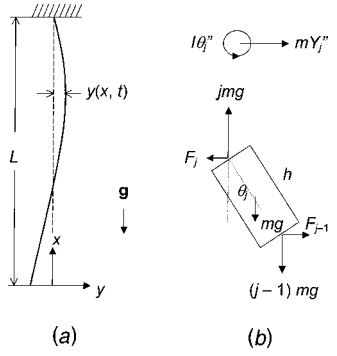

Fig. 1 A hanging chain of discrete links. (a) The coordinate system and (b) the free body diagram of the *j*th link. Counterclockwise displacement angles are taken positive.

where the linear mass density along the x-direction is given by $\lambda\equiv m/h$ and x_j is the longitudinal position coordinate of the top pivot of the jth link and can be written as x. The first term on the right side of Eq. (5) can be written as

$$(2I/h^2)(\ddot{y}_{j-1}-\ddot{y}_j)=(2I/h)\frac{d^2}{dt^2}[(y_{j-1}-y_j)/h]\approx-(2I/h)\frac{\partial^2}{\partial t^2}\left(\frac{\partial y}{\partial x}\right). \tag{7}$$

Similarly, introducing the tension due to the gravitational force at x given by $T=\lambda gx$ and replacing $(2j-1)h$ with $2x$ allow the second term on the right side of Eq. (5) to be expressed as

$$\frac{(2j-1)mg}{h}(y_{j-1}-y_j)\approx-2T\left(\frac{\partial y}{\partial x}\right). \tag{8}$$

Finally, the last term of Eq. (5) becomes

$$-(m/2)(\ddot{y}_{j-1}+\ddot{y}_j)\approx-\lambda h\ddot{y}, \tag{9}$$

which can be ignored when h is considered to be infinitesimal.

The equation of motion of a hanging chain with a large number of links can now be approximated as

$$\lambda\int_0^x\ddot{y}dx-\frac{I}{h}\frac{\partial^2}{\partial t^2}\left(\frac{\partial y}{\partial x}\right)-T\left(\frac{\partial y}{\partial x}\right)=0, \tag{10}$$

or

$$\lambda\frac{\partial^2 y}{\partial t^2}-\lambda k^2\frac{\partial^2}{\partial t^2}\left(\frac{\partial^2 y}{\partial x^2}\right)-\frac{\partial}{\partial x}\left(T\frac{\partial y}{\partial x}\right)=0. \tag{11}$$

Note that if the radius of gyration of a link, k ($I\equiv mk^2$), is taken to be zero, Eq. (11) would reduce to the well-known equation of motion governing the small transverse vibration of a hanging cable whose natural frequencies ω_n occurs when $2\omega_n(L/g)^{1/2}=\xi_n$, the nth zero of the Bessel function of the first kind, J_0 (Weng and Lee [10]). It is also worth mentioning that one could have produced Eq. (11) if the simplifying assumptions had been made at the beginning and the system had been seen as a hanging massive string with rotary inertia. As mentioned earlier, this discrete-to-continuum approach allows one to see the connection between a hanging string with rotary inertia and a hanging chain of two-dimensional links.

It is known that, near a position of stable equilibrium, a system executes harmonic oscillations. To solve Eq. (11), one is, therefore, justified to assume that the normal modes can be found by a solution with harmonic time dependence characterized by an exponential function with an angular frequency ω. Let $f(x)$ denote the spatial part of $y(x,t)$; i.e., the mode-shape function or deflection amplitude of the chain of interest and f' the first derivative of the function $f(x)$. The corresponding equation becomes

$$(gx-\omega^2k^2)f''+gf'+\omega^2f=0. \tag{12}$$

The identity manipulation of change of variables, $x=(g/4\omega^2)z^2+(\omega^2k^2/g)$, permits the above homogeneous differential equation to be obtained in the form of Bessel's differential equation of order zero,

$$z^2f''+zf'+z^2f=0, \tag{13}$$

where f is now considered a function of the variable z given by $z^2=(4\omega^2/g)(x-\omega^2k^2/g)$ and f' denotes df/dz.

The solution of Eq. (13) subjected to the requirement of finite displacements is obtained as Bessel function of the first kind of order zero, $J_0(z)$. Since $J_0(z)$ is an even function, whose maximum occurs at $z=0$ for all *real* z, the local maximum amplitude of the chain in the section of $\omega^2k^2/g\leqslant x\leqslant L$ takes place at $x=\omega^2k^2/g$. The maximum deflection amplitude of the whole

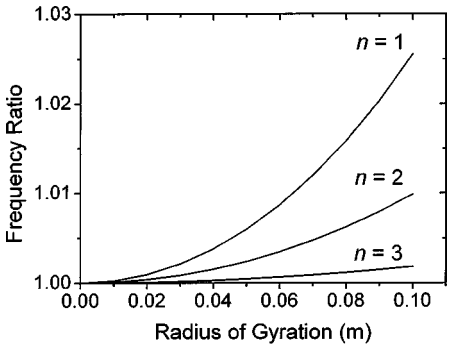

Fig. 2 A plot of frequency ratio; i.e., the natural frequency of a chain with rotational inertia divided by that of a hanging cable, versus the radius of gyration, k, for the first three modes of vibration. $L=2$ m and $g=9.8$ ms^{-2}.

chain occurs actually at the free end ($x=0$) as expected for a general continuum system. Also, since z becomes imaginary under a certain lower portion of the chain ($x<\omega^2k^2/g$), the mode shapes on the frequency-dependent regions are to be expressed as the modified Bessel function of the first kind, $I_0(z)$, with a transition to the Bessel function $J_0(z)$ above these regions. It is reminded here that the monotonically increasing function $I_0(z)$ equals to $J_0(iz)$ and $I_0(0)=J_0(0)=1$. The boundary condition at $x=L$ implies that $(4\omega^2/g)(L-\omega^2k^2/g)=\xi_n^2$, where $\xi_n=2.4048,5.5201,8.6537,\ldots$, and again, is the nth root of $J_0(z)=0$. The vibration, therefore, exists for all natural frequencies ω_n that satisfy

$$\omega_n^2=(Lg/2k^2)\{1-[1-(k/L)^2\xi_n^2]^{1/2}\}, \tag{14}$$

where the first minus sign is chosen for the solutions of the quadratic equation of ω_n^2 to reflect the physical reality concerning the proper behavior of natural frequencies of an oscillatory system. Certainly, ω_n^2 must be real to ensure a free oscillation, indicating that the number of modes is limited and that the relationship $\xi_n^2\leqslant(L/k)^2$ sets a constraint on the allowed characteristic frequencies for vibrations without dynamical absorption. Figure 2 displays a comparison of natural frequencies versus the radius of gyration of a 2-m long chain. The ordinate denotes the ratio of the angular frequency obtained from Eq. (14) and that of a hanging cable, $(g/4L)\xi_n^2$. It is clear from the figure that the deviation between these two types of frequencies becomes less pronounced for higher modes of vibration. If $k\ll L$, the binomial expansion of the square root in Eq. (14) yields an approximation for ω_n^2:

$$\omega_n^2\approx(g/4L)\xi_n^2[1+(1/4)(k/L)^2\xi_n^2], \tag{15}$$

where the third and higher powers of $(k/L)^2\xi_n^2$ in the original expansion have been neglected. Note that this expression reduces consistently to the result for a hanging cable by setting $k=0$. It is rational to expect that $k/L\ll1$ for a reasonable chain. The above equation implies that the rotary inertia will only become important for higher modes for such a long chain with many links.

It is obvious that, not only is the frequency of an oscillatory chain strongly affected by the chain length, it is also a function of the number of links and the moment of inertia of each link. It is interesting to investigate whether Eq. (15) is applicable or not for any reasonably realistic case. For a chain made of a large number of identical, two-dimensional links, it seems reasonable to obtain an approximate model by considering a link rigid while letting its length infinitesimal. On the other hand, it seems necessary to give a further explanation for the natural frequencies to increase with increasing rotary inertia as given in Eq. (15). It is also essential to examine whether Eq. (15) would provide a better approximation for a real chain than the typical hanging cable approximation does. Studies along these lines are underway.

References

[1] Watson, G. N., 1966, *Treatise on the Theory of Bessel Functions*, Cambridge University Press, Cambridge, UK, pp. 3–5.
[2] Routh, E. J., 1955, *The Advanced Part of a Treatise on the Dynamics of a System of Rigid Bodies*, 6th ed., Dover, New York, pp. 403–405.
[3] Spiegel, M. R., 1981, *Applied Differential Equations*, 3rd ed., Prentice-Hall, Englewood Cliffs, NJ, pp. 641–645.
[4] Wang, C. Y., 1994, "Stability and Large Displacements of a Heavy Rotating Linked Chain With an End Mass," Acta Mech., **107**, pp. 205–214.
[5] Timoshenko, S., Young, D. H., and Weaver, W., 1974, *Vibration Problems in Engineering*, 4th ed., John Wiley and Sons, New York, pp. 244–246.
[6] McCreech, J. P., Goodfellow, T. L., and Seville, A. H., 1975, "Vibrations of a Hanging Chain of Discrete Links," Am. J. Phys., **43**, pp. 646–648.
[7] Levinson, D. A., 1977, "Natural Frequencies of a Hanging Chain," Am. J. Phys., **45**, pp. 680–681.
[8] Sujith, R. I., and Hodges, D. H., 1995, "Exact Solution for the Free Vibration of a Hanging Cord With a Tip Mass," J. Sound Vib., **179**, pp. 359–361.
[9] Triantafyllou, M. S., and Howell, C. T., 1994, "Dynamic Responses of Cables Under Negative Tension: An Ill-Posed Problem," J. Sound Vib., **173**, pp. 433–447.
[10] Weng, P.-C., and Lee, W., 1994, "Transverse Vibrations of a Hanging Cable: The Limiting Case of a Hanging Chain," J. Sound Vib., **171**, pp. 574–576.

On Stress-Focusing Effect in a Uniformly Heated Solid Sphere

H. J. Ding[1]
Department of Civil Engineering, Zhejiang University, Hangzhou 310027, P. R. China
e-mail: wanghuiming@cmee.zju.edu.cn

H. M. Wang
Department of Mechanics, Zhejiang University, Hangzhou 310027, P. R. China

W. Q. Chen
Department of Civil Engineering, Zhejiang University, Hangzhou 310027, P. R. China

By using the separation of variables technique, the dynamic thermal stress responses in an isotropic solid sphere subjected to uniform temperature rise all over the sphere and a sudden constant pressure at the external surface are performed successfully. The analytical solutions of the radial and hoop dynamic stresses at the center are also obtained. By means of the present method, integral transform can be avoided. Numerical results denote that a very high dynamic stress peak appears periodically at the center of the isotropic solid sphere subjected to uniform temperature rise all over the sphere and a sudden constant pressure at the external surface. [DOI: 10.1115/1.1544514]

[1]To whom correspondence should be addressed.

Contributed by the Applied Mechanics Division of THE AMERICAN SOCIETY OF MECHANICAL ENGINEERS for publication in the ASME JOURNAL OF APPLIED MECHANICS. Manuscript received by the ASME Applied Mechanics Division, Oct. 10, 2001, final revision, July 26, 2002. Associate Editor: J. R. Barber.

1 Introduction

Recently, the thermally excited mechanical response of structures is of increasing interest in engineering science and many works have been done for the dynamic thermoelastic problems. Sternberg and Chakravorty [1] obtained an exact closed-form solution for the dynamic problem of a sudden temperature change at the surface of a spherical cavity in an infinite solid. Tusi and Kraus [2] discussed the thermal stress-wave propagation in an arbitrary thick-walled spherical shell due to thermal shock on the internal surface. Zaker [3] investigated the dynamic thermal stress responses in a spherical shell, which is subjected to arbitrary spherically symmetric temperature fields. The technique is based on the integral theorem of hyperbolic initial value problem, together with the construction of image temperature fields in the regions outside the actual body. Hata [4–6] obtained the dynamic thermal stress responses in a uniformly heated isotropic spherical shell and solid sphere, as well as transversely isotropic solid sphere by the ray theory. Recently, Hata [7] studied the stress-focusing effect due to an instantaneous concentrated heat source in a sphere, and Wang [8] discussed the thermal stress concentration in a spherically isotropic solid sphere.

The dynamic thermoelastic problems are usually solved by the Laplace transform technique ([1,2,4–8]). But the method will encounter the difficulty of inverse transform in some special cases. The ray theory is a good tool to complete the Laplace inversion. However, it needs a large number of rays for a very thin spherical shell and hence becomes impractical ([9]). In this paper, the separation of variables technique is applied to solve the elastodynamic problems of the solid sphere subjected to arbitrary spherically thermal and mechanical loads and thus the integral transform is avoided. Indeed, the method allows avoiding difficulties and inaccuracy of the ray theory. First, a new dependent variable is introduced to rewrite the governing equation, the boundary conditions as well as the initial conditions. Second, the thermal and mechanical loads are treated as the inhomogeneous item in the boundary conditions and a special function is introduced to transform the inhomogeneous boundary conditions to the homogeneous ones. Third, by using the orthogonal expansion technique, the equation with respect to the time variable is derived, of which the solution is easily obtained. Therefore the displacement solution for the dynamic thermoelastic problem of the solid sphere is finally obtained.

Numerical results of a uniformly heated solid sphere, which has also been studied by Hata [5], are presented by means of the present method. From the numerical results, we find that the stress responses at the center of the sphere have serious errors in Figs. 2 and 3 in Hata [5]: (a) the time histories of σ_r^* and σ_θ^* at the center ($\xi=0.0$) are different; and (*b*) the peak values of the dynamic stresses near the center appear periodically while those at the center vary smoothly with the time. The former is apparently unreasonable. The latter is also difficult to explain physically. In fact, if there are periodical peak values for the dynamic stress responses of σ_r^* and σ_θ^* at $\xi=0.01$, then what will be at $\xi=0.001$, $0.0001\ldots$? The reason related to the numerical process was mentioned by Hata [5], which implies the results would be greatly affected by the error involved in the inverse Laplace transform. By the present method, however, the integral transform is avoided and the correct results can be obtained.

2 Mathematical Formulations of the Problem

If a spherical coordinate system (r,θ,φ) with the origin identical to the center of the sphere is used, then for the spherically symmetric problem, we have $u_\theta=u_\varphi=0$, $u_r=u_r(r,t)$. So the strain-displacement relations are

$$\gamma_{rr}=\frac{\partial u_r}{\partial r},\quad \gamma_{\theta\theta}=\gamma_{\varphi\varphi}=\frac{u_r}{r},\quad \gamma_{r\theta}=\gamma_{\theta\varphi}=\gamma_{\varphi r}=0, \tag{1}$$

where γ_{ij} are the strain components. For the spherically symmetric thermoelastic problem of an isotropic solid sphere, the constitutive equations are

$$\begin{aligned}\sigma_{rr}&=(\lambda+2\mu)\gamma_{rr}+2\lambda\gamma_{\theta\theta}-(3\lambda+2\mu)\alpha T(r,t),\\ \sigma_{\theta\theta}&=\sigma_{\varphi\varphi}=\lambda\gamma_{rr}+2(\lambda+\mu)\gamma_{\theta\theta}-(3\lambda+2\mu)\alpha T(r,t),\end{aligned} \tag{2}$$

where σ_{ij} and $T(r,t)$ are the stress components and temperature increment, respectively. λ and μ are the Lamé constants and α is the coefficient of linear thermal expansion. The equation of motion is

$$\frac{\partial\sigma_{rr}}{\partial r}+2\frac{\sigma_{rr}-\sigma_{\theta\theta}}{r}=\rho\frac{\partial^2 u_r}{\partial t^2}, \tag{3}$$

where ρ is the mass density. Substituting Eq. (1) into Eq. (2), we obtain

$$\begin{aligned}\sigma_{rr}&=(\lambda+2\mu)\frac{\partial u_r}{\partial r}+2\lambda\frac{u_r}{r}-(3\lambda+2\mu)\alpha T(r,t),\\ \sigma_{\theta\theta}&=\sigma_{\varphi\varphi}=\lambda\frac{\partial u_r}{\partial r}+2(\lambda+\mu)\frac{u_r}{r}-(3\lambda+2\mu)\alpha T(r,t).\end{aligned} \tag{4}$$

Substituting Eq. (4) into Eq. (3), gives the following governing equation:

$$\frac{\partial^2 u_r}{\partial r^2}+\frac{2}{r}\frac{\partial u_r}{\partial r}-2\frac{u_r}{r^2}=\frac{1}{c_L^2}\frac{\partial^2 u_r}{\partial t^2}+\alpha\frac{(1+\nu)}{(1-\nu)}\frac{\partial T(r,t)}{\partial r}, \tag{5}$$

where ν is the Poisson's ratio and

$$c_L=\sqrt{(\lambda+2\mu)/\rho}. \tag{6}$$

The boundary conditions are

$$\begin{aligned}&r=0,\quad u_r(0,t)=0,\\ &r=b,\quad (\lambda+2\mu)\frac{\partial u_r}{\partial r}+2\lambda\frac{u_r}{r}-(3\lambda+2\mu)T(b,t)=p(t),\end{aligned} \tag{7}$$

where b is the radius of the sphere and $p(t)$ is the prescribed pressure on the external surface. The initial conditions ($t=0$) are

$$u_r(r,0)=u_0(r),\quad \dot{u}_r(r,0)=v_0(r), \tag{8}$$

where a dot over the quantity denotes its partial derivative with respect to t, and $u_0(r)$ and $v_0(r)$ are known functions.

3 The Solving Technique

First, a new dependent variable $w(r,t)$ is introduced as

$$u_r=r^{-1/2}w(r,t). \tag{9}$$

Then Eqs. (5), (7), and (8) become

$$\frac{\partial^2 w}{\partial r^2}+\frac{1}{r}\frac{\partial w}{\partial r}-\frac{9}{4}\frac{w}{r^2}=\frac{1}{c_L^2}\frac{\partial^2 w}{\partial t^2}+g(r,t), \tag{10}$$

$$r=0,\quad r^{-1/2}w(0,t)=0, \tag{11a}$$

$$r=b,\quad \frac{\partial w}{\partial r}+h\frac{w}{r}=p_b(t), \tag{11b}$$

$$w(r,0)=u_1(r),\quad \dot{w}(r,0)=v_1(r), \tag{12}$$

where

$$\begin{aligned}&g(r,t)=\beta\sqrt{r}\frac{\partial T(r,t)}{\partial r},\quad h=\frac{2\lambda}{\lambda+2\mu}-\frac{1}{2},\\ &p_b(t)=\frac{\sqrt{b}[\beta T(b,t)+p(t)]}{\lambda+2\mu},\quad \beta=\alpha\frac{(1+\nu)}{(1-\nu)},\\ &u_1(r)=\sqrt{r}u_0(r),\quad v_1(r)=\sqrt{r}v_0(r).\end{aligned} \tag{13}$$

Second, we transform the inhomogeneous boundary conditions into the homogeneous ones by assuming

$$w(r,t)=w_1(r,t)+w_2(r,t), \tag{14}$$

where $w_2(r,t)$ satisfies the inhomogeneous boundary conditions, and it can be taken as

$$w_2(r,t)=Ar^m p_b(t), \tag{15}$$

where $m=2$, and

$$A=\frac{1}{b(h+2)}. \tag{16}$$

Substituting Eq. (14) into Eqs. (10)–(12) gives

$$\frac{\partial^2 w_1}{\partial r^2}+\frac{1}{r}\frac{\partial w_1}{\partial r}-\frac{9}{4}\frac{w_1}{r^2}=\frac{1}{c_L^2}\frac{\partial^2 w_1}{\partial t^2}+g_1(r,t), \tag{17}$$

$$r=0, \quad r^{-1/2}w_1(0,t)=0, \tag{18a}$$

$$r=b, \quad \frac{\partial w_1}{\partial r}+h\frac{w_1}{r}=0, \tag{18b}$$

$$w_1(r,0)=u_2(r); \quad \dot{w}_1(r,0)=v_2(r), \tag{19}$$

where

$$g_1(r,t)=g(r,t)+\frac{1}{c_L^2}\frac{\partial w_2(r,t)}{\partial t^2}+\frac{9}{4}\frac{w_2(r,t)}{r^2}-\frac{1}{r}\frac{\partial w_2(r,t)}{\partial r}-\frac{\partial^2 w_2(r,t)}{\partial r^2},$$
$$u_2(r)=u_1(r)-w_2(r,0), \quad v_2(r)=v_1(r)-\dot{w}_2(r,0). \tag{20}$$

By using the separation of variables technique, the solution of Eq. (17) can be assumed in the following form:

$$w_1(r,t)=\sum_i J_{3/2}(k_i r)F_i(t), \tag{21}$$

where $F_i(t)$ are unknown functions of t, and $J_{3/2}(\ )$ is the Bessel function of the first kind. k_i, arranged in an ascending order, are a sequence of positive roots of the following eigenequation:

$$(h+3/2)J_{1/2}(k_i b)+(h-3/2)J_{5/2}(k_i b)=0. \tag{22}$$

We notice that

$$\lim_{r\to 0} r^{-1/2}J_{3/2}(k_i r)=0. \tag{23}$$

By virtue of Eqs. (22) and (23), we know that $w_1(r,t)$, as given in Eq. (21), satisfies the homogeneous boundary conditions in Eq. (18).

Substituting Eq. (21) into Eq. (17), gives

$$-c_L^2\sum_i k_i^2 F_i(t)J_{3/2}(k_i r)=\sum_i J_{3/2}(k_i r)\frac{d^2F_i(t)}{dt^2}+c_L^2 g_1(r,t). \tag{24}$$

By virtue of the orthogonal property of Bessel functions

$$\int_0^b rJ_{3/2}(k_i r)J_{3/2}(k_j r)dr=N_i\delta_{ij}, \tag{25}$$

where δ_{ij} is the Kronecker delta, and

$$N_i=\frac{1}{2k_i^2}\left\{b^2\left[\frac{dJ_{3/2}(k_i b)}{dr}\right]^2+\left(k_i^2 b^2-\frac{9}{4}\right)[J_{3/2}(k_i b)]^2\right\}, \tag{26}$$

where $dJ_{3/2}(k_i b)/dr=dJ_{3/2}(k_i r)/dr|_{r=b}$, we can derive the following equation from Eq. (24)

$$\frac{d^2F_i(t)}{dt^2}+\omega_i^2 F_i(t)=q_i(t), \tag{27}$$

where

$$\omega_i=k_i c_L, \quad q_i(t)=-\frac{c_L^2}{N_i}\int_0^b rg_1(r,t)J_{3/2}(k_i r)dr. \tag{28}$$

The solution of Eq. (27) is

$$F_i(t)=G_{1i}\cos\omega_i t+G_{2i}\sin\omega_i t+\frac{1}{\omega_i}\int_0^t q_i(\tau)\sin\omega_i(t-\tau)d\tau, \tag{29}$$

where

$$G_{1i}=\frac{1}{N_i}\int_0^b ru_2(r)J_{3/2}(k_i r)dr,$$
$$G_{2i}=\frac{1}{N_i\omega_i}\int_0^b rv_2(r)J_{3/2}(k_i r)dr. \tag{30}$$

Finally, the radial displacement solution can be obtained as follows:

$$u_r(r,t)=r^{-1/2}[w_1(r,t)+w_2(r,t)]. \tag{31}$$

4 Numerical Results and Discussions

Example 1. The dynamic thermoelastic responses in a uniformly heated solid sphere is considered in this example. The loads are

$$T(r,t)=T_0H(t), \quad p(t)=0.0, \tag{32}$$

where $H(t)$ denotes the Heaviside step function and T_0 is a prescribed temperature change. The Poisson's ratio of the material is taken as

$$\nu=0.3. \tag{33}$$

The following nondimensional quantities will be used:

$$t^*=\frac{c_L}{b}t, \quad \xi=\frac{r}{b}, \quad \sigma_i^*=\frac{\sigma_{ii}}{\sigma_0}, \quad (i=r,\theta,\varphi), \tag{34}$$

where

$$\sigma_0=\frac{\alpha E T_0}{1-2\nu}. \tag{35}$$

In the calculation that follows, we take $u_0(r)=0$, $v_0(r)=0$ and the first 40 terms in the series in Eq. (21).

The dynamic thermal stress responses are shown in Figs. 1–4. Comparing Fig. 1 with Fig. 3, we find that, at the center ($\xi=0.0$), the time history of σ_r^* is the same as that of σ_θ^*, and the peaks of the dynamic stresses appear periodically at an interval of $t^*=2$. The first peak values of the dynamic stresses σ_r^* and σ_θ^* at different locations are listed in Table 1. In the table, the peak values become higher and higher as the position approaches to the center, and the maximum peak values of σ_r^* and σ_θ^* both appear at $\xi=0.0$. The stress responses of σ_r^* and σ_θ^* at $\xi=0.01$, 0.1, and 0.5 are also depicted in Figs. 2 and 4. They are almost the same as those obtained by Hata [5], except that the peak values are slightly different.

According to the method presented in the paper, for the uniformly heated sphere, Eq. (15) reads as

$$w_2(r,t)=E_1 r^2, \quad E_1=\frac{\beta T_0}{\sqrt{b}(h+2)(\lambda+2\mu)}. \tag{36}$$

Also Eq. (20) becomes

$$g_1(r,t)=-\frac{7}{4}E_1, \quad u_2(r)=-E_1 r^2, \quad v_2(r)=0. \tag{37}$$

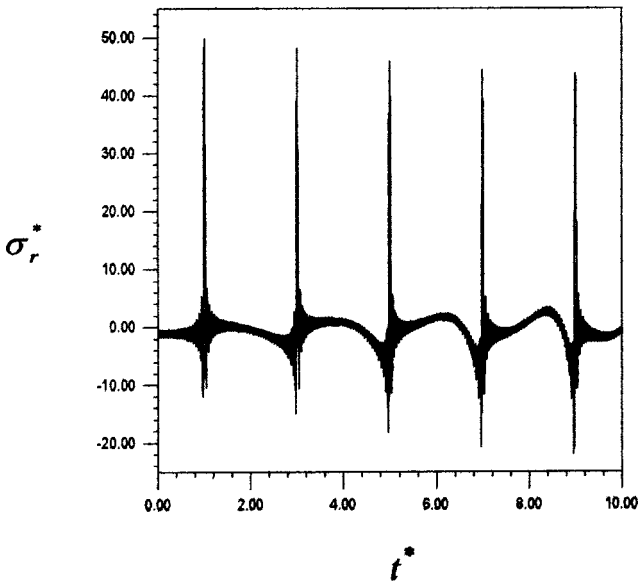

Fig. 1 History of dynamic stress σ_r^* at the center (ξ=0)

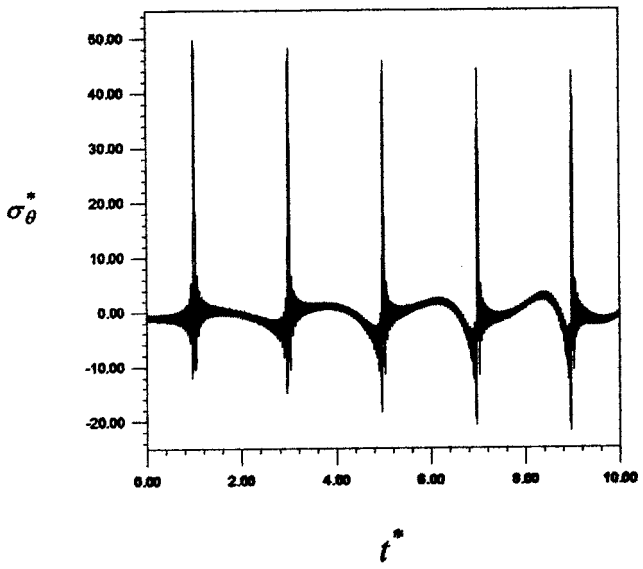

Fig. 3 History of dynamic stress σ_θ^* at the center (ξ=0)

Then $q_i(t)$ in Eq. (28) and $G_{ji}\,(j=1,2)$ in Eq. (30) have the following forms:

$$q_i(t)=E_{2i}=\frac{7c_L^2}{4N_i}E_1\int_0^b rJ_{3/2}(k_ir)dr. \tag{38}$$

$$G_{1i}=-\frac{E_1}{N_i}\int_0^b r^3J_{3/2}(k_ir)dr,\quad G_{2i}=0.0. \tag{39}$$

We then get from Eq. (29)

$$F_i(t)=\frac{E_{2i}}{\omega_i^2}+\left(G_{1i}-\frac{E_{2i}}{\omega_i^2}\right)\cos\omega_i t. \tag{40}$$

And Eq. (31) becomes

$$u_r(r,t)=r^{-1/2}\left[\sum_i J_{3/2}(k_ir)F_i(t)+E_1r^2\right]. \tag{41}$$

Utilizing Eq. (1), the components of strain at the center are obtained as follows:

$$\begin{aligned}\gamma_{rr}(0,t)&=\left.\frac{\partial u_r(r,t)}{\partial r}\right|_{r=0}=\lim_{r\to0}\left\{\frac{3}{2}E_1r^{1/2}+\sum_i\left[r^{-1/2}\frac{dJ_{3/2}(k_ir)}{dr}\right.\right.\\&\left.\left.-\frac{1}{2}r^{-3/2}J_{3/2}(k_ir)\right]F_i(t)\right\}\\&=\sum_i\lim_{r\to0}[r^{-3/2}J_{3/2}(k_ir)-k_ir^{-1/2}J_{5/2}(k_ir)]F_i(t)\\&=\sum_i\lim_{r\to0}[r^{-3/2}J_{3/2}(k_ir)]F_i(t)\\&=\sum_i\frac{1}{3}\sqrt{\frac{2}{\pi}}k_i^{3/2}\left[\frac{E_{2i}}{\omega_i^2}+\left(G_{1i}-\frac{E_{2i}}{\omega_i^2}\right)\cos\omega_i t\right]\end{aligned} \tag{42}$$

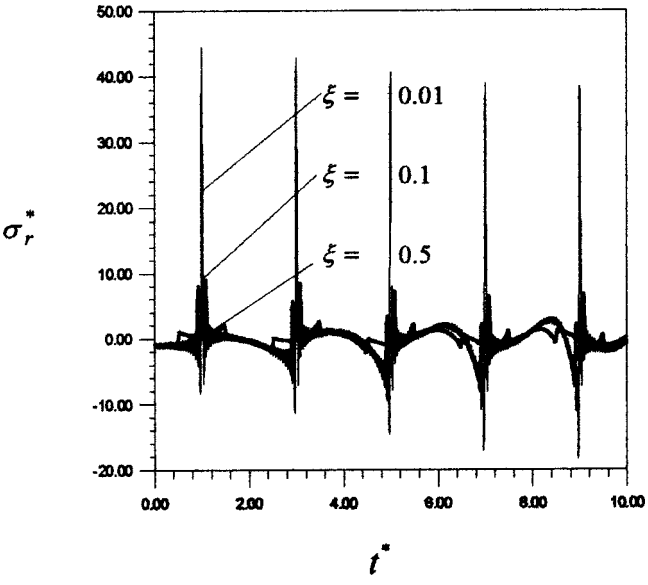

Fig. 2 History of dynamic stress σ_r^*

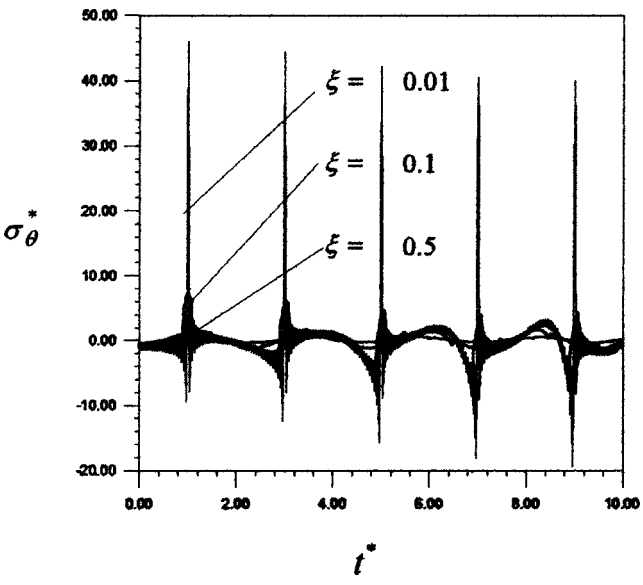

Fig. 4 History of dynamic stress σ_θ^*

Table 1 The first peak values at different positions

ξ	0.0	0.0001	0.001	0.005	0.01	0.05	0.10	0.25	0.50
σ_r^*	49.7641	49.7592	49.7251	48.4317	44.5091	14.9455	9.0218	4.2719	2.2240
σ_θ^*	49.7641	49.7582	49.7380	48.8329	46.0527	14.2610	7.1121	2.7451	1.3384

$$\gamma_{\theta\theta}(0,t)=\gamma_{\varphi\varphi}(0,t)=\left.\frac{u_r(r,t)}{r}\right|_{r=0}$$
$$=\lim_{r\to 0}\left\{E_1 r^{1/2}+\sum_i\ [r^{-3/2}J_{3/2}(k_i r)]F_i(t)\right\}$$
$$=\sum_i\ \lim_{r\to 0}[r^{-3/2}J_{3/2}(k_i r)]F_i(t)$$
$$=\sum_i\ \frac{1}{3}\sqrt{\frac{2}{\pi}}k_i^{3/2}\left[\frac{E_{2i}}{\omega_i^2}+\left(G_{1i}-\frac{E_{2i}}{\omega_i^2}\right)\cos\omega_i t\right].$$

From Eq. (42), we find that the components of strain at the center are the same with each other. Substituting Eq. (42) into Eq. (2), we obtain

$$\sigma_{rr}(0,t)=\sigma_{\theta\theta}(0,t)=\sigma_{\varphi\varphi}(0,t)=(3\lambda+2\mu)\left\{\sum_i\ \frac{1}{3}\sqrt{\frac{2}{\pi}}k_i^{3/2}\left[\frac{E_{2i}}{\omega_i^2}+\left(G_{1i}-\frac{E_{2i}}{\omega_i^2}\right)\cos\omega_i t\right]-\alpha T_0\right\}. \tag{43}$$

Obviously, the components of stresses at the center should also be identical to each other. This fact has been well illustrated by our numerical results as shown in Figs. 1 and 3.

Example 2. The elastodynamic responses in a solid sphere subjected to a sudden constant pressure at the external surface is considered in this example. The loads are

$$T(r,t)=0.0,\quad p(t)=-p_0H(t), \tag{44}$$

where p_0 is a constant pressure. The other parameters for calculation and the nondimensional quantities are the same as those in Example 1 except that $\sigma_i^*=\sigma_{ii}/p_0$, $(i=r,\theta,\varphi)$.

The dynamic responses of σ_r^* and σ_θ^* at the center are shown in Figs. 5 and 6. From the curves, we also find the stress-focusing effect. The analytical expressions for the radial and hoop stresses can also be obtained in this case.

$$\sigma_{rr}(0,t)=\sigma_{\theta\theta}(0,t)=\sigma_{\varphi\varphi}(0,t)=(3\lambda+2\mu)\left\{\sum_i\ \frac{1}{3}\sqrt{\frac{2}{\pi}}k_i^{3/2}\left[\frac{E_{4i}}{\omega_i^2}+\left(G_{3i}-\frac{E_{4i}}{\omega_i^2}\right)\cos\omega_i t\right]\right\}, \tag{45}$$

where

$$E_{4i}=\frac{7c_L^2}{4N_i}E_3\int_0^b rJ_{3/2}(k_i r)dr,$$

$$G_{3i}=-\frac{E_3}{N_i}\int_0^b r^3J_{3/2}(k_i r)dr,\quad E_3=\frac{p_0}{\sqrt{b}(h+2)(\lambda+2\mu)}. \tag{46}$$

It is noted here that the present method also can be applied to study the dynamic problems of spherical shells, for which only boundary conditions and the eigenequation should be modified. By virtue of such a method, the dynamic stress responses in a spherical shell subjected to an instantaneous constant internal radial pressure and the dynamic thermal stress responses in a uniformly heated hollow sphere can also been obtained. The results agree well with those presented in Refs. [9] and [4], respectively. Thus, the validation of the method developed in this paper is additionally supported.

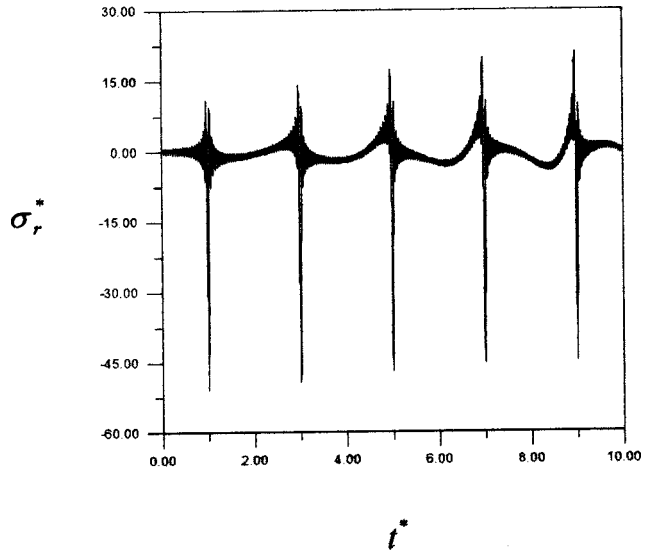

Fig. 5 History of dynamic stress σ_r^* at the center (ξ=0)

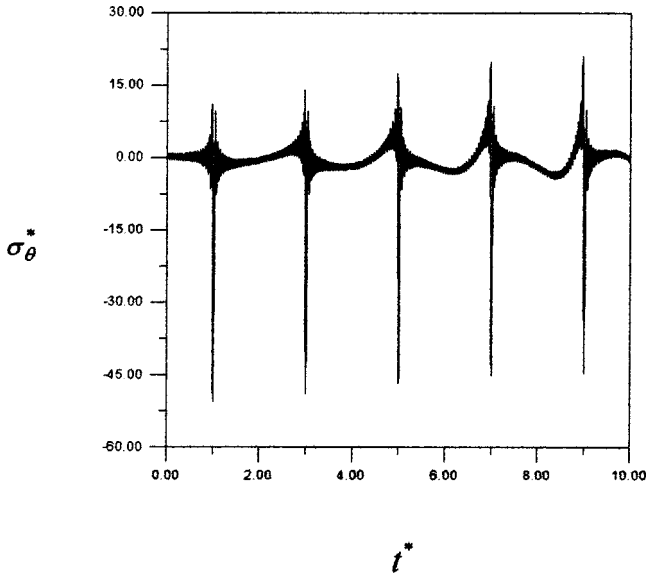

Fig. 6 History of dynamic stress σ_θ^* at the center (ξ=0)

Acknowledgments

The work was supported by the National Natural Science Foundation of China (No. 10172075 and No. 10002016).

References

[1] Sternberg, E., and Chakravorty, J. G., 1959, "Thermal Shock in an Elastic Body With a Spherical Cavity," Q. Appl. Math., **17**, pp. 205–218.
[2] Tusi, T., and Kraus, H., 1965, "Thermal Stress-Wave Propagation in Hollow Elastic Spheres," J. Acoust. Soc. Am., **37**, pp. 730–737.
[3] Zaker, T. A., 1968, "Dynamic Thermal Shock in Hollow Sphere," Q. Appl. Math., **26**, pp. 503–520.
[4] Hata, T., 1991, "Thermal Shock in a Hollow Sphere Caused by Rapid Uniform Heating," ASME J. Appl. Mech., **58**, pp. 64–69.
[5] Hata, T., 1991, "Stress-Focusing Effect in a Uniformly Heated Solid Sphere," ASME J. Appl. Mech., **58**, pp. 58–63.
[6] Hata, T., 1993, "Stress-Focusing Effect in a Uniformly Heated Transversely Isotropic Sphere," Int. J. Solids Struct., **30**, pp. 1419–1428.
[7] Hata, T., 1997, "Stress-Focusing Effect Due to an Instantaneous Concentrated Heat Source in a Sphere," J. Therm. Stresses, **20**, pp. 269–279.
[8] Wang, X., 2000, "Dynamic Thermostress-Concentration Effect in a Spherically Isotropic Sphere," Acta Mech. Sin., **32**, pp. 245–250 (in Chinese).
[9] Pao, Y. H., and Ceranoglu, A. N., 1978, "Determination of Transient Responses of a Thick-Walled Spherical Shell by the Ray Theory," ASME J. Appl. Mech., **45**, pp. 114–122.

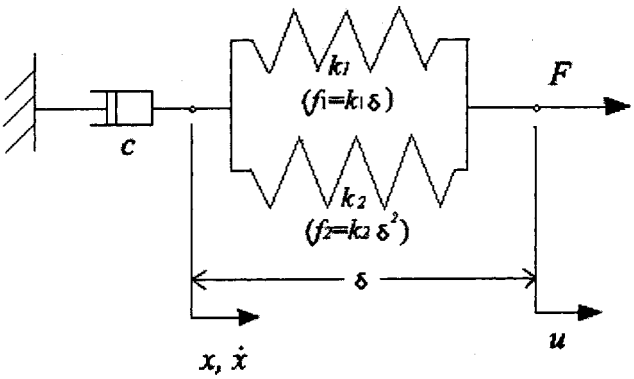

Fig. 1 The nonlinear model, consisting of a parallel arrangement of a linear spring (k_1) and a second-order spring (k_2), in series with a linear dashpot (c)

On the Nonlinear Generalized Maxwell Fluid Model

H. Hu
Department of Mathematics and Physics, Xiangtan Polytechnic University, Xiangtan 411201, Hunan, Peoples' Republic of China
e-mail: huihu2000@21cn.com

An equation describing a nonlinear generalized Maxwell fluid model is presented. Model behavior, for constant rate elongations, is investigated. A comparison of the results in this study with those in the literature has been given. The conclusion of Corr et al. that the model has two solutions is questionable.

[DOI: 10.1115/1.1544538]

Introduction

In a recent paper, [1], a nonlinear Maxwell fluid spring-and-dashpot model (Fig. 1) was developed to describe the complex nonlinear behavior of some viscoelastic materials. The closed-form solution of the model was determined for constant-rate displacement-control testing. In this study, we pursue a somewhat different avenue of research. First the differential equation of the load-displacement relationship is presented. Second, a closed-form solution is given for constant rate displacement. Finally, a comparison of the results in this study with those in Ref. [1] has been given. It is pointed out that the argument that "the closed-form solution of the model has two solutions, corresponding to the positive and negative roots of B" [1], is questionable.

Model Derivations

From Fig. 1 we have

$$\dot{u}=\dot{x}+\dot{\delta} \tag{1}$$

$$F=k_1\delta+k_2\delta^2 \tag{2}$$

$$\dot{x}=F/c \tag{3}$$

where δ and x are the displacement of the springs and dashpot from the rest position, respectively, $u=x+\delta$ is the total displacement, and the overdot denotes differentiation with respect to time t. Solving Eq. (2) for δ gives

$$\delta=\frac{\pm\sqrt{4k_2F+k_1^2}-k_1}{2k_2}. \tag{4}$$

Obviously, if $F=0$, we should have $\delta=0$. Therefore, we can only get

$$\delta=\frac{\sqrt{4k_2F+k_1^2}-k_1}{2k_2}. \tag{5}$$

Substituting Eqs. (3) and (5) into Eq. (1) gives

$$\dot{u}=\frac{\dot{F}}{\sqrt{4k_2F+k_1}}+F/c. \tag{6}$$

Integrating this equation across the point $t=0$, [2], we have

$$\sqrt{4k_2F_0+k_1^2}=2k_2u_0+k_1, \tag{7}$$

where $u_0=u(0^+)$ and $F_0=F(0^+)$.

The Characteristic When $u(t)=u_0h(t)+\alpha t$. We let

$$u(t)=u_0h(t)+\alpha t, \tag{8}$$

where α is a constant, and $h(t)$ is the Heaviside step function. In this case, Eq. (6) becomes

$$\frac{\dot{F}}{\sqrt{4k_2F+k_1^2}}+F/c=\alpha, \tag{9}$$

or

$$\frac{dF}{(F-\alpha c)\sqrt{4k_2F+k_1^2}}=-dt/c. \tag{10}$$

Integrating Eq. (10) yields

$$\frac{\sqrt{4k_2F+k_1^2}-k_1'}{\sqrt{4k_2F+k_1^2}+k_1'}=Ae^{-k_1't/c}, \tag{11}$$

where $k_1'=\sqrt{k_1^2+4k_2\alpha c}$ and A is an integration constant. Solving Eq. (11) for F gives

$$F(t)=\alpha c+\frac{Ak_1'^2e^{-k_1't/c}}{k_2(1-Ae^{-k_1't/c})^2}. \tag{12}$$

Writing Eq. (11) for $t=0^+$ and using Eq. (7), we have

Contributed by the Applied Mechanics Division of THE AMERICAN SOCIETY OF MECHANICAL ENGINEERS for publication in the ASME JOURNAL OF APPLIED MECHANICS. Manuscript received by the ASME Applied Mechanics Division, Feb. 5, 2002; final revision, Oct. 9, 2002. Associate Editor: D. A. Siginer.

$$A=\frac{2k_2u_0+k_1-k_1'}{2k_2u_0+k_1+k_1'}. \quad (13)$$

Discussion

Substituting Eq. (12) into Eq. (3), we obtain

$$\dot{x}=\alpha+\frac{Ak_1'^2e^{-k_1't/c}}{k_2c(1-Ae^{-k_1't/c})^2}. \quad (14)$$

Multiplying this equation by dt and integrating gives

$$x(t)-x(0)=\alpha t+\int_0^t\frac{Ak_1'^2e^{-k_1't/c}dt}{k_2c(1-Ae^{-k_1't/c})^2}. \quad (15)$$

Applying the initial condition $x(0)=0$, we find

$$x(t)=\alpha t+\frac{k_1'}{k_2}\left(\frac{1}{1-A}-\frac{1}{1-Ae^{-k_1't/c}}\right). \quad (16)$$

In order to compare our results with those of Corr et al. [1], we let $u_0=0$. Then, Eq. (13) becomes

$$A=\frac{k_1-k_1'}{k_1+k_1'}. \quad (17)$$

In this case, we can see that Eqs. (16) and (14) coincide with Eqs. (14) and (15) in Ref. [1], respectively, but we must take

$$B=(\mu-\sqrt{\mu^2+4\xi\alpha})/2\xi=(k_1-\sqrt{k_1^2+4_2\alpha c})/2k_2. \quad (18)$$

When

$$B=(\mu+\sqrt{\mu^2+4\xi\alpha})/2\xi=(k_1+\sqrt{k_1^2+4_2\alpha c})/2k_2, \quad (19)$$

we cannot obtain $x(t)=\dot{x}(t)=0$ even if $\alpha=0$. Our understanding of physics can simplify our mathematical calculations, and mathematical solution should make physical sense. The conclusion of Ref. [1] is questionable that ''the closed-form solution of the model has two solutions, corresponding to the positive and negative roots of *B*.''

References

[1] Corr, D. T., Starr, M. J., Vanderby, Jr., R., and Best, T. M., 2001, ''A Nonlinear Generalized Maxwell Fluid Model for Viscoelastic Materials,'' ASME J. Appl. Mech., **68**, pp. 787–790.

[2] Flügge, W., 1975, *Viscoelasticity*, 2nd Ed., Springer-Verlag, New York, pp. 6–11.